PRECISION ENGINEERING CENTER

2002 ANNUAL REPORT
VOLUME XX
January 2003

Sponsors:

3M Corporation
Biomachines
Eastman Kodak Company
IBM Corporation
Los Alamos National Laboratory
National Science Foundation
NASA Goddard Space Flight Center
Precitech, Inc.
Vistakon, Inc.

Faculty:

Thomas Dow, Editor
Greg Buckner
Jeffrey Eischen
Karl Falter
Dieter Griffis
Paul Ro
Phillip Russell
Ronald Scattergood
Albert Shih
David Youden

Graduate Students:

Stuart Clayton
Karl Freitag
David Gill
David Hood
David Kametz
Patrick Morrissey
Nobuhiko Negishi
Witoon Panusittikorn
Travis Randall
R. Sheldon Sigmon
Tao Wu

Undergraduate Students:

Elizabeth Chatham
Aaron Kiefer

Staff:

Kenneth Garrard
Alexander Sohn
Laura Underhill

TABLE OF CONTENTS

FABRICATION

SUMMARY

The goals of the Precision Engineering Center are: 1) to improve the understanding and capability of precision metrology, actuation, manufacturing and assembly processes; and 2) to train a new generation of engineers and scientists with the background and experience to transfer this new knowledge to industry. Because the problems related to precision engineering originate from a variety of sources, significant progress can only be achieved by applying a multidisciplinary approach; one in which the faculty, students, staff and sponsors work together to identify important research issues and find the optimum solutions. Such an environment has been created and nurtured at the PEC for over 20 years; the new technology that has been developed and the 85 graduates attest to the quality of the results.

The 2002 Annual Report summarizes the progress over the past year by the faculty, students and staff in the Precision Engineering Center. During the past year, this group included 10 faculty, 11 graduate students, 2 undergraduate students, 2 full-time technical staff members and 1 administrative staff member. Representing two different Departments from the College of Engineering, this diverse group of scientists and engineers provides a wealth of experience to address precision engineering problems. The format of this Annual Report separates the research effort into individual projects, however, this should not obscure the significant interaction that occurs among the faculty, staff and students. Weekly seminars by the students and faculty provide information exchange and feedback as well as practice in technical presentations. Teamwork and group interactions are a hallmark of research at the PEC and this contributes to both the quality of the research as well as the education of the graduates.

The summaries of individual projects that follow are arranged in the same order as the body of the report, that is the four broad categories of 1) metrology, 2) actuation, 3) control and 4) fabrication.

1) METROLOGY

The emphasis of the metrology projects has been to develop new techniques that can be used to predict surface shape as well as measure important parameters such as tool force.

Design and Fabrication of High-Current Density Electrical Connections

Pulse power experiments being conducted at Los Alamos National Labs require the design and assembly of joints that carry large electrical currents. The shape and interference of these joints are critical to the success of the experiments. This project involves the development of FEM analysis to visualize and quantify the stresses at the interface. The primary issues considered are: mechanics of the interference fits, definition of the contact between the components, locations joint voids and material property effects. A measurement technique has also been developed to compare distortions produced in the model to actual interference fits. Application of this model will speed the implementation of new joint design to the pulse power experiments.

Lapping Plate Charging

Lapping the air bearing surface of a ceramic hard disk head is one of the final steps in its production process. This surface is 1 mm square, must be flat to 10 nm and have a surface finish less than 1 nm. This project involved optimizing the preparation of the tin lap plate used to create this surface. The new technique starts with a spiral groove machined on the face of the tin and the lands between grooves are charged with the diamond grit; that is, a cylindrical roller is used to push the grit into the soft tin surface. The resulting lap plate can be fabricated in one-third of the time presently required, uses significantly less diamond slurry (saves money) and produces a more aggressive lapping plate.

Scribing Mechanics of Single Crystal Silicon

A project to understand the basic mechanics of single crystal silicon deformation has been initiated. It involves dragging a diamond tip across a surface at a constant speed for a range of vertical loads. The resulting grooves illustrate ductile and brittle response of the material beneath the scribe. The residual stresses resulting from the elastic-plastic constraint create a bending distortion in a scribed wafer sample. Bend deflection of these wafers was measured using an optical interferometer. With the absence of fracture in the scribe region, the amount of plastically generated material in the transformation region was found to be proportional to the bend deflection. The current scribing apparatus is being updated with a counterbalance to reduce the minimum load from 50 mN to 5 mN to generate data in the more interesting low load region.

2) ACTUATION

Real-time control is a necessary technique to improve the precision — accuracy and repeatability — of a fabrication or measurement process. The metrology activities discussed above are intended to develop tools or devices to measure shape, force or properties. Equally important are improved actuators with the ability to create the motion necessary to correct the error.

Design and Development of a Piezoelectric Drop Dispenser

This project involves the design and development of a drop dispenser that will deliver fluid droplets with a volume of 0.5 nanoliter. A fluid flow model of the process was developed using a piezoelectric bimorph as the driver. This model was then used to optimize the component dimensions to create the desired drop size. The device consists of two main parts: 1) an etched silicon/SiN fluid chamber with multiple cavities and nozzles and 2) a sheet of piezoelectric material cut into multiple beam actuators to pressurize each cavity. The components are being fabricated and will be assembled into a test fixture. The static and dynamic performance of the system will be studied and droplet volume measurements will be made using a light microscope.

Dynamic Performance of Piezoelectric Bimorph Cantilevers

Analytical prediction of the dynamic performance for piezoelectric bimorph structures was investigated. A damping ratio was assumed to find the dynamic peak amplitudes and finite element

simulations were used to validate these results. The proposed analytical method was able to predict the dynamic performance in many applications. Effects of bonding layers were also analyzed by both static and dynamic methods. The results show that the bonding influence can be minimized by selecting appropriate bonding materials and dimensions.

3) CONTROL

Control of a precision fabrication processes involves both the characterization of the electromechanical system and the selection of hardware and software to implement the control algorithm. As a consequence, studies of each of these aspects are important research topics for the PEC.

Active Control of Tool Deflection

An open-loop technique to compensate for deflection of small milling tools (diameter < 1 mm) has been demonstrated. However, it is limited due to uncertainties in part position and tool wear. A new project has been initiated to use force feedback in a real-time mode to correct for tool deflections. Two approaches are presented: 1) predicted depth based on a dynamic cutting force model and 2) predicted deflection using a model of tool stiffness. A control algorithm was written incorporating both methods allowing the user to create a variety of profile cuts using feedback from real-time cutting forces and position feedback from the machine. Experimental results are presented for force feedback closed loop machining using both approaches. For a desired depth of 80 μm, the tool deflection was on the order of 20 μm but the profile error with force feedback is only about 5 μm.

Deconvolution of Control Signals

The use of fast tool servos (FTS) to create non-rotationally symmetric optical surfaces is growing. However, the amplitude and phase response of this dynamic system can result in form errors on the machined part. The motivation for this work is to implement open-loop modifications of the input signal to the Variform fast tool servo to correct for its dynamics. An algorithm using signal deconvolution was developed to generate the appropriate input commands that produce the desired response. Deconvolution is a mathematical procedure that can produce a modified input to reverse the effects of attenuation and phase if the impulse response of the dynamic system is known. Since this modified command is not calculated from the position feedback, there is no delay in the response. The result is dramatically improved following error especially for high frequency motion.

Sliding Mode Control of a Magnetostrictive Actuator

Magnetostrictive actuators have the advantage of high strain output and broadband response but have significant hysteresis. Use of these actuators in precision applications requires advanced control schemes. A fast tool servo driven by a large magnetostrictive actuator (length = 200 mm with a maximum stroke of 300 μm) is being used to study the application of a non-linear control scheme, called sliding mode control, to this type of system. The displacement of the actuator as a

function of drive voltage has been measured and modeled as a hyperbolic tangent function. A theoretical model of the control system has been created and its application to the actuator shows improved performance.

4) FABRICATION

High-speed milling, plastic replication and a new technique for diamond turning have been the focus of the fabrication process research over the past year.

Vibration Assisted Diamond Turning

Adding high-speed vibration to the tool during diamond turning has been shown to reduce tool wear when machining difficult materials such as steel and silicon. The goal of this project is to study the details of this secondary motion and optimize its shape and frequency. A high-speed UltraMill has been fabricated to operate at frequencies up to 5000 Hz with a shape that is adjustable from linear to circular. The issues being addressed include the effect of the tool motion on surface finish of the machined part, ability to machine brittle materials and tool wear.

Force Modeling with Miniature Ball End Mills

A ball end mill creates a complicated array of forces in three orthogonal directions. Predicting these forces as a function tool rotation speed, number of flutes, depth of cut, feed rate and workpiece material is a challenging task. The model developed for diamond turning has been applied to the ball end mill geometry and these predictions have been corroborated using force measurements with a 3 axis load cell. Three different materials – structural aluminum, low carbon steel and hard tool steel – were studied. The results showed excellent agreement with the model both in terms of the reproducibility within a given material class as well as for the entire range of materials.

Co-Molding Plastic Optics

Injection molding fulfills many of the requirements for high-precision optics but still presents significant challenges. One of these challenges is the thermal stability of the molded optic. The thermal expansion of the typical molded plastic, such as PMMA, limits its performance over a large temperature range. By co-molding the optical shape onto a thermally stable substrate such as glass, the advantages of cost and performance could be simultaneously realized. Implementation of this concept requires changes to typical injection molding process with regard to substrate support, plastic flow, mold preheating and substrate preparation/coating. The results of this project indicated that this process is feasible but the results were disappointing regarding adhesion of the polymer using the selected cleaning method.

Fabrication of Non-Rotationally Symmetric Spectrometer Mirror

Challenges in fabrication and testing have historically limited the choice of surfaces for reflective optical instruments to spherical or conic mirrors. However, more degrees of freedom are needed to meet new performance and packaging requirements. In particular, single-surface astigmatism

correction in spectrographs necessitates a biconic surface, which lacks an axis of rotational symmetry. With support from NASA Goddard Space Flight Center (GSFC), a 94 by 76 mm off-axis, toroidal, biconic mirror has been fabricated using the Variform fast tool servo and the Nanoform 600 diamond turning machine. Issues related to the geometric analysis, decomposition, toolpath generation, controller interfacing, part fixture design, alignment, machining, and metrology of a pair of these mirrors are discussed.

Characterization of Mechanical Indent Effects on Polystyrene Hemispheres

Creating a residual stress field by plastic deformation (scribing or indents) has been shown to be a useful technique for precision shape modification. It has been applied to hard disk heads to control the features of the flying surface to the order of nanometers. This project expands the techniques to hemispherical components. Whereas the effects of indents on flat surfaces have been defined, loads applied in various locations on dome-shaped components can be more difficult to understand. Experiments were conducted involving identical polystyrene hemispheres that were exposed to indents with different magnitudes and geometric configurations. The shapes were measured and compared to finite element analysis (FEA) simulations.

1 FABRICATION, DISTORTION, AND METROLOGY OF SHRINK FIT ELECTRICAL CONNECTIONS

Patrick D. Morrissey
Graduate Student
Jeffrey W. Eischen
Associate Professor
Department of Mechanical and Aerospace Engineering

The fabrication of pulse power experiments at Los Alamos National Labs requires assembly of shrink fit or press fit joints that are used to carry large electrical currents. These joints are also called on to support some mechanical stresses. As a result, the shape and interference of these joints are critical to the success of the mission. The primary issues at hand include the following: mechanics of the interference fits, physical description of the contact surfaces between the liner and glide planes, joint void description, and material property effects. To investigate these issues, computer generated finite element analysis models have been created and compared to experimental data. A measurement technique has been developed to compare distortions produced in a model interference fit joint to verify the finite element simulation. Verification of the computer generated finite element model with experimental results could provide tremendous aid in accurately predicting the shape, deflection, and stress distribution of such cylindrical elements.

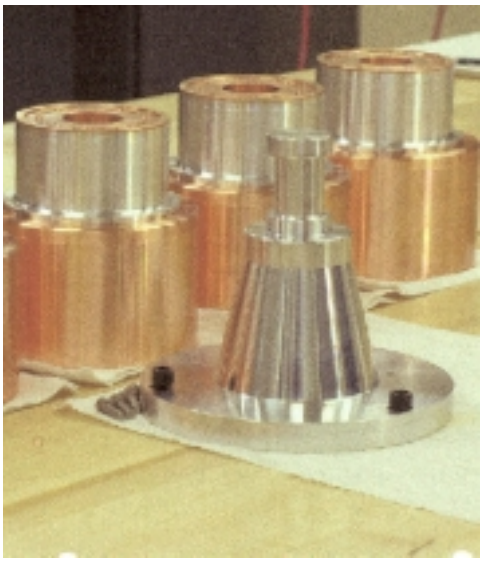

1.1 INTRODUCTION

There is a need to fabricate thin cylindrical components (called liners) for use in high-energy pulse power experiments at Los Alamos National Laboratories. The material, thickness, and shape of the liner are dictated by the physics experiment and, as a result, the fabrication technique must be flexible. The base material for the liners is typically pure aluminum (commercial 1100 series) and the glide planes are composed of copper. Early designs used a thermal shrink fit to assemble the liner and glide planes while the most recent designs use a press fit. It has also been proposed to employ composite liner structures, i.e. fabricated with nested cylindrical shells of dissimilar materials. The inner layer would normally be copper, but tantalum, stainless steel, or 6061 aluminum may be utilized.

Copper glide planes are inserted in either end of the cylindrical liner, typically via a thermal shrink fit process, though more recent designs have used a modified geometry with a mechanical press fit process. These glide planes serve as a mechanism to transfer tremendous electrical currents to the liner, which leads to a cylindrical liner implosion. To optimize the results of these experiments, it is necessary for this cylindrical implosion to occur very uniformly. Therefore, manufacturing dimensionally precise liners with minimal surface flaws is essential. Unfortunately, the shrink fit process naturally results in residual stress and distortion in the liner walls, which need to be compensated. A schematic illustrating the assembly orientation of a single wall liner with glide planes is shown in Figure 1. The nominal diameter of the liner is 100mm, the height is 55mm, the wall thickness is 1.2953mm, and the nominal interference fit is 15.24μm (0.0006in).

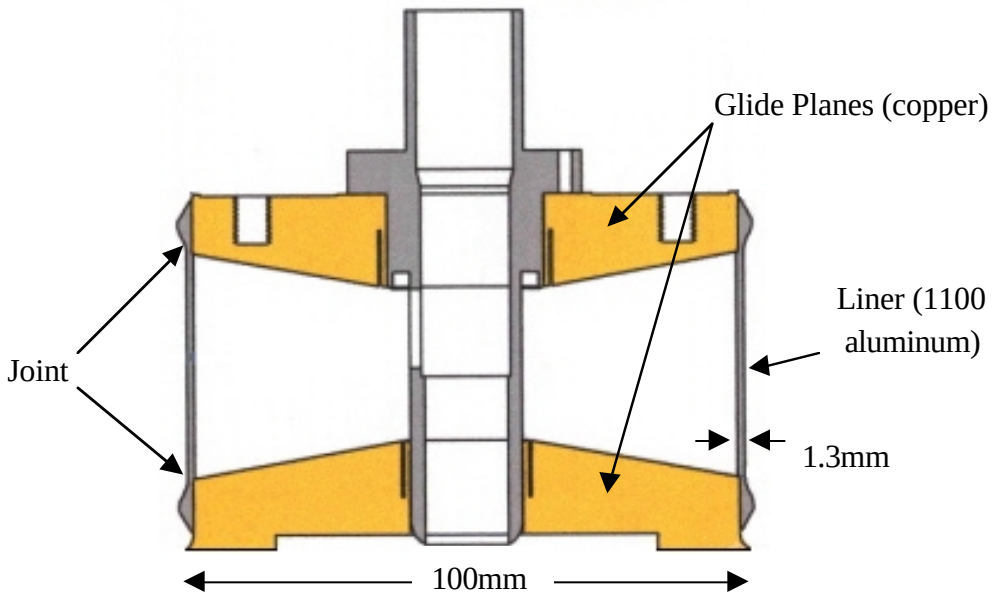

Figure 1: Cross section of liner and glide planes (NTLX Shiva Star/Atlas Configuration)

1.2 FINITE ELEMENT MODELING

1.2.1 LANL PROTOTYPE

The 3D stresses and distortions resulting from slipping the glide planes into the liner are impossible to calculate from analytical formulas. These expressions exist only for cylindrical systems in which the interference exists along the entire length of the mating cylinders. In the current problem, only a partial interference exists, since the glide planes only fit into the end portions of the liner. Finite element analysis (FEA) provides an efficient method to calculate the desired quantities for this type of structural configuration. The geometry of this particular shrink fit interface, as well as the geometry of the actual liner itself, is expected to provide results that considerably deviate from those given by standard shrink fit calculations. LS-DYNA is a powerful finite element code with the capability to model contact. This code is marketed by Livermore Software Technology Company and was used to simulate the liner/glide plane system. Each mating component was meshed as a distinct part and detection of contact was handled automatically. The code has the capability to simulate thermal shrink fits using a temperature versus time profile, or to treat press fits using specified nodal displacements. Figure 2 shows the baseline mesh modeling the geometry of this axi-symmetric system. The axi-symmetric modeling does ignore some details of the glide planes, such as holes and ports, but this is not expected to impact the results of interest in any significant way.

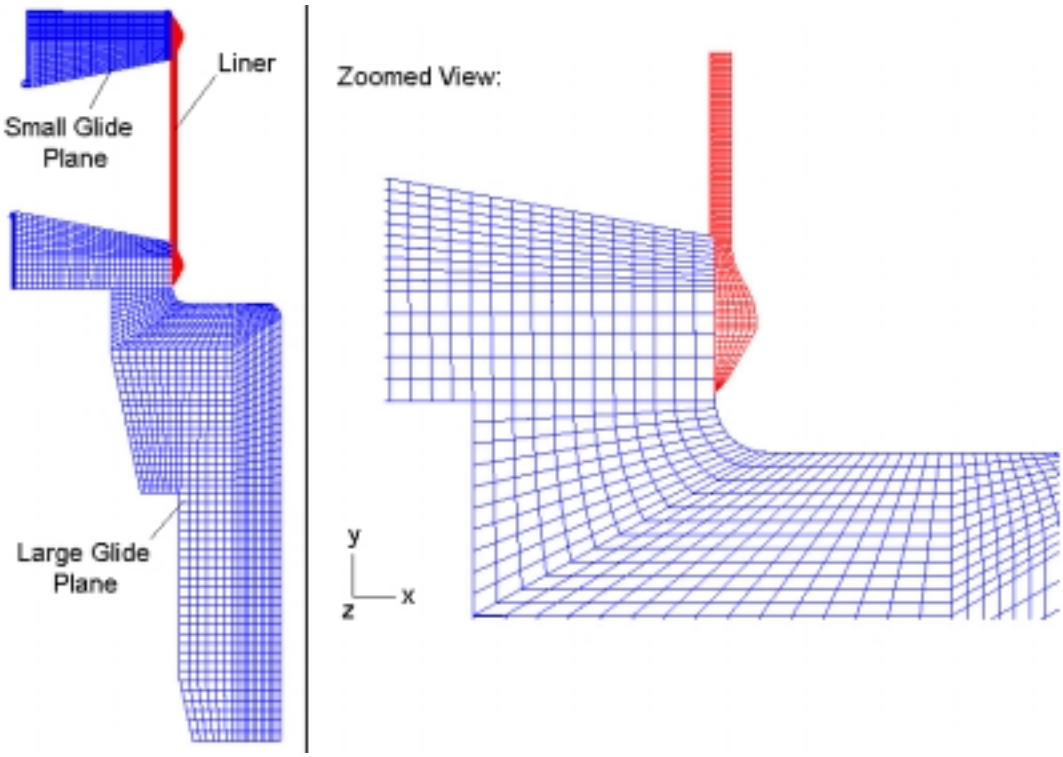

Figure 2: LS-DYNA mesh used for LANL prototype simulation

Table 1: Material properties used in LS-DYNA simulations

PARAMETER	COPPER GLIDE PLANES	1100 ALUMINUM LINER
Young's Modulus	1.5954×10^{7} psi	1.0008×10^{7} psi
Poisson's Ratio	0.35	0.33
Thermal Expansion Coefficient	1.7×10^{-5} $(°C)^{-1}$	2.36×10^{-5} $(°C)^{-1}$
Yield Strength	50,000 psi	5,000 psi

The material properties used for the liner and both glide planes corresponded to 1100 aluminum and copper, respectively. These properties are listed in Table 1. Each component was modeled in LS-DYNA as an elastic-plastic material, thus accounting for any potential yielding. The liner was composed of 1638 elements with 8 elements through the thickness, and the large and small glide planes were composed of approximately 2000 elements each. For this preliminary FEA model, a composite liner was *not* used. A uniform temperature change of -100°C was imposed on the glide planes during simulation. The parts were then slipped together, followed by a return to ambient temperature with contact modeling between the parts activated during the transition to equilibrium. The glide planes expanded during this phase, deforming the liner as expected.

1.2.2 LINER DESIGN CHANGES

Although the most significant and noticeable liner deformation occurs over the entire length of the liner, there is indeed a localized liner deformation profile at each of the two joints. To maximize the flow of current at this interface between the glide planes and the liner, it is desirable to maximize the area of the contact interface between these components. Therefore, it is necessary to investigate potential gaps or voids at the two liner-glide plane interfaces caused by the thermal shrink fit used for assembly. By plotting the coordinates of both the liner and glide plane nodes located within each of the given contact regions, gaps within the interfaces will become apparent. Figure 3 shows the nodal coordinates of the liner and glide plane located within the top contact region. The coordinates of these nodes correspond to the final time step of the LS-DYNA simulation, in which the components have reached thermal equilibrium. Since these are simply the coordinate locations of the interface nodes for both the liner and glide plane, any discrepancies in x-coordinate values at identical y-coordinate positions represent gaps. An example of such a gap can be seen in Figure 3.

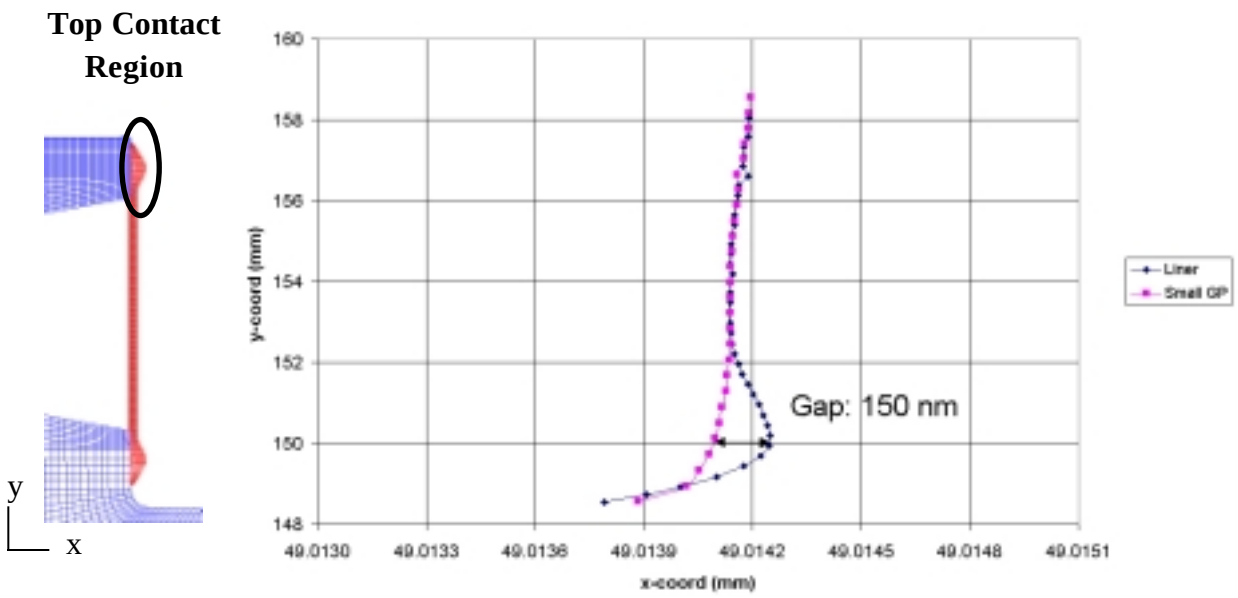

Figure 3: Coordinates of liner and glide plane nodes for the Original Design located within the top contact region

It is important to note that while the magnitude of the gap is only 150nm, the gap occurs over approximately one third of the entire contact length. This could be a significant factor in the overall performance of the ATLAS pulse-power experiments, as it could potentially lower conductivity. Although not pictured, the bottom contact region results in a very similar gap profile.

To compensate for these gaps, simulations were conducted with hypothetical liner design changes. Particular attention was paid to the bump features on either end of the liner. Figure 4 illustrates finite element meshes of three proposed liner redesigns in comparison to the original liner geometry.

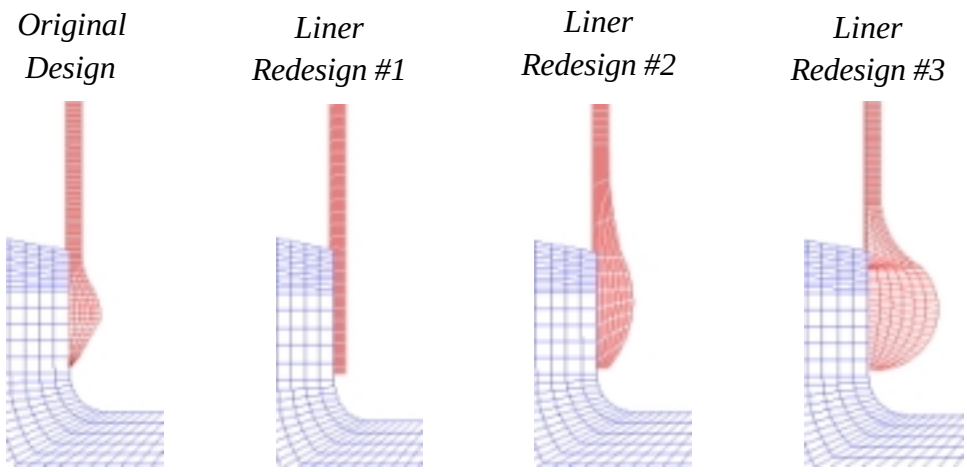

Figure 4: Liner feature redesigns in comparison with the original liner

The three liner redesigns represent three extreme design alterations: no feature on the end of the liner (Liner Redesign #1), a longer smoother feature (Liner Redesign #2), and a thicker feature (Liner Redesign #3). The feature in Liner Redesign #2 contains the same width as the Original Design (2.525mm), while Liner Redesign #3 has a feature of slightly more than twice the width (5.619mm). Note that for each of the three redesigns, the thickness of the liner portion falling within the non-contact region is equal to that of the Original Design (1.295mm). Investigating any potential gaps in each of the redesigns was done once again by plotting the coordinates of the liner and glide plane nodes falling within the interface region at the final time step of the LS-DYNA simulation. The gap resulting from Liner Redesign #1 is shown in Figure 5. It is evident that removing the liner bump feature altogether results in a much wider void in the liner-glide plane interface. Even more important, however, is the fact that this void occurs over approximately half of the total interface length.

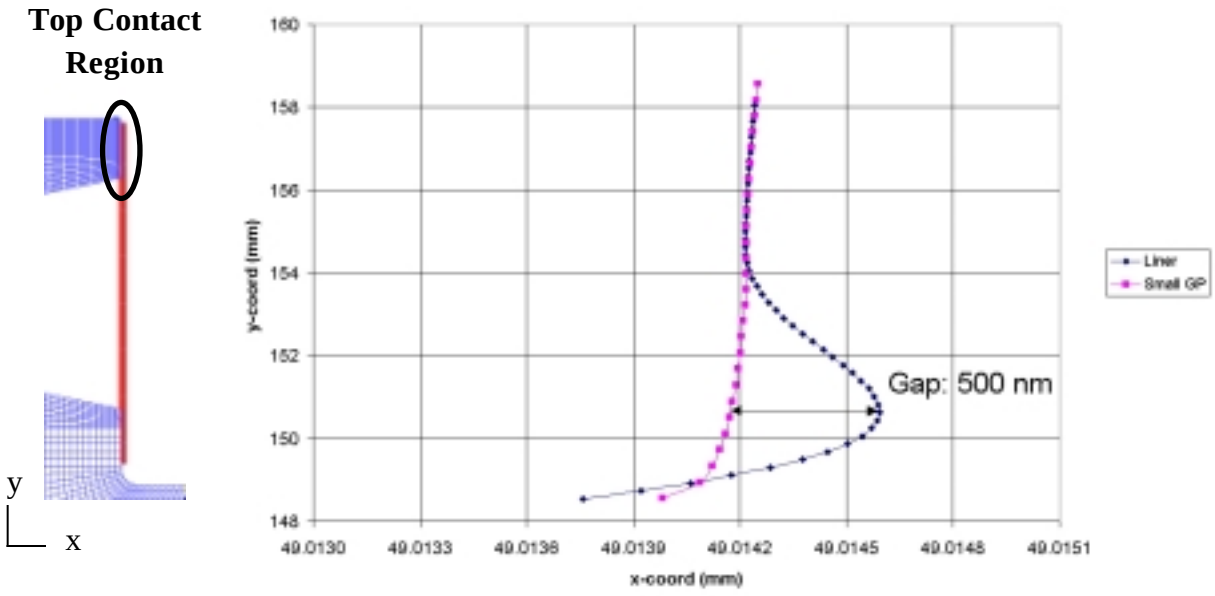

Figure 5: Coordinates of liner and glide plane nodes for Liner Redesign #1 located within the top contact region

Altering the liner bump feature to a longer, smoother geometry considerably decreases the size of the void, essentially eliminating it altogether, as shown for Liner Redesign #2 in Figure 6. The top contact region was chosen for illustration for this particular redesign, but once again, the bottom contact region (not shown) gives very similar results.

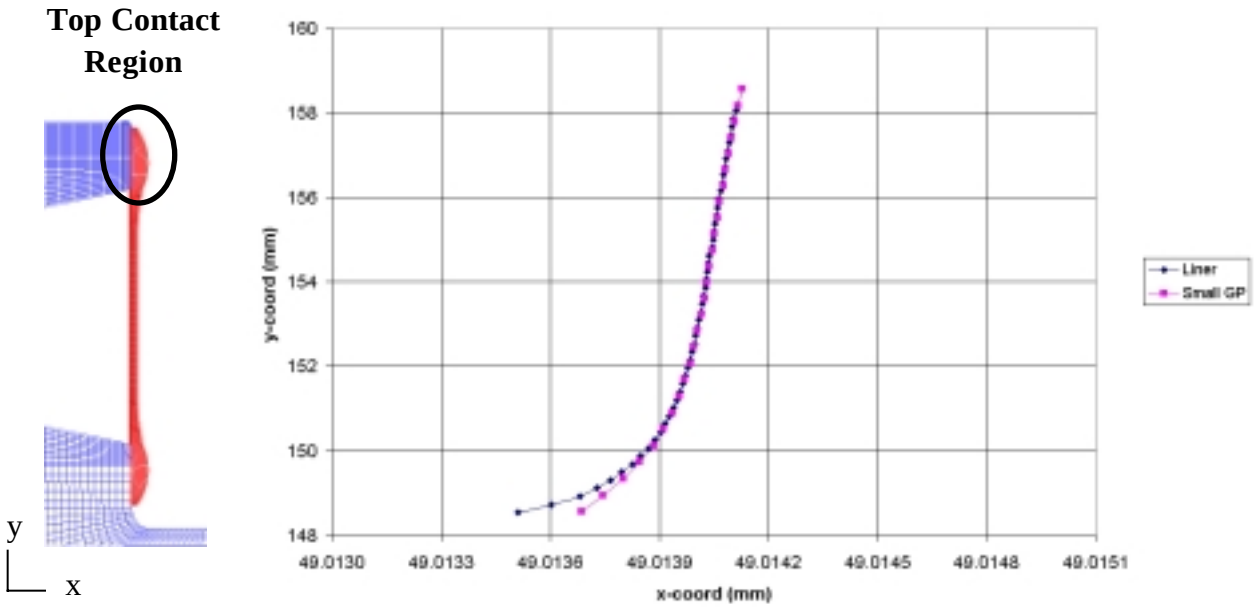

Figure 6: Coordinates of liner and glide plane nodes for Liner Redesign #2 located within the top contact region

Liner Redesign #3 produces similar void reduction. The favorable results can be seen in Figure 7, which shows the top contact region. Again, the bottom interface (not shown) gives very similar results.

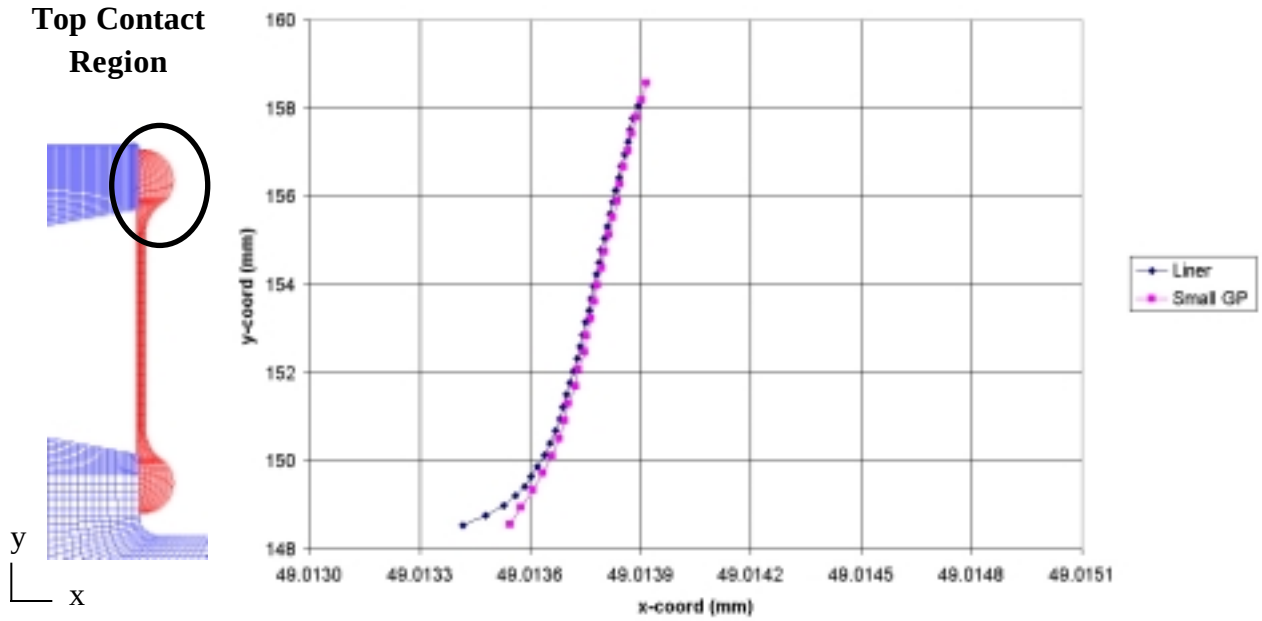

Figure 7: Coordinates of liner and glide plane nodes for Liner Redesign #3 located within the top contact region

As expected, the maximum stress levels in Liner Redesign #1 (5,350psi) exceed the yield strength of 1100 aluminum. This, coupled with the fact that the gap is greatly increased without the presence of the liner features, suggests that these liner features are crucial for the desired performance of the ATLAS pulse-power experiments. The maximum stress levels found in the liner for each liner design are summarized in Table 2.

Table 2: Maximum liner hoop stresses

GEOMETRY	MAXIMUM LINER STRESS LEVEL
Original Design	4,190 psi
Liner Redesign #1	5,350 psi
Liner Redesign #2	4,125 psi
Liner Redesign #3	3,400 psi

The maximum stress level in Liner Redesign #2 was similar to the Original Design, though this design reduced the size of the void considerably. Liner Redesign #3 significantly reduced both the maximum liner stress and the void magnitude.

1.2.3 EFFECTS OF AN OUT-OF-ROUND LINER

Improper machining or handling of these thin aluminum liners could potentially cause distortion and therefore non-axisymmetric geometries. It is believed that this could potentially alter the stress levels and effect the deflection profile for the liner. To model this scenario, a cross-section of the liner at the minimum wall thickness location was used for analysis. The shape of the non-axisymmetric liner was assumed to be elliptical, with the radial interference values being varied at two locations located 180 degrees apart. The locations of the varied radial interference value, δ^*, are shown in Figure 8.

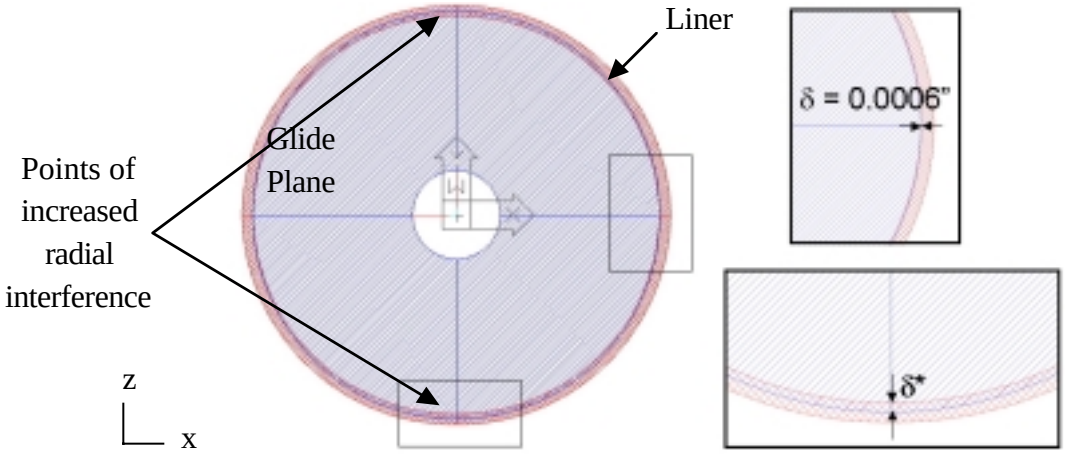

Figure 8: Cross-sectional geometry of an elliptical out-of-round liner

Attention was focused on the maximum hoop stress and its dependency on the liner eccentricity. A list of the range of variation for the radial interference values and the corresponding maximum hoop stress is shown in Table 3, and a normalized graphical representation is shown in Figure 9.

Table 3: Maximum hoop stress located in the liner for each of the liner redesigns

δ* VALUE	MAXIMUM LINER STRESS	PLASTIC STRAIN?
0.0003in (7.62μm)	3,000 psi	No
0.0006in (15.25μm)	3,590 psi	No
0.0008in (20.30μm)	4,250 psi	No
0.0010in (25.40μm)	4,920 psi	No
0.0012in (30.50μm)	5,535 psi	Yes
0.0015in (38.10μm)	5,850 psi	Yes

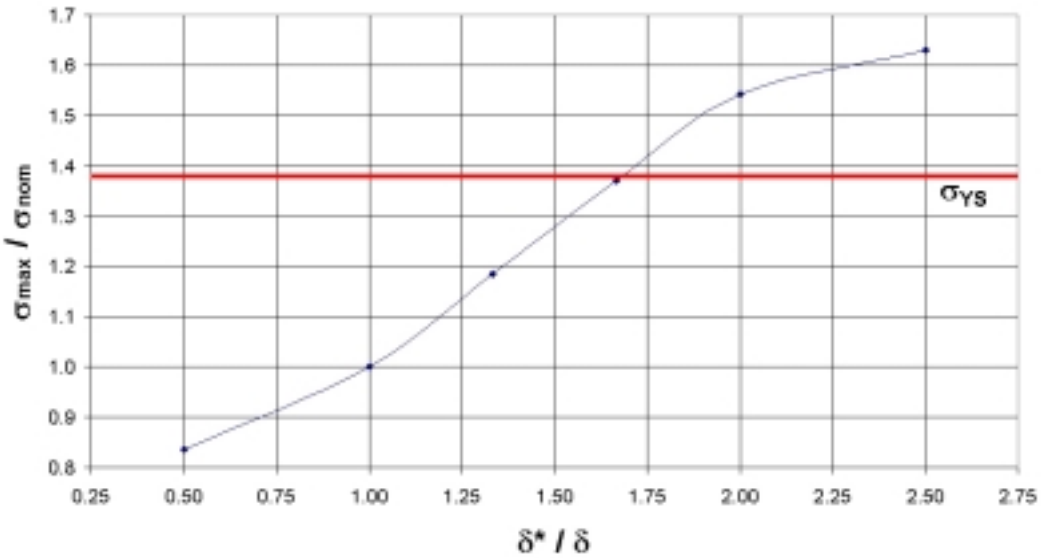

Figure 9: Normalized graph of maximum hoop stress versus liner distortion

The radial interference value of 15.24μm (0.0006in) represents the baseline value for the current liner design. Improper handling is predicted to be the main source of concern for any distortions in the liner, rather than improper machining or Diamond Turning Machine axis stability errors. To simulate this improper handling, two point loads (which simulate a pinching force that could be caused by two fingers) were imposed 180 degrees apart on the liner OD. This corresponds to the location of the varied radial interference values for the finite element model as shown in Figure 8. Such forces cause liner distortion and result in an elliptical shape, shown in Figure 10, which also coincides to the finite element model for non-axisymmetric geometries.

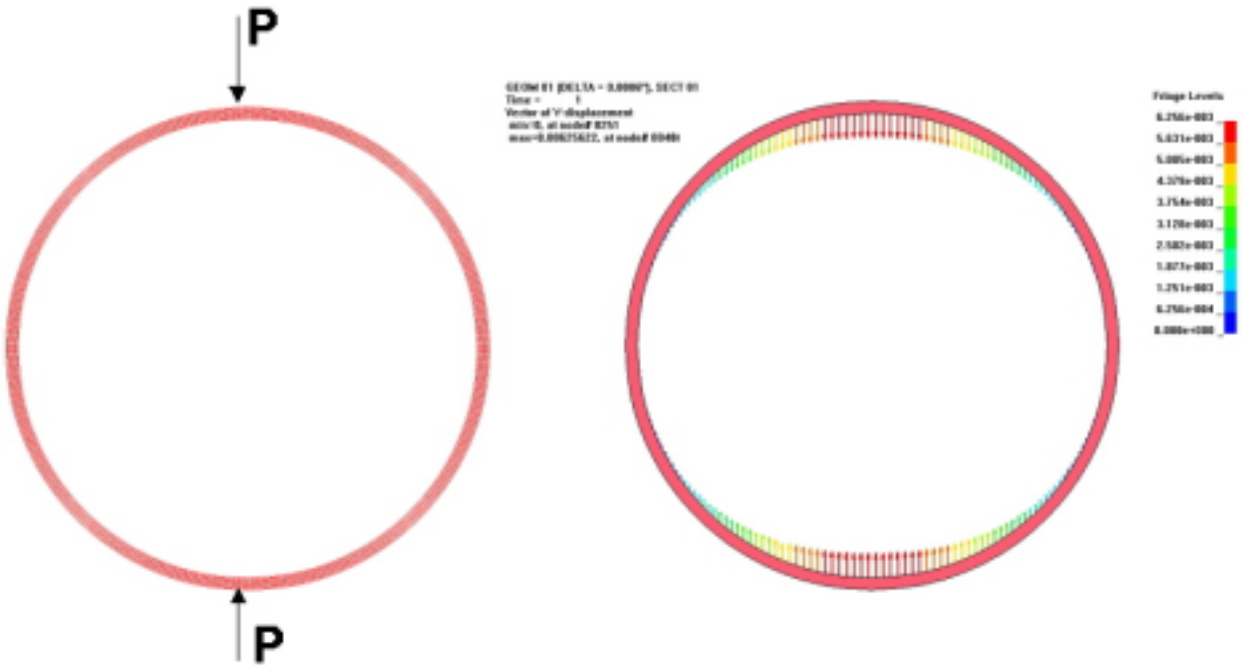

(a) (b)

Figure 10: Finite element simulation of "pinch" loads on a thin walled liner (a), and post-processor resultant displacement vectors (b)

By incrementally increasing the load *P*, the level at which the thin-walled liner could withstand prior to permanent plastic deformation was determined. A graphical representation of this load increase is shown in Figure 11.

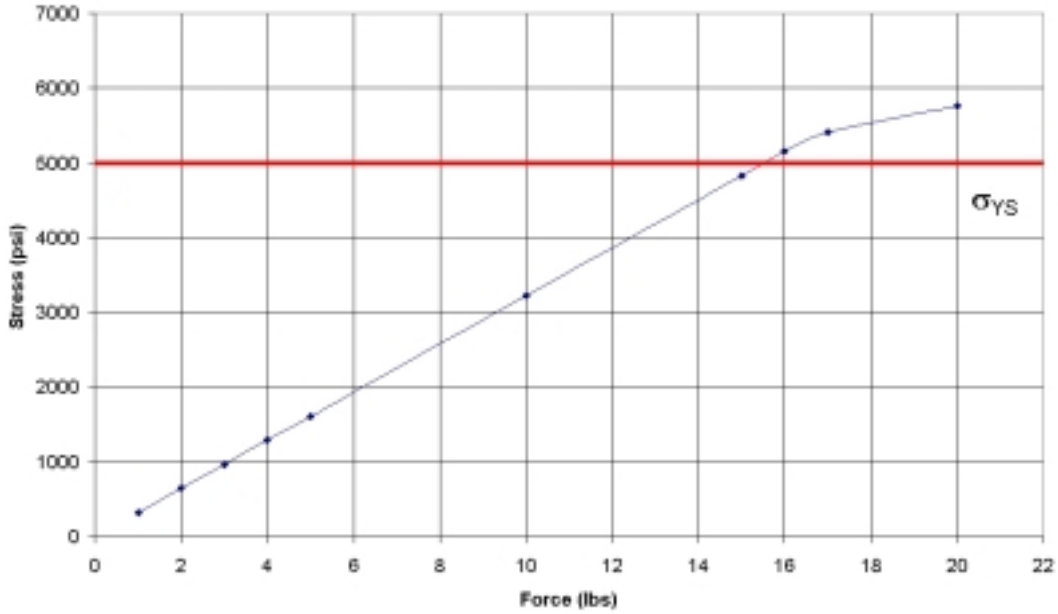

Figure 11: Resulting maximum hoop stress due to increased "pinch" loads on a thin walled liner

It is evident that relatively large "pinch" loads of approximately 15lbs are required to plastically deform the thin walled liners. Pinch loads of this magnitude would be required to lift the assembled components due to the weight of the heavy glide planes. Thus, if the components were lifted by grasping the thin walled liner, deformation of the liner could potentially be an issue.

1.3 LINER SHAPE MEASUREMENTS

1.3.1 TEST SPECIMEN DESIGN

To verify the validity of the LS-DYNA results, an experiment was conducted involving a shrink fit test specimen. The idea behind this test specimen was to measure the liner deflection (a quantifiable and measurable parameter) caused by the shrink fit and compare it to the deflection profile predicted by the LS-DYNA model. Identical deflection profiles would verify the finite element code. The model could then be used to evaluate new designs and would be a tremendous aid in determining their application to the ATLAS machine. This test specimen will be referred to as Test Specimen #3, since two similar test specimens were designed and fabricated prior to this.

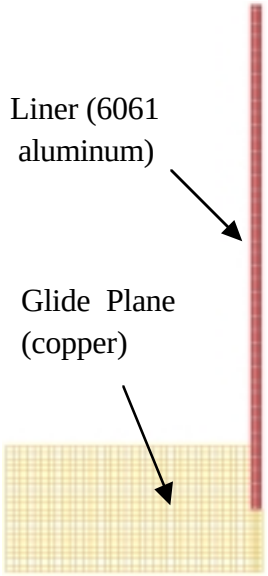

Figure 12: Test specimen mesh for LS-DYNA

To determine appropriate dimensions providing a reasonable radial interference value, the assembly of the test specimen was first simulated using LS-DYNA. Preliminary shrink fit analytical calculations were performed to determine hoop and radial stress levels and dimensions were selected to avoid yielding of either part as a result of the shrink fit process. An illustration of the axi-symmetric geometry of this test specimen can be seen in Figure 12. Note that only half the cross section of the test specimen need be modeled due to the axi-symmetric geometry. There were two components of this test specimen: a liner composed of 6061 aluminum containing no end features (for fewer machining complications) and a glide plane composed of copper. Appropriate inner and outer diameters of the test specimen liner were determined to be 48.4472mm (1.90737in) and 50.4140mm (1.98480in), respectively, and the liner length was selected to be 51mm (2.00787in). This liner wall thickness of approximately 1mm is comparable to the actual liner thickness used in the ATLAS models. The glide plane outer diameter was selected to be 48.4543mm (1.90765in) thus producing a radial interference value δ of 0.00014in or approximately 3.5μm. The hoop and radial stress values for the shrink fit assembly determined by the finite element simulation corresponded to the preliminary calculations. This confirmed that neither part would plastically deform due to yielding; therefore, these selected dimensions were deemed sufficient for experimental assembly of the test specimen components.

1.3.2 TEST SPECIMEN FABRICATION AND DIMENSIONAL MEASUREMENTS

After determining the dimensions for the test specimen, fabrication could begin using the ASG-2500 DTM to machine both components with very high surface finishes. Previously, two test specimens were fabricated consisting of the same approximate dimensions as described for Test Specimen #3, but with radial interference values of 15μm. Since the radial interference values for these test specimens were on the micrometer scale, it was essential to ensure that each component was machined and measured to a high degree of precision, particularly for radial dimensions. Formerly, components for Test Specimen #1 were measured with calipers and micrometers, which did not have the resolution necessary to ensure such accurate dimensions. The B&S Coordinate Measuring Machine (CMM) was thought to be a good alternative, but upon measuring various gage blocks to validate the accuracy of the CMM, it was found that the errors were too large for the purposes of machining and measuring these particular components. Using 0.500", 1.000", and 2.000" gage blocks, the average measurement variation along a single axis was found to be approximately 3 μm.

Since the CMM was not sufficiently accurate for measuring such components, the ASG-2500 DTM with a Federal gage and a gage block stack was used to measure the diameter of each mating component for Test Specimen #2. The apparatus is shown in Figure 13.

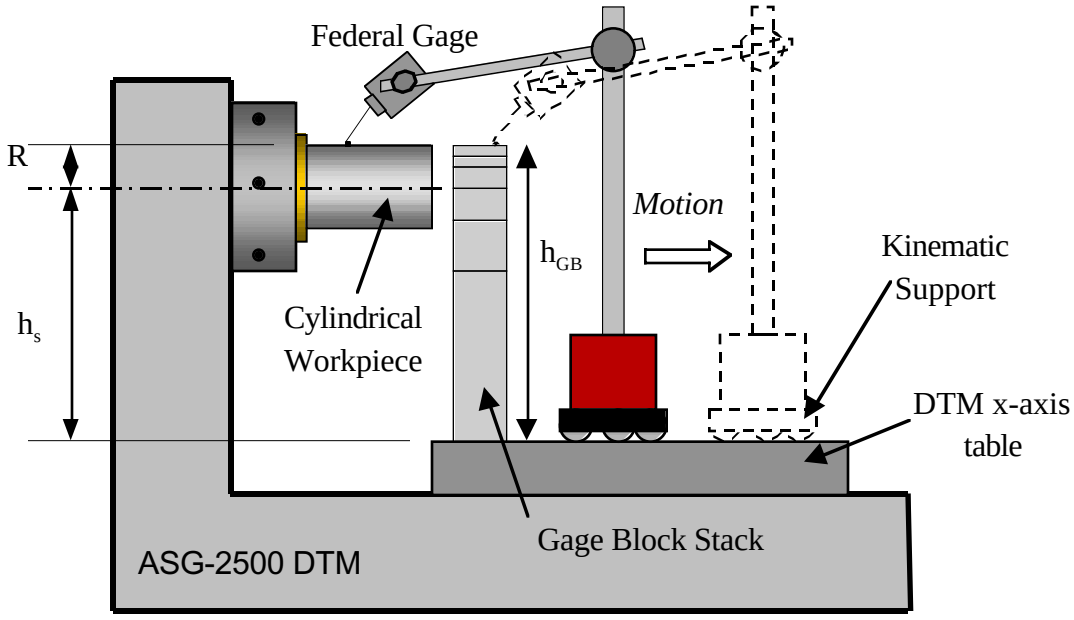

Figure 13: Apparatus used for measuring cylindrical Test Specimen #2 components

The technique consisted of moving the Federal gage from the highpoint of the cylindrical workpiece to the slightly lower surface of the gage block stack. The difference in height was indicated by the Federal gage readout ($FG_{Readout}$). Theoretically, if the precise height of the gage block (h_{GB}) and the spindle height (h_s) were both known, the radius of the workpiece, R, could be determined using Equation 1.

$$R = h_{GB} - h_s + FG_{Readout} \tag{1}$$

It is important to note that there are tolerances associated with each gage block. Six gage blocks of various dimensions had to be used to achieve the spindle height of 6.00874in (plus the radius of the workpiece). Using statistical analysis for the particular grade of gage blocks used, it was calculated that the overall positive and negative gage block stack tolerances were +400nm and –200nm, respectively. Using the Federal gage, it was determined that the repeatability of the gage stack measurement was within one micrometer. Additionally, the film thickness of the oil in between each gage block can potentially effect the measurement.

1.3.3 ALTERNATE DIMENSIONAL MEASUREMENT TECHNIQUES

GAGE BLOCK ON CYLINDER: Measuring dimensions to within a micrometer could be considered sufficient for shrink fits with radial interference magnitudes of approximately 15µm (similar to the first two test specimens). However, with smaller radial interference values of 3.5µm (corresponding to Test Specimen #3 that was described earlier), it is desirable to develop measurement techniques that ensure even higher dimensional accuracy. Therefore, two additional methods were evaluated. The first method also uses the Diamond Turning Machine and a Federal gage. However, instead of using a stack of gage blocks, a single gage block is attached to the workpiece by means of a rubber band. As usual, the diamond tool height is adjusted to match the DTM spindle centerline height using the micro-height adjuster. A schematic of this measurement technique setup is shown in Figure 14. Using this method, the Federal gage is attached to the x-axis table of the DTM using a magnetic base. By jogging the x-axis slowly, the Federal gage probe is touched off on both the inner edge of the gage block (which is essentially the outer

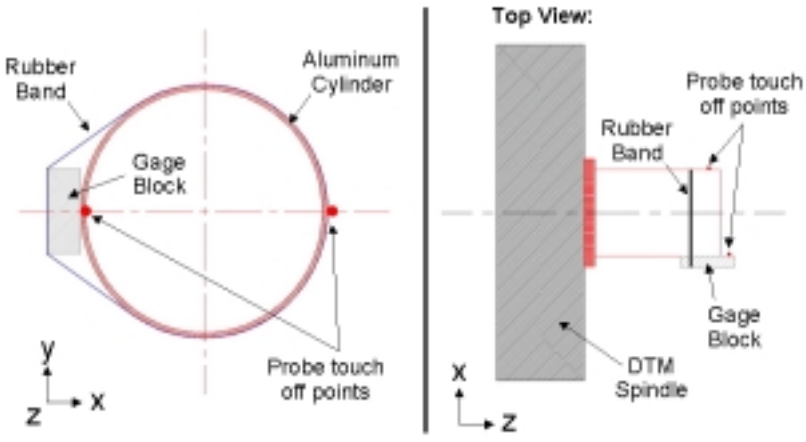

Figure 14: Schematic of an additional radial measurement technique

edge of the cylindrical workpiece at that point of contact) and on the outer diameter of the cylindrical workpiece on the opposite side. Recording the change in x-coordinates between each touch off gives the outer diameter of the cylindrical workpiece. Since the tool height has been adjusted to match the height of the spindle centerline, it is then trivial to machine the cylindrical workpiece ID to a desired dimension using the DTM coordinates. However, there are problems associated with this technique. It is imperative for the gage block to be perfectly perpendicular to the x-axis table of the DTM, and for the Federal gage probe height to closely match that of the spindle centerline. The relatively gradual curvature of a 2" OD cylindrical workpiece allows for some discrepancy between the Federal gage probe height and the spindle centerline height without remarkably sacrificing measurement accuracy. Regardless, adjusting the height of the probe tip to a desired level is not an easy procedure. Furthermore, touching a diamond turned workpiece with a gage block would undoubtedly result in a scratched workpiece. While the rubber band would not produce forces high enough to permanently deform the workpiece (refer to Figure 11), it could distort the thin walled aluminum workpiece while in use, thus tainting the diametral measurement. Based on these issues, this measurement technique was not used.

DIAMOND TOOL REFERENCE: Another measurement technique involved a simple solution: center the diamond tool. By machining centering plugs and examining them under high-resolution microscopes and the Zygo GPI Interferometer, the tool height was iteratively centered in both the horizontal and vertical directions (x- and y-directions, respectively). Once the tool was centered, the x=0 point was established at the spindle centerline. As shown in Figure 15, the diamond tool uses a different cutting edge for the centering plug and test specimen components.

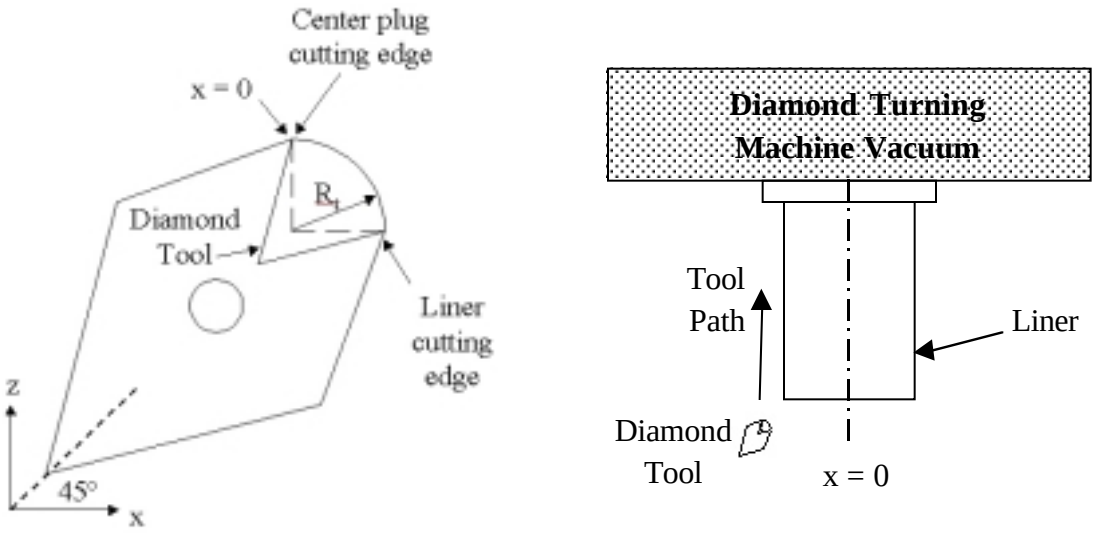

Figure 15: Diamond Turning Machine schematic for a centered tool

Since these cutting edges vary by 90 degrees, the current radius of a cylindrical workpiece was actually the x-axis coordinate *minus* the tool radius, R_t.

To accurately compensate for the radius of the tool when determining the current cutting x-coordinate, the tool radius was measured. To do this, the diamond tool was examined under the Zygo NewView, a set of points falling along the edge of the tool was taken, and a curve was fit to this set of points. The radius of this fitted curve was the tool radius, determined to be R_t=0.4808mm. By machining the centering plug, examining the resulting feature, and adjusting the tool position accordingly, the tool was centered to within 30nm of the spindle height and 250nm of the spindle x-axis centerline.

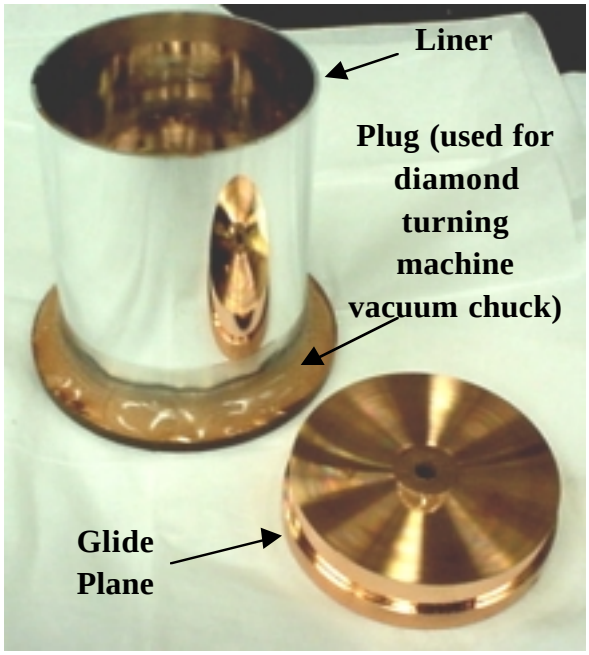

Figure 16: Typical test specimen components fabricated using the ASG-2500 Diamond Turning Machine

Regardless of the accuracy of the tool centering procedure, there is one true advantage behind this measurement technique. Assuming the same tool setup is used for machining each component, it ensures that the desired radial interference value can easily be achieved. Even if there were a discrepancy between the centered tool's position and the spindle centerline, such a discrepancy would apply to each of the mating parts, thus maintaining a desired radial interference value. One slight disadvantage of this technique is that there are no direct dimensional measurements of the finished components. However, by measuring the shape and features of the machined centering plug, the position of the tool in relation to the spindle centerline can be determined with a low degree of uncertainty. These centering plug measurements are indirectly applied to determine the radii of each test specimen component. The diamond turned components that were fabricated and measured using this technique are shown in Figure 16. The graphic portrays the unassembled test specimen components. Note that the copper piece glued to the bottom end of the liner is a simply a flat disk used to attach the aluminum cylinder to the vacuum chuck of the Diamond Turning Machine.

1.3.4 TEST SPECIMEN SURFACE MEASUREMENTS

The liner and glide planes were fabricated and assembled via a thermal shrink fit. The copper glide plane was submerged in liquid nitrogen, thus cooling the part and shrinking it to a diametral dimension such that the aluminum liner could slip onto the glide plane. After returning to thermal equilibrium, the shape of the liner was measured to compare with the FEA model. For the test

specimen that was fabricated and measured with the technique involving the gage block stack on the Diamond Turning Machine (Test Specimen #2, see Figure 13), the Zygo GPI Interferometer was used to measure the surface profile of the liner before and after the shrink fit. The difference in these two surface profiles effectively gives the deflection of the liner induced by the shrink fit. The software package for the Zygo GPI Interferometer contains a convenient "subtract data" function for two sets of data. In order for this to be useful, however, the data sets must contain identical pixel locations. Therefore, a kinematic support was designed and developed for the purpose of maintaining the same position of the test specimen for measurements before and after the shrink fit. The kinematic support illustrating the test specimen orientation is shown in Figure 17.

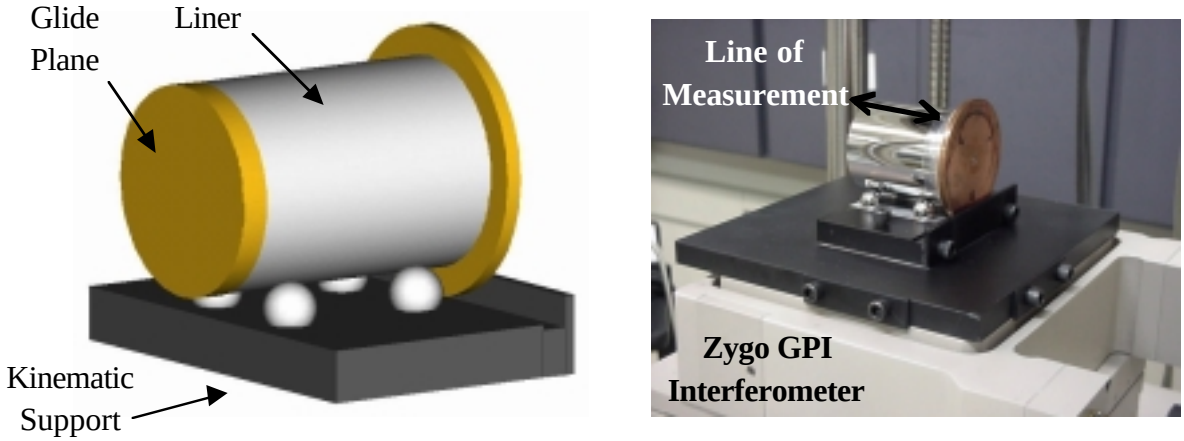

Figure 17: Kinematic support used for test specimen measurements on the Zygo GPI Interferometer. The test specimen is located by four precision chrome balls and the stop.

For the test specimen that was fabricated and measured using the technique involving a centered tool (Test Specimen #3, see Figure 15), the TalySurf Profilometer was used to measure the surface profile of the liner before and after the shrink fit. Once again, the difference in these two profiles provides the liner deflection profile resulting from the shrink fit assembly. Unlike the Zygo Interferometer software, the TalySurf software package does not contain a function that will subtract two data sets, and therefore maintaining the same position of the test specimen was not necessary. Nonetheless, the kinematic support was still used to hold the test specimen in place while measurements were taken. The TalySurf measurement setup is shown in Figure 18.

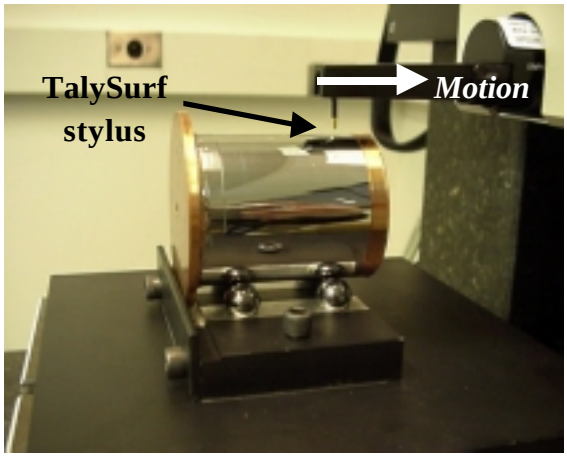

Figure 18: The TalySurf can also be used as a method for liner surface profile and deflection measurements

1.3.5 TEST SPECIMEN #2 RESULTS

The following results correspond to the test specimen that was fabricated and measured with the technique involving the gage block stack on the Diamond Turning Machine (see Figure 13). The radial deflections predicted by the FEA analysis were obtained from the LS-DYNA simulation corresponding to the test specimen geometry. These results are shown in Figure 19. The OD of the glide plane is 15μm larger than the ID of the liner, and as a result, the radial deflection of the liner is a maximum +15μm for the right portion of this curve (the region in which the shrink fit exists). The left portion of curve shows the region in which the shrink fit has no effect on the shape of the liner (zero deflection) since it is not close to the shrink fit interference. Note that the vertical magnification is 3000x that of the horizontal. The large slope in the deflection curve (*y-position* > 35 mm) resulted in a region that cannot be measured using the interferometer because it cannot resolve fringes for surfaces with large slopes. Therefore no data was obtainable near the shrink fit interference end of the liner.

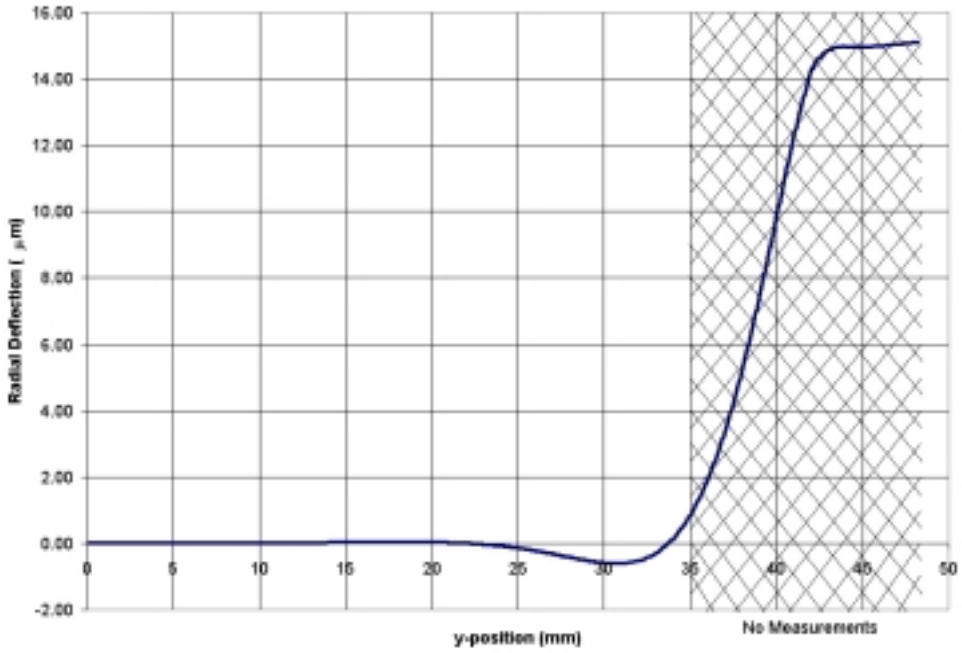

Figure 19: Liner radial deflection values predicted by LS-DYNA (test specimen geometry)

For the measurable portion of the liner (*y-position* < 35 mm), the experimental deflection curves are shown in Figures 20 (a) and (b) in comparison with the deflection curves predicted by LS-DYNA. These two graphs represent experimental deflection profiles located at two different circumferential locations around the liner.

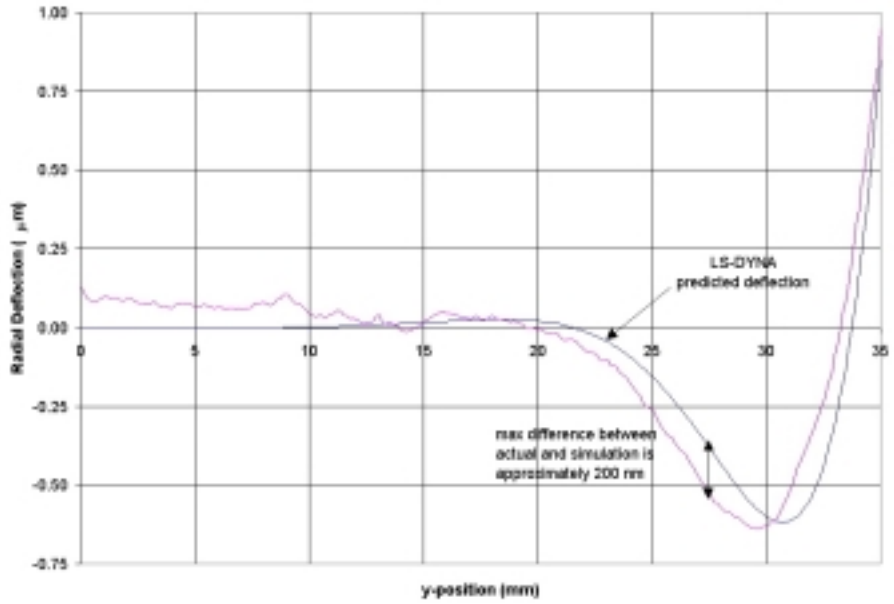

(a)

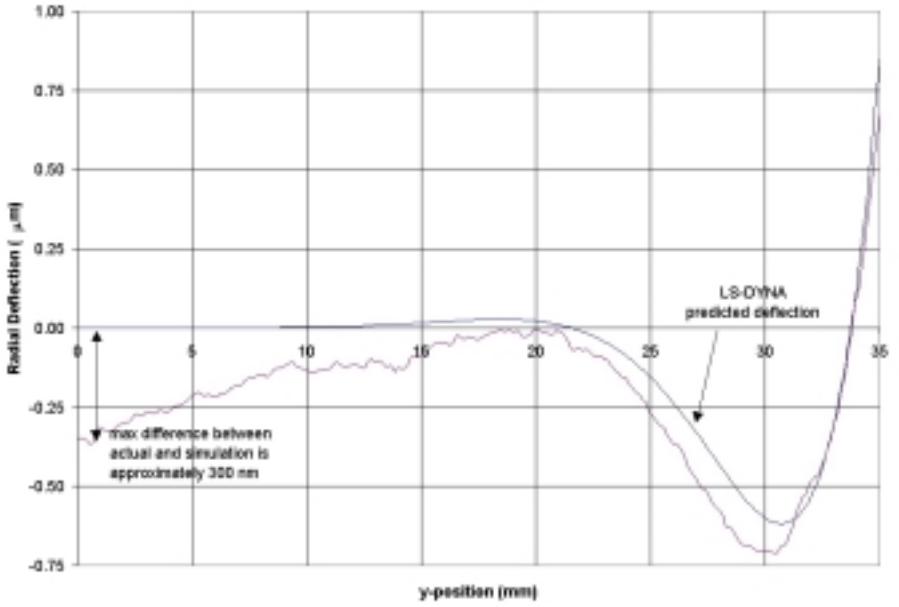

(b)

Figure 20 (a) and (b): Typical experimental liner deflection values at different circumferential locations around the liner OD in comparison with LS-DYNA simulated results.

As seen in Figure 20, the maximum difference between experimental and simulated liner deflection plots for any given region is approximately 300nm. This difference can be attributed to the uncertainty in the measurement technique. The gage block combination has a maximum uncertainty range of 600nm and the repeatability error is 1μm. Both uncertainties are greater than the experimental error.

1.3.6 TEST SPECIMEN #3 RESULTS

The following results correspond to the test specimen that was fabricated with the technique involving a centered tool on the Diamond Turning Machine (see Figure 15). As explained earlier, Test Specimens #1 and #2 had radial interferences of approximately 15μm. Such interference produced a liner slope that was too large for the Zygo GPI Interferometer to resolve fringes. Therefore, this test specimen was designed to have a much smaller radial interference value of 3.5μm, and hence smaller slope of the liner deflection profile. It was predicted that the Zygo GPI Interferometer would resolve fringes for this test specimen, though it was found that the interferometer was still unable to gather data for the entire length of the liner due to the slope of the liner after shrink fit assembly. Thus, the TalySurf Profilometer was used to gather both before and after shrink fit liner profiles, and the difference in these profiles gave liner deflection. Three lines of measurements were taken around the circumference, each 120 degrees apart in the circumferential direction. Figure 21 shows data taken from one of the measurement lines in comparison to the LS-DYNA liner deflection profile of a model with geometry identical to that of this particular test specimen. The right end of the graph represents the end on which the glide plane was attached via a thermal shrink fit.

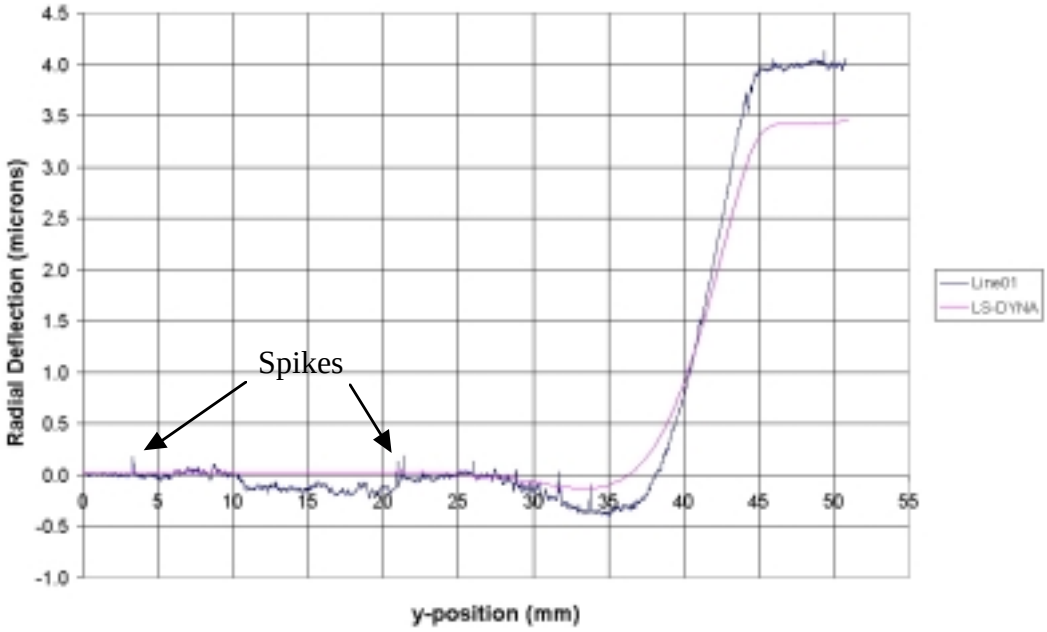

Figure 21: A typical liner deflection profile in comparison to the LS-DYNA model with identical geometry. This data was obtained using the TalySurf Profilometer.

It is obvious that the discrepancies between the experimental ("Line01") and theoretical ("LS-DYNA") data sets are located at the regions of minimum and maximum liner deflection (*y-position* = 35mm and *y-position* > 45mm, respectively). However, these are sub-micrometer variations and therefore the data is considered to be excellent. The large, non-periodic spikes seen throughout the

length of experimental liner deflection profile are due to particles that have collected on the diamond turned surface over time. The other two lines of measurement produced very similar favorable results, as seen in Figure 22.

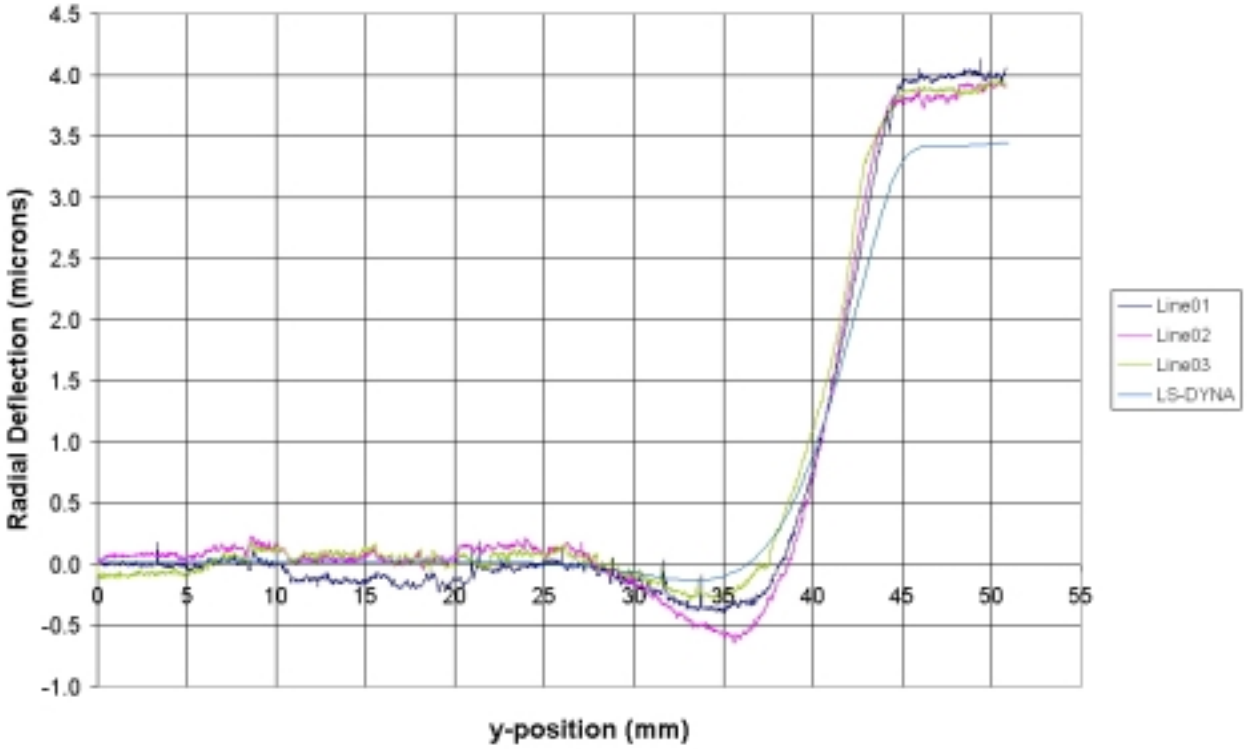

Figure 22: Compilation of all experimental liner deflection profiles in comparison to the LS-DYNA model with identical geometry. This data was obtained using the TalySurf Profilometer.

Note that any discrepancies between the experimental and theoretical data sets are within approximately 0.5μm. The 0.5μm difference in experimental and theoretical profiles can be partially attributed to the 0.25μm uncertainty in the x-axis centering of the tool, as described earlier. It was believed that the orientation of the test specimen on the base of the TalySurf Profilometer could potentially be a source of error as well. Any tilt in the liner, α, with relation to the motion of the TalySurf stylus would result in undesirable stylus drop off and therefore inaccurate data. An exaggerated example of a tilted test specimen is illustrated in Figure 23.

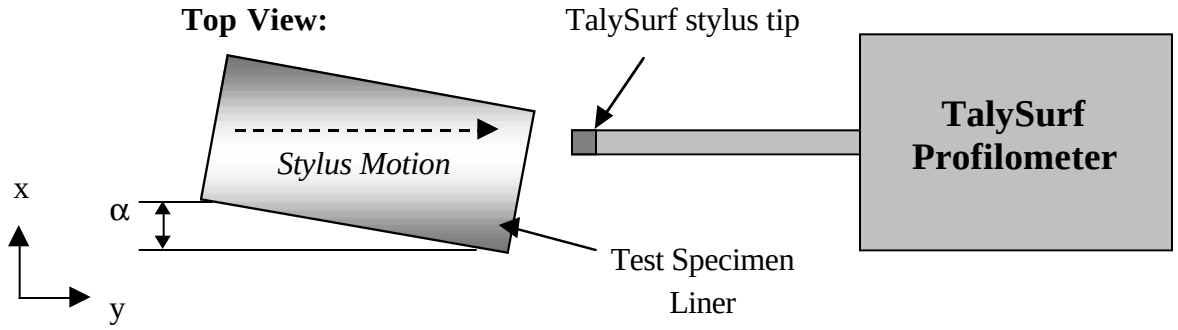

Figure 23: Tilt in the test specimen liner results in undesirable TalySurf stylus drop off and therefore inaccurate data

The test specimen position was adjusted by hand and the orientation of the liner was determined using the following method. After touching off with the stylus on one end of the liner, the liner was translated in the appropriate x-direction using an adjustable slide base upon which the kinematic support and test specimen were placed. The point of maximum stylus deflection represented the peak of the liner at that end. The position value of the slide base was then recorded. An image of the knob used to adjust the slide base can be seen in Figure 24. The slide base position was simply defined by the current numeric value. The stylus was then touched off on the opposite end of the liner and the position of the slide base corresponding to the location of the liner peak was again recorded. Any discrepancies in the two position values of the slide base represented a tilt in the test specimen as seen in Figure 23. The kinematic support that held the liner was then rotated by hand using an iterative procedure to align the y-axis of the liner with the motion of the TalySurf stylus. For each line of measurement taken, the locations of the peaks on either end of the liner were aligned to within one numeric increment on the slide base knob (each numeric increment represents 150μm of translation in the x-direction). With an OD of 50.414mm, the fall off associated with a 150μm x-axis deviation from the peak is approximately 0.5μm.

Figure 24: An adjustable slide base was used to determine the peak locations on either end of the liner.

1.4 CONCLUSIONS

1.4.1 LINER DESIGN CHANGES

From the finite element simulations performed using LS-DYNA, it is evident that gaps exist at each of the liner-glide plane interfaces. Although maximum separation between the liner and glide planes was on the order of approximately 150nm, it is important to note that the length of each gap is approximately one third the entire interface length. It is believed that this could potentially affect the performance of the ALTAS prototype. To overcome these potential performance issues, design

changes were suggested. These three altered designs to the liner included: a liner with no bump features on either end, a liner with longer smoother features, and a liner with thicker features.

As expected, the finite element analysis showed that the features on either end of the liner are essential. As seen in the first liner redesign, a thin walled liner with no end features plastically deforms due to the thermal shrink fit with a maximum liner hoop stress of 5,350psi compared to the current design's maximum stress of 4,190psi. Furthermore, the maximum separation between the liner and glide planes increases more than 200% to approximately 500nm, and the gap grows to about half of the total interface length. Conversely, the other liner redesigns essentially eliminated the occurrence of interface gaps. The longer smoother liner feature resulted in a maximum liner hoops stress of 4,125psi, which is an insignificant improvement from the current liner design. More importantly, however, is the fact that the interface gaps between the liner and glide planes are eliminated. There are indeed small voids on the order of a few nanometers along each of the interfaces, but these are mainly attributed to finite element analysis noise and are very insignificant. The third and final redesign resulted in a maximum liner hoop stress of approximately 3,400psi, the greatest improvement of all redesigns. Once again, the interface gaps were completely eliminated and for this particular design, even small gaps due to finite element noise are not present. For each of these finite element models, the interface gaps were virtually identical for the upper and lower interfaces.

1.4.2 EFFECTS OF NON-AXISYMMETRIC LINER GEOMETRY

It was also found that the effects of an out-of-round non-axisymmetric liner could be very significant, depending on the magnitude of the radial interference variation. If the radial interference magnitude increases by approximately 65% at any point around the circumference of the liner, the liner will yield. It was predicted that such elliptical shaped liners could be the result of improper machining, but most likely would be caused by improper handling. Finite element results from a model in which a thin walled liner was pinched by two opposing forces showed that the liner would not plastically deform unless the loads reached approximately 15lbs. Pinch loads of this magnitude would be required to lift the assembled components due to the weight of the heavy glide planes. Thus, if the components were lifted by grasping the thin walled liner, deformation of the liner could potentially be an issue.

1.4.3 FINITE ELEMENT CODE VERIFICATION

The results from two test specimens that were fabricated, measured, and compared to corresponding finite element models showed vast improvement from the first test specimen results. Whereas the first test specimen was measured with calipers lacking the precision necessary to target such a demanding dimensional accuracy, these final two test specimens were measured with new techniques that provided excellent results. The measurement technique involving a gage block stack

on the x-axis table of the Diamond Turning Machine provided reliable results. Unfortunately, the design of this test specimen consisted of a radial interference magnitude such that the Zygo GPI Interferometer could not obtain a full range of data along the length of the liner. The post-assembly liner had a large slope due to the shrink fit, and such a slope prevented the interferometer from resolving fringes near the liner's shrink fit end. For the data that was collected for the first half of the entire liner length, the experimental and theoretical deflection values lined up well, with a maximum deviation of approximately 0.3μm. The trend of these two deflection profiles matched well, with the LS-DYNA model accurately predicting the region of negative, inward radial deflection.

The third test specimen provided the most insightful results to date. Although the components of this test specimen were not directly measured, the measurements of the tool position in relation to the DTM spindle centerline were indeed taken and recorded. The 0.25μm uncertainty of this tool position was directly related to the uncertainty of the test specimen components' radial dimensions, as the x-axis coordinate of the tool at any given time was used to determine the current radius of the component being machined. This uncertainty was by far the lowest of the three measurement techniques employed, and this was certainly portrayed in the outstanding results. Using the TalySurf Profilometer to obtain the experimental deflection profile for the entire length of the liner, it was seen that the maximum deviation from the theoretical deflection profile was approximately 0.5μm. This maximum deviation existed only at the shrink fit end of the liner, and suggests that the effective radial interference value was slightly larger than desired. This can be attributed to both the small uncertainty involved in the tool centering procedure and the straightness of the liner in relation to the TalySurf stylus motion (any tilt in the liner with respect to the stylus path results in slight stylus drop off error). Although these errors are present, improvements made with each subsequent measurement technique resulted in a final test specimen with sub-micron error magnitudes.

2 LAPPING PLATE CHARGING

David Kametz[1]
Graduate Student
Thomas A. Dow
Professor
Department of Mechanical and Aerospace Engineering

Manufacturing hard disk heads is a challenging compromise between speed of production (cost) and quality of the read head. These heads fly over the disk surface on a layer of air and a GMR sensor detects changes in the magnetic field on the disk surface. The current thin film heads use a block of Al_2O_3TiC (1x1x0.3 mm) with a series of deposited layers on the back surface that is the actual magnetic read head. The focus of this research effort is the fabrication a lapping plate that can be used to create the final surface finish and flatness of the sliding surface. Higher data density is possible if the read head is closer to the disk surface, that is, if flying height is as small as possible. One of the factors that limit this height is the flatness of the head over the 1 x 1 mm flying face. Flying heights for current disk drives are on the order of 10Å or 1 part in 10^6 of the length of each side of the face. This is a challenging fabrication process. The achieve such flatness, the heads are lapped with a tin lap charged with small diamond particles. The soft tin serves to limit the pressure at each diamond/AlTiC contact and the small diamond size limits the force. If the tin surface can be made flat, the result is a head lapping process that can yield the results desired. The PEC has developed a fast, reliable technique to push the diamond particles into the tin surface using a cylindrical roller that reduces the preparation time by 75% and increases the material removal by a factor of 2.

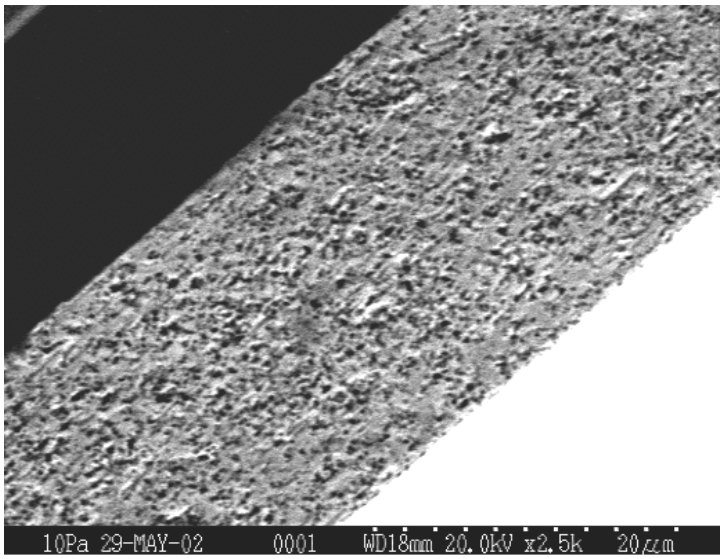

[1] Curently with NAVAIR in Putuxent River Naval Air Station, Maryland.

2.1 INTRODUCTION

The process of fabricating fixed-abrasive lapping plates used to finish hard disk heads is lengthy and demanding. The current process uses a “texturing” ring to create a series of circular scratches on the tin lap plate followed by a flat ceramic ring to create small plateaus and push the diamond abrasive into these regions. The goals of this research are to investigate the current fabrication process for improvements in surface texture quality, charging time and waste reduction of abrasive as well as to develop methods and equipment capable of estimating the lapping quality of the plate during the fabrication process. A new process for creating lapping plates has been developed that changes the surface texture from scratches of random geometry to a continuous spiral groove cut on a diamond turning machine. This texture not only has better reproducibility than the random scratches, but the geometry of the individual features can be better controlled. The charging mechanism was also changed from a large charging ring that was half the diameter of the lapping plate to a small rolling cylinder. The cylinder creates higher pressures and the ability to follow the profile of the plate. These changes resulted in shorter charging times, higher charging quality and reduced abrasive waste during the charging process. A tribometer to measure the local friction coefficient was also developed to test the charging quality of the plate during the charging process.

2.2 CHARGING TECHNIQUE

Charging was done by loading a cylindrical roller (20 mm long) against the grooved, rotating lap plate (350 mm diameter) and dripping the abrasive filled slurry onto the surface of the plate just in front of the roller. A traversing mechanism moves the roller in a radial direction to contact the entire plate as illustrated in Figure 2. The calculated yield load for this cylinder is 20 N using the long cylinder approximation on a tin plate with a land ratio of 25%. However, edge effects play a significant role in the local deformation and measurements showed the roller edge yielded the tin at the net weight of 7.3 N.

The roller material is a Hot Isostatic Pressed (HIP) alumina cylinder made by Sumitomo Special Metals Corporation. This roller had an outer diameter of 50.802 mm and a contact width of 20.96 mm. It was 25.4 mm long with a 2.2 mm relieved section at each end. The peak to valley roughness of this roller varied from 2.95 μm to 1.43 μm and the RMS roughness from 0.25 μm to 0.21 μm, depending where on the circumference the measurement was taken. Figure 1 shows the region of minimum measured roller roughness. The bearings on the roller assembly were upgraded to ABEC-7 deep groove ball bearings and a new axle was machined to produce a total run-out of 2.54 μm.

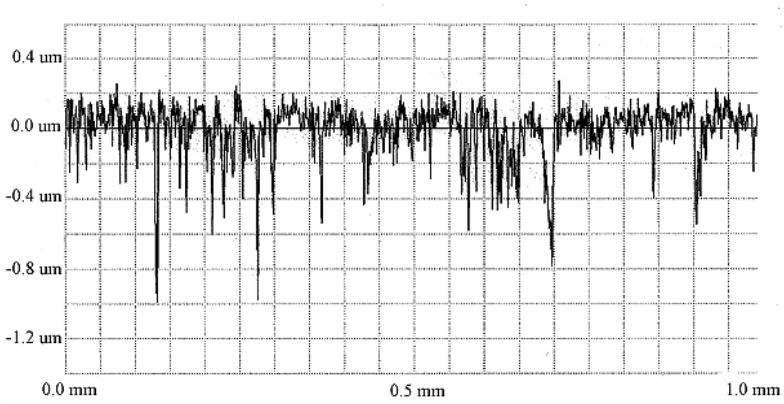

Figure 1 Talysurf profile of HIPed alumina roller

Charging tests done at a roller load of 7.3 N showed a change in land height of almost 1 µm after 60 minutes of continuous contact with the roller. Also, during charging with the roller, the initially white contact surface of the roller took on a dark coating. Tin etchant alleviates the discoloration on the roller. This is evidence of tin particles being present on the roller surface, most likely due to wear from the slip between the surfaces. The change in height is most likely due to a combination of yield due to the edge stresses as well as wear of the tin due to slip. To alleviate the applied load, a counterbalance, shown in Figure 2, was constructed to reduce the load between the plate and roller. The counterbalance was attached to the arm of the roller assembly and hung over the pivot point. Weights made of iron were placed on the stage, and in turn reduced the load of the roller onto the plate. A second charging experiment done at a roller normal load of 6.2 N showed no change in land height after charging.

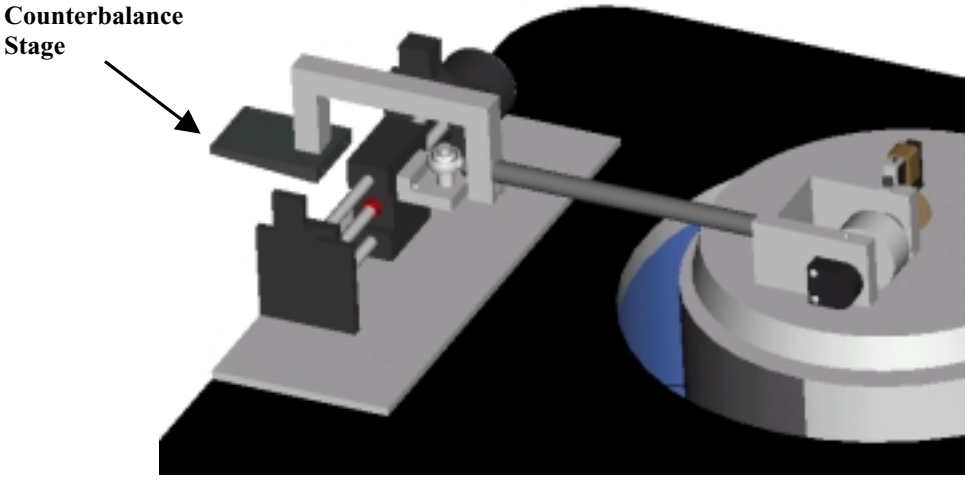

Figure 2 Illustration of roller charging mechanism with counterbalance

The slurry was changed from water-based to oil-based for this set of tests. In the quest to increase storage areal density of hard disk drives, the latest round of product development for heads involves using a Cobalt Iron Nitride layer in the read sensor. This alloy is very sensitive to corrosion due to a galvanic cell type of reaction with other alloys in the aqueous medium. Water

based lapping or cleansing steps that are currently used would destroy the active element of the head necessitating an oil-based slurry.

2.2.1 CREATING THE LAND SURFACE

To eliminate the effect of the grooving burrs, the tops of the lands were faced off using a large radius single crystal tool after the grooving cut. The grooving cut was done at a depth of 13 µm and a pitch of 80 µm with a land ratio of 0.25. This was followed with a pass using a 3.017 mm radius single crystal tool at a depth of ~3 µm and a feed of 10 $^{mm}/_{min}$. This cut could also be accomplished by cutting simultaneously with the grooving tool and the facing tool offset 10 µm in depth. It is recommended that shallow depths be used for the land-facing cuts, as previous trials have shown that a deep cut can cause a "smearing[2]" effect of the soft tin. Figure 3 shows a plug imaged at 500x before charging and 1000x after 10 minutes of charging. Trimming the lands optimizes the charging process. The elimination of the lands not only accelerated the charging quality per unit time, but also improved the overall appearance of the charged plate.

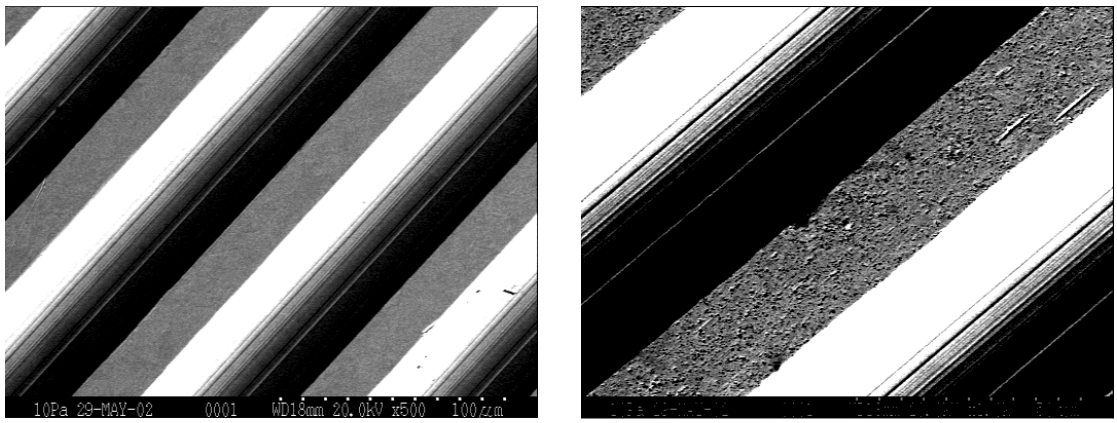

Figure 3 SEM images of plate surface after land-facing cut 500x before charging (left) and 1000x charged 10 minutes (right) with 5.5 N load - traversing roller

2.2.2 DIAMOND CONCENTRATION VS. CHARGING TIME

A study was performed to see how the diamond concentration grows with charging time using the HIPed roller. This can then be compared with the current fabrication process to estimate an optimal charging time. Using a plate with removable plugs, the HIPed roller charged the plate for a total of 60 minutes. The roller was traversed at a speed of 2.38 $^{mm}/_{sec}$ using a normal load of 5.5 N. A plug was removed every 10 minutes for observation in the SEM. This allows for an estimate of the diamond concentration on the surface of the plate. Figure 4 shows images of a plug surface after 10 minutes and 30 minutes of charging. It can be seen that the concentration of diamond grows with charging time.

[2] Creation of burrs that flow into the grooves and change the appearance of the grooved plate

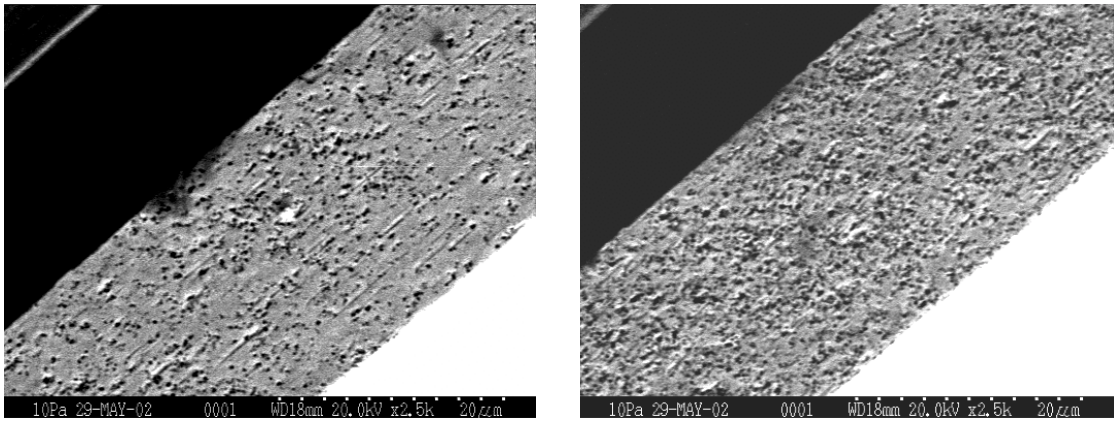

Figure 4 Images of charged surface with 5.5 N normal load at 2500x after 10 minutes (left) and 30 minutes (right) of charging – Traversing roller

Table 1 is a summary of the diamond concentration of the surface of the charged lands. The standard textured plate and charging ring process has an estimated 44.4% abrasive density in the charged areas after 60 minutes of charging. The abrasive density is an estimate of the percentage of area covered by diamond abrasive as measured by the histogram function of Adobe Photoshop.

Table 1 Summary of charged area abrasive density for various fabrication processes

	Local Abrasive Density on Land or Plateau		
Charge Time, min	**Groove Plate/ Roller**	**Grooved Plate/Ring**	**Texture Plate/ Ring**
0	0 %		
10	3.2 %		
20	6.5 %		
30	11.6 %		
40	12.1 %		
50	20.9 %		
60	21.6 %	10.1 %	44.4 %
Plate Charge Density[3]	5.4 %	2.5 %	1.8 %

One large difference between the texturing process and the grooving process is the land ratio of 4% for the textured plate versus 25% for the grooved plate. Thus, the estimated 44.4% abrasive density in charged areas is actually only 1.8% abrasive density over the entire area of the plate after 60 minutes of charging. The grooved plate and charging ring process produces an abrasive

[3] The overall plate charge density is the local density times the land ratio (25% for the grooved plate and 4% for the textured plate)

density of 10.1% in the charged areas, and a total abrasive density of 2.5% for the entire area of the plate after 60 minutes. The grooved plate and charging HIPed roller produce an approximate abrasive density of 21.6% in the charged area and a total abrasive density of 5.4% over the entire area of the plate after 60 minutes of charging.

To produce a grooved plate charged with the HIPed roller with the same material removal rate as the textured plate charged with the alumina ring process, it is estimated the plate charge density should be equivalent at 1.8%. This equates to a charged area abrasive density of 7.2% for the grooved plate/HIPed roller charging process. To create this density, the estimated charging time would be between 20 and 30 minutes. This is a significant improvement from the previous charging time of 60 minutes. The reduction of charging time not only helps accelerate the lapping plate fabrication process but also reduces the amount of diamond slurry – and the cost – needed to create the lapping plate.

2.2.3 ROLLER CHARGING AND PLATE FLATNESS

Plate flatness was determined to be an important factor for charging quality when using the standard rotating ring charging process. Due to the large contact area and large diameter of the ring, a plate figure error greater than 1 μm across the plate radius caused lower areas not to charge. To help alleviate this problem, the roller was designed to have a much smaller contact area and was given the freedom to rotate about 3 axes to follow the profile of the plate.

The flatness of a grooved plate was measured before and after charging, but this time the plate was charged using the roller. The roller had a normal load of 5.5 N during charging. The shape of the plate was measured in a spiral fashion. This was done by rotating the plate on the diamond turning machine at 50 RPM and traversing a capacitance gage from the outside edge to the center at 90 $^{mm}/_{min}$, or 1.8 $^{mm}/_{revolution}$. This traverse speed created a small overlap between each rotation of the plate. The profile of the plate was measured after grooving and again after charging. The P-V for the grooved plate is 0.7 μm and is 0.9 μm for the charged plate. Focusing on the profile of the grooved plate, as this is the profile that must be charged, the peak-to-valley is approximately the same as for the plate unsuccessfully charged during previous plate charging experiments using the charging ring. Plugs in the location of the low spot and the high spot were measured in an SEM and results in consistent charging at both locations as shown in Figure 5. This experiment verifies that the use of a roller can alleviate charging problems related with plate flatness previously encountered using the charging ring.

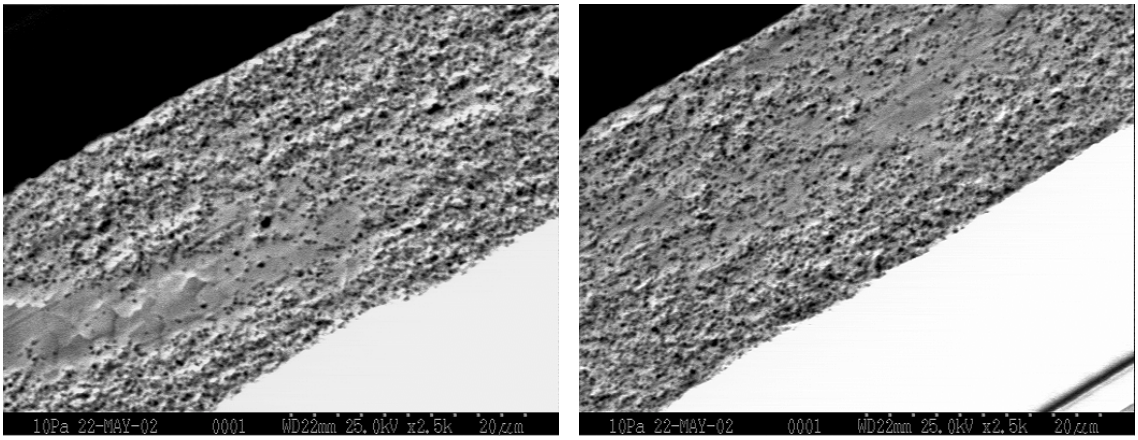

Figure 5. SEM images of tin surface charged with HIPed roller at plate radius locations low spot in the plate r=50 mm (left) and at the high spot r=120 mm (right)

2.3 LAPPING PERFORMANCE

The lapping performance of the plate charged with the HIPed roller mechanism was tested at IBM in San Jose, California. The lapping process consists of 24 AlTiC strips (1.2 mm x 47 mm) mounted to a foam pad as illustrated in Figure 6. This foam pad is vacuum chucked onto a lapping machine and is pressed onto the lapping plate with a pressure of 49 kPa. The AlTiC strips are oscillated across the lap plate in a sinusoidal motion with a 12 Hz frequency and an amplitude of 177.8 mm.

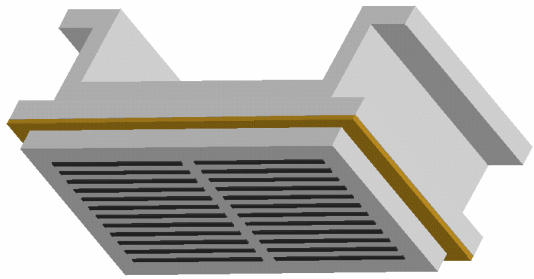

Figure 6 Vacuum chuck, foam pad and AlTiC strips

The lapping process is characterized by the material removal rate. Three grooved lapping plates were charged with the oil-based slurry using different charging mechanisms. The first plate was charged with the solid alumina charging ring. This plate had a 100 μm pitch with a land ratio of approximately 50%. The plate was charged for a total of 120 minutes using a 147.0 N weight on top of the charging ring. The slurry was applied at 10 $^{mL}/_{min}$.

The second was charged with a compliant alumina charging ring. This plate had the same geometry as the first; 100 μm pitch with a land ratio of approximately 50%. The compliant ring is similar to the solid alumina charging ring but has a small pad of rubber between the alumina

pieces and the metal ring. This rubber allows the alumina ring to conform to the shape of the plate during charging. The plate was charged for a total of 120 minutes using a 147.0 N weight on top of the charging ring. The slurry was applied at 10 $^{mL}/_{min}$.

The third plate tested was charged with the alumina charging roller. The pitch was 78 μm and the land ratio was approximately 33%. This plate was charged for a total of 30 minutes using a total normal load of 5.5 N. The slurry was applied at 9.5 $^{mL}/_{min}$.

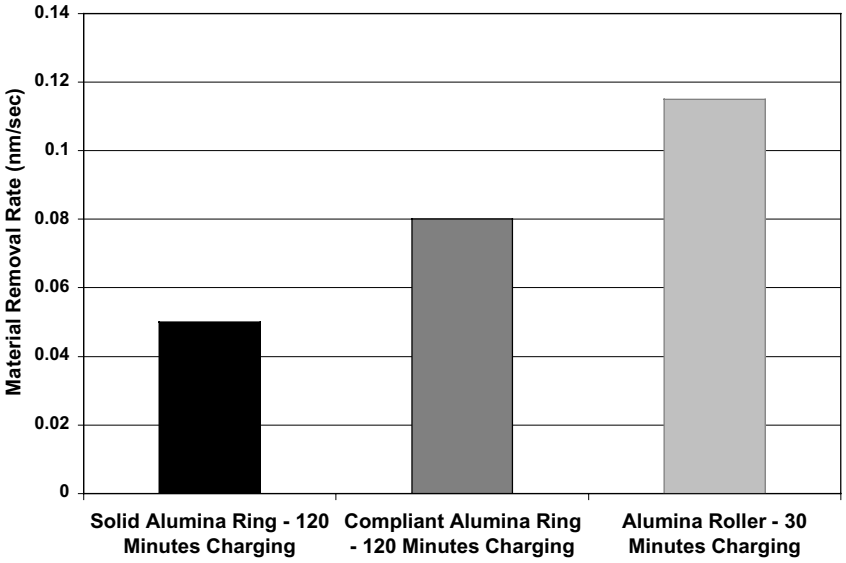

Figure 7 Material removal rates during lapping for different plate charging techniques

The material removal rates during lapping with the 3 different grooved plates are shown in Figure 7. The solid alumina charging ring has the smallest material removal rate of 0.05 $^{nm}/_{sec}$. This may be due to poor charging quality caused by a lack of full contact. The compliant charging ring has a higher material removal rate of 0.08 $^{nm}/_{sec}$ most likely due increased contact between the ring and the plate during charging.

The roller has over twice the material removal rate of the solid charging ring and about 1.5 times that of the compliant charging ring. It is important to note that the charging time for the roller charged plate is one-quarter of the other 2 methods. Thus, not only does the end product have a greater material removal rate, but the fabrication time is much lower. Also, only 285 mL of slurry was used in the roller charging process compared to 600 mL for the ring charging processes; a reduction of over 50%.

3 SCRIBING MECHANICS OF SINGLE CRYSTAL SILICON

Travis Randall
Graduate Student
Dr. Ron Scattergood
Professor
Materials Science and Engineering

A scribing apparatus was designed to translate a diamond tip across a surface at a constant rate for different loads. The diamond tip is used to produce scribes on single crystal silicon samples generating brittle-to-ductile transformation of the material beneath the scribe. The residual stresses resulting from the elastic-plastic constraint create a bending distortion in a wafer sample. Bend deflection was measured and extracted using an optical interferometer. With the absence of elastic fracture in the scribe region, the amount of plastically generated material in the transformation region was found to be proportional to the bend deflection. The current scribing apparatus has difficult attaining repeatable loading below 50 mN. A newly designed system will attempt to correct the problems associated with the current design, and is expected to attain repeatable loading in the 5-50 mN range.

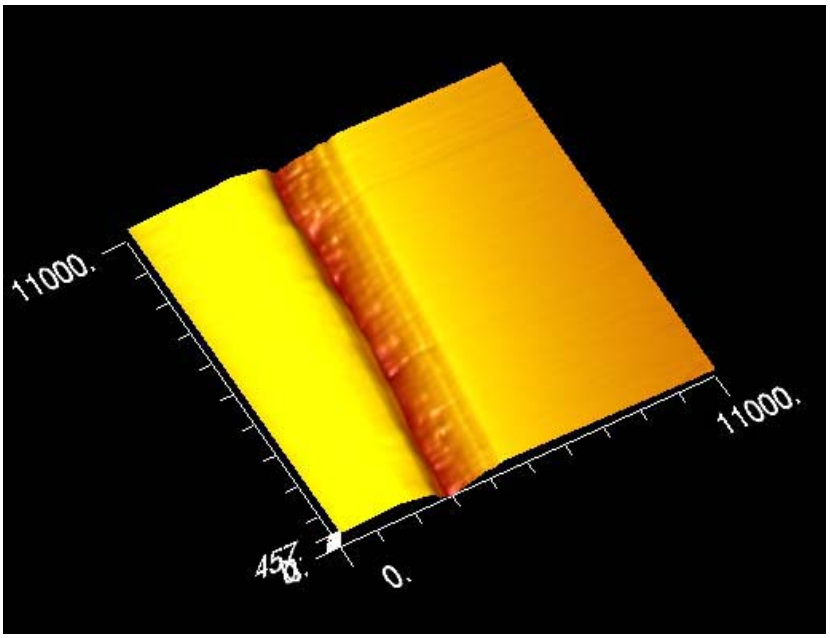

3.1 INTRODUCTION

This investigation is part a research program aimed at characterizing the effects of high pressure phase transformations of silicon, germanium, and silicon nitride during manufacturing processes such as slicing, grinding, lapping, and polishing. Subsurface fracture damage associated with material removal processes reduces part quality and lifetime. It is hoped that better understanding of the mechanics of the transformation can be used to improve the manufacturing processes of these material to produce devices at lower cost and higher quality.
The scope of this investigation is the study of the stresses generated within scribe grooves of single crystal silicon to better understand the nature of material removal during machining. Scribing tests act to model the grinding and polishing process by replicating the material deformation behavior of an individual grinding or polishing particle. Residual stresses are the result of line-force dipoles created by the elastic-plastic constraint of the deformed and displaced material. The scribes are placed on one face of a thin plate of Si. The difference in stress states on the opposing faces creates a bending distortion. This bending distortion can be used to approximate the residual stress created by the tensile dipole forces.[1] During the initial investigation, scribing data will be obtained for various directions on (100) and (111) crystallographic planes of silicon. Stress approximations will be coupled with Raman and SEM observations to aid in understanding the nature of the material deformation within the scribe zone.

3.1.1 HIGH PRESSURE PHASE TRANSFORMATION

It has been well documented that single crystal silicon undergoes phase transformation with the generation of high pressure on the surface by micro-indentation. [1-6] The nature of the microstructure in the transformation region has been examined by several methods including x-ray diffraction, Raman spectroscopy, transmission electron microscopy, and atomic force microscopy. Investigations of the transformation region created by micro-indentation report a phase transformation from diamond cubic (dc) structure to β–tin phase. Further phase transform to an amorphous phase or R8/BC8 crystal structure was seen after unloading at low and higher loads, respectively. [2] The amorphous phase is believed to exist because kinetics may prohibit the β–tin phase from returning to dc structure upon unloading. [3] (It is also suggestion that creation of amorphous phase may be due to high defect concentration or dislocation activity.) [2] The transformation to the metallic β–tin phase is thought be responsible for anomalous plastic flow behavior without fracture seen in contact loading experiments.

The implication of the ductile behavior is, that using careful machining conditions, single crystal silicon may be ground or diamond turned in the ductile regime. It is hoped that ductile-machining will reduce cracks and dislocations generated by machining on the surface and subsurface regions that can reduce the mechanical integrity and lower the operation lifetime of

the components. This study aims to employ a bend effect model to characterize residual stresses within the transformation zone as well as Raman spectroscopy to identify phases present.

3.2 EXPERIMENTAL DESIGN

3.2.1 METHOD

Topographic data is collected for the sample using a ZygoGPI Laser interferometer. Samples were then scribed at various loads ranging from 10-500 mN. The effects of multiple, adequately spaced scribes on one sample are additive and produce a more statistically significant measurement than that of a single scribe. This is also necessary to generate measurable deflection. The sample is measured again in the interferometer after scribing. Metropro, the software suite used to analyze the interferometer data, allows the user to subtract the data collected before scribing from that collected after scribing. The resulting profile created is the net bending effect. The data collected from the Zygo is then converted with a utility to an ASCII format. The Y and Z data for an X approximated as the center of the long axis is then used to create a plot of the bend profile. Microsoft Excel is used to graph these values. The generated plot is then used to approximate the angle of deflection from the initial state. This angle of deflection is correlated to the residual stresses created by scribing using the bend effect model.

Scribes will be studied with scanning electron microscopy to determine the nature of material removal within the scribe trace and to observe the fracture behavior/plastic deformation in relation to crystallography. Raman spectroscopy will be used to identify differences in structure between the untouched silicon and that within the scribe. It is hoped that an amorphous phase can be identified within the transformation zone.

The initial stages of this investigation will entail collecting bend data as well as SEM on Raman measurements for (100) and (111) crystallographic orientations of silicon. Scribing along the <100> and <110> will be studied for the (100) orientation. <110>, <112> directions will be studied for the (111) orientation. Later investigations of silicon will be to evaluate the influence of polishing slurries on scribing mechanics such as cutting depth, nature of material removal, and stresses generated within the scribe. While it was expected that use of polishing slurries would decrease the surface hardness, initial experiments by Patten have found the opposite. [7]

3.2.2 FIRST GENERATION SCRIBING SYSTEM

A Zwick microhardness tester is fitted with a Dynatex diamond tip in a custom holder as pictured in Figure 1a. To produce a scribe, the sample is translated under the diamond tip such that a cutting edge is oriented in the scribe direction. The samples are held firmly in place between two glass slides mounted to the stage with brackets. A motorized stage is used to create translation at

a constant rate of 0.250 mm per second. The holder was designed to hold the cutting edge of the tip at an angle of 3.3 degrees from the sample surface as shown in Figure 1b. The desired load is placed on the loading sleeve and the tip is positioned and contacted to the surface of the sample. The stage is translated with relation to the diamond tip producing the scribe.

A counter-balance relying on a knife edge is used for loads lower than the dead weight of the indenter and fixtures. This setup has difficult achieving repeatable loading below 50 mN, believed to be due to frictional forces in the dashpot mechanism as well as difficulties with the counterbalance system. A second generation apparatus is currently being designed and built to attain loading as low as 10 mN. A schematic is pictured in Figure 1c.

(a.) Picture of first generation scribing setup

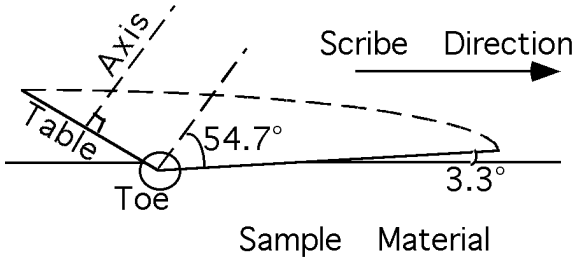

(b.) Geometry of tip to sample surface

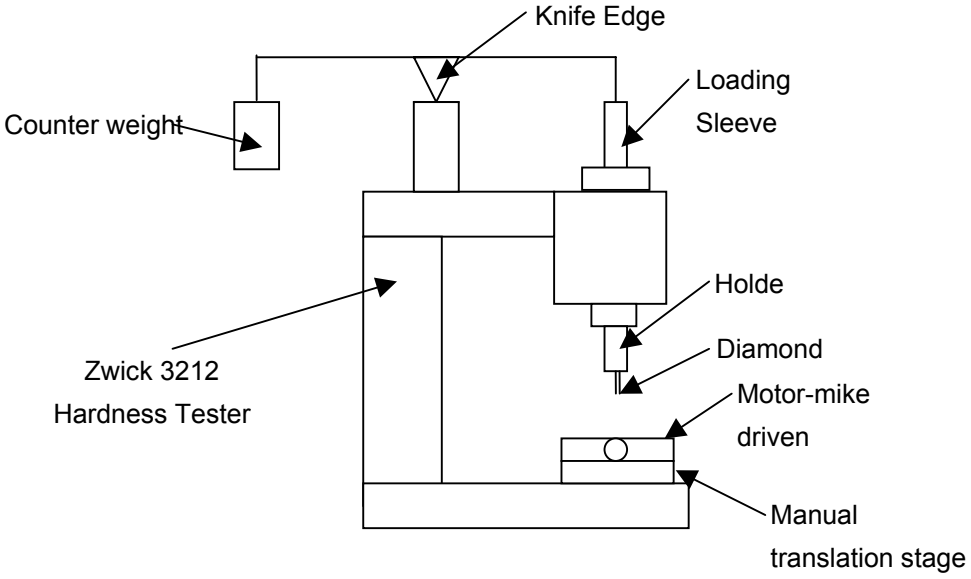

(c.) Schematic of Loading Sytem

Figure 1. First generation scribing system.

3.2.3 SECOND GENERATION SCRIBING SYSTEM

The second generation system was designed to eliminate the problems thought to create poor loading reproducibility below 50 mN. The new system has the tip holder affixed an slider air bearing to reduce friction in the loading (vertical) direction. A counter balance system between the bearing slider and the counterweight consists of two Airpot™ stock actuators connected by a hose. A vacuum is kept between the two chambers; effectively transferring the load of the counterweight to zero the weight of all moving parts (slider, holder, and tip) not intended to generate load. The head will feature a loading tray which, when loaded, will generate dead load on the tip. The whole system will be mounted between two plates and can be driven up and down into contact with the sample by an attached stepper motor. The design will most likely use the original scribe mount used to angle the tip at 3.3 degrees to the sample surface. The XY motor-mike driven stage will also be retained for this system. A schematic of the design to be built is illustrated in Figure 2.

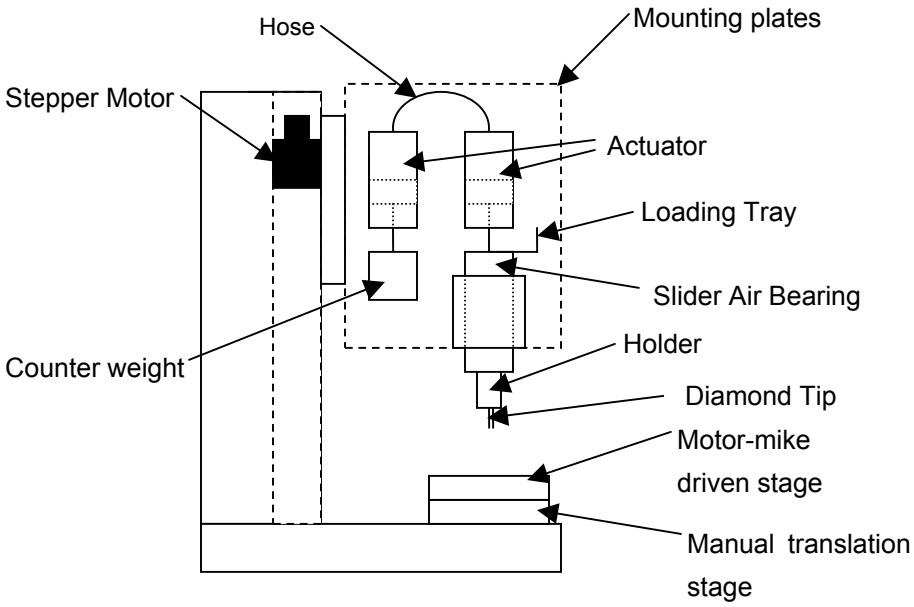

Figure 2. Schematic of second generation scribing system.

3.2.4 ANALYTICAL APPROACH

For the initial part of this investigation involving silicon, the ZygoGPI Laser interferometer was used to measure the change in profile of a sample. This is accomplished by subtracting the profile collected on an as-received sample from that of the scribed sample. Metropro allows for

the direct subtraction of the data points from each profile. The bend profile is represented by a 3-D oblique plot as shown in Figure 3. The data is then converted to a line plot format with a conversion utility. An X is selected that is estimated to be the center of the long axis. The Y and Z data for that X is used to generate a 2-D profile in which the flat portions of the profile can be fit to lines and the angle of the deflection from the flat position can be calculated. (For small angles the angle is approximately the arctan of the slope. Figure 4 illustrates an example of a 2-D bend profile generated with fitted lines.

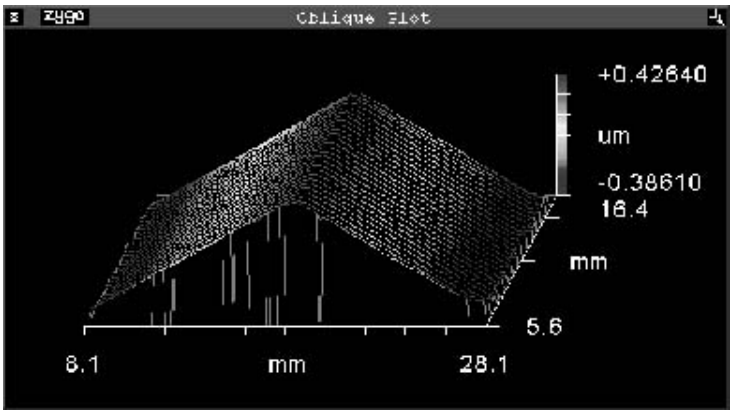

Figure 3. Oblique plot of bend angle effect generated in Metropro.

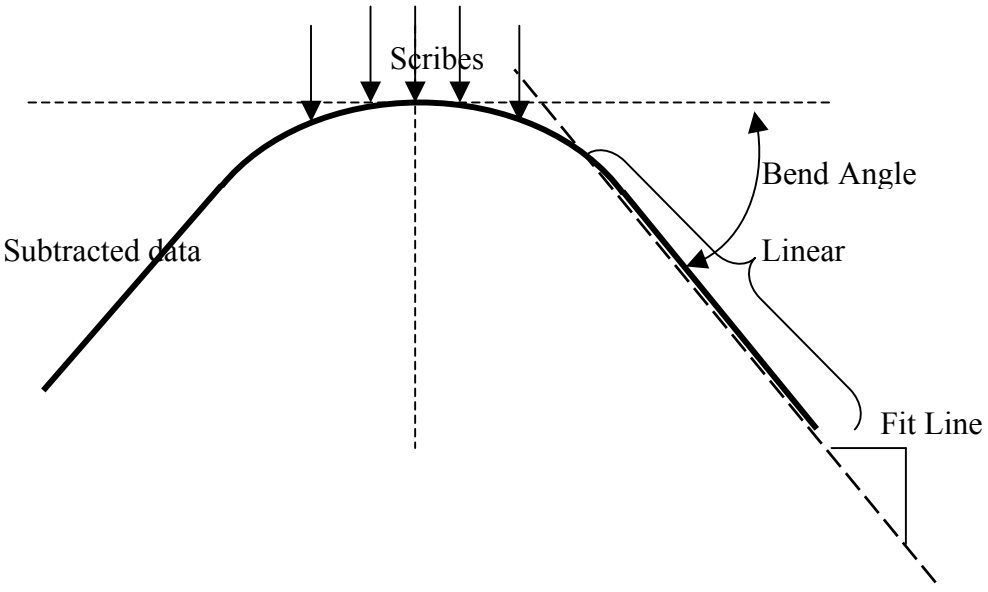

Figure 4. 2-D profile of bend effect showing line fit to flat portions and bend angle [1].

A model shown in previous work [1] to accurately reflect the bend effect generated by the line-force dipoles created from a scribe will be used to characterize residual stress in the single crystal silicon. A line-force dipole, shown in Figure 5, will be used to model the elastic-plastic

deformation zone along a scribe path. The dipole forces act outward from the scribe trace since the surrounding elastic material is forced outward by the plastically deformed material region after unloading. The line-force dipole model was extended from a model created by Yoffe [8] in which orthogonal dipole forces acting on an elastic half space describe residual forces left by indentation. The line-force dipole model is derived by the superposition of the dipole "blister" fields proposed by Yoffe. Standard elasticity solutions [9] are used to obtain the line-force dipole stresses for a limiting case of infinitesimal dipole spacing. By applying the line-force dipole stresses to a beam bending problem the stresses will be then be approximated as a function of loading and bend angle from prediction curves created in previous work.

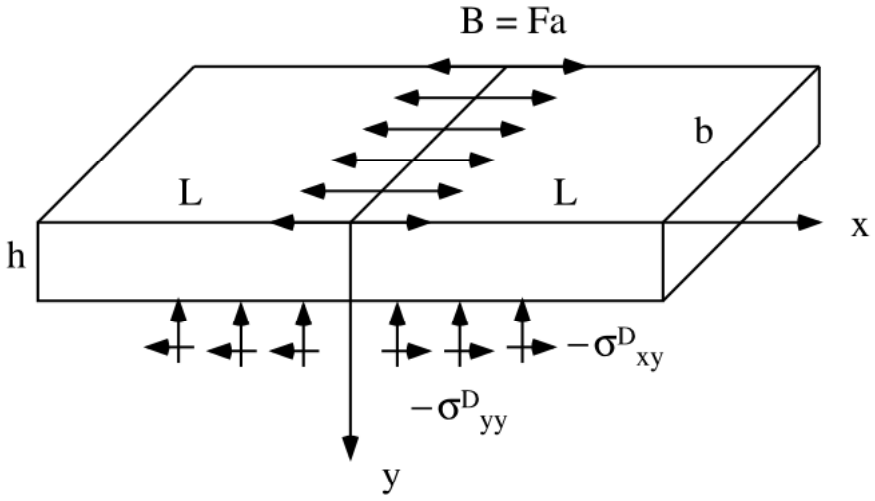

Figure 5. Line-force dipole model.

3.3 RESULTS

Load plotted versus bend angle for initial experiments done with scribing in the <011> direction on (100) silicon with the first generation setup are presented in Figure 6. Each sample was viewed under an optical microscope to make an initial observation on material removal processes. If no chipping is present along the scribe traces, it is reasoned that the material removal is mostly controlled by plastic mechanisms. If chipping is apparent, it is reasoned that the material removal is influenced by elastic fracture mechanisms, and that the plastically deformed material will be removed in the process. For the samples represented in Figure 6, chipping was not seen for samples loaded below 150 mN (15g.) These data points appear to correspond to a linear trend in the plot suggesting that bend angle is directly proportional to the plastically deformed material generated.

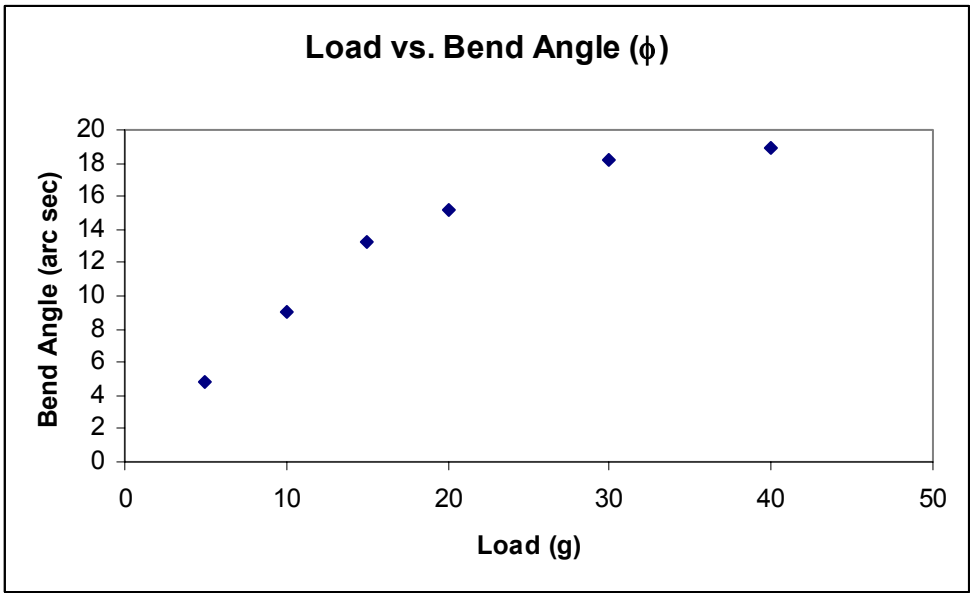

Figure 6. Load vs. Bend Angle for <011> on (100) silicon surface

Subsequent testing was done for other crystallographic directions but is incomplete and will not be reported here. The next generation scribing system is need for loading lower that 50 mN. Every crystallographic direction for the two different orientations exhibited brittle fracture at loading above 50-100 mN under 500x optical magnification. SEM and Raman measurements are currently under way, but significant data has not been collected or analyzed for presentation at this time.

3.4 CONCLUSIONS/FUTURE WORK

Preliminary results show that a bend effect is created during scribing of the surface of single crystal silicon. It is expected that the bend effect model developed in previous work can be extended to single crystal silicon to accurately characterize the residual stresses within the plastically displaced regions. The bend effect will be directly proportional to the amount of plastically displaced material. The effects become confounded as chipping due elastic fracture occurs. The current method of profile subtraction using the interferometer appears to produce accurate, easy to interpret data. Testing and data analysis methods are being refined for Raman analysis to produce better data for characterization of the transformation zone. SEM analysis will be a high priority to characterize material removal processes during scribing. The development of the second generation scribing system is expected to allow scribing with reproducible loading below 50mN.

REFERENCES

1. B. Austin. M.S. Thesis, North Carolina State University, 2000.
2. I. Zarudi, L.C. Zhang, J. Zou. "Microstructures of phases in indented silicon: A high resolution characterization." Appl. Phys. Lett. **82,** 7 (2003.)
3. B.V. Tanikella, R.O. Scattergood. "Phase transformations during microcutting tests on silicon." Appl. Phys. Lett. **69,** 19 (1996.)
4. I. Zarudi, L.C. Zhang. "Structure changes in mono-crystalline silicon subjected to indentation-experimental findings." Tribology International **32** (1999.)
5. V. Domnich, Y. Gogotsi, S. Dub. "Effect of phase transformations on the shape of unloading curve in nanoidentation of silicon." Appl. Phys. Lett. **76,** 16 (2000.)
6. X. Zhao, B. Brushan. "Material removal mechanisms of single-crystal silicon on nanoscale and at ultra low loads." Wear 223, 66-78. (1998.)
7. J. Patten, S, Mumford. "Effects of fluids on the ductile deformation of silicon." ASPE 2000 Annual Meeting, Proceeding, p. 604. (2000)
8. E. H. Yoffe, "Elastic Stress Fields Caused by Indenting Brittle Materials", Phil. Mag. A, vol. 46, no. 4, 617 (1982).
9. K. L. Johnson, "Contact Mechanics", Cambridge Univ. Press, p.17 (1985).

4 DESIGN AND DEVELOPMENT OF A DROP DISPENSOR

Elizabeth A. Chatham
Undergraduate Student
Thomas A. Dow
Professor
Department of Mechanical and Aerospace Engineering

This project involves the design and development of a piezoelectrically-driven drop dispenser that will deliver fluid droplets that have a volume on the order of 0.5 nanoliter. A fluid flow model of the process was developed based on models described in the literature. This model was then used to optimize the component dimensions to create the desired drop size. The device consists of two main parts: 1) an etched silicon/SiC fluid chamber with multiple cavities and nozzles and 2) a sheet of piezoelectric material cut into multiple beam actuators used to pressurize each cavity. The silicon wafer will be processed at MCNC based on a design developed by the PEC. Once the components are fabricated, they will be assembled into a test fixture designed at the PEC and tested. This testing will consist of static and dynamic tests of the actuator motion and light microscope examination of the droplet volume.

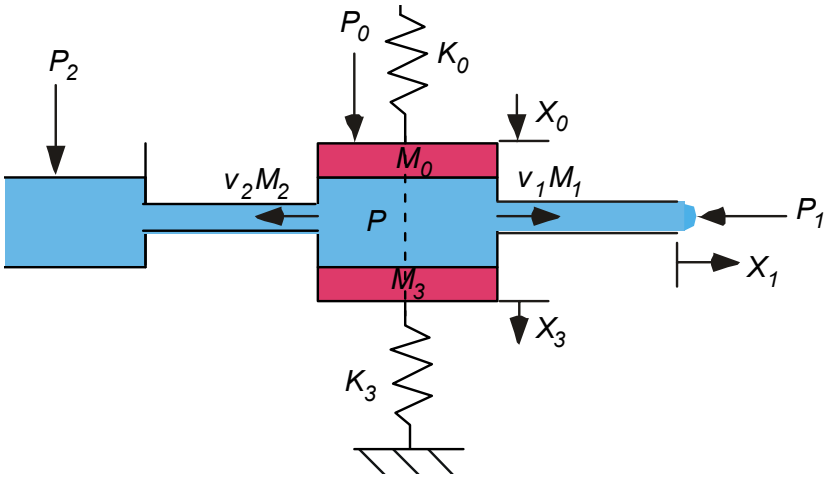

4.1 NOMENCLATURE

A_c cross sectional area of the central cavity, m^2
A cross sectional area, m^2
a acceleration, m/s^2
B bulk modulus, Pa
β viscous damping coefficient, Ns/m
b equivalent diameter, m
E modulus of Elasticity, Pa
I area moment of inertia, m^4
G_i shape function
l length, m
l_l length to the left of the dividing line of the cavity, equivalent length of the inlet, m
l_R length to the right of the dividing line of cavity, equivalent length of the outlet, m
l_C length of the cavity, m
m mass, kg
M_C mass of the fluid in the cavity, kg
M_L mass of the fluid to the left of the dividing line, kg
M_R mass of the fluid to the right of the dividing line, kg
M_T total mass of the fluid in the system ($M_C + M_L + M_R$), kg
K spring constant, N/m
P load or force, N
p pressure, Pa
r radius, m
t thickness, m
w width, m
V volume, m^3
v velocity, m/s
x position, m
$\dot{x}$ velocity, m/s
$\ddot{x}$ acceleration, m/s^2
z aspect ratio
α curvature factor
α_3 piston curvature factor
δ deflection, m
γ Possion's Ratio
η kinematic viscosity, m^2/s
ρ fluid density, kg/m^3
σ surface tension, N/m
ω_n natural frequency
τ time, s

4.2 INTRODUCTION

4.2.1 INK JET DESIGNS

Ink jet printers have been available for approximately 20 years. The first design developed simultaneously at Canon and HP (1979) involved creating a bubble by heating the fluid and that bubble forced a spurt of ink from a nozzle. The other design developed by Seiko Epson used a piezoelectric actuator to pressurize a fluid filled cavity and force a drop out of a nozzle. In the current Drop on Demand (DOD) ink jet printing systems, the bubble jet printers (thermal) have approximately twice the sales as the piezoelectric designs.

For the application of interest to the sponsor, the temperature spike due to the heating and bubble creation was not attractive so the piezoelectric type of actuation was selected.

4.2.2 PIEZOELECTRIC ACTUATION

The design of a piezoelectric actuator for a droplet generator involves a fluid cavity with one or more walls that move to pressurize the fluid. In addition, there are holes in this cavity to allow the drop to be dispensed and the cavity to be refilled. The relative size of these holes with respect to the size and shape of the fluid cavity determines the size of the drop produced.

Figure 1 shows the features of an Epson print head found in a commercial ink jet printer. Beginning at the top of the drawing, this design uses a thin sheet of piezoelectric material that has separate actuators coated on the surface to create individual actuators. Note that there are 8 individual electrodes on each side of the print head to pressure the 16 individual fluid wells of this design. These actuation electrodes are on the bottom the piezoelectric sheet. The common electrodes are on the top the sheet and are attached together. If a square wave is put on one of the actuator electrodes with respect to the common electrode, the sheet will deform in the region of the electric field.

The piezoelectric sheet is attached to a well plate containing 16 wells. Each well has a pair of holes that allow the fluid to move to the nozzle as well as refill the well from the reservoir. When the piezoelectric sheet is actuated, it bends into the well pressurizing the fluid in that particular well. The pressure pushes the fluid through holes in the bottom of the well, the reservoir sheet and through the nozzle on the lower membrane. At the end of the actuation pulse, the piezoelectric contracts and the negative pressure pulls fluid from the reservoir back into the well. The holes for the nozzle and the refill port must be sized such that the pressure pulse pushes most of the fluid out of the nozzle hole but the refill port must be large enough to refill the well after the drop is generated. The design problem is to find the optimum size of the cavity and the nozzle and refill holes.

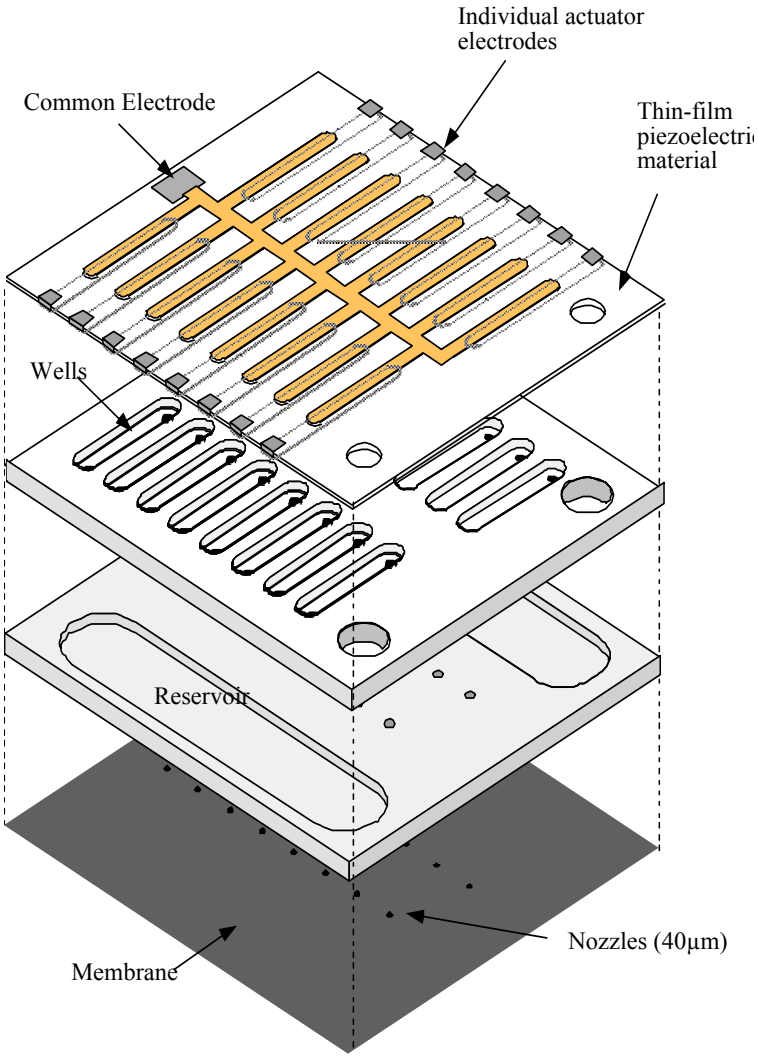

Figure 1. Drawing of an Epson Ink Jet Printer

Another similar design that fits the needs of this project was developed in Sweden by Laurell [2]. It is a similar design to the Epson print head described above. However, this design was developed for the same application as that envisioned by the sponsor; that is, rapid sample handling in chemical microsystems and automated high-throughput analysis for screening systems. Laurell used a piezoceramic bimorph to actuate the fluid. A bimorph is a pair of piezoelectric sheets that bend when actuated with an electric field. As shown in Figure 2, the upper sheet will shrink when the voltage is applied and the lower sheet will grow. This combination will make the sandwich bend toward the cavity and eject a small drop of fluid. The bimorph actuates the cavity through standoffs that have been shown to be more efficient in providing motion than gluing the piezoelectric sheet directly to the top of the fluid cavity. A single piezoelectric element could also be used but with a reduction in stroke and force.

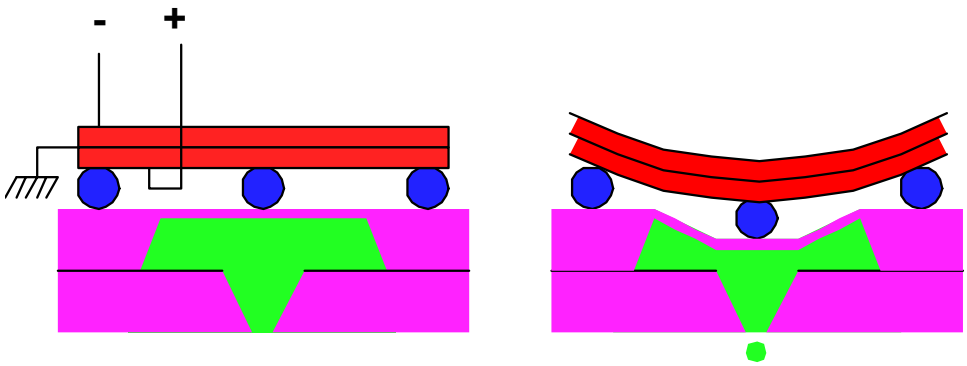

Figure 2. Side view of the Laurell design for drop dispenser

One goal of the proposed design is to provide the means to have a wide variety of different chemicals dispensed. As a result of this requirement, the drive system should be separated from the reservoir of fluid. It is desired that the reservoir be removable from the actuator so that it can be discarded and a new reservoir with different chemicals can be attached. Clearly this is an advantage of the design shown in Figure 2 over that illustrated in Figure 1. The Epson design uses the actuator as the roof of the fluid cavity whereas in the Laurell design, the actuator and the fluid cavity are separate elements.

4.3 MODEL OF DROP DISPENSOR

The system was modeled using a C program initially based upon Edmond L. Kyser's paper "Design of an Impulse Ink Jet" [1] that was modified to fit the specific parameters of this drop dispensing application.

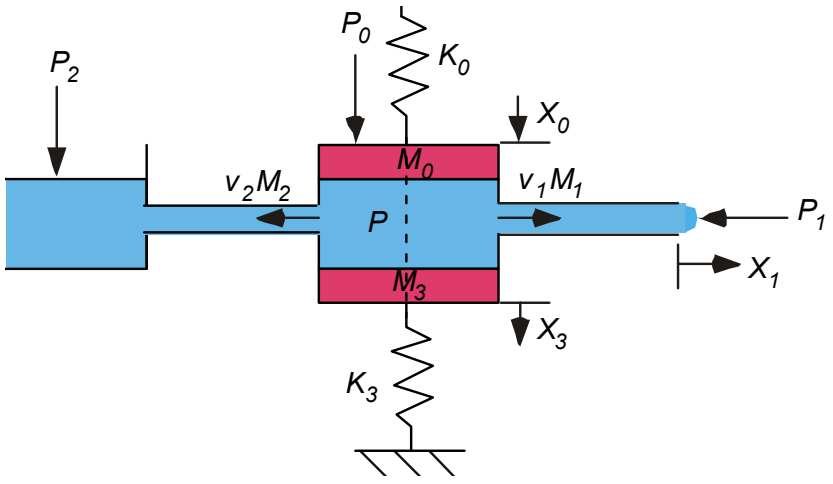

Figure 3. Impulse Ink Jet model as depicted by Kyser [1]

Kyser describes a four-part system model shown in Figure 3. The components of model are the driven element (denoted *0*), the outlet (*1*), the inlet (*2*), and the passive compliance segment (*3*). The drop (*4*) must be examined but is not part of the system as it has already been ejected. The orientation of the actual device to be built for the sponsor will be slightly different because the drops are ejected from the bottom not the right side. In Figure 3, M indicates mass, K correspond to spring constants, v stands for velocity, x for position, and p for pressure.

4.3.1 MASS CALCULATIONS

All of the mass in the system must be considered including the mass of the fluid in the central cavity, which is not directly assigned to any of the four labeled components. The geometry of the system and the density of the fluid are known so the masses are calculated by:

$$M = \text{length} \cdot \text{width} \cdot \text{thickness} \cdot \text{density} \tag{1}$$

The mass of the driven element (M_0) is the sum of the mass of the piezo and the silicon nitride layer used to transmit the force from the piezo to the fluid. Although the silicon nitride will cover the entire surface of the silicon wafer, only the portion that is suspended - and therefore deflecting - is included in this mass calculation.

The unassigned mass in the central cavity is added to the mass of the inlet fluid and the mass of the outlet fluid so that all the fluid mass is moving either toward the inlet or toward the outlet. This is done so that all the pressure created by the piezo moves fluid in these two directions. This models flow along pressure gradients, being created by the higher pressure in the central cavity and lower pressures outside the inlet and outlet. An imaginary line or plane (dotted line in Figure 3) is inserted into the cavity to divide the fluid into two regions, the placement of this division is mathematically found through the calculation of equivalent lengths and masses.

Outlet Mass The mass of the fluid in the outlet can be calculated but must include a portion of the central cavity fluid to find an equivalent mass. The equation 2 is a weighted average used to determine the equivalent length of the volume of fluid to the right (l_R) of the dotted line in Figure 3, toward the outlet.

$$l_R = l_C \left\lceil \frac{M_L + M_C}{M_T + M_C} \right\rceil \tag{2}$$

Using the definition of mass as volume multiplied by the density and canceling the density terms, the equivalent length formula can be written as follows:

$$l_R = l_C \left\lceil \frac{V_{inlet} + V_{cavity}}{\left(V_{inlet} + V_{cavity} + V_{outlet}\right) + V_{cavity}} \right\rceil \tag{3}$$

This equivalent length can now be used to find the equivalent mass of the outlet, the new M_1, shown in the equation 4 below:

$$M_1 = \left[\left(A_{cavity} l_R\right) + \left(A_{outlet} l_{outlet}\right)\right]\rho \tag{4}$$

The first volume term above is the calculation of the portion of cavity fluid being assigned to outlet; the second volume represents the fluid present in the actual outlet region. The mass is calculated from the volume and the fluid density.

Inlet Mass The calculation of the equivalent length to the left of the dotted line (l_L) is similar to that of the outlet. The equivalent length formula remains the same with the exception of the first term in the numerator.

$$l_L = l_C\left[\frac{V_{outlet} + V_{cavity}}{\left(V_{inlet} + V_{cavity} + V_{outlet}\right) + V_{cavity}}\right] \tag{5}$$

The equivalent mass (M_2) can then be calculated as in equation 6.

$$M_2 = \left[\left(A_{cavity} l_L\right) + \left(A_{inlet} l_{inlet}\right)\right]\rho \tag{6}$$

Compliance Mass The passive compliance mass(M_3) is a theoretical term representing the mass of any part of the system that will deflect due to cavity pressure. The most obvious possibilities being the silicon walls holding the fluid. In this system it is assumed that these walls will not deflect and a large mass value is used so that the cavity pressure will not be able to deflect the mass and confirming the no deflection assumption.

Drop Mass The mass of the drop (M_4) is found by calculating the volume of the cylinder formed as the fluid advances a distance (x_1) out of the outlet and then multiplying by the density of the fluid, shown below.

$$M_4 = \left(A_{outlet}\left(x_1\right)\right)\rho \tag{7}$$

4.3.2 BEAM ANALYSIS

Spring Constants

The flexibility of each member of the system controls its response to the applied forces and pressures. The spring constants of the piezo and the flexure are combined as springs in parallel to

determine K_0. The piezo is modeled as a simply supported beam with the governing deflection equation:

$$\delta = \frac{P\ L_{piezo}^3}{48\ E_{piezo}\ I_{piezo}} \tag{8}$$

The area moment of inertia is found using the formula below:

$$I = \frac{wt^3}{12} \tag{9}$$

Then using the definition of $\frac{P}{\delta} = K$ deflection, the spring constant expression is:

$$K_{piezo} = \left(\frac{48\ E_{piezo}\ I_{piezo}}{L_{piezo}^3} \right) \tag{10}$$

The silicon nitride film flexure is modeled as a flat circular plate with a fixed perimeter, the deflection formula is:

$$\delta = \frac{P\ a_{flexue}^2}{16\pi\ D} \tag{11}$$

where D is a geometric term containing both mass moment of inertia and the elasticity properties (E and ν)

$$D = \frac{E_{flexure}\ t_{flexure}^3}{12(1-\nu^2)} \tag{12}$$

and $b_{flexure}$, the characteristic length, is defined by:

$$b_{flexure} = \sqrt{\frac{A_{cavity}}{\pi}} \tag{13}$$

Using the definition of deflection the spring constant can be expressed as:

$$K_{flexure} = \frac{16\pi\ D}{b_{flexure}^2} \tag{14}$$

Using the expression for springs in parallel K_0 is determined by the following formula:

$$K_0 = K_{piezo} + K_{flexure} \tag{15}$$

The spring constant of the passive compliance portion of the system, K_3, is used to include compliance in the structure containing the fluid. The silicon structure is stiff (K_3 is high) and the small forces associated with the bimorph piezoelectric actuator will produce negligible displacement. When this value is combined with the large M_3 discussed previously, the deflection will be small and the natural frequency will be low.

The natural frequency of the piezo and the entire system can be calculated and are valuable to understand the performance of the system. When the system is operating at or near the natural frequency, it will behave differently and produce excessive vibration. The natural frequency, ω_n, can be calculated using the following formula:

$$\omega_n = \frac{1}{2\pi}\sqrt{\frac{k}{m}} \tag{16}$$

4.3.3 FLUID ANALYSIS

Damping

Unlike the structural portions of the system examined previously the orifice and reservoir are both bodies of fluid. Due to their fluid properties viscous damping values must be calculated for both masses of fluid. The viscous flow formula comes from Poiseuille's law, shown below:

$$dF = \eta G_i v_i(x) dx_i \tag{17}$$

This law describes the change in flow rate for an infinitesimal section of fluid of length dx_i and cross-sectional area $A_i(x)$. The i denotes the channel identification label, η is the symbol of kinematic viscosity, and v_i is the velocity.

The continuity relation for channel velocity shown below, states that any infinitesimal piece of fluid is traveling at the same velocity as the average channel fluid, v_c.

$$v_c A_c = v_i A_i \tag{18}$$

After dividing through by $A_i(x)$ this equation can be rewritten in terms of pressure and constant channel velocity using

$$dP = \eta\left(G_i \frac{A_c}{\left(A_i(x)\right)^2} \right) v_c dx_i \tag{19}$$

By defining a viscous damping coefficient, β, the ratio of pressure to percent of volume reduction, the formula for the viscous damping coefficient is:

$$\beta = \eta G_i(x) \left(\frac{A_c}{A_{outlet}} \right)^2 \tag{20}$$

The shape function $G_i(x)$ is known to be 8π for a circle, but neither channel in this system is circular so the shape factor formula is given by:

$$G(x) = 12 \left[0.33 + 1.02 \left(z + z^{-1} \right) \right] \tag{21}$$

where z is the aspect ratio. For square channels z is 1 because the sides are of the same length and the ratio of two adjacent sides is 1. The square geometry is used in this model.

4.3.4 FORCING FUNCTION

Force is applied to the system by the deflection of the piezoelectric bimorph in response to an applied voltage pulse. The magnitude of voltage and the shape of the pulse were designed to control the size of drop and cycle time of the system. The pulse is divided into three time periods, a pre-pulse time, a pulse time, and a decay time. The voltage used in the model is depicted in Figure 4.

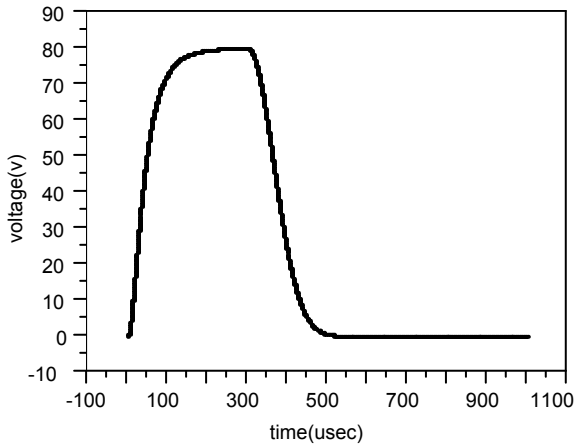

Figure 4. Example Voltage vs. Time plot for applied voltage pulse.

This applied voltage can be converted to a force using the equation below where the constant 0.023 is obtained from manufacturer's literature about the specific piezo being used.

$$Force = 0.023 \cdot Voltage \cdot \left(\frac{w_{piezo}}{l_{piezo}} \right) \tag{22}$$

4.3.5 PRESSURE

The system is controlled by the pressure created when the force is applied. There are also three fluid pressures: the cavity pressure (P), the inlet pressure (P_2), and the outlet pressure (P_1). The fluid will change volume when it is pressurized depending on the bulk modulus, B. The bulk modulus is defined as the ratio of pressure to the % decrease in volume.

$$B = \frac{P}{\frac{\Delta V}{V}} = \frac{PV}{\Delta V} \tag{23}$$

It is the inverse of compressibility. The fluid being compressed is the fluid in the central cavity upon which the piezo force is acting. The fluid pressure is reduced as a result of the compressibility and can be written as a function of a fluid spring constant, K_{fluid}, defined as:

$$K_{fluid} = \frac{B}{V_c} A_c^2 \tag{24}$$

With this stiffness, the displacement (x_4) of the piston due to the compressibility can be written.

$$x_4 = \frac{A_c}{K_{fluid}} P \tag{25}$$

The pressure gradients are created by the difference in the central cavity pressure compared to the inlet pressure and the outlet pressure. The inlet pressure in the model shown in Figure 3 is atmospheric pressure. Depending on the type of fluid inlet used for the system, P_2 could change and as a result, the pressure gradients would change.

The outlet pressure includes the meniscus pressure. A meniscus, the curved portion of fluid, forms due to the surface tension (σ) holding the fluid molecules together. The meniscus is what forms the drop in this system.

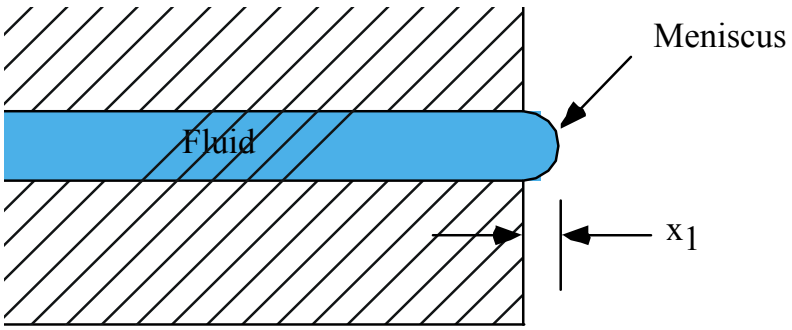

Figure 5. Forces acting on fluid

When the pressure in the fluid is greater than zero, the fluid is forced out of the outlet and forms the meniscus. The outlet pressure pushing the fluid back into the cavity has been estimated by Kyser [1] to be:

$$p_1 = \frac{2\sigma}{r_{orifice}} \sqrt{\frac{16x_1^2}{16x_1^2 + A_{orifice}}} \tag{26}$$

4.3.6 SYSTEM ACCELERATION EQUATIONS

The system is composed of four accelerations that are related through a continuity equation. Newton's second law of motion states that the sum of forces acting a body is equal to the mass of the body multiplied by the acceleration of that body. This law has been rearranged as followed and then applied to the four components of the system.

$$a = \frac{1}{m} \sum F \tag{27}$$

The spring constants, pressures, and damping coefficients can all be easily converted to forces. Hooke's law states that the spring constant multiplied by the distance the spring is deflected equals the force, the unit analysis of this is shown below.

$$F = kx = \frac{force}{deflection} deflection = force \tag{28}$$

Similarly the damping coefficient multiplied by the velocity of the fluid also results in a force, unit analysis is shown below.

$$F = \beta v = \frac{force \bullet time}{displacment} \frac{displacment}{time} = force \tag{29}$$

Pressure by definition is force per unit area so multiplying pressure by area yields force.

The motion in the system begins with the pressure produced by the deflection of the bimorph resulting from the applied voltage. The effect on the central cavity is two-fold, the fluid is compressed and accelerated away from the flexure. The acceleration equation below encompasses both of these reactions. The three terms in this equation represent the force from the piezo, the deflection of the flexure, and the compressibility of the fluid.

$$a_0 = \frac{1}{M_0} \left(F - K_0 x_0 - K_{Fluid} x_4 \right) \tag{30}$$

The acceleration of the fluid in the outlet (a_1) is driven by the pressure gradient and impeded by the damping effects of the fluid.

$$a_1 = \frac{1}{M_1}\left(A_{outlet}\left(p + p_2 - p_1\right) - \beta_1 v_1\right) \tag{31}$$

The inlet acceleration term (a_2) is also composed of the pressure driving force and the damping force.

$$a_2 = \frac{1}{M_2}\left(A_{inlet} p - \beta_2 v_2\right) \tag{32}$$

The third acceleration comes from the passive compliance components included in the system to account for the effects on the containing structures of the fluid. This term assumed to be negligible because the walls of the structure will not deflect or deform under the pressure being applied. For continuity in the system this component must still be included.

$$a_3 = \frac{1}{M_3}\left(A_3 p - K_3 x_3\right) \tag{33}$$

The continuity equation for this system is:

$$-\alpha A_0 \dot{x}_0 + A_1 \dot{x}_1 + A_2 \dot{x}_2 + \alpha_3 A_3 \dot{x}_3 + {Vp}/{B} = 0 \tag{34}$$

Where α and α_3 are curvature constants for the force generator and the passive compliance elements of the system. This can be rewritten with a series of area ratios, shown below:

$$a_4 = \frac{1}{A_c}\left(\alpha A_c\right) - \frac{1}{A_c} A_{outlet} - \frac{1}{A_c} A_{inlet} - \frac{1}{A_c}\alpha_3 A_{passive} \tag{35}$$

4.3.7 DROP FORMATION

Fluid is ejected from the outlet opening due to the pressure created in the cavity. If the applied force is a constant force not a pulse, the drops would break off when a mass of fluid extended from the end of the orifice is large enough to overcome the surface tension holding the fluid together. There would be no way to control how many drops were ejected from the system. In this system, the goal is to eject a single drop each time the voltage pulse is applied. Once the force is removed the flexure that forms the roof of the cavity deflects in the opposite direction creating a pressure gradient to pull new fluid in from the reservoir. The velocity of the fluid in the outlet (V_1) crosses from positive to negative during this time. At the point in time that this velocity is zero, a drop is assumed to be detached from the column of fluid in the outlet. This

mass of fluid (M_4) is no longer considered part of the system. The fluid remaining in the outlet is then sucked back toward the cavity a short distance. The system is returned to equilibrium by the refill action; that is, fluid is drawn in through the inlet to return the total fluid volume and cavity pressure to the initial values before force was applied.

4.4 ITERATIVE ANALYSIS USING HUEN METHOD

The Heun method, also known as the improved Euler's method, is an iterative approximation based on the trapezoidal rule used for to solve definite integrals. The trapezoidal rule can be expressed as:

$$\int_{x_0}^{x_n} f(x)dx \approx h\sum_{j=0}^{n-1}\left(\frac{f(x_j)+f(x_{j+1})}{2}\right) \tag{36}$$

where h is the incremental step size. In this report the method is applied to obtain velocity and displacement so the $f(x)$ can be expressed as an acceleration term, $\ddot{x}$. The equation is further reduced because only two values are required for the computation. Implementing these simplifications and computing the velocity from the acceleration values produces:

$$\dot{x}_n - \dot{x}_0 = h\left(\frac{\ddot{x}_n - \ddot{x}_0}{2}\right) \tag{37}$$

Replacing the subscript n and 0 notation with values representing a functions of time, t equivalent to the 0 subscript, and $\tau + \Delta\tau$ equivalent with the n. The final equation is constructed:

$$\dot{x}(\tau+\Delta\tau) = \dot{x}(\tau) + \frac{1}{2}\left(\ddot{x}(\tau)+\ddot{x}(\tau+\Delta\tau)\right)\Delta\tau \tag{38}$$

Or in words, the final velocity equals the initial velocity plus the average acceleration multiplied by the time step. Using the same methods acceleration and position formulas are obtained and are shown below.

Acceleration:
$$\ddot{x}(\tau+\Delta\tau) = \frac{1}{2}\left(\ddot{x}(\tau)+\ddot{x}(\tau+\Delta\tau)\right) \tag{39}$$

Position:
$$x(\tau+\Delta\tau) = x(\tau) + \frac{1}{2}\left(\dot{x}(\tau)+\dot{x}(\tau+\Delta\tau)\right)\Delta\tau \tag{40}$$

These calculations were performed to find the acceleration, velocity, and position values for each of the four parts of the system at each time period as the driving loop mechanism of the program.

4.5 SIMULATION

A simulation of the drop dispenser using geometric dimensions listed in Table 1 was conducted for discussion here.

Table 1. Dimensions for Simulation

Feature	**Dimensions, µm**
Flexure Side	300
Inlet Channel Depth	20
Outlet Side	35

Each time the program is run it outputs the following information, shown in Table 2. The upper portion of the table describes the system, the masses dimensions, spring constants, areas, and natural frequencies are all calculated before the iterative process begins and do not need to be recalculated at any additional points during the simulation. The remainder of the information is based on the iterative process.

Table 2. Program Input Values

Item	Symbol	value	units
mass piston	M_0	2.96555e-06	kg
mass outlet	M_{outlet}	4.2733e-08	kg
mass inlet	M_{inlet}	4.27307e-08	kg
mass passive	M_3	1e+100	kg
piezo area moment	I	1.82907e-15	m^4
Equivalent length outlet	l_R	0.000474987	m
Equivalent length inlet	l_l	0.000475013	m
spring K pressure generator	K_0	42749	N/m
spring K passive	K_3	1e-100	N/m
spring K piezo	K_{piezo}	36522.8	N/m
spring K flexure	$K_{flexure}$	6226.25	N/m
spring K compressibility	K_{fluid}	194211	N/m
viscous damping outlet	β_{outlet}	0.153819	N/m/s
viscous damping inlet	β_{inlet}	2.88618	N/m/s
shape factor	G_i	28.44	
cavity area	A_c	9e-08	m^2
outlet area	A_{outlet}	1.225e-09	m^2
inlet area	A_{inlet}	2.828e-10	m^2
passive area	A_3	9e-08	m^2
Compress area	A_c	9e-08	m^2
natural frequency(system)	$\omega_{n\ system}$	19108.7	Hz
natural frequency(piezo)	$\omega_{n\ piezo}$	12492.5	Hz

Table 3. Program Output Values

Simulation Duration		1,000,000	cycles
Delta time		0.001	µsec.
Output interval (400 cycles)		0.4 usecs	µsec.
Drop Volume		57.2885	pL
Drop Detachment Time		5.689860e+02	µsec.
Maximum pressure		9.78978e+06	Pa
Time @ maximum pressure		1.613050e+02	µsec
Minimum pressure		-1.31408e+06	Pa
Time @ minimum pressure		6.734680e+02	µsec
Maximum distance in the outlet		0.0336017	mm
Maximum distance in the inlet		0.000414026	mm

The program also creates a text file that records time, force, pressure and meniscus pressure as well as the acceleration, velocity, and positions of all elements (0, 1, 2, 3 and 4) at the end of each output interval, in this simulation every 400 iterations. The data stored in this file can be used to generate plots of any recorded variable(s) versus time or another variable for further analysis of the performance.

The applied voltage is translated into force that applies pressure on the fluid in the system. Figure 6 shows the force versus time and pressure versus time plots. The amplifier and the electrical characteristics of the system dictate the shape of the force vs. time trace. Figure 6 also illustrates the direct relationship between the pressure and applied force. The oscillation in the pressure plot is caused by the rapid excitation ringing the system at its natural frequency. That shape is also repeated in velocity and acceleration plots for most elements in the system.

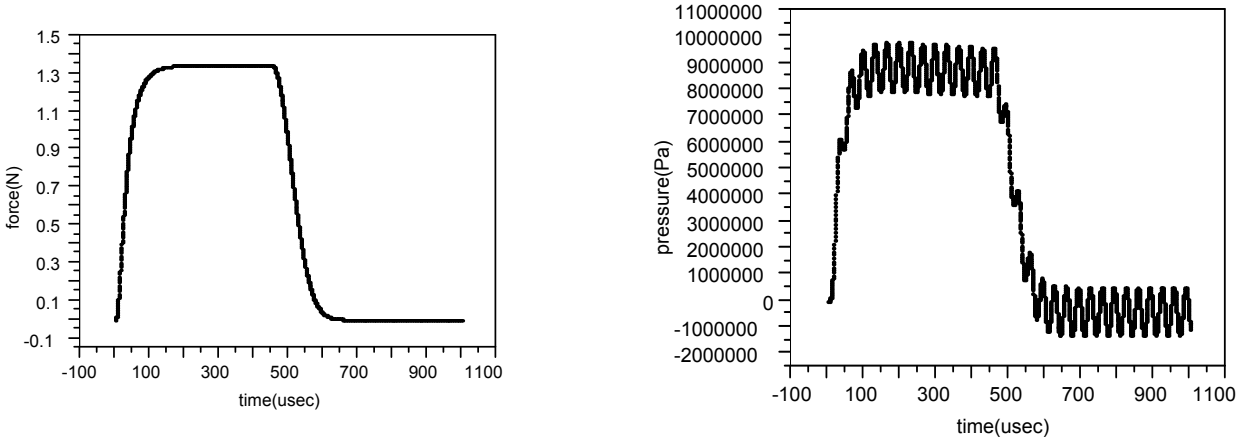

Figure 6. Force and Pressure plots from sample simulation.

The process of drop detachment is illustrated in Figure 7. This figure shows the velocity and position of the fluid in the outlet during the simulation. The velocity plot has the same shape as the pressure plot seen previously, which makes sense because the pressure is driving the velocity. The position plot has a discontinuity at the point in time that a drop detaches. The position is then negative as the cavity pressure causes the fluid to withdraw into the orifice a small distance.

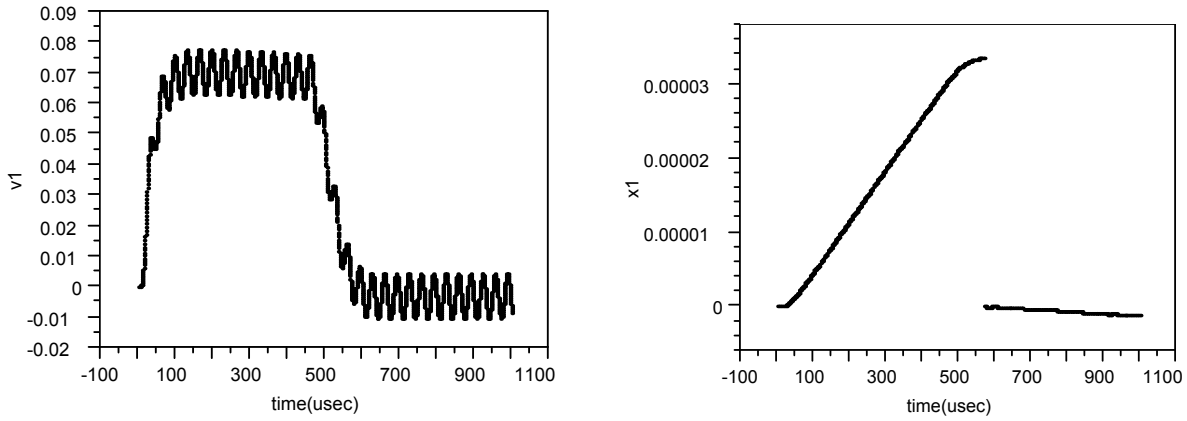

Figure 7. Outlet Velocity and Position of the Fluid in the Outlet

4.5.1 DESIGN

A series of simulations was conducted based on varying the nozzle area, flexure area, and reservoir channel depth. The nozzle dimensions were chosen based on areas varied from 400μm^2 to 4230 μm^2 in steps of 575 μm. The flexure area was set to either 200 μm or 300 μm, and the channel depths used were 20 μm, 50 μm, and 80 μm. All other aspects of the system were kept constant. The maximum pressure and drop volume was recorded for each simulation and the values are shown in Table 4.

Table 4. Simulation Results

Wafer	Design ID	Nozzle Side (μm)	Channel Depth (μm)	Flexure Side (μm)	Program Results	
					Max Pressure (psi)	Drop Volume (pL)
1	1a	20	20	200	372.71	3.419
	1b	28	20	200	159.29	19.917
	1c	37	20	200	98.86	47.034
	1d	44	20	200	69.86	64.749
2	2a	20	20	300	141.00	2.606
	2b	28	20	300	137.57	12.957
	2c	37	20	300	120.71	61.683
	2d	44	20	300	96.57	115.622
5	5a	50	50	200	35.57	46.187
	5b	55	50	300	27.71	60.709
	5c	60	50	200	21.14	76.985
	5d	65	50	200	15.71	96.893
6	6a	50	50	300	59.71	31.39
	6b	55	50	300	54.86	69.372
	6c	60	50	300	49.57	115.39
	6d	65	50	300	43.86	154.443
7	7a	50	80	200	12.14	34.345
	7b	55	80	200	10.86	46.477
	7c	60	80	200	9.71	62.35
	7d	65	80	200	5.14	82.076
8	8a	50	80	300	38.71	31.179
	8b	55	80	300	36.57	39.876
	8c	60	80	300	34.00	52.486
	8d	65	80	300	31.14	90.288

Two of the original eight wafers were eliminated from the design process after preliminary analysis of the results. Wafers 3 and 4 had drop volumes very close to zero because the reservoir was much larger than the orifice and so the majority of the fluid was forced back into the reservoir. The drop volumes of the remaining nozzles were sorted and graphed, shown in Figure 8. These drop volumes are distributed over a large range of volumes approximately centered around the target volume range of 40 to 60 pL.

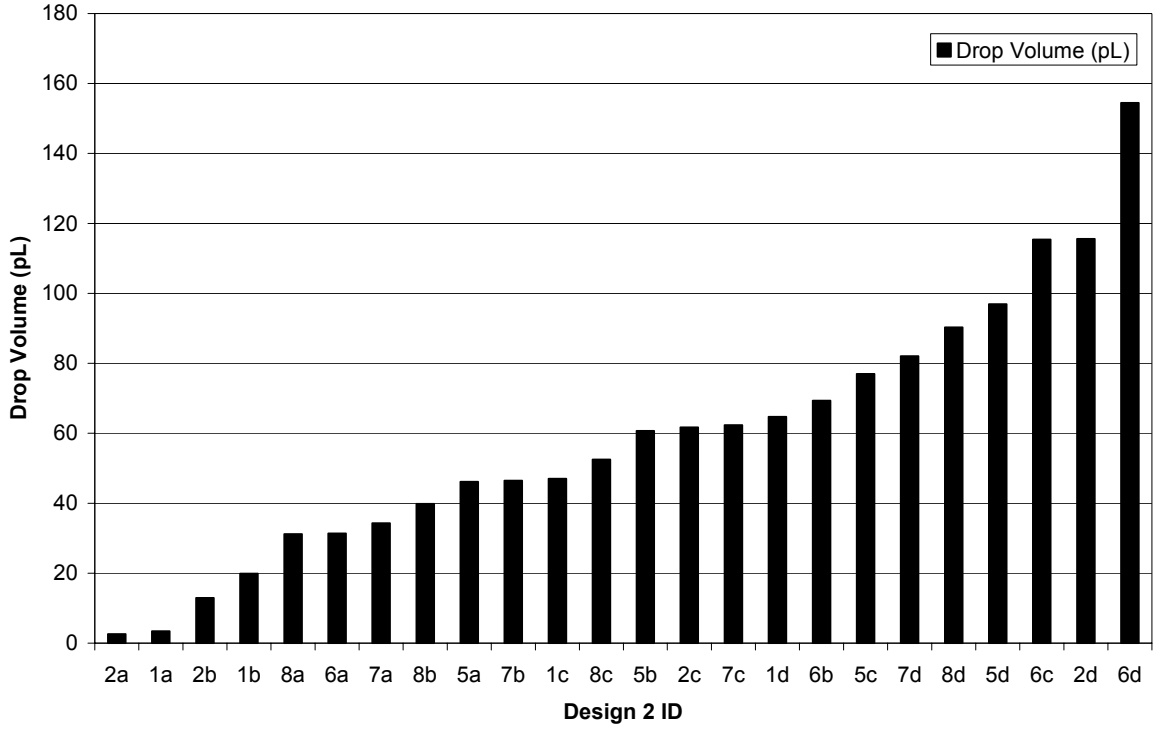

Figure 8. Sorted drop volume chart

Based on the success of the simulations of these six wafers, the designs were selected for manufacturing and testing.

4.6 DESIGN OF DROP DISPENSER

4.6.1 PIEZOELECTRIC DRIVER

The driving force to produce a droplet is a piezoelectric actuator in the form of a beam situated above the fluid cavity. An electrical pulse produces a movement of the beam toward the cavity and increases the pressure in the cavity. The properties of the piezoelectric material, its thickness and the length and width determine the force/voltage relationship.

Piezoelectric materials are ceramic with properties that allow them to be poled in a magnetic field at high temperature to produce electric dipoles. When such a material is exposed to an electric field, the dipoles will align themselves with the field and displacement will take place. The direction of poling can be arranged so that displacements in different directions can occur with a given electric field direction. For the actuators used in this design, the electric field is

applied across the thickness of the sheet and it either grows or decays in length based on the direction of the electric field.

The magnitude of the displacement of a piezoelectric element depends on the stiffness of the structure against which it acts. If the structure's stiffness is much less than the actuator, the actuator will produce its total displacement. If the stiffness of the structure is equal to the actuator, the displacement will be cut in half. If the structure is much stiffer than the actuator, the displacement will approach zero but the force will be the same in each case. Therefore, both the displacement desired and the properties of the structure must be considered when designing the actuator.

Shape and Size

A sheet of piezoelectric material was purchased from Piezo Systems, Inc. in Cambridge, MA. This was a standard product (#T215-H4CL-503X) with overall dimensions of 63.5 by 31.8 mm and a thickness of 0.38 mm. It is a sandwich of two active piezoceramic materials each poled in opposite directions so that if a voltage is applied from the top to the bottom of the sheet, the upper half will contract and the lower half will expand to produce force and displacement.

Characteristics

For the application of interest, the sheet described above was laser cut into a small size to fit into drop dispenser package. Based on the information supplied by Piezo System, the particular bimorph design selected (5 mm long by 0.4 mm wide) that is fixes at each end should produce the following results.

Capacitance The capacitance of the bimorph in nanofarads will be a function of the area of the actuator; that is the length (l in m) and width (w in m) times a constant.

$$C = 91.6\text{x}10^{3} wl = 0.183 \text{ nf} \tag{41}$$

Blocking Force The blocking force in N (maximum force against an immovable object) is a function of the ratio of the width to length.

$$F_b = 1.84\frac{w}{l} = 0.147\text{N} \tag{42}$$

Displacement The maximum displacement for 80 v excitation is a function of the length squared.

$$x_{\max} = 89\text{x}10^{-3} l^2 = 2.2\mu\text{m} \tag{43}$$

Mass The density and the volume of the actuator determines the mass.

$$m = 5.86x10^{-3}\frac{\text{gm}}{\text{mm}^3}\cdot 5\text{mm}\cdot 0.4\text{mm}\cdot 0.38\text{mm} = 4.45\text{mg} \tag{44}$$

Natural Frequency The natural frequency is a function of the mass, shape and the stiffness of the bimorph.

$$w_n = \frac{0.846}{l^2} = 34\text{KHz} \tag{45}$$

Modulus of Elasticity The material modulus is 94 GPa.

4.6.2 SILICON FLUID CAVITY

Geometric Limitations on Shape

The etching process being used to create cavities and channels in the silicon wafer imposes geometric limitations on the chosen design. The process being used etches in a square pattern, each square is slightly smaller than the previous square. Instead of the smooth walled passages and circular openings envisioned, pyramidal shapes with square openings will actually be created. The geometry of these pyramids is based on the 54.47˚ slope created on each face etched, shown in Figure 9. This geometry change alters the way dimensions are specified as well as the volumes of fluid present in the system. Dimensions must be specified by the upper openings not the lower openings. The specification of the slope allows calculation of the upper opening using the formula shown below.

$$M = \frac{2H}{\tan(54.47^\circ)} + N \tag{46}$$

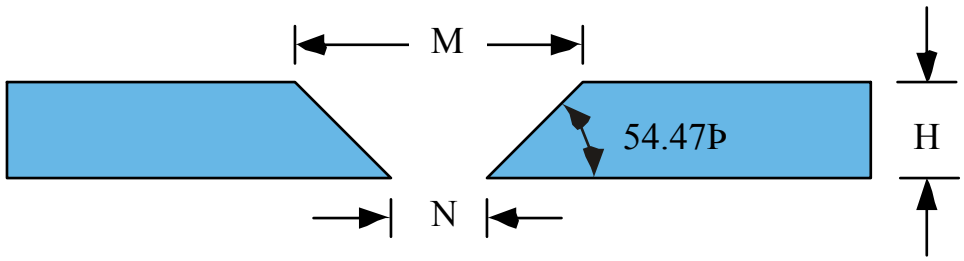

Figure 9. Etching Slopes

The reservoir channel will also be etched in this fashion but only on one of the two chips. This results in a channel with a triangular cross-section. The volumes of fluid are calculated as pyramids with square bases. The volume of a pyramid with a square base is calculated using the following formula:

$$V = \frac{1}{3}(base\,side)^2(height) \tag{47}$$

Most often the volumes are not complete pyramids, the openings create pyramids without peaks. These are calculated by separating the volume into two regions, a rectangular prism with the base having the dimension of the outer opening, and a complete pyramid with base dimensions, *M*–*N*.

$$V = N^2 H + \frac{1}{3}(M - N)^2 H \tag{48}$$

4.6.3 ASSEMBLY AND ALIGNMENT

Assembly of Driver and Fluid Cavity

The two components of the drop dispenser, the piezoelectric driver and the fluid cavity, are assembled into a fixture used to both align them and hold them together. A cross-sectional view of this fixture is shown in Figure 10. The base contains a slot into which the silicon fluid cavity is inserted and holes in the bottom that expose the 4 nozzles. The piezoelectric driver is placed on top of the fluid cavity and aligned using four 0.4 mm diameter hypodermic needles. These needles fit through 0.4 mm holes in both the piezoelectric driver and the fluid cavity and pass through larger holes in the base of the fixture. A cover is placed on the aligned components and a pair of screws are tightened to hold the assembly together.

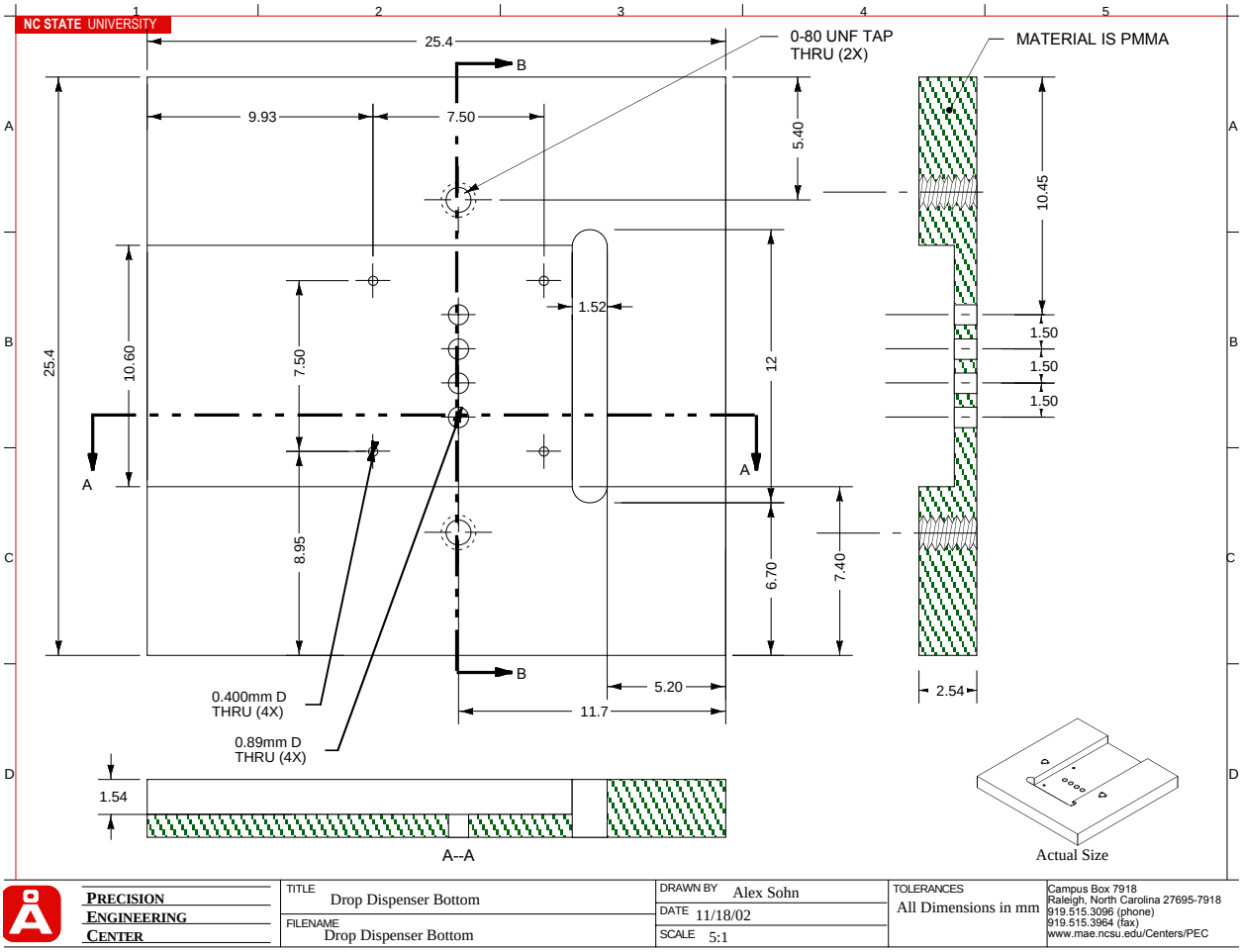

Figure 10. Drop Dispenser

Micro-ball spacer – Based on results of other drop dispenser designs, separation between the piezoelectric actuator and the fluid cavity creates larger displacements and higher pressures. To this end, a small sphere will be attached to the center of each piezoelectric driver to separate it from the silicon nitride diaphragm. The diameter of the ball will be large enough to allow manipulation and connection to the center of the piezoelectric beams yet small enough not to damage either component due excessive deflection. Plastic spheres on the order of 5-10 μm will be used.

4.7 CONCLUSION

The assembled drop dispenser will be tested to study the performance of the different configurations of fluid cavity shape built by the sponsor during the fabrication phase. Different central cavity volumes, orifice sizes and reservoir sizes were produced and should provide a variety of drop volumes. To set up the system for these measurements, other components must be assembled and tested including the amplifier. These performance measurements include:

- Static Displacement Measurement
- Pulse Shape
- Dynamic Displacement Measurement
- Drop Size and Frequency

A proposal has been submitted to extend the project to include assembly and performance testing of the drop dispenser prototypes.

REFERENCES

1. Kyser, Edmond L., "Design of an Impulse Ink Jet," Journal of Applied Photographic Engineering, Volume 7, pages 73-78, 1981.

5 ANALYSIS ON DYNAMIC PERFORMANCE OF PIEZOELECTRIC BIMORPH CANTILEVERS

Tao Wu
Graduate Student
Paul I. Ro
Professor
Mechanical and Aerospace Engineering

Analytical prediction of dynamic performance for piezoelectric bimorph structures was investigated. Damping ratio was assumed and employed to determine dynamic peak amplitudes at resonances by finding the frequency with $1/\sqrt{2}$ *of peak amplitude. Finite element simulations were used to validate the proposed improvement strategy. Results show that the peak amplitude determination method is good enough to predict the dynamic performance in many applications. Effects of bonding layers were also analyzed by both static and dynamic methods. Bonding influence can be minimized by selecting appropriate bonding materials and dimensions of structures.*

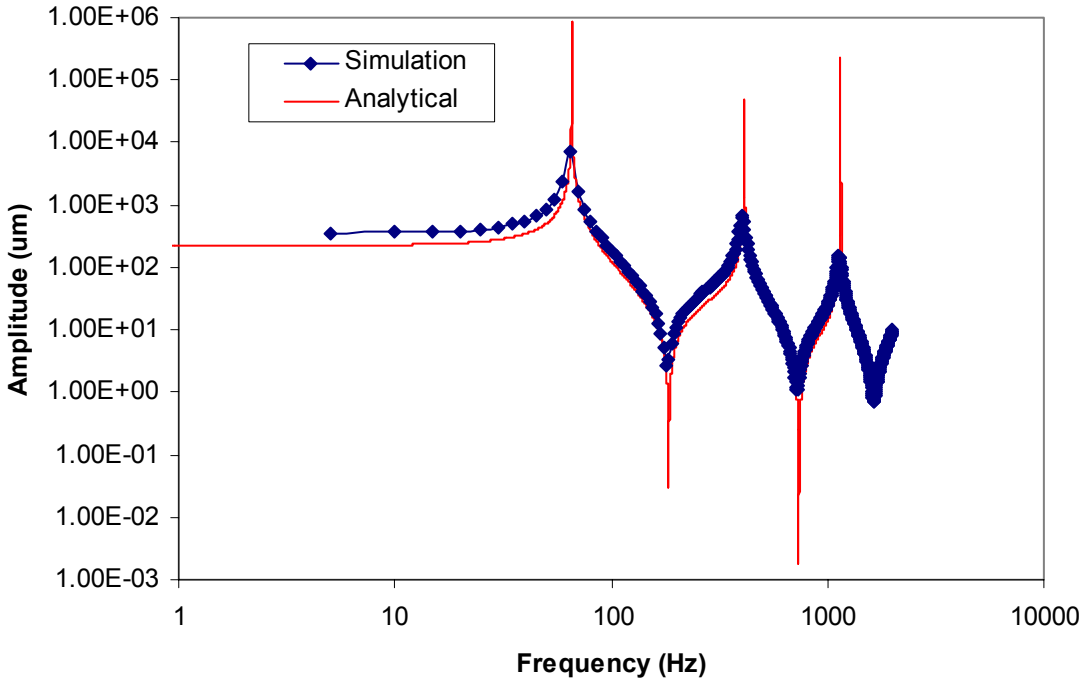

5.1 INTRODUCTION

There is growing interests in the use of piezoelectric materials in smart structures. Piezoelectric bimorphs are one of the most important structures. The principle setup of bimorph is made by bonding two piezoelectric materials to each side of a passive elastic plate. When an electric field is applied across the thickness in such a way that one piezoelectric element contracts while the other expands, the entire bimorph structure produces curvature.

Much work has been carried out to predict the static behavior of piezoelectric bimorphs [1-4]. Among the models predicting the interaction between the induced strain actuators and the structure to which they are bonded, pin-force is one of the earliest models which was derived from mechanics considerations [1]. Under "mechanics considerations", the actuator is treated as a separate body which manifests itself to the substrate only in the form of applied forces and moments. Elementary beam theory is used to compute the resulting deformations in the homogeneous beam. This model is invaluable in understanding the physics of induced strain actuator.

There are relatively fewer studies on dynamic performance prediction. Specifically, Crawley and de luis [5] presented a comprehensive static model for a piezoelectric actuator and a substructural coupled beam. These static results were then used to predict the dynamic behavior of the coupled system. The dynamic response thus obtained is approximate and needs to be qualified by direct dynamic modeling of the coupled system. Pan et al's dynamic model [6] was developed for a simply supported elastic beam with a piezoelectric actuator glued to each of its upper and lower surfaces. Their model allows the calculation of the beam surface strain at any location of the beam as a function of the voltage applied to the actuator. Smits et al. [7] have extensively analyzed the dynamic properties of bimorphs. They proposed a matrix describing the dynamic dependence of tip rotation, tip deflection, volume displacement and electrode charge as functions of the sinusoidal driving parameters: a moment at the tip, a force at the tip, a uniform body pressure and the electrode voltage. Smits' model shows to be efficient in locating the resonance and antiresonance frequencies of symmetrical bimorphs. However, the dynamic tip deflection at resonances can not be determined by Smits' expressions when electric field is applied on the bimorph structure. Hence, there is a need for studies of determining the peak amplitude at resonances which is very important in many practical applications of bimorphs, e.g., used as a cooling resonator in microelectronic systems [8].

The issue of bonding layer was also discussed in previous work. Static elastic models for surface-bonded and embedded segmented actuators exciting extension and bending in the substructure was presented in Crawley and de luis's paper [5].The existence of an elastic bonding layer of a finite thickness between the piezoelectric and the substructure led to a classic shear lag solution. When the shear lag in the bonding layer goes to zero, this solution was

reduced to a perfectly bonded piezoelectric model. One shear lag parameter was proposed to indicate the effectiveness of the shear transfer. Morris and Forster [9] utilized the finite element method to optimize the deflection of a circular bimorph consisting of a single piezoelectric actuator, bonding material and elastic plate with finite dimensions. The effect of bonding layer-to-plate thickness ratio was investigated and optimized. A finite element formulation that incorporates the effect of non-idealities (bonding layer) was proposed by De Faria et al. [10]. The formulation used an Euler-Bernoulli model for the beam and assumed the bond layer to be in a state of pure shear. Their work shows that within certain limits, the finite stiffness bond may be compensated by using higher gain in the control system. However, the finite bonding stiffness has to be considered for control system design.

A new method is proposed here to calculate the tip deflection at resonances based on the damping ratio of the structures. Finite element simulation was employed to validate the proposed method. The effect of finite stiffness bonding was analyzed by static and dynamic methods as well. Some suggestions were mentioned to minimize the bonding influence.

5.2 THEORETICAL ANALYSES

5.2.1 PERFECTLY BONDED BIMORPH

As illustrated in Figure 1, if the bonding layers are neglected, bimorphs can be regarded as a three-layer element. A bimorph cantilever beam of constant width w consisting of several materials with different Young's moduli, can be represented by an equivalent beam of the same total thickness, and of the homogeneous Young's modulus by modulating the widths of the components. A stiffness difference in the original beam results in the width difference in the new, equivalent cantilever beam.

As derived by Smits et al. [7], the dynamic tip deflection of the cantilever bimorph is given as:

$$\delta = \frac{3d_{31}V \sin \Omega L \sinh \Omega L}{4t_p{}^2 \Omega^2 (1 + \cos \Omega L \cosh \Omega L)} \tag{1}$$

where: δ is the dynamic tip deflection of the cantilever, d_{31} is the piezoelectric constant, L the length of bimorph cantilever, and t_p is the thickness of PZT layer. V is the voltage applied on piezoelectric layers.

In Eq.(1), Ω is the normalized frequency defined as:

$$\Omega = \sqrt{\frac{w}{a}} \tag{2}$$

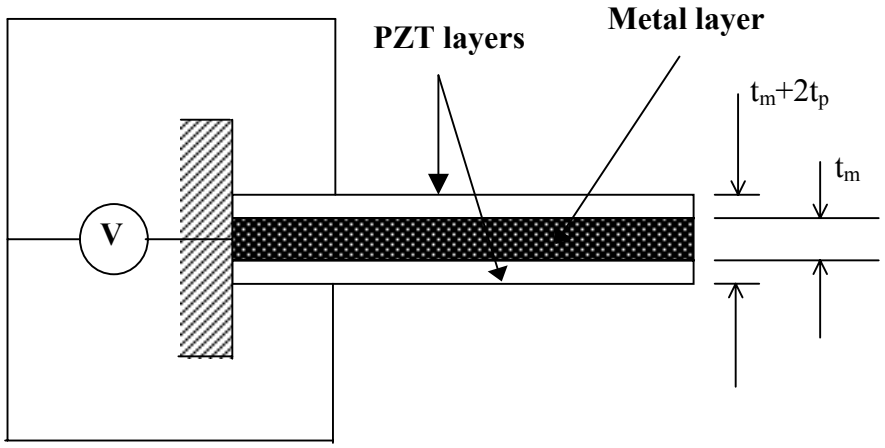

Figure 1: Structure of three-layer cantilever bimorph

$$\text{where} \qquad a = \sqrt{\frac{EI_{eff}}{\rho A_{eff}}} \tag{3}$$

a is the ratio of the bending stiffness and the mass per unit length. It plays a role in the vibrating system as a natural frequency.

The equivalent moment of inertia of the beam is:

$$I_{eff} = I_1 + I_2 + I_3 \tag{4}$$

$$I_1 = I_3 = \frac{1}{12} w_b {t_p}^3 + 2 w_b t_p \left(\frac{t_p}{2} - \bar{y} \right)^2 \tag{5}$$

$$I_2 = \frac{1}{12} \frac{E_m}{E_p} w_b {t_m}^3 \tag{6}$$

where w_b is the width of bimorph, E_m, t_m and E_p, t_p represent Young's modulus and thickness of metal and piezoelectric layers, respectively. The centroid position of the beam can be determined using the equation:

$$\bar{y} = \frac{\int_A y dA}{\int_A dA} \tag{7}$$

Due to the symmetric geometry of the bimorph, the centroid is located at the center of the total thickness.

The mass of an infinitesimally thin slice of the beam with length dx is given by $\rho A_{eff} dx = \sum_i w \rho_i t_i dx$ where t_i is the thickness for different layers. Then I_{eff} and A_{eff} can be substituted into (3) to obtain variable a.

5.2.2 DETERMINATION OF AMPLITUDE AT RESONANCE

Resonance occurs for the bimorph cantilever when the equation $1+\cos\Omega L\cosh\Omega L=0$ [11]. However, it is found from Equation (1) that $1+\cos\Omega L\cosh\Omega L$ is in the denominator and $\sin\Omega L\sinh\Omega L$ in the numerator. Figure 2 shows the plots for the values of $1+\cos\Omega L\cosh\Omega L$ and $\sin\Omega L\sinh\Omega L$ when the length of cantilever (L) is 60mm. Clearly, the values of $1+\cos\Omega L\cosh\Omega L$ and $\sin\Omega L\sinh\Omega L$ do not reach zero at the same Ω value. This indicates that when the frequency approaches the resonance, the tip deflection goes to infinity, which can not represent the real system. So some corrections should be taken for the tip deflection at the resonance.

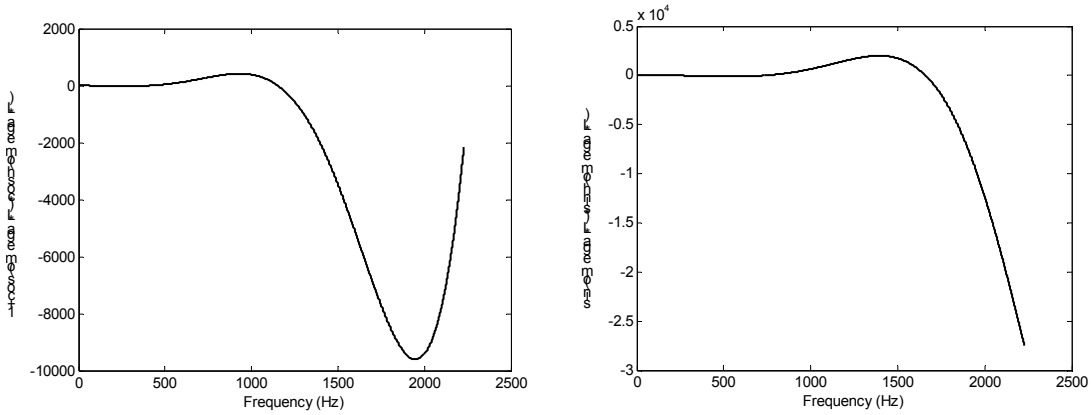

(a) (b)

Figure 2: (a) Values of $1+\cos\Omega L\cosh\Omega L$ in frequency range of [0, 2500]
(b) Values of $\sin\Omega L\sinh\Omega L$ in frequency range of [0, 2500]

Quality factor or Q factor can be a measurement of the sharpness or frequency selectivity of a resonant vibratory system having a single degree of freedom. In the mechanical system, Q factor is approximately equal to $f_r/\Delta f$, where f_r is the resonance frequency and Δf is the bandwidth between the half-power points. In Figure 3, $\Delta f = f_2 - f_1$.

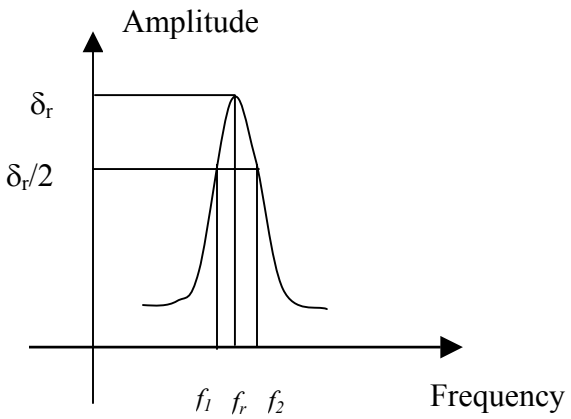

Figure 3: Damping ratio Q = f_r /(f_2 − f_1)

The relation between the quality factor and damping ratio is:

$$Q = \frac{1}{2\xi} \tag{8}$$

where ξ is the damping ratio of the mechanical system. By using the damping ratio of the system, the amplitude at the resonance can be obtained by the following flow chart.

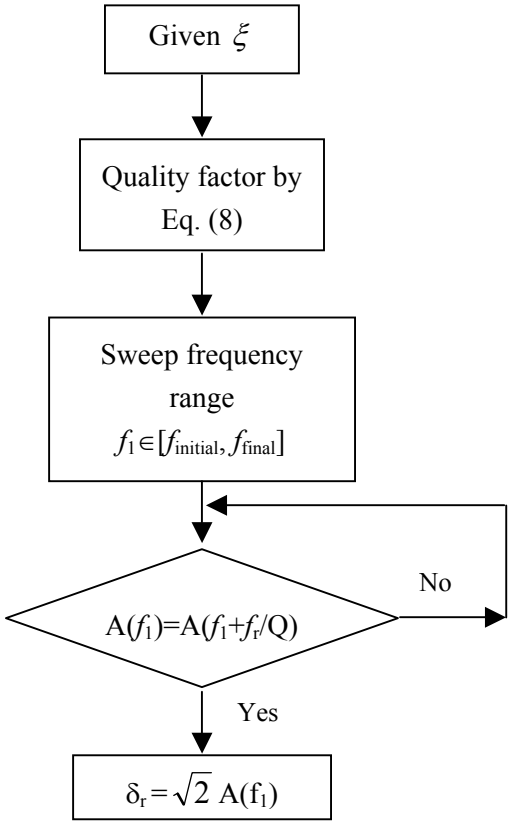

In the flow chart, A(f_1) is the amplitude at frequency f_1. δ_r is the tip amplitude at the resonance and f_r the resonance frequency. By using this method together with Smits' dynamic expression, the finite tip deflection can be determined.

5.2.3 EFFECT OF BONDING STIFFNESS

Inclusion of a finite stiffness bonding layer between the actuators and the structure will reduce the effectiveness of induced strain actuators mounted on the surface of a structure. Pin-force model is one of the most important modeling methods for piezoelectric structures. In the pin-force model, the actuator and the structure are modeled as separate structures, linked together by pins at the edges of the actuator. The shear stress is applied to the beam along the actuator-substructure interface. When the perfect bonding between the actuator and substructure is assumed, the curvature induced in the beam is [1]:

$$\kappa = \frac{12\Lambda}{t_m(6+\psi)} \tag{9}$$

where Λ is the piezoelectric strain $\Lambda = \frac{d_{31}V}{t_p}$, d_{31} piezoelectric constant, V the applied voltage on the actuator, t_p and t_m the thickness of actuator and structure layers respectively. ψ is the relative stiffness parameter $\psi = \frac{E_m t_m}{E_p t_p}$.

When a finite stiffness bonding layer with shear modulus G_b and thickness t_b is included in the model between the structure and actuator, there is imperfect actuation due to shear lag in the bonding layer. The shear lag parameter can be defined as [5]:

$$\Gamma^2 = \frac{\left(\frac{G_b}{E_p}\right)\left(\frac{t_b}{t_p}\right)}{\left(\frac{t_b}{l}\right)^2}\left(\frac{\alpha+\psi}{\psi}\right) \tag{10}$$

The geometric constant α is set to 6 for the bending. It is apparent that with the increase in G_b and decrease in t_b, the shear lag parameter Γ will be increased.

By using the shear lag parameter, the curvature induced in the case of finite stiffness bonding becomes [2]:

$$\kappa = \frac{12\Lambda}{t_m(6+\psi)}\left(1-\frac{1}{\Gamma}\frac{\sinh(\Gamma)}{\cosh(\Gamma)}\right) \tag{11}$$

For moderate value of Γ, $\cosh(\Gamma) \cong \sinh(\Gamma)$, then the ratio between the curvatures for perfect bonding and stiff bonding is:

$$ratio = 1 - \frac{1}{\Gamma} \tag{12}$$

For large Γ's, the effects of bond are minimized.

Employing the quite similar method mentioned in sections 5.2.1 and 5.2.2, effect of bonding layers can also be analyzed in terms of the dynamic amplitude and resonance frequencies. With the bonding layers, bimorph is a five-layer element and the centroid is still located at the center of the total thickness from the bottom due to the symmetry. The moment of inertia of the beam around the centroid is:

For the piezoelectric layers,

$$I_1 = I_5 = \frac{1}{12} w_b {t_p}^3 + w_b t_p \left(\frac{t_p}{2} - \bar{y} \right)^2 \tag{13}$$

For the bonding layers,

$$I_2 = I_4 = \frac{1}{12} \frac{E_b}{E_p} w_b {t_b}^3 + \frac{E_b}{E_p} w_b t_b \left(t_p + \frac{t_b}{2} - \bar{y} \right)^2 \tag{14}$$

For the middle shim layer,

$$I_3 = \frac{1}{12} \frac{E_m}{E_p} w_b {t_m}^3 \tag{15}$$

The equivalent moment of inertia of cantilever beam with bonding layers is:

$$I_{eff} = I_1 + I_2 + I_3 + I_4 + I_5 \tag{16}$$

where E_b, t_b represent Young's modulus and thickness of bonding layers. Again, the tip deflection of the bimorph cantilever is obtained by using Equation (1) as well as the resonance-amplitude determination method.

5.3 FINITE ELEMENT ANALYSIS

Dynamic, three-dimensional finite element models of a bimorph cantilever were developed based on the geometry with actuator and middle shim layers shown in Figure 1 for perfectly bonded case and five-layer structure including two bonding layers for finite stiffness bonded case. The finite element analysis program ANSYS5.6 was used to implement the models. The piezoelectric actuator patches were constructed using 3-D Coupled-Field Solid Elements SOLID5. The middle brass shim and the bonding layers were modeled by SOLID45. SOLID5 has a three-dimensional magnetic, thermal, electric, piezoelectric, and structural field capability with limited coupling between the fields. It has eight nodes with up to six degrees of freedom at each node. The underlying equations solved were the coupled linear piezoelectric equations, given as follows:

$$[M_{uu}]\{\ddot{u}\} + [C]\{\dot{u}\} + [K_{uu}]\{u\} + [K_{\varphi u}]\{\varphi\} = \{F\} \tag{17}$$

$$[K_{\varphi u}]\{u\} + [K_{\varphi\varphi}]\{\varphi\} = \{Q\} \tag{18}$$

where, u and φ are displacements and electrical potentials within the element domain, $[M_{uu}]$ and $[K_{uu}]$ are the mass and displacement stiffness matrices, $[K_{\varphi u}]$ is the piezoelectric coupling matrix, $[K_{\varphi\varphi}]$ is dielectric stiffness matrix, {F} and {Q} are respectively the mechanical force vector and the external applied electrical charge vector acting on the piezoelectric element.

The full-method harmonic analysis in ANSYS was employed to predict the dynamic behavior of the structure. The full-method harmonic analysis uses the full system matrices to calculate the harmonic response, where the matrices may be symmetric or asymmetric. The element edge length on surface boundaries of 0.4mm, 0.3mm, 0.2mm and 0.1mm were tested. Little variation in the parameters of interest, i.e., resonance frequencies and dynamic displacements, was observed between the last two smallest grid solutions, so the final meshing edge length was 0.2mm to guarantee reasonable accuracy and cost of computational time. The fixed-free boundary condition was applied by constraining the nodal displacements in x, y and z directions at one end of the beam. To simulate the electrode surfaces of the bimorph actuator, the same level of nodal electrical potential was prescribed at the nodes on the surface.

5.4 RESULTS AND DISCUSSIONS

5.4.1 PERFECTLY BONDED BIMORPH

In this work, two-layer brass reinforced piezoelectric elements from PIEZO Systems Inc. were used. The thickness of the brass shim is 0.127mm and the thickness for each of two ceramic sheets is 0.191mm (bonding layer negligible), which brings the total thickness of the piezoelectric element to 0.508mm. The properties of the PZT ceramics and brass are listed in Table 1.

Table 1 Material Properties

Materials	d_{31}	Young's Modulus (N/m^2)	Density (kg/m^3)	Poisson's ratio
PZT ceramic	190×10^{-12}	6.6×10^{10}	7800	0.31
Brass	N/A	11×10^{10}	8800	0.35

The profile of bimorph, which consists of two piezoelectric layers and one brass layer, can be calculated using the Young's moduli of these materials, which are 66GPa and 110GPa, respectively. The ratio of brass Young's modulus with respect to that of PZT is 1.6667. The cross section of the beam is shown in Figure 4, where in Figure 4(a) the actual cross-section of the beam is given and in Figure 4(b) the cross-section with the width modulated according to the different elastic stiffness. Because of the symmetric geometry of the bimorph, the centroid is located at the center of the total thickness, i.e., 254.5μm from the bottom of the bimorph. The

moment of inertia of the beam around the centroid can be calculated using Eqs. (5) and (6), hence the bending stiffness EI_{eff} is 7.328×10^{-4} Nm^2. Using the density values for the PZT and brass layers, it is found that $\rho A_{eff} = 4.1\times10^{-3} kg/m$, which results in:

$$a = \sqrt{\frac{EI_{eff}}{\rho A_{eff}}} = 0.4229 N^{1/2} m^{-3/2} kg^{-1/2} \tag{19}$$

The dynamic tip deflection of the cantilever bimorph can be found by substituting $\Omega = \sqrt{\frac{w}{a}} = \sqrt{\frac{w}{0.4229}}$ into Equation (1).

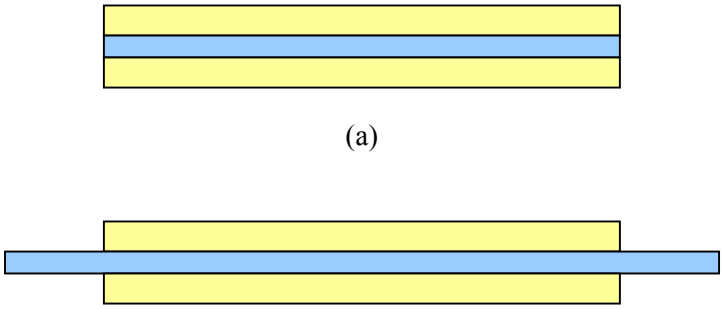

(a)

(b)

Figure 4: (a) Actual cross section of the beam
(b) The cross-section with the width modulated

The deflection of bimorph as a function of frequency is plotted in Figure 5 together with the ANSYS simulation results for $L = 0.06m$ and $w = 0.002m$. Good agreement can be found in the locations of resonance frequencies (Table 2) and the amplitude except at resonance points.

Table 2: Resonance Frequencies ($L = 0.06m$, $w = 0.002m$)

	First Resonance Frequency (Hz)	Second Resonance Frequency (Hz)	Third Resonance Frequency (Hz)
Analytical	65.7	412	1153.4
Simulation	65	405	1150

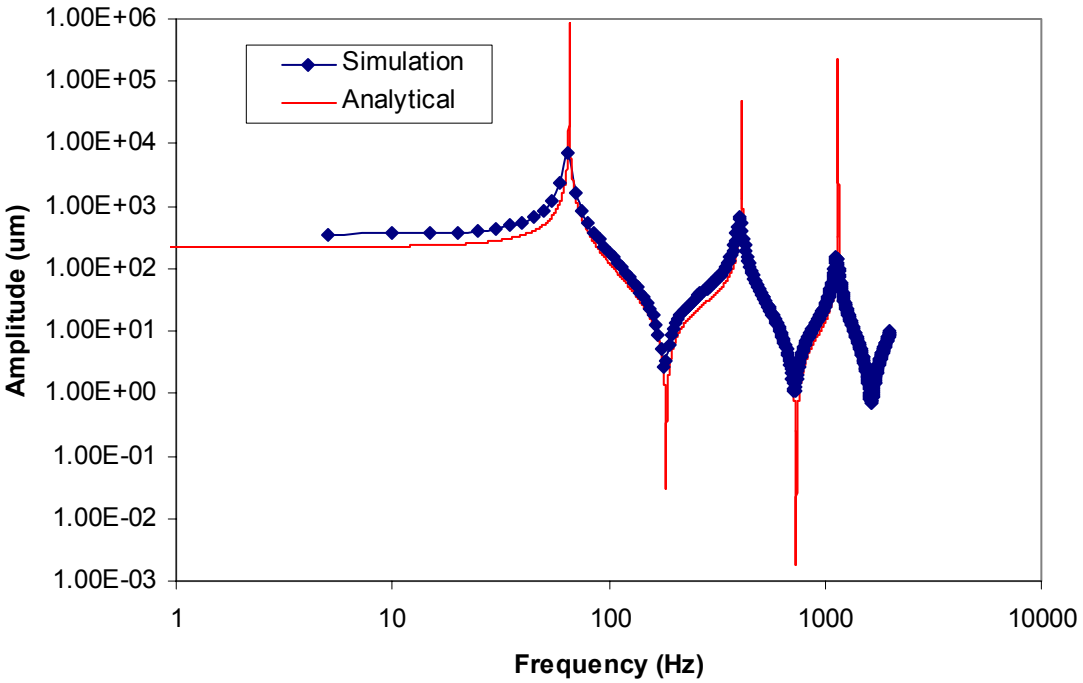

Figure 5: Spectrum analysis for $L = 0.06m$, $w = 0.002m$ beam

However, large discrepancies between the simulation and analytical calculation can be found at resonances in Figure 5. By using the proposed resonance-amplitude determination method, the corrected amplitude at resonances and simulated results are given in Table 3. The damping ratio is assumed to be 2% which is reasonable for most mechanical systems.

Table 3: Tip Deflection at Resonances ($L = 0.06m$, $w = 0.002m$)

	Tip Deflection (mm)		
	First Resonance	Second Resonance	Third Resonance
Analytical	7.2	0.62	0.13
Simulation	7.1	0.635	0.14

The good agreements between the analytical and simulated tip deflections indicate that our correction method can be used to calculate the tip deflection at resonance.

From Figure 5, another phenomenon that can be observed is the difference between the simulation and analytical calculation in the very low frequency range, which implies that the dynamic analytical expression can not be used to evaluate the quasi-static response of the system. Wang and Cross [3] developed the analytical expressions for the fundamental resonance frequency and static tip deflection of cantilever bimorph are:

$$f_r = \frac{3.52t}{4\pi L^2}\sqrt{\frac{E_p}{3\rho_p}\left[\frac{1+3(1+2B)^2+4AB^3}{4(1+B)^2(BC+1)}\right]^{1/2}} \tag{20}$$

$$\delta_s = \frac{3L^2}{2t}\frac{(1+B)(1+2B)}{AB^3+3B^2+3B+1}d_{31}E_3 \tag{21}$$

where f_r is the fundamental resonance frequency, δ_s is the static tip displacement, d_{31} the piezoelectric constant, L the length of beam. $A=\frac{E_m}{E_p}$, $B=\frac{t_m}{2t_p}$, $C=\frac{\rho_m}{\rho_p}$, where E_m, ρ_m, t_m and E_p, ρ_p, t_p represent Young's modulus, density, thickness of metal and piezoelectric layers, respectively. Total thickness of bimorph is $t = t_m + 2t_p$. E_3 is the electric field strength applied on piezoelectric layers. Using the Equation (21) and material properties given in Table 1, for the cantilever 60mm long, the static (quasi-static) deflection is 0.364mm while the simulation gives 0.356mm, and Smits' analytical expression calculates 0.225mm. The fundamental resonance frequency from Equation (20) is 65.4 Hz which is very close to both the simulation and Smits' analytical results.

With the same materials' properties, the deflection of bimorph *vs.* frequency is plotted for $L = 0.03m$ $w = 0.001m$ in Figure 6. ANSYS simulation results are included for comparison. The resonance frequencies and tip deflections for this case are given in Tables 4 and 5. The amplitudes are calculated with damping ratio of 2%.

Table 4: Resonance Frequencies ($L = 0.03m$, $w = 0.001m$)

	First Resonance Frequency (Hz)	Second Resonance Frequency (Hz)
Analytical	263	1647.9
Simulation	264	1650

Table 5: Tip Deflection at Resonances ($L = 0.03m$, $w = 0.001m$)

	Tip Deflection (mm)	
	First Resonance	Second Resonance
Analytical	1.8	0.164
Simulation	1.7	0.172

The locations of resonance frequencies from Smits' equation and corresponding tip amplitudes (Table 4 and 5) by using the method proposed in this section for *0.03m* long cantilever show the good agreement for the simulation and analytical results. The first mode shape for the cantilever of $L = 0.03m$ $w = 0.001m$ can be obtained by ANSYS simulation which is given in Figure 7. The

fundamental resonance frequency and quasi-static tip deflection from Eqs. (20) and (21) in this case are 263.25Hz and 93.2μm, while the simulation gives 92.8μm as static deflection.

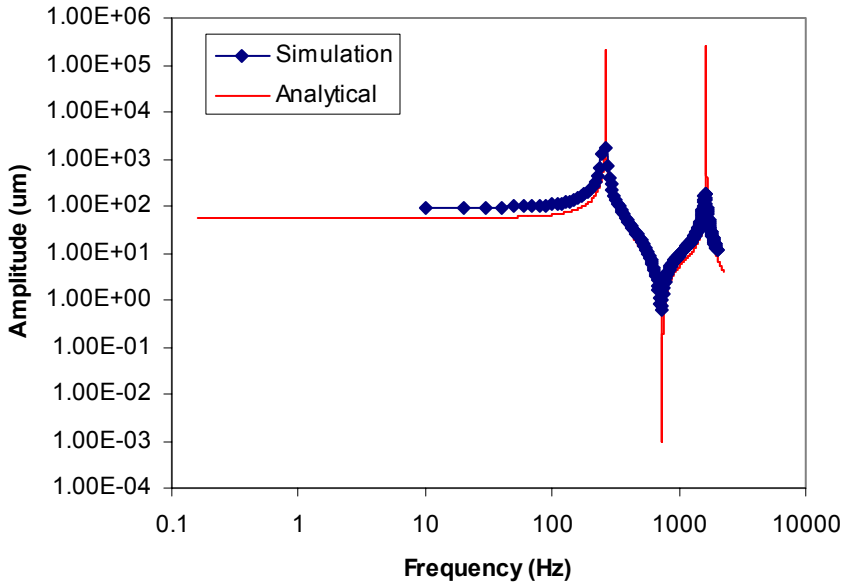

Figure 6: Spectrum analysis for $L = 0.03m$, $w = 0.002m$ beam

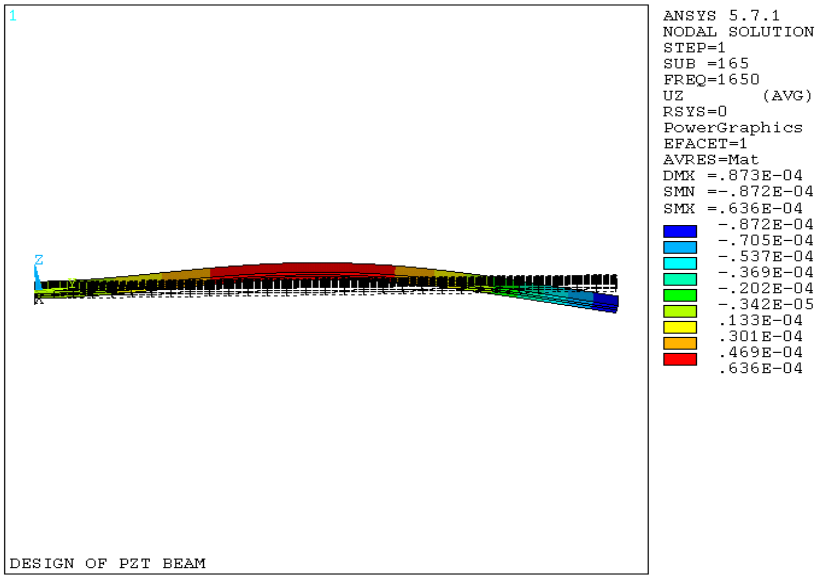

Figure 7: The first mode shape for the cantilever of $L = 0.03m$ $w = 0.001m$

5.4.2 EFFECTS OF BONDING LAYER

Based on the expression for shear lag parameter Equation (10), several factors including length of bimorph and the thickness and stiffness of bonding layer can be considered to minimize the effect of bonding stiffness. These effects are shown in Figures 8 to 11. The electric field applied on the actuator E_3 is related to the piezoelectric strain by $\Lambda = d_{31}E_3$. With an increase in electric field, the bending curvature for both perfect bonding structure and finite stiffness bonding structure increases, but different values. The difference between the tip deflection for bimorph with perfect bonding and 15μm thick bonding increases with the electric field (see Figure 8), i.e., the static tip displacement deviates much more from the perfect case for larger voltage.

Due to the fact that the shear lag parameter is proportional to the structure length, the ratio in Equation (12) tends to be unity for longer bimorphs. In Figure 9, with the increased length from 5mm to 15mm, the bending curvature expressed in Eq. (11) also increases from 0.33 to 0.443 which is closer to 0.503 in perfect bonding structure. Therefore selecting a longer structure can reduce the effect of bonding layer while keeping other conditions.

Obviously, a thicker bonding layer results in worse performance, which is also shown in Equation (10). With the increase of bonding thickness, the shear lag parameter decreases, thus increasing the curvature ratio in Equation (12). Figure 10 indicates that the static tip deflection is smaller for the structure with a thicker bonding layer.

Another factor which may minimize the effect of bonding layer in quasi-static condition is the shear modulus of bonding material. As shown in Figure 11, the tip deflection increases until it saturates when the shear modulus increases from 10^6 Pa to 10^9 Pa. Therefore a harder material makes a better bonding layer.

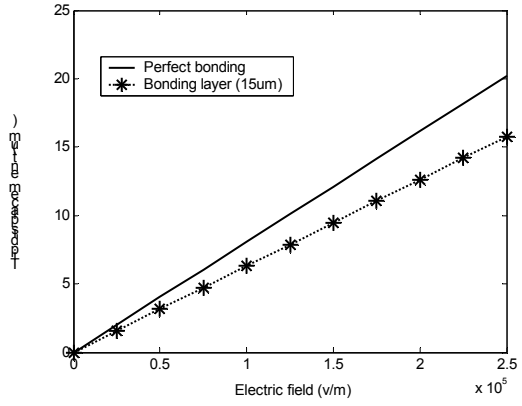

Figure 8: Quasi-static tip deflection vs. electric field

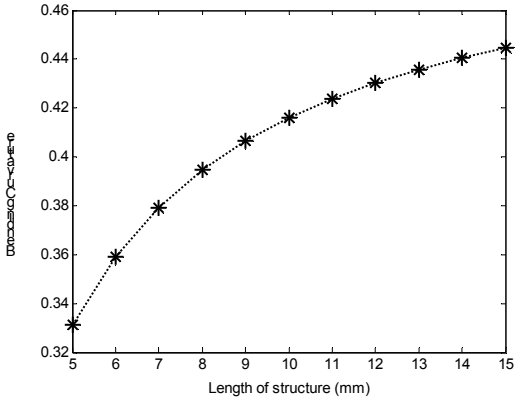

Figure 9: Effect of length on bending curvature for bimorph with bonding layers

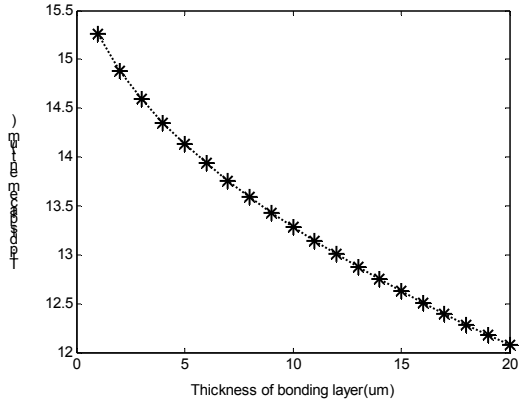

Figure 10: Effect of thickness of bonding layer on static tip deflection

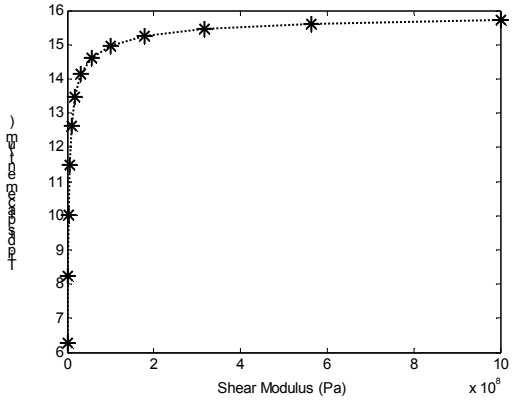

Figure 11: Effect of shear modulus of bonding materials on static tip deflection

The effect of finite stiffness bonding layer can also be examined in the viewpoint of *dynamic* tip deflection and resonance frequency. Equations (13) to (15) were employed to calculate the moment of inertia of cantilever around the centroid. The dimension of the five-layer bimorph structure (including two bonding layers) is $L = 0.06m$ $w = 0.002m$, thicknesses of piezoelectric patch and brass are 0.191mm and 0.127mm, respectively. The properties of PZT and brass are the same as shown in Table 1. The Young's modulus and density for the bonding layer are 5.17×10^9 N/m^2 and 1150 kg/m^3. Figure 12 shows the analytical dynamic amplitude as a function of frequency in the range of 0 to 2000Hz together with ANSYS simulation results with bonding layer of 15μm. Due to the large discrepancy at the resonances, a 2% damping ratio is assumed for the analytical calculation. The results are shown in Table 6.

Table 6: Comparison for bonding thickness of 15microns

	First resonance		Second resonance		Third resonance	
	Frequency (Hz)	Amplitude (mm)	Frequency (Hz)	Amplitude (mm)	Frequency (Hz)	Amplitude (mm)
Analytical	70.7	5.68	438.8	0.653	1224	0.131
Simulation	70	5.61	430	0.675	1210	0.144

Comparing the results in Tables 2, 3 to 6, the resonance frequencies increase while the amplitude at the fundamental resonance decreases when the effects of bonding layer are considered.

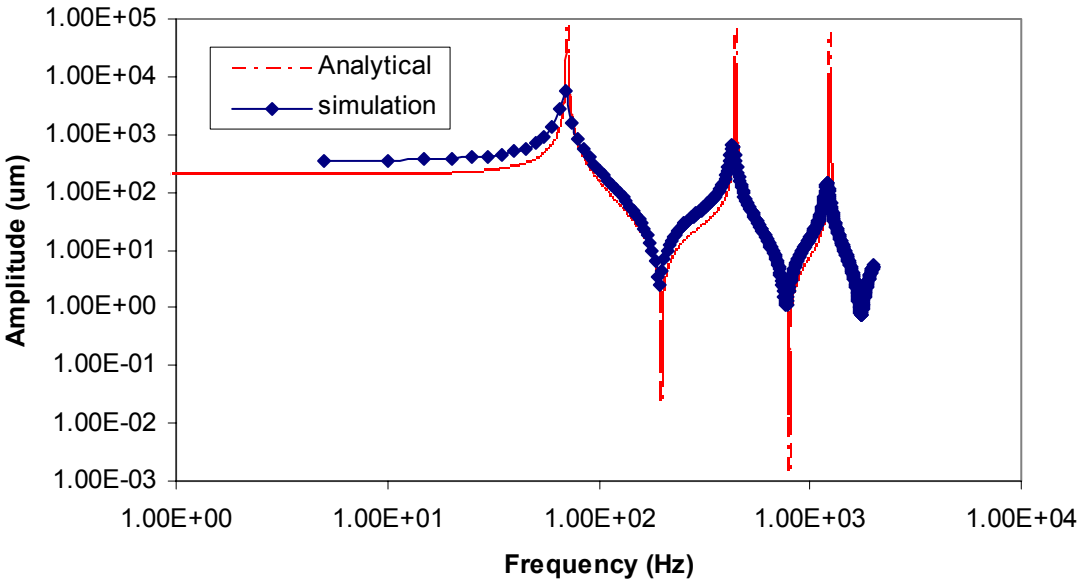

Figure 12: Spectrum analysis for $L = 0.06m$, $w = 0.002m$ beam with 15μm thick bonding layers

The effects of the bonding layer thickness on the fundamental resonance frequencies and the corresponding dynamic tip deflections are plotted in Figure 13. While keeping the other layers (piezoelectric and metal layers) constant, the fundamental resonance frequency increases linearly and the dynamic tip deflection decreases with the increase of the bonding layer thickness. This is because that the thinner the structure, the easier it is to resonate, hence the lower resonance frequency and the larger vibration amplitude.

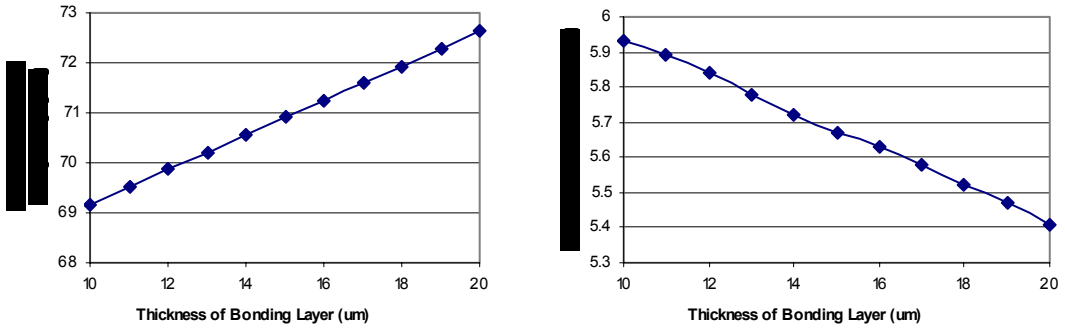

(a) (b

Figure 13: (a) Effect of bonding layer thickness on fundamental resonance frequency
(b) Effect of bonding layer thickness on dynamic amplitude at the first resonance

5.5 CONCLUSIONS

In this paper, the Smits' dynamic performance prediction has been improved by including the damping ratio of the system. Dynamic tip deflections were accurately predicted and can be employed in many applications. The effect of finite stiffness bonding layer is analyzed by using both static and dynamic methods. To minimize the bonding effect, longer structure, thinner bonding layer and harder bonding materials are preferred. Finite element simulations show that the proposed method to determine dynamic tip deflection is accurate enough to predict the performance of perfectly bonded bimorphs as well as finite bonding structures.

REFERENCES

1. Chaudhey, Z. and Rogers, C.A., "The pin-force model revisited", *Journal of Intelligent Material Systems and Structures*, 5:347-354, 1994
2. Crawley, E.F. and Anderson, E.H., "Detailed models of piezoceramic actuation of beams", *Journal of Intelligent Material Systems and Structures*, 1:4-25, 1990
3. Wang, Q.M. and Cross, L.E., "Performance analysis of piezoelectric cantilever bending actuators", *Ferroelectrics*, 215: 187-213, 1998
4. Kim, S.J. and Jones, J.D., "Quasi-static control of natural frequencies of composite beams using embedded piezoelectric actuators" *Smart Materials and Structures*, 4: 106-112, 1995
5. Crawley, E.F. and de Luis, J., "Use of piezoelectric actuators as elements of intelligent structures", *AIAA Journal*, 25(10):1373-1385, 1987
6. Pan, J., Hansen, C.H. and Snyder, S.D., "A study of the response of simply supported beam to excitation by a piezoelectric actuator", *Journal of Intelligent Material Systems and Structures,* 3: 3-16, 1992
7. Smits, J.G. and Ballato, A., "Dynamic admittance matrix of piezoelectric cantilever bimorphs", *Journal of Microelectromechanical Systems*, 3(3): 105-112, 1994
8. Wu, T., Ro, P.I., Kingon, A.I. and Mulling, J.F., "Piezoelectric resonating structures for microelectronic cooling", *Smart Materials and Structures*, in press
9. Morris, C.J. and Forster, F.K., "Optimization of a circular piezoelectric bimorph for a micropump driver", *J. Micromech. Microeng*., 10: 459-465, 2000
10. De Faria, A.R. and De Almeida, S.F.M., "Modeling of actively damped beams with piezoelectric actuators with finite stiffness bond", *Journal of Intelligent Material Systems and Structures*, 7:677-688, 1996
11. Rayleigh, J.W.S., *The theory of sound*, New York: Dover, 1976.

6 CLOSED LOOP FORCE FEEDBACK CONTROL OF MINIATURE BALL END MILLING

David Hood
Graduate Student
Dr. Greg Buckner
Assistant Professor
Mechanical and Aerospace Engineering

Previous research has focused on the prediction and compensation of error during machining with miniature ball end mills of hard steel dies used in injection molding. However, these methods used open loop compensation algorithms involving tool force models to predict deflection and off-line compensation of desired tool path to achieve dimensional tolerance and accuracy in the finished part. Accuracy relied on the cutting parameters, the accuracy of the model used to predict deflection, and part alignment on the machine. Real-time force feedback incorporated in the control algorithm would eliminate some uncertainties in parameters and further improve the accuracy of profiles created during machining. This paper demonstrates that closed loop force feedback during machining can be used to predict tool deflection and compensate for this deflection during the milling operation real-time rather than off-line beforehand. Two approaches of real-time force feedback compensation are presented here: predicted depth based on a dynamic cutting force model and predicted deflection using a model of tool stiffness. A control algorithm was written incorporating both methods of force feedback control allowing the user to create a variety of profile cuts using feedback from real-time cutting forces and encoder position of the machine. Experimental results are presented for force feedback closed loop machining using both approaches. Profile accuracy is reduced up to 80% from the non-compensated case with profile error on the order of 2 μm. These results confirm that closed loop force feedback incorporated in the control algorithm during machining can drastically improve the dimensional tolerance and accuracy of injection molds created using miniature ball end mills.

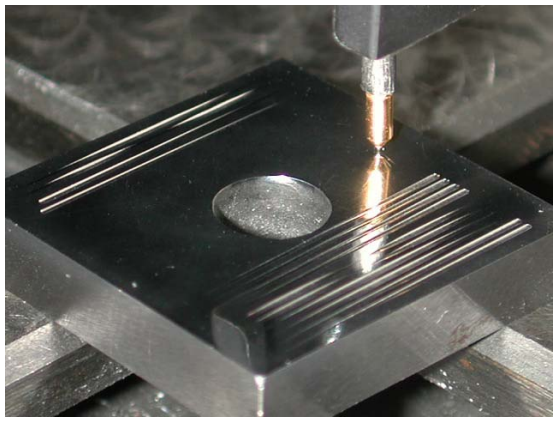

6.1 INTRODUCTION

Injection molding is an important manufacturing process for optical and mechanical components. The hard steel dies used in injection molding play a direct role in the quality of molded parts. Traditionally, fabricating the dies involved rough milling followed by heat treatment, grinding, and polishing to the desired shape. Recently, high-speed machining of heat-treated steel (hardness > 55 R_c) has become a viable approach for reducing fabrication times while retaining the necessary shape control. However, as feature sizes drop below 1 mm with dimensional tolerances on the order of 10 μm, tool deflection can create significant errors in the shape of mold surfaces. Oftentimes the deflection created from milling can be on the order of 30 μm and thus render a part out of tolerance from that specified in industry.

Machining error during milling is based on three components: incorrect geometric surface description, limited machine stiffness, and deflection of the cutting tool during machining [1]. Total error is just the superposition of the three error sources together during machining. Geometric surface error results from insufficient knowledge of the surface of the workpiece being cut. Limited machine stiffness results in changes in the machine axes position as various changing loads are applied in time. The last source of error in machining is the one most heavily concentrated on and researched in the past here at North Carolina State University. It involves deflection of the tool tip during milling based on forces imparted on the tool.

A previous research effort at the Precision Engineering Center developed open loop correction techniques for tool deflection of miniature ball end mills [2]. This effort used a tool force model developed for diamond turning to predict tool forces during milling operations. The predicted forces in milling lead to tool deflections for specified machining conditions and a given tool stiffness. Based on these predicted tool deflections, the tool path was modified before cutting. A CAD model of the surface along with the planned tool path was used to determine the depth of cut, feed rate, and normal vector to the surface. This information was then used to calculate the magnitude and direction of cutting forces causing tool deflection and the predicted tool deflection was incorporated in the tool path off-line before cutting.

Another research has focused on a dynamic model based approach to tool deflection. With the development of several tool force models, numerous amounts of data have been collected of the cutting forces during milling. Using these measured cutting forces during milling, along with measured cut profiles, many models have been refined to better predict deflection and depth given fixed cutting parameters for numerous complicated groove profiles and a variety of cutting conditions. These cutting conditions include upfeeding, down feeding, semi-circular machining, as well as more complex surfaces [3].

Despite the results obtained from open loop cutting and off-line deflection prediction based on a model, during the actual milling operation, these methods rely only on a model of the cutting operation and not on real-time data of forces causing the deflection during milling. The cutting results using an open loop approach are only as good as the prediction of cutting conditions, material properties, and parameters, as well as the cutting force model used.

During miniature ball end milling, precise prediction and measurement of the cutting parameters is very difficult and by measuring a force real-time while cutting, it is possible to better predict a deflection or depth rather than off-line calculation based on a model. Closed loop compensation for tool deflection takes the form of two paths with different approaches and different results. One approach involves depth prediction using a dynamic tool force model developed at the Precision Engineering Center. This method takes a measured force and predicts a depth based on cutting conditions including feed rate, spindle speed, material properties, and wearland of the tool. This predicted depth from cutting force is the sole feedback in the control algorithm and the only comparison with desired depth to get real-time position error during milling.

The other approach to compensation for tool deflection consists of deflection prediction using a model of tool stiffness. This involves measuring a force real-time, inferring a deflection based on tool stiffness, and using desired position, the laser encoder position of the machine, and this predicted deflection to determine position error while cutting. This method relies only on orthogonal tool stiffness measured with respect to the surface of the workpiece, and as a result precise estimation of cutting conditions is not necessary as in the predicted depth algorithm approach.

Recent efforts for open loop compensation of tool deflection using a dynamic force model has proven to be successful and errors have be reduced from 50 μm to less than 10 μm with correct knowledge of the cutting conditions and parameters [2]. Unfortunately, the proper cutting conditions and parameters are not usually known. For example, the tool or workpiece may have dimensions different than expected or be imprecisely positioned, resulting in cutting depths that are larger (or smaller) than expected. Also wearland, real-time spindle speed and feed rate, as well as material properties are often difficult to determine before hand to predict deflection. Open loop compensation cannot correct for these types of errors in part setup or error in determining cutting parameters before hand and is limited in comparison to real-time force feedback control.

In this paper, the effectiveness of a new strategy to perform closed loop milling operations using miniature ball end mills where the real-time orthogonal cutting force is used as feedback in the control algorithm is demonstrated. Thus, during the cut, the profile error is composed of a predicted depth or deflection based on an actual measured force while milling rather than an off-line calculation and prediction beforehand based on a model. Thereby, the real-time cutting

force is used to adjust the axes position on the fly and thus the algorithm is true closed loop machining with force feedback incorporated.

The results show significant improvements over those obtained with open loop compensation using a model to predict deflection and error beforehand. Error in various cut profiles was decreased 80% in certain instances when compared with a non-compensated cut and up to 50% over the open loop compensation method. Further improvement in accuracy is shown to be achievable with continued development in the methods presented.

6.2 DETAILS OF THE PROJECT

6.2.1 EXPERIMENTAL APPARATUS

This section describes the development of a real-time, force feedback control algorithm for milling operations that compensates for tool deflection during the machining process. Both methods of feedback using depth prediction and deflection prediction are used and compared. The workpiece is supported on a three-axis load cell and is machined using a miniature ball end mill driven by a high-speed (60,000 rpm) air-bearing spindle. During machining, the force output of the load cell orthogonal to the workpiece provides feedback used in the control algorithm. This orthogonal force is measured real-time and depending on the compensation method implemented a depth into the part or a deflection of the tool is inferred. In using the compensation method of depth prediction based on a dynamic cutting force model, this predicted depth is compared with the desired depth to determine a position error. With the compensation method of predicted deflection using a tool stiffness model, a calculated deflection along with encoder z-position on the machine is compared with desired position to determine a machine error.

The experiments described in this paper were conducted using a Nanoform 600 diamond turning machine (DTM) with 3 orthogonal linear axes and a high-speed milling spindle. Figure 1 is a photograph of the machine on which the experiments were conducted. The spindle is a Westwind air-bearing, air-turbine unit with a maximum speed of 60,000 rpm. The cutting tools are two-flute, ball end TuC milling cutters with a diameter of 0.8 mm and a length of 4 mm. A Kistler three-axis piezoelectric load cell supports the workpiece, and is used to measure the tool forces that are fed back in the control algorithm to correct for tool deflection. Only the force perpendicular to the workpiece surface (the z-direction component) is used to predict depth and deflection in this research. A Delta Tau Programmable Multi-Axis Controller (PMAC) system collects force data from the load cell in real time, controls the DTM milling machine, computes the corrected slide command, and incorporates constant feedback for all three axes.

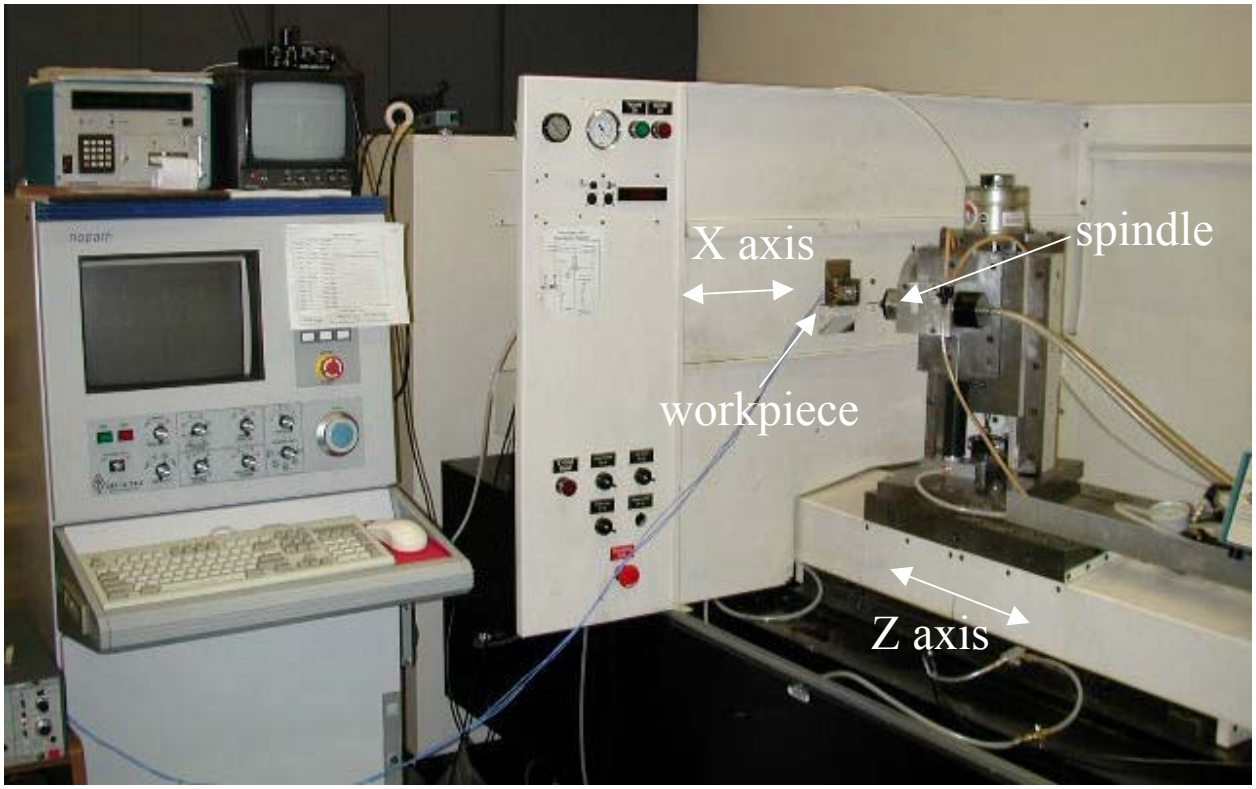

Figure 1: Nanoform DTM Machine and Setup

6.2.2 TOOL FORCES

Predicted Forces

The tool force model developed in [2] provides formulas for calculating the cutting and thrust forces developed during milling. Inputs to this model are the material properties (Rockwell Hardness, Young's Modulus) and friction at the rake and flank faces of the tool. Tool geometry (ball end radius and number of flutes), spindle speed, upfeed and cross feed, depth of cut and tilt angle of tool are used to find the cross-sectional area of the chip and the area of contact between the flank face of the tool and the workpiece. The model can be written as:

$$F_c = \frac{HA_c}{3}\left(\frac{\cot\phi}{\sqrt{3}}+1\right)+\mu_f A_f\left(0.62H\sqrt{\frac{43H}{E}}\right) \tag{1}$$

$$F_t = \mu\left[\frac{HA_c}{3}\left(\frac{\cot\phi}{\sqrt{3}}+1\right)\right]+A_f\left(0.62H\sqrt{\frac{43H}{E}}\right) \tag{2}$$

where:

A_c = cross-sectional area of the chip
A_f = area of the tool flank face
φ = shear angle in the workpiece
μ = friction coefficient on the rake face
μ_f = friction coefficient on the flank face
H = Rockwell hardness of the workpiece
E = Young's modulus of the workpiece

These forces rotate with the flank face of the milling tool, but can be readily converted to orthogonal forces (in the x, y, and z machine directions) for comparison to those measured by the load cell. Using this dynamic force model, a relation between force and predicted depth is determined. Thus during milling using a force feedback approach, a measured force can be equated to a predicted depth, and this predicted depth compared with desired depth from the user. This is the basic principle behind predicted depth compensation using a dynamic tool force model. A plot of generated depth vs. force for a spindle speed of 10,000 rpm, feed rate of 100 mm/min, material hardness of 55 R_c, tilt with respect to the workpiece of 25 degrees, and wearland of 3 µm using the dynamic cutting force model is presented in Figure 2. A quadratic trendline has been added to approximate this curve.

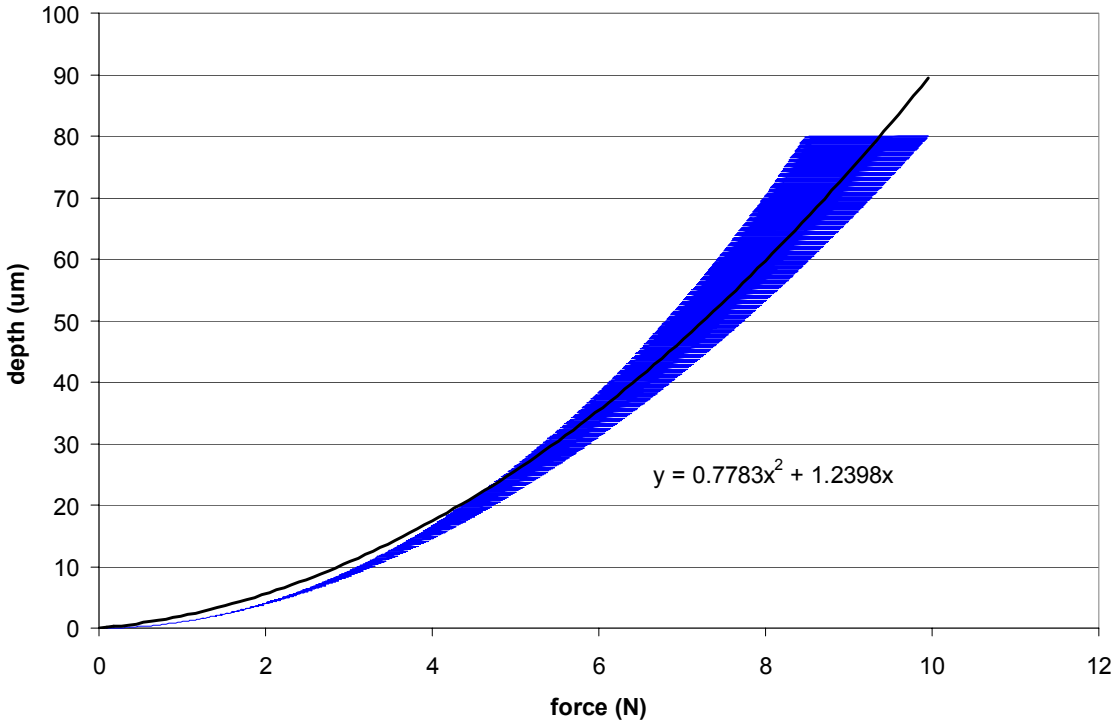

Figure 2: Depth vs. Force Curve Using a Dynamic Cutting Force Model

Measured Tool Forces

Preliminary cutting experiments were conducted to validate the tool force Equations (1) and (2). Cutting forces were measured using a Kistler 3-axis piezoelectric load cell, pictured in Figure 3. This load cell was mounted below the workpiece on the x-axis of the diamond turning machine, while the high-speed spindle was mounted on the z-axis slideway (Figure 1). Experimental results for an S-7 steel workpiece machined at a spindle speed of 10,000 rpm, a feed rate of 100 mm/min, a tool tilt of 25 degrees with respect to the workpiece, and a cutting depth of 100 µm, are presented in Figure 4. This figure compares the predicted forces using a dynamic tool force model with actual cutting forces during machining for one revolution of the tool. The z-component of force in Figure 4 is dominated by the tool thrust force (2). The x and y-force components are influenced more by the cutting force (1), which rotates in the plane of the workpiece and changes from an x-direction force to a y-direction force every quarter rotation of the tool.

Figure 3: Workpiece on Piezoelectric Load Cell

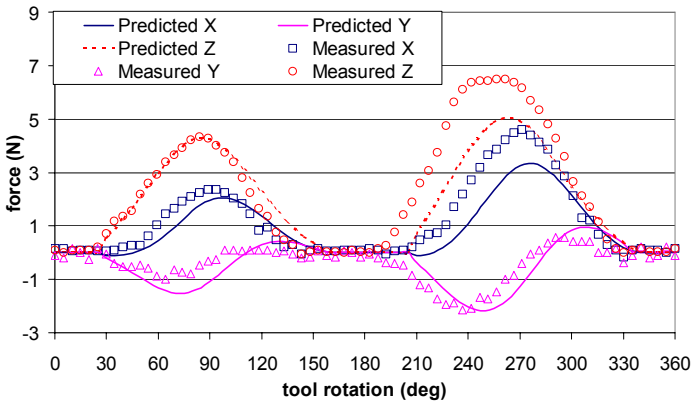

Figure 4: Typical Cutting Forces - x, y, z Coordinate System – 25 Degree Tilt

6.2.3 Tool Stiffness and Deflection

The long TuC milling tools have a 4 mm shank with a ball diameter (0.8 mm) on the end. Since a ball mill is used to fabricate free form surfaces, the tool can be loaded in the axial direction, the radial direction, or both. The stiffness of the tool is significantly less in the radial direction (see Table 1), therefore regions of a machined surface where the tool is loaded in the radial direction will create dimensional errors from deflection.

Table 1: Tool Stiffness Values for Long Shank Tool

Axial Stiffness (N/m)	1421000
Radial Stiffness (N/m)	98930
25 degree Tilt Stiffness - Calculated (N/m)	419565
25 degree Tilt Stiffness - Measured (N/m)	455120

In all the experiments, the tool was tilted at 25 degrees with respect to the workpiece. Figure 5 represents a schematic of axial and radial force components with the tool tilted at an angle with respect to the workpiece.

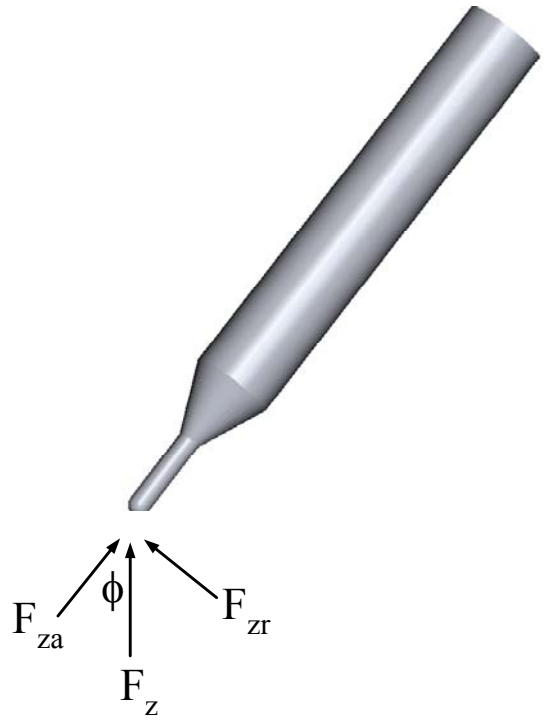

Figure 5: Schematic of Tool and Axial and Radial Forces

As a result, the stiffness of the tool in the direction orthogonal to the workpiece must be found. The relationship between orthogonal force and orthogonal deflection is given with Equation (3).

$$\delta_{orthogonal} = force_{orthogonal}\left(\frac{\cos^2\phi}{k_{axial}} + \frac{\sin^2\phi}{k_{radial}}\right) \tag{3}$$

where:
k = stiffness of tool

ϕ = tilt angle of the tool with respect to the workpiece
δ = deflection of the tool

Therefore stiffness of the tool at a tilt of 25 degree tilt is found in Equation (4).

$$k_{tilt-25\deg} = \left(\frac{k_{axial}}{\cos^2 \phi} + \frac{k_{radial}}{\sin^2 \phi} \right) \tag{4}$$

Comparison of Calculated and Measured Tool Stiffness

To experimentally measure the tool stiffness when tilted at 25 degrees, experiments were ran on the DTM that involved pushing a non-rotating tool against the load cell. A tool was placed in the high-speed spindle and the tool was angled at 25 degrees with respect to the normal vector of the surface of the workpiece. This measurement of tilt of the tool with respect to the axis of the machine was made with a precision protractor. The z-axis was moved until the tip of the tool was just in contact with the surface of the workpiece. At this time a motion program moved the z-axis into the part 50 μm while measuring the orthogonal force. Since the tool was not rotating, cutting did not occur and movement of the z-axis resulted in deflection in the tool tip. Once the experiment was complete, a measurement of the indention on the workpiece produced by the tool was made. This value of indention depth was then subtracted from the encoder position during the move. It was then assumed that deflection of the tool was equal to z encoder position during the move. This resulted in a force vs. deflection curve and experimental data to compare with the calculated value of tool stiffness at 25 degrees tilt with respect to the workpiece.

Experimentally measured tool stiffness at 25 degree tilt can be seen in Figure 6. It is seen that the experimental tool stiffness at 25 degree tilt is 455120 N/m. This is comparable with the calculated value (using Equation (4)) of 419565 N/m using the axial and radial stiffness measurements shown in Table 1.

6.2.4 CONTROL SYSTEM ON THE NANOFORM

The machine used for these experiments is not designed for fast feedrates and high acceleration. There are limits incorporated in the maximum acceleration the axes can perform without violating safety variables set internally in PMAC. Therefore, to get around these acceleration limits and also make force feedback more easily implemented and user friendly, a custom motion program was written controlling the Nanoform axes inside a motion program, rather than have PMAC do the controlling of the axes internally. In essence, internally in the built-in controller, PMAC believes all three axes to be in a dwell state. In actuality though, a control algorithm is operating in a motion program that takes care of reading encoder position, calculating error,

performing deflection compensation routines, filtering z-force, and updating voltage output to the motors controlling each axis.

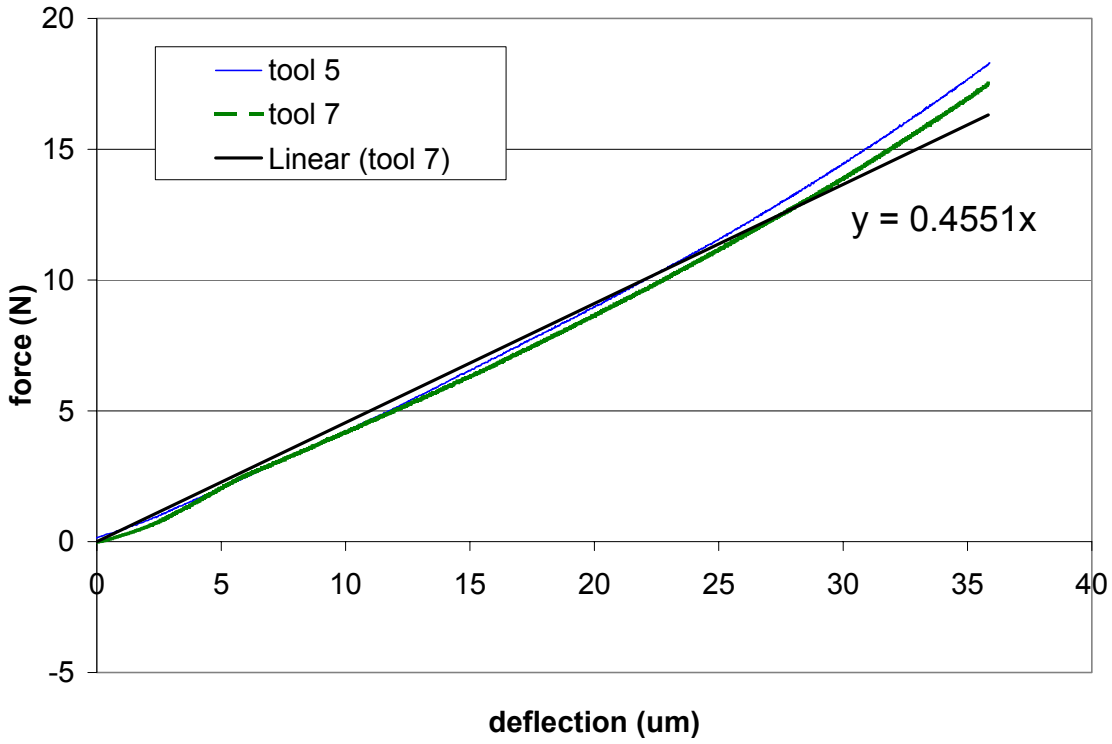

Figure 6: Experimental Tool Stiffness at 25 Degree Tilt with Linear Trendline

Determining Gains for the Axes

The control running all three axes on the Nanoform DTM is proportional-integral-derivative (PID) control with gains implemented for quick acceleration and movement. The gains were chosen to achieve satisfactory performance given a step input to each axis on the order of 100 μm. Through tuning of the PID gains rise time, overshoot, and steady state following error of each axis was reduced to a minimum without compromising system stability.

Tuning on the system started through evaluating each axis at its limit of stability. Proportional gain was increased until continuous oscillations occurred and the system became marginally stable. This produced a corresponding gain K_u (called the ultimate gain) and a period of oscillation P_u (called the ultimate period) illustrated in Figure 7. Ziegler-Nichols rules were then used to determine starting PID gain controller settings for closed loop response of the machine. Ziegler-Nichols provided a starting point for the PID gains, but further tuning was necessary to achieve desired response time, steady-state error, and system stability for the system.

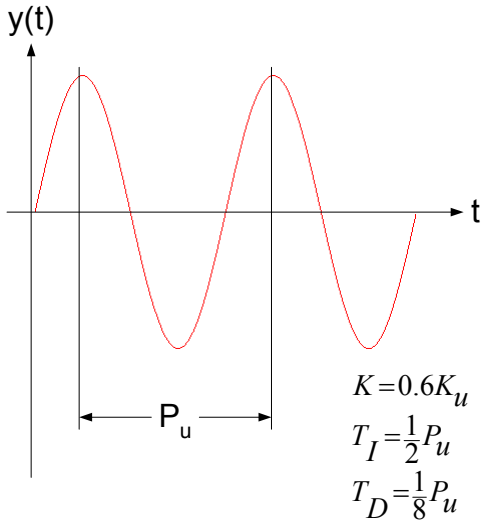

Figure 7: Ziegler-Nichols Marginal Stability Criteria

Table 2: PID Gains for Control Algorithm

axis	proportional gain	integral gain	derivative gain
x	39000	190000	373
y	45000	1400000	15
z	48000	200000	422

The gains were chosen to give good step response for each axis. Each axis was tuned to make 100 μm steps and integral control was implemented to give good steady state error response. Likewise derivative control was implemented to reduce overshoot. Final system gains for each axis is shown in Table 2 and a plot of all three axes response to the step input is shown in Figure 8.

Custom G Code Program

Control of the axes was implemented using a custom motion program performing various operations such as: reading encoder position, calculating desired position, calculating following error, filtering input force, calculating predicted depth and deflection, compensating for error in tool depth/deflection, and outputting voltage to each motor being controlled. There was also a need for this algorithm to be user friendly and to apply to a wide range of cutting conditions like current “g codes” on CNC machines in industry.

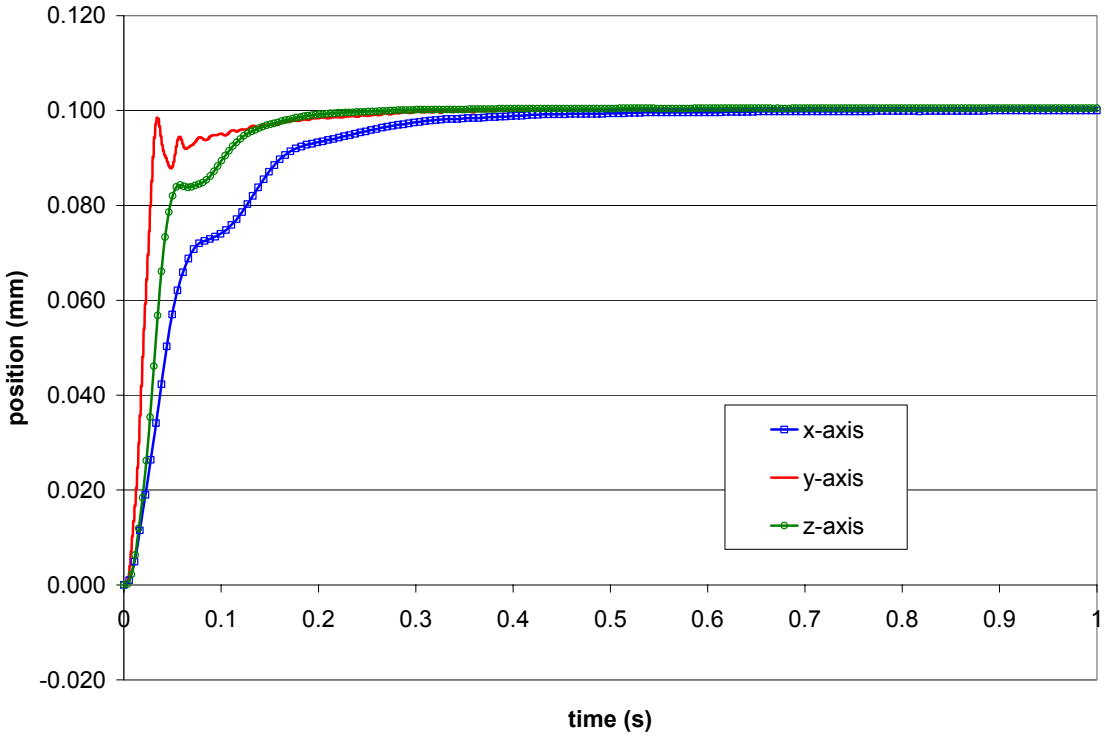

Figure 8: Axes Response to a 0.1 mm Step Input

Therefore, various subroutines were created to perform a linear move with no compensation, a linear move with force feedback implying a predicted depth based on a dynamic model, a linear move with force feedback implying a predicted deflection based on a model of tool stiffness, and a linear move in the x and y directions with a sinusoidal profile in the z-direction with no compensation, predicted depth compensation, and predicted deflection compensation. These subroutines are called from a main motion program where the user simply chooses which particular cutting operating to perform with an appropriate "callxx x0.0 y0.0 z0.0 f0.0" statement telling the motion program which subroutine to use and what kind of move to make.

Any profile can be created as long as it can be parametrically defined as a function of time with respect to each appropriate axis. Helical cuts, sinusoidal cuts, parabolic profiles, and other complex cuts are easily made as long as the movement of each axis can be defined as a mathematical function of time.

6.2.5 DIFFERENT APPROACHES TO COMPENSATION:

There are two basic approaches to error compensation using force feedback discussed in this section. One involves predicting a depth based on a dynamic cutting force model, while the other involves predicting a deflection based on a model of tool stiffness.

Depth prediction using a dynamic tool force model

A block diagram of the control algorithm predicting depth using a dynamic cutting force model is show in Figure 9. The concept behind this algorithm is straightforward: start with a desired tool path position vs. time, measure a real-time cutting force, using cutting conditions and a dynamic force model predict a depth of cut, and then calculate an error equal to desired minus predicted depth. Once this error has been calculated, PID control either holds position, moves further into the workpiece in the z-direction increasing the depth of cut, or moves out from the workpiece decreasing the depth of cut. In this way the system can correct for errors associated with tool deflection and misalignment of the workpiece. Error used in the PID control is as follows:

$$error = desired_{position} - \left(a \cdot force^2 + b \cdot force \right) \tag{5}$$

where:

a = quadratic coefficient of depth vs. force trendline generated by cutting force model (Figure 2)
b = linear coefficient of depth vs. force trendline generated by cutting force model

With a validated cutting force model, a depth vs. force curve can accurately be predicted based on cutting conditions. By measuring a real-time force, a dynamic cutting force model predicts a depth. This allows compensation for tool deflection as well as compensation for other errors involving misalignment of the part with respect to the axes of the milling machine.

Advantages to Depth Prediction

- alignment of the workpiece with respect to the axes of the machine is not necessary
- uses only-force feedback in the control algorithm so that the profile is referenced to the workpiece surface and has no relation to the z-axis of the machine

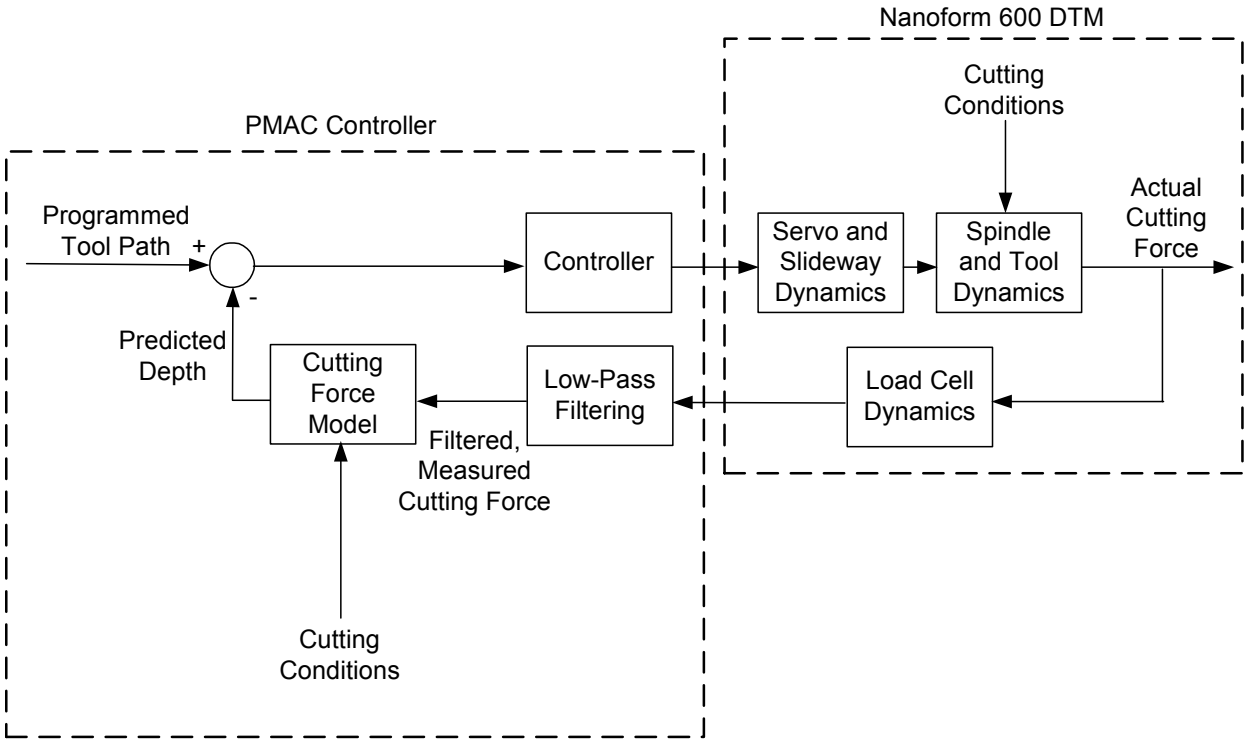

Figure 9: Block Diagram of Predicted Depth Based on Dynamic Cutting Force Model

Disadvantages to Depth Prediction

- cutting parameters are very difficult to determine (wearland, spindle speed, feed rate, material properties, etc.) to get appropriate dynamic cutting force model
- wearland of tool is difficult to measure and may change during a milling operation
- spindle speed may change during a milling operation
- relies only on force feedback to predict a depth so that stability is a major issue in the control algorithm (for instance during a tool break, interruption of cuts, etc.)
- starting and stopping during milling with only-force feedback (no encoder feedback) results in an increased required awareness as to what state in the milling operation one is in (operator needs to know exactly what's going to happen next in reference to exiting the workpiece, reaching the edge, plunging, etc.)
- tool force filtering has to be incorporated in the model before hand and has an effect on the results
- drift in the load cell as well as noise plays a larger role as this is the only method of feedback in the control algorithm
- this model is setup for milling down a groove feeding into the workpiece along the direction of tilt and does not apply to any general profile

Deflection Prediction Using a Model of Tool Stiffness

A block diagram of the control algorithm predicting deflection using a model of tool stiffness is shown in Figure 10. The concept behind this algorithm is straightforward: start with a desired tool path position vs. time, measure a real-time cutting force, using a tool stiffness model at a particular tilt of the spindle with respect to the workpiece as well as the measured force predict a deflection, calculate an error equal to desired position plus deflection minus encoder position. Once this error has been calculated, PID control either holds position, moves further into the workpiece in the z-direction increasing the depth of cut, or moves out from the workpiece decreasing the depth of cut. In this way the system can correct for errors associated with tool deflection during milling using force feedback while keeping system stability. Error used in the PID control is as follows:

$$error = desired_{position} + \left(\frac{force}{k} \right) - laser_{position} \tag{6}$$

where:

k = stiffness of tool with respect to normal of workpiece (Figure 6)

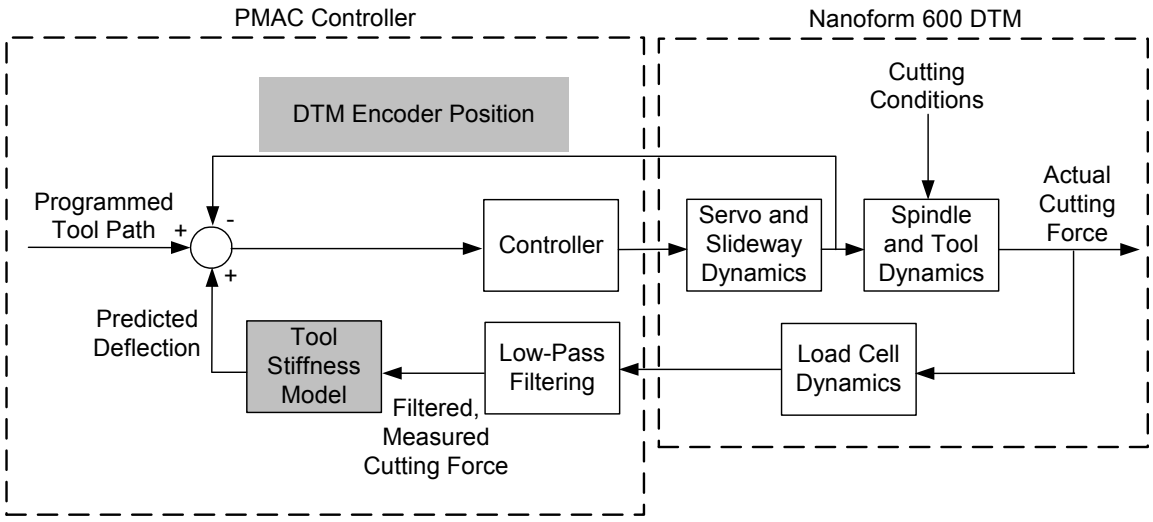

Figure 10: Block Diagram of Predicted Deflection Using a Tool Stiffness Model

With a validated stiffness model, deflection can accurately be predicted based on tool stiffness and a measured real time cutting force. This allows compensation for tool deflection to occur real-time while also having encoder position feedback to ensure greater system stability.

Advantages to Deflection Prediction

- Wearland, spindle speed, feed rate, material properties, and depth are not factors in predicting tool deflection
- Tool stiffness is easily measured at a particular tilt and can be calculated from measurements of axial and radial tool stiffness
- Deflection is dependent only on tool stiffness (which is a function of tilt of tool with respect to workpiece normal vector)
- Uses encoder feedback so program execution is more stable and reliable
- Part alignment is performed in industry in every milling operation and alignment on the order of 1 μm is easily obtainable so misalignment is not an issue
- Load cell noise and drift play less of a part in total machine stability and accuracy

Disadvantages to Depth Prediction

- part alignment with respect to the axes of the machine plays a direct result on the profile of the completed cut and misalignment can occur (however this is true in any current milling operation in industry)

6.2.6 DIGITAL CONTROL

The computer system running the algorithm used to control the Nanoform DTM and to perform closed loop force feedback compensation is a Programmable Multi-Axis Controller (PMAC). As this is a digital computer, the control system does not follow fundamental control theory of a continuous system, but instead has its own set of considerations covered under the topic of digital control and discrete systems. Digital control has its own set of limitations and understandings one must be aware of if the system is to perform similarly to a continuous system. With sampling periods and non-continuous states there is an associated phase lag and one must pay careful attention to the frequencies and update rates of the control algorithm along with data gathering frequency to ensure system stability and desired performance.

The digital system operates on samples of sensed plant output rather than on a continuous signal. Associated with this digital control is an A/D board that takes analog force input and converts it into a digital signal to be used in the PMAC. Conversion of the analog signal occurs repeatedly at instants of time specified by the clock frequency on the PMAC board. The A/D board input is captured at each instance of the servo cycle on the PMAC. The frequency at which the force is sampled through the A/D board is at 2272.72 Hz (440 μs). When comparing this sampling frequency with the frequency of the spindle during operation at 10,000 revolutions per (RPM) (166.66 Hz) it is seen that the sampling frequency of the force is 13.68 times that of the

frequency of the spindle. Therefore, for every one revolution of the spindle, force data from the A/D board is captured approximately 14 times.

Even though the force is sampled at 2272 Hz, the actual force used in the control algorithm is sampled much less frequently. As discussed earlier, the control algorithm running the axes on the DTM is PID control running inside a motion program. In a milling operation, the PMAC internal controller believes the axes to be dwelling, but in reality, the axes are controlled with PID control through a while loop running in a motion program externally with its own set of PID gains, etc.. This PID control running inside a motion program performs such operations as checking following error, derivative error, integration error, and it also scales and filters the current cutting force orthogonal to the workpiece. The execution time of this while loop is what really determines the sampling of this force, due to the fact that in every execution of the while loop, the force is measured and filtered, and then a depth/deflection is inferred to be used in the PID control algorithm. Thus the depth/deflection value is only updated once per execution of the while loop actually controlling the DTM.

With digital control and the relatively slow sampling rate equal to the while loop execution frequency, investigation to see if digital control will in fact perform like continuous control should be made. Control theory states that if the sampling rate is on the order of 20 times the bandwidth of the axis, then the system will behave like that of a continuous system. The closed loop bandwidth of the z-axis on the DTM is approximately 14.2045 Hz, and because the frequency at which the control algorithm operates is 751.8793 Hz, which is 52.93 times that of the z-axis, this system should behave like that of a continuous system.

Control theory also states that as long as the sampling frequency of a signal is twice as fast as that input signal, no aliasing will occur and the input signal is properly represented with the samples. In looking at the while loop execution frequency of 751. 8793 Hz, it is seen that the apparent force sampling frequency is in fact over twice as fast as the actual force input frequency (333.33 Hz) and thus, no aliasing will occur and the force measured properly represents the actual input force without aliasing [4].

Table 3 shows the frequencies of various components in the system. Spindle frequency is the frequency at which the spindle rotates during a machining operation. A/D board conversion frequency is the frequency at which the A/D board captures data and makes the conversion from an analog signal to a digital signal to be used in the PMAC. While loop execution frequency is the frequency at which axes position, encoder position, etc. is updated. Due to this while loop actually capturing the force and performing filtering of the force, it is at this frequency that the force is actually sampled and used. Closed loop bandwidth of the axes is simply the frequency at which each axis can respond to output commands from the PMAC.

Table 3: System Frequencies

Spindle frequency	166.66 Hz (10,000 rpm)
Apparent spindle frequency (with 2 flutes)	333.33 Hz
A/D board conversion frequency	2272.72 Hz (440e-6 s)
While loop execution frequency	751.8796 Hz (1.333e-3 s)
Apparent force sampling frequency	751.8796 Hz (1.333e-3 s)
x-axis closed loop bandwidth	13.0718 Hz
y-axis closed loop bandwidth	37.7358 Hz
z-axis closed loop bandwidth	14.2045 Hz

6.2.7 FORCE FILTERING

The execution time of the while loop is 1.33e-3 s (751.8793 Hz). When comparing this with the frequency of the spindle at 10,000 rpm, it is seen that the while loop execution frequency is approximately 4.511 times that of the spindle frequency when taking into account the number of flutes on the tool. In deflection compensation, one would like to compensate for the maximum force achieved during milling. If compensate for the maximum deflection is not made, the profile of the cut will not be what was originally desired, but will be better than a cut with no compensation at all. By only sampling realistically at 4.511 times that of the spindle frequency (or 2.25 times per flute with a two flute tool), the actual maximum machining force during each sample is not likely to be read. Therefore, some force filtering is necessary to have an average force to use in the control algorithm that can be scaled to achieve a value of the actual maximum force. The determination of this force filtering should be approached with caution however, as with all filtering, some phase lag as well as attenuation of the maximum value of the signal is expected. Due to this attenuation, a multiplication factor is needed to scale the filtered force by to achieve a value closer to the maximum force.

Force gathering was done with a PMAC Accessory-28A analog-to-digital (A/D) conversion board. This board provides four channels of high-speed, high-resolution analog input capability to the PMAC controller. The input voltages in the range of ±10 V are converted to 16-bit signed values. In the control algorithm, these forces values are simply brought into the motion program as variables and then proper scaling as well as filtering is done accordingly.

First Order Digital Filter

A first order digital filter was used to filter the input orthogonal force. Such a filter was chosen due to its simplicity and fast arithmetic operation time in the while loop. If a very complex filter was implemented, the execution time of the while loop would further decrease and thereby reduce the sampling frequency of the force. Thus a filter of the following form was used:

$$force_{filtered}(k) = \beta \cdot force_{current}(k) + \alpha \cdot force_{average}(k-1) \tag{7}$$

$$\beta = 1 - \alpha$$

The determination of the filtering coefficients is not trivial and should be determined based on the root locus of the transfer function of this first order digital filter. The transfer function of this filter is determined by taking the z-transform of the filter. The z-transform is defined with the following properties:

$$L\{F(k)\} = F(z) = \sum_{k=1}^{\infty} f(k) z^{-1} \tag{8}$$

$$L\{F(k-1)\} = z^{-1} F(z) \tag{9}$$

where F(k) is the discrete function at a particular sample k, and F(z) is the z-transform of the discrete function. L represents the z-transform operator.

The transfer function of this first order digital filter was found to be:

$$\frac{force_{average}(z)}{force_{current}(z)} = \frac{\beta}{1 - \alpha z^{-1}} \tag{10}$$

Setting the denominator of Equation (8) equal to zero gives the root locus pole location on the z-plane. The z-plane represents a graphical chart of different natural frequencies of a system as well as different damping ratios. The z-plane can be seen in Figure 11 and is used to determine the proper coefficients in the first order digital filter.

The following characteristics apply for the z-plane:

- The stability boundary is the unit circle | z | = 1
- The small vicinity around the z = +1 in the z-plane is essentially identical to the vicinity around s = 0 in the s-plane
- The z-plane locations give response information normalized to the sample rate
- The negative real z-axis always represents a frequency of $\omega_s/2$ where $\omega_s = 2\pi/T$ = sample rate in radians per second
- Vertical lines in the left half of the s-plane (the constant real part or time constant) map into circles within the unit circle of the z-plane and represent a stable system
- Horizontal lines in the s-plane (the constant imaginary part of the frequency) map into radial lines in the z-plane

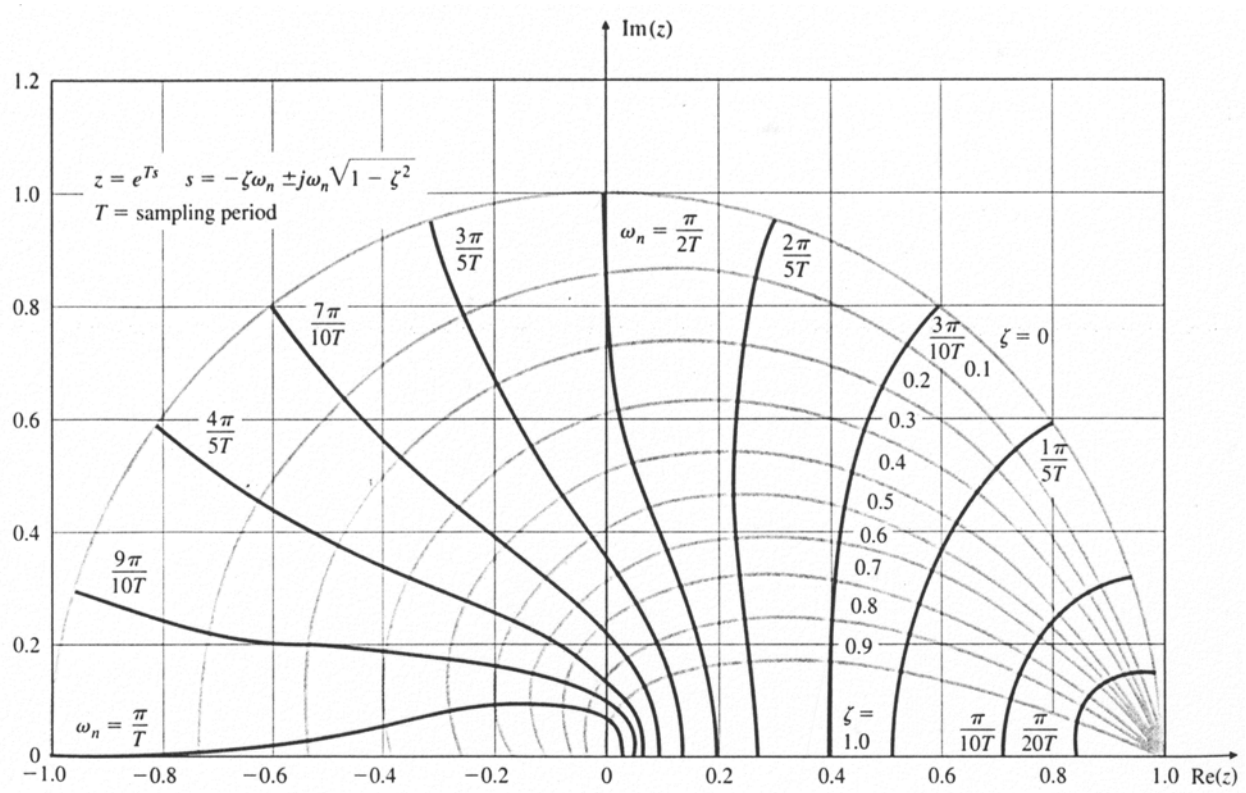

Figure 11: Z-Plane for a Discrete System

The root of the denominator is z = α and represents a traditional pole in control theory. Therefore, choosing α in the first order digital filter will determine the filtering characteristics. In looking at the z-plane, various lines of constant damping are represented with lines starting on the real axis in the left half plane and ending at 1 on the real axis. Various lines of natural frequency start on the real axis of the right half plane and end on the unit circle boundary. Determining closed loop frequency of this system, and where this frequency crosses the real axis on the right half of the z-plane will reveal the proper coefficients in the first order digital filter. The closed loop bandwidth of the z-axis is 14.2045 Hz, and therefore, this is the frequency used in determining the proper α best suiting the bandwidth of the system. Since our sample time is the time of the while loop execution (751.8796 Hz ~ 1.333e-3 s), the following Equation (11) and (12) gives the natural frequency band desirable for this system:

$$\omega_n = \frac{x\pi}{T} \tag{11}$$

$$x = 0.006027 \sim \frac{1}{168} \tag{12}$$

In taking a closer look at the z-plane (Figure 12), the corresponding root on the real axis that is at a natural frequency band position of π/170T is α = 0.99 and consequently β = 0.01. This lead

coefficient in the first order digital filter should give proper filtering for the natural frequency of the z-axis as well as the sample time used in the while loop execution.

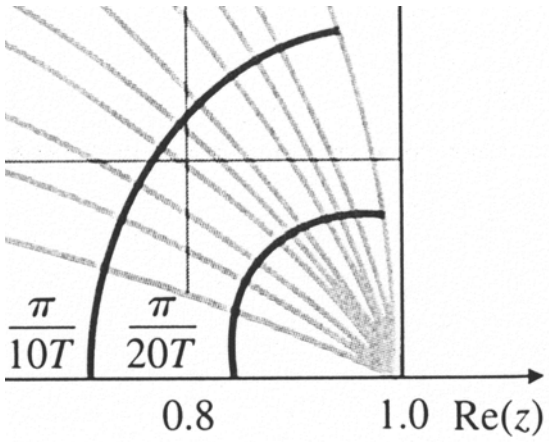

Figure 12: Enlarged Z-Plane around Area of Interest

Multiplication Factor

Compensation is done strictly by taking in consideration the orthogonal force with respect to the workpiece. The orthogonal force has a shape closely resembling a sine wave due to the shape of the ball end mill. The z-force increases as the tool rotates, but due to the tilt of the tool, the flutes on the tool are not always cutting for a whole revolution of a tool. At 25 degree tilt of the tool, orthogonal force increases to a maximum and then decreases to zero twice with every rotation of the tool due to the tool having two flutes. In looking at actual force data Figure 13, it is seen that in fact the orthogonal cutting force does resemble a sine wave.

However, due to the fact that the execution of the while loop controlling the axes is only 4.5 times as fast as the spindle frequency, data acquisition of the real time cutting force in the while loop only gives approximately four data points for every revolution of the tool. This causes the gathered force to resemble a square wave and can also be seen in Figure 13. Actual force data for a cutting operation is shown in Figure 14. Thus, due to limited force gathering and the fact that the while loop does not execute at a frequency equal to an even multiple of the spindle frequency, there is a some what random sample of the orthogonal cutting force.

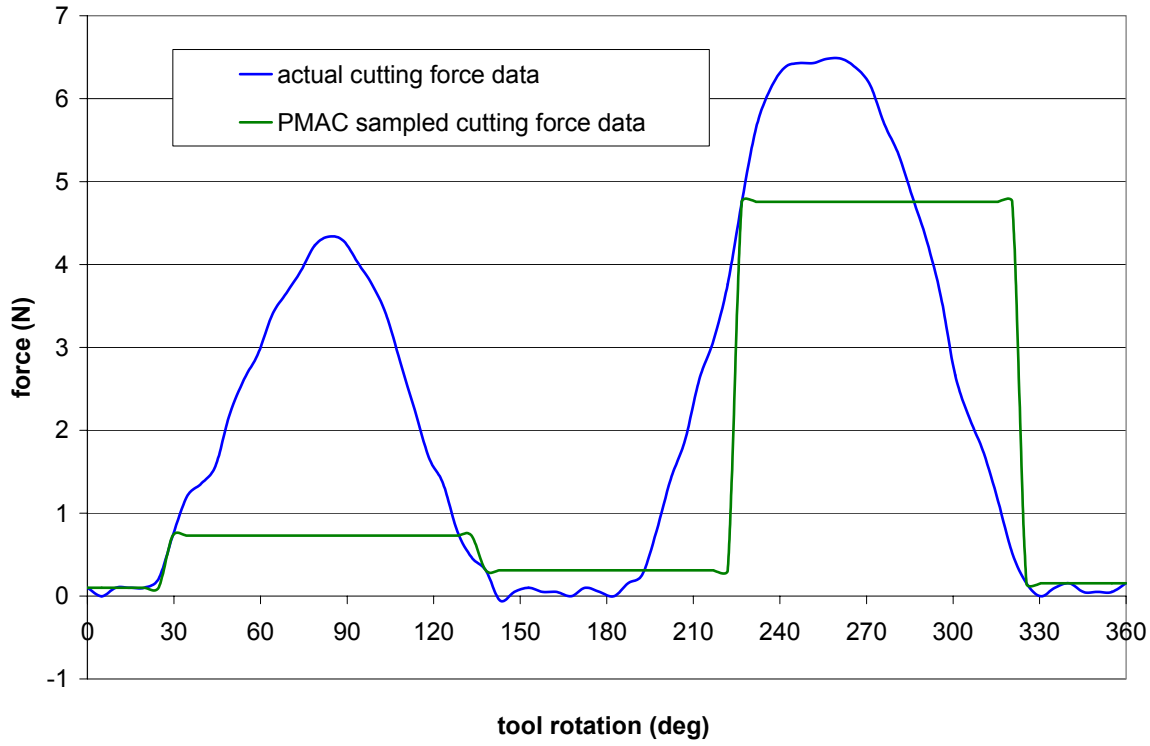

Figure 13: Z-force during 25 Degree Tilt Cutting

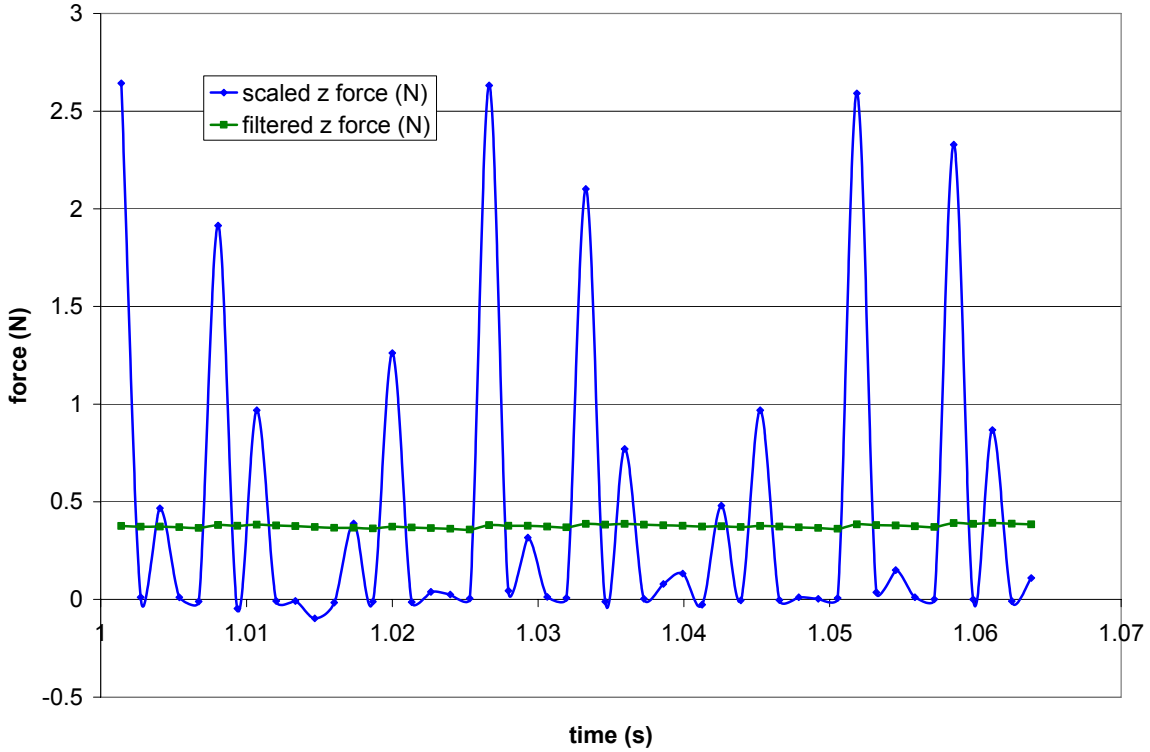

Figure 14: Actual PMAC Gathered Z-Force during Machining

This some what random sample of the orthogonal cutting force made an analytical approach to determining the multiplication factor difficult. Thus the multiplication factor was determined experimentally with an open loop groove test. For this open loop groove test, a cut was made to a depth of 80 μm open loop without force feedback implemented. During the cut, the force was measured and deflection predicted based on a model of tool stiffness. Then the groove profile was measured on the talysurf profilometer, and the actual deflection was compared with predicted deflection based on the real-time cutting force without a multiplication factor. By comparing the real deflection to predicted deflection, an experimental multiplication factor could be determined to scale the inferred deflection by to achieve the actual deflection. A plot of the predicted deflection without a multiplication factor added during machining is given in Figure 15.

It is seen that the maximum predicted deflection without a multiplication factor is 9.23 μm. The actual deflection measured on the talysurf profilometer is 26.859 μm. Therefore the experimental multiplication factor is determined to be 2.90 and this value was then used in the experiments.

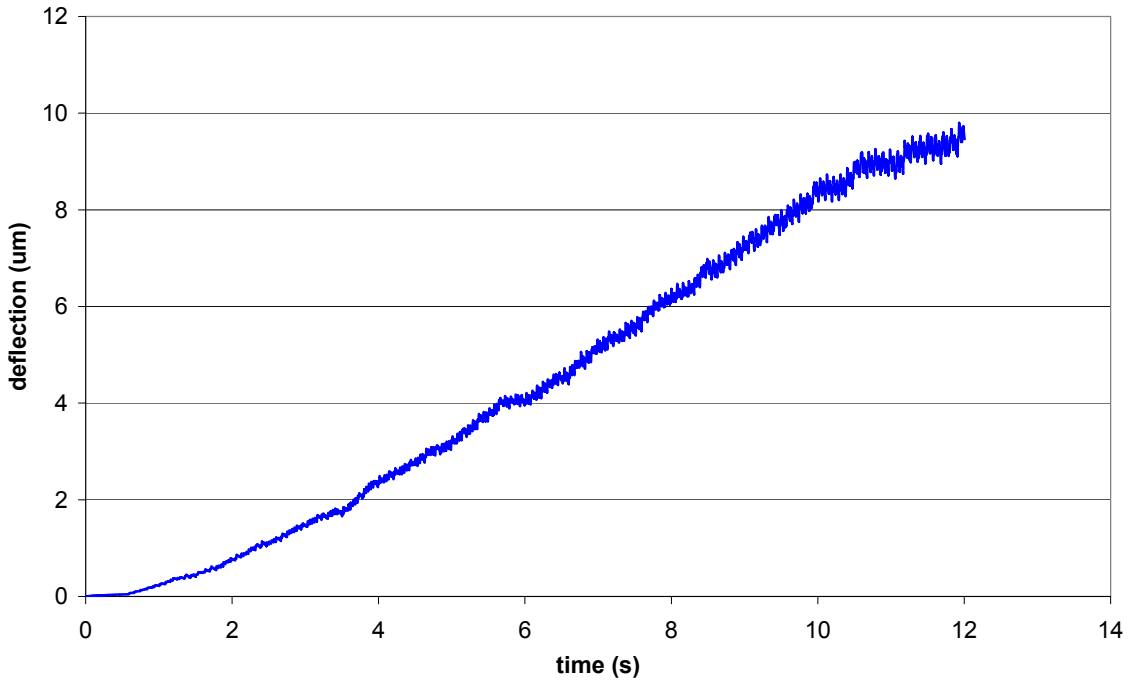

Figure 15: Predicted Deflection during an Open Loop Groove Cut without Multiplication Factor

6.2.8 EXPERIMENTAL RESULTS

Predicted Depth Based on a Dynamic Cutting Force Model

To evaluate the predicted depth based on a dynamic cutting force model compensation algorithm, a series of experiments were conducted on the Nanoform DTM. Groove profiles were machined in S-7 tool steel samples. Cuts were made with and without compensation to determine the value and error reduction with the algorithm implemented. Groove profile was then measured on the talysurf profilometer. The part was aligned with the axis of the stylus tip motion of the profilometer, and the then the tip was drug down the groove thereby giving a measurement of the depth and profile.

One set of results is shown in Figure 16. This figure shows the measured and predicted cutting depths for a tool tilted at 25˚ to the surface normal. Grooves spanning 18 mm and 0-70 µm in depth were programmed, using a spindle speed of 10,000 rpm and a feed rate of 100 mm/min. This was the 3rd cut on this particular tool. The upper line represents the uncompensated cutting depth, as measured on a Talysurf profilometer. The middle line is an actual measured groove profile of a cut made with compensation implemented. The lower line is the desired groove profile representing what the groove should look like.

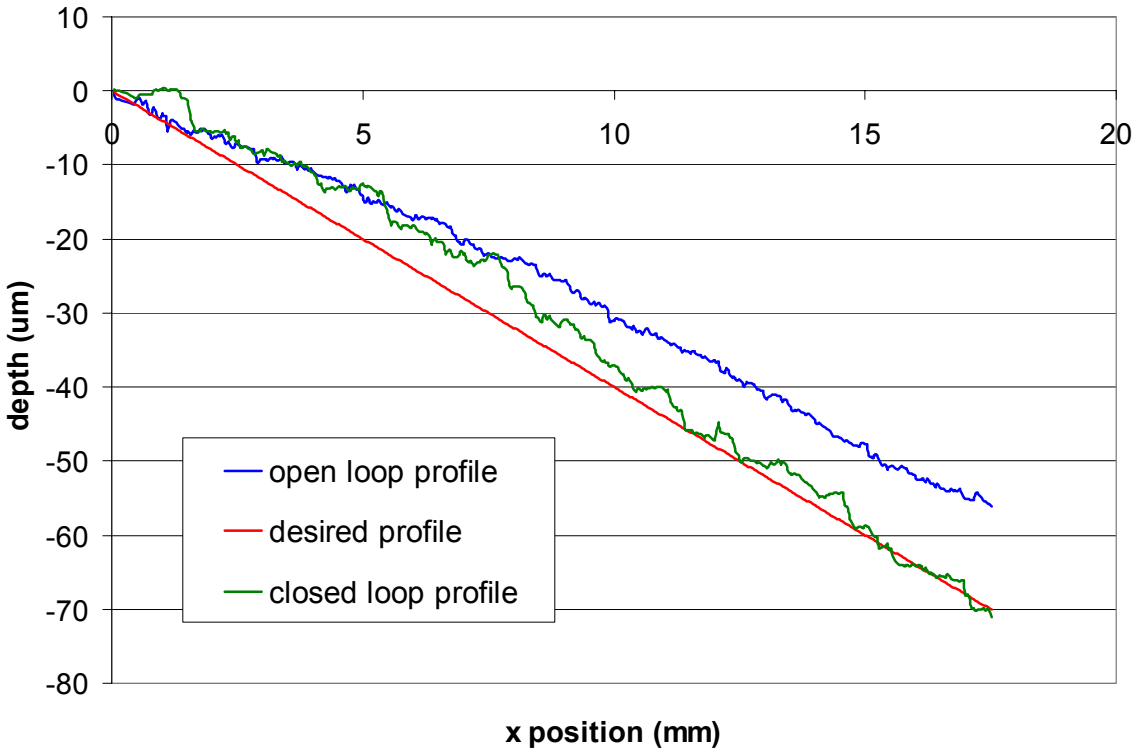

Figure 16: Predicted Depth Linear Groove Profile

Error in the groove profile is not significantly improved at the start of the groove as both error uncompensated and error compensated are approximately equal 8 mm into the groove cut. However, Figure 17 shows that beyond this point compensation based on predicted depth using a dynamic cutting force model significantly improves the error in the profile cut and produces results more desirable. Maximum error in the compensated groove is on the order of 8 μm (at a horizontal location of 8 mm), while maximum error (deflection) in the uncompensated groove reaches a maximum of 14 μm at a location of 18 mm. This equates to a 43% reduction in groove profile error.

Predicted Deflection Using a Model of Tool Stiffness

To evaluate the predicted deflection using a model of tool stiffness compensation algorithm, a series of experiments were conducted on the Nanoform DTM. Various groove profiles were machined in S-7 tool steel samples. Cuts were made with and without compensation to determine the value and error reduction with the algorithm implemented.

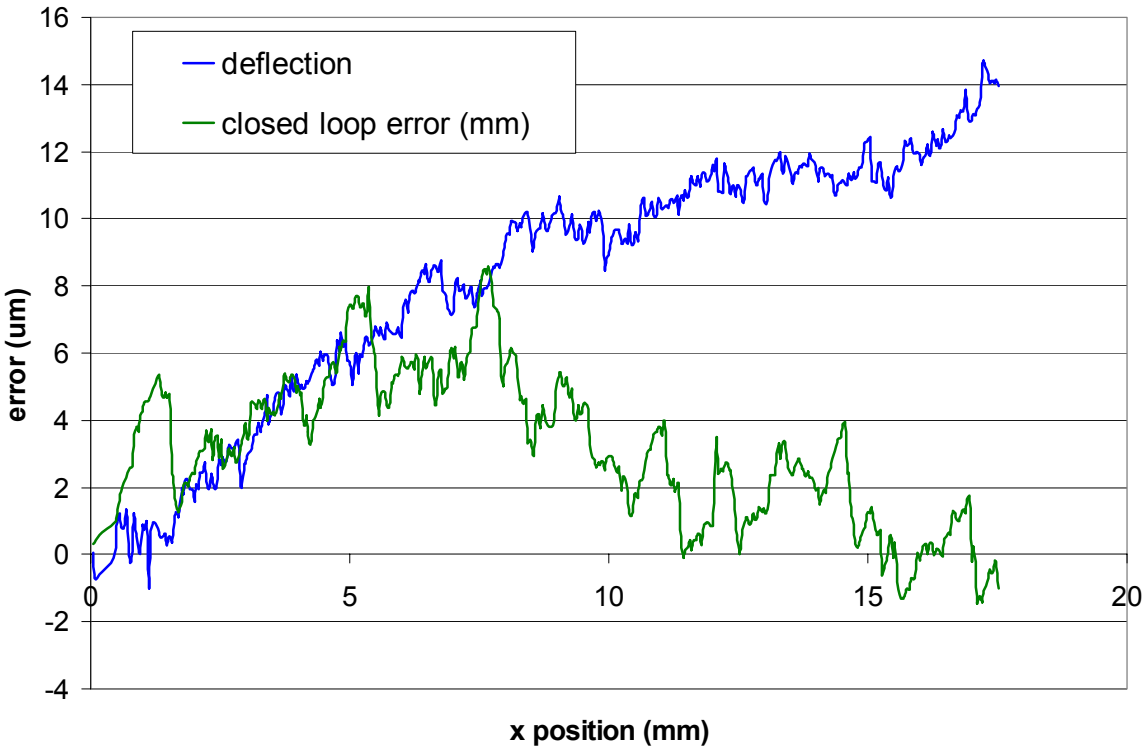

Figure 17: Predicted Depth Linear Groove Deflection and Error

Linear Groove Cut

Figure 18 shows the measured and predicted cutting depths for a tool tilted at 25˚ to the surface normal. Grooves spanning 20 mm and 0-80 μm in depth were programmed, using a spindle speed of 10,000 rpm and a feed rate of 100 mm/min with the long tool. This was the 10th cut on this particular tool. The upper line represents the uncompensated cutting depth, as measured on a Talysurf profilometer. The middle line is an actual measured groove profile of a cut made with deflection prediction compensation implemented. The lower line is the desired groove profile perfectly representing what the groove should look like.

Figure 19 shows that error in the groove profile is significantly improved throughout and the results show that this method of compensation reduced the form error from a maximum of 21 μm to just over 4 μm. This is an 80% reduction in error comparable almost to an order of magnitude decrease in groove profile form error. It can be seen that groove profile error at the start as well as during the groove cut is bound between +1 μm and –3 μm. It is only at the end of the groove that the error increases to +4 μm.

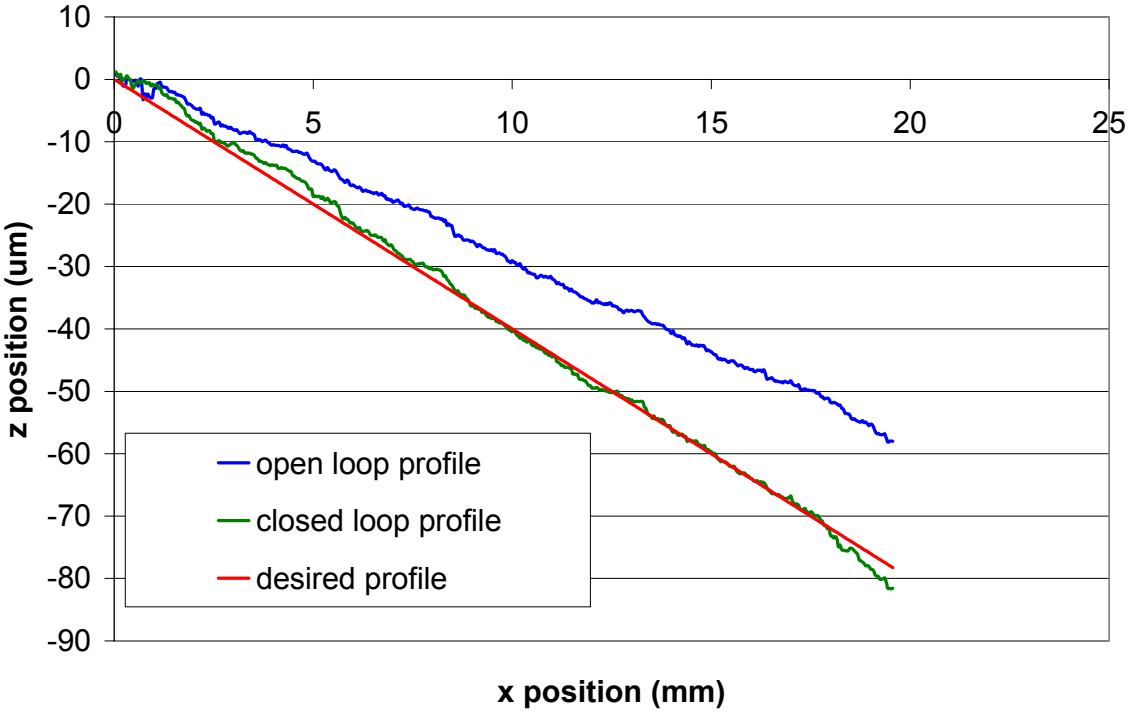

Figure 18: Predicted Deflection Linear Groove Profile

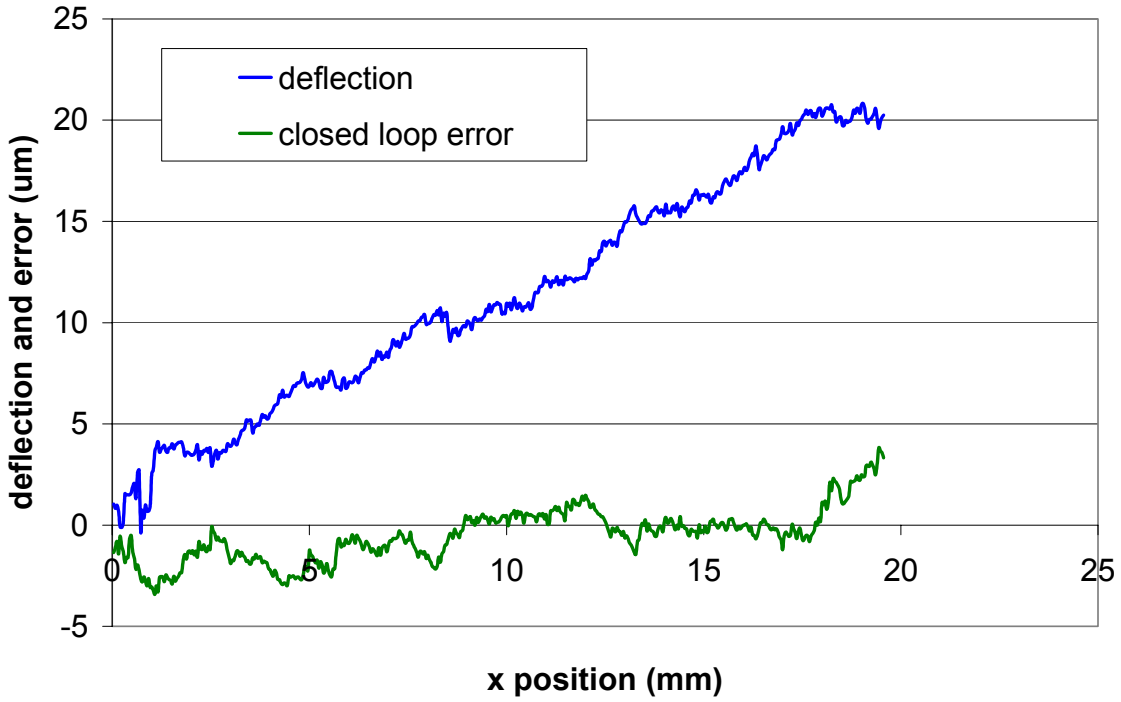

Figure 19: Predicted Deflection Linear Groove Deflection and Error

One Period Sinusoidal Wave Profile

Figure 20 shows the measured and predicted cutting depths for a tool tilted at 25˚ to the surface normal. Grooves spanning 20 mm with a one period sinusoidal profile and desired depth of 80 μm were programmed, using a spindle speed of 10,000 rpm and a feed rate of 100 mm/min with the long tool. This was the 11th cut on this particular tool. The frequency of the sine wave is 0.523 Hz. The upper line represents the uncompensated cutting depth, as measured on a Talysurf profilometer. The middle line is an actual measured groove profile of a cut made with compensation implemented. The lower line is the desired groove profile.

Figure 21 shows that error in the groove profile is significantly improved throughout and that this method of compensation reduced the form error from a maximum of 23 μm to just over 6 μm. This is a 75% reduction in error. It can be seen that groove profile error at the start as well as during the groove cut is bound between +1 μm and –5 μm.

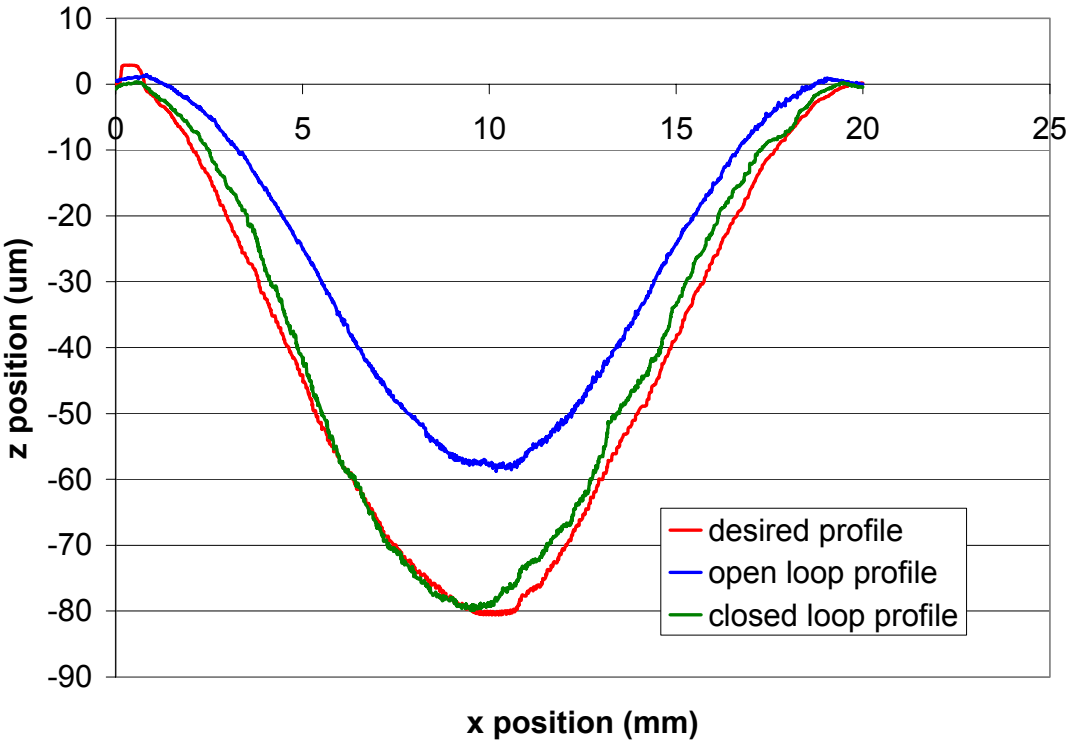

Figure 20: Predicted Deflection One Period Sine Wave Groove Profile

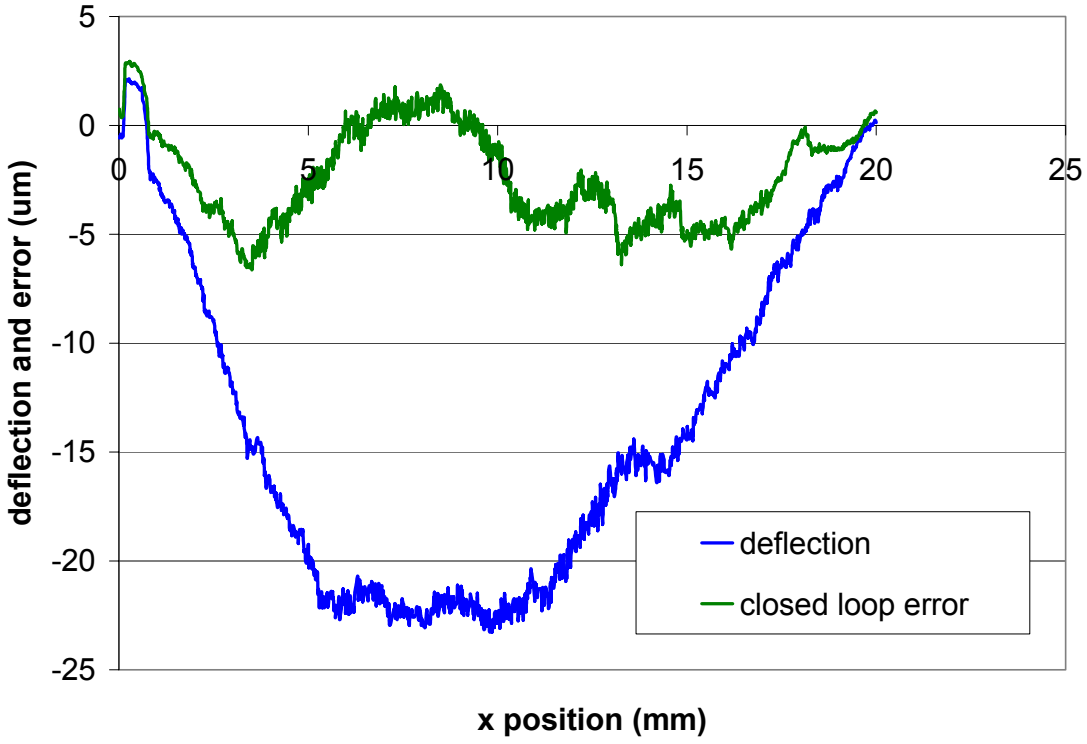

Figure 21: Predicted Deflection One Period Sine Wave Groove Open Loop Deflection and Error

Two Period Sinusoidal Wave Profile

Figure 22 shows the measured and predicted cutting depths for a tool tilted at 25˚ to the surface normal. Grooves spanning 20 mm with a two period sinusoidal profile and desired depth of 80 μm were programmed, using a spindle speed of 10,000 rpm and a feed rate of 100 mm/min with the long tool. This cut was the 12th cut on this particular tool. The frequency of the sine wave is 1.047 Hz. The upper line represents the uncompensated cutting depth, as measured on a Talysurf profilometer. The middle line is an actual measured groove profile of a cut made with compensation implemented. The lower line is the desired groove profile perfectly representing what the groove should look like.

Error in the groove profile shown in Figure 23 is significantly improved throughout and the results show that this method of compensation reduced the form error from a maximum of 27 μm to 13 μm. This is a 52% reduction in error. It can be seen that groove profile error at the start as well as during the groove cut is bound between +1 μm and –13 μm.

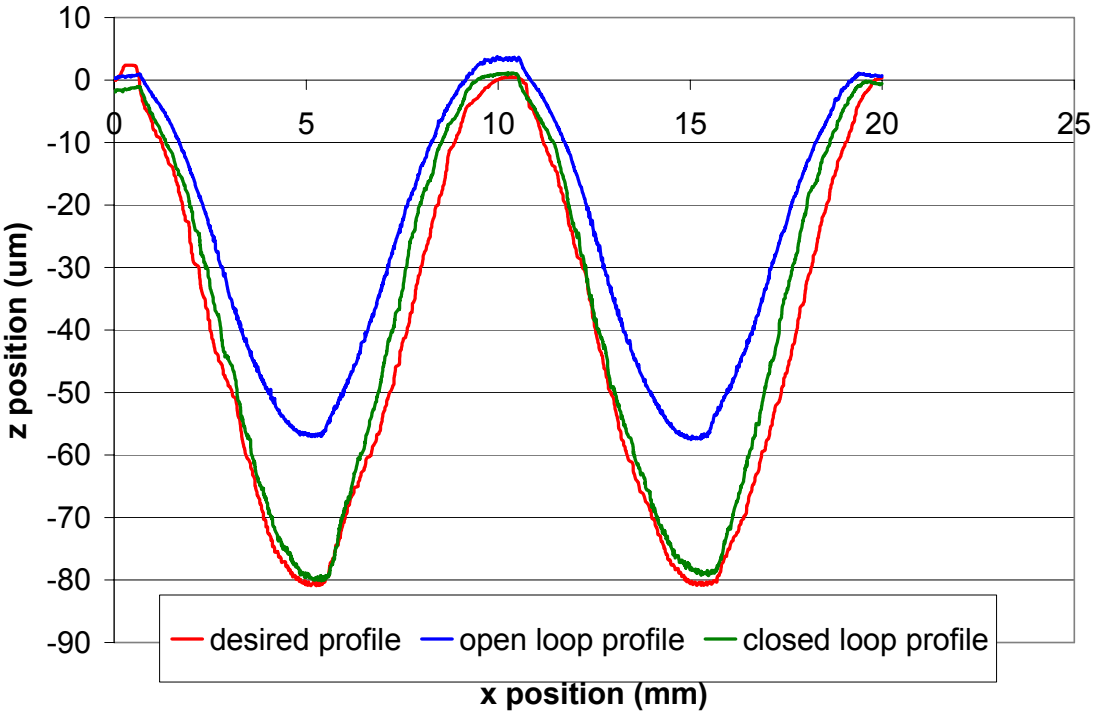

Figure 22: Predicted Deflection Two Period Sine Wave Groove Profile

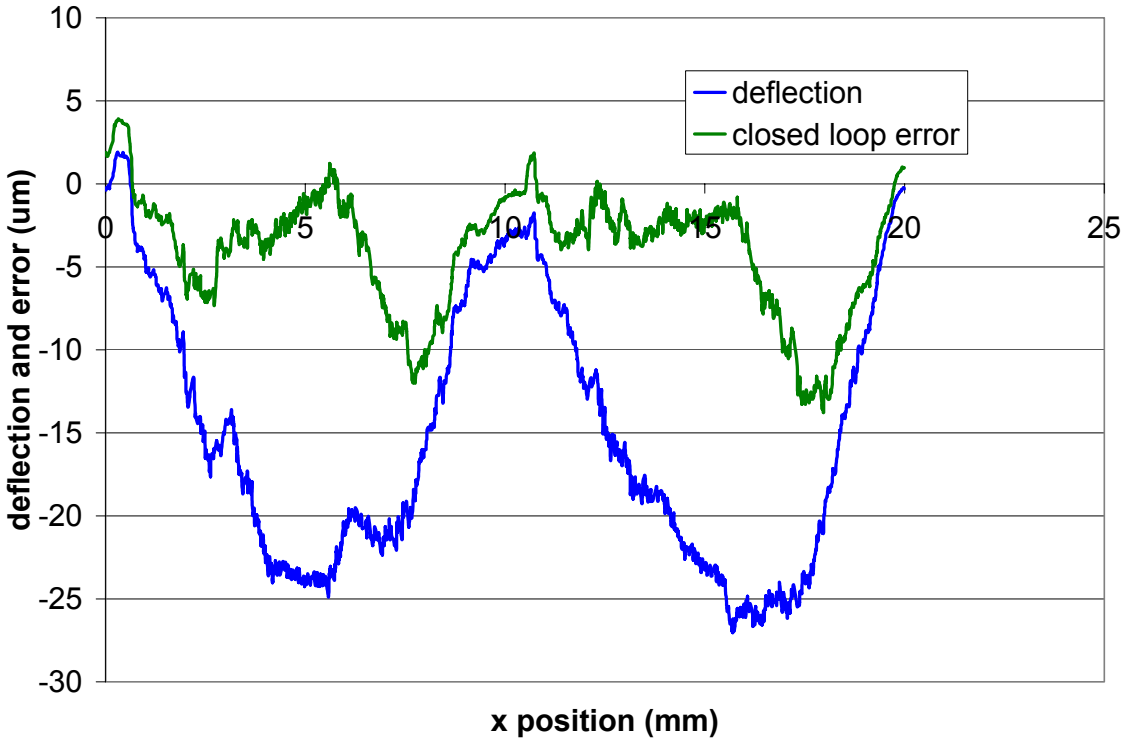

Figure 23: Predicted Deflection Two Period Sine Wave Groove Open Loop Deflection and Error

This data indicates that the tool stiffness model accurately predicts average tool deflections, as the experimental measurements of groove profile cut with predicted deflection compensation are close to the desired profile. These results show that compensation using predicted deflection based on a model of tool stiffness applies to more complex profile cuts and freeform surfaces.

The results for predicted deflection are more stable and of better quality than the predicted depth algorithm mainly due to the following reasons:

- Use of both machine position encoder feedback as well as real time cutting force feedback in the algorithm
- Less uncertainties in the tool stiffness model as the only parameters are the multiplication factor and tool stiffness (both a function of tilt of tool with respect to the workpiece)

6.3 CONCLUSION

The forces generated during milling with a miniature ball end mill are relatively small (less than 10N) because of the limited size and strength of the tool edge. However, tool deflections can be a significant source of surface errors because of the low stiffness of these ball end mills. Two approaches to tool deflection compensation are presented with advantages and disadvantages to

each. The compensation algorithms presented here provide an avenue to reduce fabrication times and improve surface accuracy for hardened steel mold dies.

Predicting depth based on a dynamic cutting force model accurately predicts depth using the real-time cutting force and developed model, and can be used to compensate errors arising from tool deflections and workpiece misalignment but is not as good as the second method of predicting a deflection based on a model of tool stiffness. Predicting deflection using a model of tool stiffness accurately predicts tool deflection and allows for compensation in profile error real-time using force feedback as well as machine encoder position feedback.

The results presented here show that the approach of predicting deflection using a tool stiffness model to compensate for profile error yields better results than those obtained from predicting depth based on a dynamic cutting force model. This is a result of several reasons, the most significant being slow execution time of the control algorithm and limited knowledge of actual cutting parameters. The reduction in error in groove profile over a non-compensated groove can be as great as 80% depending on the profile and method of compensation implemented.

REFERENCES

1. Lechniak, Z., A. Werner, K. Skalski, K. Kedzior, "Methodology of off-line software compensation for errors in the machining process on the CNC machine tool," Journal of Materials Processing Technology, vol. 76, pp. 42-48, 1998.
2. Dow, T. A., E. Miller, A. Sohn and K. Garrard, "Compensation of Tool Forces in Small Diameter End Mills," ASPE Proceedings, vol. 20, pp. 546-550 and to be published in Precision Engineering in 2003.
3. Ikua, B.W., H. Tanaka, F. Obata, S. Sakamoto, "Prediction of cutting forces and machining error in ball end milling of curved surfaces – I theoretical analysis," Journal of the International Societies for Precision Engineering and Nanotechnology, vol. 25, pp. 266-273, 2001.
4. Franklin, Gene F., J. David Powell, and Abbaas Emami-Naeini, Feedback control of dynamic systems, 2nd ed., Eddison-Wesley, Reading, Mass., (1991).

7 SURFACE DECOMPOSITION FOR DIAMOND TURNING

Witoon Panusittikorn
Graduate Student
Kenneth Garrard
Precision Engineering Center Staff
Thomas A. Dow
Professor
Department of Mechanical and Aerospace Engineering

The Variform fast tool servo (FTS) implements an internal second-order filter on its input command signal yielding improved closed-loop performance with a broader bandwidth. However, this filter delays the actuator's response resulting in form errors. Additional errors result from the varying response of the servo to the different frequency components of a command signal. An algorithm using surface decomposition was developed to generate open loop input commands that compensate for the system dynamics. Since this modified command is not calculated from the position feedback, there is no delay in the response. This paper presents an open-loop control approach based on Digital Signal Processing. By measuring the impulse response of the system, deconvolution can reverse the effects of attenuation and phase by sending a modified input signal through the actuator. The result is dramatically improved performance, especially for high frequency motion.

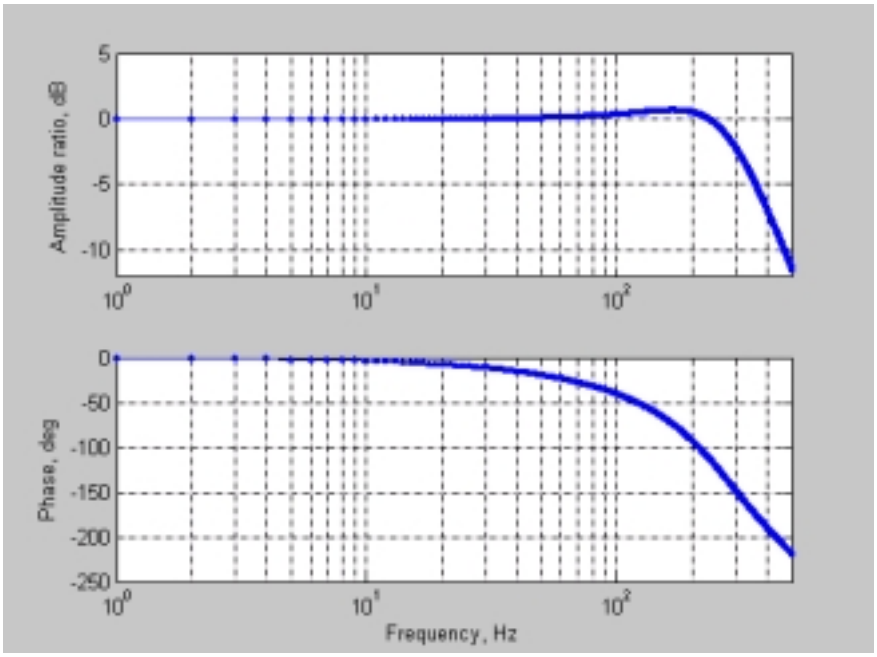

7.1 INTRODUCTION

The response of a dynamic system to an applied signal is a function of the frequency of that signal. In general, the response results in an attenuated and delayed motion of the output with respect to the input signal. When the system is a diamond turning machine and the dynamic input signal is made up of a variety of frequencies, the result is form error in the machined surface. In Figure 1, the mechanism inside of the system can be considered as a spring-mass-damper driven by a periodic function $x(t)$ with an amplitude A and a frequency of ω radians/sec. The steady-state output motion $y(t)$ is attenuated by a gain factor a and is phase shifted by an angle ϕ.

Input: $x(t) = A\sin(\omega t)$

Output: $y(t) = a\,A\sin(\omega t + \phi)$

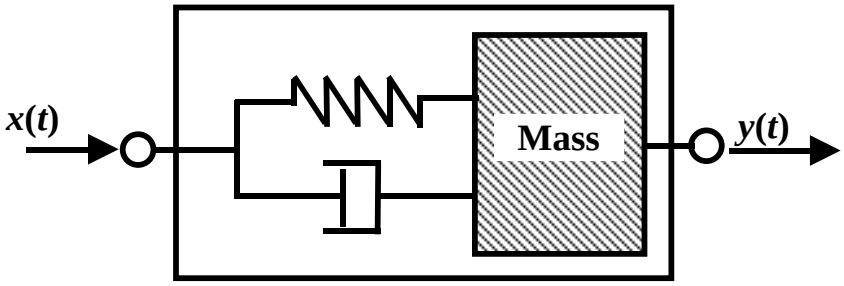

Figure 1. Spring-mass-damper system.

If the input $x(t)$ contains multiple frequencies, the corresponding output can be determined using *superposition*; that is, the input signal can be decomposed into single-frequency components each of which will be attenuated and delayed. The response of the system $y(t)$ will be the sum of these frequency components.

Input: $x(t) = \sum_i A_i \sin(\omega_i t)$

Output: $y(t) = \sum_i a_i A_i \sin(\omega_i t + \phi_i)$

To machine a desired surface profile with high fidelity, the amplitude gains and delays must be eliminated. To achieve this, the input signals are modified prior to applying them to the system such that the attenuation is canceled and the phase is compensated.

Modified Input: $x(t) = \sum_i \frac{A_i}{a_i} \sin(\omega_i t - \phi_i)$

Desired Output: $y(t) = \sum_i a_i \frac{A_i}{a_i} \sin(\omega_i t + \phi_i - \phi_i)$

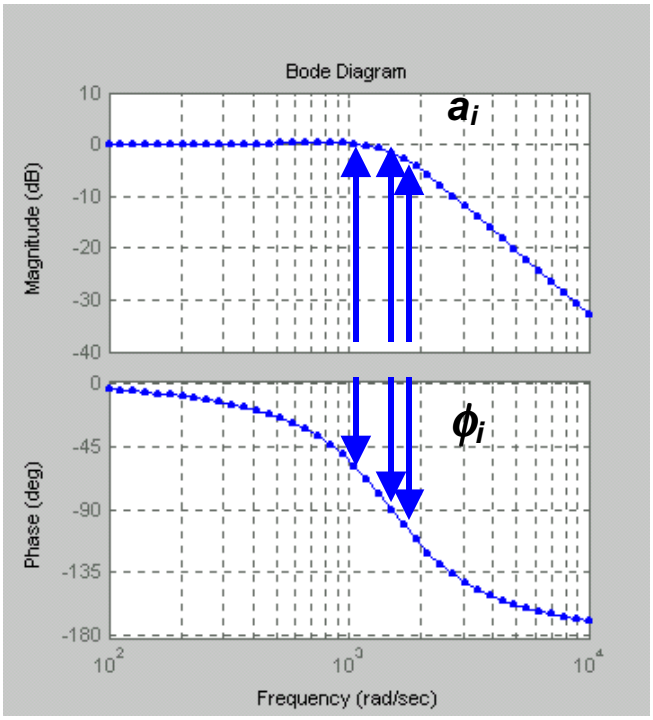

Figure 2. Manual compensation values based on system dynamic characteristics.

If the dynamics of the system are known and at the desired motion is decomposed into sinusoids, the values of amplitude and phase can be manually adjusted using a look-up table. The values can be obtained from the frequency response of the system as shown in Figure 2. This manual method is slow and cumbersome if the signal contains many frequency components. However, automation can be used to minimize the effort. The following sections describe the technique for system identification applied to the Variform FTS and the input signal modification algorithm that produces the desired output response.

7.1.1 SYSTEM DYNAMICS – VARIFORM FAST TOOL SERVO (FTS)

The Variform fast tool servo employs a lever mechanism as a motion amplifier to produce a stroke of 400 μm over a frequency range from static to 300 Hz. A pair of piezo stacks moving in opposite directions drive a T-shaped lever that is connected to the tool. The lever amplifies the piezo displacement and moves the tool normal to the axis of the stacks as shown in Figure 3. To energize the piezo stacks in this manner, the two actuator signals must be 180° out of phase; that is, the drive system needs a differential input signal, which consists of a command signal and its inverse. These drive signals are inputs to an integrated high voltage amplifier – analog control system. Tool motion is measured by an LVDT sensor that provides position feedback to the controller. This system linearizes the displacement of the tool with respect to the input signal, eliminates hysteresis by means of a reference capacitor and provides additional damping.

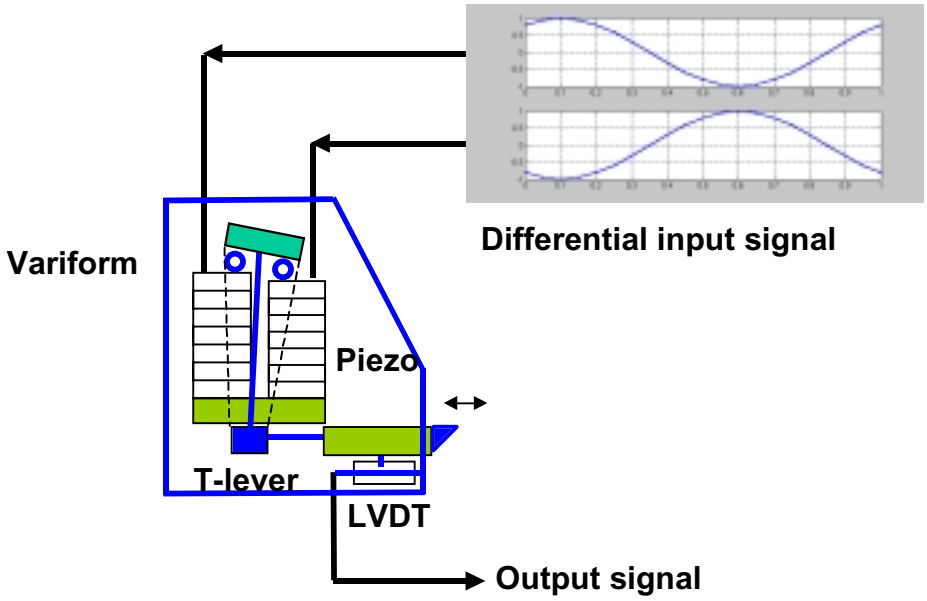

Figure 3. Variform fast tool servo motion.

Inverting Amplifier To operate the Variform from a single command signal, a second signal must be generated that is the inverse of the first. Some commercial controllers (e.g. the Delta Tau PMAC) provide this option for the output. However, to find the frequency response of the Variform using a Spectrum Analyzer's single channel output, the inverted signal must be generated. Figure 4 shows a way to accomplish this using an operational amplifier and two resistors. The gain of this circuit can be written as,

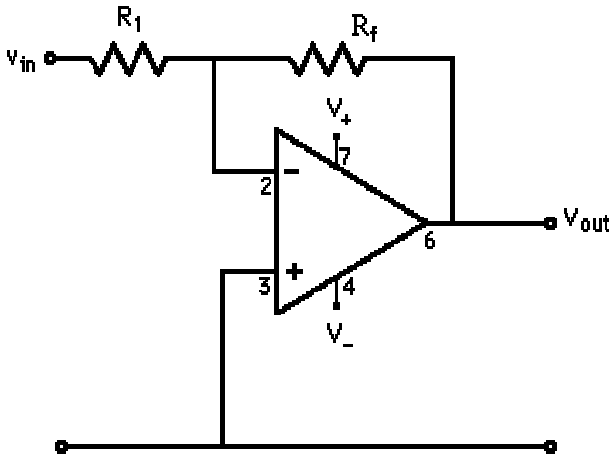

$$\frac{V_{out}}{V_{in}} = -\frac{R_f}{R_1}$$

Figure 4. Inverting amplifier.

If the two resistors are selected with the same magnitude, a unity gain inverter will be the result.

Frequency Response Measurement The dynamics of the Variform can be measured by supplying a fixed amplitude sine wave (1 volt P-P) of continuously varying frequency (0 to 3000 Hz) as input to the actuator. Figure 5 shows the experimental setup. The Spectrum Analyzer (Stanford SRS 780) generates the swept sine wave from which an inverted signal is generated and both are sent to the Variform. The motion of the tool as measured by an internal LVDT is sent back to the analyzer along with the input signal. The Stanford analyzes the amplitude and

phase at each sampling frequency and provides a measure of the dynamic response of the Variform.

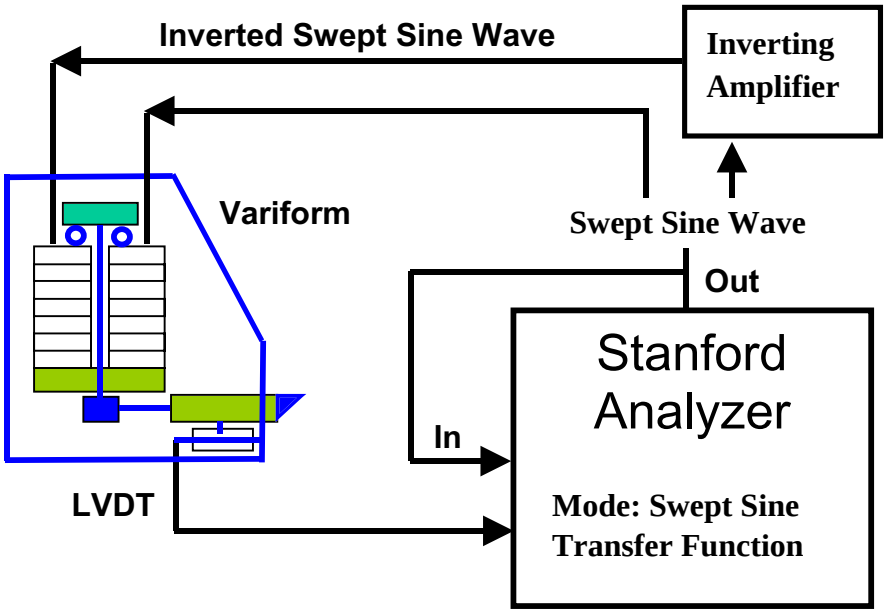

Figure 5. Diagram of frequency response measurement.

The frequency response of the system can be presented in different formats but the most widely used form is the amplitude and phase of the output with respect to the input signal. Figure 6 illustrates the amplitude and phase form of the frequency response of the Variform to a swept sine input signal. The maximum displacement of the tool for this excitation is 20 μm. The top graph shows the ratio of the amplitude of the output to the input (in dB units) as a function of frequency.

$$AR_{dB} = 20\log(AR)$$

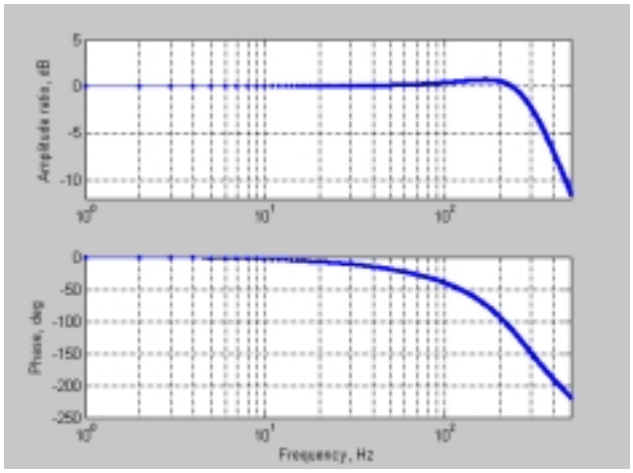

Figure 6. Frequency response of the Variform.

At low frequency, the output is equal to the input and the ratio is unity leading to a dB value of zero. As the frequency is increased, the AR peaks at about 200 Hz and then drops rapidly for higher frequencies. The lower graph shows the phase angle between the input and output. At lower frequencies, these signals are nominally in phase but as the frequency rises, the output lags the input. At 100 Hz this lag is about 45°.

7.2 DIGITAL SIGNAL PROCESSING (DSP)

Since the development of high speed computing, Digital Signal Processing is one of the innovations that have established a new revolution in science and engineering. A primary application of DSP is to reduce interference due to noise by filtering acquired data. The methodology has been fully developed in a broad range of fields: communications, feedback control, imaging, radar, sonar, and high fidelity music reproduction [1].

7.2.1 ANALOG TO DIGITAL CONVERSION

The motions of electro-mechanical systems are characterized by continuous time-dependent variables. For example, exerting a small movement input $x(t)$ to a spring-mass-damper system results in a gradual output motion $y(t)$. Although both movements change continuously with respected to time, a digital data acquisition system will not measure this continuity; it will produce a discrete time representation of that motion. In fact, both time and the motion amplitude variable must be digitized, as shown in Figure 7. In the digital realm, the continuous time t becomes,

$$t = n\delta t$$

where n = 0, 1, …, N and δt is a sampling time. As a result, a continuous motion $y(t)$ is represented as a finite series of discrete motion steps, $y[n\delta t]$, usually shortened to $y[n]$.

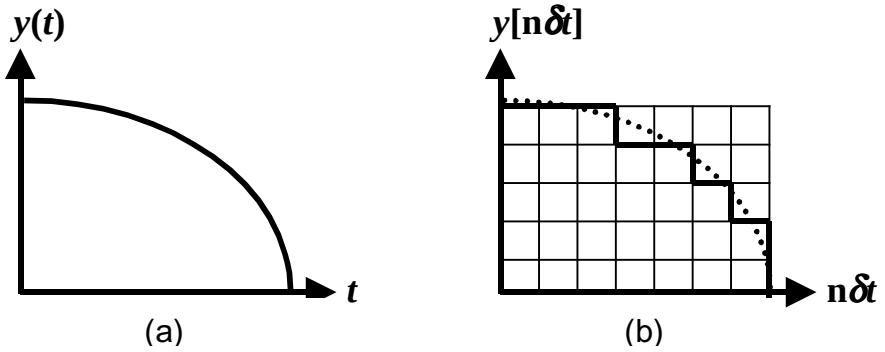

Figure 7. (a) Analog signal. (b) The same signal after digitization.

7.2.2 SAMPLING THEOREM

The basis for digital technology was provided by the Nyquist or sampling theorem and applied to communication theory in 1949 by Shannon and Weaver [2]. It establishes a formal mathematical link between the physical world of continuous signals, both periodic and aperiodic, described by Fourier transforms and Fourier series and the reality of modeling physical phenomena based upon discrete and finite observations. The theorem states that a discrete time sequence obtained by sampling a continuous function contains enough information to reproduce the function exactly, provided that the sampling rate is strictly greater than twice the highest frequency contained in the original signal. Furthermore, it provides a means of reconstructing the bandwidth limited signal given the sampled data. Equation 1 is an interpolation formula that reconstructs the value of the function f at any time $t \in \Re$ from the sequence of samples of f at the discrete time intervals, k.

$$f(t) = \sum_{k=-\infty}^{+\infty} f[k] \frac{\sin(\pi (k-t))}{\pi (k-t)} \tag{1}$$

The derivation of Equation 1 from a Fourier series yields an infinite sum. Its value is zero for all terms outside the time range of the sample, so it can be computed by adding up the values where $f[k]$ exists. Note however that if t is outside the time range of the sampled data, then there will still be a value for the reconstructed function. The result is that the sample is repeated both forwards and backwards in time. That is, the sample represents exactly one period of a continuous periodic function.

The sampling process cannot detect any frequency higher than one-half of the sampling frequency (known as the critical frequency), but obtains amplitude values from the signal nonetheless. Since the reconstruction formula, or any other Fourier series based analysis, can only consider frequencies less than the critical frequency, the total energy of the sampled signal is represented within the frequency band of the sample. If the signal being sampled is not bandwidth limited, then aliasing will occur and the reconstruction will fail to recreate the signal as illustrated in Figure 8. The aliasing phenomenon is familiar as the apparent speed ambiguity and direction reversal of a bicycle wheel as its angular velocity advances through the speed at which our vision system can detect the motion of the individual spokes (no faster than 20 Hz).

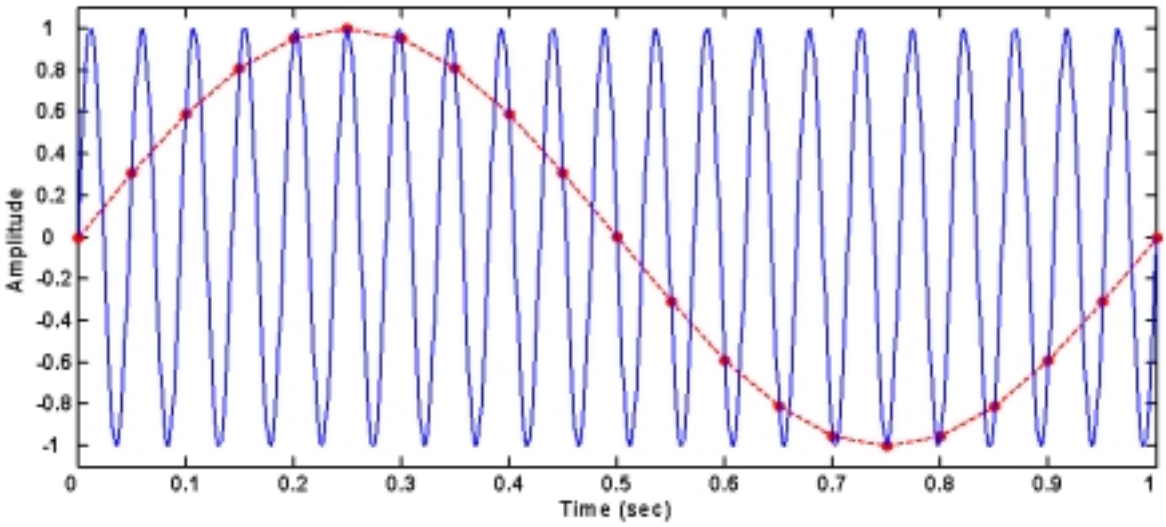

Figure 8. An example of aliasing where a 21 Hz sine wave (solid line) is sampled at 21 Hz (dots) and the reconstructed signal (dashed line with dots) is a 1 Hz sine wave.

7.2.3 DIGITAL SIGNALS AND SUPERPOSITION

The principle of *superposition* can be applied to linear-time discrete systems. Since a digital signal can be represented by a series of impulses[1] as shown in Figure 9, superposition can be used to break a complicated digital signal into a series of individual impulses. These impulses can be applied to the dynamic system and the output resulting from each impulse charted according to its magnitude and time of application. Figure 9 shows the input signal decomposed into a series of impulses, each sent through and modified by the dynamic system and finally added together to produce the final output signal. The effect that the system has on each input impulse is called the Impulse Response of the system.

[1] An impulse is defined as a signal whose magnitude is zero everywhere except at a single nonzero point.

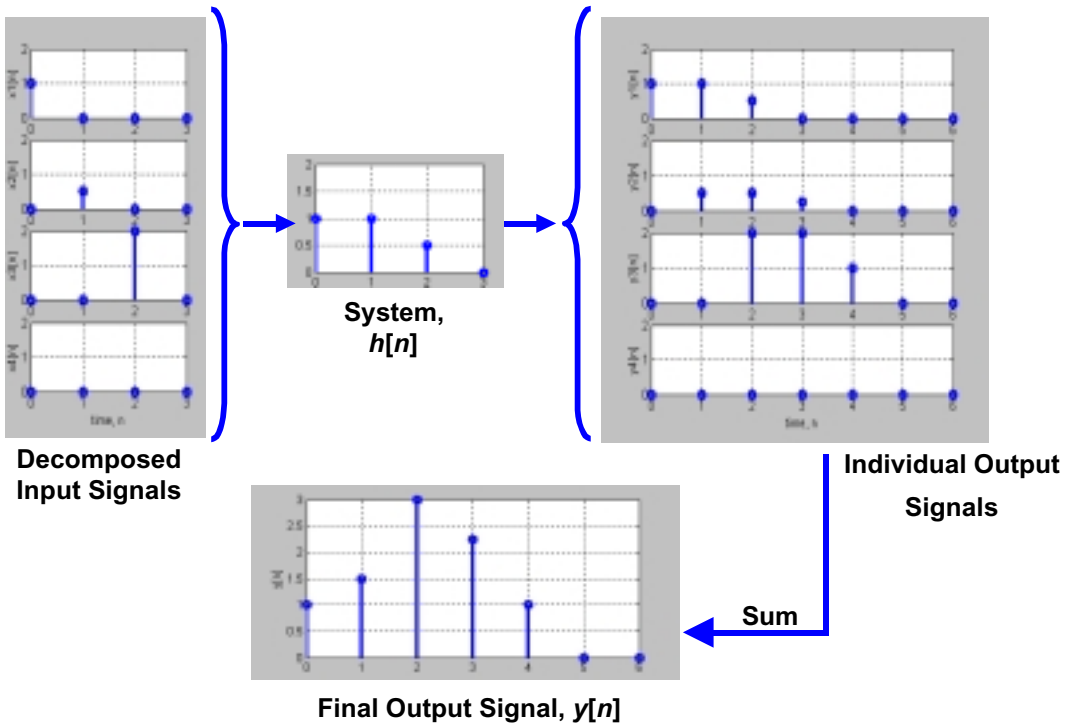

Figure 9. Superposition shows how the final output is generated.

7.2.4 IMPULSE RESPONSE

The impulse response describes the characteristics of a system with respect to time. As the name suggests, the system yields a specific response when a normalized impulse is applied as the input as shown in Figure 10. The response depicts the dynamics of the system such as attenuation and phase shift. Therefore, it is very important to know the exact impulse response in order to construct a modified signal to cancel those effects. To explain how an impulse response can show the dynamics of the system, the Fourier Transform and the frequency domain must be introduced.

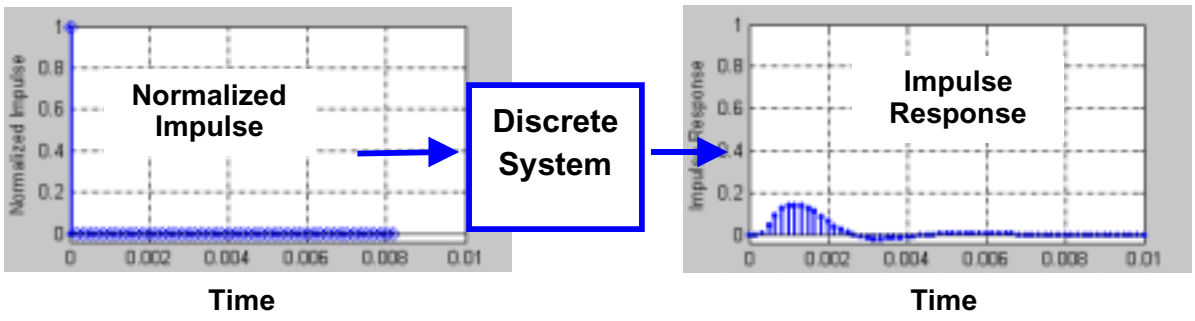

Figure 10. Impulse response is the outcome of a normalized impulse to a system.

7.2.5 CONVOLUTION

The effect of a dynamic system on an input signal of length N can be calculated by applying the so-called "convolution" operation to the input $x[n]$ and the impulse response $h[n]$ of the system. The convolution operation is represented by the * (star) operator and is expressed as

$$x[n] * h[n] = y[n]. \tag{2}$$

This operation can be mathematically described as the sum,

$$y[k] = \sum_{m=0}^{M-1} h[m]\, x[k-m] \tag{3}$$

where M is the length of the impulse response. The length of $y[n]$ is $N+M-1$.

7.2.6 DISCRETE FOURIER TRANSFORM (DFT)

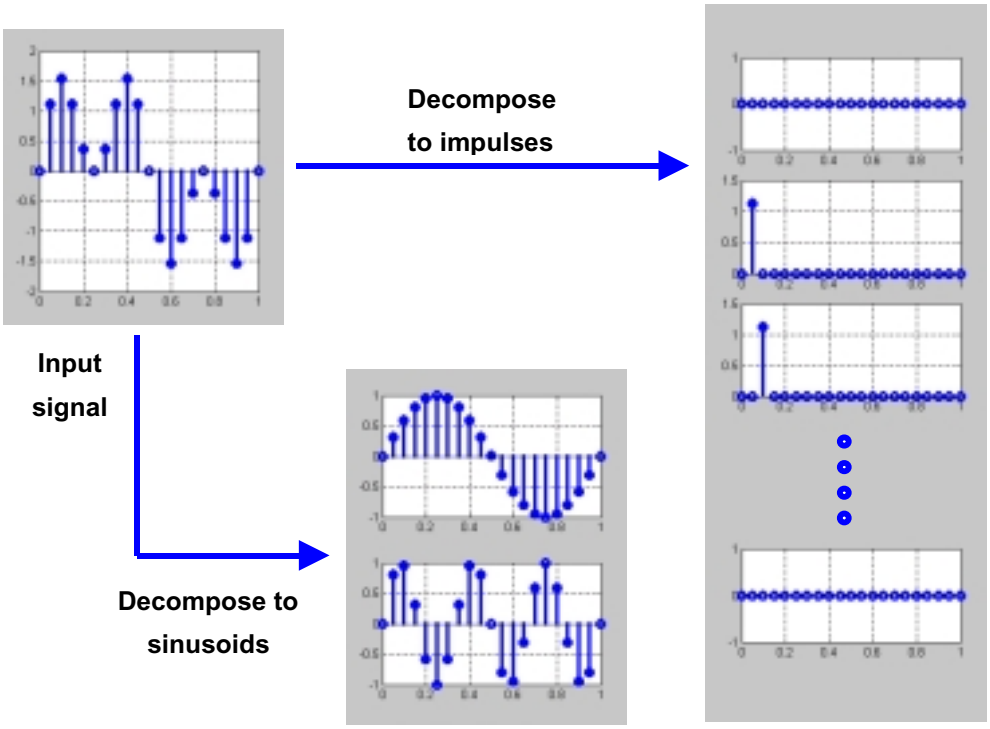

Figure 11. Input decomposition to different forms of the components.

All the operations discussed above are in the time domain; that is, the operations have been applied to a sequence of values collected as a function of time. The operations are sometimes easier to implement if they are applied in frequency domain; this is especially true for periodic signals. For example, the input signal shown in Figure 11 can be broken into either 21 impulses

in time the domain, or 2 frequency components (that is two sine waves with different frequency and magnitude) in the frequency domain. Performing the convolution operation in the frequency domain can significantly reduce the amount of memory and number of operations required in a digital computer.

Since only a digital signal with a finite length can be processed through a computer, the discrete Fourier transform (DFT) assumes that an entire signal is made up of the input signal collected over the given time period but repeated again and again. The DFT represents all signals by a sum of sine and cosine components, which facilitates analysis in the frequency domain. The DFT converts *N* samples in time to *N* samples in frequency. The more samples that are collected in a fixed time period, the finer the frequency resolution, Δf, of the resulting frequency analysis. The sampling time δt determines the highest frequency that can be represented by the transform, as was discussed in Section 8.2.2.

$$\text{sampling frequency } F_s = \frac{1}{\text{sampling time} = \delta t}$$

$$\text{frequency resolution } \Delta f = \frac{F_s}{N} = \frac{1}{N\,\delta t}$$

The DFT decomposes a signal into its constituent sinusoids and typically presents the results in terms of complex sines and cosines as shown by Equation (4). Lowercase letters indicate a signal in time domain (e.g. $h[n]$), while uppercase (e.g. $H[k]$) represents the transformed signal at a specific frequency.

$$\begin{aligned} H[k] = DFT(h[n]) &= \sum_{n=0}^{N-1} h[n] \times \left[\cos\left(2\pi (k\,\Delta f) n\,\delta t\right) - j \sin\left(2\pi (k\,\Delta f) n\,\delta t\right)\right] \\ &= \sum_{n=0}^{N-1} h[n] \times \left[\cos\left(2\pi \left(k \frac{1}{N\,\delta t}\right) n\,\delta t\right) - j \sin\left(2\pi \left(k \frac{1}{N\,\delta t}\right) n\,\delta t\right)\right] \\ &= \sum_{n=0}^{N-1} h[n] \times \left(\cos\left(\frac{2\pi\, k\, n}{N}\right) - j \sin\left(\frac{2\pi\, k\, n}{N}\right)\right) \end{aligned} \tag{4}$$

where $1 \le k \le N$.

The sampling theorem limits the highest detectable frequency to one-half of F_s over the N input samples, but there are N outputs in the DFT at frequency steps of $\Delta f = F_s / N$. This means that the DFT output contains two copies of the frequency information; one with positive frequencies and one with negative (i.e., *conjugate*) frequencies. The cosine (real) and sine (imaginary) parts of the DFT repeat themselves for every *N* samples as illustrated in Figure 12. The sampling time in this case is 50 ms to produce an F_s of 20 Hz. In this frequency domain, the data consists of 20 points distributed over the frequency range from the negative half sampling frequency ($-F_s / 2$) to

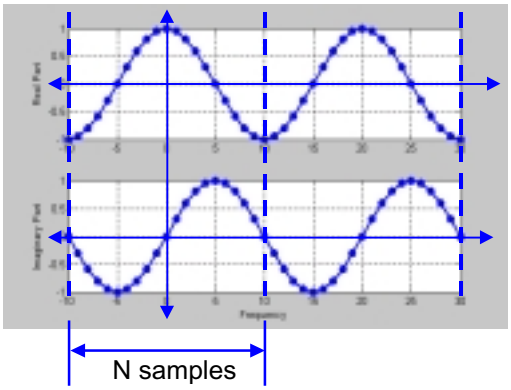

Figure 12. Real and imaginary parts of the DFT are periodic.

the positive half ($F_s / 2$) with a frequency resolution of 1 Hz. The negative frequencies usually have no physical meaning and are a mirror image, or *conjugate* pair, of those in the positive frequencies. Their real, even parts (cosine) are the same but the imaginary, odd parts (sine) are inverted to avoid a discontinuity (i.e., $\cos(-x) = \cos(x)$ and $\sin(-x) = -\sin(x)$.) Since the response is periodic, the distribution in negative frequencies reappears to the right of 10 Hz. As a result, the frequency range can also be thought of as the positive frequencies starting at 0 up to the sampling frequency F_s, which in this case is 20 Hz.

The convolution operation (Equations (2) and (3)) is mathematically equivalent to polynomial multiplication and is complex multiplication in the frequency domain. The DFT provides a convenient means of implementing convolution. An algorithm called the Fast Fourier Transform (FFT) is frequently used to accelerate the calculation by exploiting symmetries in Equation (3). MATLAB has a built-in FFT algorithm that was used in this work. The convolution theorem, Equation 2, can then be restated in the frequency domain using the FFT.

$$x[n] * h[n] = y[n] \qquad \text{(time domain)}$$
$$\mathbf{FFT}(x[n]) \times \mathbf{FFT}(h[n]) = Y[k] \qquad \text{(frequency domain)}$$

Therefore, $X[k] \times H[k] = Y[k]$.

7.2.7 Impulse Response in the Frequency Domain

In the time domain, the impulse response of a mechanical system shows how it would react to an impulse with unity magnitude applied at time zero. A different picture is created if viewed in the frequency domain. The DFT of the normalized impulse yields an array of frequency coefficients all of which have a magnitude of one as illustrated in Figure 13. The frequency content of a

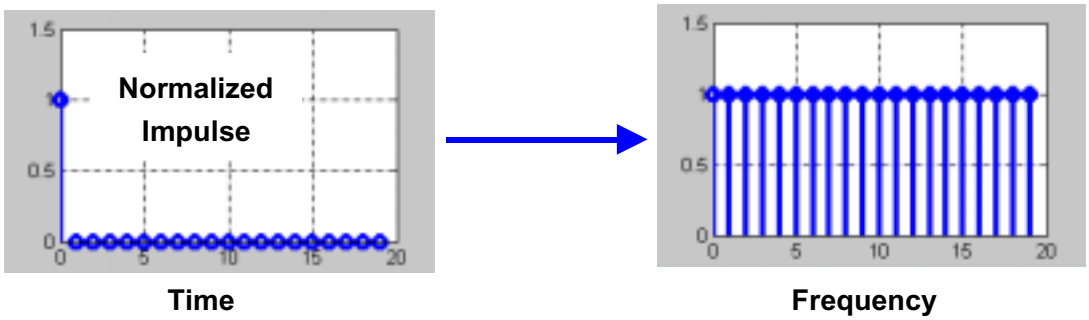

Figure 13. Discrete Fourier Transform of a normalized impulse.

swept sine wave is identical to that of a normalized impulse. This implies that the impulse response can be obtained by applying a swept sine wave to the system. Then, the frequency response $H[k]$, or transfer function of the system, is determined by

$$H[k] = \frac{Y[k]}{X[k]}.$$

$X[k]$ is the DFT of a swept sine wave signal used to excite a system and $Y[k]$ is the DFT of the time sampled response of the system. *X[k]* should be unity for all frequencies, but is usually calculated from *x[n]* (the swept sine wave) so that effects of quantization, noise and the finite range of sine frequencies are accounted for by the analysis. The transfer function is a representation of the impulse response in the frequency domain and is calculated as the Fourier transform of the impulse response.

7.2.8 DECONVOLUTION

Deconvolution is the inverse of convolution. In the frequency domain, if a desired output $Y_d[k]$ is known, the input signal *X[k]* can be determined by deconvolution or,

$$X[k] = \frac{Y_d[k]}{H[k]}.$$

For a manufacturing application when the output $y_d[n]$ is a desired excursion of a cutting tool and *H[k]* is the frequency response of an actuator, the resulting *X[k]* (in frequency domain) can be used as an open-loop control signal to the actuator. This *X[k]* can be efficiently transformed back to the time domain *x[n]* using the Inverse Fourier Transform (IFFT command in MATLAB). Concisely, the actuator input signal x[n] is obtained from Equation (5).

$$x[n] = \mathbf{IFFT}\big(X[k]\big) = \mathbf{IFFT}\left(\frac{\mathbf{FFT}\big(y_d[n]\big)}{H[k]}\right) \tag{5}$$

As an example, let the desired excursion consist of two 1.0 μm amplitude sinusoidal profiles with frequencies of 100 and 300 Hz. The digitized signal can be written as

$$y_d[n\delta t] = 1.0\times10^{-6}\sin(2\pi\times100\,n\delta t) + 1.0\times10^{-6}\sin(2\pi\times300\,n\delta t).$$

The transformed excursion $Y_d[k]$ using a sampling frequency of 6000 Hz is illustrated in Figure 14. The two peaks in the left half frequency range correspond to the given input frequencies, whereas the others (in the right half range) are their *conjugate* pairs required to perform the inverse transformation. Alternatively, the frequency representation for $Y_d[k]$ could be shown as extending from –3000 Hz to 3000 Hz with positive frequencies reflected about zero.

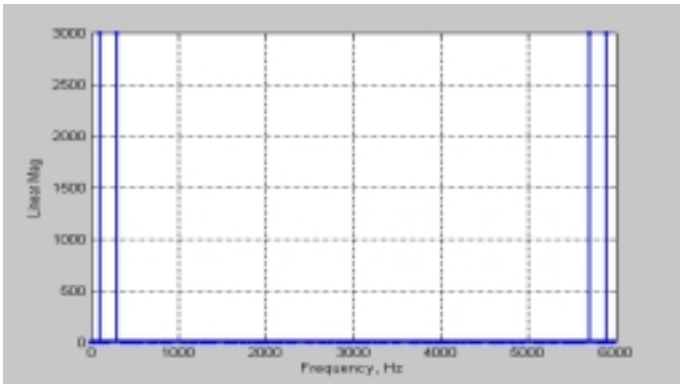

Figure 14. Frequency response of the desired excursion.

In addition to the desired excursion, the frequency response $H[k]$ or the characteristic transfer function of the actuator must be obtained to generate the modified control input $x[n]$ using deconvolution. This frequency response is specific to a particular actuator and is consequently obtained experimentally.

7.3 EXPERIMENTAL CORROBORATION

7.3.1 ANALYTICAL APPROACH

Figure 15 shows the complex number form of the Variform frequency response[2] depicted in Figure 6. As with the example from Figure 14, the frequency response of the actuator must contain both gathered data and its *conjugate* distributed within the sampling frequency.

The frequency response $H[k]$ is normalized to cancel out the gain mismatch between the Stanford SRS 780 and the LVDT and transformed back to the time domain. The impulse response is the result as shown in Figure 16.

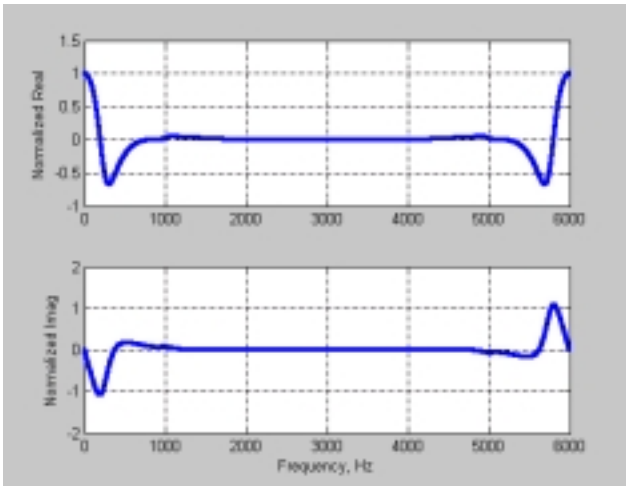

Figure 15. The complex number form of the frequency response.

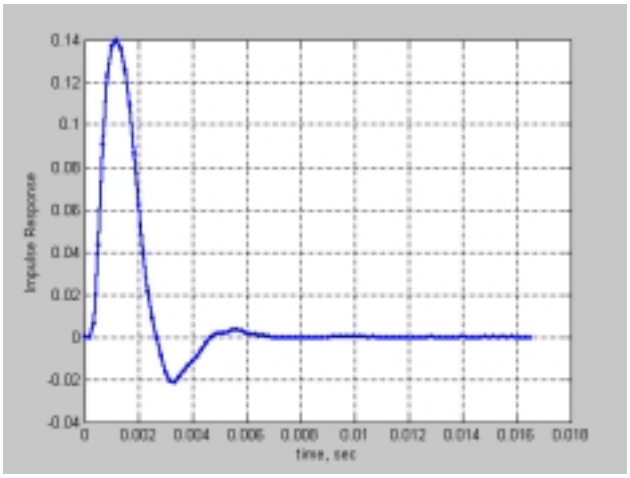

Figure 16. Impulse response of the Variform fast tool servo.

[2] The complex number form is an alternative way to present the more familar frequency response (amplitude and phase) that was in shown in Figure 6.

The modified input $x_m[n]$ that will produce the desired motion of the Variform is calculated from Equation (5) using the deconvolution operator on the desired excursion $y_d[n]$ and the frequency response of the system $H[k]$.

The altered amplitude and phase of the modified input are compared to the desired signal in Figure 17. The desired signal is advanced to compensate for the delay through the computer system that was used to command the Variform and acquire the LVDT signal demonstrating its response. All of those adjustments are carried out simultaneously in one deconvolution. Path differences in the Variform response associated with the modified input $x_m[n]$ (a line with dots) and the input without the deconvolution (a dashed line) with respect to the desired excursion $y_d[n]$ are shown in Figure 18.

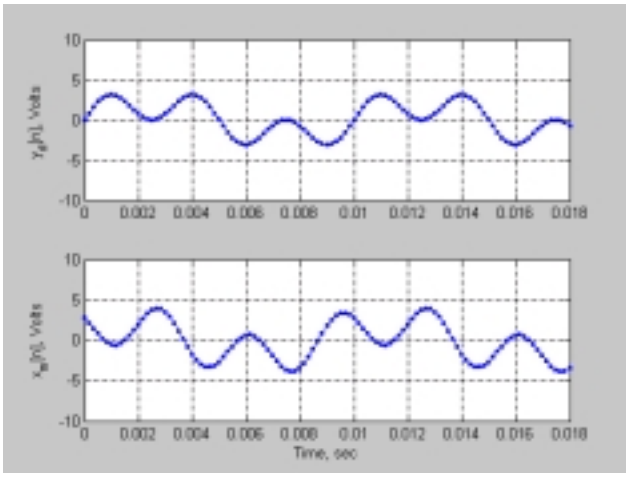

Figure 17. Desired signal $y_d[n]$ and modified input signal $x_m[n]$ obtained by deconvolution.

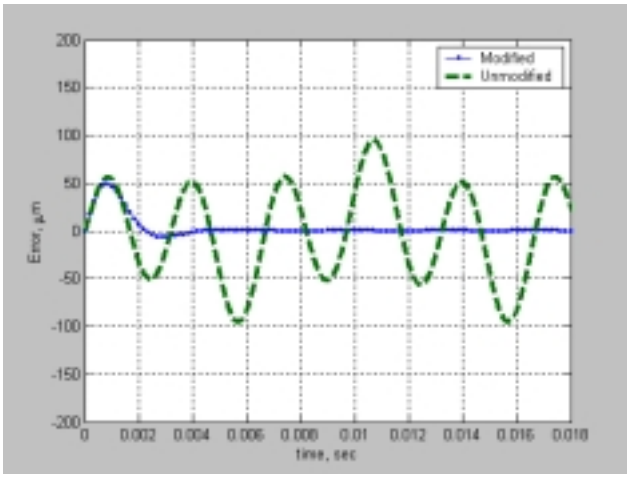

Figure 18. Path error associated with a modified input and unmodified input.

Note that in Figure 18 the system response is essentially identical to the desired signal (i.e., zero error) after about 0.004 seconds.

7.3.2 EXPERIMENTAL RESULTS

Test input signals as shown in Figures 19 and 21 were sent to the Variform. Both modified and unmodified input commands are padded zeros so that each experiment starts from a stationary state and inverted to account for the negative gain of the LVDT. To correct the phase, the modified signal leaps at the start. However, the Variform filters this discontinuity with a built-in filter and rapidly "catches up" to the desired waveform.

Figure 20 illustrates the path error in the Variform response corresponding to a small amplitude input of ±4 volts. Note the close similarity to Figure 18. The modified command signal eliminates actuator form errors due to the attenuation and phase after about 4 ms. A high

amplitude input command signal varying between ±10 volts is shown in Figure 21. In Figure 22, a significant path error appears in the response associated with the modified input command, although it is much smaller than the error produced by an unmodified command signal. The problem is that the system is saturated by the modified command signal and cannot accelerate to the desired velocity. Figure 23 shows that the speed of the actuator response is dictated by hardware limitations. The slew rate of the amplifier and natural frequency of the mechanical system constrain the velocity at which the piezo stacks deform, resulting in a path error in the response.

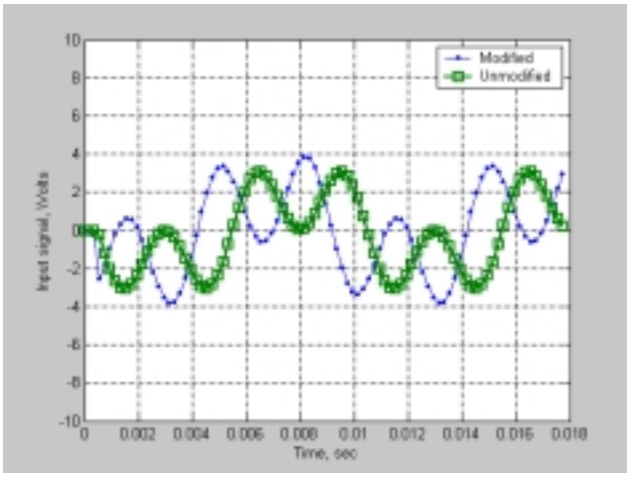

Figure 19. Modified and unmodified inputs at low amplitude (±4 volts).

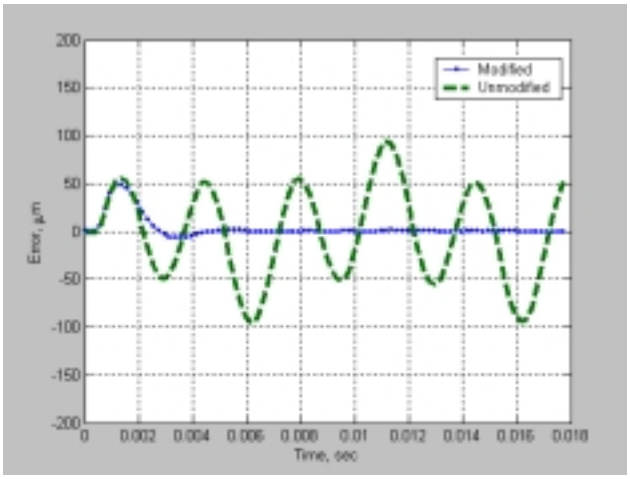

Figure 20. Path error due to modified and unmodified inputs at low amplitude (±80 µm).

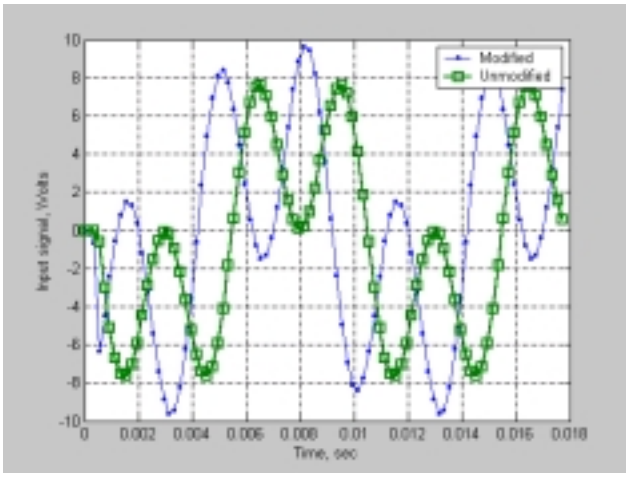

Figure 21. Modified and unmodified inputs at high amplitude (±10 volts).

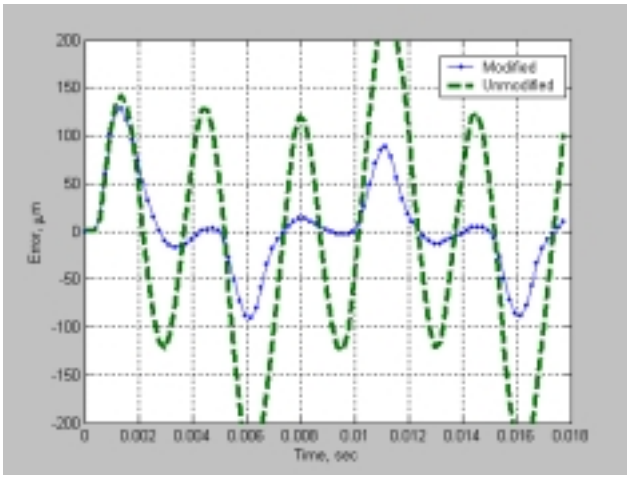

Figure 22. Path error due to modified and unmodified inputs at high amplitude (±200µm).

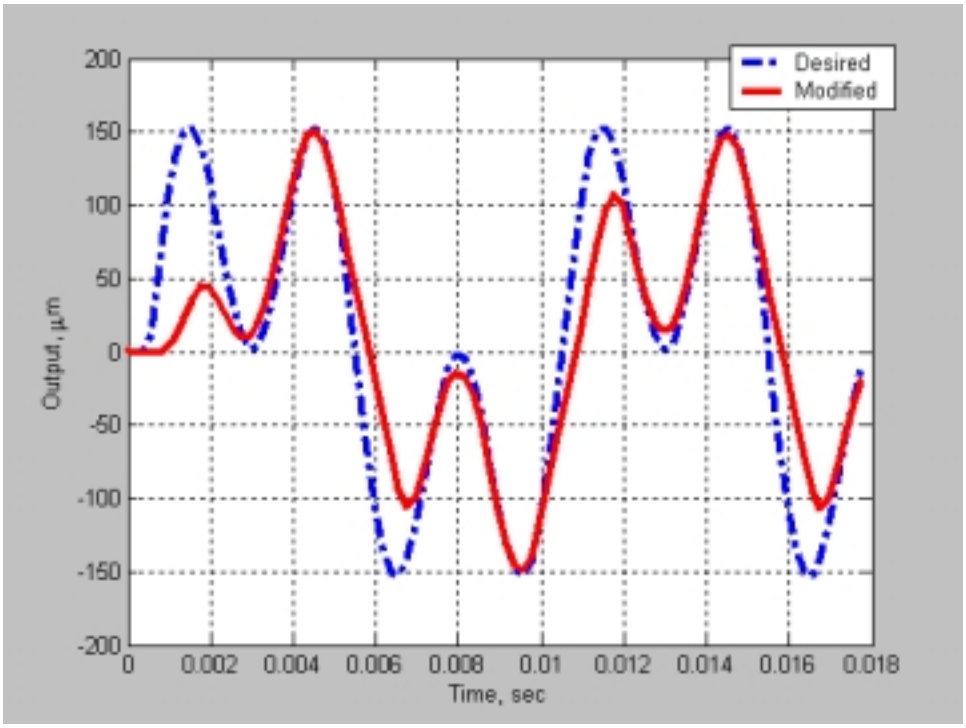

Figure 23. Velocity is constrained by hardware limitations at high frequency and high amplitude. The slope of the modified command signal response reaches a maximum value.

7.4 CONCLUSION

An open-loop control scheme using Digital Signal Processing (DSP) was proposed to correct form errors caused by the dynamics of the Variform fast tool servo. Fundamental concepts of DSP were introduced to explain the causes of attenuated and delayed excursion and to formulate a corrective algorithm. By applying deconvolution, or the inverse dynamics algorithm, to a desired motion path, the 2nd order dynamics of the actuator can be counteracted yielding a significant reduction in steady-state form errors. Not only is the magnitude of the error reduced by almost 3 orders of magnitude, the analytical simulation predicts the experimental behavior very closely. The response shows practically no delay from the desired excursion after a startup interval lasting approximately 4 ms. In practice, this startup period will occur before machining begins and thus will not effect the fidelity of a surface. Since the entire command signal needed to machine a surface can be generated *a priori*, the deconvolution is performed once for a given set of machining parameters (e.g., spindle speed, cross-feed). The technique critically depends on knowledge of the actuator impulse response.

The limitations of this technique appear with the combination of high frequencies and large amplitudes. Actuator motion is constrained by the maximum velocity of the electro-mechanical system resulting in an uncorrectable error. At frequencies above 340 Hz even a saturated input signal (±10 volts) will not produce a full magnitude tool excursion. These restrictions will be

incorporated into a procedure for automatically decomposing an arbitrary motion path into its constituent sinusoids and producing a modified command signal that drives an actuator to follow the desired profile. Inputs to this procedure will also include the actuator impulse response and the machining parameters.

REFERENCES

1. Smith, Steven W., "The Scientist and Engineer's Guide to Digital Signal Processing," 2nd edition, California Technical Publishing, (1999).
2. Shannon, C.E. and W. Weaver. *The Mathematical Theory of Communication.* The University of Illinois Press, Urbana, Illinois, (1949).

8 MODELING AND CONTROL OF A MAGNETOSTRICTIVE TOOL SERVO SYSTEM

Witoon Panusittikorn
Graduate Student
Paul I. Ro
Professor
Department of Mechanical and Aerospace Engineering

In spite of high mechanical strain output with a broadband response, a magnetostrictive actuator contains significant magnetic hysteresis and is highly nonlinear when combined with 2nd order dynamics of a tool fixture. Full utilization of these actuators requires a feedback loop as well as an advanced control scheme in response to high accuracy in a various frequency. A robust nonlinear control scheme using sliding mode control with a variable switching gain was developed. An analytical approach for equivalent control input was based on the inverse anhysteresis described in a published model. To restrain uncertainties such as noise, unmodeled dynamics, Lyapunov stability condition was introduced to calculate the switching gain. The simulation illustrates the validity of the proposed approach. The experimental results from a sliding mode controller are compared with the results from PID control and conclusions are drawn on the effectiveness of the sliding mode for the control of the magnetostrictive actuator.

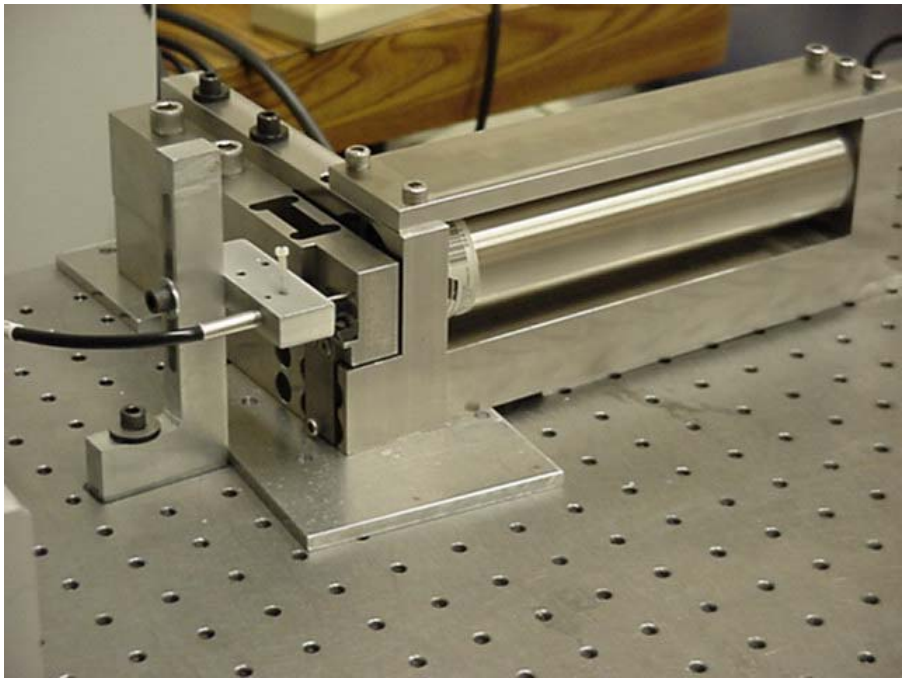

NOMENCLATURE:

V_s Input voltage

R Resistance of the induction coil

V_i Voltage across the induction coil

N, n Number of coil turns and number of turns per unit length

Φ Magnetic flux

B Magnetic flux density

A Cross section area

μ Permeability of the air closed by the magnetostrictive rod

H Magnetic field

H_{eff} Effective magnetization

M Magnetization

M_{an} Anhysteresis magnetization

M_{rev} Reversible magnetization

M_{irr} Irreversible magnetization

M_s Saturation magnetization

λ_s Saturation magnetostriction

λ Magnetostriction

α Magnetic and stress interaction

δ $\operatorname{sgn}\left(\frac{dH(t)}{dt}\right)$

P Compressive preload

E Young modulus of magnetostrictive materials

x Total elongation

$$\delta_M \begin{cases} 0 : \dot{H} < 0 \text{ and } M_{an}(H_{eff}) - M(H) > 0 \\ 0 : \dot{H} > 0 \text{ and } M_{an}(H_{eff}) - M(H) < 0 \\ 1 : \text{otherwise} \end{cases}$$

a, c, k Constants, which characterize the shape of hysteresis.

8.1 INTRODUCTION

This paper addresses a modeling and development of the nonlinear control methodology for a magnetostrictive system. As an application of smart materials, magnetostrictive transducers can generate high mechanical strain with a broadband response, and provide accurate positioning. Even though these properties characterize a good tool servo application in precision machining, full utilization of these actuators generally requires an advanced controller as well as accurate model of the transducer dynamics in response to various inputs.

In literature, two major modeling methodologies describe the mechanism of magnetostrictive materials [1]. The first approach, Preisach operators, represents hysteresis through expansions based on the global characteristic of the materials. This technique has an advantage of the generality; however, it is only in response to one particular frequency. Therefore, it is difficult to develop a dynamics model for the transducers, which usually operate in various speeds. The second approach, *quasi-macroscopic* model [2], describes the magnetostriction as a result of the movement of magnetic domain walls. This technique is an extension of the mean field theory for ferromagnetic hysteresis of Jiles *et al* [3-5]. Since it is energy based, the model can function with the frequency-dependence. The idea is analytically supported by another energy-based model, called the *bulk ferromagnetic hysteresis* model [6-7].

At moderate to high drives, the output from a magnetostrictive actuator contains significant hysteresis and, in effect, is highly nonlinear when attached to 2^{nd} order dynamics of a tool fixture. The control of this nonlinear tool servo system is quite challenging. Many sophisticated control schemes have been proposed to deal with this nonlinearity. The optimal control was employed to manipulate the vibration of a flexural cantilever beam [8]. Partial and Full Inverse hysteresis was described to linearize the actuator dynamics [9]. The inverse model was based on piecewise polynomials curve fit to the experimental data of a specific application. Preisach model was incorporated with the adaptive controller to handle the hysteresis for a specific frequency in a milling device [10]. To cross over the limited utilization of specific inputs as well as frequencies, this paper presents the development of a robust controller to maneuver a tool servo system for various inputs in the presence of highly nonlinear dynamics.

A transducer model consisting of a magnetic hysteresis in the 2^{nd} order dynamics system is summarized in Section 2. In Section 3, a simplified inverse-anhysteresis model for sliding mode control is presented to obtain an equivalent control input. A Lyapunov stability condition is introduced to determine the variable switching gain. Simulation, experimental apparatus and results are illustrated in Section 4, 5, and 6 respectively. Finally, the conclusion is drawn in Section 6.

8.2 DETAILS OF THE PROJECT

8.2.1 EXPERIMENTAL APPARATUS

Figure 1 shows the layout of a closed-loop magnetostrictive transducer. An optical probe is attached near by the tip of the actuator measuring the dynamic motion. The data is, then, acquired by using a DSP board, which incorporates with a personal computer. The control input is computed based on the displacement errors and the nonlinear control scheme. The voltage input is given back to the transducer to compensate for the hysteresis and nonlinearities, which cause the inherent displacement errors.

Based on the feedback signal from measurement, a PID and nonlinear control approach, sliding mode control are developed. A signal is generated through the D/A channel from the DSP board and directed to the actuator. This makes this system a closed loop control system.

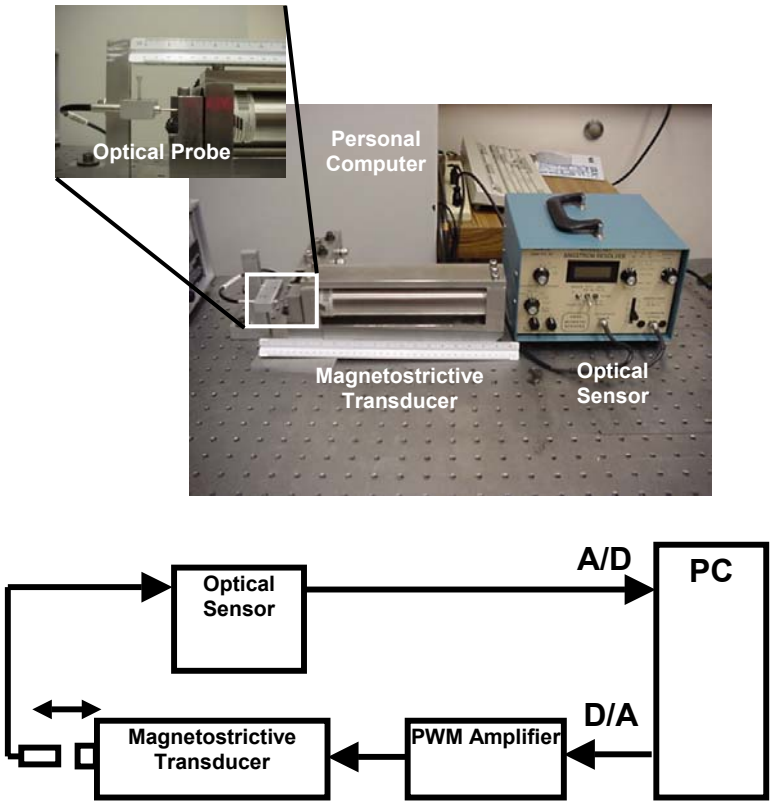

Figure 1: Closed Loop Magnetostrictive Transducer

Magnetostrictive Transducers

In the presence of a magnetic field, a magnetostrictive material, Terfenol-D, generates mechanical stroke by rotating internal magnetic domains in the direction of the field causing an elongation. The more intense the field, the more magnetic domains rotate until magnetic saturation is reached.

Figure 2 illustrates the component of the transducers. A Terfenol-D rod is surrounded by a series of electromagnetic induction coils, which produce a moving magnetic field. This traveling magnetic field causes Terfenol-D to stretch and, then contract when the field is removed, producing a stroke and force output. Preload and bias magnetic field is installed to achieve bi-directional motion. The amplitude of motion is proportional to the magnetic field provided by the coil system.

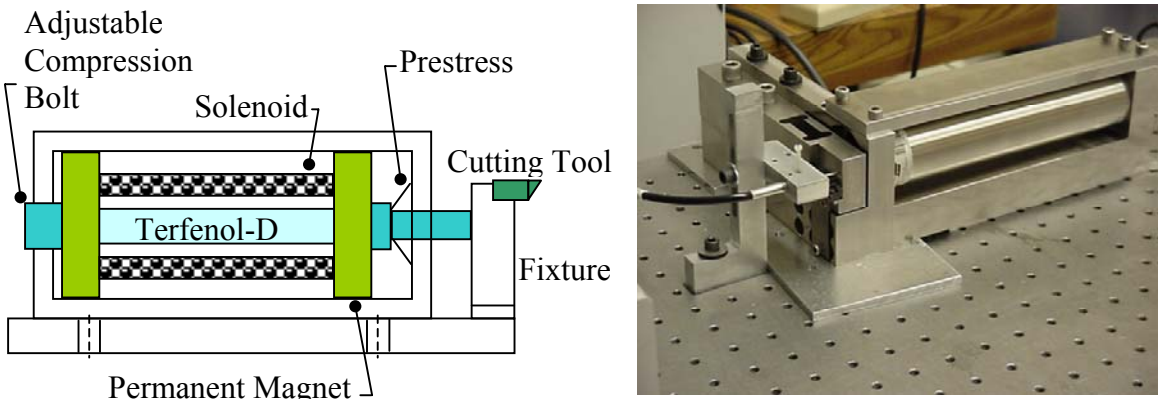

Figure 2: Component of Magnetostrictive Transducers

Such transducers are used in many applications: both civilian and military. The military application is to use smart materials to fine-tune the shape of the airfoil cross section of an aircraft wing in flight, reduce aerodynamic drag, and improve maneuverability. For civilian applications, the transducers are extensively employed for paper production, and automotive accessories [11].

Magnetic Hysteresis

When a magnetostrictive material is subjected to a magnetic field, the domains inside the material crystal rotate, resulting in changes of its shape. If the crystal is perfect, the material can expand and contract without losing energy. However, the crystal usually contains inclusions or pinning sites, which impede the rotation of the domains. The relationship between the input current and the induced magnetostriction displays significant hysteresis and saturation effects at

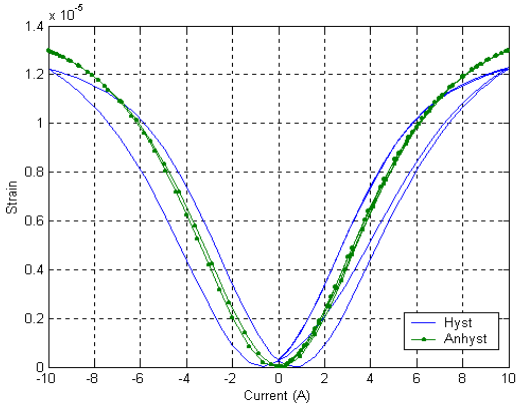

Figure 3: Hysteresis in the Relationship between Input Current and Strain

high drive levels as shown in Figure 3. The line with dots represents the anhysteretic (hysteresis-free) strain while the solid line portrays the hysteretic magnetostriction. When the input current increases, magnetostriction evolves until it reaches the saturation.

Magnetostrictive Actuator Model

The quasi-macroscopic model used to characterize the transducer dynamics is described by Calkins, Smith, and Flatau [2]. The magnetization component of this model is based on the Jiles-Atherton mean field theory for ferromagnetic materials [3-5]. Figure 4 shows the data flow in the magnetization model of a magnetostrictive core when the input current is given.

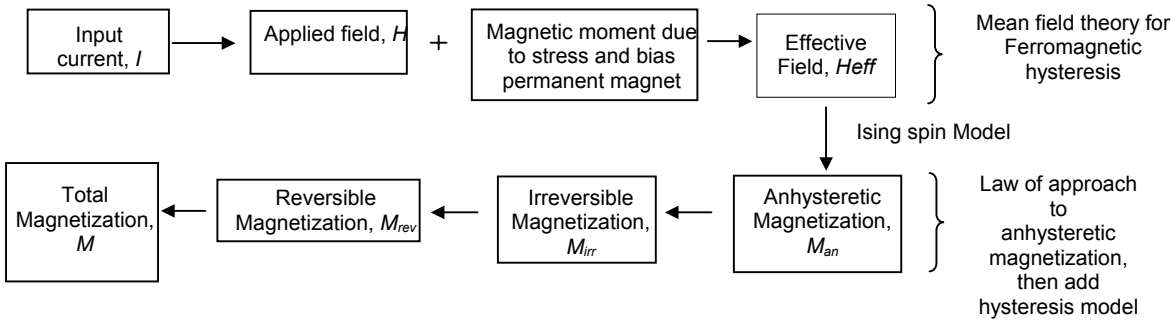

Figure 4: Flow Chart of a Computational Magnetization for a Magnetostrictive Core

The equations of the magnetization model are summarized as following:
Equation (1) and (2) show the relationship between input coil current and magnetic field

$$\boldsymbol{H(t)=nI(t)} \tag{1}$$

where

$$\boldsymbol{V_L = I(t)Z_L = \frac{d\lambda}{dt} = \frac{d(N\phi)}{dt} = \frac{d(NBA)}{dt} = \mu NA\frac{dH(t)}{dt}} \tag{2}$$

Effective field is a combination of the applied field and stress interaction as expressed in Equation (3).

$$\boldsymbol{H_{eff}(t) = H(t) + \alpha M(t) + H_\sigma} \tag{3}$$

where

$$\boldsymbol{H_\sigma = \frac{3}{2}\frac{\sigma}{\mu_o}\left(\frac{\partial\lambda}{\partial M}\right)_T}$$

Using the Ising spin model, Anhysteresis magnetization incorporated with bias magnetization $\boldsymbol{M_0}$ can be described as

$$M_{an}(t) = M_s\left[\tanh(\frac{H_{eff}(t)}{a})\right] + M_o \tag{4}$$

Then, the hysteresis loss is superimposed to anhysteresis magnetization by computing irreversible and reversible magnetization in Equation (5) to (8).

$$\frac{dM_{irr}}{dt} = \frac{dH(t)}{dt}\frac{\delta_M\left(M_{an}(t) - M_{irr}(t)\right)}{\frac{k\delta}{\mu_o} - (\alpha + \frac{3}{2}\frac{\sigma}{\mu_o}\left(\frac{\partial\lambda}{\partial M}\right)_T)(M_{an} - M_{irr})} \tag{5}$$

$$M_{rev}(t) = c\left(M_{an}(t) - M_{irr}(t)\right) \tag{6}$$

$$M(t) = M_{rev}(t) + M_{irr}(t) \tag{7}$$

The strains generated by the magnetostrictive rod are given by bulk magnetostriction in Equation (8). Applying Hook's law to obtain the amount of force is described in Equation (9).

$$\lambda(t) = \frac{3}{2}\frac{\lambda_s}{M_s^2}M^2(t) \tag{8}$$

$$F = \lambda(t)EA + P \tag{9}$$

Since the magnetostrictive rod connected to a tool fixture, the moving body develops its own 2nd order dynamics, equation (10).

$$m\ddot{x} + c\dot{x} + kx = F \tag{10}$$

The dynamics, in turns, results in an internal stress in the rod due to the output strain $\tilde{e}(t)$ incoherent to the magnetostriction $\lambda(t)$

$$\sigma = E\left[\tilde{e}(t) - \lambda(t)\right] \tag{11}$$

Since the transducer model integrates a bias magnetization M_0 and preload P to achieve a bi-directional magnetostriction, Figure 3 is re-expressed in Figure 5.

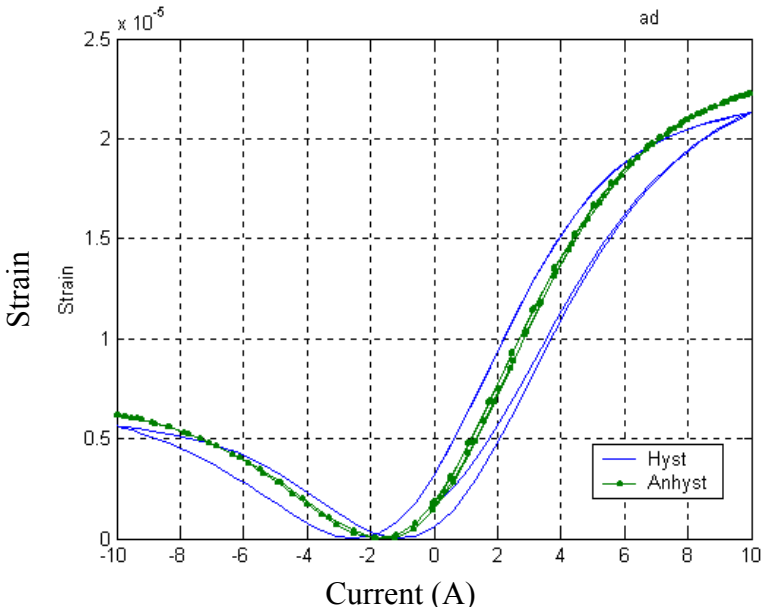

Figure 5: Profile of Magnetization With Bias Magnetization and Preload

Figure 6 illustrates the comparison of the actuator dynamics between the actual and simulation when applying a sinusoid input current at 10 Hz. The dynamics is linear to the current at low drive. At high current input, the actuator performs in a highly nonlinear manner. The simulation captures very accurately the transition of the nonlinear dynamics as the input current increases.

The effect due to inertia of the tool fixture can be exhibited by comparing the output elongation at different frequencies. In Figure 7, as the frequency increases, speed of the fixture rises up. The inertia, in turn, impedes maneuverability. As a result, the hysteresis loop becomes wider.

Figure 8 shows the profiles of forces corresponding to different current magnitudes. Anhysteretic (hysteresis-free) forces are represented by dotted lines. Since no hysteresis impedes the energy transformation, all anhysteretic forces, in effect, evolve in the same path. On the other hand, the hysteretic forces represented by solid lines develop different sized of major loops.

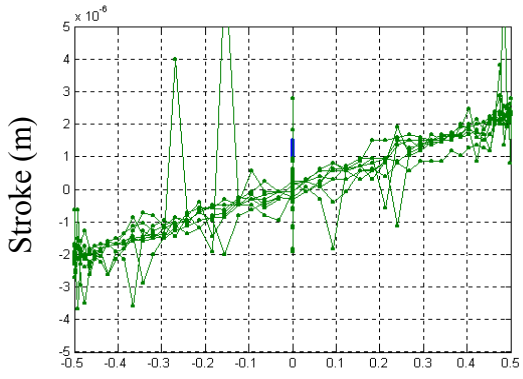

a. Actual Stroke at 0.5A

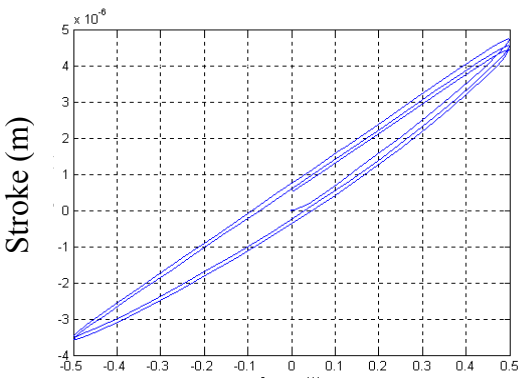

b. Estimated Stroke at 0.5A

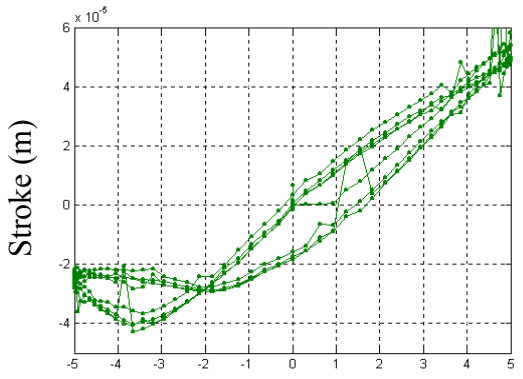

c. Actual Stroke at 5.0A

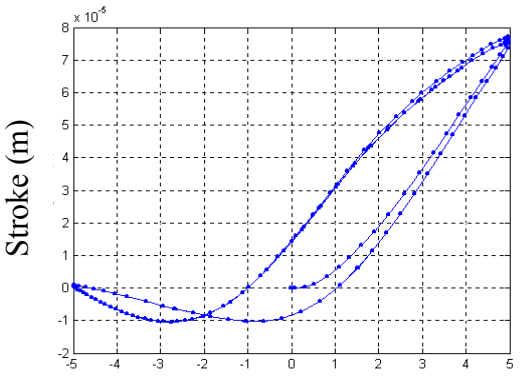

d. Estimated Stroke at 5.0A

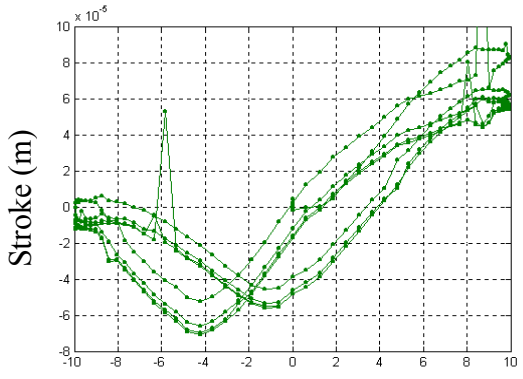

e. Actual Stroke at 9.95A

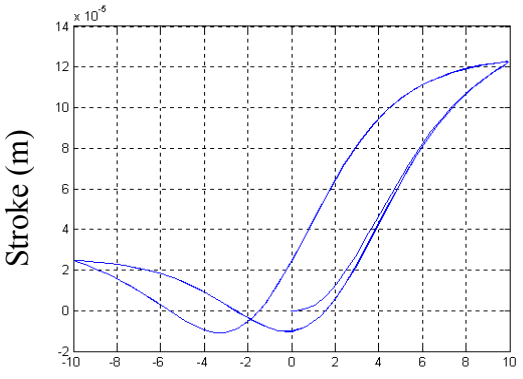

f. Estimated Stroke at 9.95A

Figure 6: Comparisons Between Actual And Estimated Elongation Evolution At 10 Hz

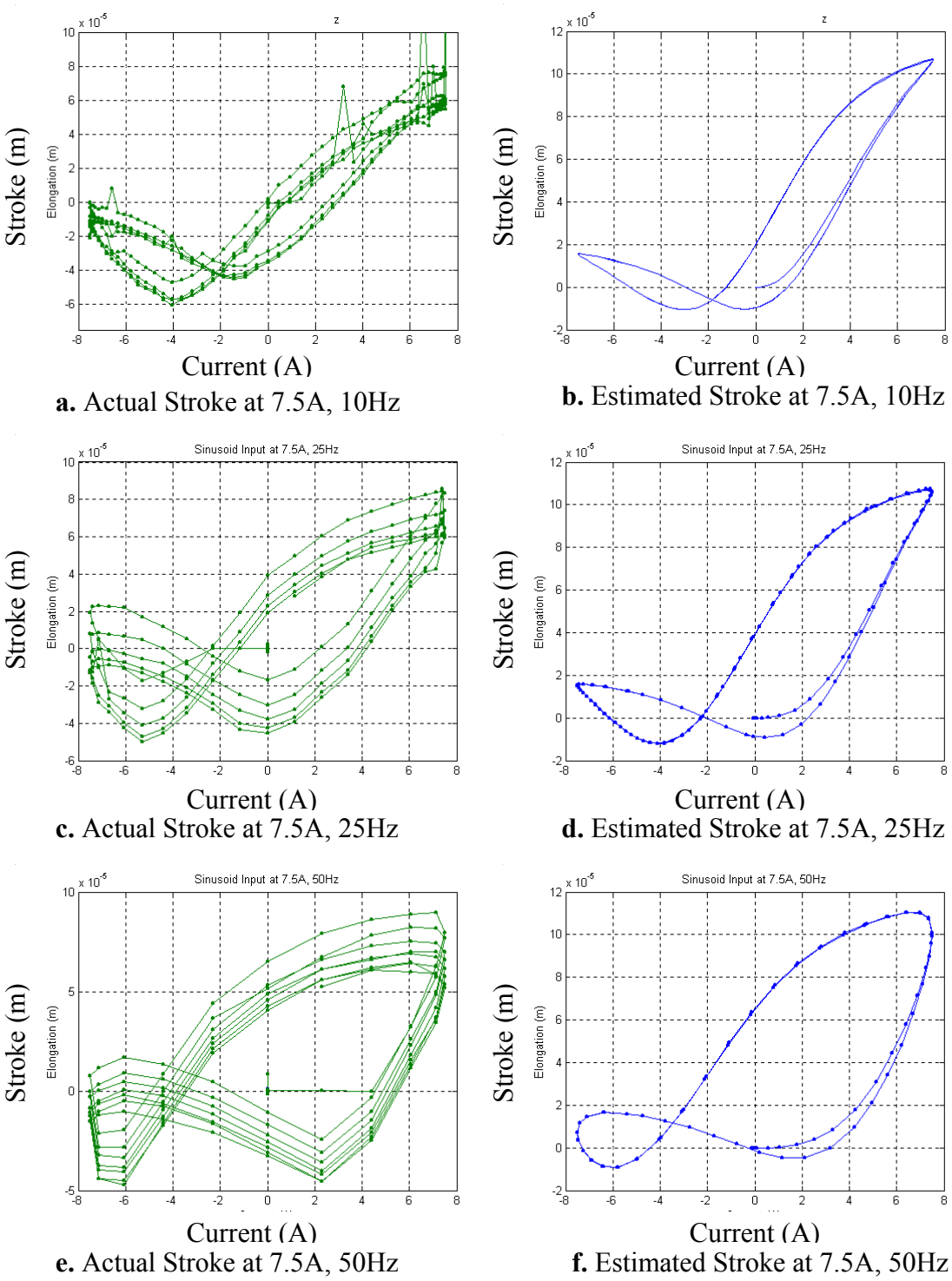

a. Actual Stroke at 7.5A, 10Hz

b. Estimated Stroke at 7.5A, 10Hz

c. Actual Stroke at 7.5A, 25Hz

d. Estimated Stroke at 7.5A, 25Hz

e. Actual Stroke at 7.5A, 50Hz

f. Estimated Stroke at 7.5A, 50Hz

Figure 7: The Effect of Tool Fixture Dynamics At Various Frequencies

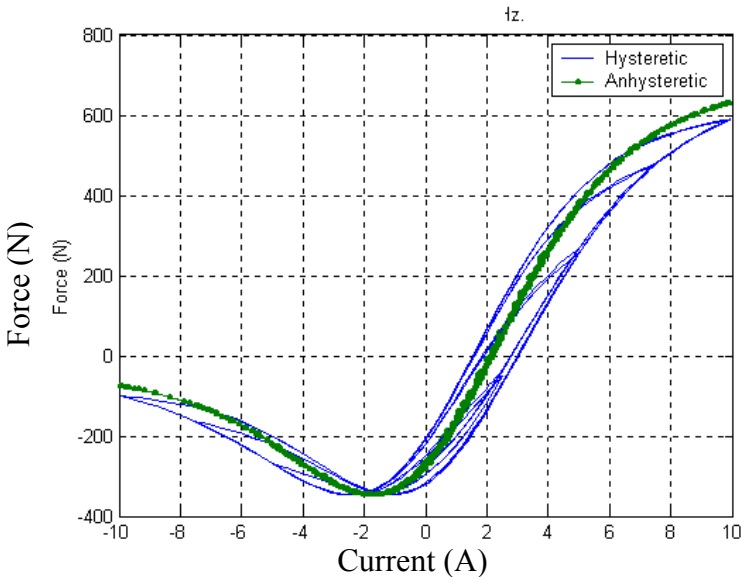

Figure 8: Anhysteretic And Hysteretic Forces Profile At 10 Hz

8.2.2 SLIDING MODE CONTROL (SMC)

As a robust control scheme, sliding mode control can offer many good properties, such as insensitivity to parameter variations or uncertainties, external disturbance rejection, and fast dynamic response. The modeling inaccuracies can have strong adverse effects on an output response. The model imprecision may come from unknown system dynamics or intentional yet very effective simplification of the system dynamics [12]. Sliding mode control is a simple approach to a robust control of systems with these problems. In the past, the authors have employed variations of the control schemes to control robots [13] as well as precision machines [14].

With this property of Sliding control, the complicated hysteresis model can be expressed in a simple representation by using an anhysteresis model as a nominal model with a correction measure to account for the effect of hysteresis gap. The previous hysteretic force $\boldsymbol{F}$ in equation (4 and 9) is, then re-written in terms of anhysteretic force $\boldsymbol{F_{an}}$ with a variable control input $\boldsymbol{U}$ (a coil current)

$$\boldsymbol{F} = \boldsymbol{K}\left[\boldsymbol{M}_s \tanh\left(\frac{\boldsymbol{U}}{\boldsymbol{A}}\right) + \boldsymbol{M}_o\right]^2 + \boldsymbol{P} \tag{12}$$

where the input $\boldsymbol{U}$ is the amount of the coil current, $\hat{\boldsymbol{U}}$ for anhysteretic force, and $\Delta\boldsymbol{U}$ for hysteresis gap.

$$\boldsymbol{U} = \hat{\boldsymbol{U}} + \Delta\boldsymbol{U} \tag{13}$$

Using anhysteretic force $\boldsymbol{F_{an}}$, the nominal equation is defined as

$$\hat{F} = \hat{K}\left[\hat{M}_s \tanh\left(\frac{\hat{U}}{\hat{A}}\right) + \hat{M}_o\right]^2 + \hat{P} \tag{14}$$

An equivalent control input U_{eq}, in turn, becomes

$$U_{eq} = \hat{U} = \hat{A}.\tanh^{-1}\left[\frac{1}{\hat{M}_s}\left(\sqrt{\frac{\hat{F}-\hat{P}}{\hat{K}}} - \hat{M}_o\right)\right]. \tag{15}$$

The 2nd order dynamic system located on top of the transducer's hysteretic force, shown in equation (10), can be written in its nominal form as

$$\hat{m}\ddot{x} + \hat{c}\dot{x} + \hat{k}x = \hat{F} \tag{16}$$

A controller must overcome both hysteresis loop and the 2nd order dynamics to achieve the desired output stroke.

The control input U can be obtained from the force in equation (12). Define a sliding surface S as a combination of estimated force errors

$$S = \lambda e + n\lambda^2 \int e dt \tag{17}$$

where the error e is the difference between the desired output force and the estimated force

$$e = \hat{k}x_d - \hat{k}x\,.$$

Once the sliding surface is reached, where the combination of force errors S is reduced to zero, the system is designed to remain on the surface with a condition of

$$\dot{S} = 0\,. \tag{18}$$

By substituting the sliding surface S from equation (17), the condition can be re-expressed as

$$\lambda\dot{e} + n\lambda^2 e = 0$$

$$\frac{\dot{e}}{n\lambda} + \left(\hat{k}x_d - \hat{k}x\right) = 0.$$

The nominal force $\hat{F}$ is obtained by replacing the estimated force $\hat{k}x$ using equation (16).

$$\frac{\dot{e}}{n\lambda} + \hat{k}x_d = \hat{k}x = \hat{F} - \hat{m}\ddot{x} - \hat{c}\dot{x}$$

$$\hat{F} = \hat{k}x_d + \hat{m}\ddot{x} + \hat{c}\dot{x} + \frac{\dot{e}}{n\lambda} \tag{19}$$

The equivalent control U_{eq} is, in effect, determined by substituting the nominal force $\hat{F}$ in equation (15).

In order to guarantee stability, the Lyapunov stability criterion is employed to drive the system to a sliding surface S=0 in a finite time. The criterion is shown as

$$S\dot{S} \le -\eta|S|$$

where η is a positive number

$$\begin{aligned} S\left(\lambda\dot{e} + n\lambda^2 e\right) &\le -\eta|S| \\ S\left[\lambda\dot{e} + n\lambda^2\left(\hat{k}x_d - \hat{k}x\right)\right] &\le -\eta|S| \\ n\lambda^2 S\left[\frac{\dot{e}}{n\lambda} + \hat{k}x_d - \hat{k}x\right] &\le -\eta|S| \end{aligned}$$

According to the equation (10) and (19), the previous condition can be rewritten as

$$n\lambda^2 S\left[\left(\hat{F} - \hat{m}\ddot{x} - \hat{c}\dot{x}\right) - \frac{\hat{k}}{k}\left(F - m\ddot{x} - c\dot{x}\right)\right] \le -\eta|S| \tag{20}$$

The condition indicates that the product of the output error and modeling error in hysteretic force F and the 2nd order dynamics must be less than a magnitude of the output error itself. Substituting hysteretic force F shows a relationship between control input and errors.

$$n\lambda^2 S\left[\begin{array}{l} \left[\left[\left(\hat{K}\left(\hat{M}_s \tanh\left(\frac{\hat{U}}{\hat{A}}\right) + \hat{M}_o\right)^2 + \hat{P}\right) - \hat{m}\ddot{x} - \hat{c}\dot{x}\right] - \right. \\ \left.\frac{\hat{k}}{k}\left[\left(K\left(M_s \tanh\left(\frac{U}{A}\right) + M_o\right)^2 + P\right) - m\ddot{x} - c\dot{x}\right]\right] \end{array} \le -\eta|S| \tag{21}$$

As shown in equation (13), the control input U is divided into two components: $\hat{U}$ and ΔU. The first component compensates for the anhysteretic force, while the other is for the hysteresis gap. Assume an existing variable control input ΔU such that the hysteretic force $F(\hat{U} + \Delta U)$ is always inside the boundary of the anhysteretic force $F_{an}(\hat{U})$ and estimated hysteresis gap $\hat{F}_{gap}(\Delta U)$:

$$\begin{aligned} &\left|F(\hat{U} + \Delta U)\right| \le \left|F_{an}(\hat{U}) + \hat{F}_{gap}(\Delta U)\right| \\ &\left|K\left[M_s \tanh\left(\frac{\hat{U} + \Delta U}{A}\right) + M_o\right]^2 + P\right| \le \left|\begin{array}{r} K\left[M_s \tanh\left(\frac{\hat{U}}{A}\right) + M_o\right]^2 + P \\ + \hat{K}\left[\hat{M}_s \tanh\left(\frac{\Delta U}{\hat{A}}\right)\right]^2 \end{array}\right| \end{aligned} \tag{22}$$

As a result, equation (21) is re-written in terms of output elongation, hysteresis gap, and estimated anhysteretic force as

$$n\lambda^2\hat{k}S\left[\begin{array}{l}\left(\frac{\hat{K}}{\hat{k}}\left(\hat{M}_s\tanh\left(\frac{\hat{U}}{\hat{A}}\right)+\hat{M}_o\right)^2+\frac{\hat{P}}{\hat{k}}\right)+\left(-\frac{\hat{m}}{\hat{k}}\ddot{x}-\frac{\hat{c}}{\hat{k}}\dot{x}\right)\\ -\left(\frac{K}{k}\left(M_s\tanh\left(\frac{\hat{U}}{A}\right)+M_o\right)^2+\frac{P}{k}\right)-\left(-\frac{m}{k}\ddot{x}-\frac{c}{k}\dot{x}\right)\\ -\left(\frac{\hat{K}}{k}\left(\hat{M}_s\tanh\left(\frac{\Delta U}{\hat{A}}\right)\right)^2\right)\end{array}\right]\le-\eta|S|$$

In the bracket, the first two terms represent the estimated anhysteretic force and the estimated 2nd order dynamics. Recombining these two components yields the estimated anhysteretic elongation $\hat{x}_{an}$. Likewise, a combination of the next two terms becomes the actual anhysteretic elongation x_{an}. Therefore, the hysteresis gap is clearly isolated. Equation (23) summarizes the Lyapunov stability criterion as

$$n\lambda^2 S\left[-\frac{\hat{k}}{k}\left(\hat{K}\left(\hat{M}_s\tanh\left(\frac{\Delta U}{\hat{A}}\right)\right)^2\right)+\hat{k}\left(\hat{x}_{an}-x_{an}\right)\right]\le-\eta|S| \tag{23}$$

Rewriting the sliding surface as

$$S=|S|\,\mathrm{sgn}(S),$$

the equation (23), then, becomes

$$\mathrm{sgn}(S)\left[-\frac{\hat{k}}{k}\hat{K}\left(\hat{M}_s\tanh\left(\frac{\Delta U}{\hat{A}}\right)\right)^2+\hat{k}\left(\hat{x}_{an}-x_{an}\right)\right]\le-\frac{\eta}{n\lambda^2} \tag{24}$$

For a positive *S*, equation (24) is re-expressed as

$$\frac{\eta}{n\lambda^2}+\hat{k}\left(\hat{x}_{an}-x_{an}\right)\le\frac{\hat{k}}{k}\hat{K}\left(\hat{M}_s\tanh\left(\frac{\Delta U}{\hat{A}}\right)\right)^2 \tag{25}$$

In order to have sufficient power to correct output displacement error, a variable control input ΔU must yield a tensile force greater than an estimated force-error due to imprecise parameters in anhysteresis and the 2nd order dynamics model. In the light of sliding mode control scheme, this estimated force error could be replaced by sliding surface S, which is a combination of the estimated force error. Accordingly, the condition becomes

$$S\le\frac{\hat{k}}{k}\hat{K}\left(\hat{M}_s\tanh\left(\frac{\Delta U}{\hat{A}}\right)\right)^2$$

Assuming the ratio between the actual and nominal stiffness as

$$\frac{\boldsymbol{k}}{\hat{\boldsymbol{k}}} = \boldsymbol{C},$$

Control input $\Delta \boldsymbol{U}$ is found as

$$\Delta \boldsymbol{U} \geq +\hat{\boldsymbol{A}}.\tanh^{-1}\left(\frac{1}{\hat{\boldsymbol{M}}_s}\left(\sqrt{\frac{\boldsymbol{C}.|\boldsymbol{S}|}{\hat{\boldsymbol{K}}}}\right)\right)$$

With the same approach for a negative $\boldsymbol{S}$, $\Delta \boldsymbol{U}$ must result in a greater compressive force than the estimated force-error due to parameter imprecision.

$$\frac{\hat{\boldsymbol{k}}}{\boldsymbol{k}}\hat{\boldsymbol{K}}\left(\hat{\boldsymbol{M}}_s \tanh\left(\frac{\Delta \boldsymbol{U}}{\hat{\boldsymbol{A}}}\right)\right)^2 \leq -\frac{\eta}{\boldsymbol{n}\lambda^2} + \hat{\boldsymbol{k}}\left(\hat{\boldsymbol{x}}_{an} - \boldsymbol{x}_{an}\right)$$

$$\Delta \boldsymbol{U} \leq -\hat{\boldsymbol{A}}.\tanh^{-1}\left(\frac{1}{\hat{\boldsymbol{M}}_s}\left(\sqrt{\frac{\boldsymbol{C}.|\boldsymbol{S}|}{\hat{\boldsymbol{K}}}}\right)\right)$$

The sign of $\Delta \boldsymbol{U}$ is incorporated with the sign of sliding surface $\boldsymbol{S}$. Therefore, input $\boldsymbol{U}$ can be expressed as

$$\boldsymbol{U} = \hat{\boldsymbol{U}}(\hat{\boldsymbol{F}}) + \Delta \boldsymbol{U}(\boldsymbol{S}).\mathrm{sgn}(\boldsymbol{S}) \tag{26}$$

where

$$\Delta \boldsymbol{U}(\boldsymbol{S}) = \hat{\boldsymbol{A}}.\tanh^{-1}\left(\frac{1}{\hat{\boldsymbol{M}}_s}\sqrt{\frac{\boldsymbol{C}.|\boldsymbol{S}|}{\hat{\boldsymbol{K}}}}\right) \tag{27}$$

As verification to the assumption in equation (22), Figure 9 illustrates that the hysteretic force $\boldsymbol{F}(\hat{\boldsymbol{U}} + \Delta \boldsymbol{U})$ evolves inside the boundary of $\hat{\boldsymbol{F}}_{an}(\hat{\boldsymbol{U}}) + \hat{\boldsymbol{F}}_{gap}(\Delta \boldsymbol{U})$. The boundary employs variable differences of anhysteretic and hysteretic force to compute $\Delta \boldsymbol{U}$. The hysteretic force is the solid line (red and green) located in proximity to the anhysteretic force (blue). While, the dashed line surrounding as an outer loop represents the boundary.

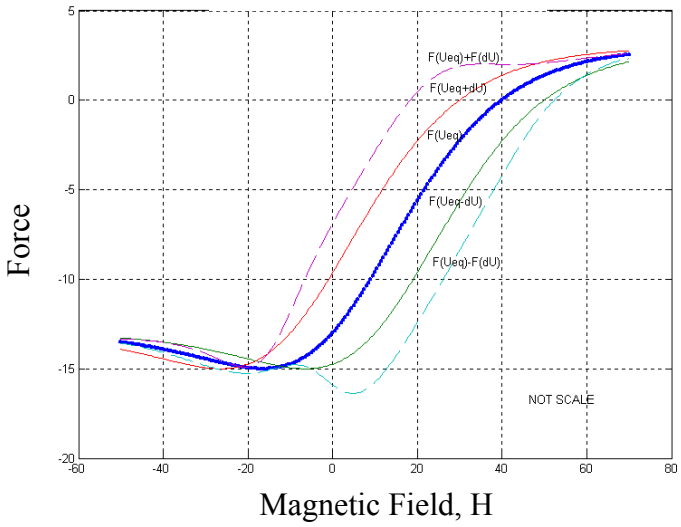

Figure 9: Demonstration of Evolving Hysteretic Force Bounded Inside Of Boundary

Figure 10 displays a comparison of the amount of current amplitude and predicted equivalent control $\hat{U}$ in order to achieve a certain elongation magnitude. The current difference indicates the effects of hysteresis gap, 2nd order dynamics, and the imprecise parameters. This difference can be corrected by applying the variable switching gain. The next section will show the controller performance through a simulation.

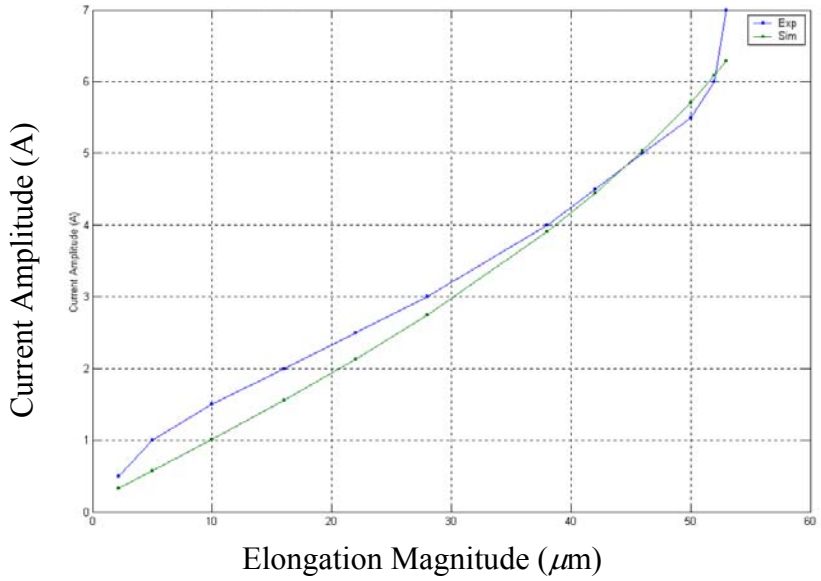

Figure 10: Comparison Between Amount of
Experimental Current and Simulated Equivalent Control

8.2.3 SIMULATION OF MAGNETOSTRICTIVE TRANSDUCER

According to the hysteresis model, the relationship between input voltages, and output strain can be depicted in Figure 11. For a given input current ***I***, the corresponding magnetic field ***H*** of the coil is computed. Then, anhysteretic, irreversible, reversible, and total magnetization are determined respectively by mean field theory for ferromagnetic hysteresis and the law of approach. The output strain is, in turn, obtained by the computation in strain subsystem. All of these function blocks are, then, contained inside of one block called "Magnetostrictive Actuator" in Figure 12. This block is integrated with the "Fixture Dynamic" block representing a complete tool servo system. The diagram of the closed loop control scheme in Figure 12 shows the overall feedback scheme.

Imprecise parameters of the fixture dynamics are given to the simulation to investigate the robustness of the control schemes. The simulated results of PID and sliding mode control (SMC) at 50 Hz and 100 Hz are demonstrated in Figure 13. PID performance is worse in term of

tracking ability especially at the peaks of command elongation. In fact, PID yields tracking errors 5 times larger than the values of SMC. The numerical results and performance comparison of the PID and the sliding controller will be demonstrated again through the experimental examples in the next section.

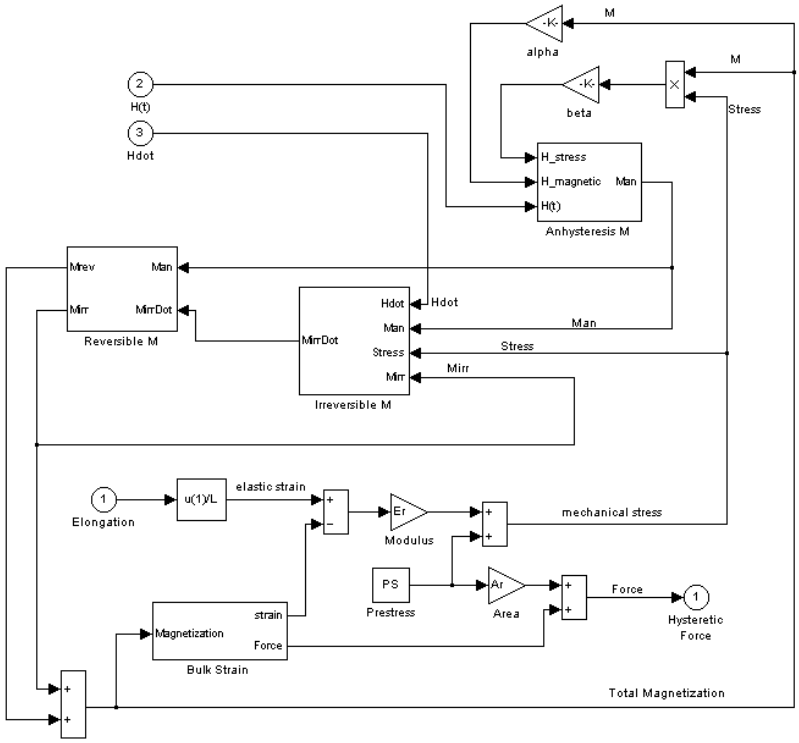

Figure 11: Block Diagram of Magnetostrictive Core

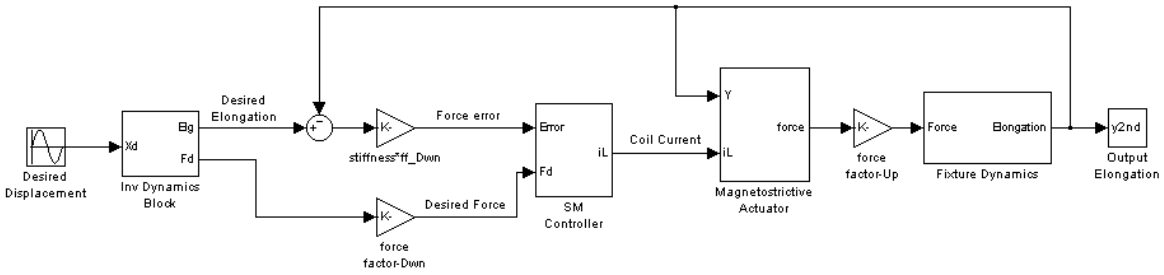

Figure 12: Closed Loop Control Diagram (Sliding Mode Control)

Note that "Inv Dynamics Block" maps a desired displacement to a desired elongation and calculates a desired estimated force as a nominal input to SMC.

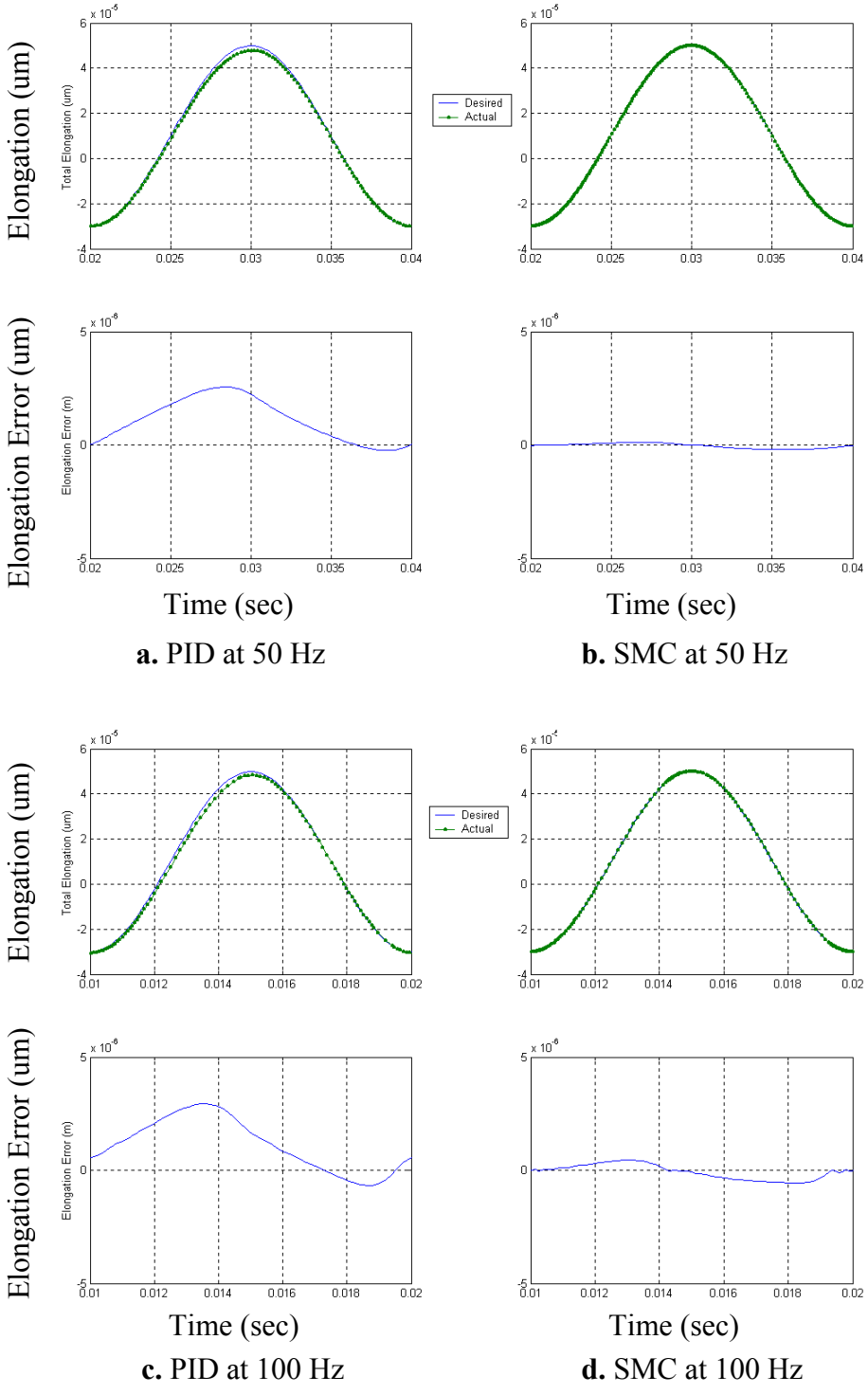

Figure 13: Comparisons of Performance Between Simulated PID And Sliding Mode Controller

8.2.4 EXPERIMENTAL RESULTS

The performance of the closed loop actuator from low to high drives was investigated. The PID gains were adjusted for a particular frequency by referring to Ziegler-Nichols stability limit technique, while the parameters of the SMC were continuously updated for every input frequency.

Typically, the performance of SMC increases as the sampling frequency increases. However, this may not be practical. Since the amount of applied magnetic field ***H*** depends on the rate change of the input current, the output force and stroke are intrinsically associated with the magnitude of SMC parameters and the sampling frequency. In the experiment, the sampling frequency was about 40 times the stroke frequency. Accordingly, to operate the transducer at 100 Hz, the sliding control should sample at 4000 Hz, for example. This factor affects bandwidth of the SMC servo system since the DSP board can acquire the measured data at the highest frequency of 10,000 Hz. Accordingly, the SMC transducer can work up to 250 Hz, while the PID system has no boundary. In general, the stroke frequency of 100 Hz is high enough to drive most applications and to study the influence of hysteresis. The SMC parameters do not need re-calibration unless the stroke frequency exceeds 250 Hz.

In Figure 14, comparison between PID and Sliding control scheme using a multiple-frequency input has shown a significant delay in PID outputs, whereas the SMC travels mostly on top of the desired trajectory.

To evaluate the performance in terms of the robustness, a mass was attached against the tool fixture. Then, the results were compared with the closed loop actuator when driving without load. The comparison is shown in Figure 15. PID output is slightly worse when operating with the load on. More wavy profile can be noticed. The SMC profile, however, is quite robust to the load variation.

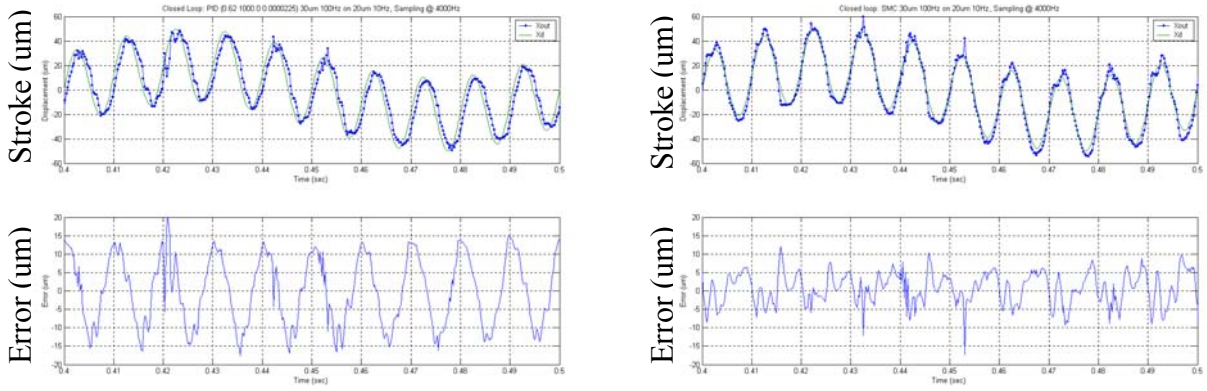

a. Output Stroke and Error of PID

b. Output Stroke and Error of SMC

Figure 14: Comparison of Path Following between PID and SMC using Multiple-Frequency Desired Displacement.

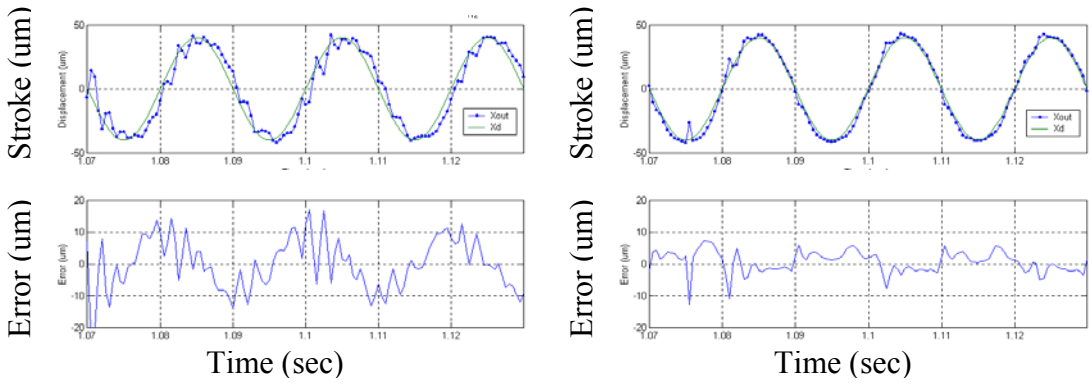

a. Output Stroke and Error of PID **b.** Output Stroke and Error of SMC

Figure 15: Comparison of Path Following between PID and SMC with Load Variation

8.3 CONCLUSION

To fully understand how to control a magnetostrictive tool servo system, the magnetostriction phenomenon including inherent hysteresis has been studied. Sliding mode control scheme with variable switching gain was presented to deal with uncertainties such as external disturbances or unmodeled dynamics. The ferromagnetic anhysteresis based on *quasi-macroscopic* model was used to compute the equivalent control. The hysteresis gap and the dynamics of the tool fixture were, then, corrected by the switching gain based on the Lyapunov stability condition. The proposed control scheme was analytically expressed and verified through numerical simulation. The experimental examples drew the comparisons between the performance of sliding mode and PID controller. PID cannot overcome the influences of hysteresis resulting a significant output delay, while sliding mode control yielded better tracking performance.

REFERENCES

1. Smith, R.C., "Modeling technique for magnetostrictive actuators," SPIE, v 3041, pp. 243-253, 1997.
2. Calkins, F.T., R.C. Smith, and A.B. Flatau, "An energy based hysteresis model for magnetostrictive transducers," ICASE Report 97-60, IEEE Transactions on Magnetics, 1997.
3. Jiles, D.C., "Introduction to magnetism and magnetic Materials," Chapman and Hall, 1991.
4. Jiles, D.C., and D.L. Atherton, "Theory of ferromagnetic hysteresis," Journal of Magnetism and Magnetic Materials, 61, pp. 48-60, 1986.
5. Jiles, D.C., J.B. Thoelke, and M.K. Devine, "Numerical determination of hysteresis parameters for the modeling of magnetic properties using the theory of ferromagnetic hysteresis," IEEE transactions on Magnetics, 28(1), pp. 27-35, 1992.

6. Venkataraman, R., and P.S. Krishnaprasad, "Qualitative analysis of a bulk ferromagnetic hysteresis model," Proceeding of the 37th IEEE conference on Decision and Control, pp. 2443-2448, December 1998.
7. Venkataraman, R., and P.S. Krishnaprasad, "A model for a thin magnetostrictive actuator, " Technical research report, Center for Dynamics and Control of smart structures, 1998.
8. Smith, R.C., "A nonlinear optimal control method for magnetostrictive actuators," Journal of Intelligent Material System and Structures, 9, pp. 468-486, 1998.
9. Smith, R.C., C. Bouton, and R. Zrostlik, "Partial and full inverse compensation for hysteresis in smart material systems," Proceedings of the American Control Conference, pp. 2750-2754, 2000.
10. Nealis, J.M., and R.C., Smith, "An adaptive control method for magnetostrictive transducers with hysteresis," Proceeding of the 40th IEEE conference on Decision and Control, pp. 4260-4265, December 2001.
11. Ashley, S., "Magnetostrictive actuators," Mechanical Engineering, 1998.
12. Slotine, J.J, and W. Li, "Applied nonlinear control," Prentice Hall, 1991.
13. Shim, W., and P.I. Ro, "Compensation of microdynamic friction by sliding mode control with variable switching gain," Proceedings of the 7th Mechatronics Forum International Conference, September 2000.
14. Ro, P.I. and, C.C., Yih, "Robust control of Passive-jointed robot and experimental validation using sliding mode," Journal of Guidance, Control and Dynamics, v 19, n 5, pp. 1039-1046, 1996.

9 HIGH SPEED VIBRATION ASSISTED MACHINING

Nobuhiko Negishi
Graduate Student
Thomas A Dow
Professor
Mechanical Engineering Department

Single crystal diamond turning has been the standard for machining high quality precision optical surfaces. However workpiece materials are limited due to tool wear and workpiece brittle fracture. Many materials with industrially useful properties such as steel, glass, silicon cannot be fabricated using single point diamond tools. Vibration-Assisted Machining (VAM) is a technique that combines linear tool motion with a secondary oscillatory motion of the tool. A subset of VAM is Elliptical Vibration-Assisted Machining or EVAM. This technique implements oscillation in both the feed and thrust directions resulting in an elliptical tool path.. The PEC has been working to create a solid understanding of the fundamental aspects of EVAM. Cutting forces have been modeled and verified with experimental results. Different chip geometries have been viewed with a SEM microscope and surface finish has been measured for various cutting conditions. The surface roughness of an EVAM fabricated part has been predicted using a technique previously developed at the PEC. This work has been conducted with a low bandwidth (0-500Hz) tool actuator developed, manufactured and assembled at the PEC called the UltraMill Low Speed. And a high bandwidth design (1000-4000Hz), the UltraMill High Speed (UMHS). The implementation of this high bandwidth tool actuator included dynamic and static structural analysis and characterization of the thermal properties of the system for efficient cooling system design. The UMHS was developed to study EVAM at higher frequencies that are more industrially viable.

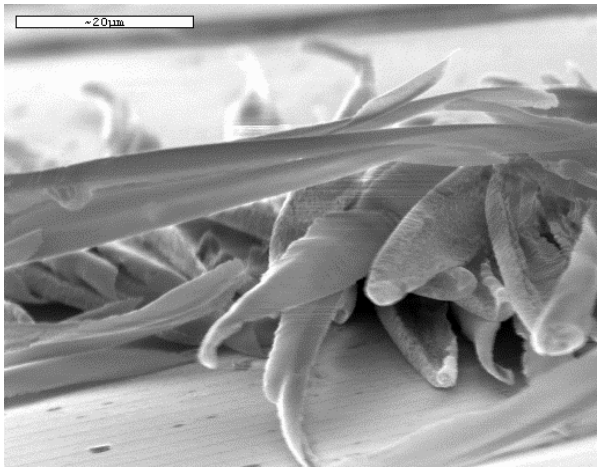

9.1 INTRODUCTION

Vibration assisted machining has been studied since the 70s with some success. Reduced cutting forces and tool wear have been reported as well promising results for machining alternative materials such as steel, silicon, or glass with a single crystal diamond tool. The significance of this finding lies in the ability to eliminate a finishing process such as polishing in a manufacturing process or the possibility of creating precision surfaces in brittle materials such as silicon or glass using a single point diamond. VAM is a complex operation with many variables whose significance has not been determined by previous research. Much of the work at the PEC deals with these VAM fundamentals. Identifying and understanding the key parameters of VAM in order to optimize this process is an important goal of this research. The PEC VAM system is a subset of VAM known as Elliptical Vibration Assisted Machining or EVAM. This process differs from standard one dimensional VAM due to the elliptical tool path generated by the mill unit. This milling unit uses two piezo electric actuators and operates below the first natural frequency of the system. The UltraMill design allows greater flexibility in oscillation frequency, tool path size and shape making the UltraMill an excellent research tool. Two versions of the UltraMill have been constructed at the PEC. The first version is a relatively low bandwidth, up to 500Hz, design that was constructed mainly to verify the advantages of EVAM. The second version is a much faster mill capable of oscillation frequencies up to 5000 Hz. The implementation of this second design was a large effort at the PEC. The UMHS will be used to study the EVAM process in greater detail then the first design.

9.2 TOOL MOTION GENERATION

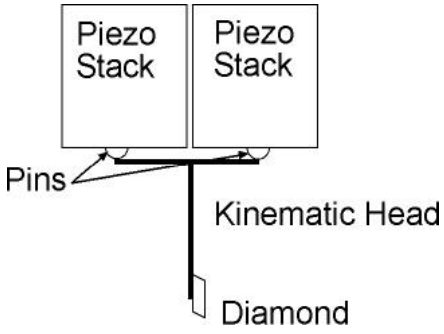

Figure 1. UltraMill Linkage

The elliptical oscillating motion of the tool is generated by attaching the diamond tool to a kinematic linkage as shown in Figure 1. This linkage consists of two 44 layer piezo stack actuators connected to a 'T' shaped kinematic head via two 1 mm radius ceramic half rounds and flexure to preload the whole system. A pair of sine waves, 90˚ out of phase, are used to drive the piezo actuators and generate the elliptical tool motion. For a given actuator displacement the

dimensions of the 'T' determine the shape and the major axis of the tool path ellipse. The Ultra-Mill High Speed has "arms" of the 'T' that are 5 mm each and a vertical beam that is 26 mm. This geometry results in an ellipse with a major axis of 40 μm and a minor axis of 8 μm for an actuator stroke of 22 μm. The piezo stack actuators are driven by two Kinetic Ceramics KC N15-1 1500 watt amplifiers with sinusoidal input from a Hewlett Packard 8904A function generator. This design is a non-resonant approach that allows research into the effects of different actuation frequencies over several octaves, amplitudes, and path tilts. The modular capability of the UMHS also permits alternate kinematic head designs to be mounted for greater performance or different experiments. An active cooling system maintains safe operating temperatures for the piezo actuators.

9.3 HEAT SOURCE

9.3.1 THEORY

High frequency, high voltage piezoelectric applications can generate appreciable amounts of heat due to losses in the material and straining of the structure. Losses in the piezoelectric ceramic material can be explained by the well known hysteretic behavior of this material. Ferroelectric materials retain some polarization even after an electric field is removed. During poling, a piezo ceramic material is subject to a large voltage field. The large voltage field aligns the crystal structure along the direction of the applied field. After the field is removed the material remains anisotropic and will display a greater piezoelectric effect along the poled axis. The manufacturing of piezoelectric actuators, sensors and other devices rely on this material property. However this property also appears during actuation voltages which are smaller then the poling voltage. This explains the hysteretic behavior found in piezo actuators during operation. The energy required to drive a piezoelectric actuator is not completely converted to mechanical strain. The efficiency of an actuator varies with piezoceramic material and construction method.

9.3.2 HYSTERESIS

Hysteresis refers to the nonlinear characteristics of a system for a linear input. For a piezo actuator this would be a voltage. An input voltage will produce a displacement that proportional to the magnitude of the input voltage. However, when a system displays hysteretic behavior there is more then one position for a given input. The output position is dependent on the previous displaced position. A plot of displacement verse input voltages will give the familiar hysteresis curve for a piezo actuator. Figure 2 is a comparison of a hysteresis plot for a piezo actuator and a plot of non-hysteretic behavior. The direction arrows show the path the hysteresis loop. The difference between the two directional paths is characterized by a percentage. For

most high voltage piezo actuators the hysteresis is about 10 to 20%. This percentage is also the amount of input power lost to heat.

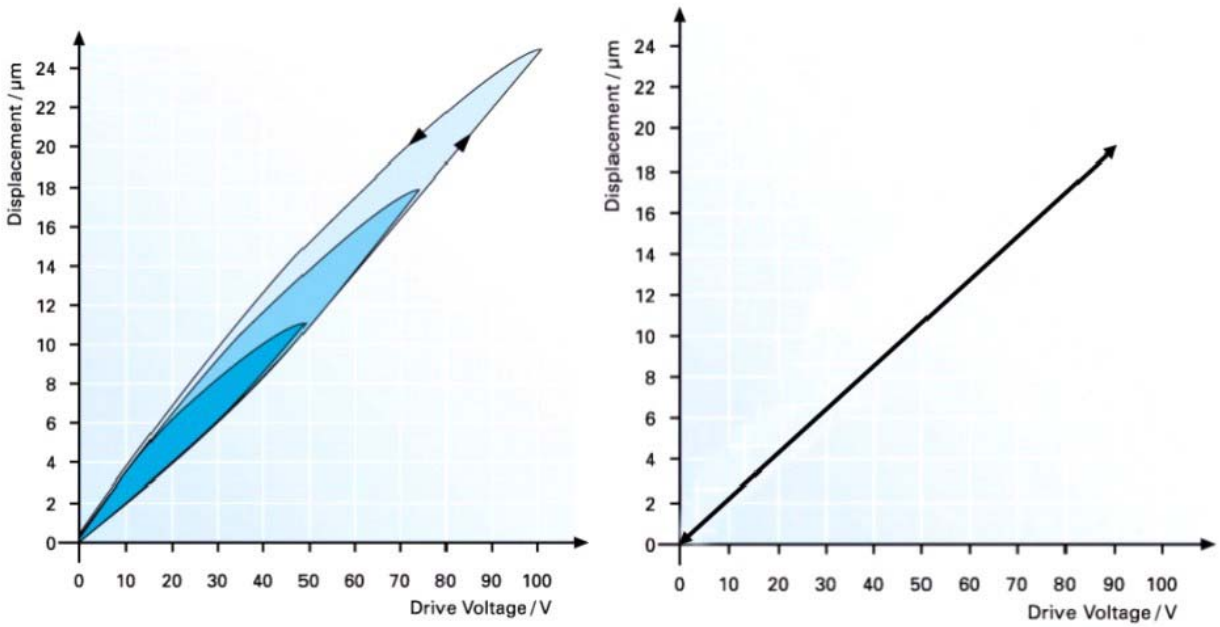

Figure 2. Effects of Hysteresis

9.3.3 HEAT GENERATION MODELS

The heat generated by a piezo motor depends on material type and application conditions. The piezoelectric properties of a ceramic are dependent on temperature, drive voltage and frequency. For small signal conditions, actuation voltages up to 100 volts, Equation (1) can be used to approximate heat generation of a piezo ceramic element.

$$P_{HEAT} = \frac{\pi}{4} Tan\delta \cdot f \cdot C \cdot V^2{}_{P-P} \qquad (1)$$

Where Tan δ is the loss angle, f is the driving frequency in Hertz, C is the capacitance in farads and $V_{P\text{-}P}$ is the peak to peak actuation voltage.

The large signal conditions and associated piezoelectric materials of high power piezo stack actuators produce larger heat to input power ratios. The percentage of input power lost to heat is on the order of 10-20 percent. A common engineering equation for predicting heat is shown in Equation (2).

$$P_{HEAT} = \left(\frac{C \cdot V_{P-P}{}^{2} \cdot f}{2} \right) \cdot K \qquad (2)$$

Where 'K' is the percentage of input power lost to heat for a given material or application.

9.4 INSULATED HEAT GENERATION EXPERIMENTS

9.4.1 OBJECTIVE

Accurately predicting the heat generated by the UltraMill piezo stack actuators was important when designing the cooling system. The parameter 'K' in Equation (2) was experimentally determined and verified again once the UltraMill was constructed. Following Equation (3), the output of a particular heat source can be measured by recording the rate of temperature increase of a known mass of material with a known specific heat that is absorbing all of the heat source's power.

$$q = m \cdot c_p \cdot \frac{dT}{dt} \qquad (3)$$

where q is the generated heat, m is the mass of the material, c_p is the specific heat of the material and $\frac{dT}{dt}$ is the rate of change in the material temperature.

9.4.2 EXPERIMENTAL APPARATUS

The ceramic material used in the construction of piezo actuators is brittle and can be easily damaged when tensile or shear stresses are placed on them. To prevent tensile stresses from damaging the piezo stacks under high frequency operation, the stacks are compressively preloaded. For this experiment the preload mechanism also acts as a thermal load to absorb the generated heat. Shown in Figure 3, the testing rig sandwiches the piezo stack actuators between two ground steel plates that are held together by two 30 mm long 8-32 steel bolts. The sectional profile of these plates maximizes stiffness to reduce stress concentrations on the edges of the piezo stacks and increases the natural frequency of the system. An alignment channel insures that the centroidal axis of the piezo stack is coplanar to the preload bolts.

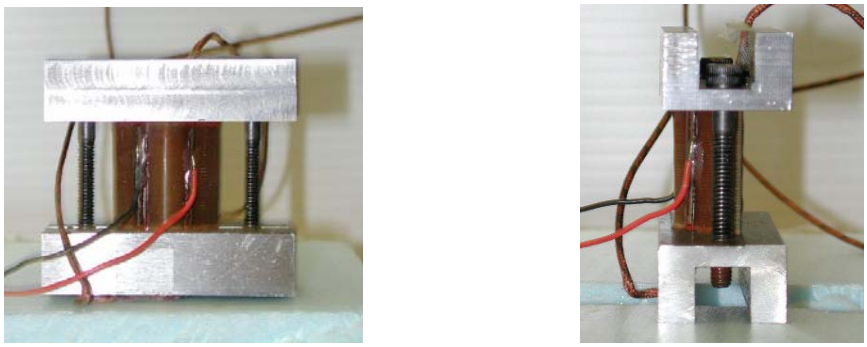

Figure 3. Preload Mechanism for Dynamic Thermal Experiment

The thermal properties of the steel plates and bolts can be easily calculated for the heat equation. The stack, plates and bolts are wrapped in insulation to create adiabatic conditions that insure the end plates absorb most of the generated heat. Thermocouples were placed on both plates and rate of temperature increase during operation was measured using a data acquisition board connected to a PC.

9.4.3 RESULTS

Eleven trials covering five different actuation conditions were conducted. The measured results were plotted against the input drive power to find the fraction of the drive power lost to heat. Figure 4 shows the plotted data for the eleven trials. The measured input power lost to heat was found to be 22%. Thus the constant 'K' in Equation (2) is 0.22 .

9.5 HEATING IN ULTRAMILL FIXTURE

9.5.1 EXPERIMENTAL APPARATUS

Once the Ultra Mill HS was assembled the stack heating was again measured to confirm the results of the insulated heating experiment. The drive actuators were attached to a steel pedestal with cyanoacrylate and preloaded by a ceramic head through half round pins attached to the top of the stacks. The side surfaces of both stacks are open to ambient air. To compare generated heating to the insulated heat experiment several assumptions were made. The heating of the stacks could be calculated by measuring the surface temperature rise rate during excitation and the piezo stack would behave as an insulated system for some initial transient heating period. The surface temperature of the piezo stack was measured with a miniature surface mount RTD (Resistance Temperature Device) that was glued to the surface of the actuator. This platinum element is a standard three wire RTD with a European curve of $\alpha = 0.385$. The transducer data was recorded using an Omega digital RTD read-out with 0.1 C° accuracy and 2.5 second update

rate connected to a PC via a data acquisition board. The piezo stacks were driven at several operating conditions to verify the range of accuracy of the heat generation equation.

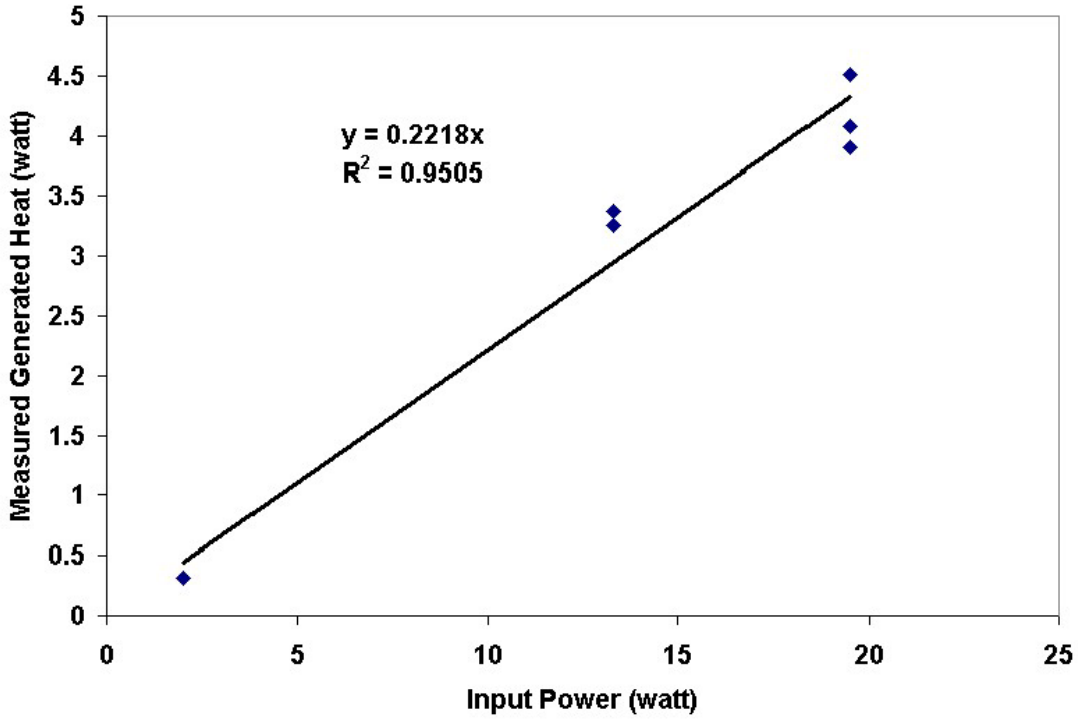

Figure 4. Input Power vs Measured Heat Generated

9.5.2 RESULTS

Piezo actuator surface temperature was recorded for 12 different actuation conditions varying both drive voltage and frequency. At the beginning of each trial the system was allowed to equilibrate with the ambient air before the stack actuators were activated. A linear curve was fit to the data to find the rate of temperature increase for each actuation condition. Shown in Figure 5, the measured heat generated was plotted against the total drive power to find the percentage of power lost to heat.

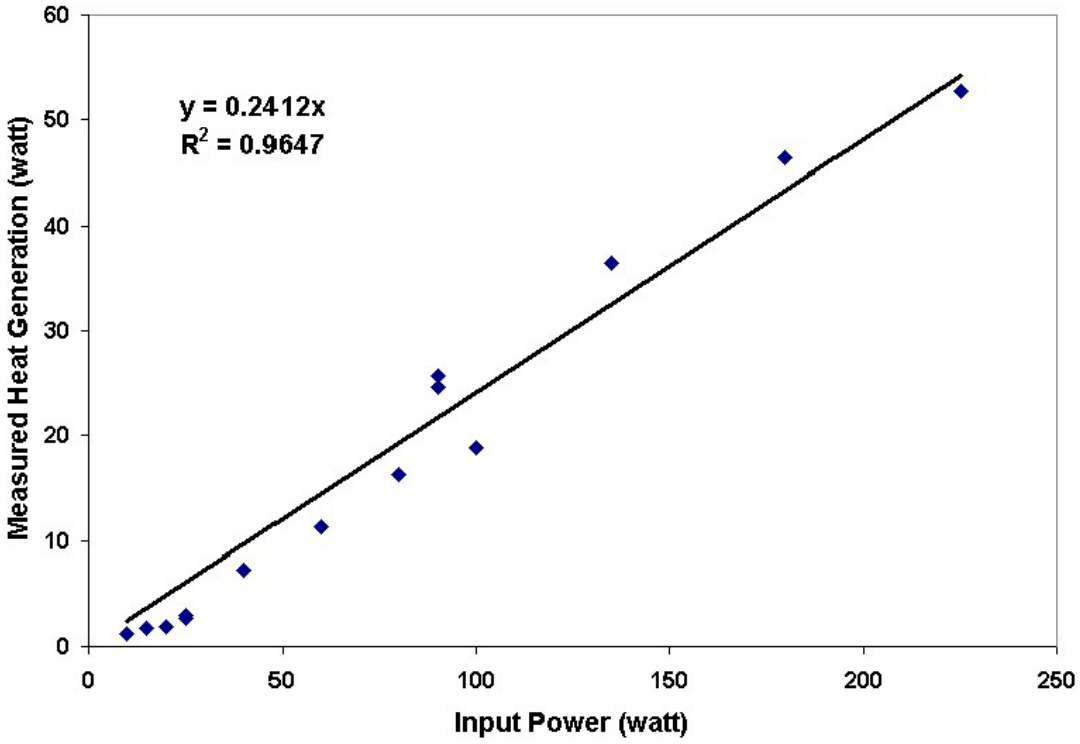

Figure 5. Input Power vs Measured Heat Generated

The experimental data shows that the generated heat is approximately 24% of the input power used to drive the stack; that is, the constant 'K' in Equation (2) is 0.24.

9.6 COMPARISON OF THEORY AND EXPERIMENTS

9.6.1 CONSISTENCY OF RESULTS

The results from the two different experiments produced similar values for percentage of input power lost to heat. This value, between 22-24% is somewhat higher then the published numbers for piezo actuators, but this was clearly the percentage value for this application.

9.6.2 DISCUSSION

The desired operating frequency and voltage of the UltraMill HS is 5000 Hz and 800 volts respectively. Using Equation (3) and a 'K" value of 0.23, the heat generated at this operating condition is 92 watts per stack or 184 watts total. The heat must be transported away from the piezo stack actuators to prevent overheating. A cooling system is necessary to facilitate the desired high power actuation.

9.7 COOLING SYSTEM DESIGN AND PERFORMANCE

Piezo electric actuators are excellent precision motion devices for small displacement actuation. They are used in high precision measuring instruments such as Atomic Force Microscopes and interferometers. The piezo ceramic material is stiff (~400n/µm) for high system natural frequencies and exhibit no stick slip effects during actuation. Due an actuation range from nanometers to tens of micrometers effective micro-positioning can be accomplished with piezoelectric devices. However piezoelectric actuators have hysteretic behavior that occurs in the form of position errors as a function of control voltage and heat generation. Position errors due to hysteresis are often compensated by feedback control systems and heat generation is negligible for low frequency/low voltage operating conditions. High frequency/high voltage applications such as the UltraMill HS require a cooling system to keep the piezo actuator temperature within the working range. Piezo stack operating temperature limits vary based on construction and piezoelectric material. The UMHS Kinetic Ceramics piezo actuators can withstand operating temperatures up to 150ºC beyond which the bonding epoxy begins to breakdown. At 250ºC the piezoelectric ceramic begins to permanently de-pole.

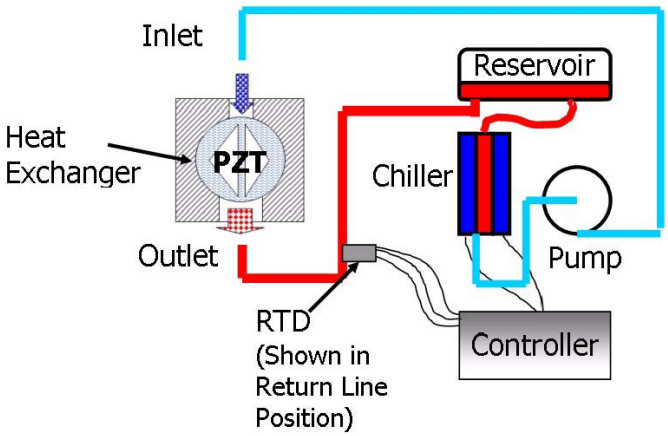

Figure 6. Cooling System Components

The UltraMill High Speed has an integrated active cooling system to regulate piezo actuator temperature during operation. Figure 6 is a diagram of the important components of the cooling system. The cooling system consists of a process fluid chiller, pump, supply and return lines, and heat exchanger. The process fluid is pumped through the heat exchanger, gaining heat from the piezo stacks and returned to the chiller unit to have this heat removed from the fluid. The chiller used in this system is a thermoelectric unit by Solid State Cooling. This 400 watt capacity chiller includes a 1 lpm diaphragm pump and PID controller that is capable of regulating outlet process fluid temperature to 0.2˚C. A submerged inline RTD in the return line is used for feed back control. The advantage of this unit is its solid state cooling element that does not require any

refrigerant or compressor. The heat exchanger removes heat from the piezo stacks into the process fluid.

Two different approaches were tested, an enclosed coil heat exchanger specified by the original design and an open flow heat exchanger devised for increased cooling capacity. The enclosed coil design pumps a process fluid such as water or an ethylene glycol mixture through a coil located in the housing with the stack actuators. The housing is filled with an intermediate dielectric fluid which acts as a thermally conductive medium between the process fluid and the stack actuator surfaces. The closed coil design relies on free convection and conduction through the dielectric fluid to transfer heat. The open flow design uses a specialized dielectric cooling fluid, Fluorinert 3283, as the process fluid and the stack actuator surfaces are subject to forced convection heat transfer. Process fluid is pumped through the piezo stack housing directly contacting the heated piezo stack surfaces.

The original closed coil heat exchanger was an ineffective method of controlling the piezo actuator temperature. The enclosed coil design has an inherently low heat transfer rate. This is because free convection is the mode for heat transport from the piezo stack actuator surface to the copper cooling coil. Low conductivity coupled with high specific heat and high viscosity cause this dielectric fluid to be unsuitable in this application. Most dielectric fluids have low heat transfer characteristics, particularly in free convection. The closed coil cooling system required a 42 ˚C temperature difference to remove 10 watts of heat from the piezo stacks. This requires low process fluid temperatures to maintain adequate piezo stack actuator temperatures. Low process fluid temperatures are undesirable because the temperature gradients produced in the UltraMill structure result in process fluid temperatures that caused condensation on fluid lines and the steel surfaces of the UltraMill. And the inefficiencies associated with maintaining process fluid temperatures below ambient conditions. These issues resulted in the redesign of the heat exchange to an open flow system.

The open flow design proved to be much more effective removing heat from the piezo stack actuators and maintaining a safe operating temperature. The analysis of the open flow design is reported below.

9.7.1 OPEN FLOW DESIGN

Description

The open flow heat exchanger design uses forced convection over the heated elements to transfer heat. Process fluid is pumped through the piezo stack housing directly contacting the heated piezo stack surfaces. The inlet flow rate through a 1/4” tube is throttled to keep the cavity full

while being emptied by gravity through the larger 3/8" outlet tube leading to the reservoir. This scheme keeps the interior of the stack housing at atmospheric pressure, reduces leaks and prevents preload reduction by fluid pressure. A miniature surface mount RTD is used to monitor stack temperatures.

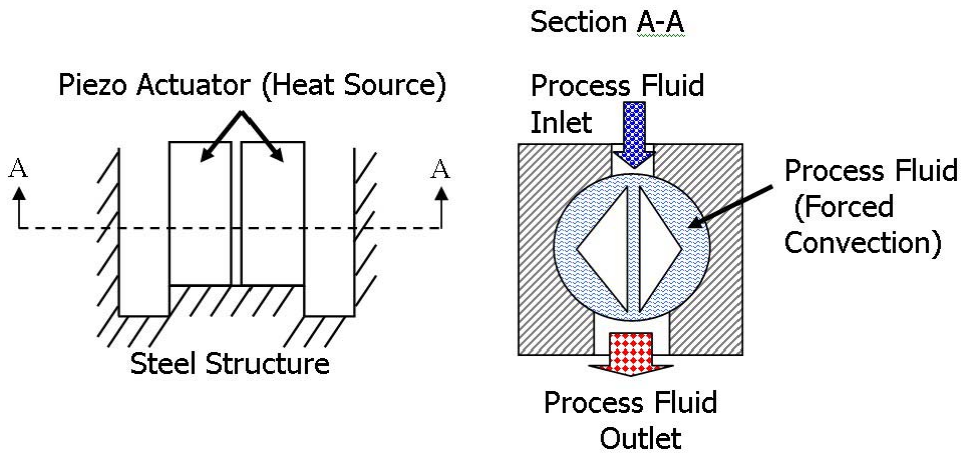

Figure 7. Open Flow Heat Exchanger Design

Process Fluids

The open flow design puts more stringent demands on the process fluid. The fluid must be dielectric, non corrosive, compatible with the piezo stack materials and chiller wetted surfaces. This fluid must also have good heat transfer properties. The cooling system uses a perfluorinated fluid by 3M called Fluorinert 3283. This is a low viscosity, high density dielectric fluid with properties that are ideal for forced convection applications. Fluorinert has a low conduction coefficient, k = 0.066, which is detrimental towards heat transfer. However Flourinert also has a low kinematic viscosity promoting turbulent convection conditions. The fluid is also non-toxic and inert towards most materials that are not fluorinated. Unfortunately, it is expensive at 366$ per gallon. This cost is off set by the low volume of the cooling system, under 500ml, and low rate of make up fluid required.

Control System

The UltraMill HS cooling system employs a closed loop controller on the chiller unit to maintain a safe operating temperature. The controller varies the process fluid inlet temperature based on a reading from a RTD located in the return line back to the chiller. This setup automatically increases or decreases cooling levels for varying heat loads.

Temperature Measurement Process fluid and piezo stack actuator temperatures are both monitored by 3-wire RTD Platinum element sensors with the European curve of $\alpha = 0.385$. The process fluid RTD is placed in direct contact with the process fluid either before returning to the fluid reservoir or immediately exiting the cold plate. It is sheathed in a stainless steel housing that fits into a standard push style fitting. The RTD that is monitoring stack temperatures is a miniature element imbedded in a thin polymide film. This film is fixed to the surface of one of the stack actuators. Using the same type of transducer allows flexibility in the position of the feedback sensor. The inlet and outlet fluid temperatures are measured using a j-type iron constantan thermocouples. The thermocouples are bonded into plastic push in fittings with the tip of the thermocouple wire exposed to the fluid flow.

Strategy for control The ideal operating condition for the UltraMill would be to have all components at ambient temperature. This results in a thermally stable setup with no transient temperature changes effecting position of the diamond tool. However due to heat loads and stack actuator cooling requirements this ideal condition cannot be achieved. The ideal condition motivates the decision to use the cooler maintain the process fluid at ambient temperature or in this case 20˚C. The chiller controller feedback transducer can be placed in several locations to monitor the process fluid temperature. Moving the location of the feedback transducer changes the nature of the cooling system. Placed in the supply process fluid flow the cooling system will maintain the set point regardless of the heat load placed on the system. This scheme is the simplest. The chiller does not control the temperature of the system. A constant outlet fluid temperature uses the return fluid temperature as the control feedback. Using the return fluid temperature as the set point allows the chiller to respond to varying load conditions and transient temperature changes. However the lag time in the system requires careful PID tuning of the controller.

Results Using the constant outlet temperature control scheme, the outlet fluid temperature was maintained at 20˚C. The UltraMill was then operated at various driving conditions to observer the effectiveness of this control scheme. Figure 8 shows the temperatures of various system components with a 20.7 watt load. The chiller set point temperature is 20˚C. The stack actuators are switch on at time zero. The cooler, which has been regulating the process fluid temperature while the stack actuators were off, responds by reducing the inlet temperature until the return temperature is 20˚C. This process takes approximately 6 minutes. Figure 8 shows the open flow cooling system can maintain a satisfactory stack actuator surface temperature under these conditions.

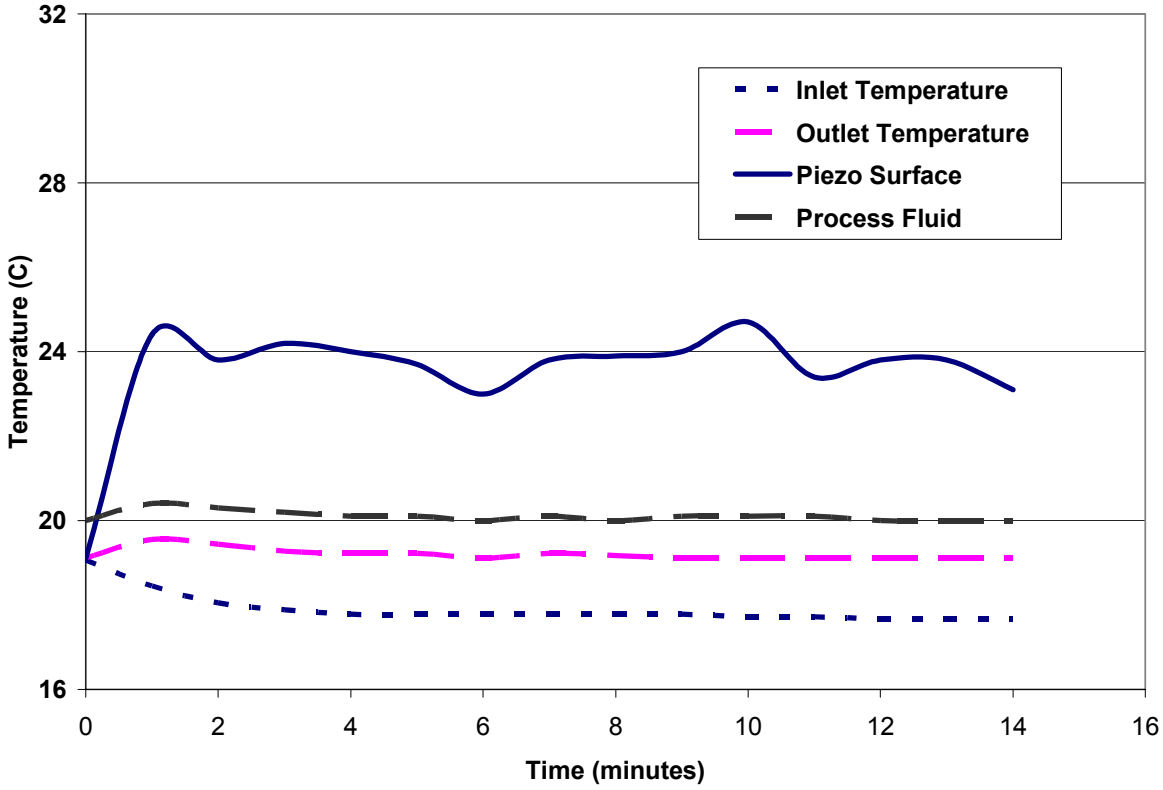

Figure 8. Component Temperatures vs Time with Heat Load of 20.7 watts

Experiments

Several experiments were conducted to analyze the effectiveness of the open flow design. The first test produces the internal stack temperatures during operation. Internal stack temperatures are an important consideration because temperature measurement only occurs on the surface of the piezo stack actuator. During operation internal temperature will most certainly be higher and thus must be accounted for with some estimation. The second experiment measures equilibrium stack temperatures under various active loads. This test defines a range of heat loads and thus operating conditions that the cooling system can handle. A third test shows the system response to a given heat load and the behavior of the system over long periods of time. This experiment will reveal temperature stability and time to component equilibrium.

Internal Piezo Stack Actuator Temperature

The internal piezo stack temperature test was conducted by running the UltraMill at an equilibrium condition then shutting down the amplifiers and cooling system simultaneously. The

subsequent temperature rise of the piezo surface is measured and recorded to a PC. A plot of this data is shown in Figure 9 below. In this experiment the cooling system process fluid was maintained at 6 ˚C and the piezo stack actuators were driven at 1000 Hz, 600 volts peak to peak. The UltraMill was allowed to equilibrate with the cooling system running, this occurs between 1 and 110 seconds in the Figure 9 below. After 115 seconds both the amplifiers and the cooling system are shut down. The subsequent rise in the piezo surface temperature is an indication of the temperatures within the piezo stacks during operation.

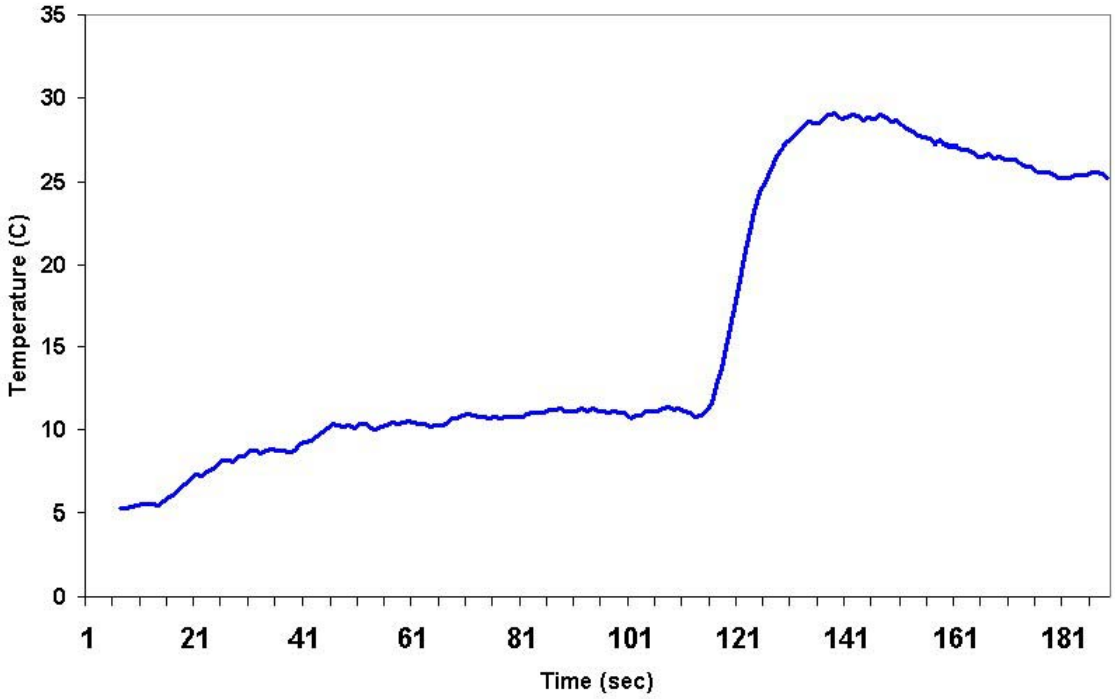

Figure 9. Piezo Surface Temperature

For this experiment the difference in internal piezo stack temperature and surface temperature is on the order of 20 ºC.

Piezo Stack Surface Temperature

Finite Element Analysis Piezo stack surface temperature is important for monitoring the piezo stack actuators for safe operation. The surface mounted RTD measures surface temperatures in an open flow condition. Ansys software was used to simulate surface temperatures of the piezo stack during operation. A 20 node brick element was selected for meshing and a heat generation was assumed for the entire piezo stack volume. Figure 10 is a diagram of the boundary conditions using for the FEA simulation.

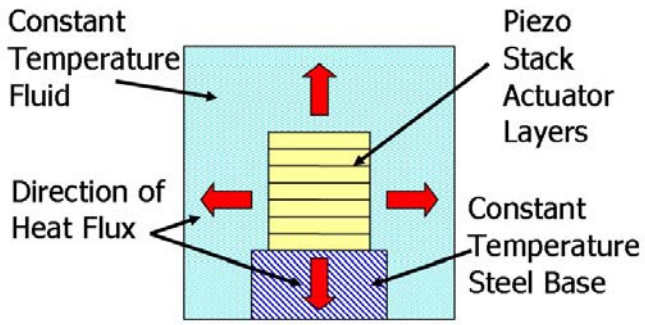

Figure 10. Diagram of FEA Model

The film coefficient was calculated using standard plane wall heat transfer equations. Thermal properties of the dielectric fluid, estimated fluid velocities and bulk temperatures were used to calculate the transport properties. Convection mode was predicted to be turbulent. The steel base was considered a thermal reservoir and the bottom piezo stack actuator surface is held at 20˚C. A 25 watt heat generation, equivalent to 4Khz, 440 volts was applied during the simulation. Table 1 lists the values used for the boundary conditions and heat generation.

Table 1. Boundry Condition Values for FEA Simulation

Convection Coefficient to Cooling Fluid	500	**W/m^2-K**
Constant Surface Temperature	20	**Celsius**
Piezo Heat Generation	25	**W**

shows the temperature contours on the surface of the piezo stack actuator for the 25 watt heat load. The maximum surface temperature for this simulation is 36.8 º C which falls with in the measured surface temperatures shown in Figure 12.

Experimental Analysis The surface temperature variation with heat load experiment was conducted by applying several different heat loads and recording the equilibrium temperature of the piezo stack actuator surface. Shown in Figure 12 the surface temperature verses heat load curve increasing linearly with increasing loading. The predicted operating limit with the open flow cooling system is 3600 Hz and 800 volt peak to peak, a heat load of 115 watts. The drive voltage corresponds to a tool path ellipse of 60 μm by 12.5 μm.

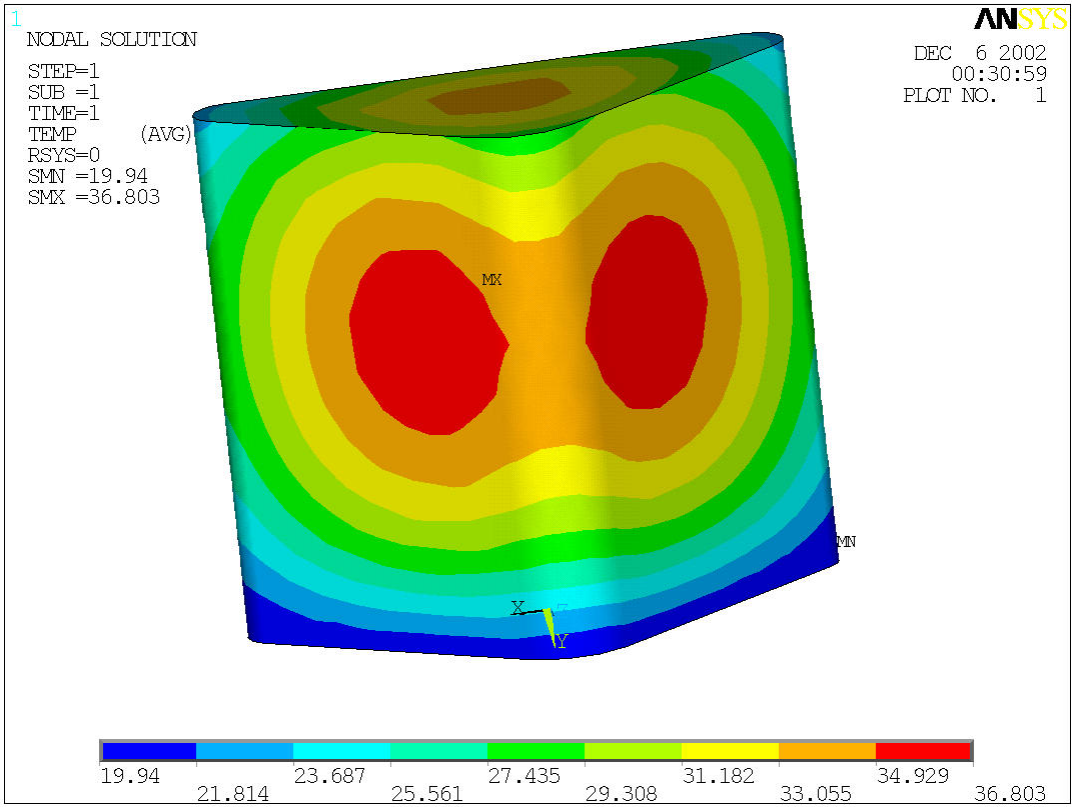

Figure 11. FEA Thermal Model of Piezo Stack Actuator (25 Watt)

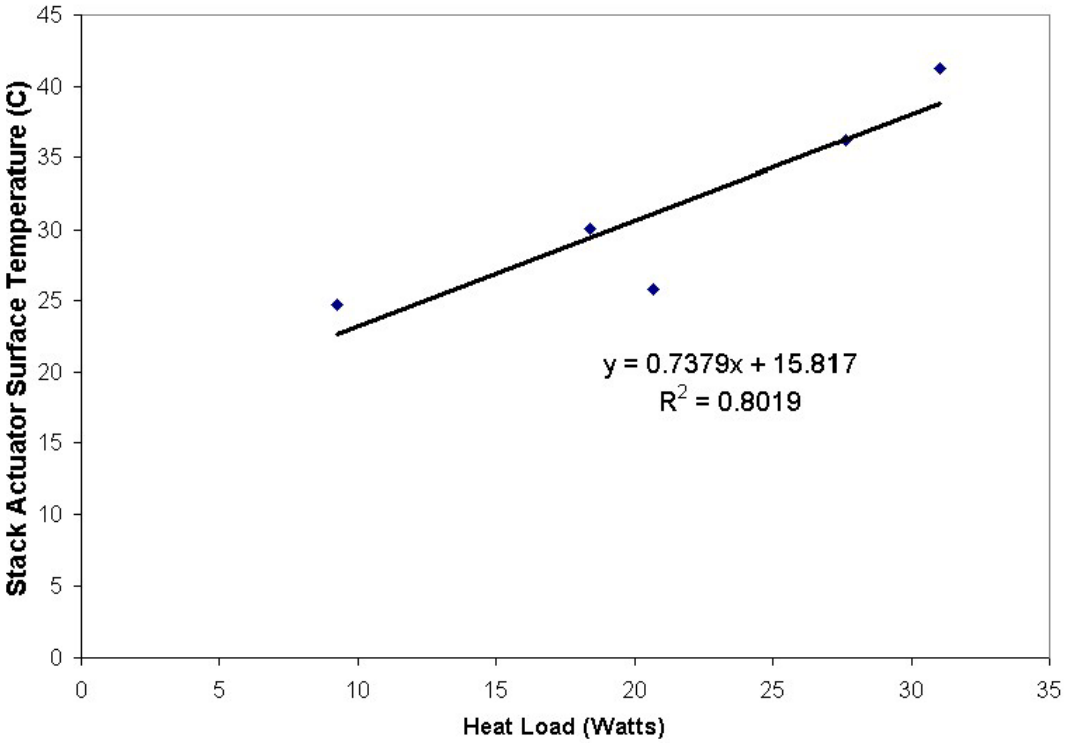

Figure 12. Stack Actuator Surface Temperature vs Heat Load

9.7.2 SYSTEM TEMPERATURE STABILITY

The third experiment tested temperature stability over long periods of time. This is an important factor for precision fabrication. Temperature changes in machine parts cause dimensional variations which result in form errors. Testing the stability of the cooling system required operating the UltraMill HS for an extended period and measuring the component temperatures. The cooler was turned on and run under an ambient load condition until an equilibrium condition occurred, approximately 10 minutes, then the piezo actuators were turned on and a new loading condition was introduced to the system. Figure 13 shows the cooling system component temperatures for two different conditions and the long term stability of the UltraMill piezo stack temperature. After 20 minutes of operation equilibrium was reached and the piezo surface temperature stabilized at 32ºC. After which the temperature variation of the piezo surface was +/- .15 ºC over 23 minutes.

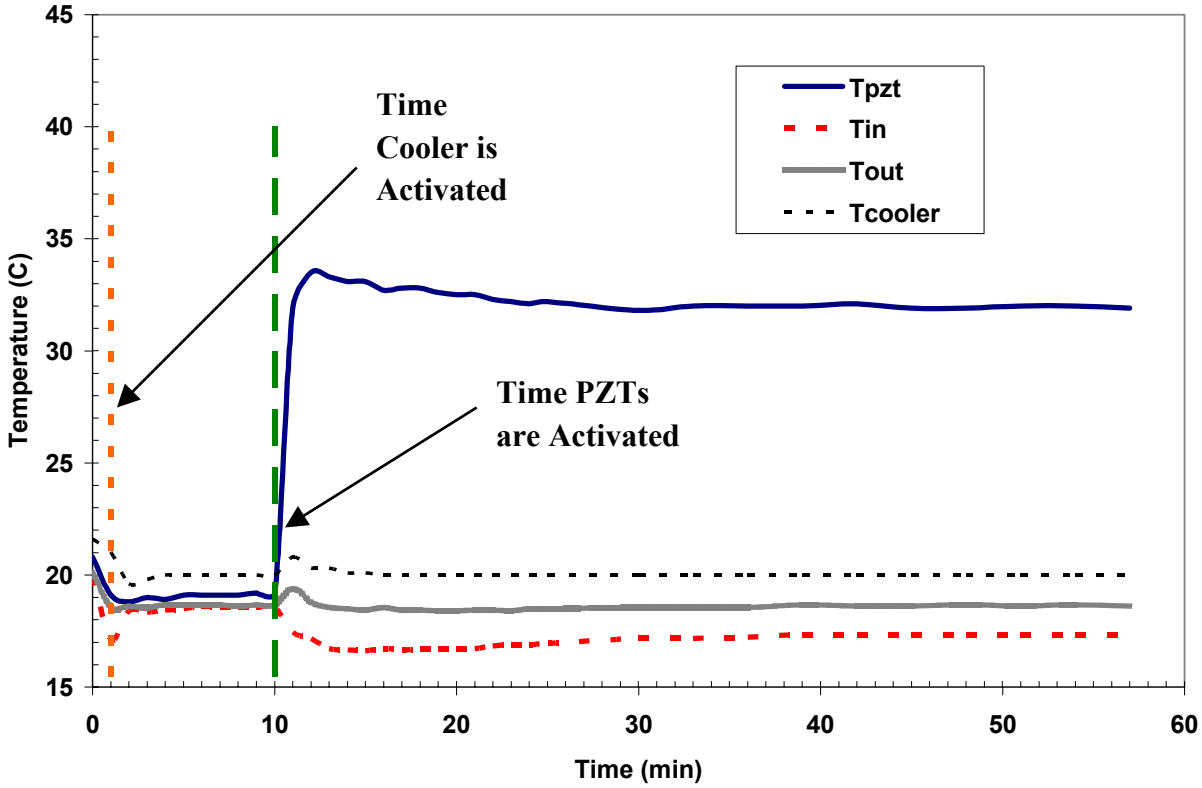

Figure 13. Long Term Temperature Stability and Equilibration

9.7.3 DISCUSSION

The forced convection cooling approach resulted in higher heat transfer rates with lower temperature gradients between the fluid and stack surface. This system required a 12˚C

temperature difference between the stack surface and the process fluid to remove 18 watts of heat. The enclosed coil cooling system was unable to maintain a safe piezo stack actuator temperature with an equivalent heat load. Higher heat transfer rates could be achieved by increasing fluid velocity, mixing and flow rate through the stack housing chamber. These properties are limited by pump design, desired pressure and imparted vibration to the system. These issues resulted in the redesign of the heat exchange to an open flow system.

9.8 TOOL MOTION

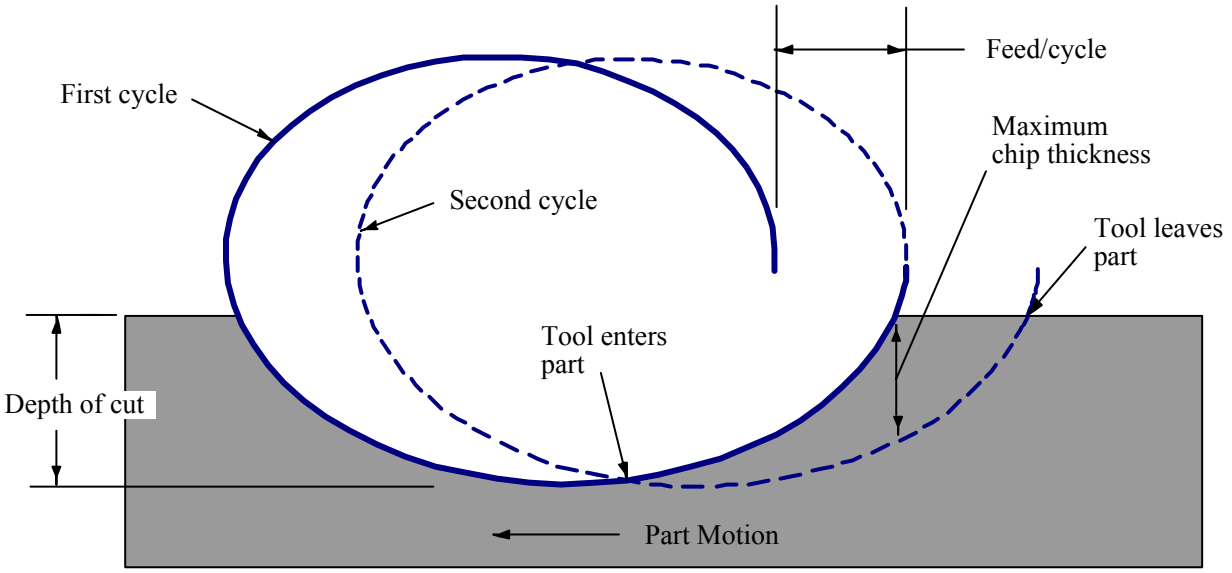

Figure 14. Tool Path

The desired tool motion for the UltraMill is generated using two piezo actuators extending out of phase with respect to the other and a kinematic tool holder attached to the end of the stacks with small pivot points. The tool holder simultaneously pivots and translates generating the tool path. The goal of this design is to operate the system below its first natural frequency so that the tool path can be manipulated in a controllable manner to study the details of the machining process. For elliptical cutting, the motion of the end of the tool is a combination of the elliptical motion from the actuator and the linear motion from the workpiece. Figure 14 shows the motion of the tool (exaggerated in the vertical direction for clarity) and defines the important parameters. Only two cycles of the tool are shown and second revolution (dotted line) which is the steady-state motion that removes material from the workpiece.

9.9 CHIP FORMATION

Figure 14 also shows the chip geometry at the center of the cut as the tool moves through its elliptical path. The thickness of the chip is reduced as the tool frequency is increased or the part speed or depth of cut are reduced. SEM micrographs of non-overlapping groove cutting experiments in aluminum illustrate that chip geometry is directly related to cutting conditions. If the depth of cut is smaller than the minor axis of the tool motion, the chips are discontinuous (Figure 15), and if larger they are connected at the center (Figure 16). The discontinuous chips have a thickness related to the feed/cycle and are as wide as the cut. The continuous chips are longer because of the increased depth of cut but are discontinuous at each edge where the round nose tool leaves the flat workpiece. Notice that the chips appear transparent in the 1000x image of Figure 16, indicating a thickness less than 10 μm.

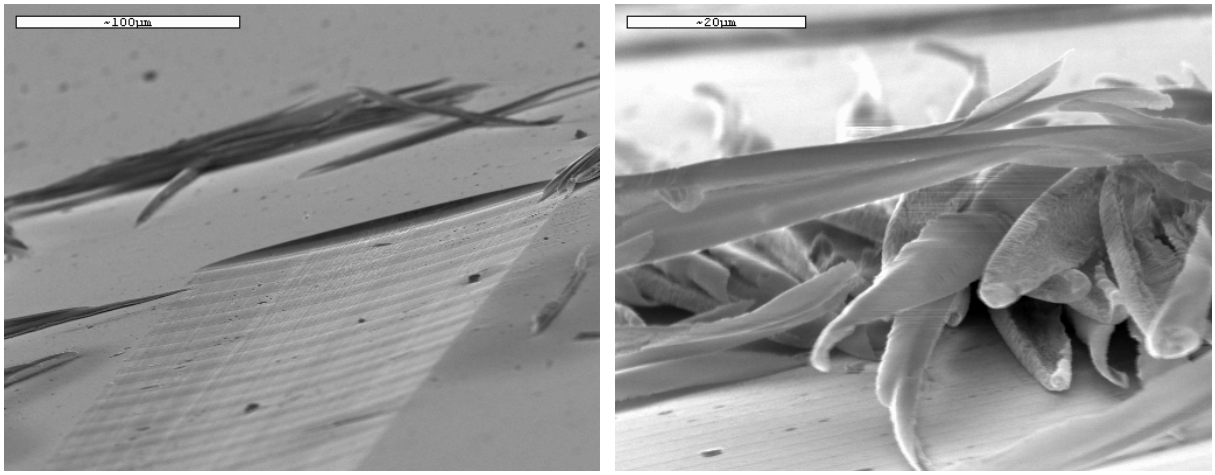

450x 1800x

Figure 15. SEM micrographs of discontinuous chip where depth of cut is 32% of the minor axis (depth = 1.4 μm and upfeed/cycle = 3.3, minor axis of elliptical motion =4.3 μm)

Continuous VAM chips have a feathered look. Each "feather" is the front of an individual chip generated by one cycle of the UltraMill. These chips are attached in the center to a continuous section of the due to their increased thickness resulting in the chip shown in Figure 16. The edge of the continuous chip consists of many relieved single chip cycle edges. The edge of each "feather" is relieved at the cut edges because the depth of cut and chip thickness is reduced enough to create a discontinuous feature.

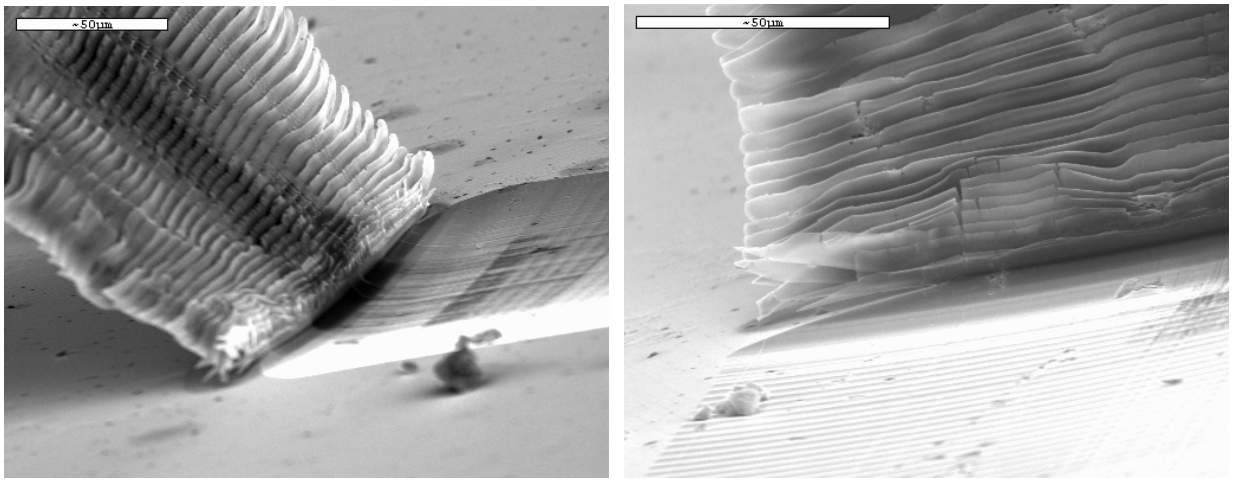

600x 1000x

Figure 16. SEM micrographs of continuous chip where the depth of cut is twice the minor axis (depth of cut = 8.9 μm and upfeed/cycle = 6.7 μm, minor axis of elliptical motion =4.3 μm)

Discontinuous VAM chips are more difficult to examine. Chip width corresponds to cut width and chip depth is dependent on the upfeed per cycle. The chips shown in Figure 15 were generated cutting a 166 μm width groove with an upfeed of 1.66 μm per cycle. Individual chip geometry has been limited to qualitative observations due to measurement logistics. The chips shown in Figure 15 are thin at the front and larger in the rear. This characteristic follows the expected discontinuous chip geometry resulting from the elliptical tool path.

9.10 TOOL FORCES

To measure the forces, a specimen was attached to a three-axis load cell mounted on the diamond turning machine. The oscillating tool was fed across the surface at a constant speed and depth of cut. The measured forces were acquired using a high-speed data acquisition system.

The measured forces in the cutting and thrust directions as a function time are shown in Figure 17. The measurements are shown as a series of points connected by a line and the predicted forces are the solid and dotted lines. The workpiece was 6061 aluminum, the vibration frequency 1000 Hz, the depth of cut 8.9 μm and the upfeed/cycle 6.6 μm. Based on the geometry shown in Figure 14, the maximum chip thickness for this condition is 7.7 μm. For these cutting conditions, the maximum force in Figure 17 is about 1 N and the tool is in contact for 0.3 ms out of a cycle time of 1 ms (at 1000 Hz operation) or a duty cycle of 30%. The thrust force was predicted to be negative once the velocity of the tool exceeded the chip velocity. This phenomenon can be seen towards the end of the cutting cycle in Figure 17. The cutting

simulation program assumes chip velocities based on a 45º shear angle for the material. The predicted values were in agreement within 0.1 N of the magnitude of the measurements. However, secondary vibrations due to the load cell dynamics are apparent, especially in the thrust direction with a 12 kHz frequency (the natural frequency of the load cell with specimen).

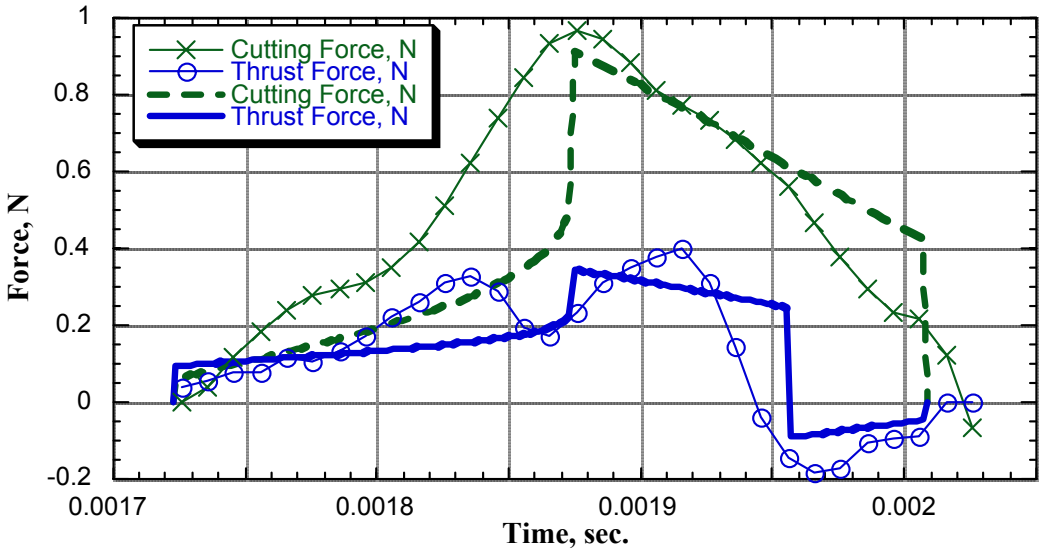

Figure 17. Theoretical and measured cutting and thrust forces during tool contact (material = 6061-T6 aluminum under same conditions as Figure 5)

9.11 SURFACE FINISH

9.11.1 THEORETICAL SURFACE FEATURE GENERATION

The idealized surface along the bottom of a single groove created by any given UltraMill tool path is determined by the features generated in the upfeed direction. The curvature and height of the features generated in the surface along the feed direction is related to the indexed section of the tool path and tool path aspect ratio. The tool path aspect ratio is defined as the ratio of the major axis and the minor axis lengths. The curvature of the groove perpendicular the feed axis is determined by the radius of the tool. However the width of the groove is dependent on depth of cut, both nominal and cyclic depth due to the oscillating tool path. Depth of cut does not effect the idealized surface unless it is smaller then the calculated Peak to Valley surface using Equation (4) shown below.

$$PV = \frac{f_{index}^{\ 2}}{8 \cdot R} \qquad (4)$$

Where R is the radius of curvature of the bottom of the tool path and f_{index} is the feed per tool cycle. Figure 18 illustrates the terms for Equation (4).

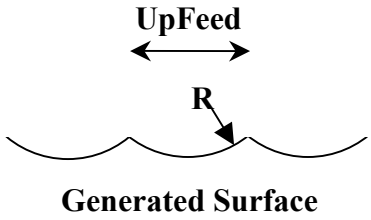

Figure 18. Surface Feature Definitions

The elliptical tool path of the UltraMill has two dominate radii of curvature. The major radius is defined by the minor and major axis as shown in Equation (5).

$$R_{major} = \frac{a^2}{b} \tag{5}$$

Where *a* and *b* are half the length of the major and minor axis respectively. From Equation (5) and the definition of tool path aspect ratio it is clear that the higher the tool path aspect ratio the large the radius of curvature and thus the lower the theoretical surface finish.

Predicting the theoretical surface finish of an area generated by the UltraMill is considerably more complicated due to phase and velocity effects inherent when combining a single frequency machining operation with a turning operation. The surface speeds of a constant rotating part vary with radius. As the tool travels toward the center of the workpiece, the surface velocity decreases. Upfeed per cycle also decreases as it is directly dependent on surface velocity. As shown in Equation (1), a decrease in f_{index}, or upfeed will cause the theoretical surface finish to decrease with the square of the feed per cycle. This effect is coupled with another effect know as phasing. Phasing is the relative position of two identical features that are side by side. In the case of the UltraMill each adjacent cusp can be 0-180º out of phase. And depending on the phase value the resultant area generated by the UltraMill will vary significantly. Surfaces generated by the UltraMill can have large differences in PV roughness due to phasing between adjacent cuts. However, phase effects are diminished as the cross feed per cycle becomes the dominating surface feature generator. In order to analyze the performance of the UltraMill the theoretical surface roughness for EVAM turned parts must be determined.

This problem is similar to the surface finish generation by precision grinding and has been studied at the PEC by Gene Storz [1]. Through his research Storz has devised a series of curves which characterize the surface roughness reduction for many different cutting conditions. Using the Storz's Curves the theoretical surface roughness of EVAM generated parts can be

approximated. The EVAM parts are descritized into smaller constant cutting conditions sections and a Storz's Curve analysis is done. The Storz Curves RMS values are calculated for a range of upfeeds per cycle and plotted against the measured values.

9.11.2 SURFACE FINISH EXPERIMENTS IN ACRYLIC

Before machining experiments were conducted on metals or ceramics surface cutting tests with acrylic were conducted. Acrylic was selected as the test material due to its high machinability and extremely low hardness which would preserve the edge of the diamond tool. Earlier research at the PEC has shown that for standard single point diamond turning the best RMS surface generated on acrylic using the ASG25000 DTM was 5 nm. This is due to an asynchronous spindle motion of 25 nm peak to peak. This value is within the manufacture's tolerance for this particular air bearing spindle.

The UltraMill experiments were conducted on one inch diameter test acrylic flats faced to 5 nm RMS finish. These turned blanks were vacuum mounted to the DTM spindle and faced by the EVAM process. Several experiments were conducted to determine the capabilities of the UltraMill HS. Initial cutting tests were performed at a spindle speed of 20 RPM and oscillation frequencies of 0 KHz, 1 KHz and 2 KHz. The samples were then cleaned and examined with the white light interferometer. Surface roughness was measured using a magnification of 50x and 0.5 zoom factor which produces a measurement area of 287 μm by 215 μm. The sample is then indexed along a line extending from the center of the part and a new measurement is taken. The surface finish measurements are shown in the Figure 19 below as a function of up feed per cycle and compared with the theoretical Storz EVAM roughness.

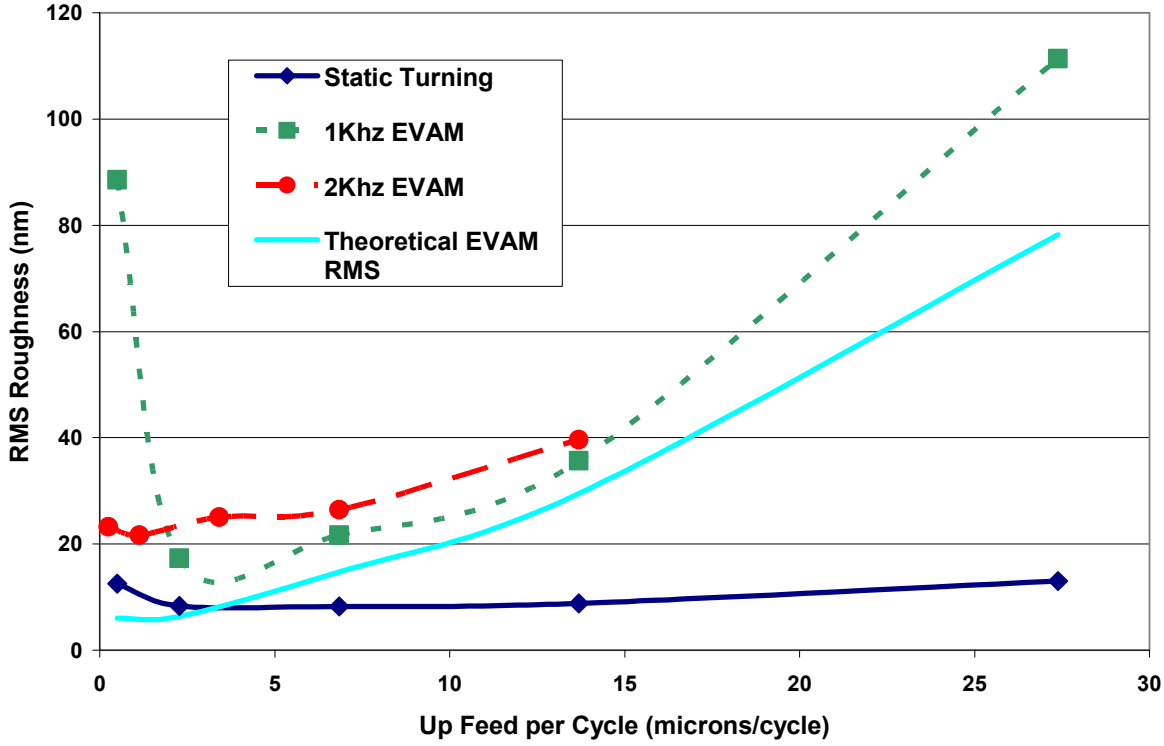

Figure 19. RMS Roughness Vs Upfeed/Cycle (21.6 RPM Spindle Speed and 0.25 mm/min cross feed)

Standard single point diamond turning generates a uniform surface finish from center to outside edge. The uniformity is caused by the constant cross feed per rev which, in conjunction with the radius of the tool, generates the surface features on the workpiece. The static turned flat, shown in Figure 19, has an essentially constant RMS roughness regardless of surface speed or radius. For these cutting conditions the theoretical RMS roughness is 6 nm. However, EVAM machined parts increase in roughness with increasing radius from the center of rotation. This behavior is due to the feed per cycle increasing as the surface speed becomes greater with increasing radius. Compared to the predicted Storz curve RMS roughness the EVAM roughness follows a similar characteristic curve. However the magnitudes of the EVAM curves are higher then predicted and the 1 KHz part suffers from center defects. A closer look at the surface reveals more about the nature of the EVAM generated surface.

The EVAM machined surface is comprised of cusps generated by the EVAM tool path. These cusps were measured at several radii and compared with theoretical values in Table 2 below. Measured and theoretical feature height and spatial frequency are listed. The theoretical spatial

frequency was determined by calculating the surface speed at a given radius and cusp height was found using the calculated surface speed and Equation (4).

Table 2. Theoretical and Measured EVAM Cusp Amplitude and Frequency

Radial Postion	Feed/Cycle (Theoretical)	Feed/Cycle (Measured)	Feature Height (Measured)	Feature Height (Theoretical)
mm	µm	µm	nm	nm
1	2.093	3.6	6	5.478
1.5	3.140	3.6	11	12.325
2.2	4.605	4.8	26	26.511
2.8	5.861	7.2	45	42.944
3	6.280	8	63	49.298
3.5	7.327	9	52	67.100
6	12.560	15.7	222	197.192

This data serves for an approximate comparison due to the uncertainty in the radius measurement, exact spindle speed, and the resolution of the interferometers CCD array which limits spatial positioning to 0.5 µm.

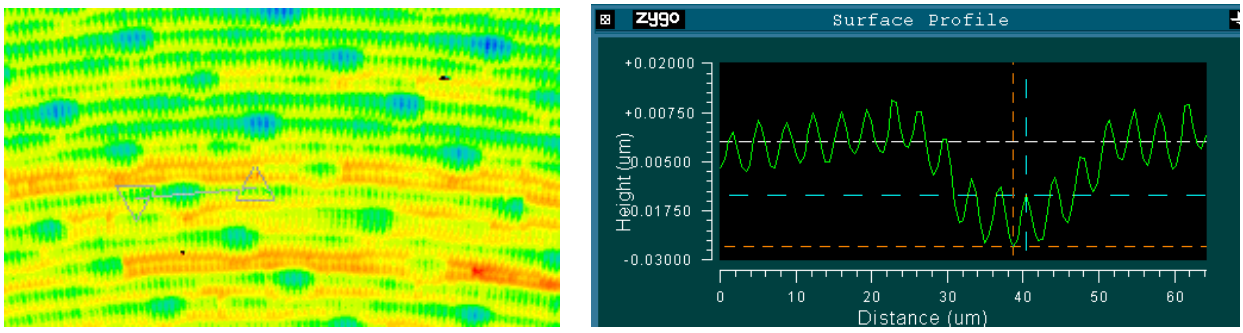

(a) EVAM Surface Image **(b)** Surface Profile of EVAM

Figure 20. Interferometer Screen Capture

The EVAM surface consists of other surface features which may explain why the resultant surface roughness greater then expected. Larger (up to 70 nm deep) indentations occur repeatedly along the circumferential tool path. Viewed with the white light interferometer, in Figure 20 (a), the surface is comprised of uniform EVAM cusps and the larger asynchronous features. A profile scan of these features with the EVAM tool cusps reveals the effect of the large

feature vibration on RMS surface roughness. A possible source of this vibration was theorized to be the asynchronous spindle vibration of 25 nm. The slow spindle speed (20 RPM) would make any such vibration more apparent and it was thought that increasing the spindle speed would increase the averaging effects and reduce the RMS surface finish. The next experiment examines this possibility by conducting several cutting trials at varying spindle speeds while the UltraMill frequency was held at 2 kHz. Experiments were conducted at 20, 40, and 100 rpm. The measurement area was reduced to 143 µm by 107 µm and the sample was indexed 140 µm for each data point leaving 40 µm between each measurement field up to 3 mm in part radius. Then the sample was indexed 500 µm for each measurement up to 5mm in part radius beyond which the sample was indexed 1 mm. This approach leads to a good resolution of surface roughness of the part. Figure 21 shows the surface roughness curves of the three trials.

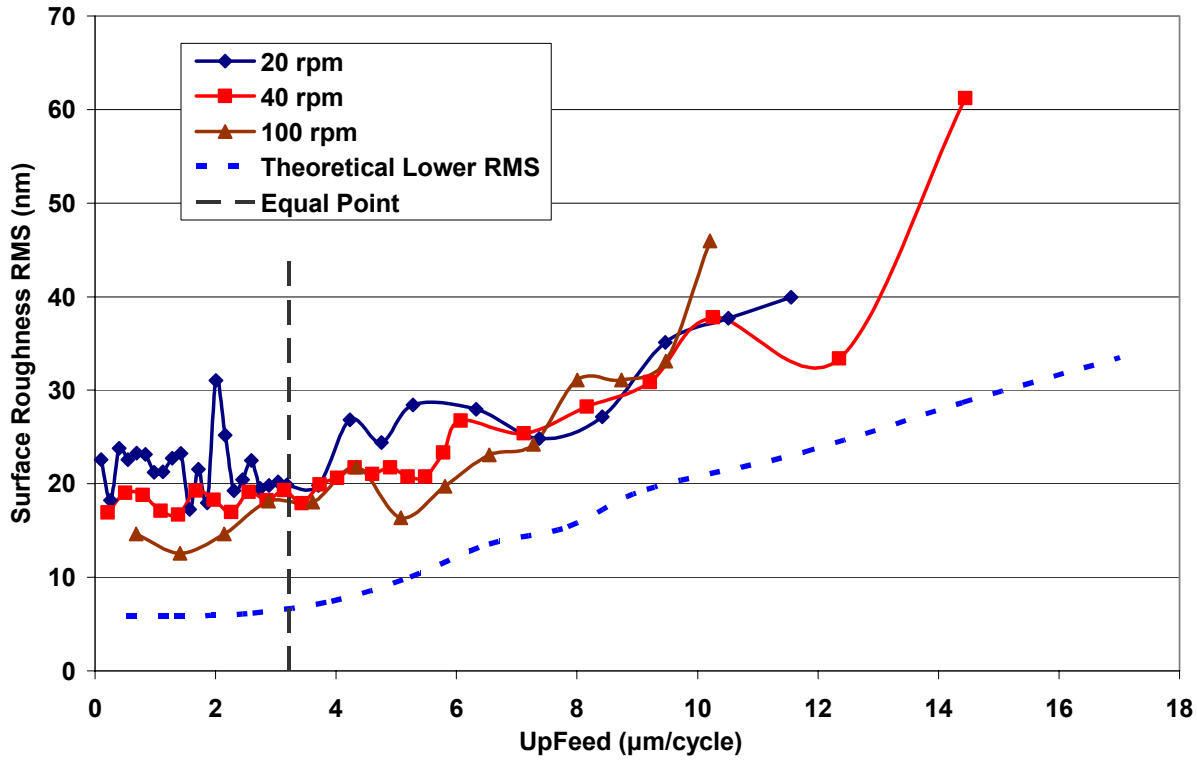

Figure 21. RMS Roughness Vs Upfeed/Cycle (2 kHz EVAM Frequency and 0.25 mm/min cross feed)

For up feeds less then 8 µm per cycle the tests show a slightly reduced RMS roughness when increasing spindle speed. The spindle speed effect reduces RMS roughness by as much as 10 nm at certain locations but is limited by the operating frequency of the UltraMill. Possible reductions gained by higher spindle speeds will be penalized with less measurable area on the part due to increased surface speeds. Compared to the theoretical roughness the measured samples are

rougher due to the asynchronous features on the surface. These features limit the best possible surface roughness to 16 nm RMS. The equal point, shown on Figure 21, is the magnitude of up feed that results in a theoretical surface finish that is identical in the radial and circumferential direction. Under these conditions the features generated by the UltraMill are equal to the roughness generated by the cross-feed. Once this condition occurs the surface roughness will not be reduced by reduction in upfeed per cycle. This behavior can be seen in Figure 21 and Figure 22 as a relatively constant roughness beyond the equal point.

The third set of experiments was conducted with 100 RPM spindle speed and a wider band of actuation frequencies,1-4 KHz to observe if the operating frequency had an effect on surface finish. The samples were all measured with a 10x magnification factor and a 2x zoom which creates a measurement field of 352 µm by 264 µm. The results of the four experiments are shown in Figure 22.

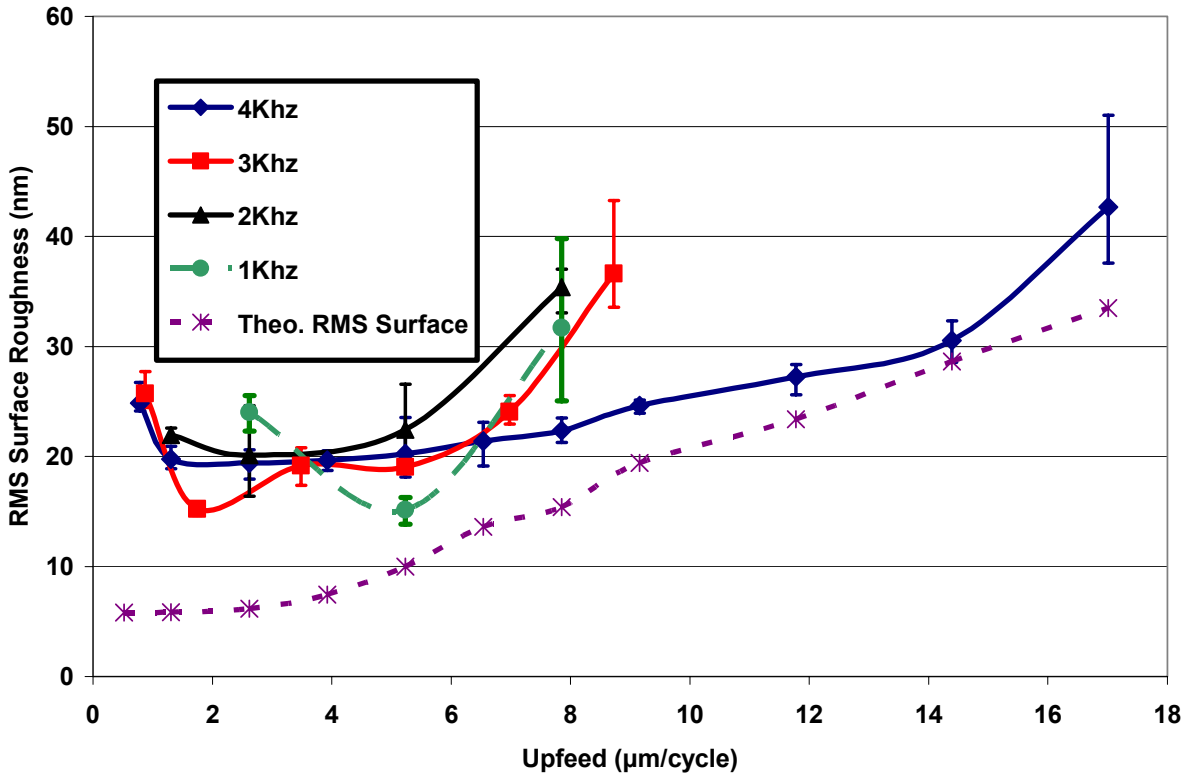

Figure 22. Surface Roughness as a Function of Upfeed per Cycle (100 rpm Spindle Speed and 1.25 mm/min Cross Feed)

The surface finish for the 1 KHz and 2 KHz improved slightly compared to the 20 rpm samples. However, the lower limit of surface roughness seems to be reached at approximately at 20 nm RMS with the best data no lower then 14 nm RMS. A view the surface revealed large,

asynchronous features occurring at 55-60 Hz, similar to the features found in the 20 rpm experiments. After this series of experiments it was clear that surface features generated by some lower frequency occurrence was dominating the surface roughness. If this source of vibration could be determined and eliminated if possible, a much better surface finish could be generated.

9.12 SOURCES OF ASYNCHRONOUS VIBRATION

To determine the cause of these large features the amplitude and frequency of the features were measured for all of the different frequencies and spindle speeds. This was done using the white light interferometer to measure the depth and distance between the features at several radii on each part. Each frequency value was obtained by averaging several frequency measurements on each part. Table 3 is a summary of the measurements for 100 RPM and 20 RPM and 1- 4 Khz UltraMill operating frequencies.

Table 3. Large Feature Frequency

	100 RPM	20 RPM
UM Freq	(Hz)	(Hz)
1 Khz	58.10	57.67
2 Khz	56.24	64.69
3 Khz	52.94	n/a
4 Khz	94.22	n/a
Average	65.38	61.18

The frequency of the large features did not vary greatly from part to part. This vibration seems to be constant regardless of spindle speed, UltraMill frequency and part radius. Due to the proximity of the 60 Hz features to the natural frequency of the z slide and the spindle, z slide excitation was considered a good possibility. Possible sources of excitation include cooler pump vibration and inertial forces from the moving parts of the UltraMill. Each of these possibilities was investigated and a discussion follows.

9.12.1 PUMP VIBRATION

The dielectric cooling fluid used to maintain the operating temperature of the piezo stack assemblies is cycled through the system with a 4 chamber diaphragm style pump that pulses 1600 times a minute or at a frequency of around 27 Hz. This value was verified in a separate test using an accelerometer attached to the outlet hose. The measured frequency of was 29 Hz. It is possible that this vibration is transferring to the surface by causing the slide to vibrate. To isolate the UltraMill and DTM from the mechanical vibrations of the chiller pump two methods were

implemented, the first was a funnel system that used gravity feed to disconnect the UltraMill from the pump on the inlet side of the UltraMill and the second isolation method was to install a section natural rubber hose in place of the hard plastic tubing between the flow valve and the inlet to the UltraMill and a section was installed from the exit of the UltraMill to the cooler return line. The flow valve and hard plastic line are mounted on a magnetic base located on a separate cabinet to further reduce vibrations. Slide vibration data was collected using the ASG positioning lasers. A hold program was implemented for four seconds while each condition was implemented and the laser positioning data was saved to a file. The data was analyzed for peak to peak vibration and standard deviation and plotted in Figure 23.

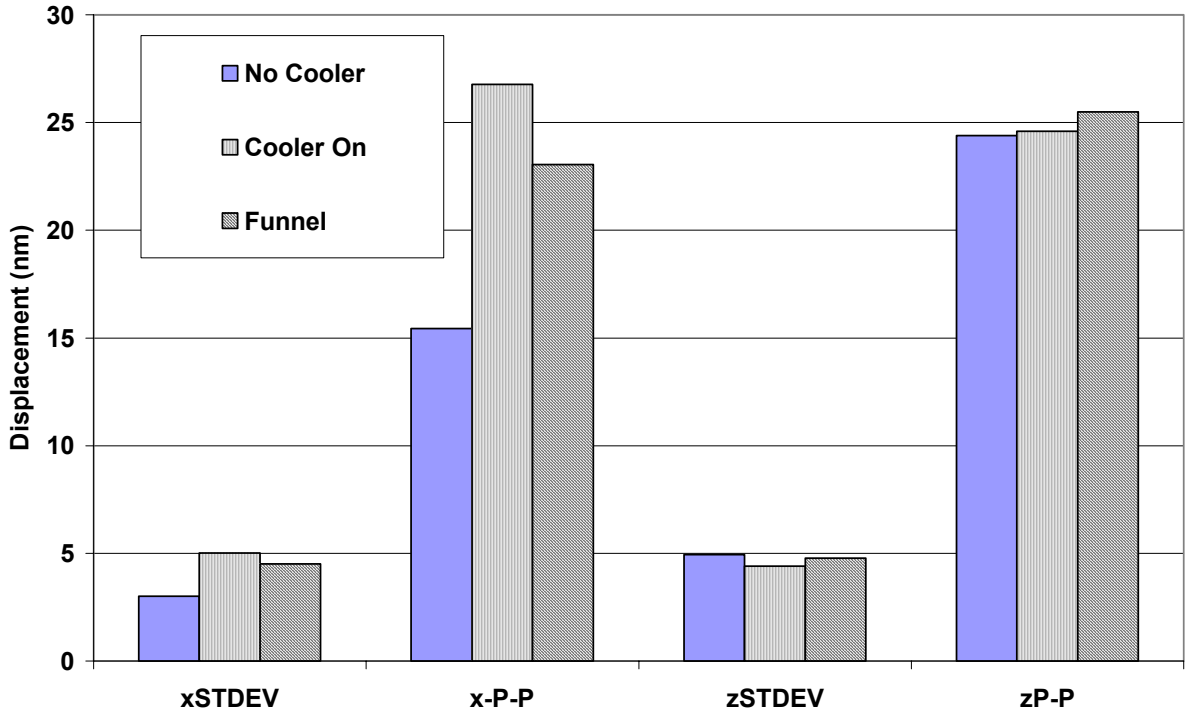

Figure 23. Peak to Peak and Standard Deviation of Slide Vibration

The positioning laser data showed increased vibration on the order of 2 nm standard deviation and 12 nm peak to peak on the x axis and no significant change in the z axis vibration when the cooler was activated. The funnel system reduced measured vibrations in the x axis but a slight increase in vibration was shown in the z axis.

9.12.2 ULTRAMILL INERTIAL FORCES

The UltraMill is bolted to the ASG 'x' carriage with the piezo stack actuators perpendicular to the direction of travel of the slide. During operation the UltraMill has a moving mass of 45.44 g most of which is from to the piezo stack actuators. The moving mass was calculated using the formula (6) below.

$$MovingMass = Mass_{KinematicHead} + 1/2 \cdot Mass_{PiezoActuators} \qquad (6)$$

At 4 Khz the maximum inertia forces are in excess of 175 N. This force is directly channeled to the 'x' slide of the DTM on which the UltraMill is connected. To study the inertial effects on the DTM slide vibration the two stacks were run 180º out of phase, theoretically canceling translational inertial forces. The laser positioning data was collected using three different conditions; a static hold position with UltraMill and cooler off, the cooler and piezo stacks at 1 Khz $400V_{P-P}$ 90º phase shift and 1 Khz $400V_{P-P}$ 180 deg phase shift. The standard deviation and peak to peak deviation was calculated for the x and z slide over 500 points or 0.27 seconds. The results are shown in Figure 24 below.

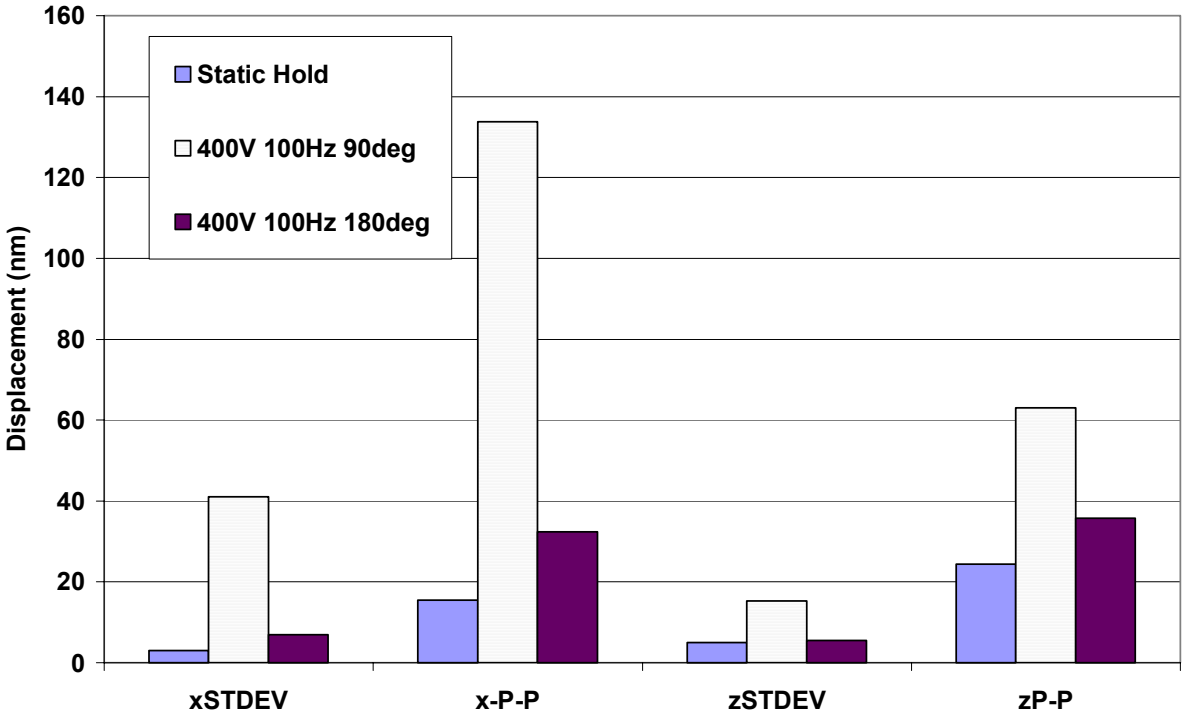

Figure 24. Peak to Peak and Standard Deviation of Slide Vibration

The largest amplitudes and deviations resulted from the UltraMill operating with 90º phase shift between the piezo stack actuators. This resulted in vibration amplitudes an order of magnitude

higher in the x slide and over 100 percent increase in the z slide. As theorized the 180º phase shift significantly reduced slide vibration compared to the 90º phase shift. 'x' slide standard deviation and peak to peak vibration was reduced 75 and 85 percent respectively and z slide standard deviation and peak to peak vibration was reduced 40 and 66 percent respectively. The inertial forces of the UltraMill have a large effect on slideway vibration and must affect the surface finish of the machined part.

9.13 PREDICTED EFFECTS OF TOOL PATH SHAPE

The significance of EVAM tool path shape has not been determined experimentally. The material properties that govern tool path dimensions are not yet understood, however ideal tool path shape and dimensions based on theoretical surface finish can be explored with a Maple computer model. In the following sections a theoretical examination of the implications of tool path shape is examined. Using tool paths that are possible with the current UltraMill design will allow these theoretical results to be compared with experimental measurements later.

9.13.1 ASPECT RATIO

The UltraMill's two actuator, non-resonant design allows for adjustments in tool path aspect ratio and tool path dimensions by changing the phase shift between the two sine wave signals. Large changes in tool path shape and size can be achieved simply by varying the phase parameter. Table 4 is a list of tool path dimensions for various phase angles between the two piezo stack actuators.

Table 4. The Effect of Phase Angle on Tool Path Aspect Ratio and Dimensions

Phase Angle (deg)	a (μm)	b (μm)	a/b
165	37.49	1.04	35.91
150	36.53	2.07	17.64
135	34.94	3.06	11.41
120	32.75	4.00	8.19
100	28.97	5.14	5.63
90	26.75	5.65	4.73
60	18.91	6.93	2.73
45	14.47	7.39	1.96
30	9.79	7.73	1.27
20	6.57	7.88	0.83

The tool path aspect ratio is defined as the quantity a/b. Where 'a' is the half the dimension of the tool path along the up feed axis and b is the dimension of the tool path perpendicular to the up feed direction. The cutting radius of an ellipsoid tool path can be approximated by the Equation 2 given earlier. From Equation 1 it is easy to see that increasing the dimension *a* decreases the PV by its square. The larger the tool path aspect ratio the lower the theoretical surface finish and increase in chip thickness reduction for a given up feed per cycle. However, for this particular system, large aspect ratio tool paths that result in large cutting radii do so at the expense of a small 'b' dimension. The 'b' dimension of the tool path dictates the formation of a discontinuous chip and reduction of tool forces for given depths. The smaller the 'b' dimension, the smaller the nominal depth of cut must be to produce a discontinuous chip. Operating in the discontinuous chip mode provides the large reductions in cutting force and is theorized to reduce tool wear. At the limit of the aspect ratio the dimension 'b' becomes so small the diamond tool is traveling in a straight path in the upfeed direction. Once this occurs the UltraMill operates in a 1-D vibration assisted mode. A similar effect occurs when the phase angle between the two actuators is zero. In this case the tool oscillates only in the axis perpendicular to the workpiece. Using the Maple EVAM cutting program a series of discrete phase angles were tested for a constant upfeed per cycle and a depth of b/2. Thus the nominal cutting depth is reduced as the

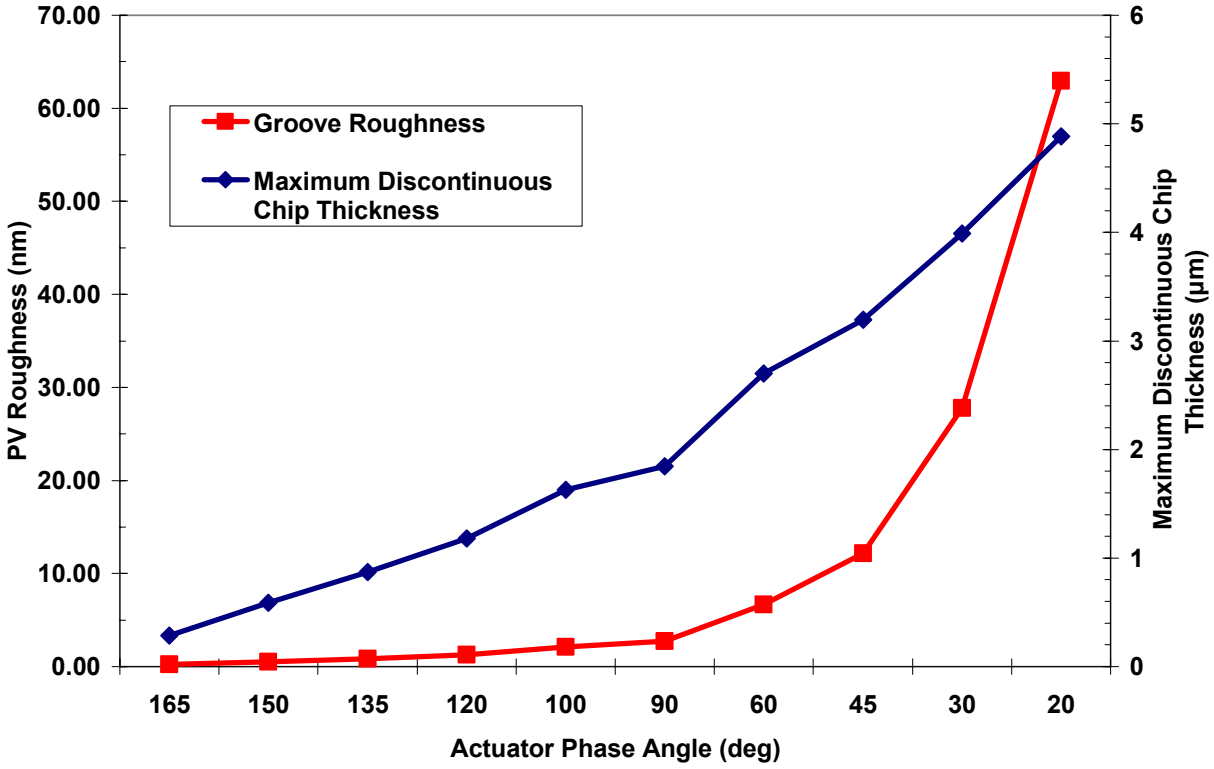

Figure 25. Percent Reduction & PV Surface Roughness as a Function of Phase Angle (a = 6.5 to 37.5, & b = 7.8 to 1 µm, Upfeed 1.6 µm/cycle)

phase angle is increased to maintain a discontinuous cutting mode. Reducing the nominal depth required by higher phase angles reduces the volume removal rate of the EVAM process. The maximum discontinuous chip thickness and theoretical surface finish was calculated for each case and plotted in Figure 25. The curves in Figure 25 show that an increase in phase angle relates to a decrease in surface roughness.

Figure 25 characteristic curves are for an of upfeed 1.6μm per cycle, higher upfeed rates result in the percent reduction curve to shift downward and the surface finish curve to shift upward.

Inertial Effects

One of the results of the aspect ratio study is the possibility of using an arbitrary 163º phase angle between the two piezo stack actuators. This would theoretically have the double benefit of reduced surface finish and reduced inertial force. To test this hypothesis the laser data was gathered comparing the UltraMill running at the same voltage and frequency with both a 90º phase shift and a 163º phase shift. The results shown below in **Figure 26** show a reduction in slide vibration amplitude of 50 to 60 percent.

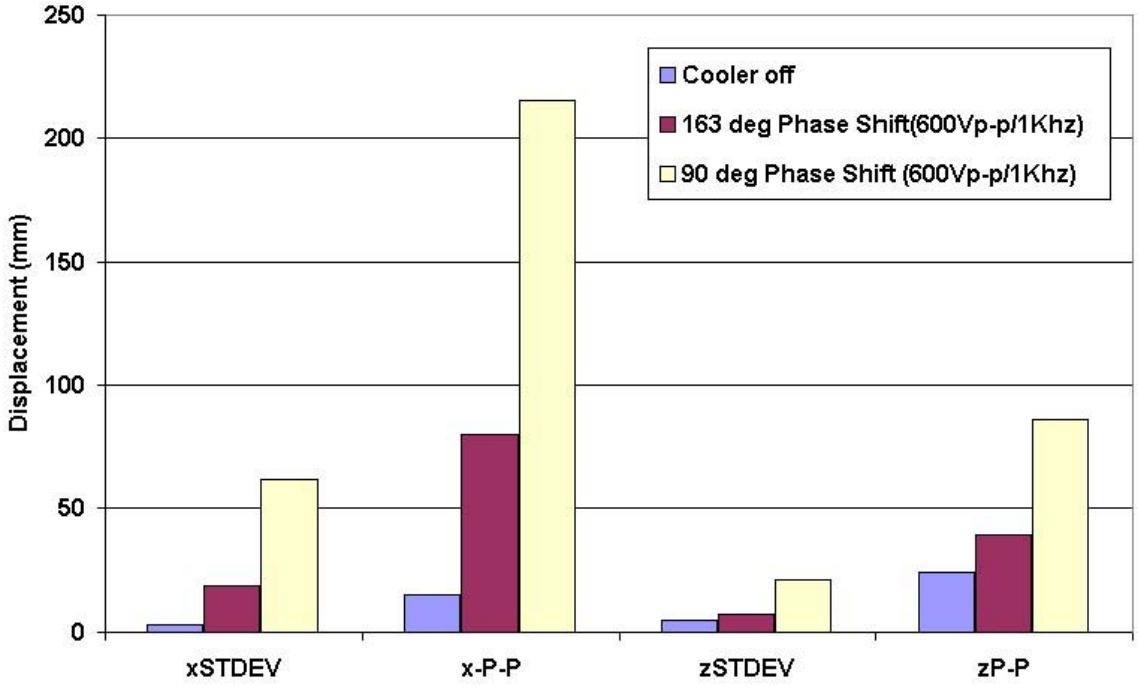

Figure 26. Laser Data Comparison of 90º and 163º Phase Angle

9.14 CONCLUSION

The UltraMill High Speed has been constructed, tested and is operational. The cooling system has been redesigned and is effective in maintaining safe piezo stack actuator operating temperatures. Multiple acrylic parts have been fabricated and tool forces in aluminum have been measured. Chip geometry and surface finish has been observed, measured and predicted. And many advances have been made toward a better understanding of generating surfaces with the EVAM process. Upfeed per cycle and tool path aspect ratio have been identified as important parameters in surface roughness of machined parts. Inertial forces have been identified as a large source of slide vibration. Several new questions have emerged. What is the lowest possible surface finish achievable with the current UltraMill setup? Can better surface finish be realized with the 163º phase angle? What is the benefit, if any, of the discontinuous chip? Is this based on material properties? Can brittle materials be successfully machined with this process? What is the ideal tool path shape and dimensions? Answering these questions remain important goals for the PEC.

REFERENCES

1. Storz, Gene Edward II, "Theoretical Modeling of Precision Contour Grinding", Masters Thesis, North Carolina State University, 1994.
2. Cerniway, M.,"Elliptical Vibration Machining with Diamond Tools", Masters Thesis, North Carolina State University, 2002.
3. Arcona, C., "Tool Force, Chip Formation and Surface Finish in Diamond Turning", Ph.D. Dissertation, North Carolina State University, 1996.
4. Nakayama, K., Arai, M., Kanda, T., "Machining Characteristics of Hard Materials", Annals of the CIRP, Vol. 37, pp. 89-93, 1988
5. Moriwaki, T., Shamoto, E., "Study on Elliptical Vibration Cutting", Annals of the CIRP, Vol. 43, pp. 35-38, 1994.
6. Moriwaki, T., Shamoto, E., "Ultra-Precision Diamond Cutting of Hardened Steel by Applying Elliptical Vibration Cutting", Annals of the CIRP, Vol. 48, pp. 35-38, 1999.

10 FORCE MODELING WITH MINIATURE BALL END MILLS

Stuart Clayton
Graduate Student
Thomas Dow
Professor
Mechanical and Aerospace Engineering

The primary objective of the proposed research is to increase the quality and productivity of precision milling operations through the development and demonstration of force-feedback machining. The utilization of force-feedback machining has the potential to increase the accuracy of precision milling while reducing time and costs. To utilize force-feedback in a control algorithm, a cutting force model must be developed and verified experimentally. A cutting force model was developed and experimental tests were conducted to compare predicted and measured force data. Experimental tests were conducted on S7 and 1018 steel along with 6061 aluminum for a variety of tool tilts and chip areas. Also, an independent force-feedback piezo-actuated spindle has been designed to compensate for tool deflection by means of the cutting force model.

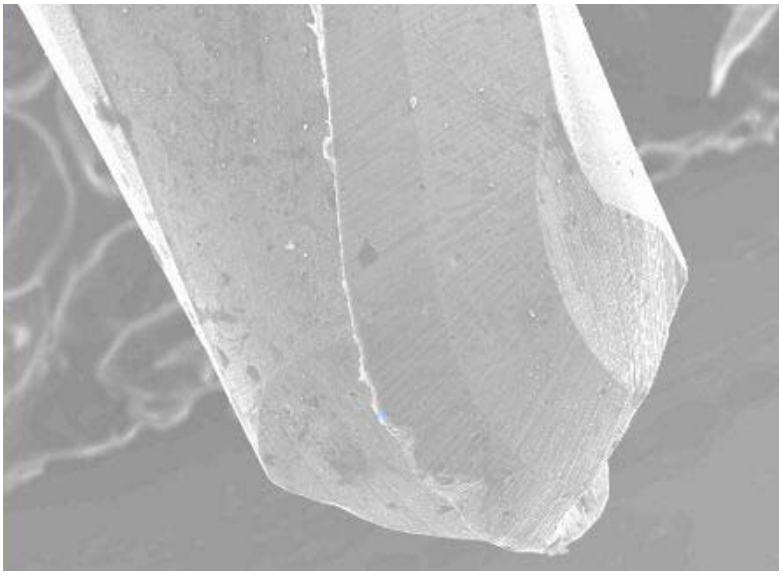

10.1 INTRODUCTION

There are a number of manufacturing processes that benefit from precision machining applications. With the increase in demand for optical systems used in computer networking and telecommunications, injection molding is one example of a precision application on the forefront of current research. Figure 1 is a picture of a lens that was created using the injection molding process. One main challenge facing the injection-molding world is to develop processes that can precisely replicate optics using high volume, low cost methods. Also for many applications, the miniaturization and increased resolution requirements will demand that the products be composed of more sophisticated components. The first step in accomplishing the above-mentioned tasks is to manufacture high quality, high accuracy steel molds that will not distort or corrode and destroy the features being produced. To create durable molds (commonly referred to as dies), hardened steels are used. These steels will typically have a hardness value near 60 H_C (Rockwell C-scale hardness)

Figure 1. Example of Lens Fabricated from Injection Molding

To create small, detailed features in the steel dies, small milling tools must be used. These tools are generally on the millimeter or sub-millimeter level and are referred to as miniature end mills. An example of 0.8 mm diameter, miniature-milling tools can be seen in Figure 2.

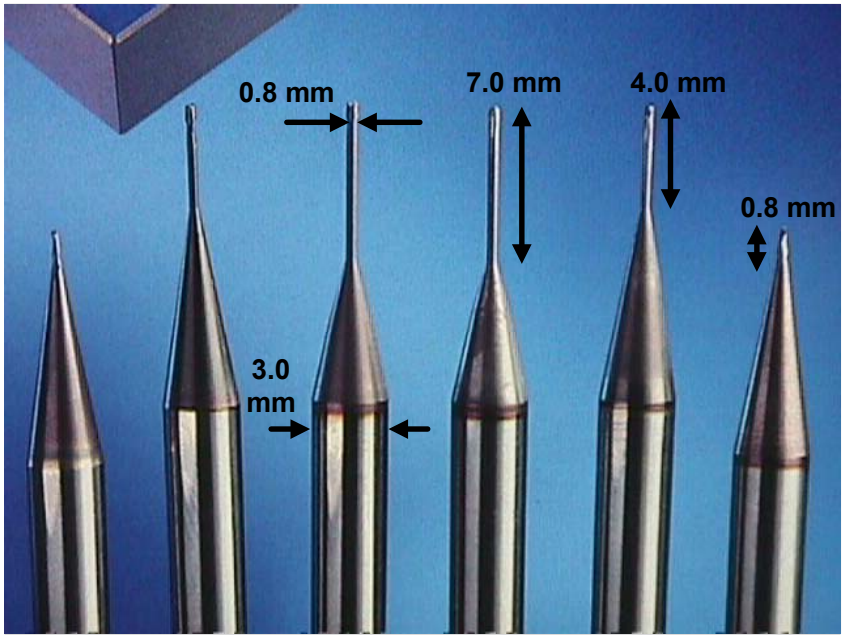

Figure 2. Picture of Miniature Ball End Mills with Different Shank Lengths

However, ball end tools (manufactured by Jabro Tools) are available in diameters ranging from to 0.2 mm up to 2.0 mm. These tools are also available in three different shank lengths – short (0.15 to 2.0 mm), long (2.5 to 10.0 mm), and extra long (4.0 to 16.0 mm). The tools are made from Tungsten Carbide coated with titanium aluminum carbide to improve wear resistance. Although these tools can produce miniature features, great care must be taken to produce accurate features. One reason for inaccurate shapes and features when using miniature end mills is the lack of stiffness of the small-diameter tools. Machining forces (especially in hardened steels) cause severe tool deflection. Once the tool begins to deflect, the desired features on the dies are no longer accurate.

An existing method to correct for tool deflection consists of an open-loop modeling technique. Here, the tool path is simulated with the cutting force model and an altered tool path is created using the knowledge of the predicted cutting forces and the tool stiffness. This technique has been proved effective by previous researchers but requires a great deal of preprocessing. An improved method may involve closed-loop control of the tool path by means of the machine axes or an independent spindle-actuation system. There are currently two main ideas to improve milling accuracies and machining time. The first concept involves tool stiffness and a measured force. Once the force is measured, the stiffness of the tool can be used to estimate the tool deflection. At this time, actions may be taken to place the tool in its desired position. However, this procedure would be effective with only tool deflection compensation in mind. A more universal method to compensate for tool deflection and/or the fabrication of part features involves force feedback only. If the cutting forces can be estimated for any desired cut, closed-

loop control can manipulate the tool path so that the measured force equals the predicted force. This method can be used whether the part is known or unknown, regardless of its geometry.

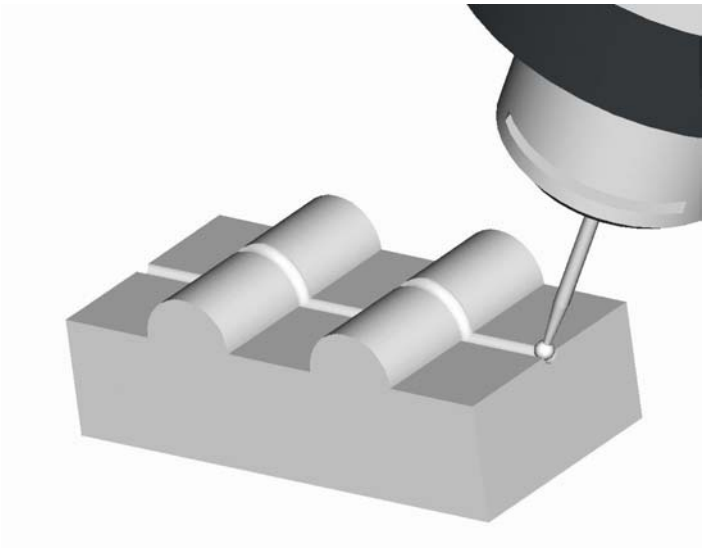

Figure 3. Generic Application of Force-Feedback Machining

The more general force-feedback method will be studied in great detail with this research. First and foremost, an accurate force model must be developed. An effective force model will account for variations in items such as depth of cut, feedrate, spindle speed, tool tilt with respect to workpiece, and material properties. Once the force model has been verified, a control algorithm can be implemented to alter the tool path based on the error between the measured and predicted forces. A simple example of an application that may be appropriate for force-feedback machining can be seen in Figure 3. Here, a constant depth groove has been machined over the length of the workpiece that has a series of raised features. Unless this geometry is known exactly, the groove depth would not be accurate across the part without force-feedback machining due to tool deflection and part uncertainties.

10.2 BACKGROUND

Cutting forces have been researched at the PEC for a number of years. Drescher [1,2] was the first student to investigate cutting forces at the PEC studying tool forces associated with diamond turning. Arcona [3] then expanded Drescher's work to reflect forces and chip formation in diamond turning. In the development of Arcona's force model, several major assumptions were made and are as follows [3]:

1. Workpiece material is regarded as elastic-perfectly plastic.
2. The normal stress acting along the shear zone, σ_S, is taken to as the uni-axial material flow stress.

3. A von-Mises failure criterion is employed so that the shear stress is given by

$$\tau_S = \frac{\sigma_S}{\sqrt{3}} \tag{1}$$

Arcona then produced Equations 2 and 3 by summing the forces in the cutting and thrust directions shown in Figure 4 using the previous three assumptions:

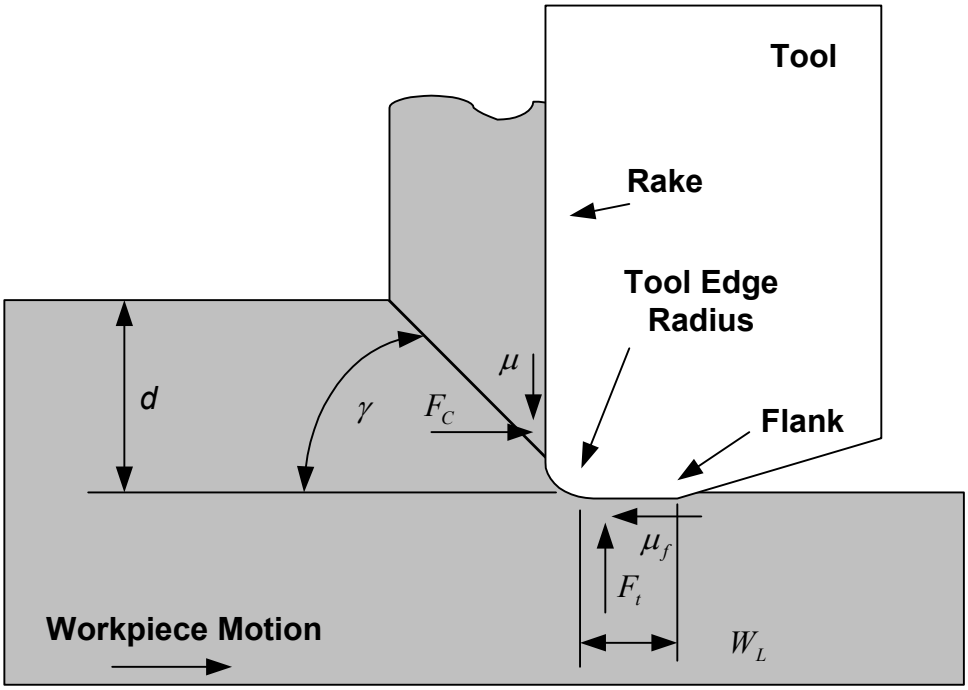

Figure 4. Cutting Force Diagram

$$F_c = \frac{HA_C}{3}\left(\frac{\cot(\gamma)}{\sqrt{3}} + 1\right) + \mu_f A_f \left(0.62H\sqrt{\frac{43H}{E}}\right) \tag{2}$$

$$F_t = \frac{\mu HA_C}{3}\left(\frac{\cot(\gamma)}{\sqrt{3}} + 1\right) + A_f \left(0.62H\sqrt{\frac{43H}{E}}\right) \tag{3}$$

where

H = hardness of workpiece material (Pa)

E = elastic modulus of workpiece material (Pa)

A_c = face area of chip (m^2)

A_f = flank area of the tool (m^2)

μ = friction coefficient acting on the tool rake face and workpiece interface

μ_f = friction coefficient acting on the tool flank face and workpiece interface
γ = shear angle of the chip (the value used in this research was 50°).

The force model was developed in polar coordinates (cutting and thrust directions). However, to compare the force model with data from the three-axis load cell, the polar coordinate forces must be transformed into a Cartesian coordinate system (x, y, and z directions). The following equations were produced from the transformation and the geometry is illustrated in Figure 5 [4].

$$F_x = F_c \cos\alpha \sin\theta - F_t \sin(0.5\phi)\cos\theta \quad (4)$$

$$F_y = -F_c \cos\alpha \cos\theta - F_t \sin(0.5\phi)\sin\theta \quad (5)$$

$$F_z = F_c \sin\alpha \cos\theta + F_t \cos(0.5\phi) \quad (6)$$

where
F_C = cutting force obtained from Equation 2 (N)
F_T = thrust force obtained from Equation 3 (N)
α = tool tilt angle, angle between centerline of tool and normal to workpiece (deg)
ϕ = contact angle between the tool and the workpiece (deg)
θ = rotational position of the tool (deg)

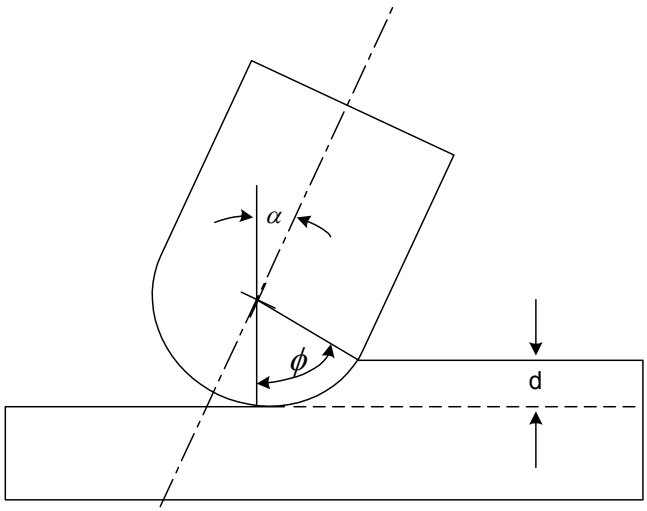

Figure 5. Diagram Illustrating Tilt Angle and Contact Angle

Miller used Arcona's model to predict cutting forces for ball end milling. Miller described the thrust and cutting forces as of two components: a chip removal force based on depth and chip thickness and a plowing force that can be related to the tool wear land and the length of contact between the tool and the workpiece. An example of a tool wear land can be seen in the SEM image of Figure 6. Miller then produced Figure 7 to illustrate chip geometry for a ball end mill [4]. Also, Miller provided Equations 7 and 8 for the chip and flank areas respectively [4].

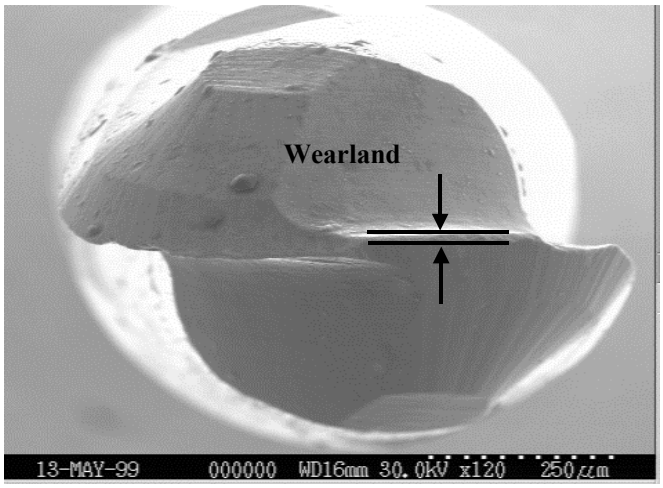

Figure 6. SEM Image of Ball End Mill

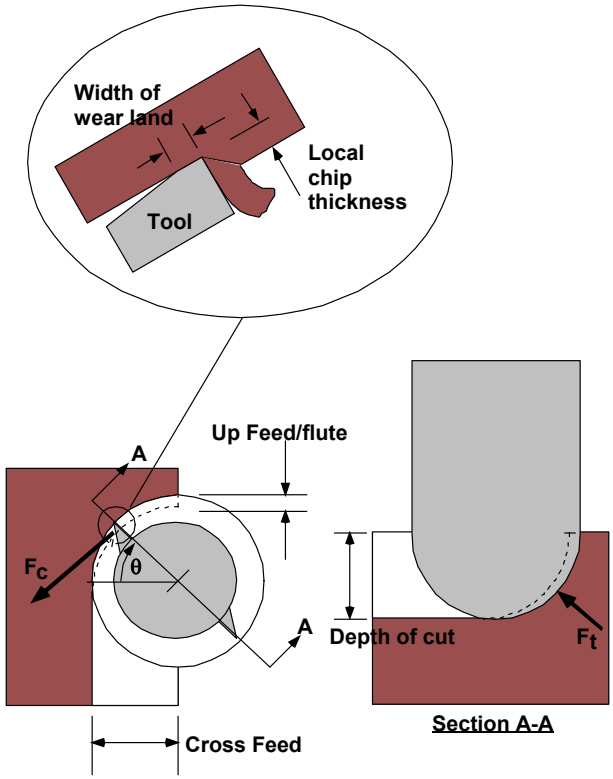

Figure 7. Chip Geometry and Tool Forces for Ball End Mills

$$A_c = d \times f \times \sin\theta \times (1 \pm \zeta) \tag{7}$$

$$A_f = R_t \times W_L \times \phi = L_c \times W_L \tag{8}$$

where

d = depth of cut (m)

f = upfeed per revolution of tool (m/rev)

ς = runout of tool/spindle (percentage that one flute cuts more than the other)

R_t = radius of tool (m)

W_L = wearland of tool (m)

L_C = tool contact length (m)

In addition to the components listed above for the flank area of the tool, an extra term was added. Miller divided the tool flank area by the term '2-sin(θ)' to empirically match the shapes of the x, y, and z forces. Although the flank area of a tool remains constant and does not change with tool rotation, Miller found this to be a suitable place to include the sinusoidal term [4].

10.3 EXPERIMENTAL APPARATUS AND METHOD

10.3.1 EXPERIMENTAL APPARATUS

All cutting experiments were performed on the Nanoform 600 diamond turning machine (DTM) controlled by a Programmable Multi-Axis Controller (PMAC) (See). A steel mount was used to contain the force transducer and workpiece, which were squared with respect to the z-axis with an electronic indicator. The steel mount was bolted to the x-axis of the DTM, while an air-bearing spindle was mounted on the y-axis, which sits on the z-axis. A Westwind D1090-01 air-bearing, air-turbine spindle was used to secure the milling tool and was capable of speeds as high as 60,000 rpm. A detailed picture of the tool-workpiece environment can be seen in the photograph in Figure 9.

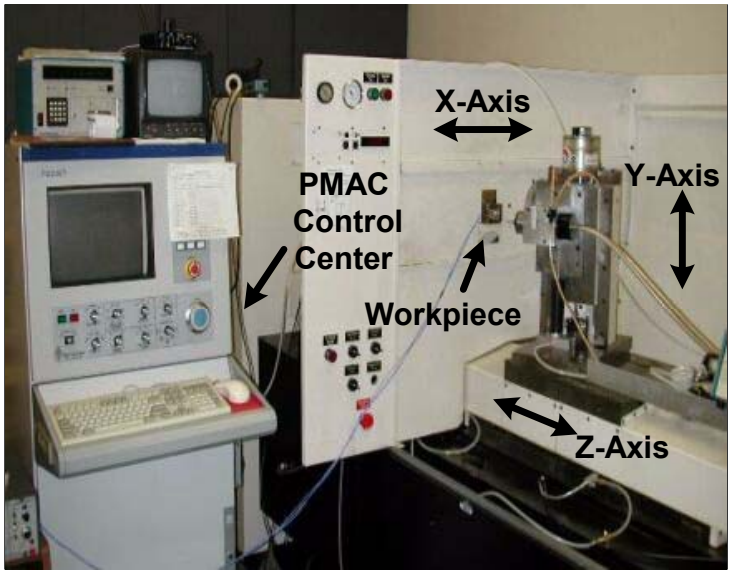

Figure 8. Photograph of Nanoform 600 DTM

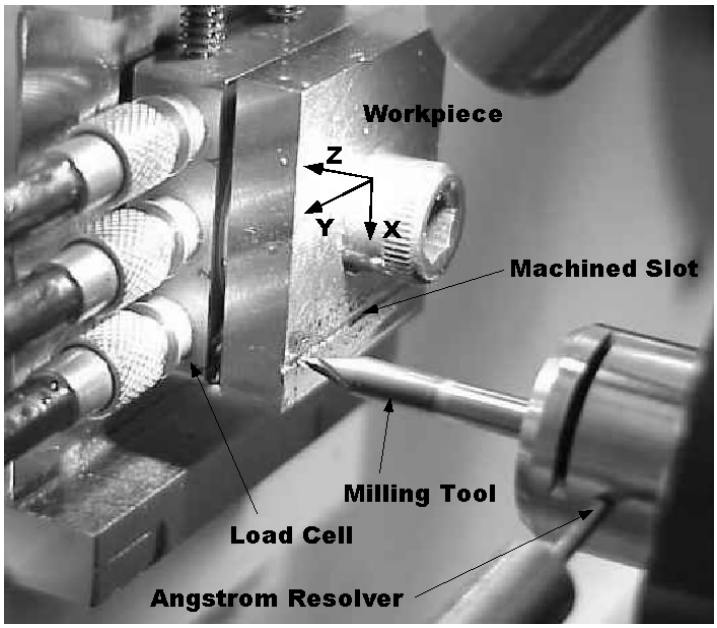

Figure 9. Tool and Workpiece Environment

10.3.2 DESCRIPTION OF DATA ACQUISITION SYSTEM

A Kistler quartz force transducer (Model 9251) was used to measure the cutting forces. The transducer consists of piezo-electric elements that were designed to decompose any acting force vector into three orthogonal components – x, y, and z. The transducer (commonly known as a load cell) is extremely rigid and consequently has a high natural frequency. The total mass of the system was found to be approximately 0.085 kg (depending on part geometry), while the stiffness of the load cell was published as 981×10^{-6} N/m and 294.3×10^{-6} N/m in the orthogonal and in-plane directions respectively. Thus, the natural frequency of the system was calculated to be about 17 kHz in the z-direction and about 9 kHz in the x and y-directions. The natural frequencies were checked experimentally and verified as the z-direction was found to be approximately 18.8 and the x and y-directions were found to be 9.7 and 11.3 kHz respectively. The natural frequencies were found by comparing the load cell output voltage to an impact hammer input voltage using a spectrum analyzer.

The load cell produces charges proportional to a given force that are fed into a three-channel charge amplifier (Kistler Model 5004). The charge becomes a voltage that is multiplied by a calibration constant (discussed later) to obtain the appropriate measured force. The voltages from the charge amplifier were then routed to a 4-channel Hewlett Packard 5400 Series oscilloscope, which acquired 500 points for each channel. The three Cartesian forces occupied three channels of the oscilloscope, while the fourth channel was used as a 1 pulse-per-spindle

revolution signal for reference and triggering purposes. This signal was obtained using an optical sensor (Angstrom Resolver Model 101). Tool speed was maintained around 10,000 rpm, and the scope was set to capture approximately 6-8 revolutions of the tool. A schematic of the data acquisition system can be seen in Figure 10 showing the major components discussed above.

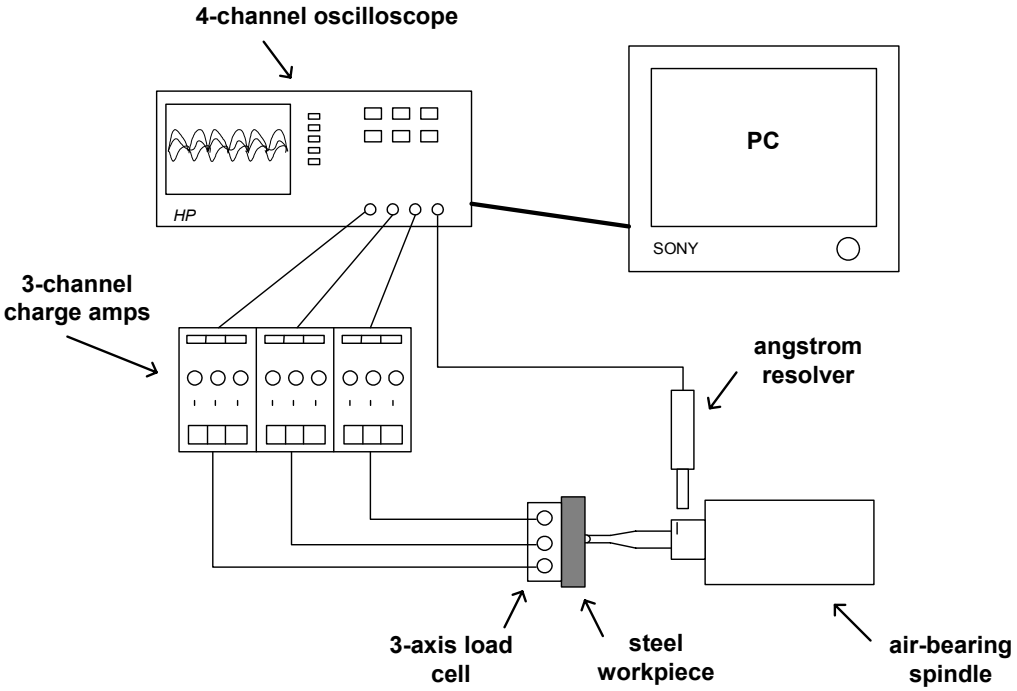

Figure 10. Schematic of Force Data Acquisition

To manipulate the cutting data, HP BenchLink Scope software was used to upload data from the oscilloscope. The data could then be saved as an image identical to the scope or in time-amplitude form for spreadsheet operations and model comparison.

10.3.3 SYSTEM CALIBRATION

For the voltages produced by the charge amplifier to be of any significance, the load cell must be calibrated under the prescribed conditions. A 1 kg mass was used to perform the calibration procedure. Here, the 1 kg mass was suspended from the load cell in each of the 3 directions. The voltage signal was zeroed and the mass was removed. Each experiment was conducted 3 times in each direction to produce average calibration values. The charge amplifier was set to 5 mechanical units per volt for S7 steel and each direction was indeed approximately 5 N/V. The calibration values for the x, y, and z directions were found to be 5.649, 5.333, and 4.547 N/V respectively for the given arrangement. Data from the calibration experiments can be found in Appendix A. The calibration values above were also used for 1018 steel, because the S7 and

1018 steel specimens were the same size and mass. However, a different set of calibration constants was used for the aluminum specimens and can also be found in Appendix A.

10.3.4 EXPERIMENTAL METHOD

Experimental force data was taken while machining three different materials – S7 hardened tool steel, Grade C-1018 low carbon steel, and 6061 aluminum. Table 1 lists a series of properties for the three materials. Different feedrates, spindle speeds, and depths of cut were used to obtain experimental data. Short flute, 0.8 mm ball end mills were used for each experiment. A short-flute tool was selected, because it has a higher radial stiffness than the long or extra long tools and therefore less deflection.

Table 1. Material Properties for S7 and 1018 Steel and 6061 Aluminum

Material	Hardness* (MPa)	Modulus (MPa)	Yield Strength (MPa)	Ultimate Tensile Strength (MPa)	Elongation to Failure (%)
S7 Steel	6710	210	1500	2000	10
1018 Steel	1760	210	290	393	40
6061 Aluminum	1090	70	275	310	23

*Measured hardness using Vickers indenter.

10.3.5 METHOD OF ACQUIRING FORCES

Constant-depth grooves were machined across the width of the workpiece. Constant-depth grooves were selected because the experimental forces were repeatable at any time during the cut. Therefore, once the tool engaged the workpiece, the force data on the scope could be captured and uploaded onto a computer through a GPIB connector. An example of captured data with a tool tilt of 25˚ can be seen in Figure 11. Notice the square wave is the once-per-revolution signal. The once-per-revolution signal was used to trigger the oscilloscope to capture all channels at the same instant in time to assure in-phase measurements. Also notice the repetitiveness of the forces for each revolution and for each flute. Each signal was then displayed as a smooth line that connected the 500 data points from the scope.

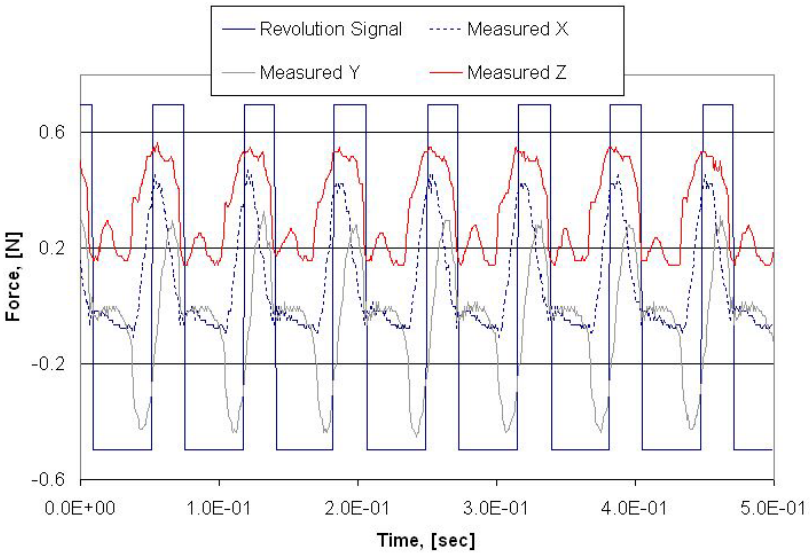

Figure 11. Example of Captured Force Data

10.3.6 DESIGN OF EXPERIMENT

Design of experiment (DOE) is a method in which a set of experimental trials are planned to determine the response of a system based on certain factors. Another goal of DOE is to verify the statistical significance of each factor. The goal of the design of experiment was to determine which cutting parameters – depth, feedrate, spindle speed, or upfeed (feed per revolution of the tool) – had the greatest effect on machining forces. For example, if feedrate and spindle speed were found to be statistically significant, while depth and upfeed was not, then feedrate and spindle speed could be varied from cut to cut with depth held constant. This would reduce the number of experimental tests needed to verify the force model while retaining the same statistical validity.

Statistics has proved that a statistically significant factor should change the mean of the response while maintaining a constant variance. JMP uses an F test to quantify the certainty of the response by analyzing the ratio of the two variances. The uncertainty or residual of the F test is called the p value and is used to quantify statistical significance. An example of an F test curve can be seen in Figure 12. In statistical terms, the p-value must be less than 5% or 0.05 to be considered statistically significant. In other words, one can be certain that the change in response was directly affected by the change in a given factor. As a matter of fact, there are three statistical categories: somewhat significant ($1\%<p<5\%$), significant ($0.1\%<p<1\%$), and very significant ($p<0.1\%$).

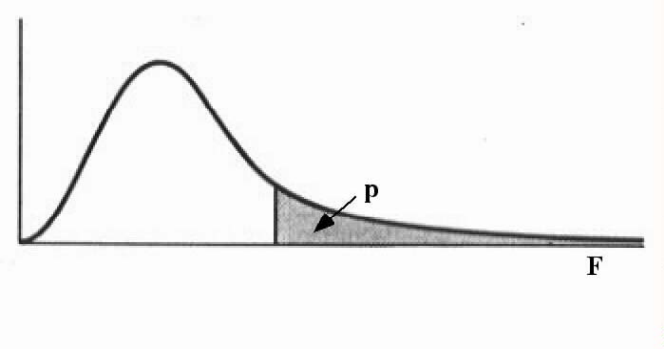

Figure 12. F Test Curve Illustrating Residual P Value [5]

Custom Design of Experiment

A custom design of experiment was chosen to identify the key factors (depth, feed, spindle speed, and upfeed) in affecting the responses (maximum x, y, and z forces). A custom design allows the designer to create special conditions that may not be allowed by a predefined design. A special condition needed for this set of experiments was the addition of the upfeed parameter, which is comprised of two other factors – feedrate and spindle speed. The first step of the process is to select a high and low value for each factor. A set of treatments, or tests, can then be developed where a high or low value is used for each factor to create a trial. Either a full factorial design or a fractional factorial design must be chosen. Fractional factorial designs are chosen to reduce the number of trials. However, since only three independent factors were being analyzed, a full factorial design was selected because there were only eight possible trials (2^3) needed for a complete design.

The Treatment Matrix

An important task in developing the design of experiment was to choose the high and low factor values appropriately. Since the force transducer can detect almost any machining force, it was important to select the factor values with the machine hardware in mind. Given that a diamond turning machine was used to create the tool path, appropriate feedrate values were selected to maintain a constant feed. The air-bearing spindle and tool geometry also provided limitations. Table 2 shows the high and low values selected for depth of cut, feedrate, and spindle speed.

Table 2. Table Illustrating Low and High Factor Values for DOE

Factor	Low Value	High Value
Depth (μm)	100	200
Feed (mm/min)	100	200
Spindle Speed (rpm)	10,000	20,000

JMP (SAS Institute Inc., Cary, NC) statistical analysis software was used to develop and randomize the matrix. The design matrix can be found in Table 3 along with the maximum forces in the x, y, and z directions. Force data was acquired for each cut and the maximum positive force value was chosen as the response for the x, y, and z directions.

Table 3. Treatment Matrix with Factor and Response Values

Trial Number	Depth (μm)	Feed (mm/min)	Spindle Speed (rpm)	Upfeed (μm/rev)	Max. X Force (N)	Max. Y Force (N)	Max Z Force (N)
1	200	200	10,000	20	5.01	3.23	0.5
2	100	200	10,000	20	2.5	2.16	0.1
3	100	200	20,000	10	2.03	1.24	0.175
4	200	200	20,000	10	4.13	2.12	0.55
5	200	100	20,000	5	2.15	0.79	0.24
6	100	100	20,000	5	1.35	0.88	0.416
7	200	100	10,000	10	3.5	2.03	0.528
8	100	100	10,000	10	1.87	1.32	0.1

Design of Experiment Results

Each row of parameters was used to machine a constant depth groove with the Nanoform 600. The treatment matrix along with the responses was then analyzed in JMP. JMP produced a series of graphs and tables regarding the statistical significance of each factor and response relationship. In other words, did a change in a particular factor directly affect the response or was the change in response due to other circumstances.

The design of experiment results found feedrate to be a statistically significant factor in all force directions. A chart of all p-values can be seen in Figure 13, while a chart of only the statistically significant p-values can be found in Figure 14. Reciprocal of the p-values were used to better illustrate the effects of each factor. The results also reveal depth to be a more significant factor than spindle speed, because depth had an average p-value twice that of spindle speed. In addition, the results reveal upfeed to be an insignificant factor in all directions. These results simply reduce the number of experiments needed to be conducted and analyzed. However, two features common to machining - chip area and upfeed - can still be analyzed by varying only depth and feedrate as the DOE suggested.

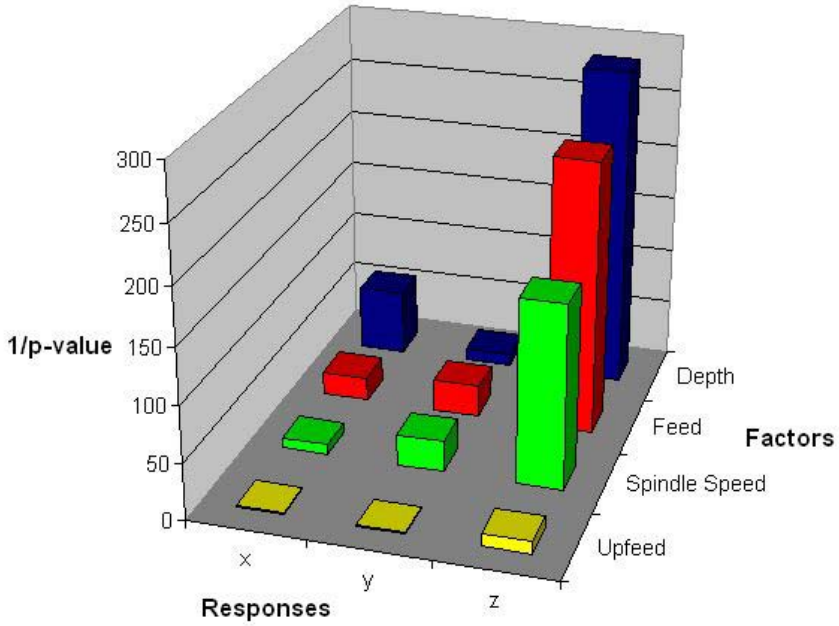

Figure 13. Graph of All P-Values from DOE

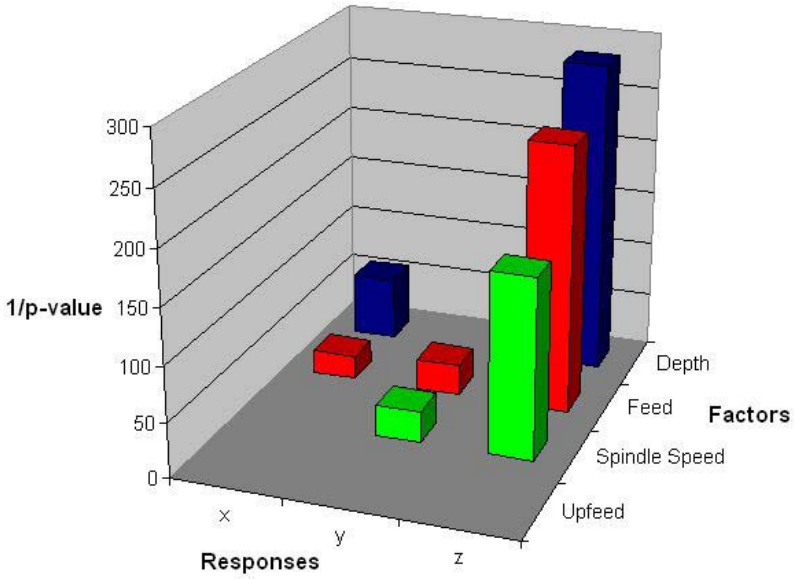

Figure 14. Graph of Significant P-Values from DOE

10.4 MEASURED AND PREDICTED FORCES

Section 10.4 will provide numerous figures where experimental forces were compared to the cutting force model. The first three sections present data for each of the three materials with varying tool tilts, depths, feedrates, and chip areas. The fourth and fifth sections then address repeatability issues and final discussions respectively. It is important to realize that three tool

revolutions were averaged to create one set of forces that rotate from 0-360°. The definition of theta can be found below. Also keep in mind that the first flute in each figure produces smaller forces than the second flute. Theta was chosen to start at the beginning of the smaller forces rather than the larger forces simply to follow the structure of the cutting force model.

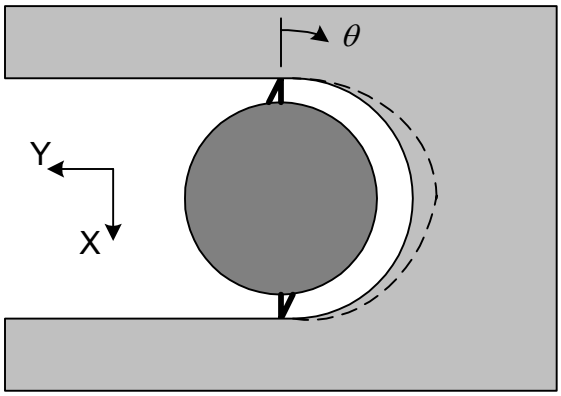

Figure 15. Definition of Tool Rotation, θ

A model parameter that presented some uncertainty was the tool wearland. The wearland rubs or slides against the workpiece material as the tool rotates. This area grows over time due to sliding frictional forces causing the flute to become dull. As wear increases, so do the forces. The wearland, usually manufactured with 2-3 μm, has been seen to increase up to 15-20 μm without visible damage to flutes. However, the wearland is not trivial to measure. A light microscope was used to view the flank of the tool. A wearland was measured by adjusting the focal point of the microscope. An SEM image of a miniature tool can be seen in Figure 16 demonstrating the wearland. The wearland value taken from the light microscope was then entered into the cutting force model.

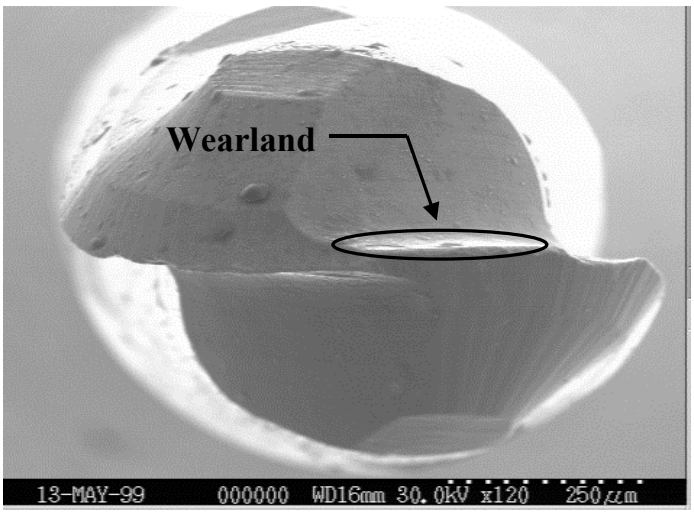

Figure 16. Wearland of a Ball End Mill

Touching off has also led to some uncertainty. A telescope was used to bring the tool close to the workpiece (within a couple hundred microns). The load cell was then used to monitor the z-force as the DTM z-slide was incremented, eventually in one or two micron increments. Once the load cell registered the rotating tool in contact with the workpiece, touchoff had occurred and the z-axis was zeroed. An example of the oscilloscope during touch-off can be seen in Figure 17. This is a touch-off procedure using the z direction of the load cell with a tilted tool. Division lines did not upload from the scope, but from the captured data shown below, the large peaks are approximately measured at 0.06 N.

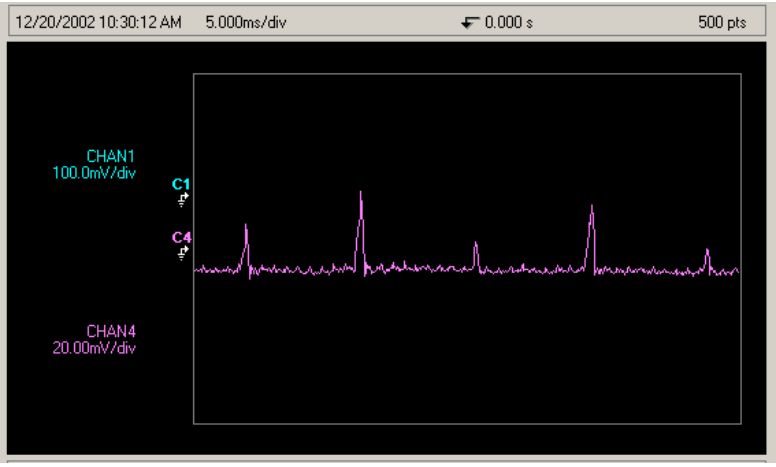

Figure 17. Snapshot of Z-Force at Touch-off

Another parameter the cutting force model accounted for was tool runout. Once the tool was mounted in the spindle, runout was measured using an electronic indicator. The electronic indicator tip was extended as close as possible to the ball of the tool. The spindle was then manually turned and runout was measured. The tool was then rotated slightly in the collet and runout was measured once again. This procedure was repeated until the tool/spindle runout was minimized. Runout could be reduced from 16-20 μm to 6-10 μm in this manner. The runout measured was exclusively the runout of the air-bearing spindle and the tool shank. The actual flute runout was not measured and is an unknown factor in the cutting force model due to the difficulties in manufacturing tools with sub-micrometer dimensions. Runout was input into the model by means of a percentage. The percentage value was calculated as the tool shank runout divided by the upfeed per revolution. For example, if the calculated upfeed and measured runout were both 10 μm, then the runout would be 100 %. This means that one flute would remove all material and the other flute would remove no material.

10.4.1 S7 STEEL RESULTS

Based on the high demand for hard steel dies in the injection molding industry, a hardened tool steel was selected for force model investigation. S7 steel was chosen and produced the highest forces tested in this research. Both small and large chip areas were tested along with varying tool tilts of 0, 10, and 25°. Table 4 provides information for the S7 steel cuts. The experimental data was then compared to the predicted forces. Figures on pages 209-213 show predicted and measured forces for each row in Table 4.

Table 4. Cutting Parameters for S7 Steel

Tool Tilt [deg]	Depth [μm]	Feed [mm/min]	Spindle Speed [rpm]	Upfeed [μm/rev]	Chip Area [μm^2/rev]	Wearland [μm]	Runout [μm]
0	25	200	10,000	20	500	7	10
0	25	200	10,000	20	500	7	10
0	100	200	10,000	20	2000	7	10
0	100	200	10,000	20	2000	5	10
10	50	100	10,000	10	500	12	5
10	100	100	10,000	10	1000	12	5
25	50	100	10,000	10	500	10	10
25	50	200	10,000	20	1000	12	10

Tool Perpendicular to Workpiece

Notice the first and second pairs of rows are identical cuts. This will give an insight to the repeatability of machining forces in S7 steel. A description of the x, y, and z forces can be found following the next two force comparisons.

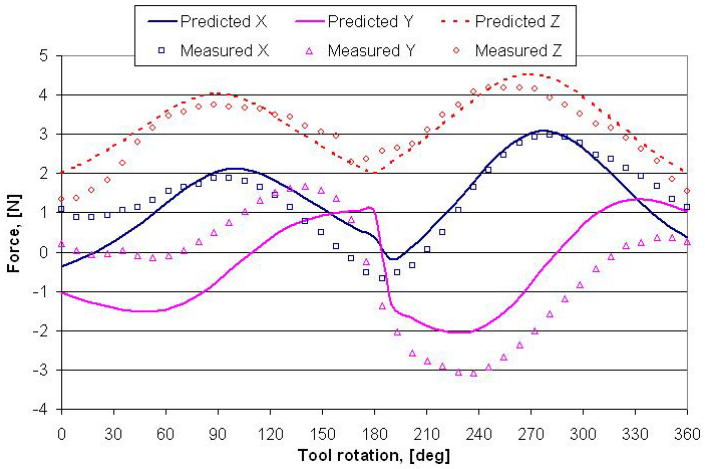

Figure 18. S7 Steel - Measured and Predicted Machining Forces. Depth = 25 µm, Feed = 200 mm/min, Spindle Speed = 10,000 rpm, Tool Tilt = 0°, Wearland = 7 µm, Runout = 10 µm

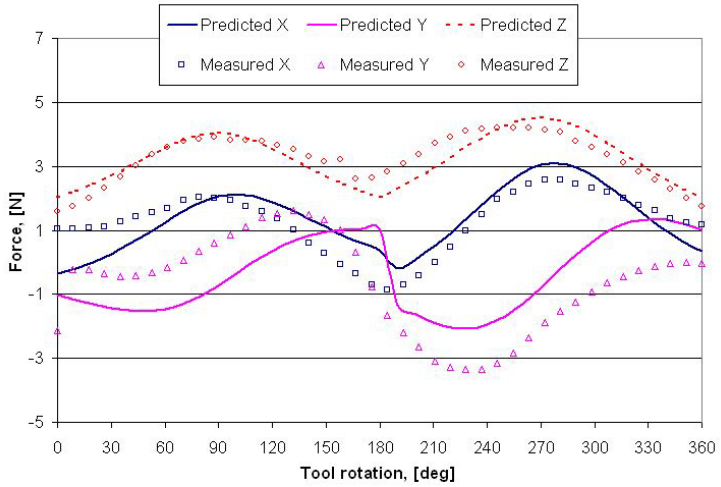

Figure 19. S7 Steel - Measured and Predicted Machining Forces. Depth = 25 µm, Feed = 200 mm/min, Spindle Speed = 10,000 rpm, Tool Tilt = 0°, Wearland = 7 µm, Runout = 10 µm

X-Force Theoretically, the machining forces should repeat every 180° in the x-direction and do indeed here. However, this is not always the case, depending on tool manufacturing and spindle runout. Certain tool flutes are manufactured where the flute transition occurs ± 30° from 180°. The x-force is the middle curve in the previous figure. At θ = 0° as defined in Figure 15, the first tool flute is vertical. The force magnitude is approximately zero in the x-direction, because the tool has just entered the cut and what cutting force is acting on the tool should be in the horizontal direction. The tool then rotates, chip thickness increases, and so does the x-force. The x-force and chip thickness reaches a maximum at 90° and returns to near zero at 180°. Notice the predicted x-force has a discontinuity at 180°. This can be explained by the change in

direction of the thrust force (with respect to the x and y directions). When flute one exits the workpiece and flute two enters, the magnitude of thrust force in the x-direction reverses and therefore explains the discontinuity. The sharpness of the tool directly affects the magnitude of this transition. For instance, a perfectly sharp tool would produce a smooth transition even in the model. However, actual data shows this event to be quite smooth.

Y-Force The y-force possesses different characteristics than either the x or z forces. While the x and z forces contain only the positive components of a rectified sine wave, the y-force reflects a complete sine wave pattern. Note that a positive y-force is the opposite of the feed direction. When the tool enters the workpiece, the cutting force vector is directly aligned with the negative y-direction. As the chip thickness increases and material is removed, the y-force grows in the negative y-direction. As the tool rotates, the cutting force vector then changes from the negative y-direction to the positive x-direction. This explains why the y-force begins increasing in the negative direction, reaches a maximum force magnitude and then once again begins to approach zero. Once the tool flute reaches 90° of rotation, the cutting force vector begins to increase in the positive y-direction, reaches a maximum force and then discontinues into the negative direction based on the magnitude of the wearland. Flute two then begins to enter the workpiece as flute one exits and the last 180° of tool rotation should theoretically mirror the first half. However, runout and the tool manufacturing process do not allow repetitive flutes as expected.

Z-Force Characteristics of the z-force are similar to the x-force in form. The z-force also begins at a minimum (some positive offset), rises to a maximum at 90°, and returns to the z-force minimum value at 180°. The second flute should follow in magnitude and shape given equivalent geometries and no spindle runout. However, the z-force is affected much differently than the x and y forces. While the x and y forces are mainly dependent on the cutting force, the z-force is mostly influenced by the thrust force. This becomes less obvious when the tool is tilted, but for perpendicular cuts as shown above and the following two figures, the z-force is only dependent upon the thrust force. Therefore, the tool wearland is the most influencing property for proper force prediction. In perpendicular cutting, the wearland defines the non-zero offset shown in the previous two figures as approximately 1.5 N. The z-force will always endure this offset because the center of the tool is constantly sliding across the workpiece. For example, had the wearland been larger in the previous figures, the minimum z-force would have also been increased. Likewise, the minimum z-force would have been smaller if a tool with a smaller wearland was used. For instance, the minimum z-force would return to zero if a perfectly sharp tool were being used.

The cutting force model can also predict forces where a larger chip area is produced. The following two figures are identical to the previous two figures, except the depth and therefore the chip area were quadrupled.

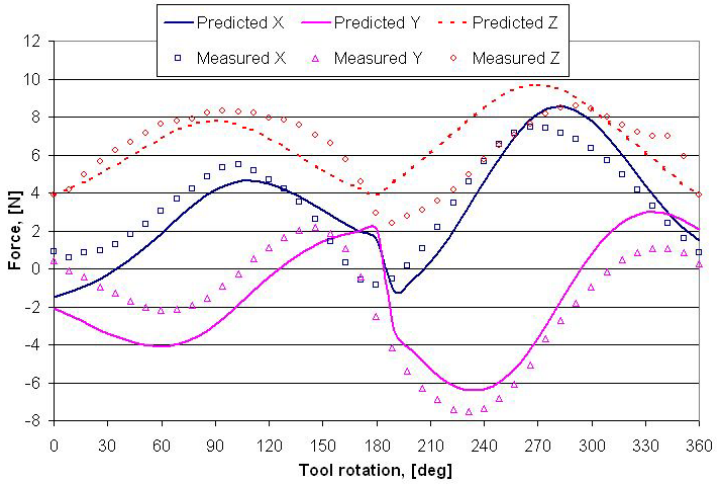

Figure 20. S7 Steel - Measured and Predicted Machining Forces. Depth = 100 µm, Feed = 200 mm/min, Spindle Speed = 10,000 rpm, Tool Tilt = 0°, Wearland = 7 µm, Runout = 10 µm

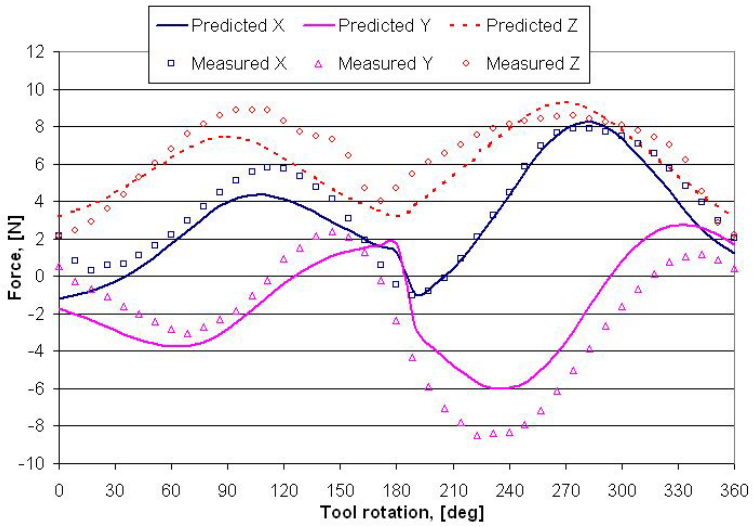

Figure 21. S7 Steel - Measured and Predicted Machining Forces. Depth = 100 µm, Feed = 200 mm/min, Spindle Speed = 10,000 rpm, Tool Tilt = 0°, Wearland = 5 µm, Runout = 10 µm

Now that an approximate model has been developed for S7 steel for perpendicular machining or 0° tool tilt, predicted forces should be compared to experimental forces for cuts with a tilted tool. There should be one major change reflected in the force model for tilted tools. Theoretically, once the tool undergoes any amount of rotation for shallow cuts, the tool should withdraw from the workpiece every revolution. In other words, the tool will leave contact with the workpiece during each revolution. A term duty cycle should now be introduced and defined as the percentage of time the tool is engaged with the workpiece. For example, perpendicular cutting yields a duty cycle of 100%, because at least the center of the tool is always in contact. However, for a tilted tool of say 25°, the duty cycle would be expected to decrease. A linear

approximation along with simple geometry was used to derive an expression for the duty cycle. Tilts of 10 and 25° were analyzed with a duty cycle of 89 and 72% respectively. In other words, the tool should be in contact with the workpiece for only 72% of the time for a tilt angle of 25°. Figure 22 and Figure 23 illustrate force modeling for 10° tilts, while Figure 24 and Figure 25 are for a tool tilt of 25°.

Tool Tilted 10°

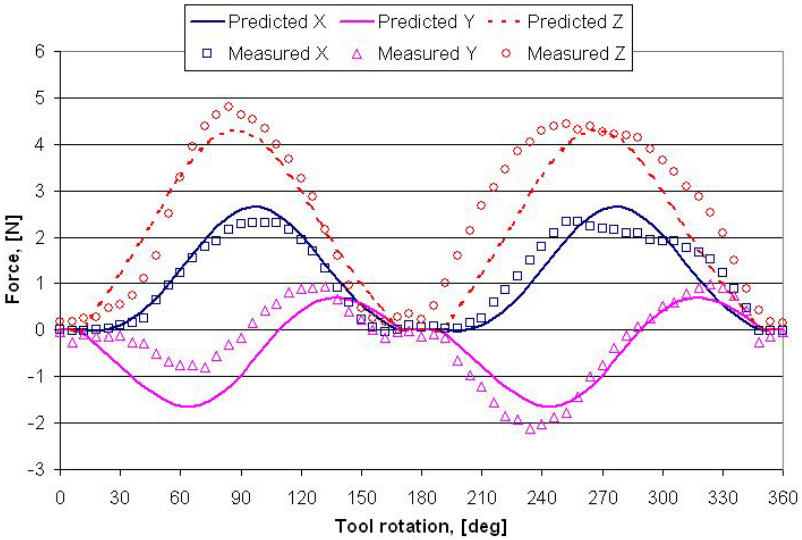

Figure 22. S7 Steel - Measured and Predicted Machining Forces. Depth = 50 µm, Feed = 100 mm/min, Spindle Speed = 10,000 rpm, Tool Tilt = 10°, Wearland = 12 µm, Runout = 5 µm

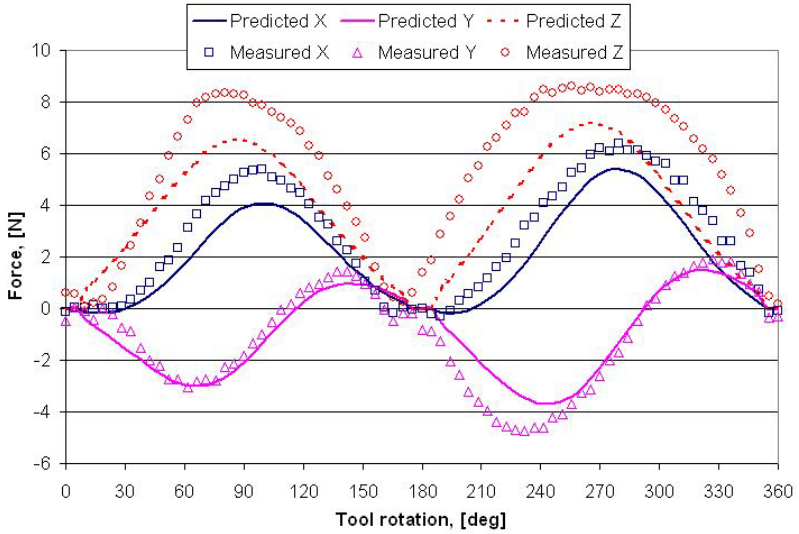

Figure 23. S7 Steel - Measured and Predicted Machining Forces. Depth = 100 µm, Feed = 100 mm/min, Spindle Speed = 10,000 rpm, Tool Tilt = 10°, Wearland = 12 µm, Runout = 5 µm

Figure 23 demonstrates the difficulty in approximating the tool wearland. Here it appears that the tool wearland was underestimated in the force model. However, notice the x and y forces are better approximated, because the x and y forces are mostly influenced by the cutting force and not the thrust force.

Tool Tilted 25°

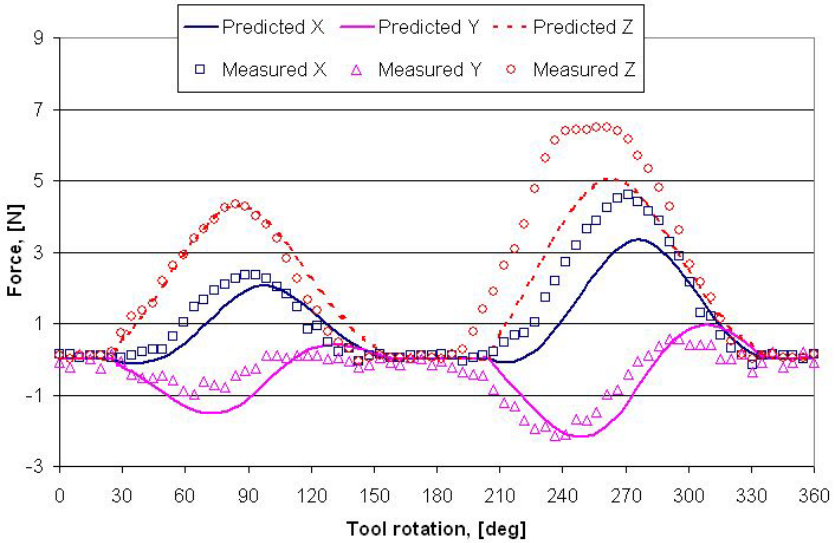

Figure 24. S7 Steel - Measured and Predicted Machining Forces. Depth = 50 µm, Feed = 100 mm/min, Spindle Speed = 10,000 rpm, Tool Tilt = 25°, Wearland = 10 µm, Runout = 10 µm

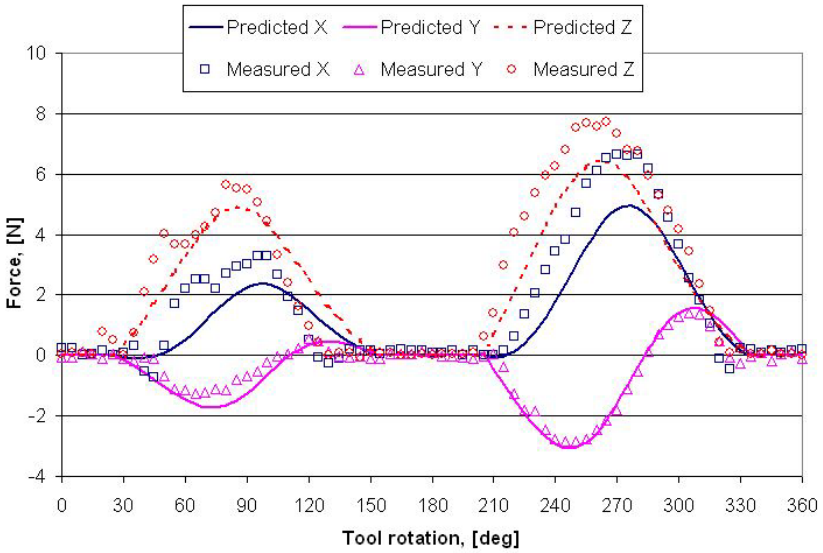

Figure 25. S7 Steel - Measured and Predicted Machining Forces. Depth = 50 µm, Feed = 200 mm/min, Spindle Speed = 10,000 rpm, Tool Tilt = 25°, Wearland = 12 µm, Runout = 10 µm

10.4.2 1018 STEEL RESULTS

The second material selected for force model verification was 1018 steel. 1018 steel is easily machined and therefore a typical steel used in industry. Tests were also performed on 1018 steel for 0°, 10°, and 25° cutting, and the cutting parameters can be found in Table 5.

Table 5. Cutting Parameters for 1018 Steel

Tool Tilt [deg]	Depth [μm]	Feed [mm/min]	Spindle Speed [rpm]	Upfeed [μm/rev]	Chip Area [μm^2/rev]	Wearland [μm]	Runout [μm]
0	75	150	10,000	15	1125	8	8
0	100	100	10,000	10	1000	9	8
10	100	50	10,000	5	500	8	5
10	100	200	10,000	20	2000	11	5
25	50	100	10,000	10	500	10	5
25	50	200	10,000	20	1000	10	10

Figure 26 and Figure 27 show the two perpendicular cuts, while the tilted tool cuts can be found on pages 214-217.

Tool Perpendicular to Workpiece

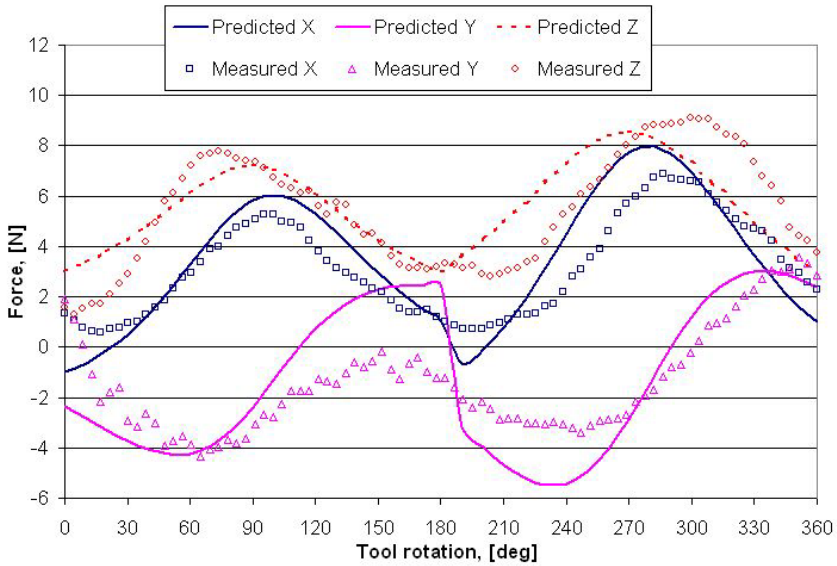

Figure 26. 1018 Steel - Measured and Predicted Machining Forces. Depth = 75 μm, Feed = 150 mm/min, Spindle Speed = 10,000 rpm, Tool Tilt = 0°, Wearland = 8 μm, Runout = 8 μm

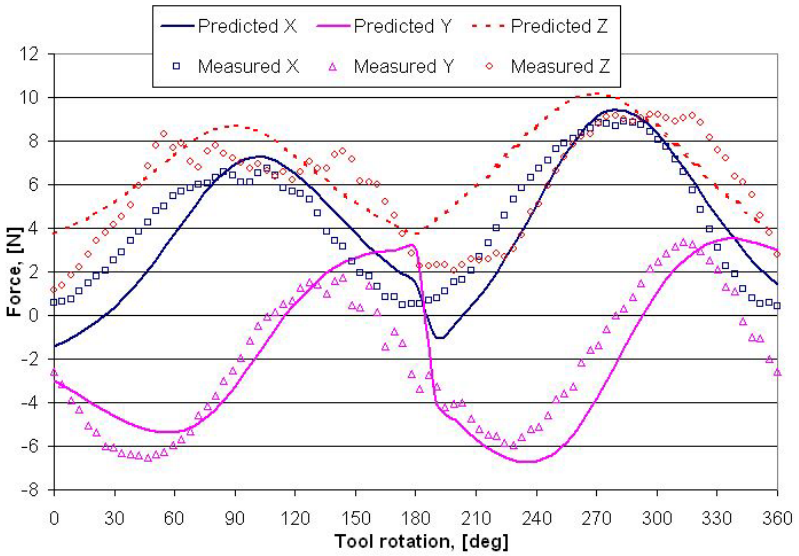

Figure 27. 1018 Steel - Measured and Predicted Machining Forces. Depth = 100 µm, Feed = 100 mm/min, Spindle Speed = 10,000 rpm, Tool Tilt = 0°, Wearland = 9 µm, Runout = 8 µm

Tool Tilted 10°

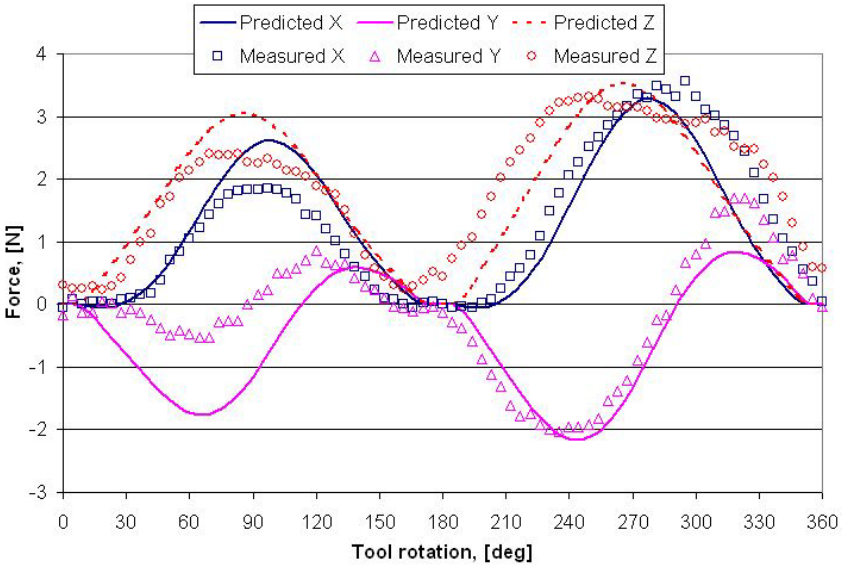

Figure 28. 1018 Steel - Measured and Predicted Machining Forces. Depth = 100 µm, Feed = 50 mm/min, Spindle Speed = 10,000 rpm, Tool Tilt = 10°, Wearland = 8 µm, Runout = 5 µm

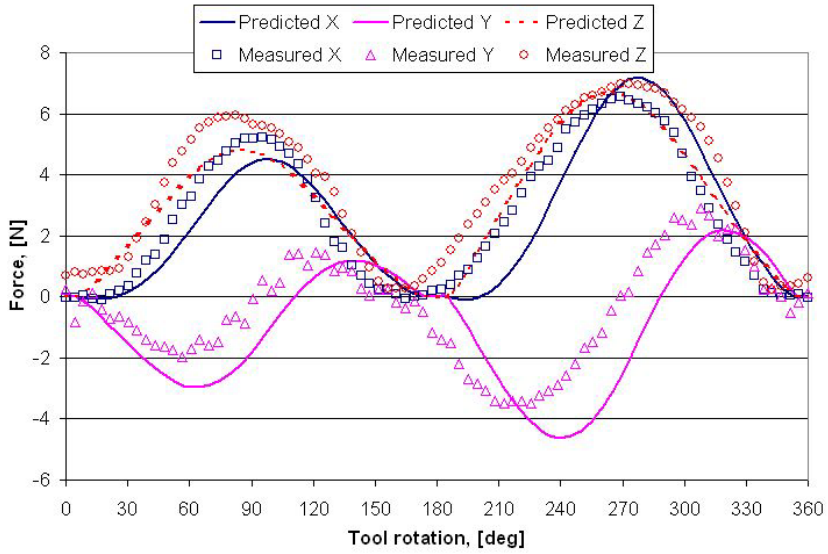

Figure 29. 1018 Steel - Measured and Predicted Machining Forces. Depth = 100 µm, Feed = 200 mm/min, Spindle Speed = 10,000 rpm, Tool Tilt = 10°, Wearland = 11 µm, Runout = 5 µm

Tool Tilted 25°

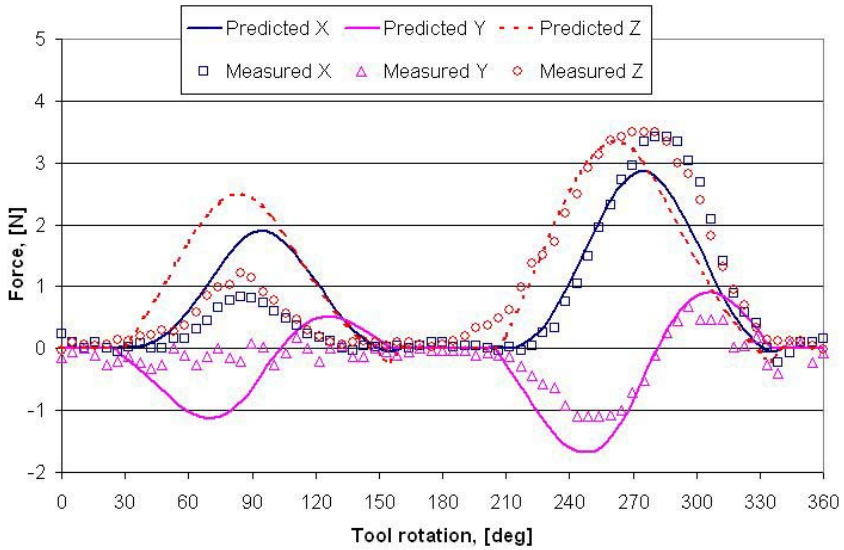

Figure 30. 1018 Steel - Measured and Predicted Machining Forces. Depth = 50 µm, Feed = 100 mm/min, Spindle Speed = 10,000 rpm, Tool Tilt = 25°, Wearland = 10 µm, Runout = 5 µm

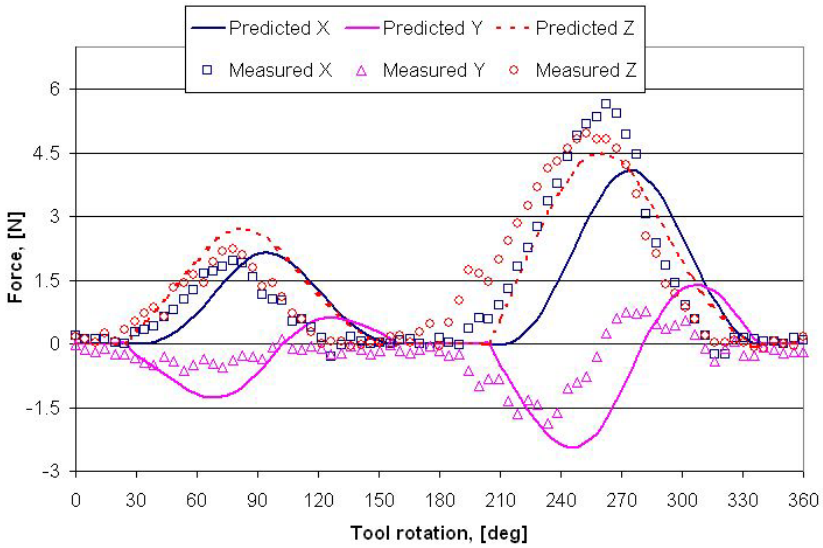

Figure 31. 1018 Steel - Measured and Predicted Machining Forces. Depth = 50 μm, Feed = 200 mm/min, Spindle Speed = 10,000 rpm, Tool Tilt = 25°, Wearland = 10 μm, Runout = 10 μm

10.4.3 6061 ALUMINUM RESULTS

Aluminum, being such a common metal for machining, was also chosen for experimental and predicted force comparison. Smaller force magnitudes were noticed while machining aluminum than either 1018 or S7 steel for a given set of cutting parameters. This phenomenon seems logical, because 6061 aluminum exhibits the smallest hardness value when compared to either type of steel. A list of cutting parameters for 6061 aluminum can be found in Table 6.

Table 6. Cutting Parameters for 6061 Aluminum

Tool Tilt [deg]	Depth [μm]	Feed [mm/min]	Spindle Speed [rpm]	Upfeed [μm/rev]	Chip Area [μm^2/rev]	Wearland [μm]	Runout [μm]
0	50	200	10,000	20	1000	4	8
0	100	200	10,000	20	2000	4	8
10	75	150	10,000	15	1125	5	8
10	75	300	10,000	30	2250	6	8
25	75	150	10,000	15	1125	4	4
25	75	300	10,000	30	2250	2	4

Force data was acquired for each row of cutting parameters above and compared to the predicted force model. The results can be found in figures on pages 218-220. Each tool tilt (0, 10, and 25 degrees) was analyzed for a small and large chip area as seen in Table 6.

Tool Perpendicular To Workpiece

Figure 32 and Figure 33 show the measured and predicted cutting forces in the x, y, and z directions (refer to Figure 9) while machining a constant depth groove in 6061 aluminum with 0° tool tilt.

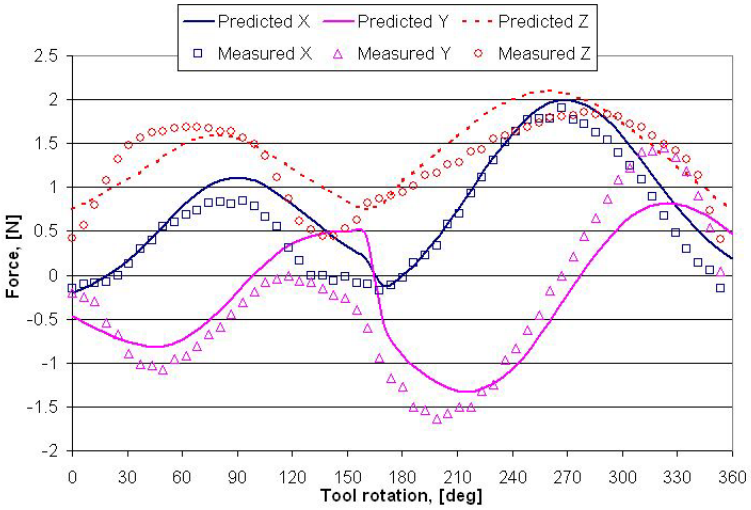

Figure 32. 6061 Alum - Measured and Predicted Machining Forces. Depth = 50 µm, Feed = 200 mm/min, Spindle Speed = 10,000 rpm, Tool Tilt = 0°, Wearland = 4 µm, Runout = 8 µm

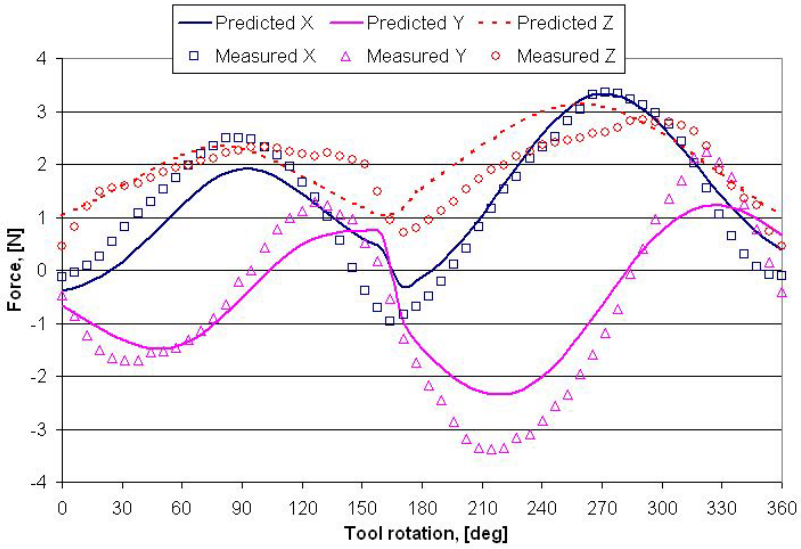

Figure 33. 6061 Alum - Measured and Predicted Machining Forces. Depth = 100 µm, Feed = 200 mm/min, Spindle Speed = 10,000 rpm, Tool Tilt = 0°, Wearland = 4 µm, Runout = 8 µm

It appears the largest error in force prediction for machining in aluminum occurs with the y-force. The modeled y-force does not predict the large amplitude swing for the second flute. A

tilted tool of 10 and 25° was then analyzed. The results can be found in the following four figures.

Tool Tilted 10°

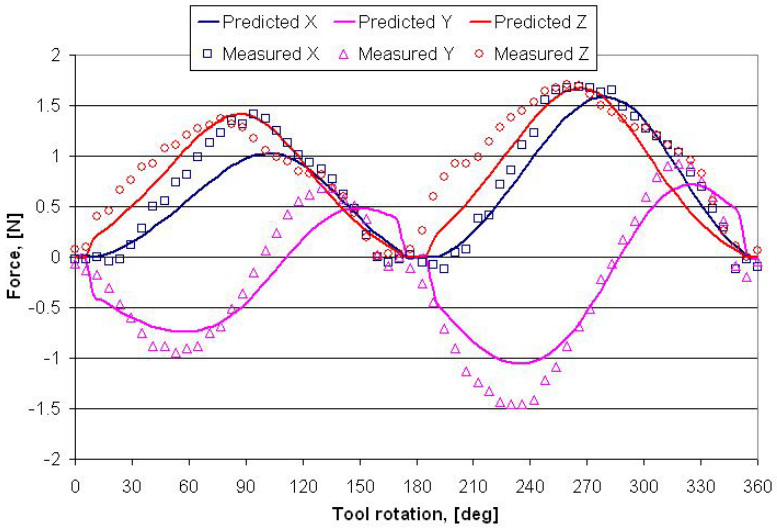

Figure 34. 6061 Alum - Measured and Predicted Machining Forces. Depth = 75 µm, Feed = 150 mm/min, Spindle Speed = 10,000 rpm, Tool Tilt = 10°, Wearland = 5 µm, Runout = 8 µm

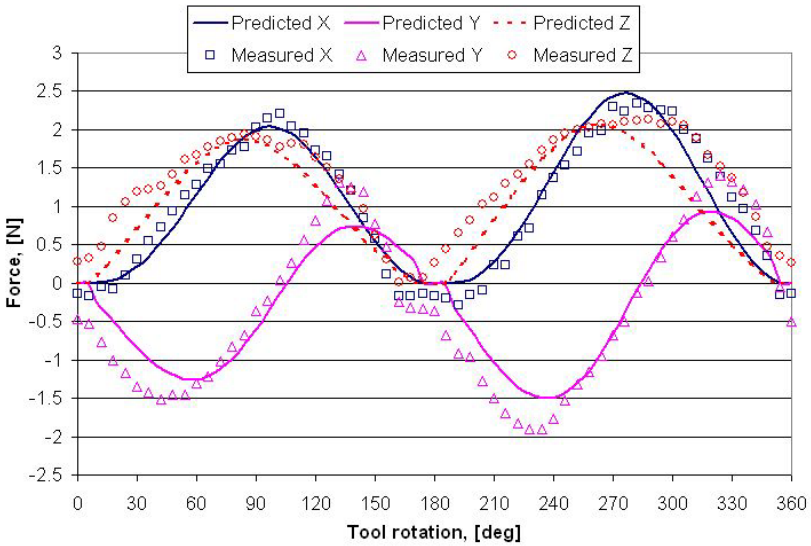

Figure 35. 6061 Alum - Measured and Predicted Machining Forces. Depth = 75 µm, Feed = 300 mm/min, Spindle Speed = 10,000 rpm, Tool Tilt = 10°, Wearland = 6 µm, Runout = 8 µm

Tool Tilted 25°

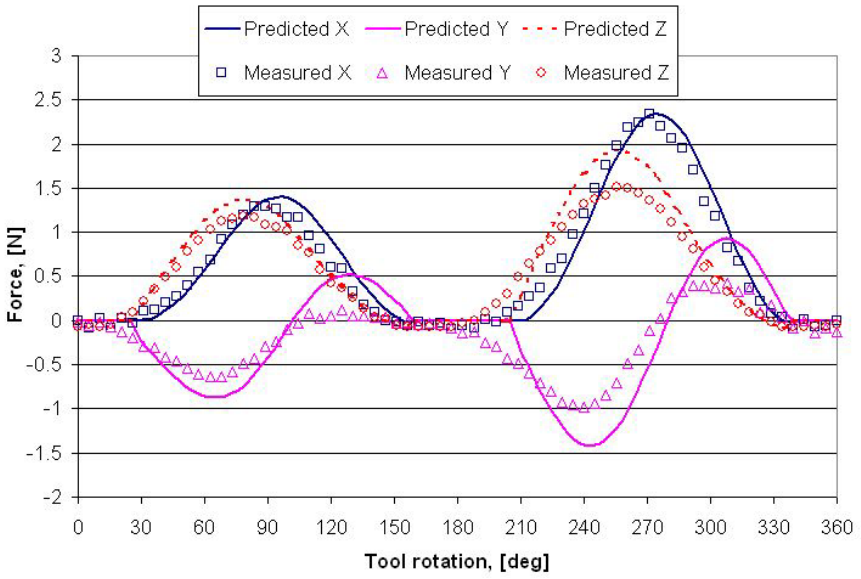

Figure 36. 6061 Alum - Measured and Predicted Machining Forces. Depth = 75 µm, Feed = 150 mm/min, Spindle Speed = 10,000 rpm, Tool Tilt = 25°, Wearland = 4 µm, Runout = 4 µm

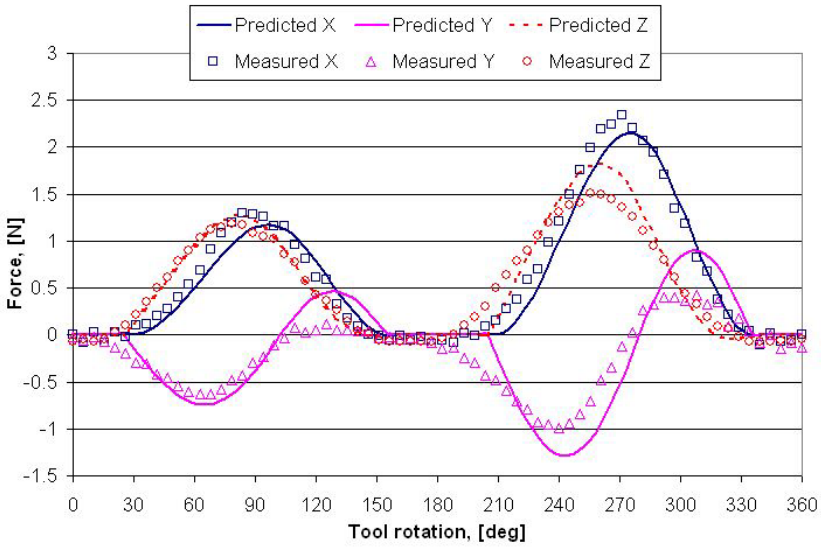

Figure 37. 6061 Alum - Measured and Predicted Machining Forces. Depth = 75 µm, Feed = 300 mm/min, Spindle Speed = 10,000 rpm, Tool Tilt = 25°, Wearland = 2 µm, Runout = 4 µm

10.4.4 REPEATABILITY

The validity of the force model is based on the assumption that the same conditions and cutting parameters will produce repeatable forces from cut to cut. The repeatability of cutting forces

was examined using a depth of 50 μm, a feed of 150 mm/min, and a tool tilt of 25°. Figure 38 illustrates the similarity of three consecutive acquired x-forces with identical parameters machined in 6061 aluminum. The same tool and experimental setup was used for the three consecutive grooves. Notice the extreme similarities in force magnitude and duration of cut for all three grooves.

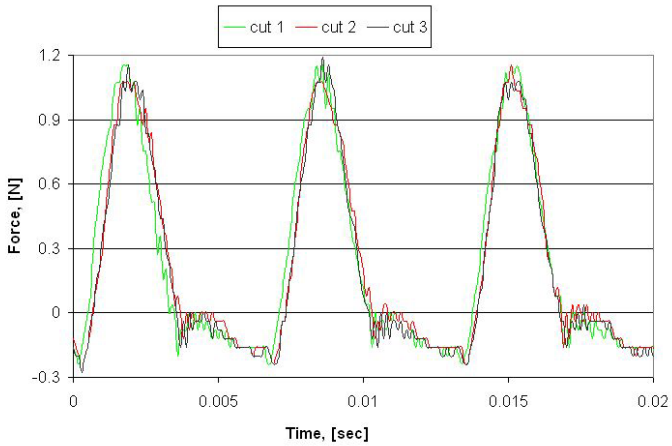

Figure 38. Measured X-Force for Three Identical Cuts

Figure 39 and Figure 40 respectively show the y and z forces for the same three cuts as Figure 38.

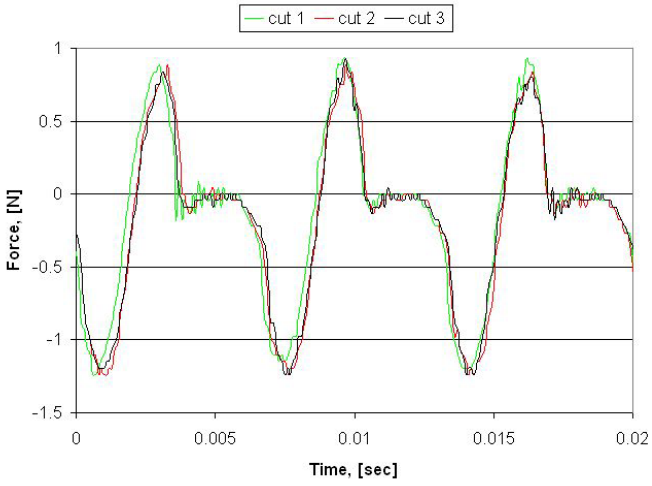

Figure 39. Measured Y-Force for Three Identical Cuts

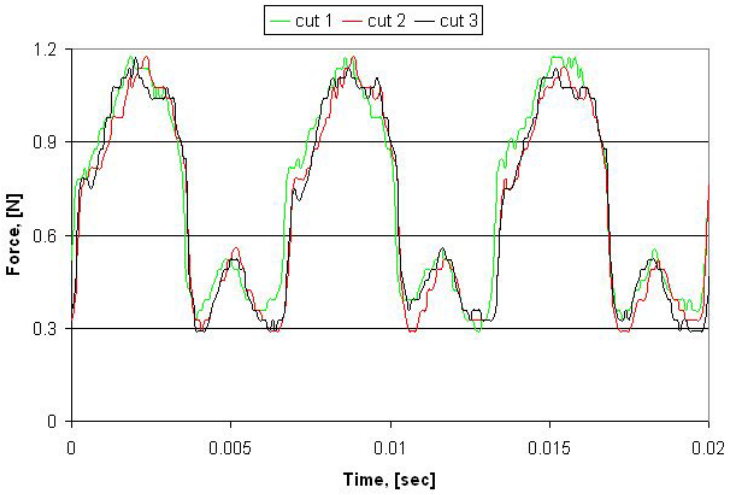

Figure 40. Measured Z-Force for Three Identical Cuts

Three different cuts were then made with the same parameters as above at a later time with a different tool and workpiece. However, identical procedures for setup and machining were conducted. The following three figures show that a change in tool and/or workpiece can cause some discrepancy in a series of similar cuts. There are really two main differences – 1) the y-force in the second set of grooves was approximately half the force of the first three cuts and 2) the z-force from the first set of cuts shows the second flute producing a small force while the z-force from the second set of cuts only shows one flute. However, the results from the two sets of groove are repeatable. The differences can possibly be attributed to the production of the cutting edges.

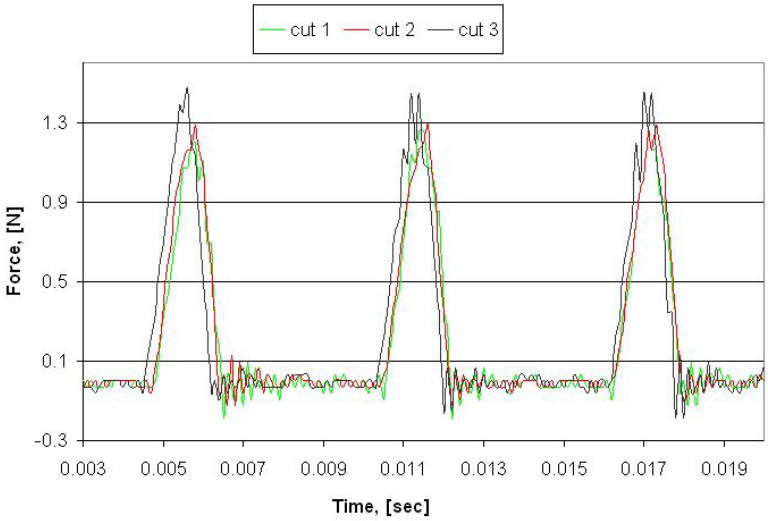

Figure 41. Measured X-Force for Three Identical Cuts

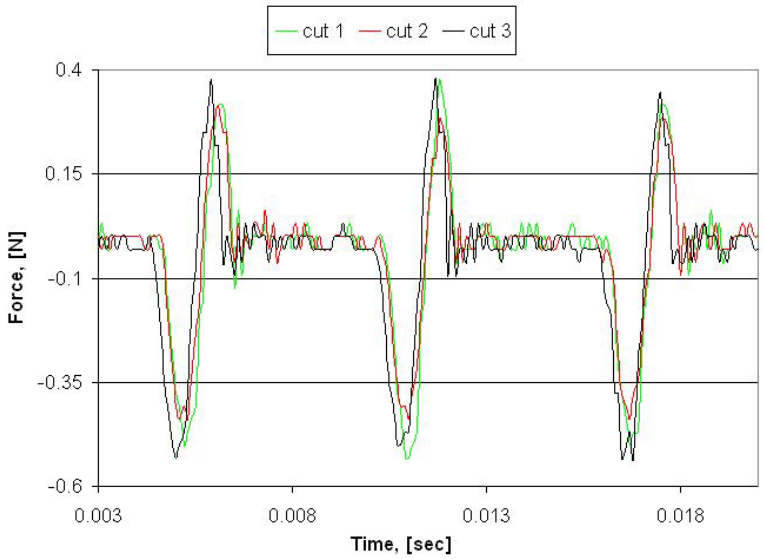

Figure 42. Measured Y-Force for Three Identical Cuts

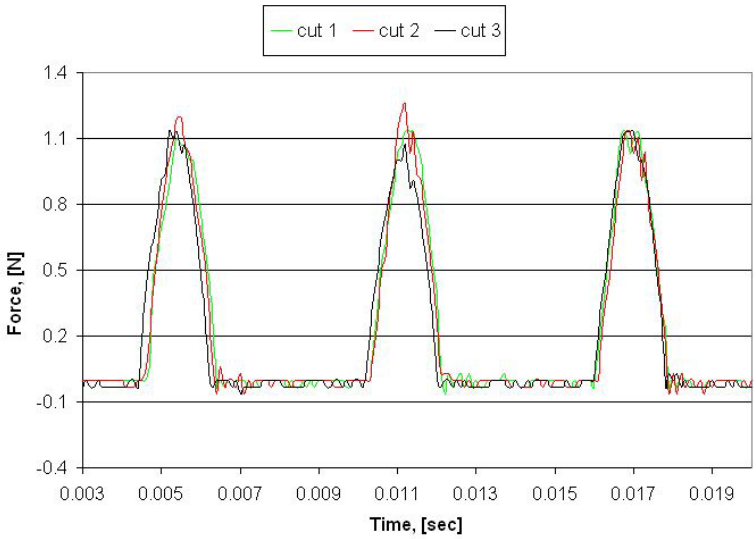

Figure 43. Measured Z-Force for Three Identical Cuts

10.4.5 DISCUSSION OF RESULTS

The force model requires a number of input parameters and material properties. Such inputs include machine parameters – depth, feed, and spindle speed; tool/spindle properties – radius, wearland, tilt, and runout; and material properties – hardness, modulus, shear angle, and friction coefficients.

Now that the cutting force model has been verified for a series of materials, tool tilts, and chip areas, it is important to understand the method and reasoning behind the modeling parameters. Figure 44 is a screen capture of an Excel worksheet environment for an aluminum simulation used to predict a cutting experiment and shows a detailed layout of the force model parameters.

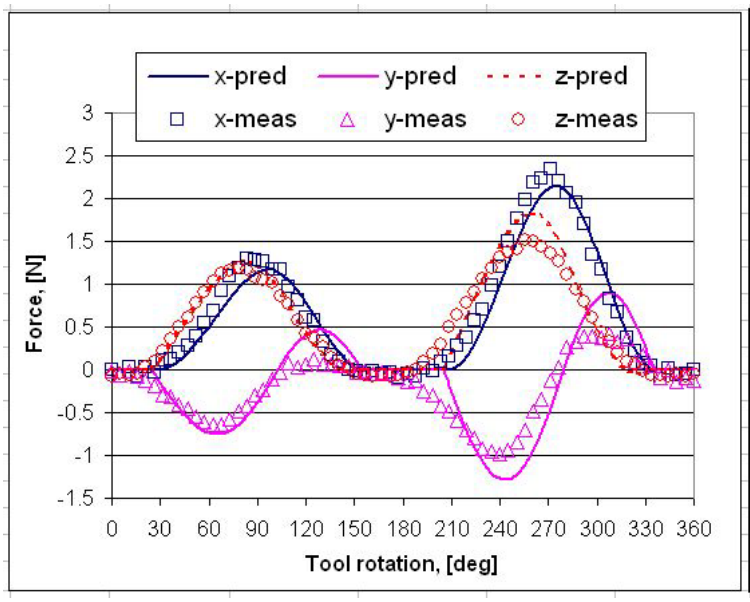

denotes INPUT		
Variable Factors		
Wear land	2.0	microns
Hardness	2.5	GPa
Runout	30	percent
Friction rake	0.46	
Friction flank	0.46	
Cutting Parameters		
Depth of cut	70	microns
Feedrate	300	mm/min
Spindle speed	9000	rpm
Tool tilt	25	degrees
Feed/flute	16.7	microns/flute
General Properties		
Modulus	70	GPa
Tool radius	400	microns
Contact angle	0.60	radians
Shear angle	50	degrees
K1	1.18E+09	Pa
K2	1.92E+09	Pa
Duty Cycle	72.41	percent

Figure 44. Screen Capture of Excel Worksheet

Volumetric Work vs. Hardness

Volumetric work can be defined as the work necessary to deform a material elastically and plastically to the point of failure. The definition of volumetric work suggests it is related to the area under a stress-strain curve and is also a measure of a material's ductility. This area is a function of a material's yield strength, tensile strength, and elongation to failure. Figure 45 is a plot showing a linear approximation of the stress-strain areas for the three materials being analyzed in this research. Although hardness has been used to describe and predict cutting forces, it may not be the most appropriate term, because it is only a function of strength. In other words, volumetric work (not hardness) can account for the energy to begin chip formation plus the energy needed to strain the material until failure.

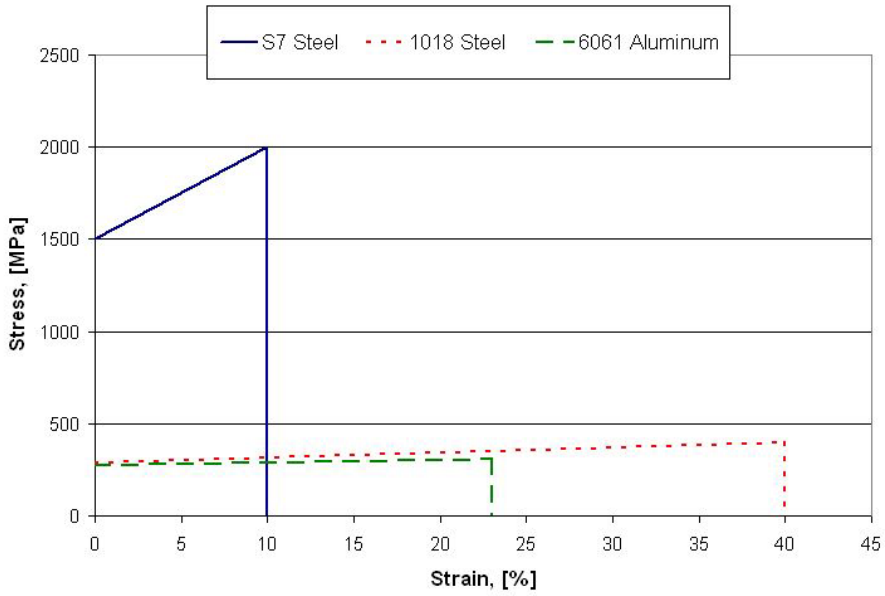

Figure 45. Area Under Stress-Strain Curves

Studies were conducted comparing both stress-strain area and hardness ratios to the empirical model parameter ratios. Figure 46 shows the comparisons of these ratios and confirms the model parameter ratios were better correlated to the area under the stress-strain curve and not the measured hardness.

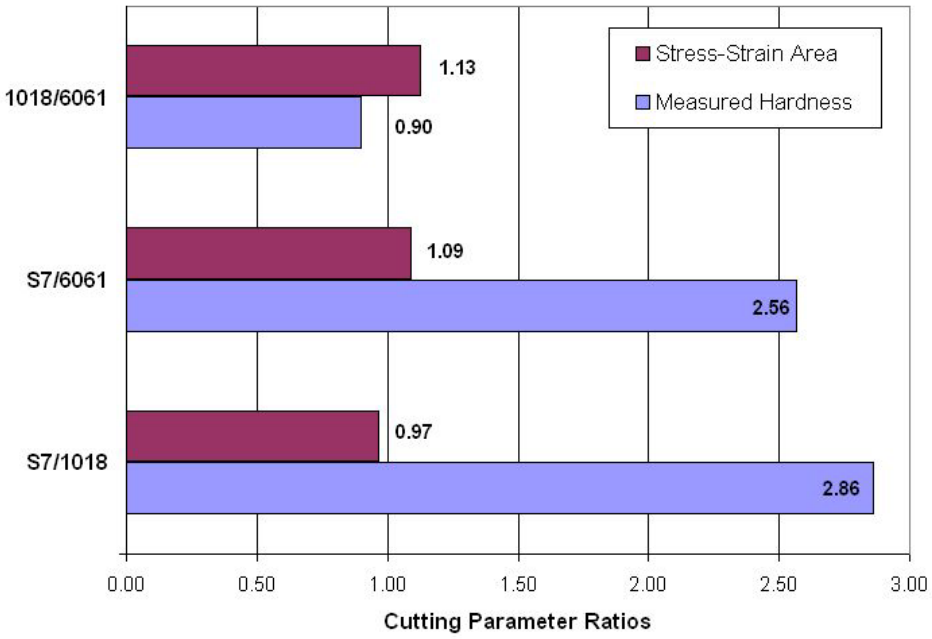

Figure 46. Stress-Strain Area and Hardness Ratios Compared to Model Parameter Ratios

Table 7 is a summary of the material properties used to verify the cutting force model parameters. These parameters were then used to simulate predicted cutting forces.

Table 7. Cutting Force Model Summary of Results

	S7 Steel	1018 Steel	6061 Aluminum
Modulus, E (GPa)	210	210	70
Friction Coefficient, Rake	0.5	0.75	0.46
Friction Coefficient, Flank	0.5	0.75	0.46
Measured Hardness (MPa)	6710	1760	1090
Empirical Hardness (MPa)	6000	4500	2500
Volumetric Work (Area) (MPa)	175	136	67

10.5 FORCE-FEEDBACK MACHINING

With the cutting force model developed and verified, predicted forces can be used to compensate for tool deflection by means of tool path manipulation. There are two options for force-feedback machining – 1) measure forces acting on the workpiece from the tool or 2) measure forces acting on the tool from the workpiece. The only difference between the two options is the placement of the force sensor.

10.5.1 DESIGN SPECIFICATIONS

A system that can operate independently and properly alter a tool path is desired, because no changes are needed to existing machining operations such as workpiece mounting or axis operation. This system must include a force sensor (such as a piezo-electric load cell used in the previous research), actuator, controller, and power supply. Figure 47 is a Pro/Engineer model of an actuation system that can manipulate a tool path in one dimension. By summing moments about the piezo centerline, the force measured by the load cell will be proportional to the force acting on the tool given by the known lever arms. The spindle collar on the right hand side of Figure 47 was designed to be compliant in the actuation direction and stiff in every other direction. The preload plate simply secures the spindle to the piezo by means of a maximum preload force of approximately 100 N. A 100 N preload allows the spindle to actuate at 250 Hz.

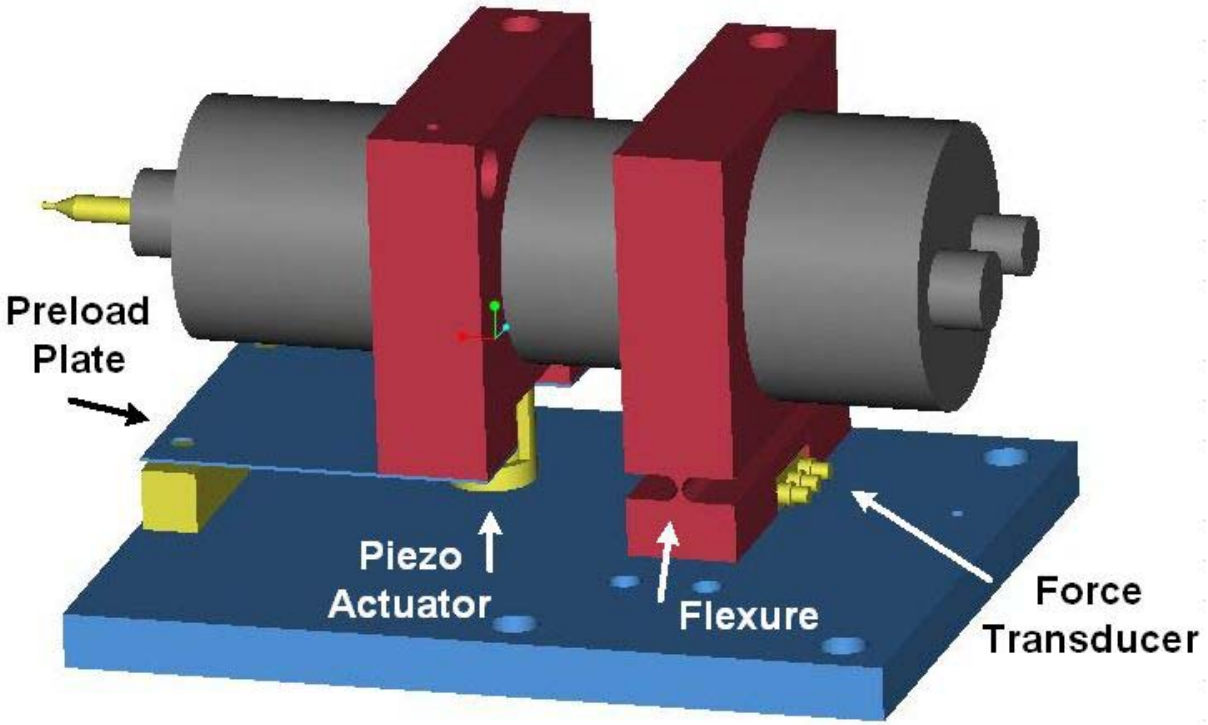

Figure 47. Solid Model of Piezo-Actuated Spindle

A piezo-electric actuator was selected due to its large stiffness and high bandwidth. The piezo-actuator chosen for this application has a maximum stroke of 15 μm, a stiffness of 400 N/μm, and can exert an actuating force up to 4,500 N. With proper placement and using the concept of mechanical advantage, tool deflections up to 40 μm can be compensated with this piezo. The load cell, which was described in Section 10.3.2, was also selected for its stiff structural properties and familiarity. The load cell/charge amp settings provide a sensitivity of around 0.04 N, which are more than enough for tool path alteration purposes. One final component other than the structural items needed is a displacement sensor. A capacitance gage was selected to monitor the actuation for closed-loop control purposes and will be mounted in line with the piezo actuator. The capacitance gage is an ADE Microsense 3401 with an output of 400 mV/μm. The spindle system has a natural frequency of approximately 160 Hz.

10.5.2 CONTROL STRATEGY

Now that a system has been designed to allow depth control by means of piezo actuation, some control issues need to be addressed. A DSP controller with a 100 kHz sampling rate will be used. There will be 2 analog inputs and 1 analog output for the board to control. The controller will also be responsible for some force filtering to obtain an overall average force signal. An example of an appropriate filter may be a running average or a digital filter with a specific lead coefficient. The controller will be responsible for filtering the measured forces, calculating a new setpoint, and providing a proper voltage signal to the piezo. This average force will then be

compared to the predicted force for that position of the tool path, which will result in some amount of error. The idea of closed-loop control is to drive that error to zero. When the error does become zero (theoretically), the forces will be equivalent and the workpiece feature should be accurate. However, feature accuracies can only be obtained if the forces are predicted properly, which previous sections have demonstrated is not a trivial task. Figure 48 is a block diagram of the control algorithm needed to properly perform force-feedback machining.

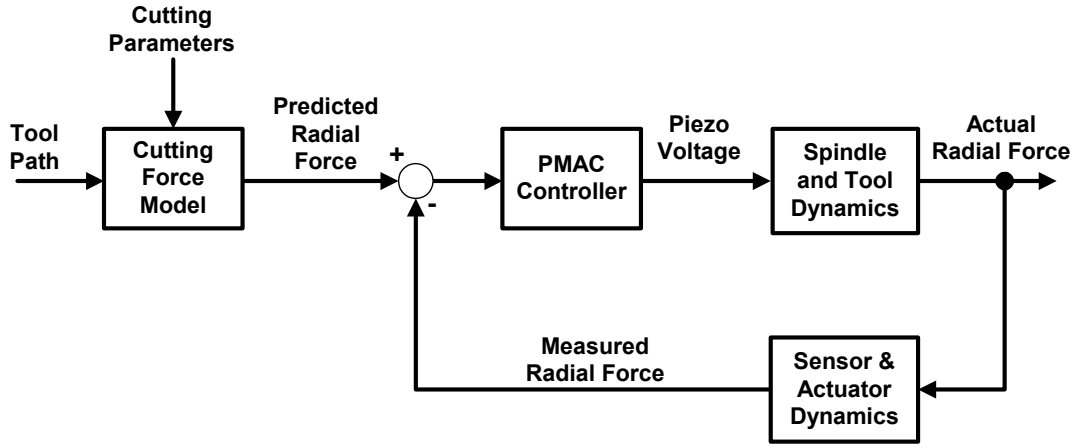

Figure 48. Force-Feedback Block Diagram

Although a proven force model has been developed for a variety of milling materials, there is another application for the piezo-actuated spindle system that does not involve force modeling. This application involves a stiffness-based feedback algorithm and can be found in Figure 49. The idea was introduced in Section 10.1 and assumes that the tool path and part are known precisely. This, however, is common in the machining process. Features are often desired on a part that has previously been faced on the same machine without workpiece movement. In this case, the part geometry is indeed known. For applications similar to those mentioned above, stiffness-based deflection compensation should be sufficient and more accurate. The idea is to monitor the actuation of the spindle with a displacement sensor, such as a capacitance gage. By measuring the radial force, knowing the radial tool stiffness and the actuated position of the tool, deflection errors can be minimized. This process should correct for tool deflection without the need for material properties, cutting parameters, or tool properties. Requirements only consist of a properly measured force, displacement, and radial tool stiffness.

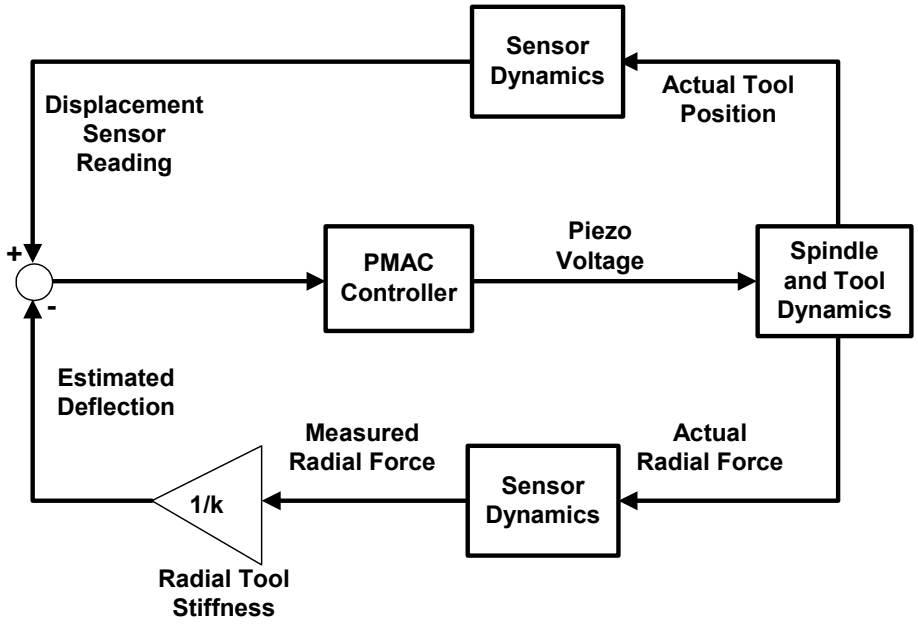

Figure 49. Stiffness-Based Block Diagram

Experimental testing will be conducted on the complete assembly of the piezo-actuated spindle system. The two control algorithms – model and stiffness based compensation – will be implemented and compared along with open-loop testing results. Open-loop testing consists of predicting tool deflection prior to machining by means of a force model and altering the tool path in the machine program. The three control strategies will be conducted and presented in future work.

10.6 CONCLUSIONS

It is evident that a cutting force model can be effective for predicting milling forces with miniature ball end mills. However, the cutting force model is comprised of numerous uncertain machining parameters such as material hardness and friction coefficients, tool runout, and tool wearland. Tool runout and wearland can be approximated with the aid of an electronic indicator and a light microscope. On the other hand, material hardness and friction coefficients were discovered empirically in the development of the force model.

It has been shown that predicted forces for a number of materials and machining parameters can approximate measured force data. Results have demonstrated that experimental data for S7 steel, 6061 aluminum, and 1018 steel can be predicted with the cutting force model with varying tool tilts, upfeeds, and chip areas. Since cutting forces can now be accurately predicted in typical machining metals, parts and molds can possibly be produced faster and cheaper. Force modeling now has the ability to introduce the machining industry to force-feedback machining. With the

addition of closed-loop cutting, part features and accuracies can be attained with only one machining pass. This development can be crucial to the injection molding industry where tool deflection is a major problem when machining hard steel dies. Deflection compensation and other applications can be improved with force-feedback machining and proper force modeling.

REFERENCES

1. Drescher, J., "Tool Force Measurements in Diamond Turning", MS Thesis, North Carolina State University, 1989.
2. Drescher, J., "Tool Force, Tool Edge and Surface Finish Relationships in Diamond Turning", Ph.D. Dissertation, North Carolina State University, 1991.
3. Arcona, C., "Tool Force, Chip Formation, and Surface Finish in Diamond Turning", Ph.D. Dissertation, North Carolina State University, 1996.
4. Miller, E., "Deflection Prediction and Error Correction of High Speed Miniature Milling Tools", MS Thesis, North Carolina State University, 2000.
5. Wonnacot, R. J., and Wonnacott, T.H. Statistics: Discovering Its Power. NY: John Wiley & Sons, 1982.

Appendix A

X DIRECTION		
	Voltage Difference [V]	Calibration [N/V]
Trial 1	1.74436	5.62384
Trial 2	1.73401	5.65741
Trial 3	1.73124	5.66646
Average	1.73654	5.64918
Standard Deviation	0.00691	0.02245

Y DIRECTION		
	Voltage Difference [V]	Calibration [N/V]
Trial 1	-1.80369	-5.43886
Trial 2	-1.86891	-5.24906
Trial 3	-1.84585	-5.31462
Average	-1.83948	-5.33302
Standard Deviation	0.03307	0.09640

Z DIRECTION		
	Voltage Difference [V]	Calibration [N/V]
Trial 1	2.09519	4.68216
Trial 2	2.29919	4.26671
Trial 3	2.07766	4.72167
Average	2.15735	4.54725
Standard Deviation	0.12316	0.25204

Figure 50. Calibration Data for S7 and 1018 Steel

X DIRECTION		
	Voltage Difference [V]	Calibration [N/V]
Trial 1	2.14313	2.28871
Trial 2	1.88527	2.60175
Trial 3	1.77894	2.75726
Average	1.93578	2.53386
Standard Deviation	0.18728	0.23865

Y DIRECTION		
	Voltage Difference [V]	Calibration [N/V]
Trial 1	1.50516	3.25879
Trial 2	1.53593	3.19351
Trial 3	2.18102	2.24895
Average	1.74070	2.81783
Standard Deviation	0.38163	0.56513

Z DIRECTION		
	Voltage Difference [V]	Calibration [N/V]
Trial 1	2.33704	2.09881
Trial 2	2.47106	1.98498
Trial 3	2.27933	2.15194
Average	2.36248	2.07621
Standard Deviation	0.09836	0.08530

Figure 51. Calibration Data for 6061 Aluminum

11 CO-MOLDING PLASTIC OPTICS

David Gill[1]
Graduate Student
Thomas A. Dow
Professor
Precision Engineering Center
Department of Mechanical and Aerospace Engineering

Mold components and tools were designed to allow the co-molding of polymer meso and micro optics directly onto thermally stable substrates. Soda lime and quartz glass slides were selected as transparent substrates for comolding due to their low coefficient of thermal expansion, elastic strength, and availability. These substrates were cleaned using the JTB1-1-1 process developed for the integrated circuit industry. The slides were then coated with a silane solution and baked. Shortly after baking, the slides were inserted into the molding machine and polymer was injected onto one side of the substrates. The slide and co-molded polymer lens were then removed from the mold using a specially designed tool and allowed to cool to room temperature. As they cooled, most of the co-molded optics separated from the substrates across the majority of their area, even though stress calculations and other researchers' experience with silane coating suggested that the lenses should maintain adhesion. The best adhesion was obtained by injecting the polymer onto the glass and then allowing the polymer to cool slowly in the mold. This method appeared to leave the polymer fully adhered to the glass slide and shear tests found the adhesion to be stronger than the plastic lens. While few co-molded optical surfaces were successfully created, the concept is feasible and usable. Possible improvements involve the use of substrates with coefficients of thermal expansion closer to the polymer, polymer with a lower melting temperature and new techniques for cleaning and silane solution handling.

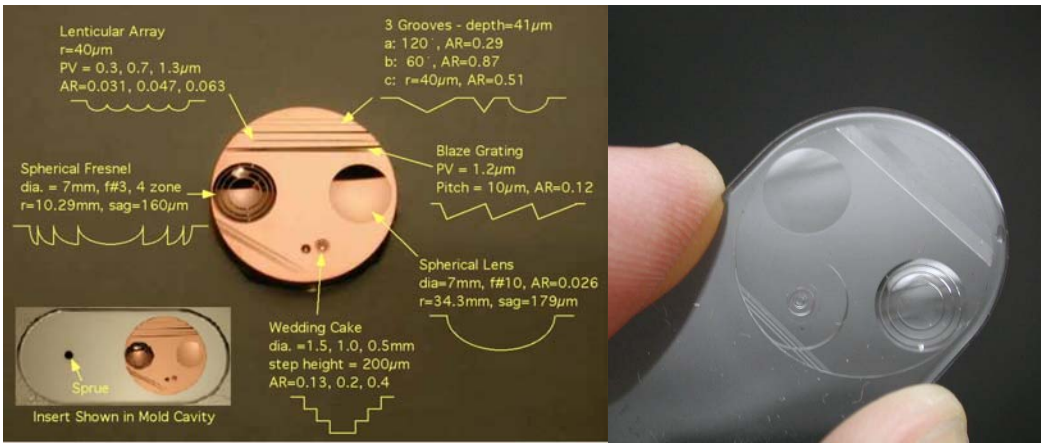

[1] Currently at Sandia National Lab in Albuquerque, NM

11.1 INTRODUCTION

Two challenges to the injection molding of precision optics are finding the conditions that could create good quality lenses in high production volume and molding on a stable substrate. The first challenge was met through increasing the understanding of the response of replication accuracy to molding factors in the injection molding of meso and micro optics. The second challenge to the acceptance of polymer lenses in precision micro optical applications was the need for thermal stability. The main problem is the high coefficient of thermal expansion of most optical polymers. This dimensional change becomes a serious problem in optics where even small changes in shape have large effects. This Section describes the background, challenges, solutions, and verifying experiments of a method of co-molding polymer optics onto thermally stable substrates. Co-molding of precision optics has not been reported using injection molding. The rewards of developing such a method are numerous, as are the challenges.

A significant challenge to substrate co-molding through injection molding is the difference in coefficient of thermal expansion (CTE) for the polymer and glass. Comparing the CTE for several optical polymers and optical glasses indicates that the polymer's CTE is approximately 10-100 times larger. When acrylic is injected onto the glass, the polymer is between 450°F and 520°F. From this point, it must cool to room temperature. Once the polymer passes the glass transition temperature, further shrinkage causes stress at the interface that attempts to break the adhesion and separate the polymer from the glass. If the bond does not separate, a large amount of stress could be locked into the polymer part. This stress, over time, can cause creep and a change in the dimensions of the optic.

11.1.1 MOLDING WITH AN INSULATED MOLD SURFACE

In conventional injection molding, both sides of the mold are carefully temperature controlled. The mold temperature was a significant factor in the replication of the blaze grating in the molding experiments. In substrate co-molding, the substrate is placed in the mold and acts as one of the mold walls. The substrate is not up to the mold temperature, and most substrates are at least somewhat insulative. The coefficient of heat transfer for glass ranges from 0.81 W/m K for standard soda-lime glass to 1.3 W/m K for Pyrex. Because the glass cannot reach the mold wall temperature before the polymer is injected into the mold (usually within 2 seconds of the glass being inserted into the mold), the mold cavity has one hot side and one cold side. Fortunately, the side with the optical features is the hot side, increasing the likelihood of filling the micro mold features. The polymer cools at different rates between the two mold cavity walls, causing internal stress in the part. Possible solutions include using extremely thin parts, heating the substrate prior to molding, or allowing the substrate to reach the mold wall temperature before injecting. Each of these solutions attempts to decrease the temperature differential

between the two materials, though only slightly, or to reduce the strength of the polymer, which will prevent the polymer from applying significant stress to the interface.

Substrate Handling The high pressure and high production volume of injection molding are not optimized for the utilization of brittle materials in the mold cavity. The clamping force of the Nissei molding machine is 69.0 KN, but larger industrial machines are often rated at 980 KN or greater with the largest machines developing 88 MN of clamping force. For the glass substrate to withstand this force, the surface supporting the glass must be very smooth, providing sufficient area to reduce the stresses on the substrate. The substrate must also be accurately positioned in the mold. The mold designed for this research uses two $^{1}/_{8}$" dowel pins to position the height of the substrate so that it spans the mold cavity.

A system for securing the substrate against the positioning pins in the mold was developed for this research as well. The system uses a spring-loaded pivot arm to press the glass against the locating dowels and back into the mold wall as is shown in Figure 1(a).

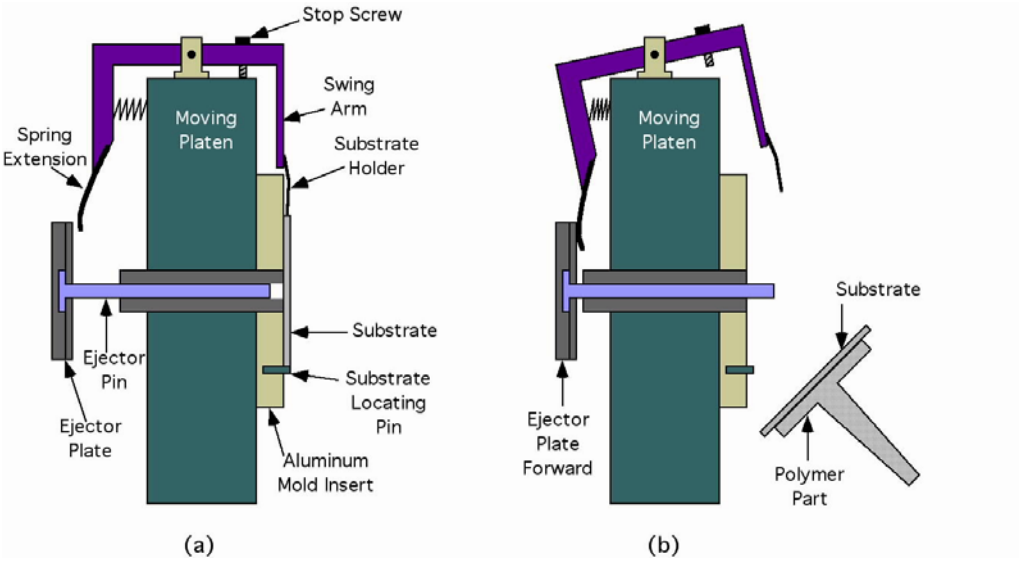

Figure 1. Side View of Mold with Substrate Holding Mechanism Shown (a) Holding the Substrate and (b) Ejecting the Co-Molded Part

The swing arm contacts the top of the substrate and presses inward and downward. The swing arm has a spring-steel extension that contacts the ejector plate in the plate's forward position. This spring extension releases the substrate just as the ejector pin comes forward to push the substrate out of the mold and into the parts chute as is shown in Figure 1(b). A stop-screw prevents the arm from swinging into the cavity if no substrate is present, and a clearance slot in the fixed side of the mold clears the swing arm and allows the mold to close fully with or without a substrate. This system permits the mold components to be brought into equilibrium by

molding polymer parts with no substrates. Then, substrates can be added when the mold has reached equilibrium.

In this research, the substrates were put into the mold by hand each time. In a production system, a pick-and-place robot could be used to place and remove the substrate optics from the mold. Systems such as this are common in industrial molding where the parts must be removed from the mold and not allowed to fall down the parts chute.

Part Features in the Fixed Side of the Mold In most molding applications, the mold features are in the moving side of the mold. When the mold opens, the molded polymer part is likely to stick in the side of the mold that has the most features. Figure 2 shows the options of molding on the fixed or the moving side of the substrate. It is desirable that the part stick to the side of the mold that has the ejector system, the moving side, so that the power of the ejector can be used to remove the part from the mold. This configuration is shown in Figure 2.

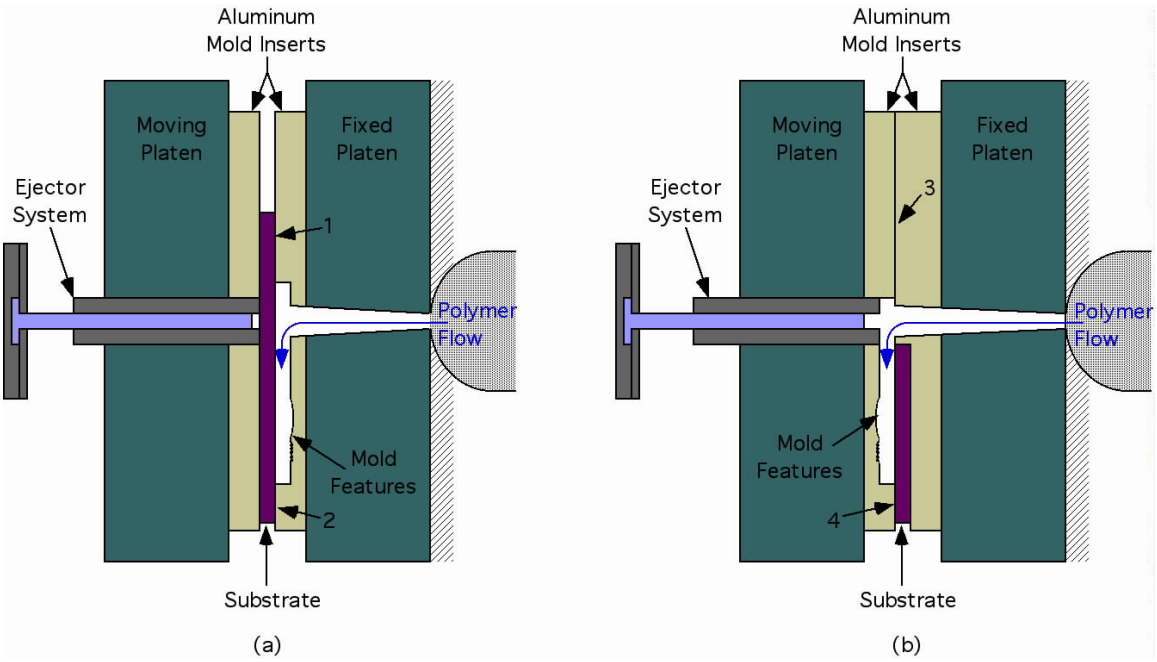

Figure 2. Top Views of Co-Molding on the (a) Fixed and (b) Moving Side of the Substrate

For this research, however, it was not possible to have the mold features on the moving side of the mold because of the placement of the substrate. The polymer must be injected on the fixed side of the mold, and it was determined that the polymer was unlikely to flow through a runner onto the far side of the substrate and along the moving side of the mold. Additionally, the fixed side of the mold would be required to fully contact both the substrate, seen at location 4 in Figure 2(b), and the moving-side's aluminum mold insert, seen at location 3. For this contact to occur, the thickness of the substrates would need to be held to a tight tolerance. Glass producers were

contacted about this requirement and most were only willing to promise a $^{\pm}$100μm tolerance on nominal thickness and only at significant expense.

The alternative was to place the mold features on the fixed side of the mold. In this configuration, shown in Figure 2(a), the mold cavity is formed by the fixed mold insert contacting the substrate at locations 1 and 2. This contact occurs regardless of the thickness of the substrate, instead requiring only that the substrate surfaces be relatively flat and parallel. The parallelism requirement is, in fact, less stringent than might be imagined due to the compliance of the sleeve bearings on which the platen rides on the tie bars. This compliance allows some non-parallelism between the platens. A requirement of the fixed-side molding configuration is that the mold inserts and features be designed so that the part can free itself from the mold upon cooling. This is necessary since the part is to travel with the moving mold plate when the mold opens. This goal was achieved by avoiding undercut features and by attempting to design relief angles into the mold features so that few feature surfaces were perpendicular to the surface of the substrate. The blaze grating was positioned so that the step features were angled to help the cooling polymer to draw back from the mold slightly. The edge of the mold cavity was rounded to help the part release from the mold and the sprue was polished and tapered to help the replicated polymer part release from the fixed side of the mold.

11.2 ADHESION OF PLASTIC ON GLASS

One of the most significant issues was not detailed above; that is the adhesion of the polymer to the glass substrate. To best understand this problem, a brief introduction to adhesion and the surface free energy theory of adhesion follows. Through this explanation, many of the important factors of adhesion will become evident.

11.2.1 ADHESION AND THE SURFACE ENERGY THEORY OF ADHESION

The phenomenon of adhesion occurs when two materials are held in contact by mechanical, electrostatic, or molecular forces. The adhesion of the materials is affected by many factors including the type of bond, condition of the two surfaces both from contamination and surface roughness aspects, surface energies, contact angles, spreadability, wettability, viscosity, internal stresses, surface density, and boundary layer strength of the two surfaces. These factors are presented below through the development of the adhesion process. This process is complicated and different theories have been proposed to explain the adhesion process. While the description below is not a rigorous one, it highlights some of the more important aspects of adhesion and the governing equations.

Adhesion Terminology and Definitions A few definitions are necessary for the discussion of adhesion.

- Adhesion – A phenomenon where two surfaces are held together by interfacial forces of attraction.
- Adhesive – A substance capable of holding materials together by surface attachment.
- Adherend – A body that is held to another body by an adhesive.
- Substrate – A material upon the surface of which adhesive is spread.
- Apparent Contact Area – The area of two overlapping surfaces as determined by the dimensions of each(e.g. length times width of overlapped area).
- Real Contact Area – The area of two materials that are within 3Å of each other, causing them to be pulled into contact by Van der Waals forces.

11.2.2 SURFACE ENERGY THEORY OF ADHESION

The surface energy theory of polymer adhesion assumes that the primary factor controlling the adhesion of materials is the surface energy. All of the other factors are either due to the surface energies of the adhesive and adherend, or are important because of the means by which they increase or overcome the materials' surface energies. Firstly, the surface energy of a material is due to the microscopic electrical (primarily Van der Waals) forces of molecules near the surface of a material. These microscopic forces produce a macroscopically measurable force perpendicular to any line lying on the surface of the material. This force, divided by the length of the line, gives the surface energy. A term that is used interchangeably with surface energy is surface tension, although surface tension only applies specifically to liquids. Van der Waal forces drop by approximately the inverse of the distance from the surface raised to the 7^{th} power causing adhesion to occur only at points where two surfaces are within 3Å of each other. When two objects are brought together, the high points of the surfaces experience adhesive bonding, but the real contact area of these tiny regions is so small that the macroscopic force is negligible.

When a force is applied to the two materials, compressing them together, the real contact area is increased and the adhesion can be felt as friction when a shear force is also applied to the materials. If the compressive force is released, the elastic recovery of the surface roughness peaks overcomes the attractive forces of the surface energies, forcing the materials apart and reducing the real contact area. If the materials are again placed under the compressive force and moved such that the so-called "ploughing force" plastically deforms the material, it is possible to reduce the elastic forces enough such that the materials remain adhered together through the process of cold or friction welding. It is possible that the ploughing force actually causes energy release from elastic hysteresis instead of actual plastic deformation. In either case, the force necessary to shear the junctions that were formed at the regions of real contact is the force labeled as the friction force. Because this force is dependent on the real area of contact and not

the apparent area of contact, friction force is generally seen to be independent of (apparent) contact area.

A conclusion of great importance can be deduced from the requirement that the surfaces have areas within 3Å of each other to achieve adhesion. The cleanliness of the surface is paramount. Even very high surface energy materials do not bond if the surface is not clean. A low energy layer of dust or oxide even as small as one molecule in thickness can prevent adhesion from occurring.

11.2.3 THE WORK OF ADHESION

A good adhesive bond can be achieved if the real contact area is maximized without significant elastic stresses present that will break the bond. The theory of adhesion is a study of the maximization of this real contact area. A convenient means of achieving maximum real contact area is to apply a liquid that spreads over the whole surface, providing contact to all points on the surface. A quantity used to predict adhesion is W_a, the reversible work of adhesion per unit area. Though it is agreed that W_a is dependent on the surface energy of the adhesive and adherend, there are several theories as to the exact form of that dependence. Measuring W_a is difficult, so most measurements are done on the reverse process of removing the adhesive from the adherend. The basic agreement among all methods is that W_a gives a quantity that is much lower than the work required to remove the adhesive. Because of this, another quantity W_a^* is defined as the quantity of work per unit area to remove the adhesive.

An approximate value for W_a is

$$W_a = 2\left(\gamma_s \gamma_l\right)^{1/2} \tag{1}$$

where γ_s = surface energy of the substrate

γ_l = surface energy of the liquid

and both the substrate and liquid surface energies have many components

$$\gamma_{s,l} = \gamma^d + \gamma^h + \gamma^p + \gamma^{ab} + \ldots$$

d=Van der Waals, *h*=hydrogen bonding, *p*=polar, *ab*=acid-base

However, the inclusion of all of the extra terms in the free energy term may be unnecessary as the Van der Waals term is widely considered to be the controlling term. The other energy terms only apply when the materials are close enough that the Van der Waals forces can take effect.

11.2.4 FREE ENERGY AND YOUNG'S CONTACT ANGLE

In a contrasting approach, the value for W_a is based on the free energy and Young's contact angle. A drop of liquid on a substrate is shown in Figure 3 and defines Young's contact angle θ and the surface energies γ_{SL°, γ_{LV°, and γ_{SV° existing at the phase boundaries of the liquid at rest

and the ° symbol denotes equilibrium conditions. SV° and LV° are the solid and liquid in equilibrium with the saturated vapor respectively.

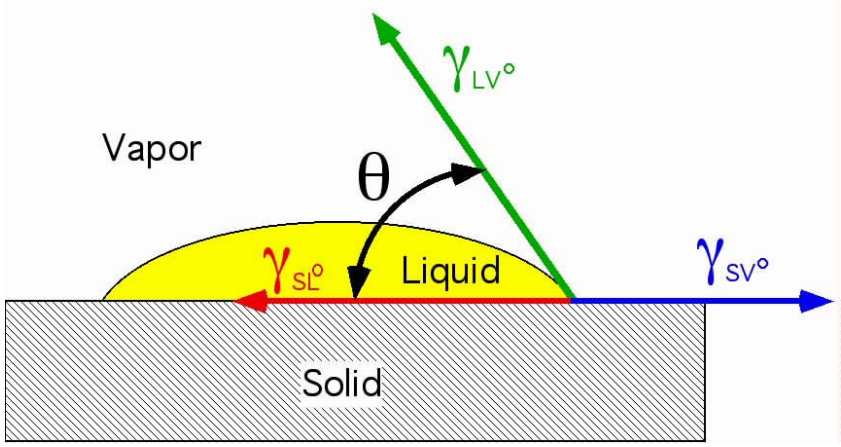

Figure 3. Contact Angle of Liquid Drop on Solid Substrate

Young's contact angle is an inverse measure of the spreadability or wettability of the liquid on the test surface. A contact angle of 0 means that the liquid is spreading, while a contact angle greater than 0 is a non-spreading liquid. The Young Equation describes the geometry shown in Figure 3 as:

$$\gamma_{sv^\circ} - \gamma_{sl} = \gamma_{lv^\circ} \cos\theta \tag{2}$$

The work of separation W_a^* has been shown to be

$$W_a^* = \gamma_{s^\circ} + \gamma_{lv^\circ} - \gamma_{sl} \tag{3}$$

where γ_{s° = equilibrium state of the solid in a vacuum

From this, it is seen that the ability of an adhesive to bond to an adherend is dependent on the surface energies of the solid, the liquid and vapor in equilibrium, and the solid and liquid in equilibrium. In fact, with further development, the work to separate the adhesive from the adherend becomes highly dependent on the surface energy of the solid and vapor in equilibrium as well. The vapor changes the apparent surface energy of the solid when the adhesive is removed.

11.2.5 Surface Roughness and Adhesion

The roughness of the surface also plays a part in the adhesion process. This is represented by the equation

$$r = \frac{\cos\theta'}{\cos\theta} \tag{4}$$

where r = a roughness factor for the surface of the solid
θ' = apparent contact angle
θ = actual contact angle

In practical applications, the roughness factor of a surface is 1.0 only if the roughness is less than 3Å so that the entire surface is within the active range of the Van der Waals forces and adhesion can occur across the entire surface. Fire polished glass is one of the few materials to achieve this surface finish. Even carefully machined and ground metal exhibits r=1.5. Because of this, the roughness exaggerates the actual contact angle in almost all cases.

Spreadability and Adhesion: Cooper developed a quantity S to signal whether a liquid would spread on a solid. If S>0, the liquid spreads, but if S<0, the liquid is non-spreading. The spreadability S is defined as

$$S = \gamma_{s^\circ} - (\gamma_{lv^\circ} + \gamma_{sl}) \tag{5}$$

but for organic liquids on organic surfaces,

$$\gamma_{sl} << \gamma_{lv^\circ} \tag{6}$$

The spreadability then becomes:

$$\begin{aligned} &S = \gamma_{s^\circ} - \gamma_{lv} \\ &or \\ &\gamma_{s^\circ} > \gamma_{lv} \end{aligned} \tag{7}$$

Therefore, for spreading to occur, the surface energy of the liquid must be less than the surface energy of the solid. Fortunately, the surface energy of liquids (except for metals) is less than 100 erg/cm^2 at room temperature, while the surface energy of solids is in the range $500<\gamma<5000$erg/cm^2 for hard solids including glass. Generally, as the hardness or melting temperature of a solid increases, so does the surface energy. One important caveat to the preceding values of surface energy is that solids have drastically lower surface energies if they adsorb liquid before adhesion is attempted.

From earlier discussion, it is apparent that the real contact area between the adhesive and the adherend must be maximized to achieve a good bond. Real surfaces have surface roughness from pores and cracks and it is desired that the adhesive penetrate and fill these pores and cracks. An equation describing the height of capillary fill, h, is

$$h = \frac{k\gamma_{lv^\circ}\cos\theta}{\rho R} \tag{8}$$

where k = a constant
ρ = liquid density
R = equivalent radius of the capillary

In the case of molten polymer, capillary filling also depends on the liquid not being so viscous that the capillary cannot be filled before the liquid cools below its glass temperature. It has been determined that the ability (Z) of the polymer melt to achieve an equilibrium contact angle can be written as:

$$Z \propto \gamma_{lv}(melt) \propto \frac{1}{\eta} \tag{9}$$

where η is the viscosity of the liquid. For injection molding, the polymer viscosity is affected by temperature and shear rate, making these factors have great importance in the success of adhesion as well.

11.2.6 CAUSES OF INTERFACIAL STRESS IN ADHESION

Often, the adhesive is applied in a liquid phase, but later cures, cross-links, or cools to a solid phase. In the ideal case, this is not a deterrent to sustaining adhesion because the adhesive bond is only 1 molecule deep. Except for any change in density or molecular orientation, the adhesive bond would be formed with the materials exhibiting the same surface energies as in the liquid phase. In reality, however, the change of phase usually causes the development of localized stress and stress concentrations. The most common cause for this stress is the difference in the coefficients of thermal expansion for the adhesive vs. the adherend. The introduction of internal stress considerably reduces the strength to a point well below the theoretical strength of the bond. There are many causes of stress concentrations in the material that magnify the effects of the internal stress. Any air pockets between the adhesive and adherend, in unfilled pores for example, act as a stress concentration. Higher values of contact angle cause higher stress concentration. It is expected that it is better to have small, high frequency, spiked roughness than relatively low frequency undulations. This is due to the propagation of cracks under stress. If the cracks are sharp and close together, one may act as a stress concentration, fracture, and propagate to the next crack, causing the radius to become larger and freeing only a small portion of the adhesive bond. Low frequency pores may cause cracks that propagate long distances parallel to the bond plane, greatly reducing the strength of the bond. The introduction of high frequency cracks is hypothesized by some to be the mechanism behind increasing bond strength by "roughing" materials before applying adhesive, though roughness can also be explained as adding significant contact area.

The strength of the boundary layer is also important to the adhesion of materials. If the boundary layer of either the adherend or the adhesive is weak, it fractures, reducing the strength of the bond. Polymers with weak boundary layers are known to generally have low coefficients of friction. Polytetrafluoroethylene has very weak boundary layers, and a coefficient of friction of 0.05-0.1. Polyethylene, on the other hand, has very strong boundary layers and a coefficient of friction of 0.6-0.8. Poly(methyl methacrylate) and polystyrene are slightly lower with 0.4-0.5 as a range for friction coefficients. The source of additional adhesion produced by surface treatments has often been attributed to surface oxidation causing a wettable polar surface with extensive interfacial contact, but it may also be due to the treatment's ability to remove the weak boundary layer from the material.

It has been noted that polymer melt is often able to form adhesive bonds, while the same polymer in solid phase would not. It is proposed that any species contributing to weak boundary layers are rejected back into the bulk by the adherend surface while the polymer is still in the melt phase. Additionally, it is known that a higher surface density increases the specific energy of the polymer. For crystalline polymers, this higher surface density is found at the adhesion interface because of the tendency for polymer crystals to nucleate at contact points in the interface.

11.2.7 Challenges to the Surface Energy Theory of Adhesion

Earlier, it was noted that the surface free energy of solids was higher than that of liquids unless the solid surface had absorbed another liquid prior to the adhesive bond forming. In fact, the requirements for adhesion are even more stringent than previously suggested. The minimum surface energy of a completely dry solid surface is approximately 500 dynes/cm. Pluddemann [3] reveals that the surface energy of soda-lime glass in air at 1% relative humidity has dropped by a factor of 10 to an astounding 47 dynes/cm. Even more drastic is the drop in surface energy at 95% relative humidity to only 29 dynes/cm. This highlights the difficulty that even a monolayer of water molecules on a glass surface reduces the surface energy so drastically that permanent adhesion is nearly impossible. Unfortunately, a monolayer of water molecules forms on glass at only 0.1% relative humidity. Even if the glass is dried and the adhesion occurs at a lower relative humidity, prolonged exposure to any higher humidity conditions causes water to penetrate through the glass or through the polymer, and the adhesion is jeopardized. One approach to overcoming the challenge of adhering polymer to glass is through the use of a silane interface.

11.2.8 Surface Modification Through Silane Chemistry

Pluddemann [3] introduces organofunctional silanes by mentioning the two challenges that degrade adhesion: 1) water hydrolyzing bonds between inorganic and organic substances, and 2)

interfacial stresses due to mismatched coefficients of thermal expansion. The proposed solution to both of these challenges is a class of coupling agents known as organofunctional silanes, hybrid organic-inorganic compounds that overcome the above mentioned challenges. Silanes were first applied to the problem of adhering polymer to glass in the 1940's for use in fiber-glass reinforced plastic composites. Since that time, much study has helped to shed light on the coupling properties of silanes. The hypothesis given in Pluddemann is that silanes work because of their ability to use the hydrolytic action of water to relieve the stresses caused by thermal expansion.

This hypothesis is a unique perspective that balances the surface free energy theory with contrasting experimental results. For example, Bascom [1] and Lee [2] showed that silanes could be used to control the surface energy of glass, but the results were not as would be expected from conventional surface energy theory. They report on the adhesion of polyethylene to glass, a process that is generally thought to require a critical surface energy of 35 dynes/cm for the glass. Some silanes were able to achieve this critical surface energy, but the silane that performed best only yielded 28 dynes/cm. Bascom and Lee propose that the reactivity of the silane is more important than the polarity or surface energy of the materials. Because this evidence does not fully support conventional adhesion theory, it is necessary to further investigate silanes and their methods of surface modification.

Silane Chemistry The silane molecules which were chosen for this research consist of a silane functional group on one end for adhesion to the silicon in the glass substrate and an organically reactive end to adhere to the polymer. Silane depositions can typically be grouped into 3 categories based on their thickness and purpose. The first category is a "surface modifier" or "finish" layer which is one to several monolayers thick. The finish must chemically modify the surface without contributing any of its own mechanical properties to the bond. The second deposition is a "primer" or "size" composed of a 0.1μm to 10μm thick layer of silane. The primer layer should be thick enough to carry the stresses developed between the adherends. The third deposition method is an "adhesive" that must be thick enough to fill gaps between two solid adherends. The silanes used for this research were developed by United Chemical Technologies Inc. (Bristol, PA) and were deposited between 3 and 8 monolayers thick, qualifying as surface modifiers, so further details in this document will only involve this deposition method. In fact, it is a good approximation to develop the chemical model assuming a monolayer deposition, even though single monolayers are very difficult to achieve.

Arkles [5] presents the steps of the chemical reaction as is presented in Figure 4. The silane combines with water in a hydrolysis reaction forming a reactive silanol intermediate and methanol as a byproduct. The hydrolysis of the silanes used in this research occurred in a mixture of 95%(by weight) ethanol, 5% water, and then sufficient silane to produce a 2% concentration solution. The reactive intermediates then bond with each other in a condensation

reaction producing silanols and a water byproduct. In addition to reacting with each other, the silanols can bond with surfaces containing hydroxyl groups through hydrogen bonding as shown in Figure 5. The hydrolyzed silane is shown in Figure 5(A) with a reactive organic end labeled "R" and a hydrolyzed end that is ready to bond with the substrate. Figure 5(B) shows the silanols bonding to the glass surface through hydrogen bonding between silicon and oxygen atoms while the polymer coil has bonded to the organic reactive end of the silane. Figure 5(C) shows the reaction as it is nearly in its completed state. The silicon-oxygen bonds are inorganic bonds with a high degree of ionic character (50%). Some oxane bonding will occur at this interface too, having an even higher degree of ionic character. The ionic bonds are dependent on equilibrium constants and concentrations, and are reversible. It is important to note that the bonding of the silane to the surface does not cause a hydrophobic coating, but instead is a process dependent on the presence of water for bonding. Any water resistant properties of the substrate surface depend on the equilibrium condition of the bonds between the surface of the glass and the silane in the presence of water.

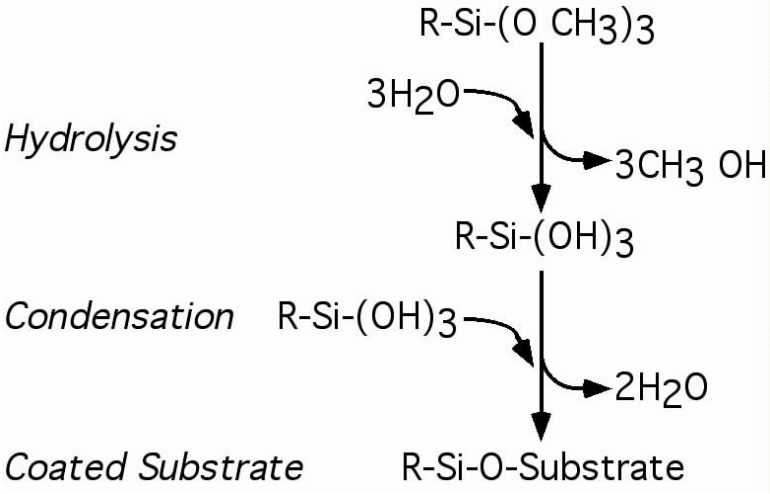

Figure 4. Chemical Reaction of Silane and Substrate

The organic reactive end of the silane molecules bonds with the polymer's organic molecules. The bonding between the silane and the polymer occurs in 3 ways. The first is through entanglement, in which the polymer coils physically entangle the reactive organic end of the silane. The second bonding method is through hydrogen bonding. The third method is through covalent bonding. Of these 3 methods, covalent bonding provides the most secure bond, hydrogen bonding next, and entanglement provides the least secure bond. One theory is that the bonding ability of entanglement is increased through a restrained layer. This theory predicts that maximum bonding and resistance to hydrolytic cleavage are achieved when the polymer near the interface has a modulus between that of the bulk resin and that of the glass. It is proposed that this increase in modulus occurs because the pressure applied during injection and bonding between silanols tightens the polymer structure at the interface and increases the holding power

of the interpenetrating networks. This tightening of the polymer coil is represented in Figure 5(B). The strength of the silane-polymer bond is also increased by the nature of covalent bond formation that is dependent on thermodynamics and kinetics in a competitive environment. An important attribute of covalent bonds is that they are not easily reversible.

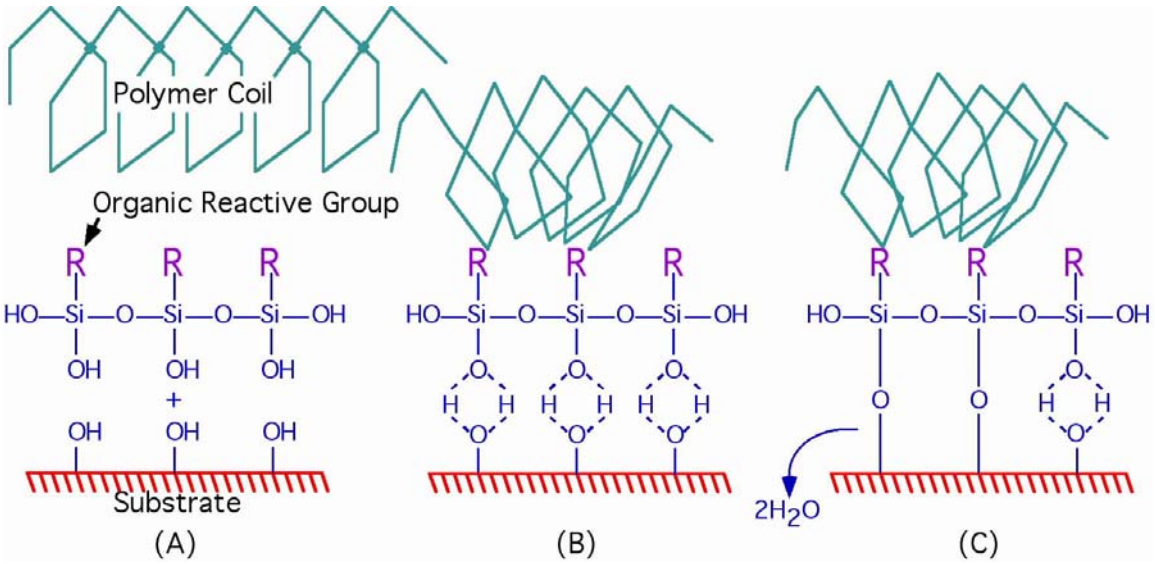

Figure 5. Silane Bonding of Polymer to a Substrate Shown (A) Before, (B) During, and (C) After Bonding Reaction Occurs (Adapted from [5])

When used as a surface modifier, it is assumed that the silane interface does not contribute any of its own mechanical properties to the interface. Tests show, however, that silane surface modifiers do have the ability to relieve stresses in the interface between polymer and a glass substrate while also maintaining the ability to adhere in the presence of water. Pluddemann [3] and other researchers suggest that this ability is due to the combination of the equilibrium dependent bond at the silane/glass interface and the rigidity of the restrained layer at the polymer/silane interface. The restrained layer prevents the silanols and the polymer chain from moving with respect to each other, while the reversible equilibrium bonding of the silanols and glass permits the breaking and reforming of bonds at adjacent sites. This theory neatly includes all of the abilities and requirements for silanol bond formation. However, for thermoplastic/silane systems, clear evidence of chemical reactions occurring between the silane and the polymer has not been found. Pluddemann completes his review of silanol chemical bonding with the following list of guidelines to achieve water resistant composite formation:

1. Use a polymer with low water absorption (permeability is not an important factor).
2. Use a water resistant substrate such as quartz.
3. Use the appropriate silane coupling agent.

Types of Silane Available Silanes can have many different molecular forms. For the adhesion of acrylic to glass, it was suggested by Dr. John H. MacMillan, Technical Manager for United Chemical Technologies, that 3 silanes be investigated (all products of United Chemical Technologies): A0397, an acryl silane, M8550, a methacryl silane, and T2507, an ureido silane. These three silane molecules are shown in Figure 6. Dr. MacMillan advised that M8550, a tri-methacryl organo-functional silane, had the greatest likelihood of providing the desired adhesion. The chemical name of this compound is 3-(Trimethoxysilyl)propyl methacrylate and has been assigned CAS#2530-85-0.

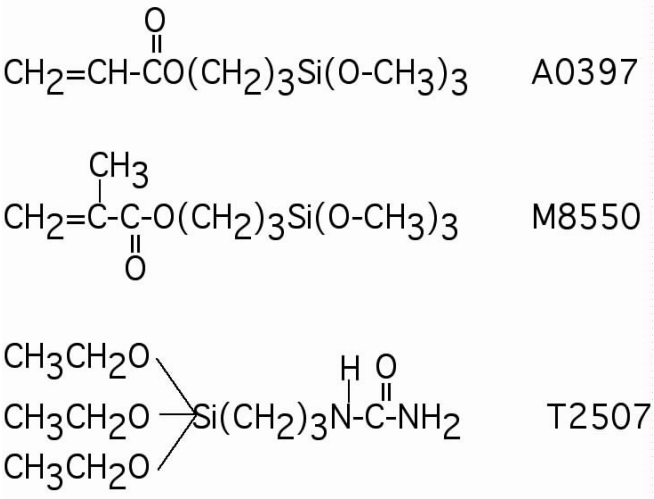

Figure 6. Three Silanes for Adhering Acrylic to Glass

11.3 METHODS OF MEASURING ADHESION

Whether bonding with silane or using conventional bonding practices (which follow the surface free energy theory), the value of W_a for adhesion is only useful as a tool for theoretical understanding. The quantity that is usually measurable is W_a^*, the work in breaking the adhesion between the adherend and adhesive. Obtaining a measurement of the effectiveness of an adhesive/adherend bond usually requires destructive testing. There are four basic types of stress encountered in structural bonding as shown in Figure 7.

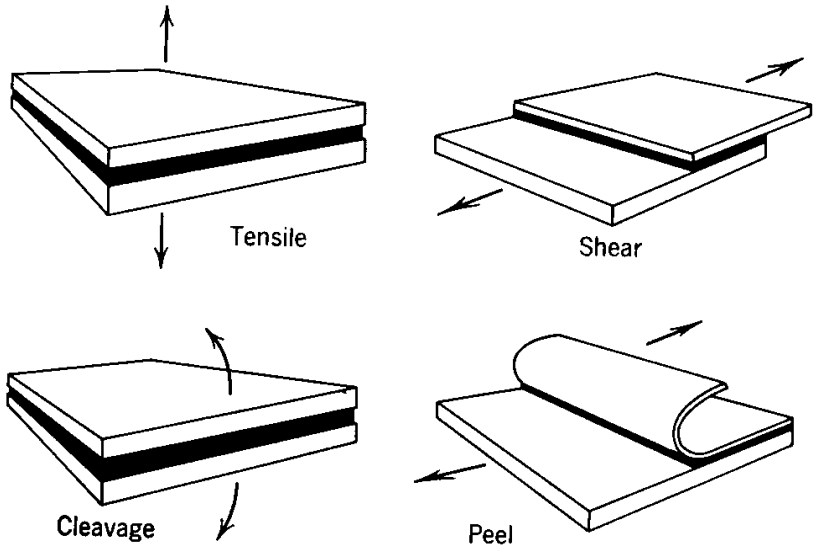

Figure 7. The Four Basic Types of Stress in Structural Bonding

The adhesive experiences loading distributed over different surface areas for the 4 types of stress. Tensile and shear loading subject the entire adhesive bond to the stress at the same time. Cleavage reduces the area of adhesive experiencing the maximum stress, and peel stress focuses the loading at a very thin line. For this reason, peel stress is used most often in an attempt to get values for W_a^* but requires that one of the adherends be flexible. When one of the adherends is not flexible, the shear test is used most often. The experimental setup for a shear test is shown in Figure 8 and a peel test is shown in Figure 9.

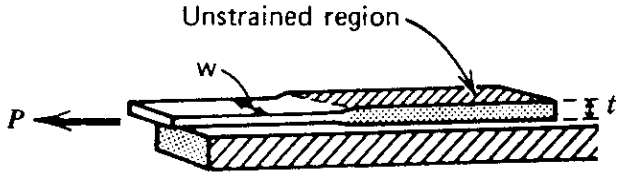

Figure 8. Lap Shear Test of Adhesion

The peel test is probably more useful for determining a number for the term W_a^* because the area over which the force acts is relatively constant throughout the test. The shear test, however, is quite useful for the injection molding of precision optics on substrates because of the ability to perform the test with no flexible adherends. This test shows whether failure is likely to occur first in the adhesive bonds of the polymer/substrate interface, or in the cohesive bonds of either the polymer or substrate materials.

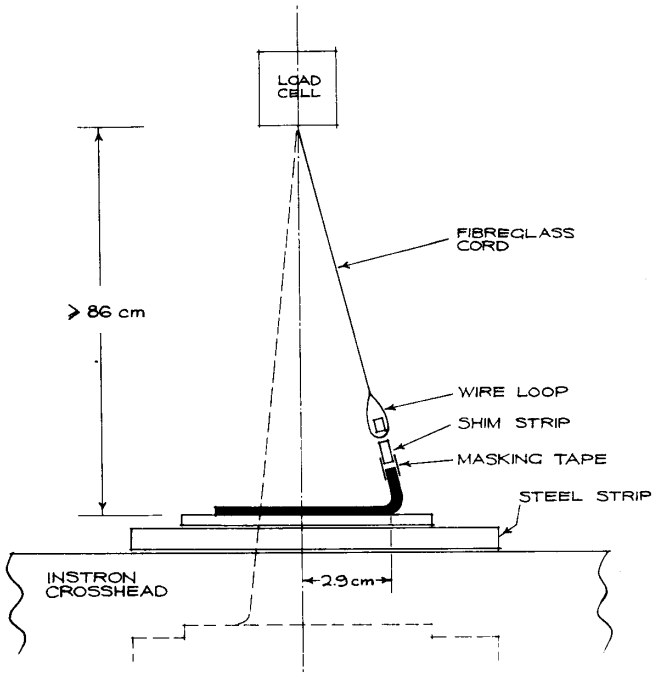

Figure 9. Experimental Setup for Adhesion Test Using Peel Stress

One method of measuring the quality of a bond is by determining the area of the surface that was wetted by the adhesive. A bond is formed between an adhesive and an adherend. The bond is then sectioned and polished and placed in an optical microscope. Any large voids may be seen at this level, but the true test of the surfaces being within 3Å must be done with a transmission electron microscope. For the optical test, however, it is often necessary to mix carbon black in the adhesive to differentiate between the adhesive and adherend. This method appears to be mostly qualitative and difficult to link back to any value for W_a^*. Coatings manufacturers use a test that drags a needle across the surface of the coating to see if the coating separates from the adherend. This method is another qualitative method with no means of determining a value of W_a^*.

Because silane adhesion is designed for use in the presence of moisture, a good test of silane adhesion is to soak the bond in water. In this test, a microscope slide is coated with silane and then the polymer is applied. The composite is placed in water either at room temperature or at an elevated temperature and the bond is rated by the length of time that the composite can be soaked before adhesion is lost. It is often the case that extremely good silane bonds will fracture the glass surface and separate carrying a layer of glass with the silane instead of fracturing at the interface.

11.4 CO-MOLDING STRESS ANALYSIS

Whether using silane surface modifiers to promote co-molding adhesion or some other method, it is important to have an understanding of the stresses that are expected at the interface between the polymer and glass substrate. Of primary concern are the peeling stress which attempts to peel one layer from the other, and the shear stress at the interface. It is also important to calculate the normal or axial stress internal to the body to check that none of the stresses are above the strengths of the polymer or glass. The shear and tensile stresses must not exceed the shear and ultimate tensile strengths of the polymer, and the peeling stress must be checked to see if the magnitude appears to be manageable.

The interfacial stresses, caused by the mismatch in the coefficients of thermal expansion between the polymer lens and the substrate, are difficult to determine due to the boundary conditions at the interface and free edges of the co-molded "sandwich". If the layers separate, the problem also takes on aspects of fracture mechanics as stress intensity factors must be used to model the crack tip. The solution of these difficulties is its own field of study and outside the scope of this work, however, several of the proposed solutions can be used as estimates of the stresses that might be present. These estimates must be used with caution, due to the simplistic nature of the solutions. Although there are several means of approaching the problem, solutions from two different methods were used here.

11.4.1 INTERFACE STRESSES BY THE THEORY OF ELASTICITY

An initial method of finding the interface stresses is a method that is consistent with the linear theory of elasticity. The description presented here follows a presentation by Dr. Barnett of the Materials Science Department at Stanford University. First, the induced thermal stresses in an N-layer elastic composite are found. Then a new temperature is selected and each layer is detached, the temperature is changed to the new temperature and the stress free length is determined. The length change for each layer is understood as a strain, so each layer is elastically deformed back to its original length. This creates a composite sandwich in which each layer is held to the length by a different externally applied stress. The layers are reattached and, because there are no end forces in the real problem, a resultant stress is found whose strain is such that there is no net axial force acting on any composite cross-section. However, the composite will have a resultant moment, causing a bending moment. The composite is modeled as a bending beam and the final residual axial stress is found in each layer based on an equilibrium radius of curvature.

Simplifications are then made with the assumption of a thin film layer on a very thick substrate, allowing semi-infinite solid solutions. However, this solution has no interfacial shear stress, so it is often solved as an infinite strip problem with periodic loading. The solution is then found

through the use of an Airy stress function, finally yielding the equations used in this approximation. The equations of the two-layer, thermal stress analysis, edge effect solution for a temperature change of ΔT are presented in Equations 11-15 with the geometry defined in Figure 10.

$$\sigma_{peel} = \sum_{n=1}^{\infty}\left\{A_n\left(\frac{n\pi}{L}\right)^2\cosh\left(\frac{n\pi y}{L}\right)+B_n\left[\left(\frac{n\pi}{L}\right)^2 y\sinh\left(\frac{n\pi y}{L}\right)+2\left(\frac{n\pi}{L}\right)\cosh\left(\frac{n\pi y}{L}\right)\right]\right\}\cos\left(\frac{n\pi x}{L}\right) \quad (10)$$

$$\sigma_{norm} = E(\alpha_s-\alpha_f)\Delta T + A_0 + \sum_{n=1}^{\infty}\left\{A_n\cosh\left(\frac{n\pi y}{L}\right)+B_n y\sinh\left(\frac{n\pi y}{L}\right)\right\}\left(\frac{n\pi}{L}\right)^2\left(-\cos\left(\frac{n\pi x}{L}\right)\right) \quad (11)$$

$$\tau_{xy} = \sum_{n=1}^{\infty}\left\{A_n\left(\frac{n\pi}{L}\right)\sinh\left(\frac{n\pi y}{L}\right)+B_n\left[\sinh\left(\frac{n\pi y}{L}\right)+\left(\frac{n\pi}{L}\right)y\cosh\left(\frac{n\pi y}{L}\right)\right]\right\}\left(\frac{n\pi}{L}\right)\sin\left(\frac{n\pi x}{L}\right) \quad (12)$$

where

$$A_0 = -E(\alpha_s-\alpha_f)\Delta T\frac{h}{L} \quad (13)$$

$$A_n = -\frac{L}{n\pi}B_n\left[1+\left(\frac{n\pi a}{L}\right)\coth\left(\frac{n\pi a}{L}\right)\right] \quad (14)$$

$$B_n = -E(\alpha_s-\alpha_f)\Delta T\left(\frac{4L}{(n\pi)^2}\right)\frac{\sinh\left(\frac{n\pi a}{L}\right)\sin\left(\frac{n\pi h}{L}\right)}{\sinh\left(\frac{2n\pi a}{L}\right)+\left(\frac{2n\pi a}{L}\right)} \quad (15)$$

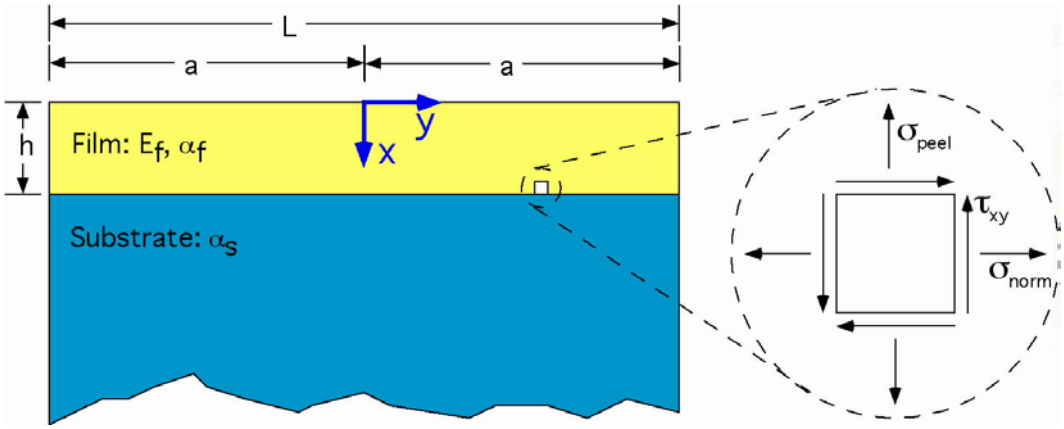

Figure 10. Geometry for Edge Effect Stress Calculation

A program was written to solve Equations 10-15 for the stresses in the layers. Software restrictions limited the number of iterations that could be used in each summation, but it was found that each term had reached a high degree of convergence, so the limitation on iterations

was not seen as a source of significant error. The stresses in the polymer were calculated and plotted for the half width of the co-molded optic along the polymer-glass interface as shown in Figure 11. Additionally, calculations were made that focused only on the final 160μm of co-molded optic so that the edge effects model's predictions could be better understood. This edge effect plot is shown in Figure 12.

As can be seen by these plots, the maximum shear stress in the co-molded optic occurs at the interface and has a magnitude of 2.657MPa which is well below the maximum shear strength of acrylic of 33.6MPa. The maximum normal or axial stress in the part has a magnitude of 9.41MPa which is well below the ultimate tensile strength of the polymer of 59MPa. The peeling stress at the interface has a maximum magnitude of 5.0MPa, but the maximum peeling stress is actually located further toward the free edge of the part and has a value of 9.6MPa. This peeling stress must be viewed with some skepticism because the edge effect solution contains a singularity in the peeling stress calculation. If the calculation were carried on for an infinite number of iterations, the value of the peeling stress would reach infinity as well. Because of the approximate nature of the calculation, it was felt that another method of approximation should be used as well to help bound the expected stress.

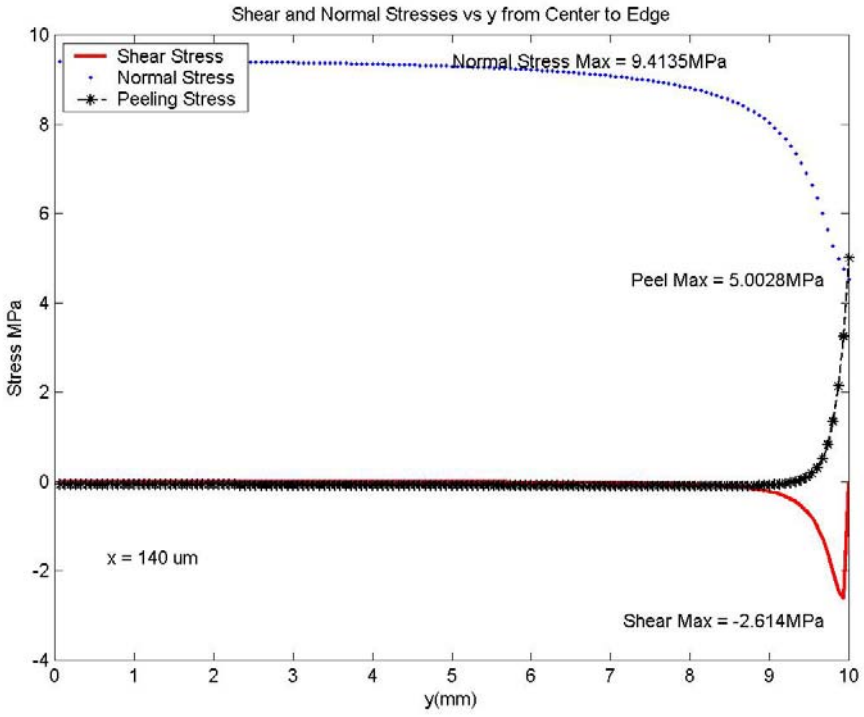

Figure 11. Thermally Induced Stresses in a Co-molded Polymer Lens at the Polymer-Glass Interface Plotted for the Lens Half Width of 10mm

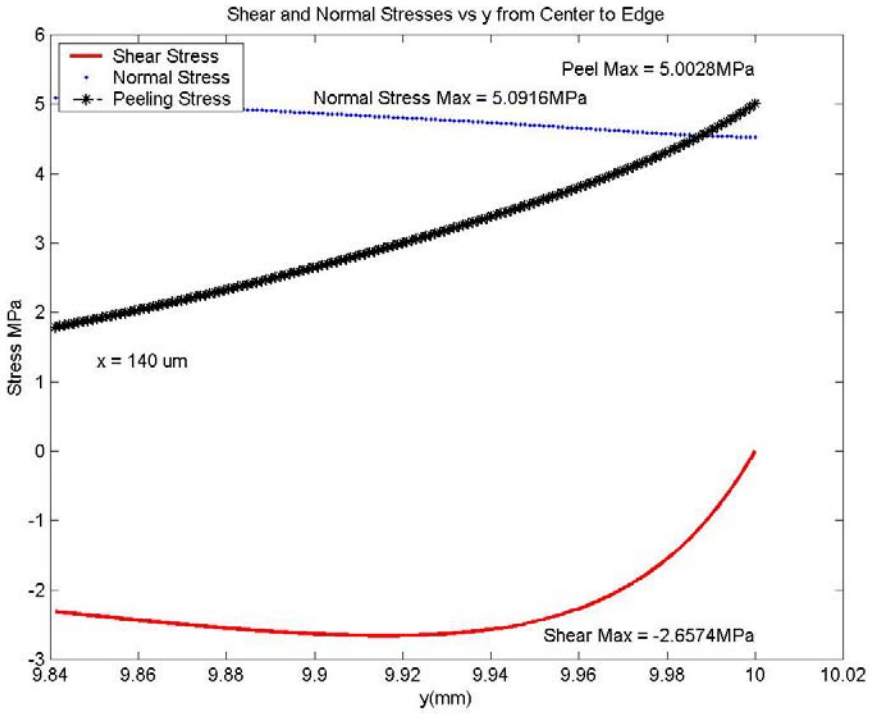

Figure 12. Thermally Induced Stresses in a Co-molded Polymer Lens at the Polymer-Glass Interface Plotted Over the Final 160 μm to the Edge of the Part

11.4.2 INTERFACE STRESSES– SUHIR METHOD

A second method of estimating the interface stresses is through a method presented by Suhir [4]. This method is an extension of the Timoshenko theory of bi-metal thermostats and can be considered to be a "strength of materials" method. There is concern as to the validity of this approach, so this method is only useful as an approximation. The development of the equations is detailed in [4] with the maximum peeling stress and shear stress given by Equations 16-21 for the geometry shown in Figure 13. These stresses are:

$$p_{\max} = \frac{\mu}{\kappa}\Delta a \Delta T \frac{\cosh(kx)}{\cosh(kl)} \tag{16}$$

$$\tau_{\max} = \frac{\Delta a \Delta T}{k\kappa}\tanh(kl) \tag{17}$$

where

$$\mu = \frac{h_2 D_1 - h_1 D_2}{2D} \tag{18}$$

$$D_1 = \frac{E_1 h_1^3}{12\left(1-\nu_1^2\right)},\ D_2 = \frac{E_2 h_2^3}{12\left(1-\nu_2^2\right)},\ D = D_1 + D_2 \tag{19}$$

$$\kappa = \frac{2(1+\upsilon_1^2)}{3E_1} h_1 + \frac{2(1+\upsilon_2^2)}{3E_2} h_2 \tag{20}$$

$$k = \sqrt{\frac{\lambda}{\kappa}} \ , \ \lambda = \frac{1}{12}\left(\frac{h_1^2}{D_1} + \frac{h_2^2}{D_2} + \frac{h^2}{D}\right) \tag{21}$$

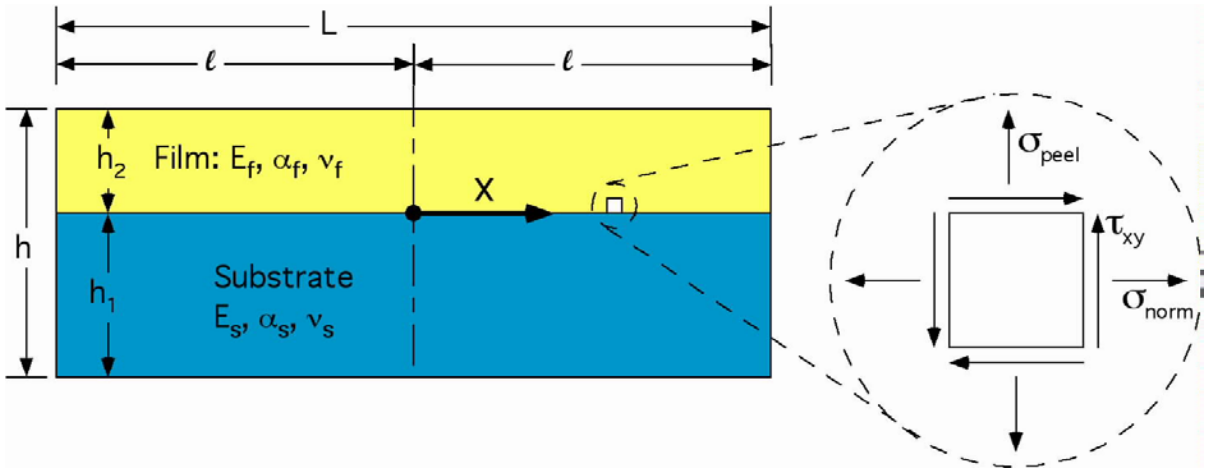

Figure 13. Geometry for Suhir Method of Stress Calculation

The Suhir method predicts that the magnitude of the maximum shear force will be 10.66MPa, a maximum axial force of 12.6MPa in the polymer, and a maximum peeling force of 4.48MPa. The stress values from the Suhir method and the edge effect method are plotted in Figure 14 along with the corresponding ultimate strength value for PMMA. This Figure shows that the predicted stresses are in fair agreement between the two methods of prediction, and all stresses lie well below the corresponding ultimate strength for PMMA. By this analysis, it is assumed that the polymer would be able to experience this stress without ultimate failure. However, no value is given for the strength of the bond in peeling. This is due to the uncertain nature of the bond between the polymer and the reactive organic end of the silane surface modifier. As was mentioned, this bond has never been seen, so it is difficult to predict a stress at this boundary. If there is failure of the adhesion, it is expected to be at this interface.

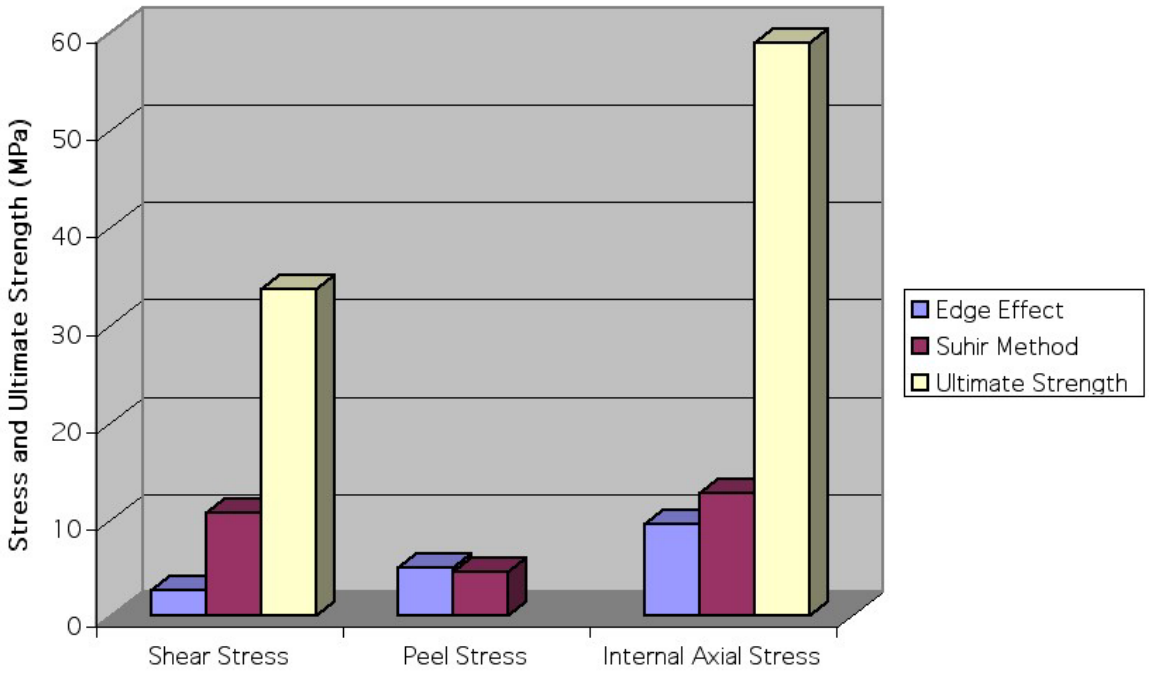

Figure 14. Magnitudes of Thermal Stresses in a Co-Molded Optic Predicted by the Edge Effect and Suhir Methods and the Corresponding Ultimate Strengths of PMMA

11.5 SUBSTRATE CO-MOLDING EXPERIMENT

Once it had been predicted that the polymer would be able to sustain the predicted stresses without failure, and that the use of silane surface modifiers was predicted to promote adhesion between the polymer and glass in the co-molded optic, a set of experiments was planned that would test the predictions to determine if co-molding was possible through injection molding.

11.5.1 EXPERIMENTAL METHOD

The co-molding of polymer onto glass required several modifications to the injection molding process. These modifications were necessary to properly prepare, co-mold, and recover the substrate. The development of these processes occurred over many molding cycles as experiments showed the methods that worked and the methods that did not. In most instances, the final methods are presented here, though in a few cases, an intermediate attempt is detailed for completeness.

Substrate Selection The substrate chosen for co-molding was glass in the form of microscope slides. Slides were chosen as an inexpensive and readily available material. Several types of glass were selected for the experiments because each offered strengths that the others did not

have. The two primary materials were soda lime glass, the material used for most commercial microscope slides, and fused silica or quartz slides. Of the two materials, soda lime is much less expensive at approximately $0.11 per slide (when purchased in small quantities) as compared to quartz at $15.00 per slide. Soda lime glass also has a coefficient of thermal expansion that is nearly 20 times that of quartz. This higher coefficient is an advantage during the molding process because it will grow and shrink more causing lower stress at the glass-polymer interface. This higher coefficient is a disadvantage in the final optical application because of the greater amount of thermal growth that the substrate will allow. The expected temperature change during operation is not extreme however and is still much better than that of the polymer alone. Quartz has many advantages due to its processing, especially in its dimensional precision and higher purity. Quartz slides are a specialty item and as such are precision ground to size with a material composition of high purity SiO_2. Soda lime glass contains other compounds leading to different properties. These additional elements and their percentage of the total are given in Table 1.

Table 1. Common Glasses and Their Primary Chemical Composition

Fused Silica (Quartz)	**Soda Lime Glass**	**Borosilicate Glass (Pyrex**
SiO_2 = 100%	SiO_2 = 75%	SiO_2 = 60-80%
	Na_2O = 15%	B_2O_3= 10-25%
	CaO = 10%	Al_2O_3= trace %

It was proposed that these additional counpounds would cause irregularities in the bond morphology and strength across the interface, causing the adhesion of the glass and polymer to be less secure. Because the silane is designed to bond with silicon in the glass substrate, bonds with other elements might not occur or, at the very least, would occur in a dissimilar manner to that of the silicon-oxygen-silicon bonds.

Substrate Preparation Process

Another difference between the two glasses was the expected cleanliness of the surfaces. To ensure that the cleanliness of the glasses would be similar, the glass slides were subjected to a rigorous cleaning before co-molding. It was suggested by Edward J. Gratrix, Director of Micro-Optics Technology for Zygo TeraOptix Corp., that the RCA method be used because it is a very common method of cleaning silicon wafers in the integrated circuit industry. After contacting individuals familiar with silicon processes at the Engineering Graduate Research Center of North Carolina State University, it was decided that the JTB1-1-1 (J. T. Baker Chemical Inc., Phillipsburg, NJ) process would be preferable. This process is a modification of the RCA method that is much more environmentally friendly, faster, and less expensive. The drawback of

the JTB1-1-1 cleaning method is that the chemicals used in the final two steps are proprietary, so some unknowns are introduced to the process.

Mr. Gratrix suggested that after cleaning, it might be advantageous to dip the slides in a 10% KOH solution to promote hydroxyl (OH) termination of the surface. The hydroxyl termination is necessary for silane to bond with the surface. This method was attempted, however, upon baking the slides for 30 minutes at 100°C as was suggested, a white residue formed on the surface of the slides. This residue could be wiped away, but the plastic would not stick to the glass after this point.

Once the slide had been cleaned thoroughly, it was ready for application of the silane interface layer. The method of application was suggested by the manufacturer of the silane stock. A solution of 95% (by weight) ethyl alcohol and 5% water (without fluoride) was created. Enough silane was then added to make a 2% concentration. This solution was allowed to sit for 2 hours during which the acidity was checked every 15 minutes using a MiniLab IQ125,handheld electronic pH meter (IQ Scientific Instruments Inc., San Diego, CA). The meter was calibrated and the manufacturer confirmed it was able to hold its calibration accuracy for up to a day after calibration, even if the unit were turned on and off. The target range of pH for complete hydrolization of the silanol was $4.5<pH<5.5$. If the mixture was too basic, acetic acid was added to return the solution to the target range. It was found that the adjustment target should be toward the basic end of the range as the solution tended to become more acidic with time.

Because silane is reactive with water vapor, it was necessary to use a nitrogen tent when the silane stock bottle was open. A tent was made from a clear plastic bag. The silane bottle, a 10 mL graduated cylinder, and a beaker containing the ethanol and water mixture was put into the bag. The bag was then sealed except for two small slots through which hands could be placed. A small cut was made in the bottom of the bag and a tube from a nitrogen gas tank was inserted. The air was removed from the tent as much as possible and then nitrogen was allowed to flow into the tent. The tent inflated with nitrogen which then flowed out the hand holes in the tent. After the nitrogen had been allowed to purge the tent for 10 minutes, the user's hands were inserted into the two hand slots and rubber bands around the wrists sealed the tent. The silane bottle was then opened, the silane measured, and added to the ethanol/water mixture. Once the silane bottle had been closed, a cut was made in the tent so that all of the items could be removed. Then the aforementioned pH monitoring could begin.

The slides were dipped in the silane solution for 3 minutes, rinsed with ethanol to prevent crosslinking of the silane layers, and then baked at 100°C for 10 minutes. Experiments were done with silane residence times of 2 to 5 minutes with little difference found in the effectiveness of the final polymer-glass bond. The silanol stock manufacturer reported that the baking could

be replaced with a drying period of 24 hours at room temperature which was also tested, but no improvements were found in the bonding of polymer to glass.

It was expected that each of the coating processes in the substrate surface preparation was time critical. After cleaning, too much time in atmospheric conditions can cause the surface to be attacked by acidic CO_2 in the atmosphere, causing the hydroxyl terminations to hydrogen bond with other molecules. Because of this time dependence and the many steps necessary to prepare the chemicals and equilibrate the molding machine, schedules were developed to determine the start times of each process. The schedules for the process with and without KOH application are presented below in Figures 15 and 16 respectively.

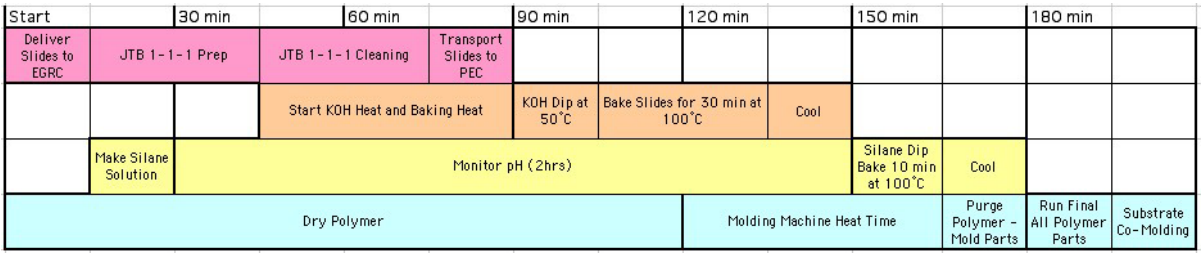

Figure 15. Processing Schedule for Substrate Co-Molding Including KOH Application

Figure 16. Processing Schedule for Substrate Co-Molding Without KOH Application

Substrate Co-Molding Process

Co-molding on a substrate requires several modifications to the injection molding process. These modifications are primarily due to the presence of the brittle substrate in the mold. For each molding session, the injection molding machine, barrel heaters, and mold heater were energized for at least 45 minutes to allow the system to come to temperature. The polymer was then purged from the barrel and new polymer was added to the hopper with some run through the barrel to purge any remaining old polymer. More than 20 parts were molded to allow the process to come to equilibrium. Once at equilibrium, a glass slide was put in the substrate holder on the moving side of the mold. The nozzle was brought into contact with the fixed side of the mold. The lower (final) mold close velocity was cut by half to 15% to protect the substrate and the mold was closed. Polymer was then injected onto the substrate. The mold remained closed for the desired cooling time. Upon opening, the co-molded part usually remained on the fixed side

of the mold due to friction in the sprue. A tool was created to push the solidified polymer out of the mold sprue. This tool, shown in 17, is inserted on the nozzle side of the fixed mold. The stepped cylindrical regions of the tool, shown in figure 17(B), fit into the holes in the fixed mold platen and fixed mold plate to guide the tool into the correct location as shown in Figure 17(A). The nozzle is then brought towards the mold, pushing on the back side of the tool. The steel push-out pin on the front of the tool pushes the solidified polymer from the sprue in a slow and controlled manner, stopping when the tool's depth stop surface contacts the back side of the aluminum mold insert. A piece of foam was inserted between the mold plates to catch the co-molded part as it was pushed from the mold. After removing the part, the machine was reset to automatic mode, molding parts and bringing the machine back to equilibrium. After a number of parts had been molded, another substrate could be co-molded.

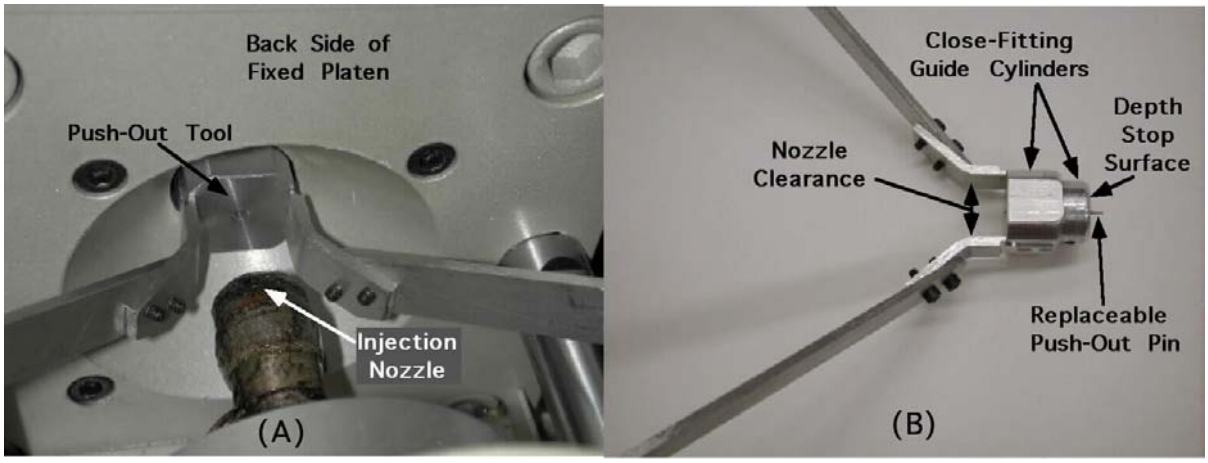

Figure17. Push-Out Tool Used to Release the Solidified Polymer Sprue from the Mold Shown (A) in Use and (B) in a Top View

11.5.2 RESULTS OF SUBSTRATE CO-MOLDING EXPERIMENTS

Many of the substrate co-molding experiments had limited success. The polymer often adhered to the glass, but as the co-molded optic cooled, the polymer popped loose from glass substrate. In locations where the polymer was separated from the glass, but still very close, it was possible to see Newton's rings due to interference caused by the increasing distance between the surfaces. By observing these fringes, it was possible to watch the separation advance across the optic from the edges toward the center. The separation happened in high speed, discrete separations, often accompanied by a loud pop. A group of cooling lenses sounded similar to a bowl of Rice Krispies in milk. Because of this separation, the effectiveness of the adhesion was measured by the amount of time that the lens remained adhered to the substrate. This number generally ranged between 0 and 20 minutes depending on the conditions of the experiment.

It was found that slides that had been cleaned using the JTB1-1-1 process were more likely to have good adhesion with the polymer than slides that had been cleaned with alcohol, acetone, or common soap. It was also found that the acrylic was more likely to adhere to soda lime glass than quartz, contrary to expectations. A possible explanation is the difference in the coefficient of thermal expansion for the two glasses. While the much lower thermal expansion of quartz might be an advantage in an optical application, this reduced ability to change with the temperature may have caused the interfacial stresses to be too high for adhesion to occur. The quartz was also more brittle and more subject to thermal shock, and thus was much more likely to shatter in the mold especially around the sprue where initial injection occurred.

The best adhesion occurred in a lens that was left in the mold overnight. After injection, the mold remained closed and maintained temperature for 1 hour. The mold was then allowed to cool slowly to room temperature and then to sit overnight. Though it appeared that the polymer was fully adhered to the substrate when the mold was opened, the lens stuck to the mold on the end opposite the sprue and was torn from the glass for some length during removal of the part from the mold. The remaining area of adhesion was approximately 5 cm^2. A shear test was attempted on this lens by grasping the glass substrate in the rubber coated jaws of a vise. The polymer was then pulled by a hand-held force gauge. The force reached 7N, and a stress of 15 KPa and then the polymer broke, leaving nothing on which to pull. The polymer remained firmly attached to the glass, and has remained that way for many weeks following the test.

A test was conducted to see if a lower coefficient of thermal expansion material might allow the polymer to adhere. Acrylic slides were used as the substrate, and the injected polymer adhered to the slides completely. This suggests that if the coefficient of thermal expansion of the substrate were closer to that of the polymer, adhesion might occur. This could be done by using a different substrate or by using a different polymer with a lower glass transition temperature.

11.6 SUMMARY OF SUBSTRATE CO-MOLDING

Mold components and tools were designed to allow the co-molding of polymer meso and micro optics directly onto thermally stable substrates. Soda lime and quartz glass slides were selected as transparent substrates for the testing due to their low coefficient of thermal expansion, elastic strength, and availability. These substrates were cleaned using the JTB1-1-1 process developed for the integrated circuit industry. The slides were then coated with a silane solution and baked. Shortly after baking, the slides were inserted into the molding machine and polymer was injected onto one side of the substrates. The slide and co-molded polymer lens were then removed from the mold using a specially designed tool and allowed to cool to room temperature. As they cooled, most of the co-molded optics separated from the substrates across the majority of their area, even though stress calculations and other researchers' experience with silane coating suggested that the lenses should maintain adhesion. Several additional methods were attempted

including coating the surfaces with KOH solution to terminate the surface in hydroxyls before silane coating, and cleaning the surfaces with different processes. These typically did not improve the adhesion, and usually worsened the adhesion of the polymer to glass.

The best adhesion was obtained by injecting the polymer onto the glass and then allowing the polymer to cool slowly in the mold for 10 hours. This method appeared to leave the polymer fully adhered to the glass slide, however, some of the polymer stuck to the mold and was torn from the substrate as the co-molded optic was removed from the mold. Shear tests on this optic found the adhesion to be stronger than the lens, with the lens tearing before the adhesion was broken. This experiment suggests that longer and more controlled cooling times would promote adhesion between the optic and the substrate.

In the co-molding experiments, slides cleaned by the JTB1-1-1 process were more likely to have polymer adhere than slides that had been cleaned by other methods, or not cleaned at all. Soda lime glass slides were more likely to have polymer adhere than fused silica slides. Slides that had been coated with M8550 silane solution were also more likely to have adhesion occur than slides that were not coated with an adhesion promoter.

It is proposed that the adhesion of polymer to substrates is still feasible and usable. Some possible solutions would be substrates with coefficients of thermal expansion that were closer to the polymer in order to create lower stress. Alternatively, polymer with a lower melting temperature such as low-density polyethylene could be used. The chemistry involved in creating the silane solution involves very small amounts and could be done with greater accuracy given better chemistry facilities and experience. Also, a means of having the polymer not stick to the silane when there was a large difference in temperature, but adhering when there was a small temperature difference might allow the optic to adhere with minimal stress and then maintain its attachment through the operating temperature cycles. This would most likely be a chemistry solution outside the expertise of these researchers.

REFERENCES

1. Bascom, W.D., *Journal of Colloid Interface Science*, Vol 27, 1968, p 789.
2. Lee, L.H., *Journal of Colloid Interface Science*, Vol 27, 1968, p 751.
3. Pluddemann, E., Silane Coupling Agents, New York, NY, Plenum Press, 1982
4. Suhir, E. Transaction of the ASME, Vol 53, Sept 1986, pg 657.
5. Arkles, B. “Silane Coupling Agent Chemistry”, Silicon Compounds: Register and Review, 1991, p 59-64.

12 OFF-AXIS BICONIC MIRROR FABRICATION

Ken Garrard
Alex Sohn
PEC Staff Members

Challenges in fabrication and testing have historically limited the choice of surfaces available for the design of reflective optical instruments. Spherical and conic mirrors are common, but more degrees of freedom are necessary to meet challenging performance and packaging requirements. In particular, single-surface astigmatism correction in spectrographs necessitates a toroidal surface, which lacks an axis of rotational symmetry. With support from NASA Goddard Space Flight Center (GSFC), a 94 by 76 mm off-axis, toroidal, biconic mirror has been fabricated using the Variform fast tool servo and the Nanoform 600 diamond turning machine. Issues related to the geometric analysis, decomposition, toolpath generation, controller interfacing, part fixture design, alignment, machining and metrology of a pair of these mirrors are discussed.

12.1 INTRODUCTION

The Infrared Multi-Object Spectrograph (IRMOS) is a facility instrument for the Kitt Peak National Observatory's Mayall Telescope (3.8m) and an engineering prototype for a possible design of the Next Generation Space Telescope (NGST) multi-object spectrograph. IRMOS utilizes unconventional optics to reduce package size and improve performance. As shown in Figure 1, the use of a Digital Micro-Mirror (DMM) array results in a tilted, discontinuous focal plane which leads to astigmatism in two planes. The mirror designated M4 corrects this astigmatism and is the final reflective optic before the detector. M4 is the most challenging of the IRMOS optical elements to fabricate due to its non-rotationally symmetric (NRS) form and tight tolerances [1].

The surface of M4 is an off-axis segment of an ellipsoidal toroid, meaning that it is not rotationally symmetric about any axis. Two principal methods for fabricating such an optic exist: milling or flycutting with a multiaxis ultraprecision machine or diamond turning using a fast tool servo (FTS). The former method requires large amounts of machining time – sometimes weeks – and must deal with all the complications associated with those longer machining times (e.g., temperature stability, transient noise). The latter, on the other hand, takes no longer than an ordinary turning operation and is therefore cheaper and more reliable than milling. By decomposing M4 into a rotationally symmetric (RS) surface and a residual NRS surface the range requirement of the FTS can be determined. The RS and NRS surfaces are machined simultaneously by a diamond turning machine (DTM) and the FTS, respectively, to produce the desired shape. It does, however, require that the deviation from a rotationally symmetric toolpath be within the available FTS range and that such a toolpath be within the DTM machining envelope. These requirements are met by the Variform FTS with 400 µm of travel and the PEC's Nanoform 600 DTM with its 600 mm diameter part capacity.

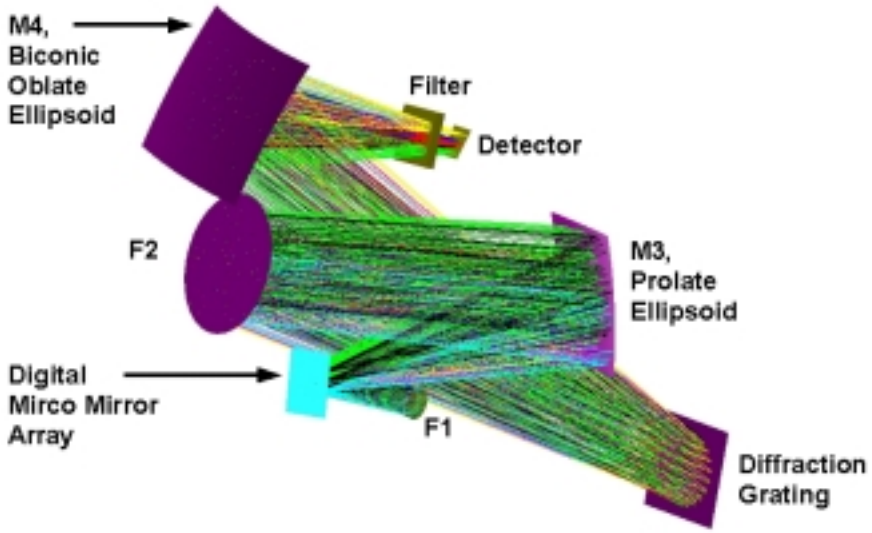

Figure 1. IRMOS detector optics.

Novel surfaces like M4 pose unique challenges for measuring figure error (i.e., surface error at spatial periods of 2 mm). Several methods are applied and evaluated for their merits and drawbacks. The use of computer-generated holographic (CGH) null elements in interferometry allow high-resolution measurements; however, alignment of the test setup can be time-consuming since the alignment tolerances are tight. This issue is addressed with a set of custom alignment fiducials built-in to the CGH and the M4 mirror. Additionally, CGH masks normally cannot be directly verified with a known standard. Stylus profilometry, on the other hand, is traceable since the instrument can be calibrated using known standards. Even with minimal probing forces the contact process can be destructive if local contact stresses leave witness marks on the surface. Depending on the system, profilometry data may also be time consuming and difficult to assemble and interpret.

12.2 M4 MIRROR DESCRIPTION

The IRMOS mirror M4 is an off-axis biconic toroidal surface. The surface is a blending of oblate ellipses of different curvature and eccentricity in the XZ and YZ planes. As such it has no axis of rotational symmetry. Figure 2 shows a section of the biconic surface as a wire frame and the aperture of the mirror blank as a solid.

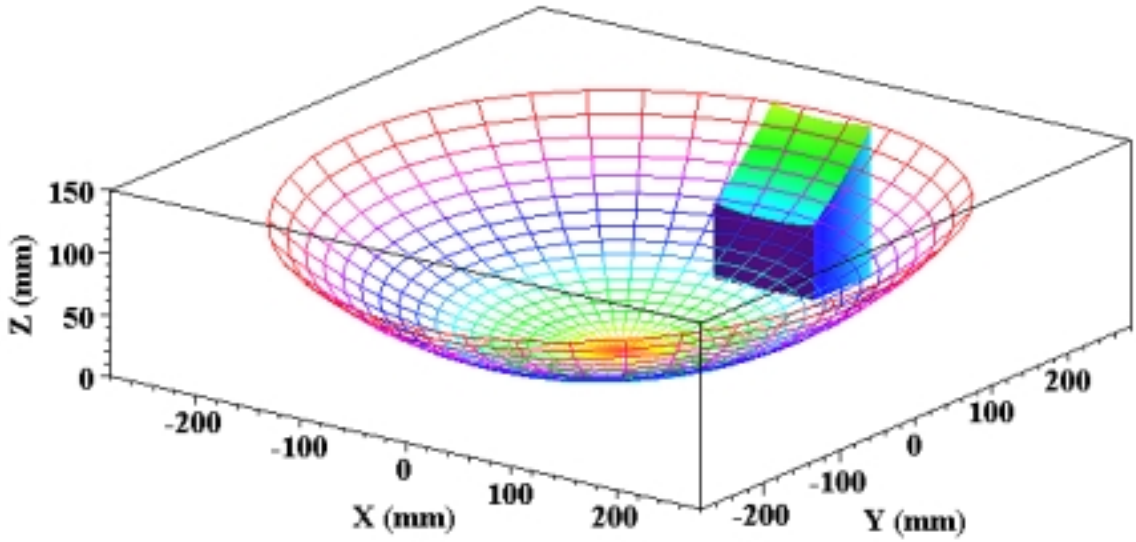

Figure 2. The biconic optic M4.

A general biconic optical surface can be defined in rectangular coordinates as,

$$M4(x,y) = \frac{c_{XZ}\cdot(x-x_0)^2 + c_{YZ}\cdot(y-y_0)^2}{1+\sqrt{1-(1+k_{XZ})\cdot(x-x_0)^2\cdot c_{XZ}^2-(1+k_{YZ})\cdot(y-y_0)^2\cdot c_{YZ}^2}} \quad (1)$$

With the origin at $(x_0, y_0, 0)$, the parameters in Equation (1) that specify the shape of M4 are:

	c_{XZ} = 0.002650	is the surface curvature in the XZ plane,
	c_{YZ} = 0.002458	is the surface curvature in the YZ plane,
	k_{XZ} = 0.0778	is an oblate ellipse in the XZ plane,
and	k_{YZ} = 0.1265	is an oblate ellipse in the YZ plane.

The aperture of the mirror is 94 mm by 76 mm and its center is located at x_0 = -2.01 mm and y_0 = 227.41 mm. The mirror surface is tilted 35.3° with respect to the optical axis so that the average normal from the front surface is parallel to the back surface.

12.3 GEOMETRIC ANALYSIS

M4 has 7.549 mm of sag with respect to a plane parallel to its back surface. If a best-fit, rotationally symmetric asphere is also subtracted from M4, the sag of the resulting surface is 4.582 mm. This is far beyond the 400 µm range of the Variform FTS. Clearly, on-axis machining of the mirror with a fast tool servo is not feasible without further geometric manipulation (i.e., tip, tilt and translation) to reduce the residual NRS excursion. The solution must also keep the mirror blanks and mounting fixture within the 600 mm turning capability of the Nanoform.

12.3.1 ON-AXIS ORIENTATION

It is possible to orient M4 on-axis, that is, with the mirror blank intersecting the centerline of the DTM spindle, in such a way that the required FTS excursion does not exceed the range of the Variform. Instead of leveling the mirror blank with respect to its back surface, a least-squares procedure was used to find the angles that "level" the mirror's front surface. Then on-axis translation followed by an small tilt about the X axis and asphere subtraction results in a surface requiring only 112 µm of FTS excursion. The least squares leveling procedure tilts the mirror -35.1° about the X axis and -0.316° about the Y axis. The on-axis translation parameters are then x_0 = 1.629, y_0 = -229.718 and z_0 = 70.407. The final rotation about the X axis is -0.1101°. The RS asphere subtracted from the resulting on-axis surface is described by Equation (2) and the residual NRS surface that would be machined by the FTS is shown in Figure 3. Note that the 4th order coefficient is nearly zero for this aspheric surface and there is no cubic term.

$$A4(R) = -3.07426 + \left(0.0013323 + 0.2596177 \cdot 10^{-8} \cdot R^2\right) \cdot R^2 \qquad (2)$$

For several reasons, this on-axis orientation was not used for fabrication of M4. The off-axis solution described in Section 12.3.2 was pursued first and work on the part fixture had already begun. Also a suitable means of locating and aligning the part via fiducial markings is more complex with an on-axis mounting. Off-axis mounting (see Section 12.5.1) facilitates access

through the vacuum chuck to the fiducial marks on the back surface of the mirror blanks. This access would be greatly restricted with on-axis mounting.

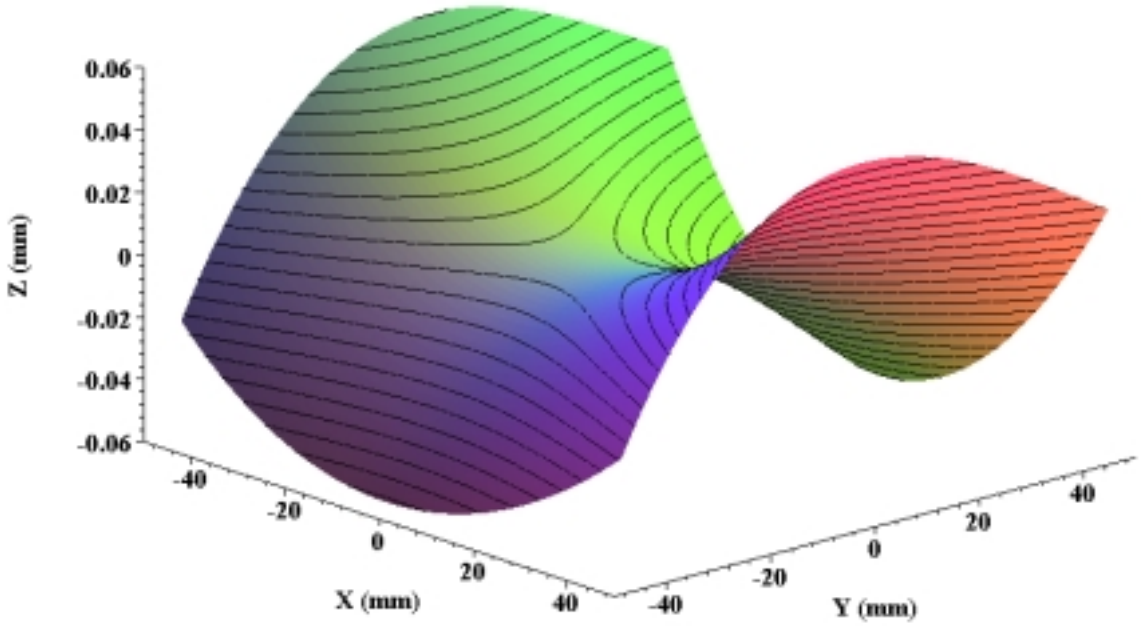

Figure 3. FTS motion for on-axis machining of M4.

12.3.2 OFF-AXIS ORIENTATION

If the optical axis of the M4 mirror is aligned with the spindle centerline on the Nanoform DTM and machined off-axis (i.e., the mirror is machined in its defining coordinate system), then M4 is within the capabilities of the Variform and Nanoform. Removal of a best-fit 4th order asphere results in a residual FTS excursion of 360 µm and the outermost corner of the mirror blank is 280 mm from the spindle center. However, it is possible to do much better than this as will be seen below.

Three other issues also must be resolved. First, tool radius compensation must be performed to machine the correct shape. Since the surface slope changes as a function of spindle rotation as well as axial distance, this compensation is three dimensional. Second, it is desirable to decompose M4 into RS and NRS components such that the excursion of the FTS is minimized. Third, if the Variform is aligned with the Nanoform Z axis, an unusually long tool shank must be used to provide clearance from the FTS for the rotating concave mirror blanks. The solution is to rotate the tool axis to an appropriate angle, for example, normal to the center of the workpiece. This has the benefit of reducing the range of motion required of the FTS, but significantly complicates calculation of its trajectory across an NRS surface.

3D Tool Radius Compensation

To compensate for the tool radius in three dimensions a parallel biconic surface was derived that is offset from M4 by the radius of the tool. Since M4 is concave, this new surface, denominated Q4, has greater curvature than M4, but a smaller aperture. Q4 defines the trajectory of the tool center that generates the surface of M4 at the tool edge as a function of tool radius *d*, radial position *R* and spindle angle θ. The parameters of Q4 can be found by noting that parallel ellipses in a plane separated by a fixed distance, *d*, simply have *A* (major axis) and *B* (minor axis) parameters that differ by *d*. So, Q4 can be derived by finding *A* and *B* for M4, subtracting the tool radius (since Q4 is smaller than M4) and then calculating the conic constant and curvature for the new ellipse. This can be done independently for the XZ and YZ planes of the biconic and the parameters substituted into Equation (1) to generate data points on Q4. The values of *A* and *B* for an oblate ellipse as functions of curvature and conic constant are,

$$A = \frac{\sqrt{k+1}}{c \cdot (k+1)} \tag{3}$$

$$B = \frac{1}{c \cdot (k+1)} \tag{4}$$

Solving Equations (3) and (4) simultaneously for *c* and *k* gives,

$$c = \frac{B}{A^2} \tag{5}$$

$$k = \frac{B^2}{\left(A^2 - B^2\right)} \tag{6}$$

The shape parameters for M4 and Q4 are summarized in Table 1 for the 2.9646 mm radius tool that was used to machine the M4 mirrors.

Table 1. M4 and Q4 biconic shape parameters.

	Plane	A	B	k	c
M4	XZ	363.518	350.152	0.0778	0.002650
	YZ	383.357	361.192	0.1265	0.002458
Q4	XZ	360.553	347.187	0.07847	0.002670
	YZ	380.393	358.227	0.12757	0.002475

The coordinates of the center points of Q4 when the tool edge is at the corners of M4 can be found by intersecting normal lines from each M4 corner with the surface of Q4. For any continuous, differentiable surface a normal line is perpendicular to any two tangent lines that intersect at a right angle. In particular, the tangent lines that lie in the XZ and YZ planes define a

plane tangent to the surface and can be used to find the normal. Parametric expressions for these two lines tangent to *F* of length *u* are,

$$L_{XZ}(u,x,y)=\left[x+u,\ y,\ F(x,y)+u\cdot\left(\frac{\partial F}{\partial x}\right)(x,y)\right] \tag{7}$$

$$L_{YZ}(u,x,y)=\left[x,\ y+u,\ F(x,y)+u\cdot\left(\frac{\partial F}{\partial y}\right)(x,y)\right] \tag{8}$$

The normalized cross product of unit length tangent lines, L_{XZ} and L_{YZ}, evaluated at any *(x,y)* defines a normal to the surface at *(x,y)* as shown in Equation (9).

$$NL(x,y)=\left\|\left[L_{XZ}(1,x,y)-L_{XZ}(0,x,y)\right]\times\left[L_{YZ}(1,x,y)-L_{YZ}(0,x,y)\right]\right\| \tag{9}$$

A function that gives the coordinates of the endpoints of a normal line of length *u* is then defined as,

$$PNL(u,x,y)=\left[x+u\cdot NL(x,y)_1,\ y+u\cdot NL(x,y)_2,\ F(x,y)+u\cdot NL(x,y)_3\right] \tag{10}$$

Substituting the function *M4* of Equation (1) for *F* in Equation (10) and evaluating it with *u* set to the radius of the tool gives the coordinates on Q4 (tool center) for any point *(x,y)* on M4 (biconic surface). These calculations are easily performed in Maple™ for any radius tool. Figure 4 shows M4 (tiled surface) and Q4 (wireframe) along with the normal (red) and tangent (blue) lines at selected *(x,y)* locations.

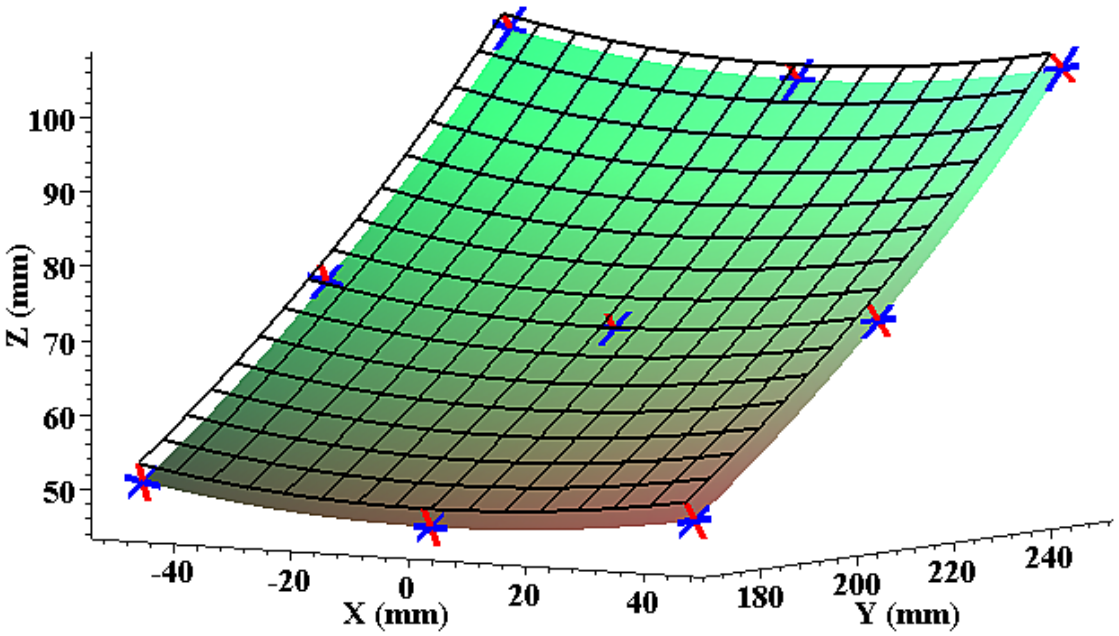

Figure 4. M4 and the parallel surface Q4.

Surface Decomposition into NRS and RS components

By considering off-axis translations and tilt angles other than that of the best fit plane, the range of NRS motion required to machine the surface can be dramatically reduced. Translations were considered first to avoid the complications of shimming the mirror blanks on a vacuum fixture. The procedure was to generate a grid of data points on Q4 using Equation (1), calculate the radius, *R*, of each point from the optical center, and fit a 4th order polynomial in *R* to this data. The range of the residuals gives the FTS excursion required to machine the mirror. A Y offset of -17 mm was found to reduce the residual range to 76 µm, 19% of the maximum range of the Variform. Data reduction was initially performed using the **pro Fit** software package and replicated using JMP®. Algebraic and numerical verification were obtained with Maple. The resulting NRS surface that must be created by the Variform is shown in Figure 5. The best-fit 4th order polynomial defining the asphere to be machined by the Nanoform is given in Equation (11). Higher order polynomials yield no significant improvement.

$$P4(R) = 46.126 + \left(-0.896 + \left(8.532 \times 10^{-3} + \left(-2.552 \times 10^{-5} + 3.752 \times 10^{-8} \cdot R\right) \cdot R\right) \cdot R\right) \cdot R \qquad (11)$$

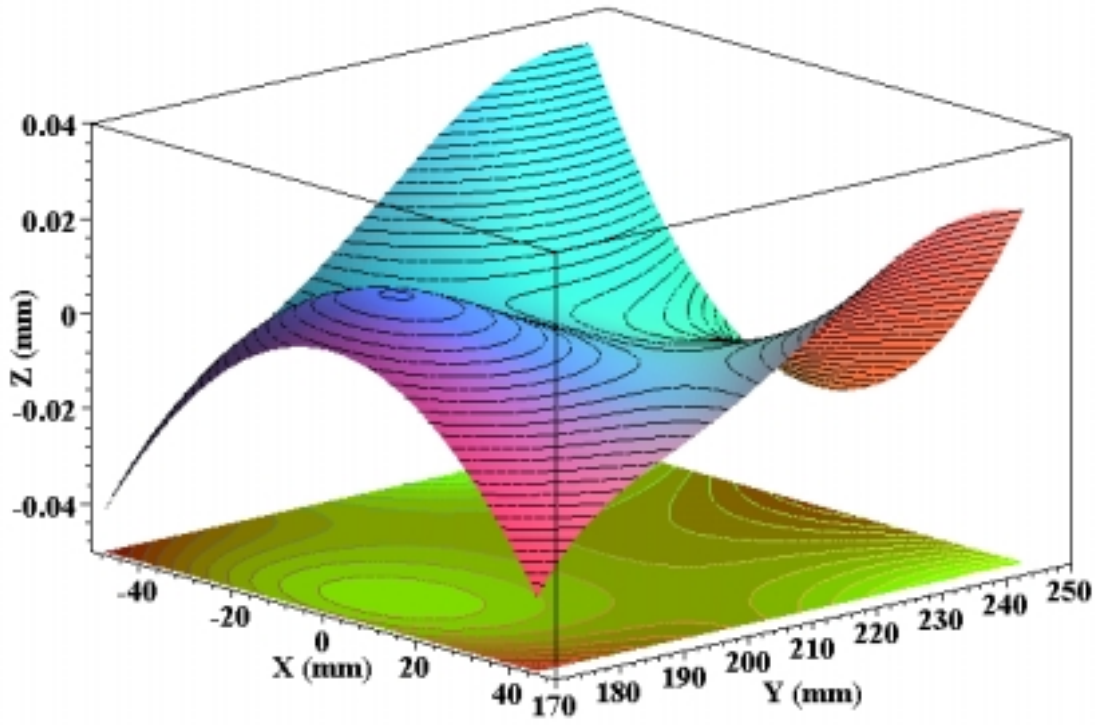

Figure 5. FTS toolpath component for Q4.

Careful examination of Figure 5 reveals that while the maximum range of FTS travel along any given radius is approximately 65 µm, that excursion must be accomplished within an angular space of about 15°. By transforming the equation defining the NRS motion into 3D polar

coordinates and taking the first derivative with respect to θ, the velocity required of the FTS can be determined for any given spindle speed. A plot of this slope function in Figure 6 shows that a maximum velocity of 4.1 mm/sec per Hz of spindle rotation is needed to machine M4. Since the Variform is capable of a velocity of 20 mm/sec, a spindle speed of 120 rpm (2 Hz) is feasible and will yield reasonable machining times.

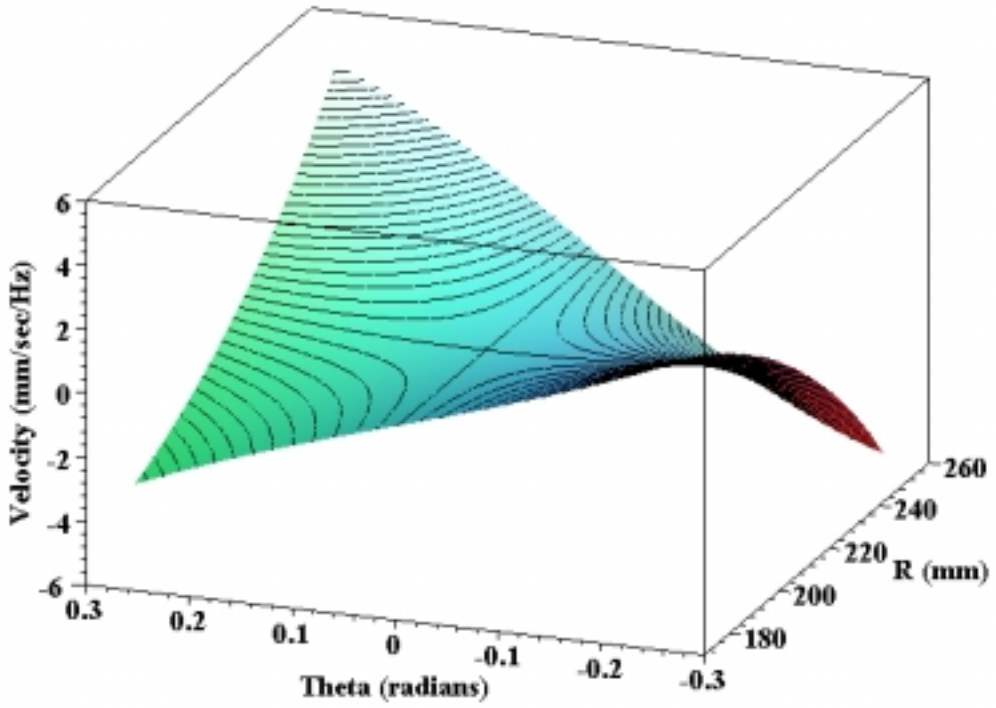

Figure 6. FTS velocity.

Tool Axis Tilt Compensation

To provide clearance to the mirror blanks as they rotate past the Variform structure, the tool post is mounted at an angle of -35.3° with respect to the Z axis of the DTM. The FTS trajectory calculations described above give tool positions as a function of R and θ that are co-linear with the Z axis. However, as the tilted FTS moves in the Z direction it also moves in the R direction. Since the FTS controller cannot change R by moving the DTM X axis as a function of θ, it must move the FTS such that the center of the tool always lies on Q4 (and hence the cutting edge machines M4). This requires finding the intersection of a line along the tool axis through P4 at R with Q4. This line varies as a function of both R and θ and is given in Equation (12).

$$T(R,r) = \frac{(r-R)}{\tan\varphi} + P4(R) \tag{12}$$

where R is a radius on P4 as defined by the DTM X axis, φ is the tilt angle of the tool axis and r is the radius on Q4 of the desired intersection point. For a given R and θ, tool center locations for the tilted tool may be determined by first solving Equation (13) for r,

$$0 = M4\left(r \cdot \sin\theta, r \cdot \cos\theta\right) - T(R,r) \tag{13}$$

and then evaluating Equation (14) to find the required FTS excursion in the tool axis direction.

$$FTS(R,r,\theta) = \frac{\left[M4\left(r \cdot \sin\theta,\ r \cdot \cos\theta\right) - P4(R)\right]}{\cos\varphi} \tag{14}$$

Figure 7 shows both the compensated and uncompensated FTS tool center locations that generate the NRS component of the Q4 surface. The contoured surface in the figure is uncompensated and the shaded surface is with tilt compensation. Note that the two surfaces intersect and the compensated surface is flatter, requiring 62 µm of FTS excursion.

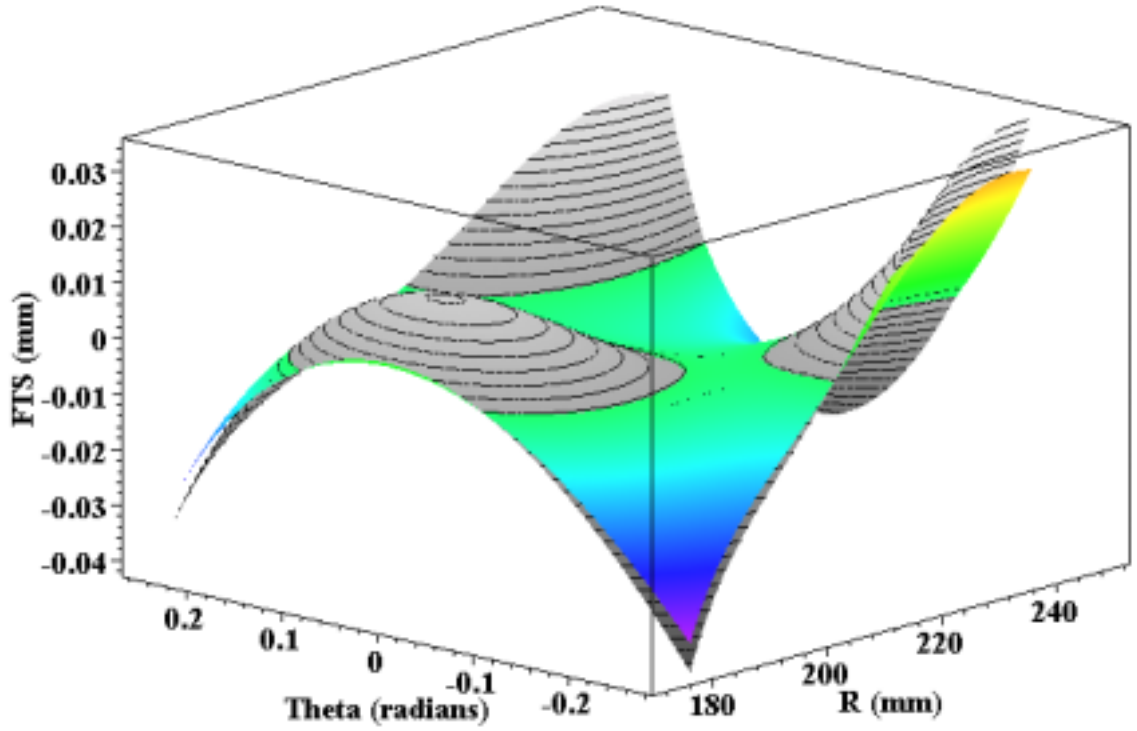

Figure 7. Tool tilt compensation for Q4.

12.4 TOOLPATH GENERATION

Unfortunately there is no closed form algebraic solution for Equation (13). For given values of R and θ the FTS excursion can be found numerically with a root finding algorithm such as bisection search or Newton-Raphson. This presents a performance problem when calculating

FTS tool locations *on-the-fly* as the best-fit asphere is being machined. Three possible options were considered.

1. Purchase a faster controller to solve the equations in real-time.
2. Derive some other, simpler function that approximates the correct answer.
3. Interpolate over a grid of exact tool locations calculated offline.

Option 1 is clearly the best; however sufficient project resources (time and money) were not available. Option 2 was pursued to the extent that a 9^{th} order interpolating polynomial was derived for r as a function of R and θ. This polynomial gives acceptably small residuals, but the time needed to evaluate the interpolating function was deemed excessive for real-time implementation with the available controller. Two-dimensional interpolation algorithms were evaluated to find an technique that generates the M4 surface from a reasonable size grid with small residual error.

12.4.1 BILINEAR INTERPOLATION

To find the FTS locations at each point on the M4 surface during machining a bilinear interpolation algorithm over a grid of 168 (R) by 68 (θ) machine axis locations was used. The interpolation is expressed in 3D polar coordinates since the Nanoform cross-feed axis (X) and spindle define a polar space. This size table is easily managed by the control system and yields an FTS toolpath with residual errors smaller than the positioning accuracy of the Variform. The basic idea of multi-dimensional interpolation is to find the neighborhood of an untabulated value in the table and construct a weighted average of the values of the nearest points as an estimate of the unknown value. For a two dimensional table, there are four nearest points to consider. A linear estimator uses the product of the distance ratios from the untabulated point to the grid lines intersecting each neighbor point in each dimension as the weighting factor for that tabulated neighbor point. Higher order estimators that use cubic functions, splines and tabulated derivatives can produce smoother, more accurate interpolators; all at the cost of more computation time and larger tables.

The interpolation grid covers an area somewhat larger than the aperture of the mirror to avoid edge discontinuities that induce vibrations and degrade surface finish. The interpolation grid is also extended in the negative X direction (i.e., the X decenter of M4 is removed) so that the leading and trailing edges of the table in the θ direction contain the same FTS values. Thus when the mirror rotates beyond the θ boundary of the table the FTS will be in the correct position when the mirror re-enters the tabulated range as it completes a revolution. To properly balance the spindle, two mirror blanks are machined at a time. The spindle angle, θ, must be manipulated so that the interpolation table is used twice per revolution (without storing the table twice). It is

also convenient for the angle to range from -π/2 to +π/2. This is easily accomplished with the conditional function in Equation (15) over input θ values ranging from zero to 2π,

$$\Omega = \left\{ \begin{array}{cc} \theta - 2\pi & \text{for } \theta \geq \frac{3}{2}\pi \\ \theta - \pi & \text{for } \theta \geq \frac{1}{2}\pi \\ \theta & \text{otherwise} \end{array} \right\} \tag{15}$$

Bilinear interpolation for Q4 expressed in polar coordinates means first finding the two rows and columns that bound an input *(R, Ω)* data point. Saturation instead of extrapolation at the table boundaries accomplishes the objective of having the tool position not change as a function of spindle rotation outside the aperture of the two rotating mirrors. For an equally spaced rectangular grid the indices of nearest neighbor tabulated points to *(R, Ω)*, can be found by calculating,

$$ri = \left\lfloor \frac{R - r_{\min}}{r_{delta}} \right\rfloor \quad \text{and} \quad ti = \left\lfloor \frac{\Omega - \theta_{\min}}{\theta_{delta}} \right\rfloor \tag{16}$$

where r_{delta} and θ_{delta} are the radial and angular grid spacings and r_{min} and θ_{min} are the lower boundaries of the interpolation table, respectively. The four nearest points are located at [row, column] positions: *[ri, ti], [ri+1, ti], [ri, ti+1],* and *[ri+1, ti+1]*. Weighting factors for the radial and angular dimensions are,

$$w_r = \frac{\left(R - Vr_{ri}\right)}{r_{delta}} \quad \text{and} \quad w_t = \frac{\left(\Omega - Vt_{ti}\right)}{\theta_{delta}} \tag{17}$$

where *Vr* and *Vt* are vectors of the radius and angle values defining the interpolation grid. The FTS position is estimated as,

$$z_{FTS} = w_r \cdot w_t \cdot Mz_{ri+1,ti+1} + w_r \cdot \left(1 - w_t\right) \cdot Mz_{ri+1,ti} + \left(1 - w_r\right) \cdot w_t \cdot Mz_{ri_i,ti+1} + \left(1 - w_r\right) \cdot \left(1 - w_t\right) \cdot Mz_{ri_i,ti} \tag{18}$$

where *Mz* is the two dimensional interpolation table of exact tool locations.

12.4.2 TOOLPATH VERIFICATION

Prior to machining, a C program was written to simulate the use of bilinear interpolation as a toolpath trajectory generation method for Q4. The program iterates through all possible combinations of *R* and θ locations at the feedback resolution of the system (approximately 1.5 million data points in the aperture of a single mirror blank). A plot of the resulting surface is shown in Figure 8. At each point, a comparison was made between the interpolation value for the FTS position obtained from Equation (18) and a more accurate value calculated from Equations (12-14) with a bisection search determining the root of Equation (13). The termination

criterion for the bisection algorithm was set to 10^{-10} mm. These reference values were also calculated at the 11,424 interpolation table grid points and compared with those found by Maple's numeric equation solver. Examination of the residual error in the z_{FTS} calculation revealed a very small slope as a function of *R*. A final step was added to the bilinear interpolator to remove this slope by applying Equation (19) to z_{FTS} values from Equation (18).

$$z'_{FTS} = z_{FTS} + (0.0703787466 - R \cdot 0.0003333488) \cdot 0.001 \tag{19}$$

The residuals errors from the modified interpolator are normally distributed with a mean of -0.3 nm, a standard deviation of 3.45 nm, a minimum of -12.82 nm and a maximum of 13.97 nm. The error distribution is leptokurtic with more than 75% of the data points having an error of less than 2.5 nm.

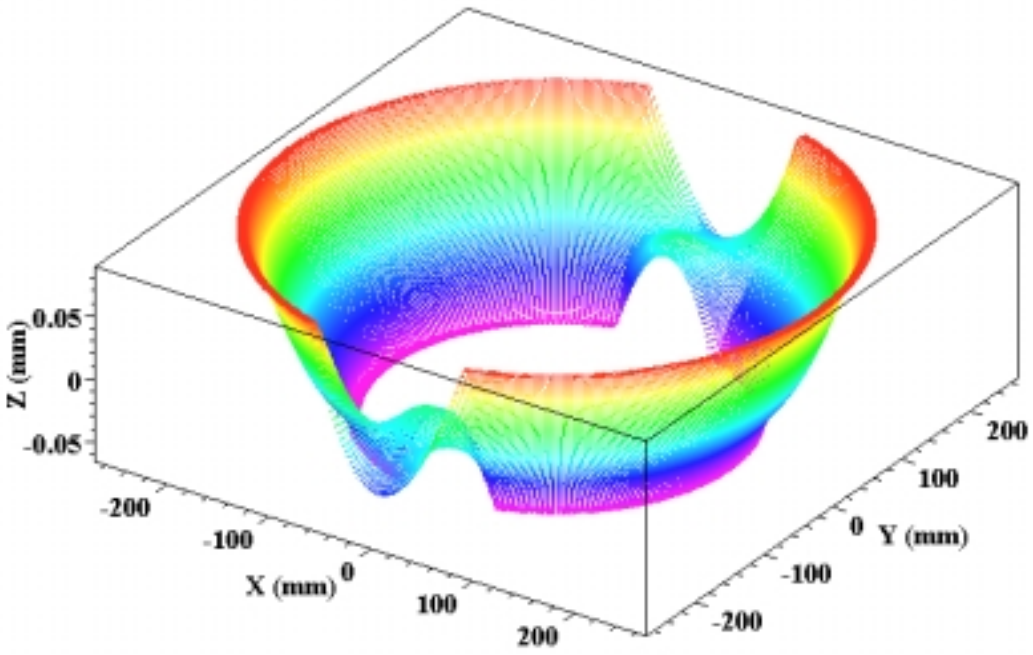

Figure 8. Simulated FTS motion for interpolated Q4 toolpath.

12.5 MACHINE SETUP

Figure 9 shows the aluminum vacuum chuck that was designed and built to hold the M4 mirror blanks and the tool centering fixture. The diamond machined chuck dimensions are 580 mm x 127 mm x 135 mm (to the top of the pedestals) and its mass is approximately 18 kg. Due to the low spindle speeds and large cross section of the chuck, deflection due to centripetal forces is minimal. The figure shows PMMA test parts mounted on the pedestals in place of the heat treated Al 6061 M4 mirror blanks. A pair of mirrors, located 180° apart on the chuck, are machined at the same time. A video camera is placed behind the DTM splash shield to observe

fiducial marks on the rear of the mirrors for part alignment in the radial and angular directions. As the parts rotate, the tool is guided by the DTM's X and Z axes to machine the RS portion of the mirror surface (i.e., the best-fit asphere) while the FTS moves in synchronization with the spindle and X axis to produce the NRS surface. To provide clearance between the rotating parts and the Variform structure, the FTS is shown mounted at a 35.3° angle.

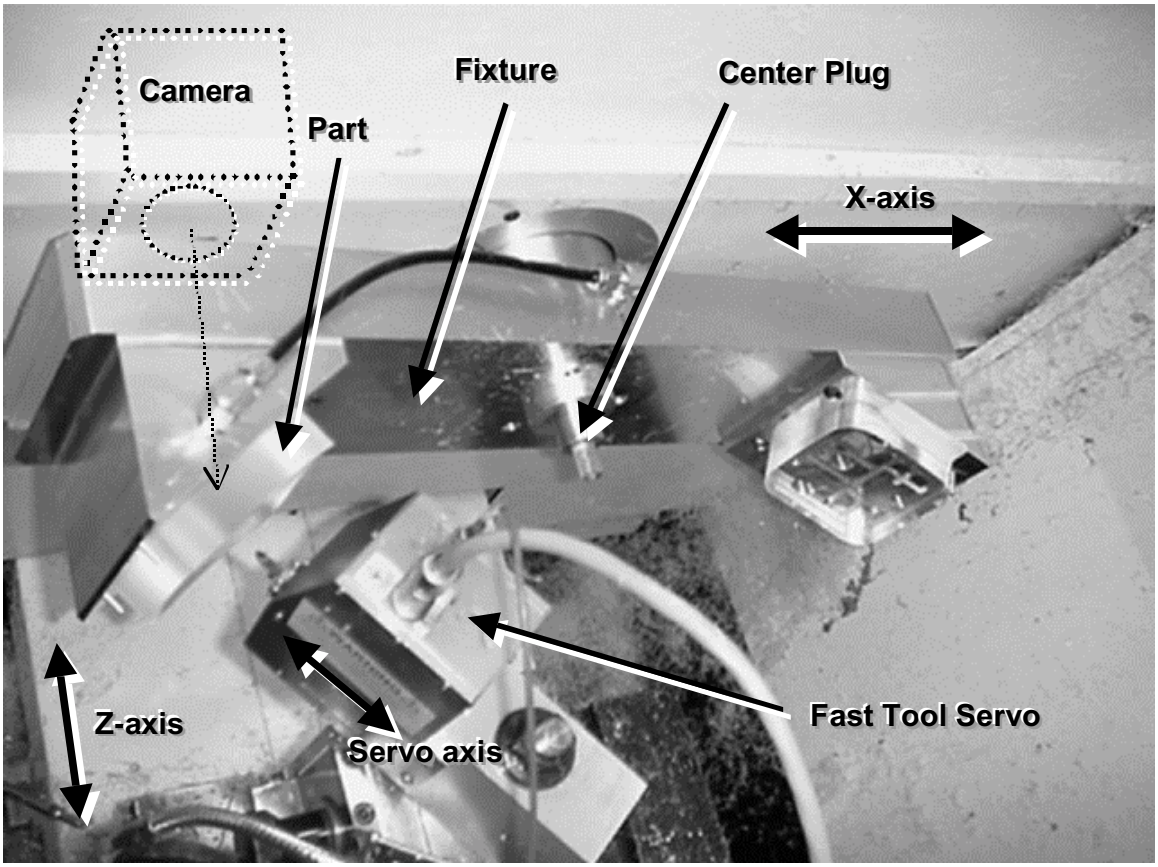

Figure 9. Machine setup. PMMA test blanks are mounted on the vacuum pedestals. The alignment camera is behind the splash shield.

12.5.1 ALIGNMENT

Alignment of both the mirror blanks and the single-crystal diamond tool required several specialized procedures. The freshly lapped diamond tool radius had to be determined over the full 80° window to allow for accurate radius compensation and alignment. This was done using a Zygo NewView 5000 white-light interferometric microscope. The instrument comes equipped with precision X, Y, and Z stages for stitching multiple images to produce a large scale surface map. In this case, the NewView was used as an optical coordinate measurement machine (CMM) by turning the microscope objective into a high resolution alignment tool and collecting position data on the tool edge in X, Y, and Z. A simple least-squares circular curve fit found the tool

radius to be 2.9646 mm. The tool was aligned to the DTM spindle axis using the PMMA centering plug shown in Figure 9.

The pair of M4 mirror blanks had to be aligned with six degrees of freedom to the machine axes. The biconic surface is located with respect to fiducials machined onto the back and sides of each mirror blank. The blanks were constrained to a plane which was diamond flycut at 35.3° onto the pedestals of the chuck. These surfaces mate with the flat flycut surface on the back of each blank. The correct angle was ensured using the DTM axes to probe the surface of the wedge-shaped pedestals with an electronic indicator. The radial position, rotation on the pedestal and angular position with respect to the spindle were aligned using two crosshair marks machined into the rear surface of the parts. A video vision system was positioned behind the X axis splash shield and aligned to the X axis and spindle using a needle. The needle had been previously located with respect to the spindle centerline and was subsequently moved to a known radius given by the X axis positions of the fiducial crosshairs. At this X position a pair of camera crosshairs were aligned with the needle. The camera could then be used to accurately position the parts by aligning the part fiducials with the camera crosshairs using a set of holes bored through the chuck. This provided a method for placement of each part to within 25 μm in X and Z and 120 μm in the direction of spindle rotation (i.e., the Y direction).

12.5.2 SYSTEM CONFIGURATION

The machining system, shown schematically in Figure 10, consists primarily of the diamond turning machine, the fast tool servo and two controllers. The DTM is commanded by a Delta Tau PMAC controller using standard lathe G-codes. This controller issues position commands to the machine axes via linear servo amplifiers to produce the aspheric rotationally symmetric portion of the part surface. It also executes a PLC which sends a simulated, pulsed encoder signal of X axis position information to the PC31 digital signal processor (DSP) that is executing the FTS trajectory generator. These pulses occur at 50 μm intervals. The DSP calculates the FTS toolpath according to current position information from the spindle (via its own encoder interface) and the simulated X axis position output. A custom counter interface circuit was built to count and buffer both position signals for digital input to the PC31. The FTS toolpath signal is an open-loop analog waveform since the Variform amplifier electronics contain both an analog closed-loop controller and a hysteresis compensator.

12.5.3 TESTING

The system was tested by machining a tilted flat. This method consists of commanding the FTS to follow a sine wave with a period of one spindle revolution whose amplitude is a linearly varying function of radial position from the spindle centerline. This allows the range and frequency requirements of the FTS for machining the M4 optics to be exercised while still

allowing the resultant part to be easily measured with an interferometer. The final results of this test produced a surface finish of 8-16 nm rms and a form error of 43 nm rms; both acceptable with respect to the specifications of 10 nm and 63 nm, respectively.

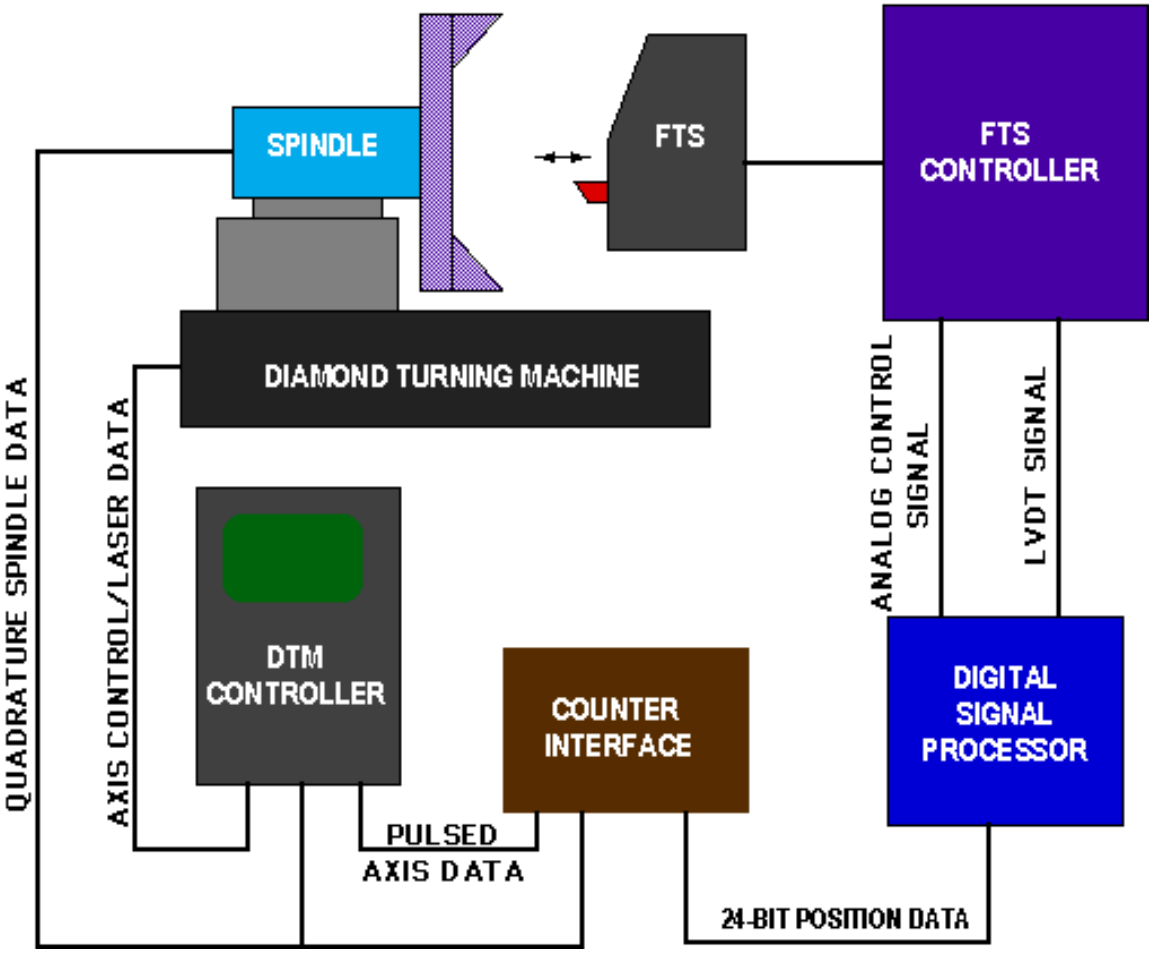

Figure 10. Schematic of the machine layout and control interfaces.

12.6 MACHINING

Before machining the biconic, the part fixture and alignment procedures were tested with PMMA test blanks mounted in place of the 6061 aluminum blanks. The FTS was commanded to follow a sine wave that mimics the Q4 NRS toolpath excursion in amplitude and location on the blanks. There were two reasons for doing this: acrylic is much more forgiving of a large depth of cut if there is an error and the aluminum blanks had significant processing invested in them (e.g., E.D.M. mounting tabs, stress relieving, crosshair fiducials, diamond flycut reference surfaces and a milled biconic front surface). Though the PMMA blanks were not stable enough to allow accurate form measurements, they did provide a good general test and an evaluation of the surface finish.

Machining of the aluminum blanks occurred in two phases: roughing and finishing. Several roughing passes were performed without FTS excursion. Cuts 10 µm deep were made with the spindle rotating 250 rpm at a feedrate of 25 mm/min. 250 µm of material were removed in this manner until the entire surface of each part was fully machined. The tool was then replaced with a freshly lapped tool which was centered using an acrylic centerplug. At this point, the servo was activated and another 140 µm was removed in 10 µm intervals. Once the entire surface of the parts was machined, a final finishing cut was made. A 1 µm deep finish pass was made with the spindle rotating 125 rpm at a crossfeed of 0.25 mm/min. The theoretical surface finish of 0.2 nm for this cut was far in excess of what was practically possible to ensure that this would not be a limitation. Chips were removed with a low-volume oil spray during the final cut.

12.7 RESULTS

12.7.1 SURFACE FINISH

The finished mirrors were measured for both form and surface finish. The visual appearance of the surface was poor, with significant scratching in the machining direction. As shown in Figure 11, measurements made with the Zygo NewView 5000 microscope revealed that most of the surface had a finish of 16-18 nm (rms). However, these relatively flat regions were interspersed with cusps on the order of 400 nm deep, occurring every 0.5 to 1.0 mm in the feed direction. Furthermore, their width (98 µm) is consistent with radius of the tool and the feature depth. This causes the overall finish to worsen considerably, but allows figure measurements to be made on an interferometer. The marks may have been caused by errant motions of the machine axes or, more likely, noise in the Variform LVDT feedback signal or the PC31 analog command signal. Both the LVDT and the analog command signals contain noise of sufficient amplitude to account for these surface cusps.

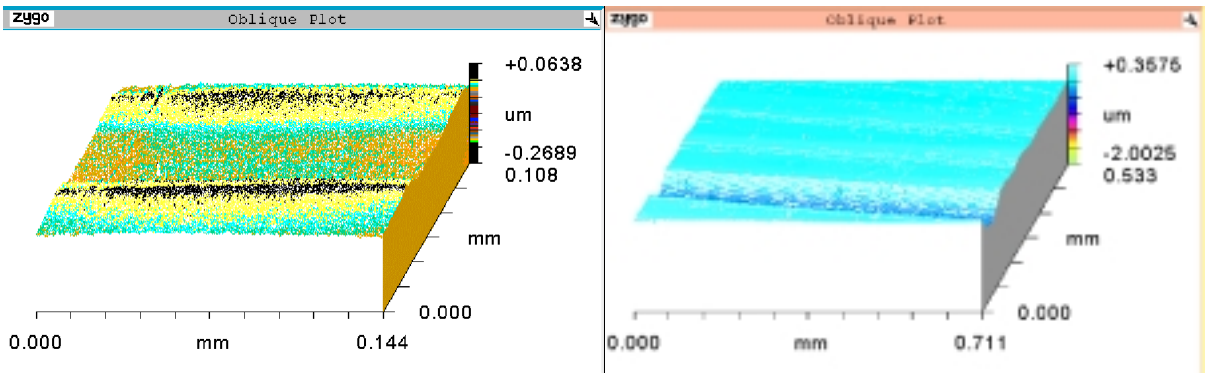

Figure 11. Surface finish is dominated by 16 nm rms regions (left) although frequent occurrence of 400 nm deep cusps causes finish to worsen considerably over larger areas (right).

12.7.2 FORM

CGH Interferometry

While the idea of using a tailored diffractive element to measure non-standard surface shapes in an interferometer is certainly not new [2], the degree of sophistication for CGH metrology has dramatically improved with in the last few years. Now commercially available, the CGH masks are equipped with alignment fiducials essential in setting up a measurement [3]. Figure 12 shows the CGH for M4. The central region is the null mask for the M4 surface and is surrounded by an alignment region. This aids in both aligning the mask to the interferometer as well as aligning the sample to the mask. Since traditional methods of finding fringes often do not apply for free-form surfaces, such tools are indispensable for CGH metrology. Unfortunately, this also means that fiducials must be applied to the sample and other alignment tools such as theodolites are required. In the case of M4, a diamond flycut back surface was used to align tip and tilt and several crosshairs were used to align translation (see Section 12.5.1). The fiducials do, however, serve another function in that they may later be used to align the mirror in the optical system.

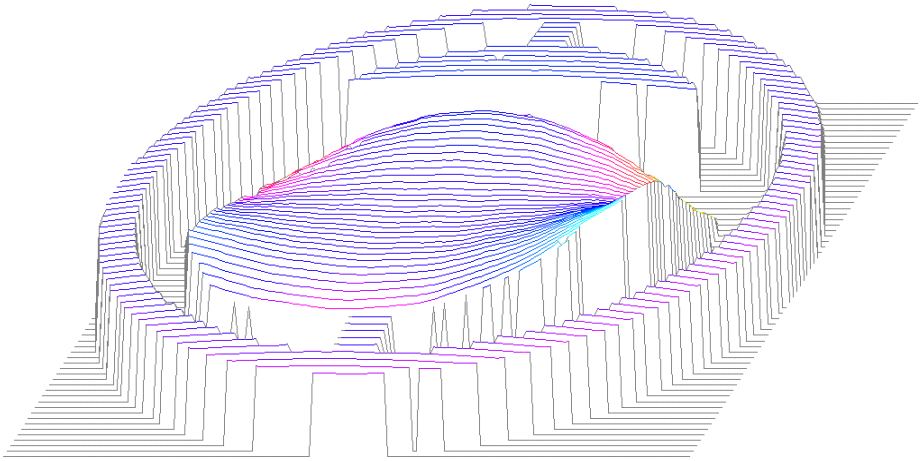

Figure 12. Interferogram of the CGH reference mask for M4.

CGH Results

Initial alignment of the CGH and mirror using fiducials immediately showed fringes and allowed data collection as shown in Figure 13(a). However a left-right offset is apparent. Systematic translation of the sample was used to minimize the error. This known translation was later correlated with a phase shift present in the FTS system (see Figure 14.) The residual error on the optimally aligned sample, shown in Figure 13(b), revealed a trefoil pattern identical to that of the servo excursion shown in Figure 5. This residual error has the same shape and orientation as the NRS motion of Figure 12 and shows that the part is "too large" (i.e., the servo amplitude was too great). While the amplitude of the measured error was about 8% of the servo excursion, the

shape correlation led to the discovery of a scaling error in the FTS output that had to be corrected. Coincidentally, the PC31 output signal was scaled with a gain of 1.0811 to achieve the correct servo amplitude as measured by the Variform LVDT with an oscilloscope during system setup and testing. A numerically generated reference surface confirmed these CGH results. A distorted (i.e., phase shifted and scaled) NRS component was added to the least squares aspheric component and compared with the interferometer data. These results show clearly that through the use of a CGH and proper alignment fiducials, one can troubleshoot a machining system in much the same way it would be done with a spherical or flat surface.

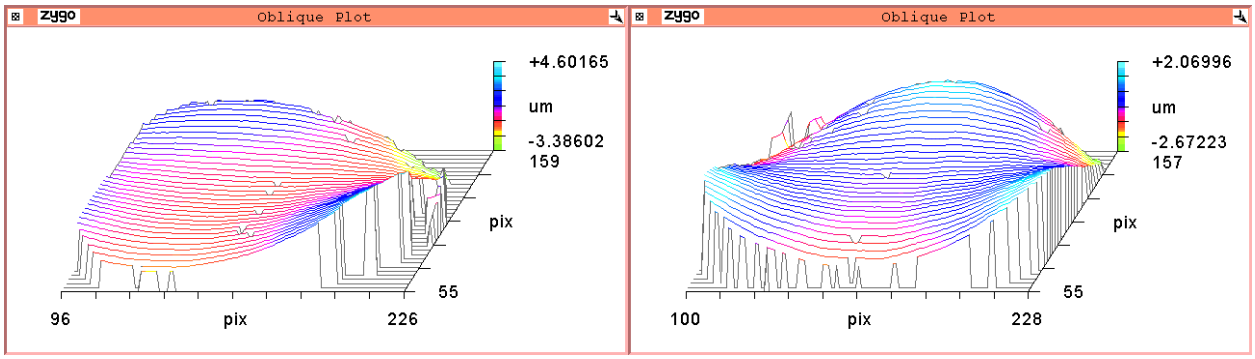

(a) (b)

Figure 13. M4 figure error with CGH null. (a) CGH alignment via fiducials. (b) Optimal CGH alignment. The error is dominated by the shape of the FTS excursion with a magnitude of 8% that of the servo. (Compare with Figures 5 and 12).

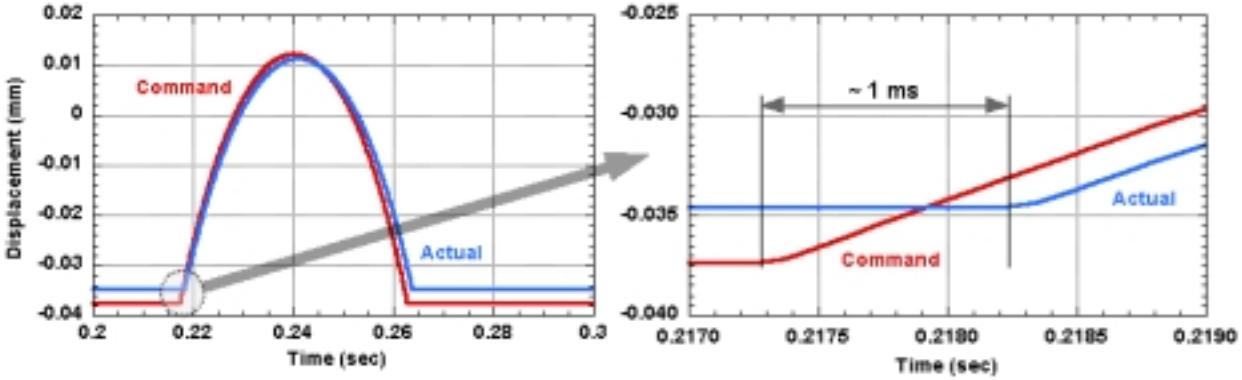

Figure 14. Variform FTS response to Q4 command signal at R = 180 mm. Actuator response is delayed about 1 msec and attenuated by 8%.

Profilometry

Since the CGH cannot be directly tested against a known standard, it is generally prudent to perform additional measurements with a method that can. While ultraprecision CMM's or multiaxis profilometers would be expertly suited to this task, they are not commonly available. Three-dimensional surface data can, however, be acquired by assembling multiple linear traces from a standard profilometer. One method, called the *Union Jack* [4], allows this assembly to be performed without the use of multiple axes. Fiducials placed on the surface of the part are used to relate the positions of the traces to each other. All of the intersections of the traces are then joined to assemble the data, as shown in Figure 15. Since each trace has multiple intersections, the redundant intersections can be used to test for alignment and measurement errors. This assembly process is tedious and errors may be introduced by interpolation at the trace intersections. If the assembled data and a reference data set are "aligned" in the same coordinate system then an error surface can be created by subtracting the measured data from the reference data.

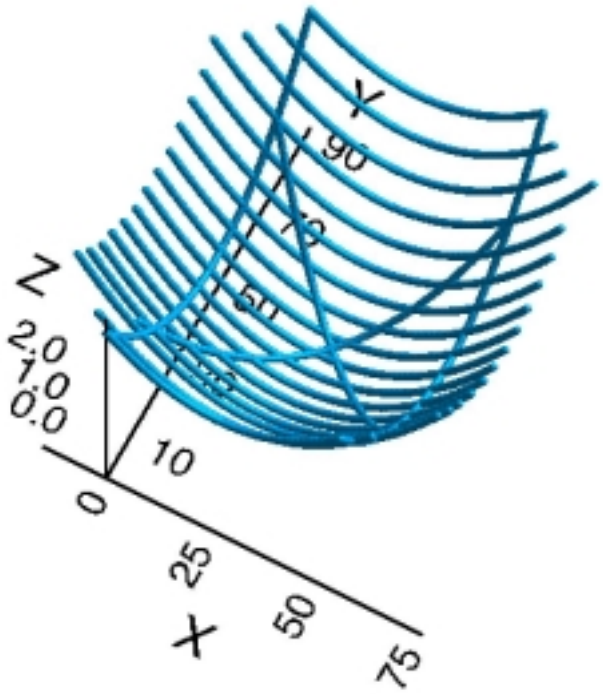

Figure 15. Profilometry measurements assembled into a 3-D surface using the *Union Jack* method.

Data Manipulation and Surface Fitting

Matlab™ software for automating 3D surface evaluation was developed. Two data sets are input for comparison. One is a measurement, presumably either a profilometer or interferometer data set and the other is a reference datum. The reference may be an analytic function (e.g., a biconic equation) or an [***x,y,z***] point cloud. An algorithm for registration of the measurement and reference data sets is illustrated in Figure 16. The problem is to find an alignment of the two surfaces (i.e., an orientation of one data set in the coordinate system of the other) that minimizes the difference between them. Figure 17 shows a reference data set for M4 that was generated from Equation (1), along with the assembled Talysurf measurement data from Figure 15. The measurement data is in the coordinate system of the Talysurf and does not overlap the reference data. To speed up the alignment process and reduce the probability of convergence to a local minimum, a preliminary coarse alignment is performed. The measurement data is translated so

that its center is coincident with the center of the reference data (see Figure 18) and then rotated about that center point so that it has the same normal vector as the reference data (see Figure 19). The Levenberg-Marquardt unconstrained nonlinear optimization algorithm is used for the final alignment of the two surfaces. The optimization merit function is the residual sum of squares error in either the parent ***z*** direction or the normal direction of the measurement. The optimization parameters are the elements of a homogeneous transformation matrix (HTM) that is used to locate the measurement data set with 6 degrees of freedom.

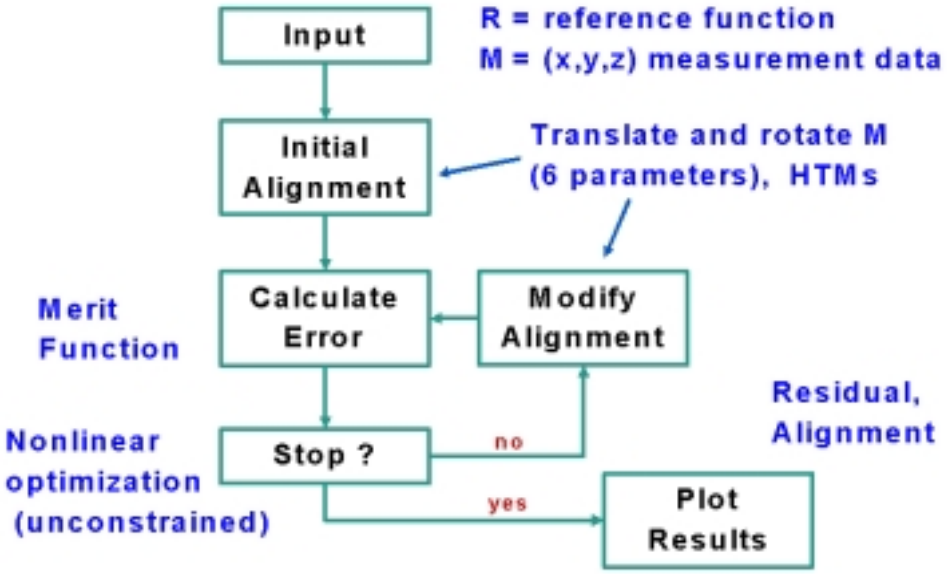

Figure 16. Surface alignment algorithm.

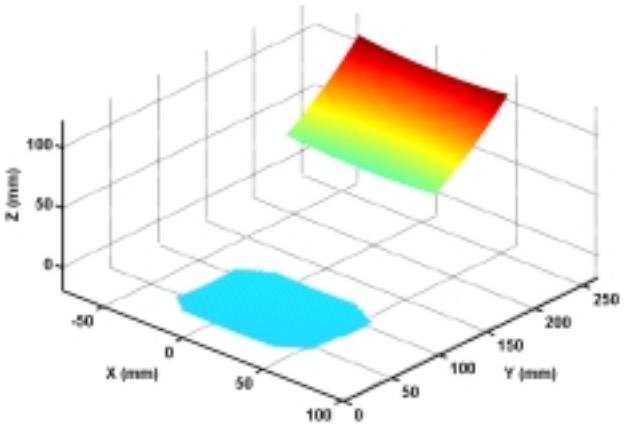

Figure 17. Initial orientation of measurement and reference surfaces.

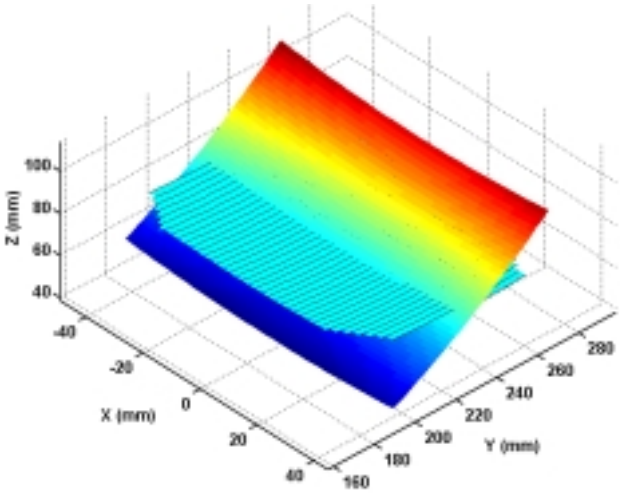

Figure 18. Surfaces after initial translation alignment operation.

Alignment modification translates the measurement data in the reference coordinate system and rotates it about a coordinate system whose origin is the geometric moment of the data set and whose ***z*** axis is normal to the surface. This is done to enhance the sensitivity of rotations for far off-axis data sets such as M4; otherwise small angle rotations are difficult to distinguish from translations. The output of the surface alignment algorithm is the residual error and the composite HTM that produces the optimal alignment. Standard metrology statistics can be calculated from the residuals. Throughout the process, the reference surface remains at its original location in the parent coordinate system.

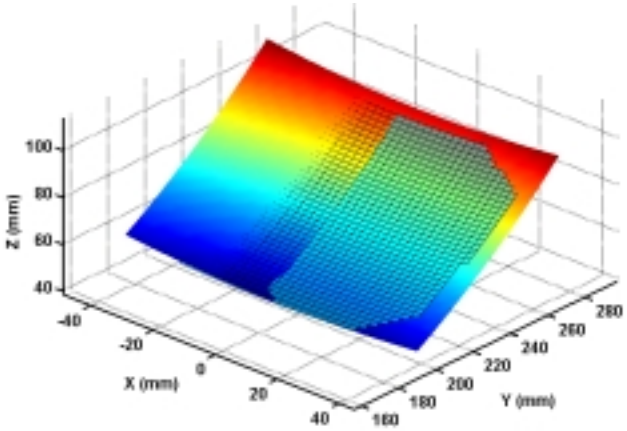

Figure 19. Surfaces after initial rotation.

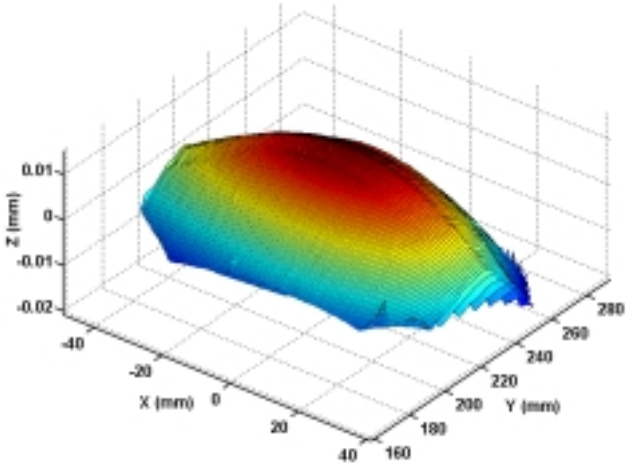

Figure 20. Residual error (z direction) after alignment optimization.

If an analytic function is not available as a reference datum, then the residual must be formed by interpolation. Either the reference surface can be triangulated onto the [***x,y***] grid of the measured data or vice versus or both data sets can be interpolated onto a common grid. This must be done on each evaluation of the merit function since parameter adjustments necessarily misalign the data. Figure 20 shows the final residual error obtained by subtracting the measurement data from the reference data in the ***z*** direction (i.e., $residual = Z_r - Z_m$). Note that the pillow shape of the residual error does not resemble the CGH residual surfaces shown in Figure 13. This is because in the interferometer, light passing through the CGH mask would be normal to a perfect test mirror. Hence the resulting fringes represent a subtraction of the object surface from the reference mask in a direction normal to the surface of the mirror, not simply in the ***z*** direction. For surfaces such as M4 with a fairly large range of slopes the difference can be large This situation is depicted in Figure 21 in two dimensions. The vector **E** is the ***z*** direction residual, but the vector **L** is the actual minimal distance between the two surfaces. The length of **L** can be approximated as the scalar projection of **E** onto the surface normal from a point in the measurement data. As shown in the figure, this operation requires calculation of the direction cosines at each point; however only the ***z*** direction cosine is needed since the vector **E** is [0 0 1]. Figure 22 is the final result after optimization and residual error calculation using surface normal estimates. The overall shape now resembles the error shape obtained with the CGH, but the

result is not completely satisfactory. Surface normal estimation is undefined at the edges of the mirror, so that data has been trimmed off in the figure. Also the estimated normal length is more sensitive to noise in the closely space ***x*** direction than in the widely spaced ***y*** direction. This could possibly be improved by interpolating the data onto an evenly spaced grid. Finally, the normal length is still an approximation. The true length could be found by a bisection algorithm to determine the intersection of the each normal vector with the reference surface. But, without accurate direction cosines for each data point, the exact intersection would not necessarily be the actual distance between the reference and measurement surfaces.

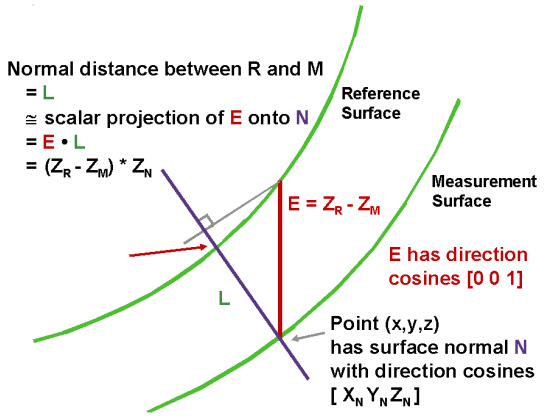

Figure 21. Error estimation normal to the measurement surface.

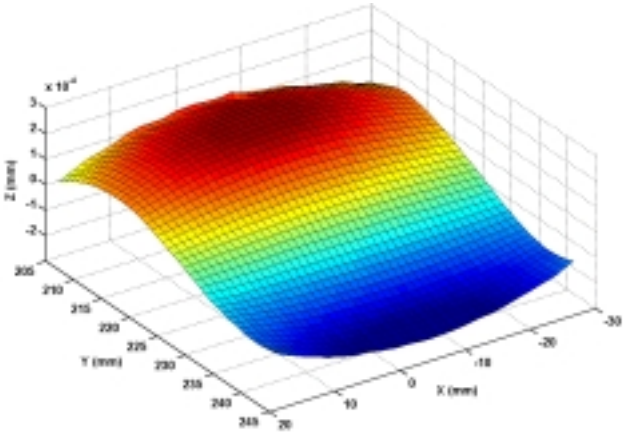

Figure 22. Residual error (normal direction).

12.8 CONCLUSIONS

The M4 mirror geometry has been thoroughly analyzed and a procedure developed that allowed it to be machined with the Variform FTS and the Nanoform 600. A special vacuum chuck was also designed and built to mount and align the mirror blanks. A custom hardware interface provides X axis and spindle position information in real-time to the PC31 DSP. In this way commanded motion of the Variform is synchronized with the movement of the Nanoform axes to produce non-rotationally symmetric surfaces on the diamond turning machine.

The aluminum M4 mirrors fabricated have proven that the method for machining these biconic surfaces is sound. With the elimination two anomalies, the specified surface finish of 10 nm (rms) and figure error of 63 nm (rms) should be achievable. Notwithstanding, the machining experiments have produced a pair of engineering prototypes suitable for preliminary testing of the assembly and operation of IRMOS.

The expanded use of free-form surfaces in optical systems is inevitable. As demonstrated in the case of the biconic mirror M4, figure metrology of these surfaces presents some unique challenges. While tools are available for measuring these surfaces, the techniques for doing so

expediently and economically are not yet mature. CGH reference masks may take weeks to design and fabricate and 3-D profilometer measurements require an arduous process of data reduction before meaningful results are available. Nevertheless, once results are obtained, they can be used in much the same way as standard ones for quality control, troubleshooting and performance assessment.

REFERENCES

1. Garrard, K.P., A. Sohn, R.G. Ohl, R. Mink, and V.J. Chambers. *Off-Axis Biconic Mirror Fabrication.* Proceedings of the Third International Meeting of EUSPEN, (2002).
2. MacGovern, A.J., and J.C. Wyant, *Computer Generated Holograms for Testing Optical Elements.* Applied Optics, 10, pp 691, (1971).
3. Diffraction International. Minnetonka, Minnesota, http://www.diffraction.com.
4. Hume, K.J. Engineering Metrology, 3rd ed., Macdonald & Co. Ltd, London (1970).

13 CHARACTERIZATION OF MECHANICAL INDENT EFFECTS ON POLYSTYRENE HEMISPHERES

Patrick D. Morrissey
Graduate Student
Jeffrey W. Eischen
Associate Professor
Department of Mechanical and Aerospace Engineering

Creating a residual stress field by plastic deformation (scribing or indents) has been shown to be a useful technique for precision shape modification. It has been applied to hard disk heads to control the features of the flying surface to the order of nanometers. This section discusses the result of the indents in polystyrene hemispheres. Whereas the effects of indents on flat surfaces have been defined, loads applied in various locations on dome-shaped components can be more difficult to understand. Therefore, experiments were conducted involving identical polystyrene hemispheres that were exposed to various load magnitudes and geometric configurations using a standard Rockwell C indenter apparatus. Measuring the shapes of these hemispheres after the indent experiments were performed gives insight to deformation behavior. Furthermore, finite element analysis (FEA) simulations were used to verify these results. Deformation results predicted by the simulations that correspond to the actual experiments could provide tremendous aid in accurately predicting and controlling the shape of 3D surfaces when exposed to various loads.

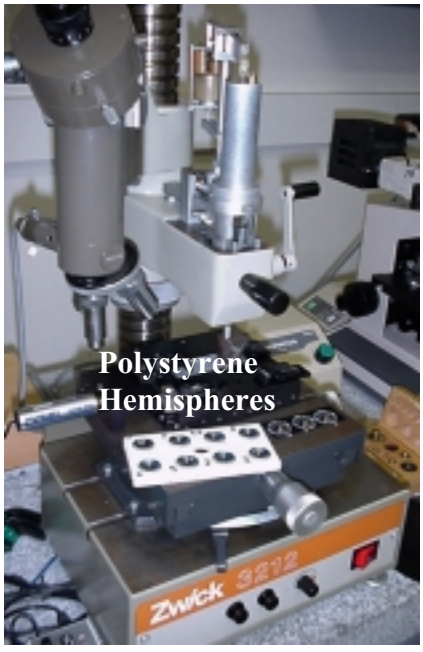

13.1 INTRODUCTION

Accurate shape control of 3D surfaces has applications in many industries. It often happens that final dimensional accuracy cannot be achieved by conventional techniques such as machining, lapping, or molding. Final adjustment of curvature on either a flat or curved surface may require changes in the range of several nanometers to micrometers. Recent work at the Precision Engineering Center has demonstrated the feasibility of using indentation and scribing techniques to induce shape changes on initially flat ceramic surfaces. Mechanical scribing—performed by dragging a diamond stylus across a surface—induces a localized layer of compressive stress, resulting in curvature away from the scribe (negative curvature). The focus of this exploratory research project was on investigating the magnitude of shape changes that could be induced on a polystyrene hemisphere. Because of the initial curvature of the surface and the constraint imposed by the shape, different results were expected for this geometry. Measurements have been made to quantify the nature of residual deformation induced by single indents and prescribed patterns of indents. Finite element simulations have been performed to validate a simulation model of the indent process.

13.2 INDENTING

13.2.1 EXPERIMENTAL APPARATUS

Three batches of polystyrene hemispherical parts with a inner radii and wall thicknesses of 6.7mm and 0.6mm, respectively, were used for the experiments. The parts were fabricated with an integral annular ring that tended to stiffen the basic hemispherical shape, see Figure 1. The indents were made using a hardness test machine containing a Rockwell C hardness tip, 120° conical tip with 0.2mm radius. For each experiment, the parts were supported around the periphery of the integral ring with a plastic tray providing support forces R_1 and R_2, as shown in Figure 1. The shape of each part prior to the indention process was measured using the Zygo GPI Interferometer. When a load was applied, the surface of the hemisphere would either bulge outward leaving a bump on the outer surface, or deform inward as the indenter was pulled away, leaving an indent or "dimple". These experiments were conducted to study the

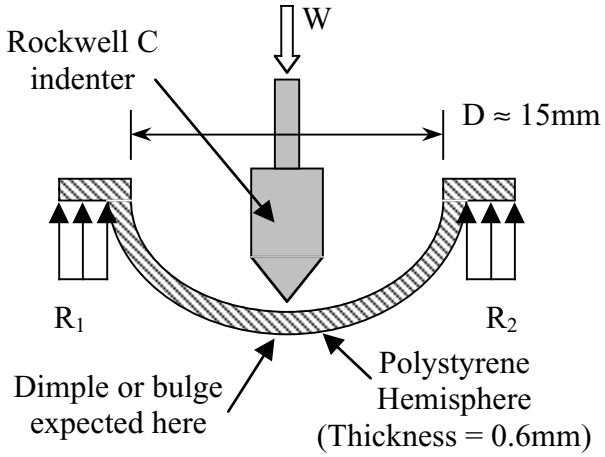

Figure 1: Setup for the indent experiments

effects of different indenter loads and geometries and to determine which combinations created bulges and which ones created dimples.

The goal of the procedure was to produce dimple depths on the order of 10_m in depth. Following the indenting process, each part was re-measured and compared to the original shape to ascertain the degree of permanent distortion induced. The load magnitude on the hardness tester, *W*, was adjusted systematically to achieve desired results.

Parts were measured in three separate batches. Data from the first batch is summarized in Table 1. These initial experiments identified the load threshold that would result in "bulging" rather than "dimpling". For loads greater than 1.5 – 1.7kg, bulges were generally the result, and for loads below 1.5kg, dimple depths decreased with a decreasing load. Results for this batch involving multiple indents correspond to a line pattern, except for one case in which a grid pattern was used. For this first batch, the grid pattern resulted in the deepest dimple depth, 1.10_m, significantly less than the desired depth.

Table 1: Experimental results for batch #1

Part #	Load (kg)	# of Indents	Spacing (_m)	Dimple Depth (_m)
1	3.0	5	10	(bulge)
2	2.0	1	N/A	(bulge)
3	1.7	1	N/A	(bulge)
4	1.5	10	10	(bulge)
5	1.5	1	N/A	1.00
6	1.3	25 (grid)	10	1.10
7	1.3	20	10	0.80
8	1.0	15	10	0.75
9	0.7	10	10	0.55
10	0.7	5	10	0.50
11	0.7	1	N/A	0.40

The second batch of indents was used to study dimple behavior resulting from a series of indents arranged in a circular pattern of varying diameter. This arrangement resulted in deeper dimples, and thus data from the second batch of parts was more encouraging. The largest circle achieving usable results had a diameter equal to 1.5mm. Several parts were indented with concentric circles. The deepest dimple depth achieved was 5.37_m by using 16 indents arranged in two concentric circles of 1.0mm and 0.5mm diameters, as seen for part #12 listed in Table 2. Figure 2 shows the interferometer plot for this case. This figure represents the difference between the before- and after-indent profiles for the outer surface of the part. In this set of experiments, it

was discovered that increasing the diameter of the ring of indents beyond 1.5mm generally led to undesirable bulges.

Table 2: Experimental results for batch #2

Part #	Load (kg)	# of Indents	Diam. (mm)	Dimple Depth (_m)
1	1.3	16	6.0	N/A
2	1.3	8	2.0	(bulge)
3	1.3	8	2.0	(bulge)
4	1.3	8	1.5	(bulge)
5	1.3	8	1.5	1.26
6	1.3	8	1.5	1.20
7	1.3	8	1.0	2.80
8	1.3	8	1.0	4.00
9	1.3	8	1.0	2.45
10	1.3	8	1.0	(bulge)
11	1.3	16	$D_1 = 1.0$ $D_2 = 0.5$	4.00
12	1.3	16	$D_1 = 1.0$ $D_2 = 0.5$	5.37
13	1.0	24	$D_1 = 1.5$ $D_2 = 1.0$ $D_3 = 0.5$	2.02

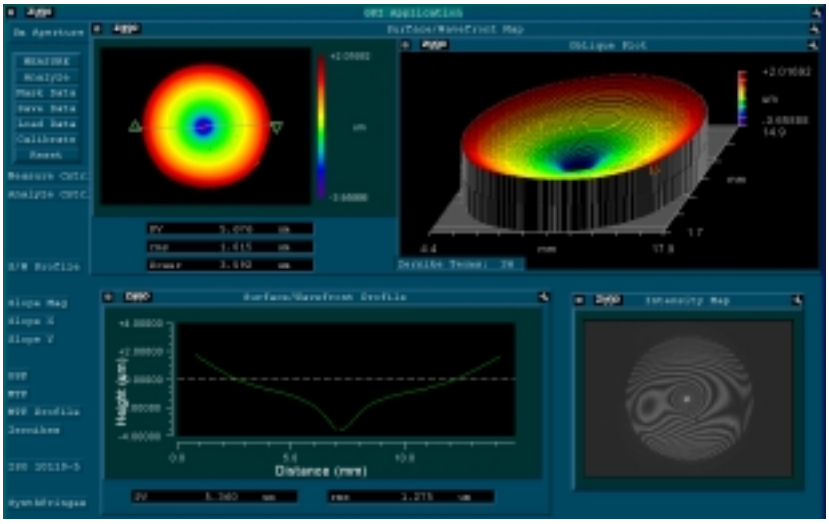

Figure 2: Interferometer plot of Part 12 from batch #2, showing a typical dimple.

In testing the third batch of parts, the goal was to spread out the indent pattern (grid) by increasing the dimensions to a 6–8mm range. These tests were generally unsuccessful due to fixture instability. The fixture allowed the parts to shift laterally as the indents were induced, and thus the desired indent patterns could not be achieved and measured. Where measurable results were successfully obtained (grid widths less than or equal to 2mm), placing several indents in a grid pattern generally led to a bulge formation. These results are summarized in Table 3, with Figure 3 showing a typical bulge profile. Note the two-peak profile of the bulge from the radial profile, with a dimple between the two bulge peaks.

Table 3: Experimental results for batch #3. All grids square, all loads 1.3 kg.

Part #	Grid Width (kg)	# of Indents	Spacing (mm)	Dimple Depth (_m)
1	6.0	36 (grid)	1.000	N/A
2	4.0	16 (grid)	1.000	N/A
3	2.0	25 (grid)	0.500	(bulge)
4	1.5	25 (grid)	0.375	(bulge)
5	1.0	25 (grid)	0.250	(bulge)
6	1.0	9 (grid)	0.500	1.68

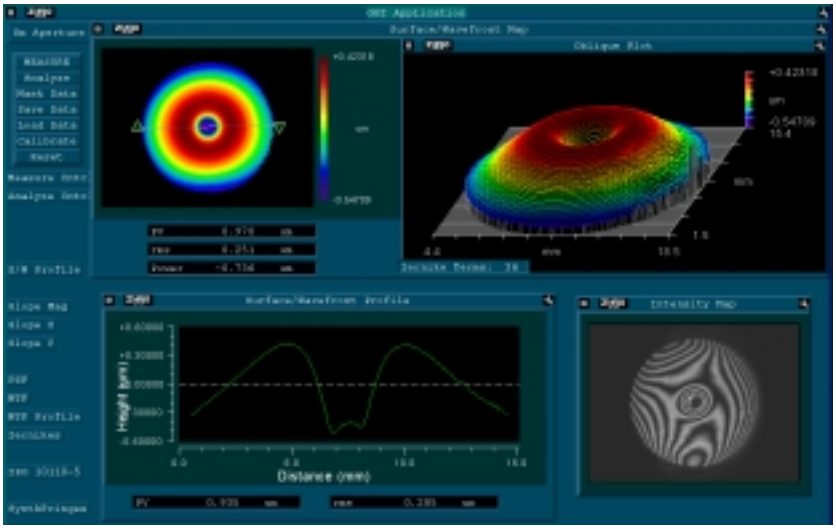

Figure 3: Interferometer plot of Part 3 from batch #3, showing a typical bulge.

13.2.2 NUMERICAL SIMULATIONS

Finite element analysis (FEA) simulations were conducted to compliment the experimental results. A two-dimensional arch model was used, with the acknowledgement that the arch is less stiff than the hemispherical shape of the actual parts. With the 2D approximations, the stiffness

deficit would be expected lead to FEA calculations of deeper dimples than experimentally measured. The commercial software code LS-DYNA was used for the study.

Figure 4 shows a typical finite element mesh. Fixed boundary conditions were imposed at the base of the arch on both sides (to account for the integral stiffening ring), and the indent event was modeled by imposing specified displacements at the apex on the inner surface. These displacements simulated the indenter's wedging action. The indent "stroke" was chosen to bring the stresses in the material to just above the yielding point, resulting in a residual stress after load removal and a dimple on the outer surface, just opposite the indent location on the inner surface. Figure 4 shows a typical finite element mesh.

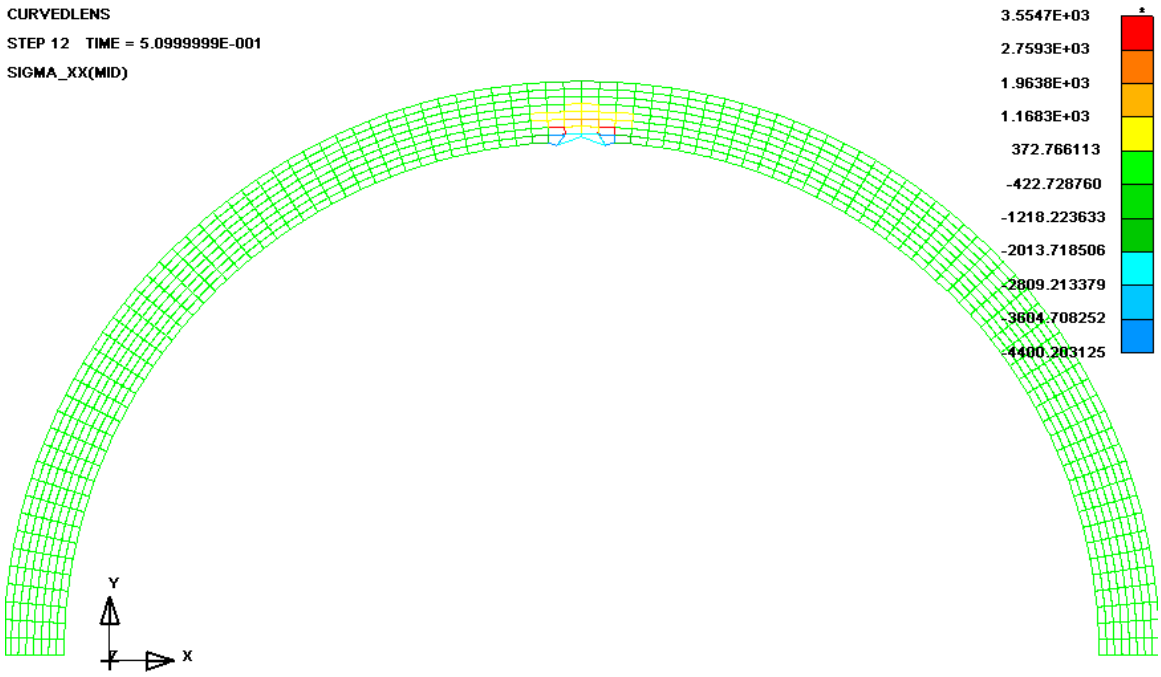

Figure 4: Finite element analysis mesh created with the LS-DYNA software.

While a crude model of the process, the results were in rough agreement with the experiments (predicted dimples deeper than measured). Table 4 is a summary of these results. For the baseline part (6.7mm inner radius, 0.6mm wall thickness), the FEA predicted a dimple depth in the range of 10.2_m – 12.4_m, depending on the indent stroke. This range is somewhat above the maximum measured values, but is not unreasonable given the modeling assumptions. Decreasing the wall thickness achieved greater dimple depths. A 20% reduction resulted in dimple depths in the range 14.3_m – 15.3_m.

Table 4: Dimple depth dependence on part thickness for FEA simulations.

Part Configuration	Indent Stroke = 0.003 in	Indent Stroke = 0.004 in
Baseline Thickness	10.2 _m	12.4 _m
20% Thinner	14.3 _m	15.3 _m

13.3 CONCLUSIONS

The preliminary experiments performed with the three batches of polystyrene parts provided a foundation for understanding the effects of various indent loads and geometries. Single indent loads greater than 1.5kg – 1.7kg generally produced bulges, while linear patterns of indents using a lower load produced dimples, though of lesser depth than desired (depth less than 1_m). Indent grids with sub-millimeter dimensions increased the dimple depths, but not considerably. The largest and most desirable dimple depths corresponded to experiments using multiple indents in a circular geometry. The greatest dimple depth, 5.37_m, was achieved using indents in a concentric circle pattern. Increasing the grid or circle pattern dimensions beyond 2.0mm resulted in instability of the measurement apparatus. The FEA simulation results corresponded rather well with the experimental results. Additionally, these simulations demonstrated that decreasing wall thickness would further increase dimple depths.

Designing a fixture that secures the parts during the indentation process would be desirable. The indenter tip should remain normal to the surface while a grid or circle of indents is being produced, which would require re-orienting the hemispherical part during the process. Such a fixture would allow for a wider range of indent grid and circle sizes, thus potentially increasing the dimple depths to desirable magnitudes.

FACULTY, STAFF, AND STUDENTS OF THE PRECISION ENGINEERING CENTER

Standing (L to R): T. Dow, K. Freitag, T. Randall, S. Clayton, R. Scattergood, G. Buckner, A. Sohn, P. Morrissey, J. Eischen, and W. Panusittikorn

Sitting: (L to R): P. Ro, B. Chatham, T. Wu, L. Underhill, K. Garrard, and N. Negishi

Students Not Pictured: D. Hood, D. Gill, D. Kametz, S. Sigmon, and A. Kiefer

Faculty Not Pictured: K. Falter, D. Griffis, P. Russell, A. Shih, and D. Youden

FACULTY

THOMAS A. DOW

Director, Precision Engineering Center
Professor, Department of Mechanical and Aerospace Engineering

BS, Mechanical Engineering, Virginia Polytechnical Institute, 1966
MS, Engineering Design, Case Institute of Technology, 1968
PhD, Mechanical Engineering, Northwestern University, 1972

After receiving his PhD degree from Northwestern University in 1972, Dr. Dow joined the Tribology Section of Battelle Columbus Laboratories and worked there for ten years. His research interests were in the areas of friction and wear and included studies on a wide variety of topics from lubrication of cold-rolling mills using oil-in-water emulsions to wet braking effectiveness of bicycle brakes to elastohydrodynamic lubricant film generation in ball and roller bearings. He developed experimental apparatuses, established analytical models, and corroborated those analyses with experimental measurements. Dr. Dow joined the faculty at North Carolina State University in 1982 and was instrumental in developing the academic and research program in precision engineering. His current research interests include the design of precision machining systems, real-time control, and metrology. He was one of the founders of the American Society for Precision Engineering and currently acts as the Executive Director.

GREGORY D. BUCKNER

Assistant Professor, Department of Mechanical and Aerospace Engineering

BS, Mechanical Engineering, Louisiana State University, 1986
MS, Mechanical Engineering, Virginia Polytechnic Institute, 1987
PhD, Mechanical Engineering, University of Texas at Austin, 1996

After receiving his PhD degree from the University of Texas at Austin in 1996, Dr. Buckner joined the University of Texas Center for Electromechanics (UT-CEM), where he served as a research engineer until 1999. His research at UT-CEM focused on the design and implementation of advanced controllers for electromechanical systems. Applications included self-learning control systems for active vehicle suspensions, magnetic bearings for flywheel systems, and manufacturing processes. Dr. Buckner joined the faculty at North Carolina State University in 1999 as an Assistant Professor of Mechanical and Aerospace Engineering. Dr. Buckner's research and teaching interests focus on the design and control of electromechanical systems, with an emphasis on self-learning algorithms. Current research topics include electromechanical actuators for system identification of milling processes, and magnetic bearings for flywheel and milling applications.

JEFFREY W. EISCHEN

Associate Professor
Department of Mechanical and Aerospace Engineering

BS, Mechanical Engineering, UCLA, 1978
MS, Mechanical Engineering, Stanford University, 1981
PhD, Mechanical Engineering, Stanford University, 1986

Dr. Eischen has been with N.C. State since 1986 and his research areas of interest include computational solid mechanics, elasticity, fracture mechanics and structural dynamics. Dr. Eischen worked with Failure Analysis Associates from June 1978 - June 1986 as a Mechanical Engineer. His primary responsibilities included analysis and prevention of industrial equipment failures.

KARL J. FALTER

Senior Development Engineer, Eastman Kodak Company
Adjunct Assistant Professor, Department of Mechanical and Aerospace Engineering

BS, Mechanical Engineering NC State University, 1988
MS, Mechanical Engineering NC State University, 1990
PhD, Mechanical Engineering NC State University, 1992

Prior to joining Eastman Kodak's Manufacturing Systems Technology Division in 1997, Dr. Falter was a Research Engineer for Rank-Pneumo, a division of Rank-Taylor Hobson. He also assisted the Rank-Taylor fellows in their research at the Precision Engineering Center. Dr. Falter previously worked as a post graduate researcher at the Precision Engineering Center on a variety of projects. These projects ranged from study of the acoustic disturbance of a diamond turning machine to finite element analysis of diamond tools. Dr. Falter's PhD dissertation concerned simplifications of finite element models used in the shock response analysis of electronic assemblies. His MS thesis, which concerned a laboratory technique used to measure power flow in vibrating structures, was completed as a student in the Precision Engineering Center.

PAUL I. RO

Associate Professor
Mechanical and Aerospace Engineering Department

BS, Mechanical Engineering, University of Minnesota, 1982
MS, Mechanical Engineering, Massachusetts Institute of Technology, 1985
PhD, Mechanical Engineering, Massachusetts Institute of Technology, 1989

Dr. Ro joined the faculty of North Carolina State University in January 1989, as an Assistant Professor in the Mechanical & Aerospace Engineering Department. He became an Associate Professor in July 1994. Dr. Ro has developed two graduate courses in the department (multivariable Control and Robotics) and has taught undergraduate Automatic Control and Dynamics courses. His research covers a wide range of controls and various applications of control theories in the following three areas: Precision Engineering, Robotics and Intelligent Vehicle Control.

In precision engineering, Dr. Ro's research concentrates on the characterization and control of microdynamic behaviors of precision slide systems (ball-screw, traction drive, piezo-electric drive, electrostatic drives and magnetic servo levitated drive) to enhance their nano-motion capabilities, development of advanced control schemes and experimental verifications to improve diamond turning process using force and position sensory feedbacks, design of a long-range fast tool servo system using magnetic servo levitated actuators, and active control of precision slide vibration using piezo-electric drives. In robotics, some of the on-going projects include design and implementation of free-floating non-holonomic space robot and a planar passive-joint robot for fuel consumption minimization, neural-fuzzy hybrid scheme for mobile robot path planning, and two-arm coordinated motion control for fixtureless assembly. In intelligent vehicle control, on-going projects include nonlinear tire model identification by Artificial Neural Network, hybrid neural-sliding mode control of 4 Wheel steering for robust handling, semi-active suspension control using
energy based Fuzzy Logic scheme, and others.

PHILLIP E. RUSSELL

Professor
Department of Materials Science and Engineering

BS, Physics, Appalachian State University, 1975
MS, Physics, West Virginia University, 1977
PhD, Materials Science and Engineering, University of Florida, 1982

After graduate work at the University of Florida, Dr. Russell joined the Solar Energy Research Institute (a DOE lab) in Golden Co. in 1980. There he developed a photovoltic materials and device characterization laboratory with emphasis on electron and ion beam analytical instrumentation. After three years at SERI, Dr. Russell joined JEOL, Inc. in Boston, Massachusetts, an electron optical instrumentation company where he led the technical and application groups. One of his major projects was the development of an electron beam based integrated circuit metrology system. He was also involved in the development and application of focused ion beam systems and electron beam lithography systems, as well as numerous analytical instrumentation projects.

On joining North Carolina State University, Dr. Russell took on the role of Director of the Analytical Instrumentation Facility and has established graduate level courses in electron optics and electron optical instrumentation techniques. He was awarded the NSF Presidential Young Investigator Award in 1987. His research at NCSU and the Precision Engineering Center are in the areas of Scanned Probe Microscopy, Focused Ion Beam Technology, Scanning Electron Microscopy, Lithography metrology and beam testing of integrated circuits.

RONALD O. SCATTERGOOD

Professor
Materials Science and Engineering Department

BS, Metallurgical Engineering, Lehigh University, 1961
MS, Metallurgy, Massachusetts Institute of Technology, 1963
PhD, Metallurgy, Massachusetts Institute of Technology, 1968

R.O. Scattergood is a Professor in the Department of Materials Science and Engineering. He received BS degrees in Mining Engineering and Metallurgical Engineering from Lehigh University. His MS and PhD degrees were obtained in Metallurgy from M.I.T. In 1968 he became a member of the basic research staff in the Materials Science Division at the Argonne National Laboratory. In 1981, he joined the faculty as a Professor of Materials Engineering at North Carolina State University.

Professor Scattergood's major research interests have been focused on the mechanical behavior of solids. He has worked in the areas of strengthening mechanisms in solids, continuum theory of defects, radiation effects, wear and fracture processes in ceramics, and precision engineering with emphasis on machining processes. He has expertise in both analytical and computer modeling as well as in mechanical testing methods and microscopy. He has published over 140 technical papers, books and reports.

ALBERT J. SHIH

Associate Professor
Mechanical and Aerospace Engineering

BSME, National Cheng Kung University, Taiwan, 1984
MSME, National Cheng Kung University, Taiwan, 1986
PhD, Purdue University, 1991

Before joining N.C. State University in 1998, Dr. Shih worked in the Fuel Systems and Technical Center of Cummins Engine Company for seven years. He developed innovative and cost-effective manufacturing processes for sub-micron precision grinding of ceramic and hardened steel diesel engine components. He also worked in teams to implement the sub-micron precision ceramic plungers for diesel fuel systems. He led a team of three companies, Cummins Engine Co., Milacron, Inc. and Goldcrown (part of the UNOVA) to win a NIST ATP (Advanced Technology Program) grant on "Sub-micron Precision Grinding of Advanced Engineering Materials" in 1997. At Cummins, he continued to conduct basic research and publish results in the broad area of mechanical engineering.

DAVID YOUDEN

Technical Associate, Eastman Kodak Company
Adjunct Lecturer, Department of Mechanical and Aerospace Engineering

ASME, Central New England College, Worcester, MA, 1965

Prior to joining Eastman Kodak's Manufacturing Systems Technology Division in 1997, Mr. Youden was Research and Development Manager at Rank Pneumo, a division of Rank Taylor Hobson Inc. for ten years. Before that, he was Director of Engineering at the Cone Blanchard Machine Company. He has also worked at Ocean Systems, Inc. of Reston, Virginia and the Heald Machine Company, a division of Cincinnati Milacron. During his professional career, Mr. Youden has been granted numerous patents in the field of machine tools, and he has published and presented technical papers on the design and testing of ultra-precision machine tools in the US, Japan, and Germany.

Mr. Youden graduated from Central New England College and attended Worcester Polytechnic Institute and Clark University. He is a charter member of the American Society for Precision Engineering.

STAFF

KENNETH P. GARRARD

Research Assistant
Precision Engineering Center

BS, Computer Science, North Carolina State University, 1979
MS, Computer Studies, North Carolina State University, 1983

As a full-time research assistant, Mr. Garrard is studying the design of systems software that supports the development of high-speed real-time applications for special purpose multiprocessor computer systems. He has several years experience in academia and industry designing and implementing real-time systems. As a Precision Engineering Center staff member, Mr. Garrard's current activities include the design and implementation of software for Diamond Turning Machine and Fast Tool Servo controller projects.

ALEXANDER SOHN

Research Assistant/Lecturer
Precision Engineering Center

B.S., Physics, University of Texas at Arlington, 1992
M.S., Physics, University of Texas at Arlington, 1994

Mr. Sohn joined the Precision Engineering Center in August, 1997 as a member of the technical staff. His current research interests range from machine design and metrology to the design and fabrication of nonimaging optics. Mr. Sohn's varied research activities began in microwave optics and atomic physics as a student at the University of Texas at Arlington and later progressed to precision machine design, design and fabrication of plastic optics as well as automation and machine vision at Fresnel Technologies, Inc. in Fort Worth, Texas.

LAURA UNDERHILL

Administrative Assistant
Precision Engineering Center

BA, Education, University of North Florida, 1994

Ms. Underhill became a member of the PEC Staff in August 2001. Previously she was an administrative assistant at North Florida Shipyards in Jacksonville, FL, and Computer Source in Jacksonville, FL. Ms. Underhill brings to the Center many years of administrative experience. Ms. Underhill provides the overall administrative support for the Center.

GRADUATE STUDENTS DURING 2002

STUART CLAYTON received his BS degree in Mechanical Engineering from NC State University in May of 2001. After taking a summer off from school, Stuart enrolled in graduate school here at the PEC. Currently, he is pursuing a Master's of Science degree in Mechanical Engineering. His research involves an investigation of deflections of high-speed miniature milling tools and the ability to compensate for tool deflections using magnetic bearing spindles.

KARL FREITAG graduated from Clarkson University in 1995 with a BS in Mechanical Engineering. After graduation he went to work in the automotive industry for New Venture Gear's Transfer Case Division in Syracse, NY. At NVG, he worked as a product engineer and worked on the transfer case design for the 1998 Dodge Durango. After NVG, Karl has been working for the past 7 years as a Senior Engineer in Optical Fiber Manufacturing for Corning, Inc. in Wilmington, NC. Upon completion of his master's degree in Spring 2004, Karl plans to continue on in pursuit of a PhD in Mechanical Engineering.

DAVID GILL received his BS degree in Mechanical Engineering from Texas Tech University in 1994. He completed a MS degree in Mechanical Engineering from Purdue University in 1997 in the area of Computer Aided Design and Manufacturing. Prior to coming to N. C. State in 1999, he worked in Manufacturing Engineering and Product Engineering at Caterpillar, Inc. Currently he is working towards a Ph.D. in Mechanical Engineering. His specific area of study and research is precision replication of optics.

DAVID HOOD received his BS degree in mechanical engineering from NC State University in 2001. The next semester he enrolled at NC State and is currently pursuing his MS degree in Mechanical Engineering. His research involves active magnetic bearings and compensation for high-speed miniature milling tools and the ability to compensate for tool deflections.

DAVID KAMETZ received his BS degree in Mechanical Engineering in August of 2000 at Clarkson University in Potsdam, NY. David had a second major in Aeronautical Engineering while at Clarkson, but did not complete the program in order to enroll in graduate school. While at Clarkson he was the team leader of his senior design group in both his mechanical engineering and aeronautical engineering programs. His first semester at NCSU was spent as a teaching assistant in the machine shop, where he taught welding, machining and fabrication. David's research for IBM involves the improvement of both manufacturing lapping plates and the lapping process.

PATRICK MORRISSEY received his BS degree from NC State University in December of 2000. During his undergraduate studies he worked at Guilford Mills in Greensboro, NC for two summers where he worked on improving the heating system used to dry dyed fabrics.

He is currently pursuing his MS in Mechanical Engineering, and has been a member of the PEC since August of 2001. He is now working on a project with Los Alamos National Laboratories that involves the design of thin composite cylinders.

NOBUHIKO NEGISHI received his BS degree in Mechanical Engineering from NC State University in May of 2001. The next semester he enrolled at NC State and is currently pursuing his MS degree in Mechanical Engineering. His research involves elliptical vibration assisted machining with single point diamond tools.

WITOON PANUSITTIKORN received his MIE degree in Industrial Engineering from NC State University in 1998, and MS degree in Mechanical Engineering from NC State University in 2001. For his Master's thesis, he designed a nonlinear controller to manipulate a friction-based object transport system. He is currently pursing a PhD degree in Mechanical Engineering. His research involves the nonlinear controller design to compensate magnetic hysteresis in a magnetostrictive transducer.

TRAVIS RANDALL received his BS in Ceramic Engineering from Alfred University in May 2002. Originally from Ann Arbor, MI, Travis spent most of his life in upstate New York. He started working with the PEC and NC State in August 2002. Prior to arriving at NC State, he worked for NYS Department of Transportation and Alcoa Chemical. His research at the PEC entails the study of scribing mechanics in single crystal silicon.

QUN WAN received his BS degree in Thermophysics from University of Science and Technology of China in 1996. After working as manufacturing engineer in Teling (TRANE CHINA) Air-Conditioning Co. Ltd for one year, he came to the National University of Singapore, where he received his M.S. degree in Mechanical and Production Engineering in 2000. Prior to come to NC State University in Fall 2000, Qun had worked as software engineer in Vector Technology Co. Ltd (Singapore). Currently, he is a PhD student under Dr. Andrey Kuznetsov and his research focuses on Numeric Simulation on Cooling Effect of Ultrasonic Acoustic Streaming.

TAO WU received her BS and MS degree in Electrical Engineering from Northwestern Polytechnic University, China in 1993 and 1996. Prior to coming to NCSU in August 2000, She also received her PhD degree in Electrical Engineering in Shanghai Jiaotong University, China in 1999 and studied in University of Virginia for one year. Currently she is a PhD student in Mechanical and Aerospace Engineering and her research focuses on the development of a novel ultrasonic cooling concept for microelectronics.

UNDERGRADUATE STUDENTS DURING 2002

ELIZABETH CHATHAM began her undergraduate education at NCSU in the fall of 1999. Since then she has worked for the university in a variety of positions while attending classes. Her experiences include writing and teaching labs for the computer science department and working as an undergraduate research assistant for professors in the mechanical engineering department. She is also an active member and the current president of Pi Tau Sigma, the Mechanical Engineering Honorary Fraternity. Beth is planning to pursue a masters in mechanical engineering upon her graduation in the spring of 2003.

GRADUATES OF THE PRECISION ENGINEERING CENTER

Student	Degree	Date	Company/Location
Jeffrey Abler	PhD	December 1994	ETEC Systems, Inc. Tucson, AZ
William Allen	PhD	December 1994	North Carolina State Univ. Raleigh, NC
Kelly Allred	MS	June 1988	
Christopher Arcona	PhD	May 1993	Norton Worcester, MA
Bradford Austin	MS	June 2000	IBM Corporation Fishkill, NY
Markus Bauer	PhD	December 2001	SCYNEXIS Chemistry & Automation, Inc. Research Triangle Park, NC
Tom Bifano	PhD	June 1988	Boston University Boston, MA
Scott Blackley	MS	May 1990	Motorola Austin, TX
Peter Blake	PhD	December 1988	NASA Goddard Greenbelt, MD
Mark Cagle	MS	June 1986	NASA-Langley Norfolk, VA
John Carroll	PhD	January 1986	Cummins Engine Co. Columbus, IN
Matthew Cerniway	MS	October 2001	Naval Surface Warfare Ctr West Bethesda, MD
Damon Christenbury	MS	June 1985	Michelin Tire Co. Spartanburg, SC
James Cuttino	PhD	December 1994	UNC – Charlotte Charlotte, NC
Bob Day	PhD	July 1998	Los Alamos National Lab Los Alamos, NM

Joseph Drescher	PhD	May 1992	Pratt & Whitney East Hartford, CT
William Enloe	MS	December 1988	ITT Roanoke, VA
Karl Falter	MS	December 1989	Eastman Kodak Company Raleigh, NC
Peter Falter	PhD	May 1990	Lockheed-Martin Orlando, Florida
John Fasick	MS	May 1998	Kodak Rochester, NY
Steven Fawcett	PhD	June 1991	MicroE Natick, MA
Andre Fredette	PhD	May 1993	IBM Research Triangle Park, NC
David Gill	PhD	August 2002	Sandia National Laboratories Albuquerque, NM
Jim Gleeson	MS	June 1986	Battelle Columbus Labs Columbus, OH
Mary Smith Golding	MS	May 1990	Harris Corporation Melbourne, FL
David Grigg	PhD	August 1992	Zygo Corporation Middlefield, CT
Hector Gutierrez	PhD	October 1997	Florida Inst. Of Tech. Melbourne, FL.
Christian Haeuber	MS	December 1996	Harris Corporation Melbourne, FL
Matias Heinrich	MS	July 2001	Vistakon Jacksonville, FL
Gary Hiatt	PhD	May 1992	Caterpiller Zebulon, NC
Peter Hubbel	MS	December 1991	Delco Electronics Kokomo, IN
Konrad Jarausch	PhD	December 1999	Intel Corporation San Jose, CA

Bradley Jared	PhD	December 1999	3M Cincinnati, OH
David Kametz	MS	August 2002	Naval Air Warfare Center Aircraft Division Patuxent River, MD
Jerry Kannel	PhD	June 1986	Battelle Columbus Labs Columbus, OH
Byron Knight	MS	May 1990	Harris Corporation Melbourne, FL
Mark Landy	MS	June 1986	Battelle Columbus Labs Columbus, OH
Mike Loewenthal	MS	December 1988	SVG Norwalk, CT
Michael Long	PhD	June 2000	Eastman Kodak Rochester, NY
Bryan Love	MS	May 2001	Virginia Tech
Michael Hung-Tai Luh	MS	June 1989	Proctor and Gamble Cincinnati, OH
Dan Luttrell	MS	1987	Luttrell, Inc. New Boston, NH
Edward Marino	MS	September 1999	Pratt Whitney Hartford, CT
Edward Miller	MS	December 2000	General Electric Greenville, SC
Michele Miller	PhD	December 1994	Michigan Tech. University Houghton, MI
Paul Minor	MS	September 1998	Hartford, CT
Gary Mitchum	MS	June 1987	Harris Corporation Melbourne, FL
Charles Mooney	MS	December 1994	JEOL Peabody, MA
Larry Mosley	PhD	June 1987	Intel Corporation Chandler, AZ
Patrick Moyer	PhD	May 1993	UNC-Charlotte Charlotte, NC

Ayodele Oyewole	MS	October 1997	Pratt & Whitney East Hartford, CT
Hakan Ozisik	PhD	December 1989	
John Pellerin	MS	May 1990	Sematech Austin, TX
Ganesh Rao	MS	December 1994	Oak Ridge National Lab Oak Ridge, TN
John Richards	MS	September 1997	Intel Corporation San Jose, CA
Walter Rosenberger	MS	May 1993	The East Group Kinston, NC
Alex Ruxton	MS	December 1996	Pratt &Whitney Palm Beach, Florida
Anthony Santavy	MS	August 1996	Ford Dearborn, MI
Keith Sharp	PhD	May 1998	Morgan Crucible Dunn, NC
Gordon Shedd	PhD	March 1991	
Wonbo Shim	PhD	May 2000	Seagate Inc. Oklahoma City, OK
Robert Skolnick	MS	September 1997	San Diego, CA
Denise Skroch	MS	May 1989	IBM Corporation Raleigh, NC
Elizabeth Smith	MS	April 1989	
Stanley Smith	PhD	May 1993	
Ronald Sparks	PhD	May 1991	Alcoa Corporation Pittsburg, PA
Brent Stancil	MS	December 1996	Harris Corporation Melbourne, FL
Gene Storz	MS	May 1994	
Anand Tanikella	PhD	August 1996	Norton Industrial Ceramics Northboro, MA
Donna Thaus	MS	May 1996	Northern Telecom Research Triangle Park, NC

John Thornton	MS	December 1993	Digital Instruments Santa Barbara, CA
Michael Tidwell	MS	December 1991	
John Tyner	MS	June 1995	Naval Depot - Cherry Point

ACADEMIC PROGRAM

Problems and limitations associated with precision manufacturing can originate in the machine, the process, or the material. In fact, most problems will probably be caused by a combination of these factors. Therefore, improvement of current processes and development of new manufacturing methods will require knowledge of a multi-disciplinary array of subjects. The educational goal of the Precision Engineering Center is to develop an academic program which will educate scientists and engineers in metrology, control, materials, and the manufacturing methods of precision engineering.

The graduate students involved in the Precision Engineering Center have an annual stipend as research assistants. They can take up to 3 classes each semester while spending about 20 hours per week on their research projects. These students also work in the Center full-time during the summer months.

The Precision Engineering Center began in 1982 with an emphasis on the mechanical engineering problems associated with precision engineering. As a result, the original academic program proposed was biased toward courses related to mechanical design and analysis. However, as the research program has developed, the need for complementary research in sensors, materials, and computers has become obvious. A graduate student capable of making valuable contributions in the computer area, for example, will require a significantly different academic program than in mechanical engineering. For this reason, the Center faculty have set a core curriculum and each student in the program is required to take at least 3 of these core courses. The remainder of the courses for the MS or the PhD degree are determined by the university or department requirements and the faculty committee of the student.

The required courses are:

- MAE 545 Metrology in Precision Manufacturing
- PY 516 Physical Optics
- MAT 700 Modern Concepts in Materials Science
- CSC (ECE) 714 Real Time Computer Systems

PhD DEGREE PROGRAM

The PhD program in Precision Engineering has been set up as a multi-disciplinary program, drawing upon courses throughout the University to provide background and expertise for the students. It should contain required courses to insure solid grounding in the fundamentals plus electives to prepare the student in his area of specialization. Because Precision Engineering is concerned with an integrated manufacturing process, students interested in computer control, materials, machine structure, and measurement and actuation systems are involved in the program. Student research projects include the wide variety of topics addressed in this report. Each student's thesis should have an experimental component because Precision Engineering is basically a hands-on technology.

MS DEGREE PROGRAM

The Master of Science degree will have a higher percentage of application courses than the PhD degree. The emphasis will be to develop the foundation for involvement in precision engineering research and development. A total of 30 credits including 6 credits for the MS thesis is required. The thesis, while less comprehensive than the PhD dissertation, will be directed at important problems in Precision Engineering. Typically the MS program will take four semesters plus one summer.

UNDERGRADUATE PROGRAM

The undergraduate degree broadly prepares an engineering student for industrial activities ranging from product design and engineering sales to production implementation. Because a large share of engineers only have the BS degree, these will be the people who must implement the new technology developed in research programs like the Precision Engineering Center. Therefore, a way must be found to acquaint engineers at the BS level with the techniques, problems, and potential of precision manufacturing.

In most undergraduate degree programs only limited time is available for technical electives. However, these electives offer the student the opportunity to expand his knowledge in many different directions. Beginning graduate courses (such as metrology) can be used as undergraduate electives.

Undergraduate projects and summer employment have also been utilized to include undergraduate students into the research program of the Center. During the 1998-1999 academic year, four undergraduate students in Mechanical Engineering were involved various projects at the PEC.

STUDY PLANS

Study plans for several example students are given below both for the MS and the PhD degree. Because of the breadth of the field and the wide range of thesis topics, few if any study plans will be exactly the same. The plan will depend upon the student's background, his interests, his thesis topic, the department, and the chairman and members of his committee.

PhD PROGRAM IN MECHANICAL ENGINEERING

Major Courses:

- MAE 740 Advanced Machine Design I
- MAE 741 Advanced Machine Design II
- MAE 706 Heat Transfer Theory & Applications
- MAE 713 Principles of Structural Vibration
- MAE 760 Computational Fluid Mechanics and Heat Transfer
- MAE 545 Metrology in Precision Manufacturing
- MAE 715 Nonlinear Vibrations
- MAE 716 Random Vibration
- MAE 714 Analytical Methods in Structural Vibration
- MAE 742 Mechanical Design for Automated Assembly
- MAE 895 Doctoral Dissertation Research

Minor Courses:

- MA 511 Advanced Calculus I
- MA 775 Mathematical Methods in the Physical Sciences I
- CSC 780 Numerical Analysis II
- PY 516 Physical Optics
- ECE 716 System Control Engineering
- MAT 700 Modern Concepts in Materials Science
- ECE 726 Advanced Feedback Control
- ECE 764 Digital Image Processing

PhD PROGRAM IN MATERIALS ENGINEERING

Major Courses:

- MAT 710 Elements of Crystallography and Diffraction
- MAT 700 Modern Concepts in Materials Science
- MAT 556 Composite Materials
- MAT 715 Transmission Electron Microscopy
- MAT 795 Defect Analysis/Advanced Materials Experiments
- MAT 753 Advanced Mechanical Properties of Materials
- MAT 712 Scanning Electron Microscopy
- MAT 895 Doctoral Dissertation Research

Minor Courses:

- PY 414 Electromagnetism I
- ST 502 Experimental Statistics for Engineers I
- MAE 740 Advanced Machine Design I
- MAE 741 Advanced Machine Design II
- MAE 545 Metrology in Precision Manufacturing
- PY 516 Physical Optics
- MA 401 Applied Differential Equations II

PhD PROGRAM IN ME (FOR STUDENT WITH MS DEGREE)

- ECE 716 System Control Engineering
- ECE 791 Gate Array Design
- MAT 700 Modern Concepts in Materials Science
- PY 516 Physical Optics
- MA 502 Advanced Mathematics for Engineers and Scientists II
- MA 775 Mathematical Methods in the Physical Sciences I
- MA 780 Numerical Analysis II
- MAE 732 Fundamentals of Metal Machining Theory
- MAE 740 Advanced Machine Design I
- MAE 741 Advanced Machine Design II
- MAE 545 Metrology in Precision Manufacturing
- MAE 716 Random Vibration

MS PROGRAM FOR ME STUDENT

- MAE 713 Principles of Structural Vibration
- MAE 740 Advanced Machine Design I
- MAE 545 Metrology in Precision Manufacturing
- MAT 700 Modern Concepts in Materials Science
- PY 516 Physical Optics
- MA 501 Advanced Math for Engineers and Scientists I
- MA 502 Advanced Math for Engineers and Scientists II
- MAE 695 Master's Thesis Research

MS PROGRAM FOR COMPUTER SCIENCE STUDENT

- CSC 501 Operating Systems Principles
- CSC 506 Architecture of Parallel Computers
- CSC 512 Compiler Construction
- ECE 521 Computer Design and Technology
- CSC 715 Concurrent Software Systems
- MAE 545 Metrology for Precision Manufacturing
- MAE 789 Digital Control Systems
- ECE 764 Digital Image Processing

MS PROGRAM FOR MATERIALS SCIENCE STUDENT

- MAT 700 Modern Concepts in Material Science
- MAT 710 Elements of Crystallography and Diffraction
- MAT 715 Transmission Electron Microscopy
- MAT 712 Scanning Electron Microscopy
- MAT 722 Advanced Scanning Electron Microscopy and Surface Analysis
- MAE 545 Metrology for Precision Manufacturing
- PY 516 Physical Optics
- ECE 738 IC Technology and Fabrication
- MAT 695 Master's Thesis Research

MS PROGRAM FOR PHYSICS STUDENT

- PY 516 Physical Optics
- PY 552 Introduction to Structure of Solids I
- PY 753 Introduction to Structure of Solids II
- PY 781 Quantum Mechanics I
- PY 782 Quantum Mechanics II
- PY 783 Advanced Classical Mechanics
- PY 785 Advanced Electricity and Magnetism I
- PY 786 Advanced Electricity and Magnetism II
- MAT 700 Modern Concepts in Material Science
- MAE 545 Metrology for Precision Manufacturing
- PY 695 Master's Thesis Research

SHORT COURSES AND TV COURSES

Six graduate level courses: Scanning Electron Microscopy (MAT 712), Advanced SEM Surface Analysis (MAT 722), Modern Concepts in Material Science (MAT 700), Mechanical Properties of Materials (MAT 705), and Metrology (MAE 545) have been offered as video courses nationwide via National Technological University. In a typical year, approximately 120 students from industry and national laboratories participate in these courses. Future plans call for a MS program in Precision Engineering to be offered via the television network.

TECHNICAL REPORTS

Volume 1 - 1983	December 1983	136 pages
Volume 2 - 1984	January 1985	168 pages
Volume 3 - 1985	January 1986	294 pages
Volume 4 - 1986	January 1987	255 pages
Volume 5 - 1987	December 1987	336 pages
Volume 6 - 1988	December 1988	362 pages
Volume 7 - 1989	March 1990	357 pages
Volume 8 - 1990	March 1991	385 pages
Volume 9 - 1991	March 1992	382 pages
Volume 10 - 1992	March 1993	289 pages
Volume 11 - 1993	March 1994	316 pages
Volume 12 - 1994	March 1995	268 pages
Volume 13 - 1995	January 1996	251 pages
Volume 14 - 1996	January 1997	232 pages
Volume 15 - 1997	January 1998	298 pages

Volume 16 – 1998	January 1999	258 pages
Volume 17 – 1999	January 2000	232 pages
Volume 18 – 2000	January 2001	274 pages
Volume 19 – 2001	January 2002	201 pages
Volume 20 – 2002	January 2003	328 pages

PUBLICATIONS

PAPERS PUBLISHED

1. Buckner, G.D., "Intelligent Bounding of Modeling Uncertainties: Applications to Robust Control", *IEEE Transactions on Systems, Man, and Cybernetics – Part C: Applications and Reviews, Special Issue on Fusion of Soft Computing and Hard Computing in Industrial Applications,* vol. 32, no. 2, pp. 113-124, May 2002.

2. Dow, T.A., N. Negishi, and A. Sohn, "Elliptical Vibration Assisted Diamond Turning", *Proceedings from ASPE 2002 Annual Meeting,* pp. 115-119.

3. Garrard, K., A. Sohn, R.G. Ohl, R. Mink, and V.J. Chambers. "Off-Axis Biconic Mirror Fabrication." *Proceedings from the European Society for Precision Engineering and Nanotechnology 2002 Annual Meeting*, 2002.

4. Garrell, M, .A. J. Shih, E. Lara-Curzio and R. O. Scattergood, "FEM Analysis of Stress Concentration in ASTM D 639 Tension Specimens", *J. of Testing and Evaluation*, Paper ID JTE11402_311, available at www.astm.org.

5. Gibson, N. and G.D. Buckner, "Real-Time Adaptive Control of Active Magnetic Bearings using Linear Parameter Varying Models", *Proceedings of IEEE Southeast Con 2002*, vol. 1, no. 1, pp. 268-272, 2002.

6. Gill, D.D., T.A. Dow and A. Sohn, "Substrate Co-Molding of Micro and Meso Optics", *Proceedings from ASPE 2002 Annual Meeting,* pp. 618-621.

7. Hood, D., S. Clayton, G.D. Buckner, T.A. Dow, and K. Garrard, "Closed Loop Control of Milling Tool Deflection", *Proceedings of the American Society of Precision Engineering 17th Annual Meeting*, October 2002.

8. Hood, D., S. Clayton, G.D. Buckner, T.A. Dow, and K.P. Garrard, "Closed Loop Control of Milling Tool Deflection", *Proceedings from ASPE 2002 Annual Meeting,* pp. 622-625.

9. Jayanth, V., H. Choi, and G.D. Buckner, "Identification and Control of Flexible Structures Supported on Active Magnetic Bearings", Proceedings of IEEE Southeast Con 2002, vol. 1, no. 1, pp. 273-278, 2002.

10. Kim, C. and P.I. Ro, "An Accurate Full Car Ride Model using Model Reduction Technique, *ASME Journal of Mechanical Design*, pp. 697-705.

11. Lawrence, B.M., G.D. Buckner, and G.A. Mirka, "Nonlinear System Identification Applied to the Biomechanical Response of the Human Trunk during Sudden Loading", *Proceedings*

of the Human Factors and Ergonomics Society's 46th Annual Meeting, Baltimore, MD, Sept 30-Oct 4, 2002.

12. Ohl, R.G., W. Preuss, A. Sohn, S. Conkey, K. Garrard, J.G. Hagopian, J.M. Howard, J.E. Hylan, S.M. Irish, J.E. Mentzell, M. Schroeder, L.M. Sparr, R.S. Winsor, S.W. Zewari, M.A. Greenhouse, and J.W. MacKenty. "Design and Fabrication of Diamond Machined, Aspheric Mirrors for Ground-Based, Near-IR Astronomy." *Proceedings of the SPIE,* **4841**, 2002.

13. Saadat, S., F.G. Yuan, M.N. Noori, and G.D. Buckner, "Estimation of Wind Load on Structures", *Proceedings of the 15th ASCE Engineering Mechanics Conference*, June 2002.

14. Sohn, A., K.P. Garrard, R.G. Ohl, R. Mink, and V.J. Chambers, "Figure Metrology of a Free-Form Optical Surface", *Proceedings from ASPE 2002 Annual Meeting*, pp. 73-76.

15. Zhang, X., H. Wang, R.O. Scattergood, J. Narayan, and C.C. Koch, "Modulated Oscillatory Hardening and Dynamic Recrystallization in Cryomilled Nanocrystalline Zinc." *Acta Materiala*, (50), 3995.

16. Zhang, X., H. Wang, R. O. Scattergood, J. Narayan and C. C. Koch, "Mechanical Properties of Cryomilled Nanocrystalline Zinc Studied by the Miniaturized Disk Bend Test", *Acta Materialia,* (50), 3527.

17. Zhang, X., H. Wang, R. O. Scattergood, J. Narayan, C. C. Koch, A. V. Sergueeva and A. K. Mukherjee, "Studies of Deformation Mechanisms is Ultra-fine-grained and Nanocrystalline Zinc", *Acta Materialia,* (50), 4823.

REPORTS PUBLISHED

1. Clayton, S.H., D.W. Hood, G. Buckner, T.A. Dow, and K. Garrard, "Closed Loop Control of Milling Tool Deflection", 2002 Precision Engineering Center Interim Report, pp. 29-35, August 2002.

2. Garrard, K. and A. Sohn, "Figure Metrology of a Free-Form Optical Surface", 2002 Precision Engineering Center Interim Report, pp. 1-5, August 2002.

3. Gill, D.D., T.A. Dow, and A. Sohn, "Co-Molding of Micro and Meso Optics", 2002 Precision Engineering Center Interim Report, pp. 43-47, August 2002.

4. Kametz, D. and T.A. Dow, "Lapping Plate Charging", 2002 Precision Engineering Center Interim Report, pp. 7-13, August 2002.

5. Morrissey, P. and J.W. Eischen, "Distortion of Thin Cylinders", 2002 Precision Engineering Center Interim Report, pp. 15-20, August 2002.

6. Morrissey, P. and J.W. Eischen, "Characterization of Mechanical Indent Effects on Polystrene Hemispheres", 2002 Precision Engineering Center Interim Report, pp. 57-63, August 2002.

7. Negishi, N., T.A. Dow, and A. Sohn, "Elliptical Vibration Assisted Diamond Turning", 2002 Precision Engineering Center Interim Report, pp. 49-55, August 2002.

8. Panusittikorn, W. and P.I. Ro, "Sliding Mode Control for a Magnetostrictive Tool Servo System", 2002 Precision Engineering Center Interim Report, pp. 37-42, August 2002.

9. Wu, T. and P.I. Ro, "Enhancement of Heat Transfer by the Vibration of Piezoelectric Structures", 2002 Precision Engineering Center Interim Report, pp. 21-28, August 2002.

PAPERS SUBMITTED OR ACCEPTED FOR PUBLICATION AND PRESENTATIONS

1. Caprio, M.T., G.D. Buckner, and W.F. Weldon, "Switched Rotor Ballast Networks for Active Control of Wound-Rotor Induction Motors", in review, *IEEE Transactions on Industrial Electronics*.

2. Craft, M.J. and G.D. Buckner, "Fuzzy Logic Control Algorithms for Magneshock Semi-Active Vehicle Shock Absorbers: Design and Experimental Evaluations", accepted, *SPIE's 10th Annual International Symposium on Smart Structures and Materials*, March 2003.

3. Dixit, R.K. and G.D. Buckner, "Sliding Mode Control and Observation for Semiactive Vehicle Suspensions", in review, *Vehicle System Dynamics*.

4. Panusittikorn, W., M.C. Lee and P.I. Ro, "Modeling and Sliding Mode Control of Friction-based Object Transport using Two-mode Ultrasonic Excitation", submitted, *IEEE Trans. on Industrial Electronics*.

5. Panusittikorn, W. and P.I. Ro, "Modeling and Control of a Magnetostrictive Tool Servo System", submitted, *ASME Journal of Dynamic Systems, Measurement and Control*.

6. Saadat, S.A., G.D. Buckner, T. Furukawa, and M.N. Noori, "An Intelligent Parameter Varying (IPV) Approach for Non-Linear System Identification of Base Excited Structures", accepted, *International Journal of Non-Linear Mechanics*.

7. Saadat, S.A., G.D. Buckner, T. Furukawa, and M.N. Noori, "An Intelligent Parameter Varying (IPV) Approach for Non-Linear System Identification of Base Excited Structures", accepted, *SPIE's 10th Annual International Symposium on Smart Structures and Materials, March 2003*.

8. Stevens, J.M. and G.D. Buckner, "Intelligent Control of a Micro-Manipulator Actuated with Shape Memory Alloy Tendons", accepted, *SPIE's 10th Annual International Symposium on Smart Structures and Materials*, March 2003.

9. Stevens, J.M. and G.D. Buckner, "Actuation and Control Strategies for Miniature Robotic Surgical Systems, in review, *ASME Journal of Biomedical Engineering*.

10. Wu, T., P.I. Ro, A.I. Kingon and J.F. Mulling, "Piezoelectric Resonating Structure for Microelectronics Cooling", accepted, *Smart Materials and Structures*.

PENDING PATENTS

1. Sohn, A., K.P. Garrard, and T.A. Dow, "Polar Coordinate-Based Profilometer and Methods", November 2002.

THESES AND DISSERTATIONS

1. Gill, David, *Precision Replication of Co-Molded Meso and Micro Optics through Injection Molding*, Ph.D. Dissertation, North Carolina State University, August 2002.

2. Kametz, David, *Precision Fabrication and Development of Charging and Testing Methods of Fixed Abrasive Lapping Plates*, MS Thesis, North Carolina State University, August 2002.